BEND AND ORIFICE PLATE INTERACTIONS AND THEIR INFLUENCE ON THE PRESSURE LOSSES IN INTERNAL FLOW SYSTEMS

By

HÜSEYİN ŞALVARLI

Thesis Presented For the Degree of

Doctor of Philosophy.

Department of Mechanical Engineering,
Brunel University,
Uxbridge,
Middlesex UB8 3PH,
England.

July 1980.

TO MY PARENTS

HASAN ŞALVARLI and

EMİNE ŞALVARLI

ACKNOWLEDGMENTS

In various ways many people have assisted with the research which has led to the production of this thesis, and I am indebted to them all.

However, I would particularly like to express my sincere gratitude to my supervisor, Professor A.W. Crook, and to Dr. A.J. Ward-Smith for their continued help, guidance and encouragement during this work.

My thanks are also due to Mrs. R. Clarke and Mrs. D. Woodrow for the typing of the manuscript, and finally to the Turkish Ministry of Education for its financial support.

CONTENTS

SUMMARY

Experimental work has been carried out with a hydraulic flow test rig in which flows of water up to 65 kgs^{-1} can be measured with a weigh-tank and its diverter valve to an accurary of ± 0.2%.

The nature of the experimental work has been to investigate the system pressure losses due to the components in line

(i) For interference free flow;

(ii) For interactions.

The components used are 90 degree circular bends and orifice plates. Bends of radius ratios from R/D = 1.49 to 4.89 and nominally standard single-hole and multi-hole orifice plates of area ratios from m = 0.170 to 0.508 have been tested. To investigate the interaction effects arising from an orifice plate in proximity to bends, various bend-orifice plate (in a few instances orifice plate-bend) combinations have been arranged.

The bore diameter of duct (or pipe) and bend is approximately D = 145.05 mm and tests have been performed for Reynolds numbers ranging from $Re_D = 0.7 \times 10^5$ to 6×10^5.

In those instances in which results from the experimental work can be compared directly with published results, agreement is good. However, many of the experimental results, particularly the measurements of interactions between bends and orifice plates, are new.

List of Principal Symbols continued

θ	bend angle (degree)
ν	kinematic viscosity (stokes)
ρ	density of fluid (kg/m^3)
ψ	pressure drop parameter

Meaning of other symbols is given where they appear in the text.

CHAPTER I

GENERAL INTRODUCTION

1.0 INTRODUCTION

Pressure losses (or head losses) in duct systems and components have been much investigated, and extensive data drawn from the experiments are available [e.g. Miller (1971), Ward-Smith (1980)]. Differences do exist between the data, and have been explained in terms of experimental error and in a lack of understanding of the more detailed physical effects which contribute to the pressure drop. Theoretical studies can, and have improved the understanding of internal flows, and consequently have contributed to the better interpretation of experimental data [e.g. Patankar and Spalding (1967), Ward-Smith (1971), Cebeci and Smith (1974)].

Unfortunately, the basic equation of fluid mechanics, i.e. Navier-Stokes equation, which embraces three-dimensional compressible and incompressible flows, including laminar and turbulent conditions, can only be solved in a small number of particular instances, and in general the solutions are approximate and rely upon an input from experimental observations [e.g. Schlichting (1979)].

In this thesis the procedure for calculating system pressure losses is based on the one-dimensional equations for the steady turbulent flow of an incompressible fluid by the use of loss coefficients found by experiment. From a design point of view this approach is adequate when the relevant loss coefficients are available. However, in many instances the upstream and downstream conditions which prevail in the experimental determination of the pressure loss coefficient do not prevail in the system through which

the flow is to be predicted. There are two principal causes of error:

(i) Pressure losses arising from practical causes such as joints, variations from nominal dimensions, dents, aging, etc.,

(ii) Interaction or interference effects.

In systems which contain long lengths of straight ducts of constant cross section the system pressure loss is dominated by the pressure losses in the straight ducts and any uncertainty in the loss coefficients associated with components such as bends and valves is of little consequence in the overall pressure loss. That is not so in systems in which the components are closely spaced and in which very complex flow phenomena will occur. The presence of adverse pressure gradients is one of the main causes for energy dissipation over and above the normal pressure loss due to friction. The combined losses of the interacting components may be either greater or smaller than the sum of the individual losses in interference free flow. In such systems an improved knowledge of the interference effects of interacting components becomes important.

Although the problem of interference is not a new topic it has not been studied comprehensively, and there are gaps in the published data. Fortunately, excellent data are available on certain component interactions such as those of bend into bend, bend into diffuser, diffuser into bend [e.g. Ito (1959), Miller (1971)]. The present work is principally concerned with the interactions between bends and orifice plates. The combined head loss coefficients, interaction coefficients, and the variations in the orifice plate discharge coefficients have been found for various

combinations of 90 degree bend, orifice plate and straight duct spacer lengths. Circular cross-sectional bends of various radius ratios and both single-hole and multi-hole orifice plates of various area ratios have been used. The experimental apparatus, test procedures and results are presented in Chapters II and III respectively. However, before the interference effects can be identified it is necessary to determine the performance of each component in interference free flow. This will be discussed in the following paragraphs.

1.1 FLUID FLOW AND PRESSURE LOSSES IN DUCT SYSTEMS

In a system the pressure (or head) losses arise primarily from frictional resistance and changes in direction or cross-sectional area of the ducting. The contributions to the overall loss due to changes in direction or area will be larger if flow separation occurs, for instance, at sharp bends and at orifice plates. Additionally, a small percentage of energy is also lost in turbulent flow by the formation and decay of turbulent eddies [Bradshaw (1971)]. Many systems consist of a series of components which are closely spaced. When the downstream velocity profile from one component affects the pressure drop of the next it is necessary to take the interaction effects into account.

1.1.1 Flow in a Duct

1.1.1.1 The One-Dimensional Equations for the Steady Flow of an Incompressible Ideal Fluid

An ideal fluid is assumed to be inviscid. With the further assumption of incompressibility the rate of change of the potential and kinetic energies of the fluid is equal to the rate at which the pressure does work on the fluid at any arbitrary points on the streamline, and this is expressed in Bernoulli's equation as

$$z_1 + \frac{p_1}{\gamma} + \frac{V_1^2}{2g} = z_2 + \frac{p_2}{\gamma} + \frac{V_2^2}{2g} = \text{constant} \qquad (1)$$

or

$$\rho g z_1 + p_1 + \rho\frac{V_1^2}{2} = \rho g z_2 + \frac{p_2}{\gamma} + \rho\frac{V_2^2}{2} = \text{constant} \qquad (2)$$

or

substituting ($\rho gz + p$) with the piezometric pressure, p^*, Eq. (2) becomes

$$p_1^* + \rho\frac{V_1^2}{2} = p_2^* + \rho\frac{V_2^2}{2} = \text{constant} \qquad (3)$$

where z = elevation above a datum

$\frac{p}{\gamma}$ = static pressure head, h

$\frac{V^2}{2g}$ = velocity head

p = static pressure

$\rho\frac{V^2}{2}$ = dynamic head

γ = specific weight of fluid, ρg

ρ = density of fluid

g = acceleration due to gravity.

In addition, incompressibility by itself gives the continuity of volume flow which is expressed by

$$Q = A_1 V_1 = A_2 V_2 = \text{constant} \qquad (4)$$

where Q = volumetric flow rate

A = cross section of duct

V = velocity of fluid.

1.1.1.2 The Equations for the Steady Flow of an Incompressible Real Fluid

To account for the effect of the non-uniform velocity profile and surface friction, Bernoulli's equation has the modified form

$$z_1 + \frac{p_1}{\gamma} + \alpha_1 \frac{V_1^2}{2g} = z_2 + \frac{p_2}{\gamma} + \alpha_2 \frac{V_2^2}{2g} + h_{L_{1-2}} \tag{5}$$

or

$$\rho g z_1 + p_1 + \alpha_1 \rho \frac{V_1^2}{2} = \rho g z_2 + p_2 + \alpha_2 \rho \frac{V_2^2}{2} + p_{L_{1-2}} \tag{6}$$

or

$$p_1^* + \alpha_1 \rho \frac{V_1^2}{2} = p_2^* + \alpha_2 \rho \frac{V_2^2}{2} + p_{L_{1-2}} \tag{7}$$

where z = elevation above a datum

$\frac{p}{\gamma}$ = mean static pressure head, h

α = kinetic energy correction factor

$\frac{V^2}{2g}$ = mean velocity head

$h_{L_{1-2}}$ = head loss due to frictional effects between stations 1 and 2

γ = mean specific weight of fluid, ρg

ρ = mean density of fluid

g = acceleration due to gravity

p = mean static pressure

$\rho\frac{V^2}{2}$ = mean dynamic head

$p_{L_{1-2}}$ = pressure loss due to frictional effects between stations 1 and 2

p^* = mean piezometric head.

In most duct problems stations 1 and 2 may be suitably selected so that α may be omitted [Ward-Smith (1980)]. Thus, for a uniform distribution of velocity, i.e. $\alpha_1 = \alpha_2 = 1$, the energy equation, Eq. (5), becomes

$$z_1 + \frac{p_1}{\gamma} + \frac{V_1^2}{2g} = z_2 + \frac{p_2}{\gamma} + \frac{V_2^2}{2g} + h_{L_{1-2}} \tag{8}$$

where z = elevation above a datum

$\frac{p}{\gamma}$ = mean static pressure head, h

$\frac{V^2}{2g}$ = mean velocity head

$h_{L_{1-2}}$ = head loss due to frictional effects between stations 1 and 2

The equation of continuity is

$$Q = A_1 V_1 = A_2 V_2 \tag{9}$$

where Q = mean volumetric flow rate

A = cross section of duct

V = mean velocity of fluid.

In ducts of constant cross section of sufficient length, conditions become established at some distance downstream of the entry to the duct such that the velocity profile takes a form which does not change, and then the flow is said to be fully developed. About that there is a general agreement but there are differences

in the values of the entry length given in the literature necessary for fully developed flow to obtain [e.g. Barbin and Jones (1963), Miller (1971), Ward-Smith (1980)].

Pressure drop due to frictional effects, p_L or h_L, may be expressed in terms of the kinetic energy based on mean fluid velocity, length as expressed in equivalent diameter of duct and in terms of a friction factor which is determined experimentally. That is:

$$h_L = f \frac{L}{D} \frac{V^2}{2g} \tag{10}$$

where f = friction factor

L = length of duct

D = equivalent diameter of duct, 4A/P

$\frac{V^2}{2g}$ = mean velocity head.

1.1.1.3 Friction Factor

The friction factor expressed in Eq. (10) is known as the "Darcy equation", whereas the friction factor given by Fanning is in the form of

$$h_L = 4f \frac{L}{D} \frac{V^2}{2g} \tag{11}$$

In the remainder of this work the Darcy form of the equation will be used.

It has been found experimentally that the decrease in the roughness of the duct wall below a certain value which depends upon Reynolds number, Re = $\frac{VxD}{\nu}$, produces no decrease in frictional loss.

With such roughness the duct is said to be hydraulically smooth and in those circumstances the experimentally determined friction factors are described by the Kármán-Prandtl expression

$$\frac{1}{\sqrt{f}} = 2 \log_{10} (Re \sqrt{f}) - 0.8 \qquad (12)$$

which is valid for $3 \times 10^3 < Re < 3 \times 10^6$.

If the duct is not hydraulically smooth, e.g. commercial ducts, the experimentally determined friction factors are described by the Colebrook-White expression

$$\frac{1}{\sqrt{f}} = -2 \log_{10} \left[\frac{2.51}{Re\sqrt{f}} + \frac{k}{3.7D} \right] \qquad (13)$$

where k = mean roughness height

D = equivalent diameter of duct

Re = Reynolds number based on equivalent diameter of duct.

It should be noted that the Colebrook-White expression essentially reduces to the Kármán-Prandtl expression for k = 0.

If the Reynolds number is less than about 2300 the fluid flow is laminar, and is dominated by viscous shear rather than inertial effects. It follows from the Hagen-Poiseuille equation for the pressure drop in a long circular duct with laminar viscous flow that when the pressure drop is expressed in velocity heads, the friction factor is given by

$$f = \frac{64}{Re} \qquad (14)$$

1.1.1.4 Definition of Friction Loss Coefficient in a Straight Duct

Head loss coefficient of a straight duct is defined by

$$K_f = f\frac{L}{D} \tag{15}$$

and total head loss, h_t, in the system is then given by

$$h_t = \sum K_f \frac{V^2}{2g} \tag{16}$$

or

$$h_t = \sum f \frac{L}{D} \frac{V^2}{2g} \tag{17}$$

where K_f = friction loss coefficient

$\frac{V^2}{2g}$ = mean velocity head

L = length of duct

D = equivalent diameter of duct

f = friction factor

1.1.1.5 Definition of Component Head Loss Coefficient

With reference to Figure 1 in the straight ducts, both upstream and downstream of the component, uniform rates of head loss with position exist. This is expressed in the same figure as the upstream and downstream tangents, and the component head loss is defined by the difference between the head losses measured from far upstream to far downstream within the tangents. Then, the component head loss coefficient, K_c, is given by:

$$K_c = \frac{h_L}{V^2/2g} \tag{18}$$

With this definition all the head losses of the component, including the head losses arising from the re-development of velocity profile after the component, are included in the component head loss coefficient. However, if the cross-sectional areas at stations 1 and 2 of the upstream and downstream tangents differ, the mean velocity head, $V^2/2g$, may be defined at either point, and K_c may be based upon the upstream conditions so that

$$K_c = \frac{h_L}{V_1^2/2g} \tag{19}$$

or may be based upon the downstream conditions, when it will assume a different numerical value, and the definition then becomes

$$K_c = \frac{h_L}{V_2^2/2g} \tag{20}$$

In such circumstances the velocity upon which K_c is based must be stated clearly.

1.1.1.6 Definition of System Head Loss Coefficient

The system head loss coefficient, K_s, is defined as the ratio of the head loss divided by a mean velocity head, i.e. $K_s = \frac{h}{V^2/2g}$, as illustrated in Figure 2. When the distribution of head loss in a component is unknown the component is shown as having zero length.

1.1.2. Flow in Bends

An extensive literature is available on the flow through bends,

and the necessary references can be found in many textbooks. For example, Zanker and Brock (1967) have presented the most readily available references together.

Flow through bends is obviously more complicated than the flow in straight ducts, and more variables such as the radius ratio ($R/_D$) and deflection angle (θ) of the bend are involved. For design purposes reliance must be placed upon the results of experimental measurements even if these results differ in some ways [Gray (1945)]. However, some theoretical discussions of the flow through bends have been published, and various dimensionless variables have been proposed, e.g. $Re\ (D/_{2R})^{\frac{1}{2}}$, $Re(D/_{2R})^2$ and $\theta(2R/_D)^{\frac{1}{2}}$. A theory for the pressure losses in the curved ducts under conditions of laminar flow was first presented by Dean (1927). The theory relates to the steady flow of incompressible fluid through a curved duct of circular cross section together with the assumption that a laminar flow is established at entry to the bend. Dean concluded that pressure losses may be expressed in terms of the parameter, $Re(D/_{2R})^{\frac{1}{2}}$, and the relevance of this parameter was confirmed by the experiments of some investigators [e.g. Eustice (1911), White (1929)]. Ito (1956) has also investigated the similar variables on the pressure losses for turbulent flow in smooth duct bends of circular cross section theoretically and experimentally, and expressed his results (bend head loss coefficients) as a function of two dimensionless numbers, $Re(D/_{2R})^2$ and $\theta(2R/_D)^{\frac{1}{2}}$. The analysis in terms of these dimensionless variables belongs to $R/D \geq 5.0$, $\theta\sqrt{2R/_D} \geq 4.7$ and to $Re \leq 2 \times 10^5$. The Reynolds numbers, Re, of the present work start within Ito's range, but extend beyond 2×10^5. However, the radius ratios, $R/_D$, of

the bends used in the present work are less than 5.0; consequently complete correspondence with Ito's work is not to be expected. However, there are other published data which are relevant, and the experimental results from the present work, which are described in Paragraph 2.3.3, are compared with some published data in Chapter III (see Para. 3.5.1).

In the following paragraphs some general background data for the interpretation of the results is given.

1.1.2.1 Definition of Bend Geometry

The geometrical parameters of a circular bend of constant cross section are, in general, defined from the basic dimensions as illustrated in Figure 3

in which R = radius of curvature of bend

D = internal diameter of bend

$\frac{R}{D}$ = radius ratio

θ = bend angle.

1.1.2.2 Definition of Bend Head Loss Coefficient

To obtain a bend head loss coefficient, the head loss coefficients measured from far upstream to far downstream are plotted against the axial length of the duct expressed in diameters as described in Paragraph 2.3.3. A typical example taken from present work is shown in Figure 4. For the purposes of the present work

it was not necessary to measure the pressure distribution around the bend itself, but this was done by Ito (1960) and a typical pressure distribution around the bend is shown in Figure 5 With reference to both Figures 4 and 5 it is clear that a considerable amount of energy is lost in the downstream tangent. As also reported by Miller (1971), up to 50 per cent of the bend pressure loss may, in fact, occur in the downstream tangent. Under these circumstances, it is particularly necessary to define a meaningful bend head loss coefficient.

In general, three different bend head loss coefficients may be defined as illustrated in Figure 6, where the curves of $A-B-B^1-C^1-D^1$ and $A-B-C-D$ represent the actual hydraulic gradient and the hydraulic gradient in a corresponding straight duct respectively

(i) Bend head loss coefficient based upon the head loss over the bend itself, which is denoted by K_e

$$K_e = \frac{h_e}{V^2/2g} \qquad (21)$$

(ii) Bend head loss coefficient based upon the head loss at some approximate point in the downstream tangent, which is denoted by K_d

$$K_d = \frac{h_d}{V^2/2g} \qquad (22)$$

(iii) Bend head loss coefficient based upon the head loss at some point in the downstream tangent far from the bend, e.g.

$L/_D > 50$, which is denoted by K_b

$$K_b = \frac{h}{V^2/2g} \tag{23}$$

It should be noted that Fig. 6 relates to an ideal system in which all internal diameters are the same, and there are no imperfections at the connecting flanges. In actual systems where differences in diameter may occur, and which will have imperfections at the joints, the pressure losses due to these imperfections may be considerable [Eastwood and Sarginson (1960)].

1.1.2.3 Flow Through a Bend

The principal causes of the pressure losses particular to bend will now be discussed.

With reference to Fig. 7, which relates to flow of an ideal incompressible fluid of uniform velocity approaching a bend, the total head at the entry to the bend is $(P/_\gamma + V^2/2g)$. As the flow passes into the bend there exists a pressure gradient across the bend to balance the centrifugal force on the fluid due to its curved streamline since the total head $(P/_\gamma + V^2/2g)$ remains constant along any streamline. At the outside of the bend a change of head takes place, and the velocity head, $V^2/2g$, is converted to pressure head, $P/_\gamma$. Then, the velocity increases on the inside of the bend as the pressure head is converted to velocity head. At the bend exit plane the flow process is reversed on both sides.

For flow of an incompressible real fluid through a bend the flow process will be different from that of a flow of an incompressible

ideal fluid. The factors such as bend geometry will also affect the flow in a bend. For example, the effects of the smaller bend radius ratios, e.g. $R/_D$ = 1.0, on the separation and pressure loss have been already reported by Miller (1971). It was also found by Weske and Providence (1948) that for the flow in curved circular ducts of constant cross section at very large Reynolds numbers, e.g. $Re_D = 5 \times 10^5$, the effect of viscosity might be disregarded except in a very thin layer adjacent to the wall, and the net pressure drop would be a function of radius ratio , $R/_D$,and Reynolds number, Re_D In the straight duct before the bend, for turbulent flow of a real fluid, due to viscosity the velocity varies from zero at the wall to a velocity of approximately 1.2 times the mean in the central core. As the flow passes into the bend the faster moving fluid in the central core is acted on by a larger centrifugal force than the slower moving fluid near the duct walls. Then, across the bend a smaller pressure gradient is required to balance the smaller centrifugal force on the fluid. Consequently, a secondary flow occurs in which the fluid in the central core moves outwards and the slower moving fluid inwards towards the centre of curvature as illustrated in Fig. 8. The secondary flows move at a considerable angle to the mean flow direction. Since the mean axial velocity of fluid must remain unchanged the mean actual velocity will be greater due to the superposition of the secondary flow [Eastwood and Sarginson (1960), Ward-Smith (1980)]. Thus, there will be an increase in the velocity head and a corresponding drop in the pressure head. After the fluid leaves the bend exit plane much of this velocity head may not be converted back into pressure head, and will be dissipated in boundary friction and

turbulence losses in the immediate downstream tangent of the bend exit plane.

It is also evident in Fig. 5 that variations in static pressure at a cross section start before the bend entry plane. While the fluid flows through the bend, at some stage before the bend exit plane, the static pressure reaches a maximum and a minimum on the outer and inner walls respectively. Then, at the bend exit plane a favourable pressure gradient is established on the outer wall while an adverse pressure gradient develops on the inner wall. Some appreciable variations in static pressure at a section persist approximately up to 2 duct diameters [Ito (1960), Ward-Smith (1963, 1968, 1971), Miller (1971)]. As will be seen, the severity of the adverse pressure gradient on the inner wall is the main factor for the pressure loss through sharp bends. A separation of flow occurs when the radius ratio of 90 degree bend is less than 1.5, and bend head loss becomes independent of Reynolds number below 10^6 [Miller (1971)].

1.1.2.4 Factors Affecting a Bend Performance

As previously mentioned, extensive data are available on pressure losses due to bends. The effects of $R/_D$, θ, Re_D and the cross-sectional shapes on the magnitude of the bend head loss coefficient have been reported by many investigators [e.g. Ito (1956), Ward-Smith (1980)].

1.1.2.4.1 Upstream Tangent Conditions

In a system in which a long upstream tangent exists fully developed flow is established, and the velocity profile in a smooth duct is dependent only upon the Reynolds number. When the length of the upstream tangent is reduced, e.g. $L/_D < 15$, the velocity profile will be changed, thus the change in pressure distribution will affect the basic frictional characteristics of the bend. However, the experimental data indicate that the effect of the upstream tangent conditions has a smaller effect on the pressure loss due to bend than the downstream tangent conditions [Ito (1960)].

1.1.2.4.2 Downstream Tangent Conditions

Assuming a fully developed flow exists in the upstream tangent, three types of downstream tangents are suggested:

(i) Long tangents for which $L/_D$ is greater than about 50;

(ii) Medium tangents for which $L/_D$ is in the approximate range $5 < L/_D < 50$;

(iii) Short tangents for which $L/_D$ is smaller than about 5, i.e. $0 \leq L/_D < 5$.

With reference to Fig. 9, which has been given by Ward-Smith (1976), it is concluded that the large adverse pressure gradients will be associated with small values of $R/_D$ and $L/_D$, and bends having such properties would be expected to have high pressure losses. Meanwhile, in the same Fig. 9 the effect of the length of the downstream tangent on the bend head loss coefficient may be seen.

1.1.3 Flow Through Orifice Plates

The orifice plate is one of the pressure difference flow measurement devices, which is widely used in industry. There are many forms of orifice plates which differ in the detail of the profile of the hole, e.g. square-edged, conical-entrance and quarter -circle. These variations and the flow characteristics which go with them have been extensively investigated and the results are tabulated in Standards such as B.S. 1042 (1964, 1965) and A.S.M.E. (1961, 1971).

In addition to the varieties of orifice plates there are several alternatives in mounting, and in the measurement of the pressure difference. An orifice plate might be mounted directly between flanges or be set in a carrier ring which is then mounted between flanges. The pressure difference might be measured between corner tappings (tappings close to each side of the orifice plate), or between flange tappings (tappings one inch upstream and one inch downstream from the orifice plate), vena contracta tappings (tappings one duct diameter upstream and half a duct diameter downstream from the orifice plate), D and D/2 tappings (the same as vena contracta tappings), or duct tappings (tappings two and a half duct diameters upstream and eight duct diameters downstream from the orifice plate). Again the characteristics of the various combinations are given in appropriate Standard Codes. In the present work the nominally thin square-edged orifice plate has been used, mounted in a carrier ring with corner tappings (because existing material had to be used the present test carrier rings and orifice plates do not quite satisfy the standard dimensions given by B.S. 1042 (1964), but the experimental results indicate that these deviations are insignificant).

For standard calibrations, in contrast with in situ calibrations, it is necessary that there should be a straight duct upstream of the orifice plate of at least 50 duct diameters [see, for example, B.S. 1042 (1964) and Patel (1974)]. It was thought that multi-hole orifice plates might be less sensitive in this respect, and that their calibrations would be less affected by the proximity of a bend. For that reason the square-edged multi-hole orifice plates have been included in the tests.

1.1.3.1 Definition of Orifice Plate Geometry

A standard single-hole orifice plate with corner tappings is shown in Fig. 10, in which the orifice plate installation is either by a mounting between the duct flanges or by a carrier ring. For design purposes the necessary requirements, specifications and recommendations are extensively given in References [e.g. B.S.1042 (1964, 1965), Clark (1965)]. All primary characteristics of the test carrier ring and orifice plates are as shown in Figs. 11 to 16 and in Table 1 respectively.

With reference to Fig. 17 it may be seen that the main geometric parameters are expressed as the ratios of the total orifice area to the duct area, the hole diameter to the duct diameter, the hole edge (or plate in the figure) thickness to the hole diameter, and the pitch to the hole diameter. For a circular duct of constant cross section and a single-hole orifice plate or a multi-hole orifice plate with regularly spaced equal circular openings, these ratios become $m = \frac{A_o}{A} = N\frac{d^2}{D^2}$, $\beta = \frac{d}{D}$, $\frac{t}{d}$, $\frac{p}{d}$

where m = area ratio

β = diameter ratio

t/d = thickness/diameter ratio

p/d = pitch/diameter ratio

N = number of holes

D = internal diameter of duct

d = diameter of hole.

1.1.3.2 Fluid Flow Through An Orifice Plate

Typical incompressible fluid flow through an orifice (for turbulent conditions, e.g. $Re_D > 4 \times 10^3$) is illustrated in Fig.18 As the fluid approaches the orifice the fluid accelerates and an abrupt change takes place. The cross section of the stream passing through the orifice continues to decrease for a short distance downstream from the orifice and reaches a minimum which is called the "vena contracta". Between the orifice entry and the vena contracta, the stream shows a favourable pressure gradient; then it gradually diverges until it fills the duct in a region of turbulent mixing dominated by an adverse pressure gradient. When the flow of fluid reattaches to the duct wall an amount of fluid is returned to the separated region which also satisfies the continuity condition within the separated region.

It is to be noted that the discussion given above embodies a flow model of a free jet together with a separation flow region. A general analysis of flow regimes for various orifice geometries has been studied by Ward-Smith (1971), and extensive data have been

made available on flows through orifice plates.

1.1.3.3 Characteristics of Fluid Flow Through an Orifice Plate

When an area change occurs by means of an orifice plate in line, the area of the "vena contracta" becomes an important factor for the flow characteristics. A contraction coefficient, C_c, is defined as the ratio of the "vena contracta" area to the orifice area. By extensive experimental measurements, it has been found that C_c depends primarily upon m (or β), orifice geometry, and the properties of fluid flowing, and C_c decreases as m decreases, e.g. see Ward-Smith (1971) in which Ward-Smith has deduced the relationship between C_c and m for both the square-edged single-hole and multi-hole orifice plates.

Experimental measurements have also shown that the static pressure of the fluid flowing through an orifice increases to a maximum at the corner of the orifice and duct wall in the upstream tangent, whereas in the downstream tangent, the static pressure decreases to a minimum approximately in the plane of the "vena contracta" [Engel (1931), Engel and Davies (1938)]. The distance from the orifice is typically between $\frac{1}{2}$D and 1D [A.S.M.E. (1971)]. This distance is dependent upon m, and becomes less as m becomes larger. For an incompressible fluid the position of the vena contracta is not very dependent upon the rate of flow.

1.1.3.4 Classical Derivation of Orifice Plate Discharge Coefficient

In Fig. 18 the geometry and flow pattern are given. As described in Para. 1.1.1.1 , the basic one-dimensional equations for an incompressible flow are the equations of continuity and Bernoulli (or energy). For the development of the theoretical equations of flow the following conditions will be imposed:

(i) $z_1 = z_2$;

(ii) The fluid performs no external work when it flows from the point 1 to 2;

(iii) The flow is steady, axial, and inviscid;

(iv) The velocity profile is uniform (which implies the kinetic energy correction factor is unity, i.e. $\alpha_1 = \alpha_2 = 1$);

(v) There is no normal stream turbulence.

Then, the equations are expressed by

(i) The continuity equation

$$A_1 V_1 = A_2 V_2 \tag{24}$$

(ii) The energy equation

$$\frac{P_1}{\gamma} + \frac{V_1^2}{2g} = \frac{P_2}{\gamma} + \frac{V_2^2}{2g} \tag{25}$$

and it then follows that

$$V_2 = \sqrt{\frac{2(P_1 - P_2)}{\rho\left[1 - \left(\frac{A_2}{A_1}\right)^2\right]}} \tag{26}$$

or

$$V_2 = \sqrt{\frac{2gh}{1 - \left(\frac{A_2}{A_1}\right)^2}} \tag{27}$$

The theoretical equation for the mass flow rate or the volume rate of flow is given by

$$\dot{M}_{th} = \rho A_2 V_2 = \rho A_2 \sqrt{\frac{2gh}{1 - \left(\frac{A_2}{A_1}\right)^2}} \qquad (28)$$

$$\text{or} \quad Q_{th} = A_2 V_2 = A_2 \sqrt{\frac{2gh}{1 - \left(\frac{A_2}{A_1}\right)^2}} \qquad (29)$$

where $\dot{M}_{th}$ = theoretical mass rate of flow through orifice

Q_{th} = theoretical volume rate of flow through orifice

A = area

V = velocity of fluid

p = static pressure

h = static pressure head, p/γ

γ = specific weight of fluid, ρg

ρ = density of fluid

g = acceleration due to gravity.

In practice, the effects of real fluid flow exist and theoretical equation for $\dot{M}_{th}$ or Q_{th} must be modified to the actual flow conditions. To obtain the actual flow from the theoretical equation a "discharge coefficient" is introduced.

In its principal aspect the discharge coefficient, C_d, is simply an experimentally derived coefficient which reconciles the idealized flow model with the much more complicated actual circumstances. The complications of the real circumstances are reflected in the way in which C_d, as an empirical coefficient, varies with a number of parameters such as area ratio, Reynolds

number, Mach number, duct size, duct roughness, velocity profile, orifice geometry, orifice bore finish, orifice plate surface finish, tapping size and location. In the classical approach the definition of C_d is given by

$$C_d = \frac{\text{actual rate of flow } (Q_A)}{\text{theoretical rate of flow } (Q_{th})} \qquad (30)$$

With reference to Fig. 18, , for a flow of a real incompressible fluid, the discharge coefficient, C_d, is

$$C_d = \frac{Q_A}{A_o E\sqrt{2gh}} \qquad (31)$$

where Q_A = actual flow rate

A_o = total orifice area

E = velocity approach factor, $1/\sqrt{(1-m^2)}$

m = area ratio, A_o/A

A = duct area

g = acceleration due to gravity

h = differential head across the orifice plate.

1.1.3.5 Derivation of Orifice Plate Discharge Coefficient Using Dimensional Analysis

Ward-Smith (1980) and others have defined the discharge coefficient in a way which is an improvement upon the classical approach and is more closely in accord with current knowledge of fluid mechanics. For a given orifice plate in the system the discharge coefficient, C_d, can be written as

$$C_d = \frac{\dot{M}(1-m)^{\frac{1}{2}}}{A_2(2\rho\Delta p_{ud})^{\frac{1}{2}}} = \text{function}\left(m, \frac{\varepsilon}{D_1}, \frac{\rho V_1 D_1}{\mu}\right) \qquad (32)$$

where $\dot{M}$ = mass flow rate

m = area ratio, $\left(\frac{D_2}{D_1}\right)^2$

A_2 = orifice plate throat area, $\frac{\pi D_2^2}{4}$

ρ = density of fluid

Δp_{ud} = pressure difference across the orifice plate, $(p_u - p_d)$ where p_u and p_d are measured in the upstream and downstream ductings respectively

$\frac{\varepsilon}{D_1}$ = measure of the effect of the roughness of the duct wall

V_1 = mean flow velocity in the upstream duct

D_1 = internal diameter of the upstream duct

μ = dynamic viscosity.

From this analysis it has been found that the discharge coefficient, C_d, is, in general, a function of

(i) The geometry of the flow path;

(ii) The position of the pressure tappings;

(iii) The area ratio;

(iv) The detailed design of the internal face and upstream edge of the orifice;

(v) The flow Reynolds number;

(vi) The size of the duct (due to surface roughness effects);

(vii) The quality of the flow entering and leaving the orifice plate.

1.1.3.6 Factors Affecting Orifice Plate Discharge Coefficient

It is seen from the definition of C_d that C_d is based on experimental measurements. A complicated relationship exists between C_d and the variables such as area ratio, Reynolds number, orifice geometry, etc. Clark (1965) has also given extensive data on the overall accuracy of flow measurement, and has pointed out the importance of the variables such as duct roughness, operating conditions, etc., affecting C_d for the standardization of installations such as Class - A Standard and Class- B Standard. If the ducting is smooth and is maintained in this condition whilst in service the installation is said to be Class - A Standard with the overall tolerance, corresponding to 95% confidence, up to $\pm$ 1.8%. A Class - B Standard will apply to normal service conditions by covering more correction factors for the flow measurement, where the permissible overall tolerance corresponding to 95% confidence may be up to $\pm$ 4%. The installations where the overall tolerance exceeds $\pm$ 4% are unclassified.

It is also seen from the interpretations on C_d given above that there are many variables affecting C_d. Those variables and recommendations with respect to the effects of each of them have been extensively given in Standard Codes [e.g. B.S.1042 (1965)]. In the following paragraphs, some of the most important effects will be introduced for both square-edged single-hole and multi-hole orifice plates concerning an incompressible fluid flow through the orifice plate.

1.1.3.6.1 The Effect of Reynolds Number

It is known from the tests of Johansen (1929) on thin, square-edged orifice plates that the relationship between Re_d and C_d is as illustrated in Fig. 19. At very low values of Re_D, C_d inreases as Re_D increases. With a further increase in Re_D, e.g. $Re_D > 10^3$, C_d decreases as Re_D increases and at very high values of Re_D, C_d will reach an essentially constant limit somewhere between C_{do} = 0.58 and 0.60, although, Halmi (1973) has indicated that C_d does not become exactly constant even though Re_D increases up to a value of 10×10^6. (The Re_D sensitivity changes with duct size, area ratio, and type of tappings).

1.1.3.6.2 The Effect of Geometrical Parameters

The basic parameters such as the area ratio, m, and the thickness/diameter ratio, t/d, can be formed from the dimensions of the orifice plate as previously described in Para.1.1.3.1. In the case of the multi-hole orifice plate there are additional factors. Thus, the number of holes, N; the pattern of holes on the orifice plate; the pitch/diameter ratio, p/d; and free area of holes/ maximum free area possible ratio, A_f/A_t, are found to affect C_d as also indicated by Kolodzie and Van Winkle (1957). The effects of m and t/d for various flow regimes of orifice flow have been described by Ward-Smith (1971), and for a given m and Re_D, C_d will increase as t/d increases.

Meanwhile, as shown in Standard Codes [e.g. B.S. 1042: 1964], for a single-hole orifice plate with corner tappings C_d

increases as m increases, and at higher area ratios, e.g. m > 0.4, C_d becomes lower.

1.1.3.6.3 The Effect of Installation

A number of factors can affect C_d with respect to either the variations in the design of orifice plate and carrier ring or the characteristics of the duct line. The specifications and requirements of the standard orifice plate do indicate that C_d is very much affected by the design conditions. For example, even a slight rounding on the upstream edge of the orifice plate will create a larger vena contracta, then C_d will be correspondingly greater depending upon the degree of roundness of the upstream edge and the diameters of duct and orifice.

It is known that, for rapid and easy installation, easy change of orifice plates can be done by the use of carrier ring. Like an orifice plate a carrier ring must also be designed as recommended in the Standard Codes [e.g. B.S. 1042 (1964)]. The carrier ring must never be less in diameter than the internal diameter of the upstream duct but may be greater by up to 3% providing the recess is not wider than 0.1 D. If the carrier ring is smaller in diameter than the duct C_d will increase or decrease depending upon the other flow conditions.

The other practical factors affecting C_d are the duct lines and operating conditions. As might be expected these factors have been interpreted in different ways by various investigators, and some recommendations have been made, of which the most relevant

points are as follows:

(i) Upstream and downstream ducting before and after the orifice plate must be uniform and straight without any other obstructions such as valves, bends,etc., for certain specified distances;

(ii) If the internal surface of the duct upstream tangent is not adequately smooth it will effect C_d depending upon the values of the duct roughness and area ratio, m;

(iii) If a reduction in a straight duct upstream of the orifice plate is required it can be done by the use of smaller m values;

(iv) Asymmetric jointing of the orifice plate must be prevented.

1.1.3.7 Definition of Orifice Plate Head Loss Coefficient

With reference to Fig. 18 the orifice plate head loss is taken as the difference in the head losses between the two static pressure tappings, which are not in the immediate pressure field of the orifice plate, less the friction loss. The orifice head loss coefficient is then defined by

$$K_o = \frac{h}{V^2/2g} \tag{33}$$

where K_o = orifice plate head loss coefficient

h = head loss

$V^2/2g$ = mean velocity head.

In standard codes [e.g. B.S.1042 (1964)],the net pressure loss has been also expressed as a percentage of pressure difference across orifice plate, and as expected, the percentage net pressure loss decreases when area ratio, m, increases.

1.1.3.8 Factors Affecting Orifice Plate Head Loss Coefficient

To measure a meaningful loss coefficient, the static pressure tappings before and after the orifice plate must be located at some distances where the straight duct friction gradients are not substantially affected by the static pressure distribution due to the orifice plate in line. From examination of experimental results [Engineering Sciences Data (1972)], the recovery plane where the positive friction gradient is again established is shown to be approximately 6D downstream from a single-hole orifice plate, and for a multi-hole orifice plate this distance may have a value of $6d/\sqrt{m}$.

As indicated in Para. 1.1.3.3, the contraction coefficient, C_c, and area ratio, m, are very important factors which affect the characteristics of flow through an orifice. Assuming a one-dimensional incompressible flow and the equations of the Bernoulli and continuity applied to the "vena contracta", and writing the momentum balance between the vena contracta and the recovery plane, it has previously been shown [e.g. Ward-Smith (1971)] that the orifice plate headloss coefficient, K_o, is

$$K_o = \left[\frac{1 - C_c m}{C_c m}\right]^2 \qquad (34)$$

where C_c is a function of m and t/d. Zanker (1961) has also shown that for a more precise value of K_o the momentum balance equation could be written by the use of the improved flow equations, where the kinetic energy correction factors, α, and momentum factors, β, enter the basic flow equations. However, these variables tended to be self-compensating and effects on the orifice plate head loss coefficient, K_o, were small when compared to the Eq. (34).

Extensive data given by Ward-Smith (1968) have also been used to obtain an expression correlating K_o as a function of t/d and m. The expression for $t/d < 0.8$ is as follows:

$$K_o = \left[\frac{1}{0.608m\ (1-m^{2\cdot6})(1+(t/d)^{3\cdot5})+m^{3\cdot6}} - 1\right]^2 \qquad (35)$$

which correlates the experimental data in the ranges

$$0 < t/d < 0.6, \quad 0 < m < 0.75, \quad 0.57 < K_o < 35000$$

with a root-mean-square error of 9.5 per cent.

It may be seen from the relationship between K_o and C_c and m that the variations of K_o with Re_D will be small at high values of Re_D.

For a multi-hole orifice plate it is obvious that the additional geometrical factors will also affect K_o depending upon the number of holes, N, the pattern of holes on the plate, the pitch/diameter ratio, p/d, etc. Some experiments will be performed to observe the effects of these variables on K_o as described in Para.2.3.4.

1.1.4 Component Interactions

System pressure losses are usually estimated by summing the individual pressure losses of each component in a system. This approach may not be so reliable when the components are closely spaced to one another. Under these circumstances an interaction or interference will occur between the components, and the pressure losses of these interacting components will be either greater or smaller than the sum of the individual losses in interference free flow. Thus, the interaction effects may become important on the overall pressure losses in a system.

Various component interactions have been studied and reported in the literature. For example, Ward-Smith (1971) has particularly considered the effects of the length of the downstream tangent on the performance of a single bend. It has been shown that the static pressure differences extend about 1.5 to 2 duct diameters before and after the isolated bends, therefore, the minimum spacer length for which the static pressure distributions in two adjacent bends are independent is about 3 or 4 duct diameters. Below this value a primary interaction occurs depending upon the configuration of the two bends. Miller (1971) has extensively reported the effects of combinations of bend-bend, bend-diffuser, diffuser-bend, and found the interaction coefficients for various combinations and spacer lengths. On the other hand, extensive data and recommendations have also been tabulated in Standard Codes such as B.S.1042 (1964, 1965) and A.S.M.E. (1971).

The flow characteristics of both bends and orifice plates in isolation have been previously described in Paras.1.1.2 and 1.1.3.

The question now arises how the combined bends and orifice plates affect the overall pressure loss in system. In the present work, the effects of closely spaced bends and orifice plates will be covered, and typical measurements for various combinations will be presented in Para. 2.3.5.

1.1.4.1 Interaction Effects

A component with upstream and downstream tangents of constant cross section, sufficiently long for a fully developed flow to be attained, is free from interference effects. The characteristics of a fully developed flow are the velocity profile and turbulence parameters being independent of axial distance. The static pressure is constant at a cross section, except for the small order turbulence perturbations, and the axial static pressure gradient becomes constant. Thus, with fully developed flow conditions, the static pressure distribution of a component can be defined in interference free flow. In practice, the component head loss coefficients are obtained with long upstream and downstream tangents. When the components are closely spaced the basic component head loss coefficients no longer apply. Two main interaction effects can be considered:

(i) Primary effects associated with the interaction of the static pressure distributions of the components;

(ii) Secondary effects associated with the upstream velocity profile and turbulence distribution at entry to the second component.

More complex flow phenomena will occur for very short spacer lengths. The presence of adverse pressure gradients will affect the overall pressure loss depending upon the dominant parameters of the components in controlling interactions.

An interaction can be either favourable or unfavourable. If the pressure loss across a combination of components decreases as the spacer length also decreases, the interaction will be described as favourable; otherwise the interaction is unfavourable.

1.1.4.2 Interactions Between Two Components

It may be seen from the static pressure distributions of each component such as a bend and orifice plate that there will be a critical spacer length for two interacting components. Below the values of the critical spacer length the static pressure distributions will interfere, and primary interactions will arise. For the values above the critical spacer length only the secondary interactions will occur, where the effects of the upstream velocity profile and turbulence distribution on the second component are dominant in controlling interactions.

With the available data in the literature, the pressure losses of an interacting bend and orifice plate in combination are less easily predicted. However, it is obvious that if the spacer length increases the secondary interactions will also be gradually decreased. For further increase in the spacer length each component in the system will be expected to show their individual characteristics as in interference free flow.

It has been shown that the primary interactions are of much greater importance than the secondary interactions for specific component combinations such as bend-bend, bend-diffuser, and these effects have been extensively discussed in References [e.g. Ito (1959), Miller (1971), Ward-Smith (1971)]. In the present work, the bend-orifice plate combinations will be particularly studied.

1.1.4.2.1 Combination of a Bend and Orifice Plate

Consider a system in which a bend of constant cross section is followed by an orifice plate, and an incompressible fluid flows through the combination. For an insufficient spacer length an interaction will occur between the bend and orifice plate. Thus, the calculation of the total pressure loss will differ from that for interference free conditions. As discussed in Para. 1.1.2.3, when the fluid leaves the bend, the non-uniform flow conditions exist and a fully developed flow can be established in the down-stream tangent only some 40 duct diameters or more after the bend. However, if a bend is closely spaced with an orifice plate the flow characteristics will vary depending upon the parameters of the combination. The important parameters affecting bend-orifice plate interactions are:

(i) Bend cross-sectional shape;

(ii) Bend deflection angle;

(iii) Bend radius ratio;

(iv) Spacer length;

(v) Orifice plate shape;

(vi) Orifice plate area ratio;

(vii) Reynolds number.

Based on the work of Ward-Smith (1976), a primary interaction between a bend and orifice plate is anticipated for critical spacer length values less than about 2 duct diameters as deduced from the separate static pressure distributions of both the bend and of the orifice plate. Under these circumstances, it is anticipated that the adverse pressure gradient on the inner wall at the exit from the bend will tend to interact favourably with the pressure gradient in the orifice plate. From these considerations it may be then anticipated that the interactions will become increasingly favourable.

(i) As the spacer length is reduced to values of less than 2 duct diameters;

(ii) As the bend radius ratio is decreased;

(iii) For larger orifice area ratios.

For the values of the spacer length larger than 2 duct diameters a secondary interaction will occur. The secondary effects can be explained by the variation of velocity profile with the spacer length. As described in Para. 1.1.2.3, a velocity profile from a bend exit is non-uniform and includes a secondary flow which often increases the energy dissipation. The secondary flows will be slowly damped and exist for over 40 duct diameters or so after the bend [Miller (1971)]. When this non-uniform velocity profile enters to the orifice plate the performance of the orifice plate, e.g., C_d, may also be significantly changed depending upon the complicated relation between the contraction coefficient, C_c, the kinetic energy correction factor, α, and the orifice plate area ratio, m [Zanker (1961)]. As also indicated by B.S. 1042 (1965), for a 90 degree single bend upstream of a single-hole orifice plate,

a negative error (or variation) in C_d occurs and the error in C_d decreases as the spacer length, L_s/D_s, increases.

A typical result from the present tests (e.g. Fig. 20) suggests that an unfavourable interaction occurs after the critical spacer length. The head loss of the combination decreases until a minimum is reached at a value of the spacer length between 5 and 10 duct diameters. Then, the head loss again increases favourably as the velocity profile is re-developed with increasing spacer length. As will be expected, for large values of the spacer length these interaction effects disappear, and the head loss of the combination will be equal to the sum of the head losses of the bend and orifice plate in interference free flow.

1.1.4.2.2 Combination of an Orifice Plate and Bend

When an orifice plate is closely spaced upstream of a bend both primary and secondary interactions will again be anticipated. The parameters affecting bend-orifice plate interactions would be the same as those given above in Para. 1.1.4.2.1. A primary interaction may be expected for values of the critical spacer length less than about 7 duct diameters where the adverse pressure gradient at the immediate downstream of the orifice plate will interact unfavourably with the adverse pressure gradient on the outer wall at the entry to the bend. Thus, as the spacer length decreases to zero the head loss of the combination will be expected to increase. For larger values of the spacer length the secondary interactions will exist and be controlled by the changed flow characteristics such as the non-uniform velocity profile at outlet

from the orifice plate. As described in Para. 1.1.3.8 for a flow through an orifice plate, extensive regions of flow separation occur, and the static pressure recovery plane is about 6 duct diameters downstream of the orifice plate. Ito (1960) and Miller (1971) have also indicated that the effect of the upstream tangent conditions has a small effect on the bend performance. With a developing velocity profile approaching the bend, the bend head loss in the downstream tangent will be reduced when compared with those for a developed upstream velocity profile. It may then be expected that the head loss of the combination will decrease until a minimum is reached at a value of the spacer length, generally, between 5 and 10 duct diameters. For further large values of the spacer length, e.g. 20 duct diameters, there will be no interaction between the orifice plate and bend, and the state of interference free flow will be observed for the pressure losses.

According to B.S. 1042 (1965), the error (or variation) in C_d is positive by up to ½% for a single-hole orifice plate-bend combination with a spacer length less than about 3 duct diameters. This indicates that the error in C_d increases as the spacer length, L_s/D_s, decreases to $\frac{L_s}{D_s} = 0$.

1.1.4.3 Definition of Interaction Coefficient

For the combined components with upstream and downstream tangents the system head loss coefficient, K_s, in the general form is given by

$$K_s = K_{f_u} + K_{f_d} + K_{f_s} + [\Sigma K_c] \times C_i \qquad (36)$$

where K_{f_u} = friction loss coefficient for the upstream tangent

K_{f_s} = friction loss coefficient for the spacer length

K_{f_d} = friction loss coefficient for the downstream tangent

K_c = component head loss coefficient for interference free flow

C_i = interaction coefficient.

However, it should be noted that in Eqn. (36) K_c are defined in terms of the upstream velocity head of the first component.

In a system in which the cross-sectional area is constant, assuming a fully developed flow in the spacer length, the interaction coefficient, C_i, is then expressed by

$$C_i = \frac{K_s - K_f}{\sum K_c} \tag{37}$$

where K_s = system head loss coefficient

K_f = straight duct friction loss coefficient

K_c = component head loss coefficient for interference free flow.

Thus, for the present work C_i becomes

$$C_i = \frac{K_{com}}{K_o + K_b} \tag{38}$$

where K_{com} = head loss coefficient of the bend-orifice plate or the orifice plate-bend combination.

K_o = orifice plate head loss coefficient for interference free flow

K_b = bend head loss coefficient for interference free flow.

CHAPTER II

EXPERIMENTAL APPARATUS AND TESTS

2.0 INTRODUCTION

The apparatus comprises a sump, a pump, an upper tank approximately 17m off the ground, a downcomer, a weigh-tank with a diverter valve and drain back to sump. The bore of the duct work is, in general, 145.05mm in diameter, and the maximum flow rate of the apparatus is 65Kgs^{-1}. The general arrangement of the test rig is shown in Fig. 21.

The first test which had to be carried out was aimed at establishing the accuracy with which the flow rate can be measured with the weigh-tank and its diverter valve. These tests were followed by measurements of the discharge coefficient of a sharp-edged single-hole orifice plate, upstream of which was a run of straight duct over 80 duct diameters long. Downstream of the orifice plate there was a further run of straight duct of 100 diameters. Discharge coefficients so obtained were compared with the values published in B.S.1042 (1964). The comparison was very satisfactory and provided additional confirmation of the high basic accuracy of the test rig, which is estimated to be within $\pm$ 0.2%. In these tests, the configuration of duct work downstream of where the downcomer turns into the horizontal direction is shown in Fig. 22.

The principal experimental work was carried out with regard to the interactions of various bends and orifice plates in combination for various spacer lengths. For these tests the general run of duct work had to be re-arranged as far as the duct-location in the laboratory allowed. A typical arrangement for a bend and orifice plate combination is as shown in Fig .23. where

the upstream and downstream tangents of the test bend are approximately 120 and 50 duct diameters. With the results of the preliminary tests, which were obtained for each test bend and orifice plate alone for an interference free flow, the interaction coefficients were found experimentally.

In the following paragraphs the apparatus, tests and typical results will be described in detail.

2.1 EXPERIMENTAL APPARATUS

2.1.1 Upper Tank and Height Over Weir Gauge

The constant level upper tank with the capacity of 32,500kg is supplied with water from a sump below the floor level of approximately 30,000kg capacity by means of a centrifugal pump driven by 50HP variable speed motor. The weir of the upper tank is provided by means of the subsidiary tank as illustrated in Fig.24 The constant head only obtains if water is flowing over the weir, and a glass section is provided in the overflow ducting at laboratory level to provide visual confirmation that overflow exists. In addition, an electrical level gauge is provided in a stilling compartment within the subsidiary tank. The gauge comprises a float and a linear potentiometer, and is read remotely at the control position in the laboratory by means of a voltmeter. This height meter indicates the level within $\pm$ 0.5mm. During the test the weigh-tank becomes filled and the level of the water in the sump falls with the consequence that the head across the pump increases. In principle, this requires continuous adjustment of the speed to maintain constant flow. However, from the flow equation between the upper tank and the sump it becomes evident

that the adjustment of the speed is small. The flow equation may be written in the form

$$h = K \frac{V^2}{2g} \qquad (1)$$

and consequently

$$\frac{\Delta h}{h} = \frac{2 \Delta V}{V} \qquad (2)$$

where h = static head

K = head loss coefficient between stations at the upper tank and the sump

$\frac{V^2}{2g}$ = mean velocity head

V = mean velocity of fluid in duct

Δh = change in static head

ΔV = change in velocity.

By taking the values of h = 17m, Δh = 1.5mm

$$\frac{\Delta V}{V} = 4 \times 10^{-5} \qquad (3)$$

which is insignificant.

However, in practice, it was found for a flow rate of 60kgs^{-1} with 8000kg of water flowing to the weigh-tank the suction head of the pump increased by more than 0.7m (water level in the sump fell below the range of the sump pneumatic gauge), and the height over the weir fell by 1.5mm. For smaller flow rates, e.g. 11 kgs^{-1}, with a similar amount of water to the weigh-tank, the height over the weir changes more, but as the time to the weigh-tank is so long the minor adjustment of pump speed needed to keep within a similar limit is made easily.

In addition to the means of precise control of level in the upper tank, pneumatic gauges are provided in both the upper tank

and the sump to give an approximate measure of water levels in these components. The time constant with which the level in the upper tank responds to an adjustment at the pump is approximately 3 minutes, and consequently early knowledge of when the level in the upper tank is approaching its overflow value is essential in controlling the pump effectively. The pneumatic gauge in the sump is essential for avoiding overflow of the sump, and also judging whether there is sufficient water in the sump for the next test.

2.1.2 Ducts

All ducts are of smooth PVC tubing except the downcomer from the upper tank which is not necessarily hydraulically smooth. (However, the tests for the friction factors have indicated that the PVC tubing are not exactly hydraulically smooth as described in Para. 2.3.2). The glassfibre bends of various ratios of R/D = 1.49, 3.42 and 4.89 were expected to be smooth, and the measured bend head loss coefficients have indicated that they are smooth. The method of making glassfibre bends is described in Appendix A , and relatively small defects in the product are noted. The dimensions of the bends which have been tested are given in Table 2. Lengths of the upstream and downstream tangents have been selected to be sufficiently long as far as the duct-location in the laboratory allows. The dimensions of the straight ducts are shown in Table 3. The fourteen metal flanges made of Mild Steel are screwed onto the short pieces of spacer ducts, but the PVC flanges have been fitted on both ends of longer ducts by PVC cement. A metal flange is shown in Fig. 25.

The horizontal sections of the main line in the laboratory have been well braced, and there is no disturbance of the ducting

for the flow of water.

Diagrams of the duct line with the various test bends and the pressure tapping connections are given in Figs. 26 to 29.

2.1.3 Diverter

In order to divert water to the weigh-tank, and then back to the drain the diverter is actuated in both directions. From previous tests [Crook (1974)] it has been shown that the mean setting error using the diverter is

$$-1 \times 10^{-3} < \left\{\frac{\Delta T/T}{\Delta M/M}\right\} < +1 \times 10^{-3} \qquad (4)$$

where $\frac{\Delta T}{T}$ = error in time to the weigh-tank

$\frac{\Delta M}{M}$ = error in mass to the weigh-tank.

The mechanical principle of the diverter is illustrated in Fig. 30. The assembly of all fourteen tubes in line is rocked by a double acting hydraulic power cylinder, fed from the outlet of the main pump, and controlled by a pneumatically actuated spool valve. There are fourteen flexible tubes (in 31.75mm bore) connected to the diverter.

Each tube (in 25.4mm bore) is connected flexibly with a valve bank at the end of the main line (in 145.05mm bore). The valves are either fully open or fully closed so any tube in use runs full. Flow rate is set by the number of valves open.

2.1.4 Switch

The main elements of the switch are shown in Fig. 31. The spindle is connected co-axially with the diverter and rotates with it. The body of the switch is held against rotation by the spring and setting screw. Switching occurs when the wiper passes

across the boundary between the insulating inner body and the gold plated strip. There are no forces which can cause bouncing of the wiper. The switch and clock are connected by up to 30m of co-axial cable of 100pF per metre. The delay because of the capacitance of the cable is too small to be of consequence. The order of magnitude of the delay is

$$16.7 \times 10^{3} \times 100 \times 10^{-12} \times 30 = 50 \ \mu s.$$

2.1.5 Clock

The electronic time counter (Fig. 32) reads to one thousandth of a second with a specified error of no more than $\pm$ 1 count in 1×10^{6}. The counter was checked against the Racal Instruments Universal Counter Timer Model 835.

2.1.6 Weighbridge

In previous tests the weighbridge had been calibrated against substandard weights of the Inspector of Weights and Measures. The substandard weights were used to calibrate a smaller weighbridge which was then used to define the values of cast iron masses which were then used to calibrate the large weighbridge. The result of calibration was a random error of less than $\pm$ 0.1% and a systematic error of less than $\pm$ 0.1%. The weighbridge has a capacity of 20,000kg and is graduated in intervals of 5kg. The weighbridge can be read to within $\pm$ 1.0kg.

2.1.7 Thermometer

Temperatures of the flowing water are measured to the nearest hundredth of a degree centigrade by a mercury thermometer set in the drain to sump of the diverter valve.

2.1.8 Manometers

Pressure differences are measured by a differential air-water manometer for moderate pressure differences, and a water-mercury manometer for large pressure differences (Fig. 33). The scale is graduated in millimeters, and a tenth of a millimeter is estimated. The manometer glass tubes are made of 12.7mm internal diameter bore. The ranges of those differential manometers are shown in Table 4. It is estimated that pressure differences are read to within ± 1.0%.

2.1.9 Static Pressure Tapping Connections

The location of the static pressure tapping connections is shown in Fig. 34. At each location two tappings of 6.35mm bore are provided at 180° intervals. The neighboring static pressure holes were spaced at least 29cm apart to keep clear of any interference effects among themselves [Ito (1955, 1956)].

The pipe wall thickness is approximately 10.5mm (actual 10.5 ± 1.5mm).

To communicate the pressure of the water flowing accurately to the manometer, the length of the static pressure tappings should be at least twice the diameter of the bore of the tapping [Miyadzu (1936)]. The greater length was obtained by screwing brass bushes with a bore of 6.35mm diameter into the wall of the duct as illustrated in Fig.35.

The problem arises of connecting any single tapping selected from a large number of tappings to one or other of the two manometers.

The solution to this problem which was adopted was to connect the static pressure tappings to a manifold via diaphragm valves so that any selected static pressure tapping could be connected with either of the manometers. The system of ducting, valves and manifold is illustrated in Fig. 36. PVC tubing of 7.94mm bore and approximately 12m length ($\frac{L}{D}$ = 1511) was used for the connections.

Some preliminary tests were made on similar ducts with the static pressure holes, 11.5mm and 1.05mm in diameter respectively, which were drilled at 90° intervals in the circumference as illustrated in Fig. 37. It was found from these tests (see Figs. 345 to 354) that neither the 11.5mm nor the 1.05mm diameter tappings gave consistent results, and that the variations were greater with the 1.05mm holes. The reason for the larger error with the 1.05mm diameter static pressure tapping might be because of the heights of burrs relative to the hole size or specks of dust [Shaw (1958, 1959)]. As a result of these tests the former static pressure tapping shown in Fig. 35. was adopted. With this design of tapping, the length of the tapping is approximately 6.55 diameters of its bore, and satisfies the criterion that the length should exceed 2 diameters.

Care was taken in drilling and tapping the duct wall, and the inner surface of the duct was carefully de-burred.

2.1.10 Orifice Plates and Carrier Rings

All square-edged single-hole and multi-hole orifice plates

were made of approximately 3.17mm thick H/H brass sheet, except the two single-hole orifice plates with area ratios of m = 0.389 (one of them was originally m = 0.386 before it was finally re-bored to m = 0.389) which were made of EN 58 J stainless steel. The orifice plate holes were bored to produce sharp upstream edges, and care was also taken to satisfy the dimensional and constructional requirements of B.S.1042 (1964). The downstream edge of the orifice plate was not bevelled, but the tests showed that the thickness of the orifice plate (approximately 3.17mm) had no significant effect on the discharge and head loss coefficients when compared with the Standard values. The measured values are compared with the values of B.S.1042 (1964) in Paras. 3.3 and 3.5.2.

All orifice plates were drawn across fine grade emery paper laid on a flat surface to remove burrs. To determine the orifice diameter, the average of four measurements of diameters were taken by an inside micrometer and were confirmed with a vernier gauge. Errors of measurement in diameter are assessed as less than $\pm$ 0.05%.

Both carrier rings were made of mild steel and were nominally identical. They produced very consistent values of orifice plate discharge coefficients. Some measurements for the single-hole orifice plate with area ratio of m = 0.387 are given in Fig. 38. The low and high pressure connections of the carrier ring, which were at 180° intervals in the circumference, were connected to the water-mercury manometer by PVC tubing of

7.94mm bore. Each orifice plate is fitted into the carrier ring by 16 screws (2BAx$\frac{1}{2}$" CSK SS screws).

The details of the carrier ring and every orifice plate tested are shown in Figs. 11 through 16, and the primary characteristics of all orifice plates are also given in Table 1.

2.2 PROVING OF THE APPARATUS

All of the work which will be described subsequently depends upon the accuracy with which flow rates may be measured by the weigh-tank apparatus. The calibration of the weighbridge itself has been referred to already, and the possible errors due to the errors in the weighbridge itself are a random error of less than $\pm$ 0.1% and a systematic error of less than $\pm$ 0.1%.

The other principal measurement is the measurement of the time during which the weigh-tank is being filled, and in practical terms this resolves itself in to setting the instants at which the clock is switched on and is switched off. This may be said because with a crystal controlled clock, which has been checked against standard time signals, the percentage error in the clock itself is too small to be of any significance. A check of the clock which was made indicated the clock error to be within $\pm$ 0.001% which only increased to within $\pm$ 0.003% when the temperature of the envelope of the crystal was raised by 20°C.

The principle of the setting of the switch correctly will be

discussed with reference to Fig. 39a and 39b. In Fig. 39a the angular position of the diverter drum is shown as a function of time. Actual measurements with a linear transducer demonstrated that over the important part of its travel the drum moves with a constant velocity as is indicated in the figure. The switching point in the figure is at position "y" to give the switching instants T_1 and T_2. In Fig. 39b the flow rate to the weigh-tank is shown as a function of time. The reasonable assumption will be made that the way in which flow rate rises to its full value, and the way in which flow rate falls back to zero are highly reproducible although the exact forms are not known. The problem now can be expressed as finding that value of "y" which in turn gives times T_1 and T_2, such that the area ABCD is equal to the area OEFG. If now two occasions of diverting are considered in which in the first instance for the sake of definiteness a time of diversion to the weigh-tank of 100 seconds is given by the clock, and in the second instance the time given by the clock is 200 seconds, then if "y" is set correctly the masses to the weigh-tank should be precisely in the ratio of 2 to 1. If "y" is set too low, i.e. y^1, then the ratio will be slightly greater than 2. Let it be assumed that the value of "y" in Fig. 39a is correct, then a lower value of "y", y^1, will add a time ΔT to the interval between switching on and off the clock whilst that makes no difference at all to the timing of the diversion of the flow. The mass to the weigh-tank in the first instance, M_1, may be expressed as

$$M_1 = \dot{M} (100 - \Delta T) \tag{5}$$

and it follows in the second instance

$$M_2 = \dot{M} (200 - \Delta T) \tag{6}$$

then the ratio

$$\frac{M_2}{M_1} = 2 \left(1 + \frac{\Delta T}{200}\right) \tag{7}$$

In this $\dot{M}$ is the actual flow rate, whereas the calculated flow rates, $\dot{M}^1$, are given by

$$\dot{M}^1_1 = \frac{M_1}{100} = \dot{M} \left(1 - \frac{\Delta T}{100} \right) \tag{8}$$

and

$$\dot{M}^1_2 = \frac{M_2}{200} = \dot{M} \left(1 - \frac{\Delta T}{200} \right) \tag{9}$$

consequently

$$\frac{\dot{M}^1_2}{\dot{M}^1_1} = 1 + \frac{\Delta T}{200} \tag{10}$$

in which the terms in ΔT^2 and higher powers are ignored. Consequently, if there is an error in timing the flow rates, as calculated from the mass to the weigh-tank and the time to the weigh-tank as shown by the clock, it will appear to depend upon the time for which the flow is diverted to the weigh-tank. That is an impossibility.

Partial differentiation of

$$\dot{M} = \frac{M}{T} \tag{11}$$

gives the proportional error as

$$\frac{\Delta \dot{M}}{\dot{M}} \cong \frac{\Delta M}{M} - \frac{\Delta T}{T} \tag{12}$$

The intention with respect to errors will be expressed as

$$-1x10^{-3} < \begin{Bmatrix} \Delta T/T \\ \Delta M/M \end{Bmatrix} < +1x10^{-3} \qquad (13)$$

The weighbridge can be balanced and read to within ±1.0kg. It follows that to satisfy the intention with respect to error, a mass of 1000kg or greater must be sent to the weigh-tank. For a typical flow rate of 60kg/sec the time of diversion to the weigh-tank would be 16.66 seconds, and to satisfy the intention with respect to time, a timing error within ±16.66 milliseconds would be required. The time taken for the tubes of the diverter drum to pass over the separator plate is 230 milliseconds, and a timing error of 16.66 milliseconds in positional terms implies that at the instance of switching on and switching off the clock the tubes are away from a central position over the separator by d/27.61 where d is diameter of the tubes. In actual dimensions (d=25.4mm) this would mean that switching occurs when the tubes are displaced 0.92mm from the intended position of switching. This would be a large displacement, and in positional terms the switch can be set to within ±0.5mm.

In Fig. 40 the effects upon the measured flow rates caused by various postulated errors in the instants of switching are shown.

It has been assumed above that the flow rate, $\dot{M}$, depends solely upon the number of valves which is open. However the flow rate, as found experimentally and indeed as one might expect, varies with the temperature of water flowing in the system. It

is therefore important that comparisons between the calculated flow rates, $\dot{M}_1^1$ and $\dot{M}_2^1$, should be made at the same temperature of the water. An example of such a comparison is shown in Fig. 41 in which flow rate, as deduced from the mass to the weigh-tank and the time by the clock, is plotted as a function of temperature. The various points relate to times of diversion of 70 to 140 seconds. All of the points lie within 0.1% of the regression line, and do not give any evidence of a timing error [Crook (1974)].

2.3 PROCEDURE OF TESTS

The test procedure generally consisted of:

(i) Measuring the flow rates;

(ii) Measuring the friction factors for the straight duct, and obtaining the experimental friction factors;

(iii) Measuring the pressure drops in the duct line due to the bends, and obtaining the experimental bend head loss coefficients;

(iv) Measuring the pressure drops in the duct line due to the orifice plates, and obtaining the experimental orifice plate discharge coefficients and head loss coefficients;

(v) Measuring the system pressure drops due to the various combinations of bends and orifice plates, and obtaining the variations of the orifice plate discharge coefficients and the interaction coefficients.

The lines to the manometers were purged carefully before the readings of the pressure differences were taken.

2.3.1 Measurement of Flow Rates

Each flow rate which was desired has been determined by the number of valves open. In making the measurement of actual flow rate by the weigh-tank apparatus, the water flowing in the system was diverted to the weigh-tank typically for 60 seconds, and the net mass to the weigh-tank was measured by the weighbridge. The temperature of the water was also measured to read the density of the water. By means of those measured values the mass flow rate was calculated by

$$\dot{M} = \frac{M}{T} \tag{14}$$

and then the volume flow rate itself was deduced by

$$Q = \frac{\dot{M}}{\rho} \tag{15}$$

where $\dot{M}$ = mass flow rate

M = net mass to the weigh-tank measured by the weighbridge

T = time to the weigh-tank measured by the electronic time counter

Q = volume flow rate

ρ = density of the water at the time of measurement.

For each test in which the flow was diverted to the weigh-tank the procedure in measuring the flow rate was repeated, and the mean flow rate was obtained by dividing the measured mean mass flow rate

by the mean density of the water. A typical plot of mass flow rate, $\dot{M}$, against the number of valves open, n, is shown in Fig. 42.

2.3.2 Measurement of Duct Friction Factors

The location of the static pressure tappings is shown in Fig. 43. For the duct friction factors, the pressure drops were measured by the air-water manometer between the static pressure tappings 'A' to 'D' spaced at a distance of 635.4cm (43.7D) and 100cm (6.7D) respectively upstream of the test bend of R/D = 1.49. The distance between the downcomer and the static pressure tapping 'A' was over 1250cm (86D). This would indicate a fully developed turbulent flow for each test. The plane at 'A' was adopted as the reference and pressure drops were measured between 'AB', 'AC' and 'AD' for both top and bottom static pressure tappings. The experimental values of friction factor were obtained from the measurements of pressure drop, and the mean friction factors were taken as the slope of the plots of K (head loss coefficient due to duct friction) versus L/D (axial length in duct diameters). Typical plots are shown in Fig.44 in which the head loss coefficients are those given by the bottom static pressure tappings (the reason for choosing the bottom readings is explained in this paragraph). The curve of Fig.44a relates to the lowest Reynolds number used in the work and the curve of Fig. 44c relates to the highest Reynolds number used in the work. The lines must pass through (0,0), and for each instance 3 experimental points provide 3 slopes. These slopes are always within $\pm$ 3.0% of the mean. Fig.43 illustrates

the system duct work, and shows a straight piece of duct upstream of the bend of R/D = 1.49 and a straight piece of duct downstream of the bend. Both upstream and downstream straight lengths carry static pressure tappings, in the instance of the upstream tangent in 4 planes, and in the instance of the downstream tangent in 6 planes. In each plane diametrically opposite static pressure tappings were provided which were normally at the bottom and the top as mentioned in Para. 2.1.9. The pressure differences between the various planes should be the same irrespective of whether the pressure differences are measured between top static pressure tappings or between bottom static pressure tappings. In Fig. 45 typical plot of system head loss coefficients, K_s, is shown, and it is clear from the plot that whereas there is little difference between top and bottom head loss measurements in the downstream tangent, there is a substantial difference between top and bottom head loss measurements in the upstream tangent. The plot clearly suggests that some of the static pressure tappings in the upstream tangent are giving false readings. This was confirmed by rotating the upstream tangent about its axis through 90 and 180- degree. It was found that the pressure differences were associated with the static pressure tappings and were unaffected by rotation of the tangent, and it is concluded that some of the static pressure tappings in the upstream tangent are defective.

The problem arises of identifying the defective static pressure tappings, and indeed of justifying whether any of the static pressure tappings are to be relied upon. It may be seen from Fig. 45 that if the pressure differences given by

the bottom readings of the upstream tangent are regarded as reliable, then the slopes, which indicate friction factor in the straight duct are substantially the same both upstream and downstream of the bend. This was found to be so in all circumstances, i.e. over the range of Reynolds numbers employed and for all of the various radius ratios of the bends tested. It should be noted that in order to determine the straight duct friction gradient in the downstream tangent strictly it is the gradient of the asymptote of plots which should be taken. The local effect of the bend is confined to within approximately 30 diameters downstream of the bend. It is the point beyond the $L/D = 30$ which should be used for the estimation of the straight duct friction gradient (see, for example, Figs. 50 to 77).

Additional evidence is provided by calculating friction factors from the head losses. In Fig. 46 some typical results of duct friction factors measured from top and bottom static pressure tappings in the upstream tangent are presented, and in the same Fig. 46 the Kármán-Prandtl curve is also plotted as a function of Reynolds number $Re_D = \frac{VxD}{\nu}$, i.e. the curve

$$\frac{1}{\sqrt{f}} = 2.0 \log (Re_D \sqrt{f}) - 0.8 \qquad (16)$$

which is relevent for $3x10^3 < Re_D < 3x10^6$. It may be seen that the friction factors derived from the bottom readings are close to the Kármán-Prandtl curve from the lowest $Re_D = 0.85x10^5$ up to $Re_D = 3x10^5$, and that thereafter the friction factors lie

above the Kármán-Prandtl curve. This would indicate a duct with the relative roughness of approximately $\frac{e}{D} = 1x10^{-5}$, and is consistent with the data from the duct manufacturer, who quote the same value of relative roughness [Chemidus Wavin (1975)]. Hereafter all pressure differences for the upstream tangent will be based upon the bottom readings which give results which are internally consistent and externally consistent with the Moody diagram [Moody (1944)].

The reason why some static pressure tappings in the upstream tangent are not reliable is not known definitely but is possibly due to the difficulty of making the static pressure tappings. The form of the static pressure tapping is shown in Fig. 35 and possibly in the early tappings the wall of the duct was distorted by pressure from the tap when the thread was cut in the blind hole, and also by pressure from the bush connected to the valve when it was fitted to the pressure hole. Detailed internal inspection of the static pressure tappings was not practicable because of the difficulty of access. It is probable that the greater reliability of the static pressure tappings in the downstream tangent reflects the greater experience which had been acquired when they were drilled.

2.3.3 Measurement of Bend Head Loss Coefficients

Some typical arrangements for the test bends are shown in Figs. 26 through 29. Three 90-degree glassfibre bends with radius ratios of R/D = 1.43, 3.42 and 4.89 and one 90-degree PVC bend with radius ratio of R/D = 4.18 were tested, and their bend head loss coefficients were measured.

For each bend, the procedure for obtaining the bend head loss coefficients for a range of Reynolds numbers was the same. The pressure drops for the duct plus bend were obtained by measuring pressure differences (by means of the air-water manometer) between the static pressure tappings located at 'A', 40 diameters or so upstream of the bend entry plane, to 'P', 45 diameters or so downstream of the bend exit plane where the flow is again fully developed.

With reference to Fig. 43 the pressure drops were measured from the top and bottom static pressure tappings at planes 'B', 'C', 'D', 'E', 'F', 'G', 'H', 'J' and 'P' relative to the plane 'A' for each selected flow rate, then the mean system head loss coefficients (except for the upstream tangent where only the more reliable bottom readings were used), $K_s = \frac{h}{V^2/2g}$,

were plotted against the distances from plane 'A' as shown typically by Fig. 47. As is to be expected these plots fall in two straight lines separated by an apparent discontinuity over the bend. The distribution of head loss in the bend is unknown, therefore, the bend is represented as having zero system length, i.e. L/D = 0 (see diagram inset in Fig. 47), and consequently the apparent discontinuity represents the gross head loss coefficient over the bend. The gross bend head loss coefficient is not quite the gross bend head loss coefficient because there will be small pressure drops attributable to disruption of a continuous smooth bore at the flanges (see Fig. 48). However, because no numerical value can be given to such losses, they have not been taken into consideration and the gross bend

head loss coefficient and bend head loss coefficient will be treated as identical. In some instances, which did occur, the bend was connected to the main duct work by short lengths of ducts whose diameters differed slightly from that of the main duct work. It is also to be noted that the actual bores of the bends tested differ slightly from the bore of the main duct work as is shown in Tables 2 - 3. Some typical arrangements are illustrated in Fig. 49.
and their mean diameters are also indicated. In all these instances the gross bend head loss coefficient was corrected for the pressure losses due to sudden enlargements and contractions. In the plots of the system head loss coefficient, K_s, against the axial length to duct diameter, L/D, the D always stands for the actual bore, i.e. a piece of connecting duct of smaller diameter and length of equal diameter is represented by 1 unit of L/D. In principle, an additional correction should be made on account of the changed velocity of flow through the connecting ducts, i.e. change in friction factor due to change in Reynolds number. In practice this correction is extremely small, and has not been applied.

For all instances shown in Figs. 50 through 77.
the apparent discontinuity in the head loss coefficients consists of the head loss coefficient attributable to the bend plus the head loss coefficient attributable to the connecting ducts in the line. For each bend tested these gross head loss coefficients were plotted against the

Reynolds numbers as shown typically by Fig. 78.
As is to be expected the gross bend head loss coefficient decreases as the Reynolds number increases.

With reference to Fig. 43 the system head loss between 'A' and 'P' can be regarded as the straight duct friction loss which would occur if the bend was removed and the downstream tangent was joined to the upstream tangent in line, plus the head loss due to the presence of the bend. Consequently, the system head loss coefficient between 'A' and 'P' is given by

$$K_s = K_b + K_f \qquad (17)$$

In these instances in which connecting duct work of different diameters was used the measured system head los coefficient will include the sum of local head loss coefficient due to sudden enlargements and contractions, and then becomes

$$K_s = K_b + K_f + \sum K_L \qquad (18)$$

from which

$$K_b = K_s - K_f - \sum K_L \qquad (19)$$

or $$K_b = K_G - \sum K_L \qquad (20)$$

where K_b = bend head loss coefficient

K_s = system head loss coefficient

K_f = friction loss coefficient

K_L = local head loss coefficient

K_G = gross bend head loss coefficient.

The problem now arises of assessing the sum of the local head loss coefficients, $\sum K_L$. The correction has in fact been made by setting down the various diameters present and

applying appropriate head loss coefficients for sudden enlargement and contraction as given in Fig. 49.

To provide some experimental verification of this procedure connecting ducts were made up with various short lengths of various diameter ducts. The head loss coefficients for these various configurations were measured and the differences between them were compared with the calculated differences based upon the theoretical head loss coefficients due to sudden enlargement and contraction. The experimentally found differences are compared with the predicted values in Table 5, and the two sets are in fair agreement. This gives some experimental justification for the way in which the sum of local head loss coefficients, $\sum K_L$, has been in fact evaluated. Typical results are given in Figs. 79 to 81.

Very careful and accurate measurements are necessary to obtain consistent bend head loss coefficients as is also indicated by Ito (1956) and Miller (1971). For a typical instance the numerical values from Fig. 51 can be given as follows:

$K_s = 1.613$

$K_f = 1.326$

$\sum K_L = 0.050$

$f = 0.01472$

$L/D = 90.1$

$R/D = 1.49$

$Re_D = 2.72 \times 10^5$

To find the bend head loss coefficient, K_b, the friction loss coefficient, $K_f = f \times \frac{L}{D}$, plus the sum of local head loss coefficients, $\sum K_L$, is subtracted from the system head loss coefficient, K_s. That is:

$$K_b = K_s - K_f - \sum K_L \qquad (21)$$

from which

$$K_b = 1.613 - 1.326 - 0.050$$

then becomes

$$K_b = 0.237$$

The accuracy of the system head loss coefficient, K_s, and the friction loss coefficient, K_f, is estimated to be within $\pm$ 0.2 and 1.0% respectively. Estimating the accuracy of the sum of the local head loss coefficient, $\sum K_L$, which is substantially a small value, to be within $\pm$ 10.0% the overall accuracy of the bend head loss coefficient, K_b, is estimated to be within $\pm$ 9.0%. From this instance it may be seen that the accuracy of the bend head loss coefficients largely depends on the accuracy of the measured duct friction factors for fully developed flow and the geometry of the duct work.

The measured gross bend head loss coefficients, K_G, in Figs.50 through 77 were corrected for the sum of the local head loss coefficients, $\sum K_L$, and then the bend head loss coefficients, K_b, were found over a range of Reynolds numbers for a number of different bend geometries. The results are presented as the bend head loss coefficient, K_b, as a function of the Reynolds number,

Re_D, and also the bend head loss coefficient, K_b, as a function of the radius ratio, R/D, for a number of specific Reynolds numbers, Re_D. The results are given in typical Figs. 82 and 83.

2.3.4 Measurements of Orifice Plate Discharge Coefficients and Head Loss Coefficients

The geometry of all orifice plates tested are given in Table 1. The orifice diameters were carefully measured at four places with inside micrometers, and the mean value of four readings was taken as the orifice diameter as previously mentioned in Para.2.1.10. To calculate the area ratio, m, of each orifice plate, the mean internal diameter of the duct was taken from four readings measured at a point about two duct diameters (2D) upstream of the orifice plate as indicated in Standard Codes [e.g. B.S.1042 (1964)]. Eight single-hole and nine multi-hole orifice plates of various area ratios were tested to measure the additional pressure drop in the line due to the orifice plates, their discharge coefficients, C_d, and head loss coefficients, K_o (except for the single-hole orifice plates with the area ratios of m = 0.386 and 0.387). The procedure for obtaining the orifice plate discharge coefficients and head loss coefficients for a range of Reynolds numbers was the same in all instances. The carrier ring containing a given orifice plate was inserted in the line between two flanges where there were upstream and downstream straight sections of over 1200cm (82D) and 600cm (41D) respectively. For the range of Reynolds numbers tested, the flow approaching the orifice plate was therefore fully developed and turbulent.

The location of static pressure tappings is shown in Fig. 84 The plane at 'A' was adopted as the reference, and the pressure drops between the static pressure tappings 'A' (14.5cm=1D) upstream and 'B' (252.5cm=17.4D), 'C' (455.5cm=31.4D), and 'D' (585.5cm=40.3D) downstream of the orifice plate were measured by the water-mercury manometer for both top and bottom static pressure tappings (in this instance, because of the relatively large pressure drops, the disparity between the pressure difference readings given by the top and bottom static pressure tappings is of no significance). The pressure drop between the high and low pressure corner tappings of the carrier ring was also measured.

For each test, the orifice plate which was always fitted into the carrier ring by the screws as mentioned in Para.2.1.10 was carefully inserted in the line between two flanges (care was taken to adjust the high and low pressure tappings connections of the carrier ring into a horizontal plane, i.e. normal to the plane of the top and bottom pressure tappings). With the water flowing in the duct work the air was removed from the ducts and each line connected to the manometer. The flow was set at a desired flow rate by opening an appropriate number of the 14 valves, and the constant head was obtained by adjusting the pump speed for the conditions as described in Para.2.1.1. When the flow conditions were stable the weighbridge was balanced and the temperature of the water was measured at the beginning of each test. Then the orifice plate pressure difference, $h_{O.P.}$, was usually measured when the flow had been diverted into the weigh-tank, which was

for a period of approximately 60 seconds. The weighbridge was again balanced and the net mass to the weigh-tank was found in order to derive the mass flow rate. The pressure differences were measured for both top and bottom static pressure tappings located between 'A' to 'D'. Each test was repeated and the mean values were used to calculate the orifice plate discharge coefficients and head loss coefficients.

It should be noted that, because of the existing screw tappings on the carrier ring, unless otherwise stated, the normal position of each multi-hole orifice plate when fixed into the carrier ring was used as illustrated in Fig. 85.

To obtain the experimental orifice plate discharge coefficients, C_d, the Eq.(31) given in Para. 1.1.3.4 was used. Some typical plots of the orifice plate discharge coefficients, C_d, versus the Reynolds numbers, Re_D, are shown in Figs. 86 through 101 and in these instances the different dates of measurements are also indicated. For each orifice plate tested C_d decreases when Re_D increases, and tends to an asymptotic value at the higher values of Re_D.

To find the orifice plate head loss coefficient, K_o, the calculated friction loss coefficient, K_f, in the straight duct was subtracted from the measured system head loss coefficient, K_s, between the static pressure tappings 'A' (1D) upstream and 'B' (17.4D) downstream of the orifice plate. The same procedure was also applied between the static pressure tappings 'A' (1D)

upstream and 'C' (31.4D) and 'D' (40.3D) downstream of the orifice plate. Then, the mean value of the top and bottom readings was taken as the experimental orifice plate head loss coefficient. Some typical plots of the orifice plate head loss coefficients, K_o, versus the Reynolds numbers, Re_D, are shown in Figs. 102 through 115 with the dates of measurements as indicated. Tests show that the orifice plate head loss coefficient tends to an asymptotic value at the higher Reynolds numbers.

All the experimental results as presented have fully taken into account any effects arising from variations in temperature, both in respect of the flow of water and also with respect to the manometer reading. The sump water has been treated as having unit density at $4^{o}C$. The density of water was measured from time to time and values of the specific gravity of the sump water about 1.0006 were obtained. The enhanced density of water was attributed to the presence of salts from the concrete sump, and the system was periodically emptied and refilled with tap water. The error in C_d due to the density variation is within $\pm$ 0.06%, and has been regarded as too small to be of significance.

2.3.5 Measurement of Interaction Effects Between Bends and Orifice Plates in Combination

In Paras. 2.3.3 - 2.3.4. the experimental head loss coefficients of the bends and orifice plates were given. In this paragraph the method of measuring the effects of the interaction between orifice plates and bends in combination will be described, and results will be reported. In general, the orifice plates were placed downstream of the bends, but in a few instances they were placed

upstream. The glassfibre bends with radius ratios of R/D = 1.43, 3.42 and 4.89 and the PVC bend with radius ratio of R/D = 4.18 were used, and were combined with both single-hole and multi-hole orifice plates of various area ratios, m. Spacers, with lengths ranging from L_s/D_s = 0.55 to L_s/D_s = 16.49, were used. The arrangement of the test line is illustrated in Fig. 23 The quantities deduced from the tests are the head loss coefficients of the various bends and orifice plates in combination, K_{b-o}, the interaction coefficients, C_i, and the orifice plate discharge coefficients, C_d. In this work the disparities between the readings of the top and bottom static pressure tappings, which had to be considered in detail when the duct friction loss was being considered in Para. 2.3.3 , are too small to be significant in the context of this paragraph.

The experimental procedure for obtaining the head loss coefficients of the combinations of the various bend and orifice plates, K_{b-o}, and the discharge coefficients of the orifice plates, C_d, in each combination was the same in all instances, and the tests covered a range of Reynolds numbers, Re_D. For each combination, with the bend upstream of the orifice plate or with the orifice plate upstream of the bend, the carrier ring containing a given orifice plate was inserted in the duct line between two flanges at a chosen spacer length of the line, and with the water flowing in the duct work all lines were carefully purged. The water flow was established and a constant head was maintained by adjusting the speed of the pump as previously described in Para. 2.1.1. When the flow conditions

were stable, with reference to Fig. 23 , the pressure differences between the static pressure tappings 'A' to 'P' were measured with the water-mercury manometer for both top and bottom static pressure tappings. The pressure difference across the orifice plate as given by the low and high pressure connections of the carrier ring was also measured with the water-mercury manometer. At the beginning of each test the temperature of the water flowing was read, and the mass flow rate was measured by means of the weigh-tank apparatus. The period of diversion to the weigh-tank was approximately 60 seconds. The flow rate was changed by opening various numbers of the valves of the valve bank. Each test was repeated and the mean values of the readings were used to calculate the combined bend and orifice plate head loss coefficients and discharge coefficients of the orifice plate in combination. For each combination, the pressure differences were usually measured at three Reynolds numbers.

2.3.5.1 Variations in Orifice Plate Discharge Coefficients

One purpose of this work was to find out the variations in the orifice plate discharge coefficient when the orifice plate was close to the bend. The calculation procedures were based on the apparent area ratios of the orifice plates, $m_s = A_o/A_s$, depending upon the internal diameters of the connecting ducts measured at the upstream side of each orifice plate installed in the duct line. With this assumption the discharge coefficients of the orifice plates in combinations have been found, and some typical plots of the orifice plate discharge coefficients, C_{di}, versus the Reynolds numbers, Re_D,

are presented in Figs. 116 to 134. As is to be expected, for the same spacer length, the discharge coefficient decreases when the Reynolds number increases. This difference between the discharge coefficient of the orifice plate in combination with the bend and the discharge coefficient of the same orifice plate as measured in the straight length for an interference free flow was expressed as a percentage of the latter discharge coefficient

$$\text{Variation in } C_d \ (\%) = \frac{C_{di} - C_d}{C_d} \qquad (22)$$

where C_{di} = discharge coefficient of the orifice plate when there is an interaction between the orifice plate and bend

C_d = discharge coefficient of the orifice plate when the orifice plate is in isolation.

As previously described, the discharge coefficients of each orifice plate in an interference free flow had been found, and the orifice plate discharge coefficients, C_d, versus the Reynolds numbers, Re_D, are shown in Figs. 86 to 101 . To calculate the variations in C_d due to the various bend and orifice plate combinations at the same Reynolds numbers, Re_D, the orifice plate discharge coefficients were taken from the figures for both instances. For each combination the mean percentage variations in C_d were obtained in the range of the Reynolds numbers, and some typical plots of the mean percentage variations in C_d versus the spacer lengths, Ls/D_s, are presented in Figs. 135 to 142.

It is concluded from the test results that

(i) With the single-hole orifice plate downstream of

the bend the percentage variation in C_d is always a negative value, and rises to a maximum magnitude, e.g. -3%, between L_s/D_s = 4 and 7 (Fig. 135);

(ii) With the multi-hole orifice plate downstream of the bend the percentage variation in C_d is usually a positive value depending on the geometry of the multi-hole orifice plate, and falls to a minimum, e.g. -0.4%, between L_s/D_s = 8 and 12 (Fig. 136);

(iii) With the various orifice plates upstream of the PVC bend of R/D = 4.18 the percentage variation in C_d rises up to +1.0% at the spacer lengths of L_s/D_s = 0.7 and 3.28 (Fig. 141), and with the single-hole and multi-hole orifice plates of m = 0.232 and 0.231 respectively upstream of the glassfibre bend of $R/_D$ = 1.49 the percentage variation in C_d is sensitive to the diameter difference at L_s/D_s = 0.55 for the single-hole orifice plate, e.g. it rises to +3% (Fig.142).

2.3.5.2 Interaction Coefficients

Another purpose of this work was to obtain the interaction coefficient, C_i, which expresses the change in the sum of the head losses over the bend and orifice plate arising from their close combination in the line. With reference to Fig.23 the system head loss coefficient, K_s, between 'A' and 'P', for example, may be expressed as

$$K_s = (K_b + K_o)\, C_i + K_f \qquad (23)$$

with $$K_{b-o} = K_s - K_f = (K_b + K_o)C_i \qquad (24)$$

it then follows

$$C_i = \frac{K_{b-o}}{K_b + K_o} \qquad (25)$$

where K_{b-o} is the measured head loss coefficient for the bend and orifice plate in combination, K_b and K_o are the measured head loss coefficients for the bend and orifice plate each in isolation, K_f is the measured friction loss coefficient for all straight sections of the line between 'A' and 'P', and C_i is the interaction coefficient for the bend and orifice plate in combination. Obviously, with a sufficient spacer length, L_s/D_s, between the bend and orifice plate they will not interact and the value of the interaction coefficient, C_i, will be unity. However, with an insufficient spacer length, L_s/D_s, the flow between the bend and orifice plate does not recover to a fully developed velocity profile. Then, for short spacer lengths there may be a static pressure interference between the bend and orifice plate, and the interaction coefficient, C_i, will differ from unity. The slope of the curve of C_i against L_s/D_s may be positive or negative. If the slope is positive the interaction is said to be favourable and if the slope is negative the interaction is said to be unfavourable as previously described in Para. 1.1.4.1.

The system loss coefficient, K_s, is not necessarily measured between 'A' and 'P' but may be taken from any point upstream of the combination to any point downstream of the

combination. The system head loss coefficient, K_s, was measured as a function of the axial length, L/D. By the system head loss coefficient is meant the pressure loss in velocity heads between any two static pressure tappings, and by the axial length is meant the length in duct diameters between the two static pressure tappings minus the circumferential length around the bend if the bend should intervene. Fig. 143a, which is purely illustrative, illustrates the reckoning of the axial length, L/D, where the 'D' always stands for the actual bore, e.g. a piece of connecting duct of larger diameter and length of equal diameter is represented by 1 unit of L/D. It is to be noted that each test bend is terminated as the 90 degree bend. Both integral tangents of the bend are included in L/D, and then are treated as an axial length in bend diameters, i.e. L/D = 0.55, 1.1 and 2.0 for the glassfibre bends with radius ratios of R/D = 1.49, 3.42 and 4.89 respectively, and L/D = 0.7 for the PVC bend with radius ratio of R/D = 4.18. Fig. 143b illustrates the plotting of the system head loss coefficients in which the static pressure tapping 'A' is taken as reference. The slopes of the lines upstream of the bend and downstream of the orifice plate substantially represent the straight duct (or pipe) friction loss, and separation of the lines which is denoted by 'K_{b-o}'gives the head loss coefficient due to the bend and orifice plate in combination. The separation denoted by 'K_{s-l}' represent the head loss coefficient for the spacer length which separates the bend and orifice plate.

For each combination the head loss coefficient, K_{b-o}, was

found by plotting the system head loss coefficients as typically shown in Figs. 144 to 248 , by drawing the best two straight lines, and by noting the separation. The system head loss coefficients upstream of the first component in the combination were based upon the readings from the more reliable bottom static pressure tappings (Para. 2.3.2), and the mean values taken from the top and bottom static pressure tappings were used as the system head loss coefficients downstream of the second component in the combination. Although this was done to obtain the best possible accuracy any disparity between the pressure difference readings given by the top and bottom static pressure tappings are of less consequence in this context than they were in Para. 2.3.3 because the head loss coefficient of the orifice plate is very much greater than that due to the bend. However, the measured head loss coefficients for the various bend and orifice plate combinations as indicated by the figures will include the sum of the local head loss coefficients due to the use of connecting duct work of slightly different diameters. To find the net head loss coefficient for the bend and orifice plate in the combination the value of the sum of the local head losses has to be subtracted from the measured gross head loss coefficient (the measured gross and net head loss coefficients of a bend-orifice plate combination will then be symbolized by K^*_{b-o} and K_{b-o} respectively). The sum of the local head loss coefficients, $\sum K_L$, due to sudden enlargement and contraction were evaluated as previously described in Para. 2.3.3 . Thus, Eq.(23) for the system head loss coefficient may be re-written as

$$K_s = K_{b-o} + K_f + \sum K_L \qquad (26)$$

Some typical plots of the net head loss coefficients, K_{b-o}, for the various bend and orifice plate combinations versus the Reynolds numbers, Re_D, are presented for the various spacer lengths, L_s/D_s, in Figs. 249 to 269. For the same spacer length, the tests indicate that the head loss coefficient for the bend and orifice plate in the combination increases when the Reynolds number increases.

The interaction coefficient, C_i, was then calculated from

$$C_i = \frac{K_{b-o}}{K_b + K_o} \tag{27}$$

in which all values of K_{b-o} and K_b have been corrected for the local head losses, $\sum K_L$ (the measured value of K_o is not affected by the $\sum K_L$). The net values of K_{b-o} and K_b were drawn from Figs. 82 and 249 - 269 respectively. Some typical plots of the interaction coefficients, C_i, versus the Reynolds numbers, Re_D, are shown in Figs. 270 to 289 for the various bend and orifice plate combinations and spacer lengths, L_s/D_s. It is to be noted that there is no substantial variation of C_i averaged over the range of Re_D employed, some typical plots of those mean interaction coefficients, $\bar{C}_i$, against the spacer lengths, L_s/D_s, are presented for the combinations with the various bends upstream of the various single-hole or multi-hole orifice plates as shown in Figs. 290 to 295 . The trend of the curves in general is the same for each combination. The interaction coefficient rises to a maximum at approximately $L_s/D_s = 4$ and falls to a minimum

at approximately L_s/D_s = 7 as in Fig. 290 which is for the combination of the PVC bend of R/D = 4.18 and the single-hole orifice plate of m = 0.389. However, it is noticeable that there are some exceptions to the general trend at small values of L_s/D_s, which occur when certain glassfibre bends of R/D = 1.49, 3.42 and 4.89 were used, and these were known to produce small sudden changes in the areas at their connections to the line. This effect may be seen in Figs. 292 to 295 where L_s/D_s = 0.55, 1.1 and 2.0 are for the bends of R/D = 1.49 3.42 and 4.89 respectively; the points for the glassfibre bends rise above the general trend, but at larger values of L_s/D_s the points for the bends are in conformity with the general trend.

In Fig. 296 , the interaction coefficients, C_i, are plotted against the spacer lengths, L_s/D_s, for the various orifice plates upstream of the PVC bend of R/D = 4.18. The tests indicate that there is an unfavourable interaction for thoseinstances as the spacer length decreases from L_s/D_s = 3.28 to 0.7. It was also predicted by Ward-Smith (1976) that the interaction coefficient would fall to a minimum value between L_s/D_s = 5 and 10, and would be unity at the large values of L_s/D_s. In Fig.297 the interaction coefficients, C_i, are also plotted against the spacer lengths, L_s/D_s,for the single-hole and multi-hole orifice plates with area ratios of m = 0.232 and 0.231 respectively upstream of the glassfibre bend with radius ratio of R/D = 1.49. In this instance the trend of the curve is the same but the effect of the larger bend diameter at L_s/D_s = 0.55 introduces a larger interaction coefficient, e.g. C_i = 1.04.

Some tests were also performed to measure the head loss coefficients for the various orifice plates upstream of the glassfibre bend with radius ratio of R/D = 3.42 when the spacer length was 45 duct diameters. The test procedure was the same but the reference plane 'A' was at 1 duct diameter upstream of each orifice plate inserted in the duct line, and the pressure differences were measured between 'A' to 'P' as illustrated in Fig. 84 . Some typical plots of the system head loss coefficients, K_s, versus the distances from the reference plane 'A', L/D, are presented in Figs. 298 to 333, and in the same figures K_o, K^*_{o-b}, $K_{O.P.}$ and C_i are also indicated.

CHAPTER III

TEST RESULTS

3.1. The Effect of Temperature

It was soon discovered in testing that the measured mass flow rate, $\dot{M}$, to the weigh-tank varied with the temperature of the water, θ, to a greater extent than is implied by changes in the density of the water. This is illustrated in Fig. 41 where over a 6-hour period the temperature of the water rose by approximately 3°C and the measured mass flow rate rose by approximately 0.4%. The figure contains points relating to the various mass flow rates and various masses to the weigh-tank, but dispositions of these points are mixed and there is no consistent segregation as would be given by timing error (see Fig. 40). The implication is that the spread of the points is due to random errors in measurement.

The line through points is the regression line of M upon θ. The standard deviation, σ, of $\dot{M}$ about the regression line was calculated, and the bar in the figure is for $\pm 2\sigma$, i.e. indicates the 95% confidence limits. The arrowed line indicates an error of 0.1% (not $\pm$ 0.1%). It may be seen from the figure that the random error is less than $\pm$ 0.1%.

3.2. Mass Flow Rate and Number of Open Valves

The mass flow rate, $\dot{M}$, was measured with 2 to 14 valves open which gives a range of Reynolds numbers, Re_D, based upon duct diameter, from $Re_D = 0.7 \times 10^5$ to 6×10^5. The mass flow rate to be expected was also calculated from the system head loss. Terms appropriate for the constrictions of the valves, for the flexible tubes connecting valves to the diverter, and for the discharge from

the tubes were included but the accuracy of these terms is not important because the major system head loss comes from the main duct friction loss. Fig. 334 shows a close correspondence between the measured and the calculated mass flow rates. It should be noted that on the scale of this figure the temperature effect is too small to be of any significance.

3.3. Measured Orifice Plate Discharge Coefficients

3.3.1 Single-hole Orifice Plate Discharge Coefficients

As an additional check upon the measured mass flow rate the single-hole orifice plates with area ratios from m = 0.171 to m = 0.508 were arranged in the line for interference free flow (80D upstream and typically 100D downstream from the orifice plate).

The measured discharge coefficients, C_d, for the single-hole orifice plate of m = 0.386 and those given by B.S. 1042 (1964) are shown in Fig. 335 as a function of Reynolds number, Re_D. It may be seen from the figure that the measured single-hole orifice plate discharge coefficients differ from B.S. values by less than $\pm$ 0.3%.

In Fig. 336 the measured values of single-hole orifice plate discharge coefficients and B.S. 1042 (1964) values and their tolerances are compared. The figure relates to a $Re_d = 5 \times 10^5$ based on the orifice plate hole diameter. It may be seen from the figure that the C_d values are within the tolerances given by B.S. 1042 (1964).

It was noted in Para.2.1.10 that the orifice plates tested do not quite satisfy the standard dimensions given by B.S. 1042 (1964) as regards the larger orifice edge thickness and non-bevelled downstream edge. This may explain why the measured values of the orifice plate discharge coefficients tend to be towards the upper bounds of the B.S. values. The accuracy of the measurement by the weigh-tank apparatus has been described already in Para. 2.2, but it is of some interest to use also the measured orifice plate discharge coefficient to obtain another estimate of accuracy by the process given by B.S. 1042 (1964) and Clark (1965). The results of doing this indicate the system may be classified as Class-A Standard, 95% confidence limits of measurements ± 0.5%.

3.3.2 Multi-hole Orifice Plate Discharge Coefficients

As previously mentioned in Para. 1.1.3, the multi-hole orifice plates with area ratios from m = 0.170 to m = 0.387 were also included in tests to measure the discharge coefficients for interference free flow. The test results cannot be directly compared with B.S. 1042 (1964) values because there are no B.S. values for the multi-hole orifice plate discharge coefficients. However, Fig. 337 shows that the mean values of the discharge coefficients, $\overline{C}_d$, is very much dependent upon the number of holes in the orifice plate, N, and area ratio, m.

The additional parameters affecting the discharge coefficients of the multi-hole orifice plates have been previously mentioned in Para.1.1.3.6.2,and Kolodzie and Van Winkle (1957) have also reported

the effects of these parameters for Reynolds numbers less than 2×10^4. For the present work C_d is, to a greater or lesser extent, found to be affected by

(i) The number of holes, N;

(ii) The pitch/diameter ratio, $p/_d$;

(iii) The thickness/diameter ratio, $t/_d$;

(iv) The area ratio, m;

(v) The orientation of the orifice plate relative to the connections of the high and low pressure tappings of the carrier ring;

(vi) The Reynolds number, Re_D or Re_d.

In Fig. 338 it may be seen that for the orifice plates with the same area ratio of m = 0.17, the largest values of C_d are measured with the 9-hole orifice plate, and the lowest values of C_d are obtained by the 3-hole orifice plate. The maximum difference in C_d is about 5.5%. In the same figure the comparison for the two 4-hole orifice plates shows that, with a constant value of t/d, C_d increases as p/d increases. The maximum difference in C_d is 0.2%.

In Fig. 339 the plots of C_d against Re_D are shown for the 4-hole and 3-hole orifice plates with the same area ratio of m = 0.231. An investigation of the orientation of the orifice plate relative to the pressure tappings of the carrier ring is made for the 4-hole orifice plate. It may be seen that there is a variation in C_d, which is about 0.5% .

3.4 Static Pressure Tappings

In Para. 2.3.2 the difficulties, which were experienced with the static pressure tappings in obtaining reliable static pressure readings, were described. It is to be expected that the static pressure gradient far upstream and downstream of the bend should be substantially equal, and should correspond with the straight duct friction gradient. Figs. 340 to 344 show test results of that nature and it may be seen that the static pressure tappings of 6.35 mm. diameter give the head loss coefficients which correspond most closely with the expectation. In particular, it may be seen from Fig.344 that the most satisfactory static pressure measurements are obtained by taking the bottom readings upstream of the bend, and either top, bottom or mean values downstream of the bend. In Figs. 345 to 354 the measured upstream head loss coefficients and expected friction gradient (hydraulically smooth) are plotted. The plots are given from $Re_D = 0.8 \times 10^5$ to $Re_D = 6.1 \times 10^5$. It may be seen from Fig. 44 that the bottom static pressure tappings of 6.35 mm diameter give head loss coefficients accurately consistent with the expected friction gradient. From the totality of these tests it was concluded that the bottom static pressure tappings upstream, and both top and bottom static pressure tappings downstream, yield reliable static pressure measurements.

3.5. Head Loss Coefficients of Bends and Orifice Plates for Interference Free Flow

The derivation of interaction coefficients, C_i, requires the measurement of component head loss coefficients, i.e. K_b and K_o,

in interference free flow and the measurement of the head loss coefficients of the componenents, i.e. K_{b-o} or K_{o-b}, in combination. The test results in interference free flow are described in this paragraph. In these tests only the preferred static pressure tappings, as described in the previous paragraph, were used (see Para. 2.3.4 for the orifice plates).

3.5.1. Bend Head Loss Coefficients

In Figs. 50 to 77 the test results, and the derivation from them of the values of K_G (the gross bend head loss coefficient) are shown. In setting up the various bends in the line it was necessary to insert straight lengths of make up pieces downstream and upstream of the bend. These make up pieces and bends themselves had their defects. They were not all of precisely the same bore. The effect of all defects is present in K_G, but allowances for them have been made in the calculation of K_b (net bend head loss coefficient). The Figs. 50 to 77 cover tests with the bends of $R/_D$ = 1.49, 3.42, 4.18 and 4.89 and Reynolds numbers of $Re_D = 0.8 \times 10^5$ to $Re_D = 5.6 \times 10^5$.

The plots of K_b versus Re_D are shown in Fig. 82. It may be seen that K_b decreases as Re_D increases for each bend tested. In Fig. 83 the plots of K_b versus $R/_D$ are given at constant values of Re_D, and it may be seen that the bend head loss coefficient, K_b, has a larger value at the radius ratio of $R/_D$ = 1.49 because of the predominant effect of the sudden change in flow direction, and a smaller value at the radius ratio of $R/_D$ = 3.42. With the bend of radius ratio of $R/_D$ = 4.89 the bend head loss coefficient, K_b, increases again as the friction losses in the bend tend to become proportional to the axial length of bend itself.

In Fig. 355 a comparison of the present values of K_b with the published values of K_b for different cross sections is shown. K_b is presented as a function of $R/_D$ and the experimental results are presented for $Re_D = 1 \times 10^5$. The figure shows good agreement between the present values and existing published values.

3.5.2 Orifice Plate Head Loss Coefficients

In Figs. 102 to 115 the plots of the measured head loss coefficients, K_o, versus the Reynolds numbers, Re_D, are shown for both single-hole and multi-hole orifice plates. It may be seen from the figures that K_o increases as Re_D increases, and approaches limiting values asymptotically at the higher values of Re_D.

In Fig. 356 the mean values of the measured orifice plate head loss coefficients are compared with those given by B.S. 1042 (1964). The orifice plate head loss coefficients are presented as a function of the area ratios, m. It may be seen that agreement seems satisfactory. Another presentation can also be made by calculating the percentage net pressure loss of each orifice plate which is defined as the ratio of orifice plate pressure loss to the maximum pressure difference across the orifice plate, i.e. $K_o/K_{O.P.}$. For this reason, in Figs. 357 and 358, the percentage net pressure losses are plotted against the Reynolds numbers, Re_D. Then, the mean values of the percentage net pressure losses are shown as a function of the area ratios in Fig. 359 together with the curve given by B.S. 1042 (1964). The values obtained for the single-hole orifice plates are in close agreement with B.S. values. For the multi-hole orifice plates there are no

B.S. values but Fig. 359 shows that the percentage net pressure loss of multi-hole orifice plate is larger than the percentage net pressure loss of the single-hole orifice plate of the same area ratio.

As previously mentioned in Para. 1.1.3.8 the head loss coefficients of the multi-hole orifice plates are also dependent upon other additional parameters such as the number of holes on the orifice plate (N), the pitch/diameter ratio (P/d), etc. For both single-hole and multi-hole orifice plates of the same area ratios of m = 0.38 and 0.23 the plots of K_o versus Re_D are shown in Figs. 360 and 361 . It may be seen from these figures that for a constant value of Re_D, which was ranging from $Re_D = 0.9 \times 10^5$ to $Re_D = 5 \times 10^5$, K_o for the multi-hole orifice plate has a smaller value than K_o for the single-hole orifice plate with the same area ratio. The maximum difference in K_o is 1.4% for the area ratio of m = 0.23. Another presentation of Figs. 360-361 may be seen in Figs.362-363, in which the Reynolds numbers, Re_d, are based on each of the hole diameters of the orifice plates with area ratios of m = 0.38 and 0.23, and for a constant value of Re_d the difference in K_o were found to be smaller, e.g. 1.1% instead of 1.4% for m = 0.23 given in Fig. 361 , than when the comparison was made at the same value of Re_D.

In Fig. 364 the test results of K_o versus Re_D for various multi-hole orifice plates with the same area ratio of m = 0.17 are shown. It may be seen that a maximum pressure loss occurs with the 3-hole orifice plate, and a minimum with the 9-hole orifice plate according to the data given in the same figure. In the case of the

4-hole orifice plate it is also evident that K_o decreases as p/d increases.

3.6 Interaction Effects Between Bends and Orifice Plates in Combination

To obtain the interaction effects between various bends and orifice plates measurements were made with the various spacer lengths ranging from L_s/D_s = 0.55 to L_s/D_s = 16.4. In this paragraph the test results are described for interacting bends and orifice plates in combination.

3.6.1 Variations (or errors) in Orifice Plate Discharge Coefficients

In Figs. 116 through 134 the test results for the orifice plate discharge coefficients, C_{di}, versus the Reynolds numbers, Re_D, are shown. With various spacer lengths, various bends of R/D = 1.49, 3.42, 4.18 and 4.89 have been combined with various orifice plates from m = 0.171 to m = 0.508 as indicated in the figures. The test results cover Reynolds numbers from Re_D = 0.9×10^5 to $Re_D = 5.5 \times 10^5$. The derivation of the variation in C_d was made as previously described in Para. 2.3.5.1, and the plots of mean variations in C_d versus the spacer lengths, L_s/D_s, for various bend-orifice plate combinations are shown in Figs. 135 and 142 . From these test results it was concluded that

(i) With the single-hole orifice plate downstream of the bend the percentage variation in C_d is always a negative value,

and rises to a maximum magnitude, e.g. -3%, between $L_s/D_s = 4$ and 7. The percentage variation has larger magnitudes as the area ratio , m, increases, and larger spacer lengths are needed for larger area ratios for a zero error in C_d;

(ii) With the multi-hole orifice plate downstream of the bend the percentage variation in C_d is usually a positive value depending on the geometry of the multi-hole orifice plate, and falls to a minimum e.g.,-0.4%, between L_s/D_s = 8 and 12.

(iii) With the various orifice plates upstream of the PVC bend of R/D = 4.18 the percentage variation in C_d rises up to + 1.0% as the spacer length, L_s/D_s, falls from L_s/D_s = 3.28 to L_s/D_s = 0.7. (This percentage variation in C_d is shown to be less than + 0.5% at spacer lengths, L_s/D_s, between 1 and 3 according to B.S. 1042 (1964)). With the single-hole and multi-hole orifice plates of m = 0.232 and 0.231 respectively upstream of the glassfibre bend of R/D = 1.49 the percentage variation in C_d is sensitive to the diameter difference at L_s/D_s = 0.55 (see Tables 2 and 3 for the diameter differences between the main duct and bends) for the single-hole orifice plate, e.g. it rises to + 3%.

In Figs. 365 and 366 a comparison of the percentage mean variations in C_d against L_s/D_s for single-hole and multi-hole orifice plates of the same area ratios are shown. It may be seen that the multi-hole orifice plates are not always less sensitive to the changes than the single-hole orifice plates as was thought. Another presentation is given in Figs. 367-371 where the orifice plates have been combined with various test bends, and plots of the

percentage mean variations in C_d against the spacer lengths, L_s/D_s, are shown. It may be concluded that the percentage mean variation in C_d is lesser for the combination of multi-hole orifice plate and bend of $R/_D = 1.49$.

3.6.2 Interaction Coefficients

In Figs. 144 through 248 the test results and the derivation of K^*_{b-o} and K^*_{o-b} (the gross head loss coefficients of combined bend and orifice plate) are shown. In each figure the characteristic data for the combination is also indicated. The values of K^*_{b-o} and K^*_{o-b} have been corrected, as described in Para. 2.3.5.2 for local head losses due to sudden enlargement and contraction. The net head loss coefficients, K_{b-o} and K_{o-b}, of bends and orifice plates in combination are presented as a function of the Reynolds numbers, Re_D, in Figs. 249 to 269 The figures relate to the various combinations of bends, orifice plates, and spacer lengths, L_s/D_s.

Interaction coefficients, C_i, were calculated from

$$C_i = \frac{K_{b-o}}{K_b+K_o} \text{ or } C_i = \frac{K_{o-b}}{K_o+K_b}$$ where K_b and K_o for approximate values of Re_D have been taken from Figs.82 and 102-115. The plots of C_i against Re_D are shown in Figs. 270 to 289 for various combinations with various L_s/D_s. The test results generally indicate that C_i does not vary substantially with Re_D.

In Figs. 290 to 297 the mean interaction coefficients, $\overline{C}_i$, are plotted against the spacer lengths, L_s/D_s. It may be

concluded that

(i) With the single-hole orifice plate downstream of the bend $\overline{C}_i$ rises as L_s/D_s increases and has a maximum value between L_s/D_s = 3 and 4, and then $\overline{C}_i$ falls to a minimum value between L_s/D_s = 5 and 11. At larger values of L_s/D_s, $\overline{C}_i$ tends to become unity. The variation in $\overline{C}_i$ is larger the larger the area ratio, m;

(ii) It may be seen in some instances, e.g. Figs. 292 and 294 , instead of $\overline{C}_i$ rising as L_s/D_s increases from small values that $\overline{C}_i$ has a relatively large value at small L_s/D_s, that falls with L_s/D_s and then subsequently shows a maximum and minimum. This more complicated behaviour occurred in tests in which the glassfibre bends were used in which there is a known difference in internal diameters between the duct work and bend;

(iii) With the multi-hole orifice plate downstream of the bend the curves show the same trends as those given by the single-hole orifice plate downstream of the bend;

(iv) With the various orifice plates upstream of the bend $\overline{C}_i$ becomes less than unity and then increases as L_s/D_s decreases to L_s/D_s = 0. The variations in $\overline{C}_i$ with area ratio is small. If the sudden diameter change in the vicinity of the orifice plate, e.g. with the glassfibre bend downstream of the orifice plate, occurs $\overline{C}_i$ becomes larger, and is more affected by the multi-hole orifice plate of the same area ratio.

In Figs. 372 and 373 a comparison of $\overline{C}_i$ against L_s/D_s for single-hole and multi-hole orifice plates of the same area

ratios are shown. It may be seen that the curves give the same trend, but the values of $\overline{C}_i$ for the multi-hole orifice plates are below the values of $\overline{C}_i$ plotted for the single-hole orifice plates. The effect of the larger diameter of the glassfibre bend of $R/D = 1.49$ becomes evident at $L_s/D_s = 0.55$, and the multi-hole orifice plates seem less sensitive to this diameter change.

In Figs. 374 to 379 the values of $\overline{C}_i$ are plotted against L_s/D_s for the various bends upstream of an orifice plate. In these figures the effect of the greater differences with regard to the glassfibre bend diameters of $R/D = 1.49$, 3.42 and 4.89 at $L_s/D_s = 0.55$, 1.1 and 2.0 respectively may be seen. It seems that a larger variation in $\overline{C}_i$ occurs with the glassfibre bend of $R/D = 1.49$ and a smaller variation with the glassfibre bend of $R/D = 3.42$.

In Figs. 298 to 333 the test results show that C_i is close to unity for $L_s/D_s = 45$.

CHAPTER IV

DISCUSSION

4.1 Orifice Plates in Interference Free Flow

The pressure (or head) loss coefficient of an orifice plate, K_o, varies rapidly with the area ratio, m. Other parameters, such as the orifice edge thickness/diameter ratio (t/d), Reynolds number (Re_D) and in the case of multi-hole orifice plates the pitch/diameter ratio (p/d), the orientation of the holes, have some influence on K_o. However, when the results of head loss tests on orifice plates with different area ratios are compared directly using K_o values, these smaller variations due to the secondary parameters can often be masked. In order to highlight the effects of these other parameters, Ward-Smith (1968) has introduced an alternative dimensionless quantity. The pressure drop parameter, ψ_o, is defined by the relation

$$\psi_o = \frac{1}{m(1 + \sqrt{K_o})} \qquad (1)$$

Ward-Smith (1968) provides a full discussion of the variation of ψ_o with m and t/d. In particular, for the free jet flow regime, with which the present tests correspond, a simple one-dimensional analysis of the flow shows that $\psi_o \approx C_c$ (see Para. 1.1.3.8).

For each orifice plate tested the experimental pressure drop parameters, ψ_o, are plotted against the Reynolds numbers, Re_D in Figs. 380 and 381. It may be seen that ψ_o slightly decreases as Re_D increases and tends to an asymptotic value at the higher Reynolds numbers and the smaller area ratios. From these figures the mean values of the pressure drop parameters, $\overline{\psi_o}$, are obtained, and

the plots of $\overline{\psi}_o$ versus m are shown in Fig. 382. In B.S. 1042 (1964) it is assumed that C_c is given by

$$C_c(m,0) = \frac{1}{m(1 + \sqrt{K_o})} \qquad (2)$$

To compare the present test results the values of C_c given by B.S. 1042 (1964) are also plotted in Fig. 382. It may be seen that the results for the single-hole orifice plates are in close agreement. The reason why the $\overline{\psi}_o$ values for the multi-hole orifice plates are generally higher, e.g. the maximum difference in $\overline{\psi}_o$ is 3.0% for the 9-hole orifice plate of m = 0.171, may be explained by the relationships given in Fig. 356 and Eq. (1) itself.

Ward-Smith (1968) has also developed correlations for published experimental values of ψ_o and K_o where, at the high Reynolds numbers under consideration, it was assumed that ψ_o and K_o were independent of Re_D. These correlations are

$$\text{(i)} \quad \psi_c = 0.6081\left[1 + (t/d)^{3.5}\right]\left[1 - m^{2.6}\right] + m^{2.6} \qquad (3)$$

where ψ_c = correlated orifice plate pressure drop parameter

t/d = thickness ratio

m = area ratio.

Eq. (3) is given for $0 < t/d < 0.8$.

$$\text{(ii)} \quad K_c = \left[\frac{1}{0.608\,m\,(1 - m^{2.6})(1 + (t/d)^{3.5}) + m^{3.6}} - 1\right]^2 \qquad (4)$$

where K_c = correlated orifice plate head loss coefficient

t/d = thickness ratio

m = area ratio

Eq. (4) is said to correlate the experimental data in the ranges

$$0 < t/d < 0.6, \quad 0 < m < 0.75, \quad 0.57 < K_o < 35000$$

The overall root-mean-square errors in ψ_c and K_c are also said to be 3.1% and 9.5% respectively. The above correlations were obtained over a wide range of experimental data, including precision-made orifice plates and multi-hole plates which were crudely fabricated, which explains the large tolerance bands.

In Table 6 values of $\overline{\psi}_o$ and $\overline{K}_o$ as derived from the present tests are compared with values of ψ_c and K_c calculated from Eqs. (3) and (4). It may be seen that the errors in $\overline{\psi}_o/\psi_c$ and $\overline{K}_o/K_c$ are within 3.1% and 6.6% respectively, i.e. $\overline{\psi}_o > \psi_c$ and $\overline{K}_o < K_c$. However, it is to be noted that the values of $\overline{\psi}_o$ and $\overline{K}_o$ have been obtained by averaging the values for each orifice plate at the various Reynolds numbers.

As mentioned in Paras. 1.1.3.4 and 1.1.3.5., the derivations of the discharge coefficient, C_d, for orifice plates have been studied by many investigators. Fig. 336 shows that the present test results of C_d for the single-hole orifice plates are within the limits of B.S. 1042 (1964) values. In Fig. 337, in the range of Re_D employed, the mean values of C_d are plotted against m. It may be seen from this figure that the parameters involved in multi-hole orifice plates produce different discharge coefficients which are larger than the discharge coefficients for the single-hole orifice plates of the same ratio. The additional parameters such as p/d, N, A_f/A_t, etc., will also affect C_d. These effects are apparent in Fig. 364.

4.2. Interaction Effects

From the test results it has become evident that an interaction occurs between closely spaced bends and orifice bends.

4.2.1. Effects of Bends Upon Discharge Coefficients

As mentioned in Para. 1.1.3.6.3., the orifice plate discharge coefficients are also affected by upstream and downstream conditions. The effect of installation has been described in Standard Codes, e.g. B.S. 1042 (1965), and recommendations have also been given. It is shown in B.S. 1042 (1965) that

i) For an orifice plate downstream of a single 90^{o} bend the error (or variation) in C_d is negative, and has a larger magnitude as the spacer length decreases from $L_s/D_s = 12$ to $L_s/D_s = 4$; for example the error in C_d is about - 2% at $L_s/D_s = 4$ for an orifice plate of $m = 0.3$, and - 6% for $m = 0.6$;

ii) For an orifice plate upstream of a single 90^{o} bend the error in C_d is positive, of small magnitude, and is less than + 0.5% between $L_s/D_s = 1$ and 3 for all sizes of orifice plates.

It should be noted that B.S. 1042 values are given for single-hole orifice plates, and may not be valid for multi-hole orifice plates. It is in fact evident from Figs. 135 and 141 that the present test results for single-hole orifice plates are in fair agreement with B.S. values but the results for multi-hole orifice plates show a quite different trend (see, for example, Fig. 136). The magnitude and direction of the error in C_d will depend upon the conditions existing in the flow and the geometry of multi-hole

orifice plate in combination. The magnitude of error in C_d is usually positive as typically shown in Figs. 136 and 141 (see also Para. 3.6.1.).

4.2.2. Interaction Coefficients

In Para. 1.1.4.3 the definition of the interaction coefficient, C_i, has been given. For closely spaced bends and orifice plates the primary and secondary interactions will occur and affect the pressure loss in the system as previously mentioned in Para. 1.1.4.1. With a bend upstream of the orifice plate, as based on the work of Ward-Smith (1976), a favourable interaction may be expected for the spacer lengths less than $L_s/D_s = 2$. At the higher values of L_s/D_s the secondary interaction will be dominant and C_i will be unity when the velocity profile is completely re-developed. With an orifice plate upstream of the bend, as described in Para. 1.1.4.2.2, an unfavourable interaction will be expected for the spacer lengths less that $L_s/D_s = 7$. Again at the higher values of L_s/D_s, C_i will approach to unity.

Test results, such as those of Figs. 290 and 291, have provided some experimental confirmation of the predictions given by Ward-Smith (1976), although it has been found that the interactions are more complex than predicted. From test results (Figs. 290 - 295) it may also be seen that C_i has a maximum between $L_s/D_s = 3$ and 4 and a minimum between $L_s/D_s = 5$ and 11. The magnitude of C_i becomes larger for larger area ratios, m. (e.g., in Fig. 290, at $L_s/D_s = 4$, $C_i \simeq 1.06$ for $m = 0.508$ and $C_i \simeq 1.02$ for $m = 0.232$. At $L_s/D_s \simeq 9$, $C_i \simeq 0.97$ for $m \simeq 0.508$ and $C_i \simeq 1.0$ for $m = 0.232$).

It is also evident in Fig. 372 that C_i shows the same trend for the combinations of bends and multi-hole orifice plates but the values of C_i are smaller than the values of C_i for the same combinations of bends and single-hole orifice plates. The effect of interactions on multi-hole orifice plates of various area ratios for $L_s/D_s \leq 4$ is less than the effect on single-hole orifice plates as shown in Fig. 372. However, in the case of orifice plate-bend combinations C_i does not vary substantially, but for a change in diameter at $L_s/D_s = 0.55$ multi-hole orifice plate of $m = 0.231$ is more sensitive than single-hole orifice plate of $m = 0.232$. (See Figs. 296 - 297).

It is seen in Fig. 290 that C_i falls to a minimum from a maximum between $L_s/D_s = 3$ and 7. As was described in Para. 1.1.4.2.1., the primary interactions will occur between the adverse (positive) pressure gradient on the inner wall of the bend and the negative pressure gradient in the orifice plate when they are combined with a spacer length of $L_s/D_s \leq 2$. With longer spacers and at greater distances away from the bend the static pressure gradient becomes negative, and the non-uniform velocity profile leaving the bend exit will be re-developed. For an insufficient spacer length the flow does not become fully developed between the components, and an unfavourable secondary interaction can occur. As proposed by Ward-Smith (1976) the physical considerations applied to bend and diffuser combinations may be applied for bend and orifice plate combinations.

An attempt will now be made to explain the interactions, and a schematic representation of the effects of spacer length and

configuration on the static pressure distribution will be illustrated as shown in Figs. 383 and 384. In Fig. 383a the static pressure distributions around a bend and an orifice plate are illustrated, and the static pressures on both walls are shown to coincide between 1 and 2 duct diameters downstream of the bend. In Fig. 383b it is supposed that the orifice plate is positioned within those 1 to 2 duct diameters. The postulated effect of this is that the negative pressure gradient associated with the orifice plate limits the region of the adverse pressure gradient associated with the inner wall of the bend. It is also postulated that the effect of this limitation is to reduce the system pressure loss below that which would be associated with the system if a fully developed flow existed with these components. These postulates lead to an initial value of C_i less than 1.0 and a value of C_i which increases as the distance between bend and orifice plate is increased up to approximately 2 duct diameters. In Fig. 383c the orifice plate is at the greater spacer where the interaction of the pressure gradients become less, and the flow in the spacer moves towards the fully developed state as the spacer length is increased. In the limit the value of C_i must be unity, and if it is assumed that non-uniform velocity distribution in the spacer upstream of the orifice plate leads to a greater system loss, then it follows C_i must approach unit value with C_i increasing as the spacer length increases. The simplest consequence of these arguments is that C_i rises monotonically from an initial low value to unit value as the spacer length increases as illustrated in Fig. 383d. However, experimental results are different in that there is a maximum and a minimum in the curve of C_i against L_s/D_s for small values of L_s/D_s (see, for example, Figs.

290 and 291). From the above arguments and experimental results it would seem that, although the broad trends have been satisfactorily predicted, the notion of the interactions of the static pressure gradients is insufficiently refined to account for all the details of the observations. It is possible that the existing small adverse pressure gradient immediately upstream of the orifice plate may affect the interactions of the static pressure gradients; that has not been taken into consideration for the qualitative predictions.

For an orifice plate upstream of the bend the same arguments may be illustrated as shown in Fig. 384. The critical spacer length is about 7 duct diameters, and the adverse pressure gradient after the vena contracta plane of the orifice plate will unfavourably interact with the adverse pressure gradient on the outer wall of the bend (Fig. 384b). Consequently, the value of C_i will be minimum at about $L_s/D_s = 7$. At larger values of L_s/D_s C_i will approach $C_i = 1.0$ as in interference free flow (Fig. 384c). No experiments were made in this range of L_s/D_s. However, for values of L_s/D_s in the range $0 < L_s/D_s < 6$ experiments were made and these are shown in Figs. 296 and 297, where the interaction coefficient is plotted. These figures show a reduction of C_i with L_s/D_s. It may be seen in Fig. 384d that the results are in accord with the predictions of Ward-Smith (1976).

For various bend-orifice plate combinations it is also evident from the test results that

(i) The interaction effect of bends on single-hole orifice plates is dependent upon the area ratio, m, and the value of C_i is

larger than 1.0 between L_s/D_s = 0 and 4 (see Figs. 290 and 374 to 376);

(ii) The interaction effect of bends on multi-hole orifice plates shows the same trend for the curve of C_i against L_s/D_s, but C_i does not vary substantially with m and the initial value of C_i is smaller than 1.0. A maximum value of C_i ($C_i \approx 1.0$) can be seen at about L_s/D_s = 3 - 4 (see Figs. 291 and 377 to 379);

(iii) A comparison of interaction coefficients for single and multi-hole orifice plates of the same area ratios (see, for example, Fig. 372) suggests that the favourable interactions show less variation for a bend and multi-hole orifice plate combination between L_s/D_s = 0 and 4. At higher values of L_s/D_s the values of C_i for multi-hole orifice plates become smaller than the C_i values for single-hole orifice plates. However, it should be noted that for smaller area ratios (e.g. m = 0.23 in Fig. 372), the values of C_i become coincident at about L_s/D_s = 10. It then seems that the effect of secondary interactions can be reduced by the use of smaller area ratios Consequently, provided greater system pressure loss is acceptable, and assuming a fix spacer length, from the point of view of interaction coefficient it is preferable to use orifice plates of small area ratios. The inconvenience of higher system pressure loss is somewhat ameliorated if multi-hole orifice plates are used.

An important outcome of these experimental results is the demonstration that the performance of multi-hole orifice

plates is, in general, less sensitive than that of single hole orifice plates of the same area ratios to interaction effects. This has important implications in the field of flow metering.

It is quite clear that much remains to be done in elucidating the flow phenomena which lie behind the experimental observations. Now that the overall behaviour of combinations of bends and orifice plates has been observed, it would seem that more detailed investigations in a few well chosen instances, are required. The investigations in mind are

(i) Measurement of pressure distributions which will include measurement of the static pressures on both outer and inner walls of the bend;

(ii) Measurement of velocity profiles both upstream and downstream of the orifice plate;

(iii) Flow visulation tests with transparent ducts with air or with water. These tests may have to be limited to low Reynolds numbers;

(iv) If measurements those of such as (i), (ii), (iii) above are carried out with air then turbulence levels could also be measured by means of hot wire anemometers.

However in the opinion of the writer the most fruitful investigation is likely to be the measurement of static pressure distributions.

CHAPTER V

CONCLUSIONS

(i) Measurements of the overall accuracy of the apparatus indicate that the system is a Class-A Standard;

(ii) Tests have been made on orifice plates, including single-hole and multi-hole types, and bends in both interference free and interacting conditions. Measurements have been taken at high flow rates of water, and the Reynolds numbers are in the range $0.7 \times 10^5 < Re_D < 6 \times 10^5$;

(iii) For the same area ratios and flow conditions, the discharge coefficients obtained with multi-hole orifice plates exceed those of single-hole orifice plates;

(iv) Detailed measurements show that the discharge coefficients and head loss coefficients of multi-hole orifice plates are affected by additional factors such as the number of holes, spacing of holes, orientation of holes relative to the pressure connections of the carrier ring, etc.;

(v) Head loss coefficients of both single-hole and multi-hole orifice plates vary with Reynolds number in the range $0.8 \times 10^5 < Re_D < 5.3 \times 10^5$ and rises to a limit at the higher values of Reynolds number ($Re_D \approx 5 \times 10^5$);

(vi) For the same area ratios, the head loss coefficients of multi-hole orifice plates are smaller than those of the corresponding single-hole orifice plates;

(vii) Measurements of the head loss coefficients of 90^{o} bends in interference free flow have been obtained for a range of radius ratios and Reynolds numbers. Where comparisons could be made with existing measurements, good agreement was found;

(viii) For various bend and orifice plate combinations with various spacer lengths ranging from $L_s/D_s = 0$ to $L_s/D_s = 16.5$ it has been found that the effect of the bends on the discharge coefficients of multi-hole orifice plates is, generally, less than that for single-hole orifice plates;

(ix) Interaction effects between bends and orifice plates have been measured, and a wide range of conditions have been investigated. Comparisons have been made between these measurements and the qualitative predictions of Ward-Smith (1976). Some agreement has been observed, but in some circumstances it is found that the interaction is more complex than was predicted;

(x) It is necessary to make more detailed observations in a few instances, to elucidate the evidently complex flow phenomena which occur;

(xi) Some of the experimental data which has been required is potentially of value in appropriate design circumstances.

REFERENCES

A.S.M.E. (1961) "Flowmeter Computation Handbook". American Society of Mechanical Engineers, New York.

A.S.M.E. (1971) "Fluid Meters. Their Theory and Application". Sixth Edition, American Society of Mechanical Engineers, New York.

BARBIN, A.R. and JONES, J.B. (1963) "Turbulent Flow in the Inlet Region of a Smooth Pipe". Trans. ASME, J. Basic Engineering, 85, 29-34.

BRADSHAW, P. (1971) "An Introduction to Turbulence and its Measurement". Pergamon Press, Oxford.

B.S. 1042 (1964) "Methods for the Measurement of Fluid Flow in Pipes". Part 1. British Standards Institution, London.

B.S. 1042 (1965) "Methods for the Measurement of Fluid Flow in Pipes". Part 3. British Standards Institution, London.

CEBECI, T. and SMITH, A.M.O. (1974) "Analysis of Turbulent Boundary Layers". Academic Press, New York.

CHEMIDUS WAVIN (1975) "Pressure Pipes for Water Distribution and Sewage Pumping Mains". Product Literature No. 5. Chemidus Wavin Ltd., Durham.

CLARK, W.J. (1965) "Flow Measurement by Square-Edged Orifice Plate Using Corner Tappings". Pergamon Press, Oxford.

CROOK, A.W. (1974) "The Commissioning of the Hydraulic Rig". Brunel Univ., Dept. of Mech.Eng., Uxbridge.

DEAN, W.R. (1927) "Note On The Motion of Fluid In A Curved Pipe". Phil. Mag., Ser. 7, 4 (20), 208-223.

EASTWOOD, D.W. and SARGINSON, E.J. (1960) "The Effect of A Transition Curve On The Loss of Head At A Bend In A Pipeline". Proc. Inst. Civil Engnrs., 16, 129-142.

ENGEL, F.V.A.E. (1931) "Measurement of Fluid Flow. Tests On The Flow of Water Through Orifice Plates". Civ. Eng., Vol. 26 (306), 21-27.

ENGEL, F.V.A.E. and DAVIES, A.J. (1938) "Velocity Profiles and Flow of Fluids Through A Contracted Pipe Line". The Engineer, London, 166 (4329), 720-722.

ENGINEERING SCIENCES DATA (1972) "Pressure Losses Across Perforated Plates, Orifice Plates and Cylindrical Tube Orifices in Ducts". Engineering Science Data Unit. London. Item No. 72010. 15 pages.

EUSTICE, J. (1911) "Experiments on Stream-Line Motion in Curved Pipes". Proc. Roy. Soc. A., 85, 119-131.

GRAY, S. (1945) "A Survey of Existing Information On The Flow In Bent Channels and The Losses Involved". Power Jets Report No. R1104.

HALMI, D. (1973) "Practical Guide to the Evaluation of the Metering Performance of Differential Producers". J. Fluid Engng., Trans. ASME, 95, 127-141.

HOFMANN, A. (1929) "Der Verlust in 90° - Rohrkrümmern mit gleichbleibendem Kreisquerschnitt". Mitteilungen des Hydraulischen Instituts der Technischen Hochschule, München, 3, 45-67.

ITŌ, H. (1955) "Theoretical and Experimental Investigation Concerning the Flow through Pipe Bends (Report 4. On the Flow through 180° Pipe Bends)". Memoirs Inst. High Speed Mechanics, Tōhoku Univ., Japan, Vol. 11, No. 109, 171.

ITŌ, H. (1956) "On The Pressure Losses For Turbulent Flow In Smooth Pipe Bends". RIHSM. Tōhoku Univ., Japan, Vol. 6, No. 54, 55-102.

ITŌ, H. (1959) "Friction Factors for Turbulent Flow in Curved Pipes". Trans. ASME, Ser. D, 81, 123-134.

ITŌ, H. (1960) "Pressure Losses in Smooth Pipe Bends". Trans. ASME, Ser. D, 82 (1), 131-143.

JOHANSEN, F.C. (1929) "Flow Through Pipe Orifices At Low Reynolds Numbers". Aeronautical Research Committee. Reports and Memoranda No. 1252.

KOLODZIE JR, P.A. and WINKLE, M. VAN (1957) "Discharge Coefficients Through Perforated Plates". A.I.Ch.E. Jnl., Vol 3(3), 305-312.

MILLER, D.S. (1971) "Internal Flow. A Guide To Losses In Pipe and Duct Systems". British Hydromechanics Research Association.

MIYADZU, A. (1936) "Über den Einfluß der Bohrungen auf die Druckanzeige". Ingenieur-Archiv, VII. Band, 35-41.

MOODY, L.F. (1944) "Friction Factors For Pipe Flow". Trans. ASME, 66, 671-684.

PATANKAR, S.V. and SPALDING, D.B. (1967) "Procedure For Solving The Equations of the Two-Dimensional Boundary Layer". Int. J. Heat Mass Transfer, Vol. 10, 1389-1411.

PATEL, R.J. (1974) "A Note On Fully-Developed Turbulent Flow Down A Pipe". Aeronaut. J., 78, 93-97.

SCHLICHTING, H. (1979) "Boundary-Layer Theory". Seventh Edition. New York. McGraw-Hill.

SHAW, R. (1958) "The Measurement of Static Pressure". Report Advisory Group For Aeronautical Research & Development, 163, 1-12.

SHAW, R. (1959) "The Influence of Hole Dimensions On Static Pressure Measurements". J.Fluid Mech., 7 (4), 550-564.

STRAND GLASSFIBRE BROCHURE (1976) "Technical Data Sheets". Strand Glass Company Limited, Brentford.

WARD-SMITH, A.J. (1963) "The Flow and Pressure Losses In Smooth Pipe Bends of Constant Cross Section". J.Roy. Aeronaut. Soc., 67, 631, 437-447.

WARD-SMITH, A.J. (1968) "Some Aspects of Fluid Flow In Ducts". D. Phil. Thesis, University of Oxford.

WARD-SMITH, A.J. (1971) "Pressure Losses In Ducted Flows". Butterworths, London.

WARD-SMITH, A.J. (1976) " Component Interactions and Their Influence On The Pressure Losses In Internal Flow System". Proc. Inst.Mech. Engrs, 190 (8/76), 349-358.

WARD-SMITH, A.J. (1980) "Internal Fluid Flow". Oxford University Press.

WESKE, J.R. and PROVIDENCE, R.I. (1948) "Investigations of the Flow In Curved Ducts At Large Reynolds Numbers". J. App. Mech., 15, 4, 344-348.

WHITE, C.M. (1929) "Streamline Flow Through Curved Pipes". Proc. Roy. Soc. A, 123, 645-663.

ZANKER, K.J. (1961) "Orifice Plate Discharge Coefficients". British Hydromechanics Research Association.

ZANKER, K.J. and BROCK, T.E. (1967) "A Review of the Literature On Fluid Flow Through Closed Conduit Bends". British Hydromechanics Research Association.

BIBLIOGRAPHY

BAINES, W.D. and PETERSON, E.G. (1951) "An Investigation of Flow Through Screens". Trans. ASME, 73, 467-480.

BEITLER, S.R. and BUCHER, P. (1930) "The Flow of Fluids Through Orifices in Six-Inch Pipes". Trans. ASME, 52, 77-87.

BLOOM, G. (1965) "Errorless Orifices". Product Eng., 25, 61-64.

BRADSHAW, P. (1971) "Calculation of Three-Dimensional Turbulent Boundary Layers". J.Fluid Mech., 46, 3, 417-445.

BUCKINGHAM, E. (1956) "Notes on Some Recently Published Experiments on Orifice Meters". Trans. ASME, 78 (2), 379-387.

CUMING, H.G. (1952) "The Secondary Flow in Curved Pipes". ARC, Reports and Memoranda No. 2880, 17 pages.

DIMMOCK, N.A. and PARKER, R. (1957) "A Multi-hole Orifice Plate for Airflow Measurement and Its Calibration by Traversing A Nozzle". NGTE Memo M306, ARC 19876.

DOWDELL, R.B. and CHEN, YU-LIN (1970) "A Statistical Approach to the Prediction of Discharge Coefficients for Concentric Orifice Plates". Trans. ASME, J. Basic Engng., 92, 3, 752-765.

EICHENBERGER, H.P. (1953) "Secondary Flow Within A Bend". J. Math. and Physics, 32, 34-42.

ENGINEERING SCIENCES DATA (1966) "Friction Losses for Fully-Developed Flow In Straight Pipes". Engineering Science Data Unit, London. Item No. 66027. 23 pages.

ENGINEERING SCIENCES DATA (1966) "Pressure Losses in Flowmetering Devices". Engineering Science Data Unit. London. Item No. 66030. 23 pages.

FERRON, A.G. (1963) "Velocity Profile Effects On The Discharge Coefficient of Pressure-Differential Meters". Trans. ASME, 85, Ser. D, 3, 338-346.

HAWTHORNE, W.R. (1950) "Secondary Circulation in Fluid Flow". Proc.Roy.Soc. A., 206, 374-387.

HAWTHORNE, W.R. (1961) "Flow in Bent Pipes". Proc. Sem. on Aer. Sc., 305-333.

HEDMAN, S. (1957) "Method For Computing The Velocity Distribution In A Curved Duct". KTH AERO TN 36. Sweden.

HOWLETT, D.P. (1962) "Pressure Losses In Duct Systems: Part 1". Engng. Materials & Design, 5, 806 -810.

HOWLETT, D.P. (1962) "Pressure Losses In Duct Systems: Part 2". Engng. Materials & Design, 5, 904-909.

HUDIMOTO, B. (1965) "A Method For The Calculation Of The Turbulent Boundary Layer With Pressure Gradient". Kyoto Univ., Faculty Eng. Memoirs, 27, 4, 433-442.

HUNT, B.W. (1968) "Numerical Solution Of An Integral Equation For Flow From A Circular Orifice". J. Fluid Mech., 31, 361-377.

JEPPSON, R.W. (1970) "Inverse Formulation and Finite Difference Solution for Flow from A Circular Orifice". J.Fluid Mech., 40, 215-223.

JUDD, H. (1916) "Experiments On Water Flow Through Pipe Orifices". Trans. ASME, 38, 331-366.

KEULEGAN, G.H. and BEIJ, K.H. (1937) "Pressure Losses for Fluid Flow In Curved Pipes". J.Res.Nat. Bureau of Standards, 18, 89-114.

MARTIN, M.E. and DEVERSON, E.C. (1960) "The Effect of Bend Outlet Conditions In The Pressure Losses In Bent Circular Pipes". ARC CP No. 505.

MASEK, J.A. (1967) "How To Design Orifice Meter Piping for Accurate Flow Measurement". Heating, Piping & Air Conditioning, Vol.39, N.1, 167-172.

MILLS, R.D. (1968) "Numerical Solutions of Viscous Flow Through A Pipe Orifice At Low Reynolds Numbers". J.Mech.Eng.Sci., 10, 133-140.

MORGAN, P.G. (1960) "High Speed Flow Through Perforated Plates". J.Roy.Aer.Soc., 64, 103-105.

MURDOCK, J.W. (1961) "Two-Phase Flow Measurement With Orifices". ASME. Paper 61-WA-27, 14 pages.

McVEIGH, J.C. (1962) "Further Investigations Into the Effect of Roughness of the Orifice Plate on the Discharge Coefficient". Inst.Engrs., 3, 112-113.

OOSTHUIZEN, P.H. (1964) "An Approximate Method for Predicting The Effect of Small Changes In The Initial Velocity Profile On The Coefficient of Discharge of an Orifice Plate". South Africa,Mech.Eng., 238-243.

PIGOTT, R.J.S. (1957) "Losses In Pipe And Fittings". Trans. ASME, 79, 1767-1783.

PUTTASWAMY, T.B. (1964) "The Effect of Upstream Velocity Distribution On Head-Loss Coefficient for Flow Through 90-degree Pipe Bends". Master Thesis. Worcester Polytechnic Inst. Alden Hydraulic Lab.

ROSS, D. (1956) "Turbulent Flow In The Entrance Region Of A Pipe". Trans. ASME, 78, 915-923.

ROUSE, H.and ABUL-FETOUH, A-H. (1950) "Characteristics of Irrotational Flow Through Axially Symmetric Orifices". Trans. ASME,J.App.Mech., 72, 421-426.

SHERMAN, J., GROCHOWSKI,F.A. and SHARBAUGH, J.E. (1960) "Variable Flow Resistance With Adjustable Multi-hole Orifice Plates In Series". Trans. ASME, J.Basic Eng., 645-653.

SPENCER, E.A. and McNULTY, P.J. (1958) "Initial Tests On Two-and Six-Inch Orifice Plates". MERL Fluids Note No. 61, 11 pages, 11 figures.

SPITZGLASS, J.M. (1922) "Orifice Coefficients - Data and Results of Tests". Trans. ASME, 14, 919-974.

SPRENGER, H. (1969) "Pressure Head Losses in 90^{o} Bends for Tubes or Ducting of Rectangular Cross-section". BHRA TT 1027, Translation from Schweizerische Bauzeitung, 87, 13, 223-231. (1969).

SPRENKLE, R.E. (1945) "Piping Arrangements for Acceptable Flow Meter Accuracy". Trans. ASME, 67, 345-360.

STUART, M.C. and YARNALL, D.R. (1944) "Fluid Flow Through Two Orifices in Series - II". Trans. ASME, 66, 5, 387-398.

TECHO, R., TICKNER, R.R. and JAMES, R.E. (1965) "An Accurate Equation for the Computation of the Friction Factor for Smooth Pipes From the Reynolds Number". Trans. ASME, Ser. E, Vol. 32, No.2, P.443.

YARNEL, D.L. and NAGLER, F.A. (1935) "Flow of Water Around Bends in Pipes". Trans. ASCE, Vol. 100, 1018-1043.

WATSON, G.A. (1978) "Flowmeter Types and Their Usage". CME, 27-32.

TABLE 1. Primary Characteristics of Orifice Plates Tested.

Name	Spacing and Number of Holes	Diameter of Hole (d) mm	Area Ratio $m = \frac{d^2}{D^2}$	Velocity Approach Factor $E = \frac{1}{\sqrt{1-m^2}}$	Total Area of Hole $A_o = \frac{N\pi d^2}{4}$ mm^2	Thickness of Hole Edge (t) mm	Pitch (p) mm	Ratio of Thickness to Diameter t/d	Ratio of Pitch to Diameter p/d
S-1	Single Hole	103.41	0.508	1.1609	8398.7	3.152	-	0.030	-
S-2	Single Hole	90.51	0.389	1.0854	6434.0	3.256	-	0.035	-
$S-2_1$	Single Hole	90.30	0.387	1.0845	6404.2	3.256	-	0.036	-
$S-2_2$	Single Hole	90.19	0.386	1.0840	6389.3	3.256	-	0.036	-
S-3	Single Hole	80.05	0.304	1.0496	5032.8	3.151	-	0.039	-
S-4	Single Hole	69.98	0.232	1.0280	3846.2	3.142	-	0.044	-
S-5	Single Hole	67.72	0.218	1.0246	3601.8	3.140	-	0.046	-
S-6	Single Hole	60.10	0.171	1.0149	2836.8	3.140	-	0.052	-

TABLE 1 continued

Name	Spacing and Number of Holes	Diameter of Hole (d) mm	Area Ratio $m = \frac{d^2}{D^2}$	Velocity Approach Factor $E = \frac{1}{\sqrt{1-m^2}}$	Total Area of Hole $A_o = \frac{N\pi d^2}{4}$ mm^2	Thickness of Hole Edge (t) mm	Pitch (p) mm	Ratio of Thickness to Diameter t/d	Ratio of Pitch to Diameter p/d
M-1	Square, 4 Holes	45.12	0.387	1.0845	6395.6	3.225	52.08	0.071	1.154
M-2	Square, 4 Holes	34.90	0.231	1.0277	3826.5	3.090	52.80	0.088	1.512
M-3	Triangle, 3 Holes	40.27	0.231	1.0277	3820.9	3.120	60.62	0.077	1.505
M-4	Square, 5 Holes	29.94	0.213	1.0234	3520.1	3.132	42.56	0.104	1.421
M-5	Square, 9 Holes	19.98	0.171	0.0149	2821.7	3.148	34.82	0.157	1.742
M-6	Square, 6 Holes	24.40	0.170	1.0147	2805.5	3.180	36.68	0.130	1.503
M-7	Square 4 Holes	29.93	0.170	1.0147	2814.2	3.144	52.47	0.105	1.753
M-8	Square, 4 Holes	29.94	0.170	1.0147	2816.1	3.140	44.80	0.104	1.496
M-9	Triangle, 3 Holes	34.51	0.170	1.0147	2806.0	3.144	62.15	0.091	1.800

TABLE 2. Actual Dimensions of the 90° Bends Tested

Name	Radius of Curvature (R) mm	Mean Internal Diameter (D) mm	Integral Tangent mm	Radius Ratio R/D
G.F. - 1.5	228.6	152.79	84.6	1.49
G.F. - 3.5	533.4	155.59	176.0	3.42
PVC - 4.0	604.7	144.47	101.2	4.18
G.F. - 5.0	762.0	155.76	306.5	4.89

TABLE 3. Actual Dimensions of the Straight Ducts

Name	Length (L) mm	Internal Diameter (D) mm
U.T. -1	6000	145.66
U.T. -2	6000	145.05
S.L. -1	152	144.65
S.L. -2	375	144.80
S.L. -3	375	144.93
S.L. -4	760	141.14
S.L. -5	760	145.18
S.L. -6	1370	146.49
S.L. -7	1545	146.01
D.T. -1	5115	144.60

TABLE 4. Manometers Used for Tests

Name of Manometer	Measured Pressure Difference
(Water-Mercury)	0 - 1500 mm of Mercury
(Air - Water)	0 - 1500 mm of Water

TABLE 5. Differences in Local Loss Coefficients Due to Change in Diameter of Spacer Lengths

Arrangement (see figures)	Calculated by Sudden Enlargement and Contraction	Measured at Re_D		
		$1x10^5$	$3x10^5$	$5x10^5$
Fig. 79	0.007	0.007	0.014	0.019
Fig. 80	0.010	0.009	0.019	0.017
Fig. 81	0.014	0.019	0.026	0.031

TABLE 6. Comparisons of Present Test Results

Name	m	t/d	p/d	$\overline{\psi}_o$	ψ_c	$\overline{\psi}_o/\psi_c$	$\overline{K}_o$	K_c	$\overline{K}_o/K_c$
S-1	0.508	0.030	-	0.675	0.675	1.000	3.660	3.665	0.998
S-2	0.389	0.035	-	0.644	0.641	1.004	8.919	9.037	0.986
S-3	0.304	0.039	-	0.632	0.625	1.011	17.603	18.121	0.971
S-4	0.232	0.044	-	0.620	0.616	1.006	35.386	35.859	0.986
S-5	0.218	0.046	-	0.616	0.615	1.001	41.472	41.640	0.995
S-6	0.171	0.052	-	0.613	0.612	1.001	72.758	73.198	0.993

TABLE 6 continued

Name	m	t/d	p/d	$\overline{\psi}_o$	ψ_c	$\overline{\psi}_o/\psi_c$	$\overline{K}_o$	K_c	$\overline{K}_o/K_c$
M-1	0.387	0.071	1.154	0.649	0.641	1.012	8.857	9.177	0.965
M-2	0.231	0.088	1.512	0.626	0.616	1.016	34.881	36.221	0.963
M-3	0.231	0.077	1.505	0.624	0.616	1.012	35.132	36.227	0.969
M-4	0.213	0.104	1.421	0.631	0.615	1.026	41.374	43.966	0.941
M-5	0.171	0.157	1.742	0.631	0.612	1.031	68.170	72.954	0.934
M-6	0.170	0.130	1.503	0.624	0.612	1.019	70.819	74.054	0.956
M-7	0.170	0.105	1.753	0.618	0.612	1.009	72.462	74.123	0.977
M-8	0.170	0.104	1.496	0.617	0.612	1.008	72.733	74.124	0.981
M-9	0.170	0.091	1.800	0.612	0.612	1.000	73.995	74.147	0.997

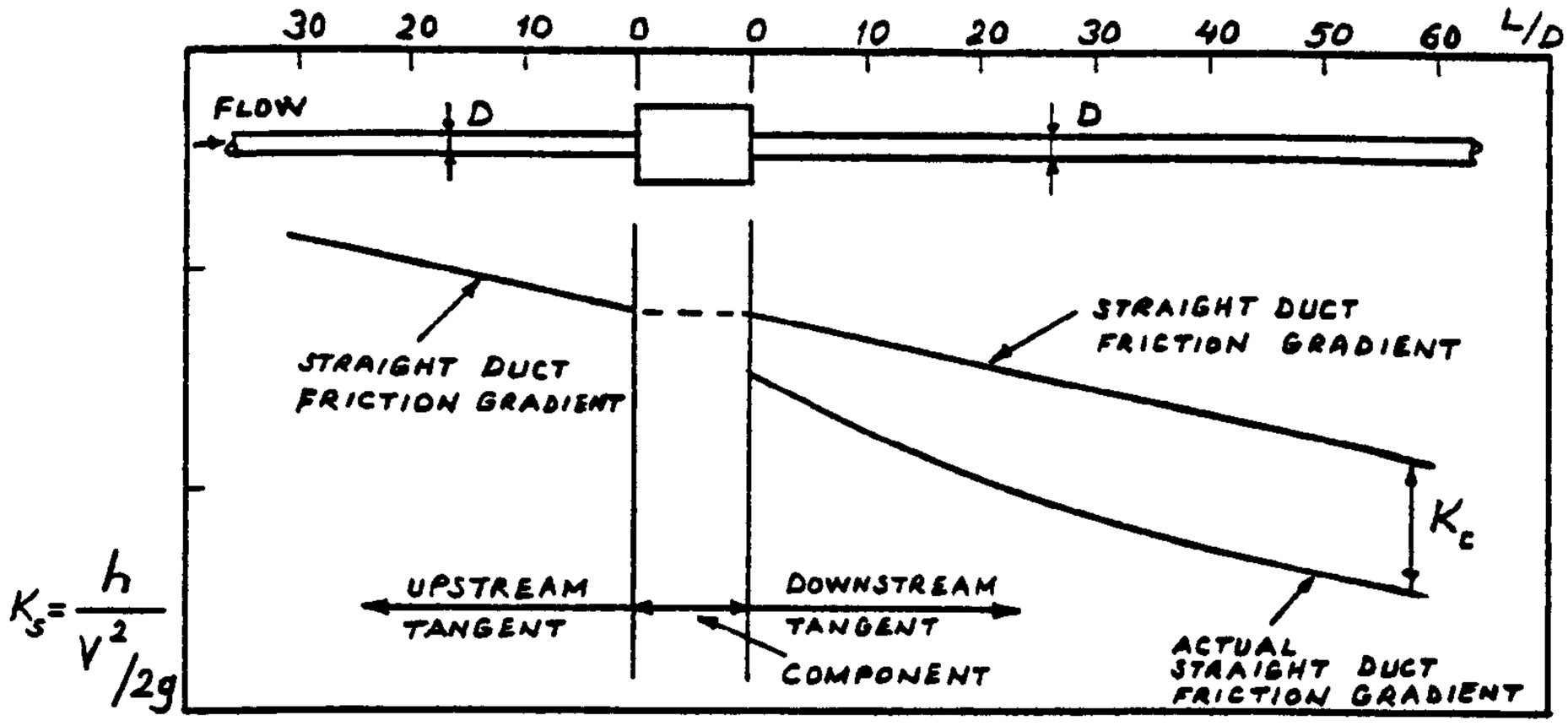

Fig. 1. Definition of component head loss coefficient

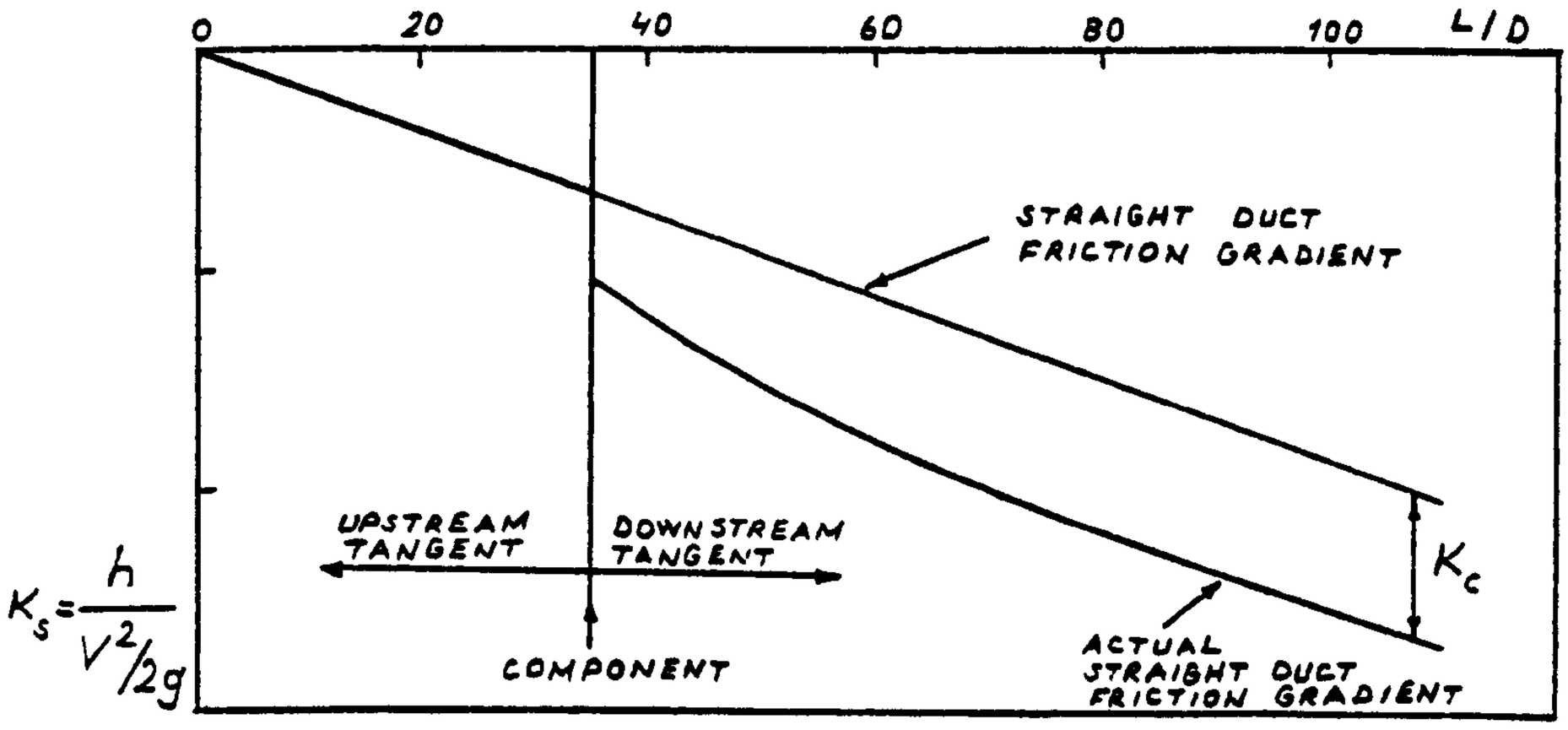

Fig. 2. Definition of system head loss coefficient

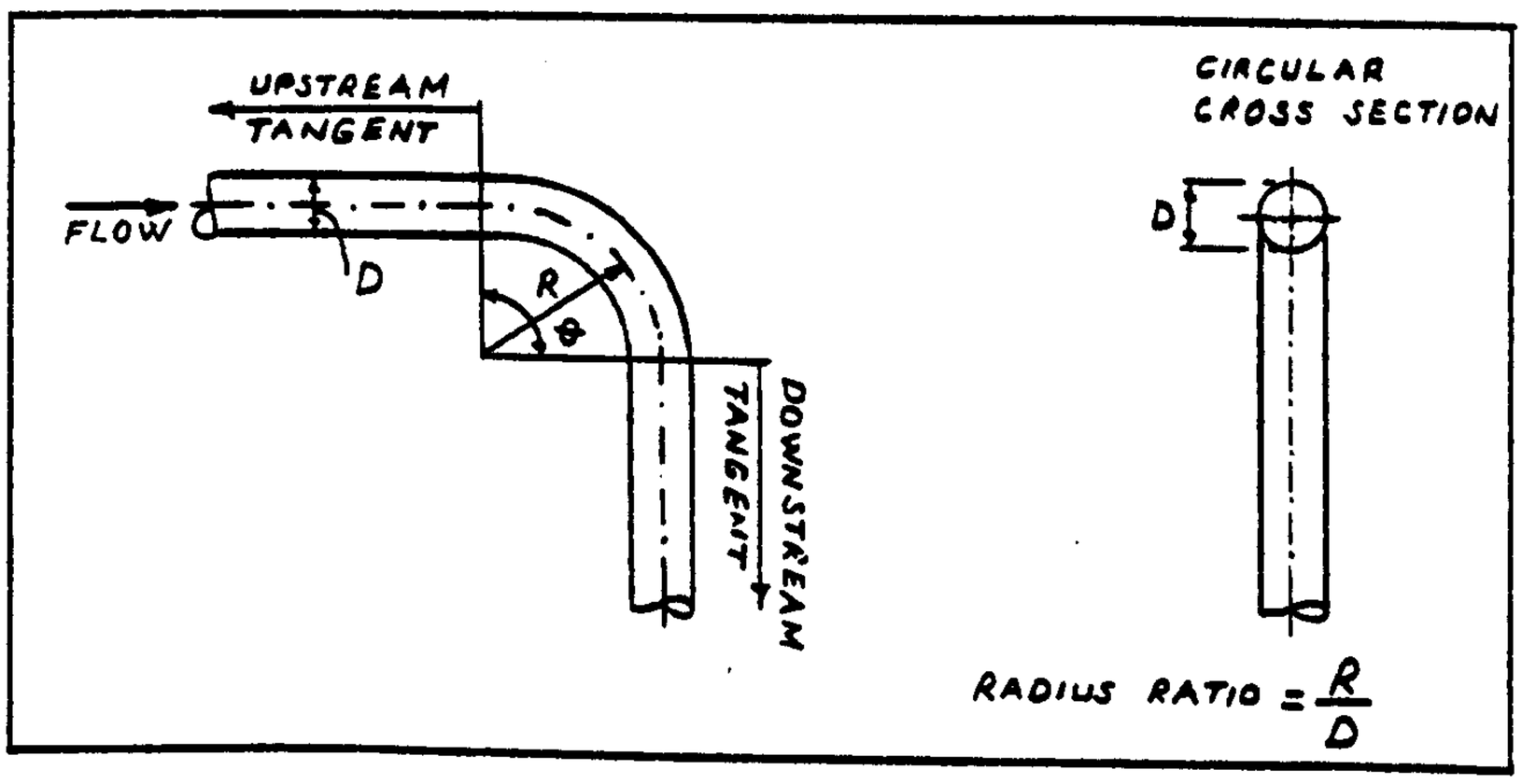

Fig. 3. Definition of bend geometry

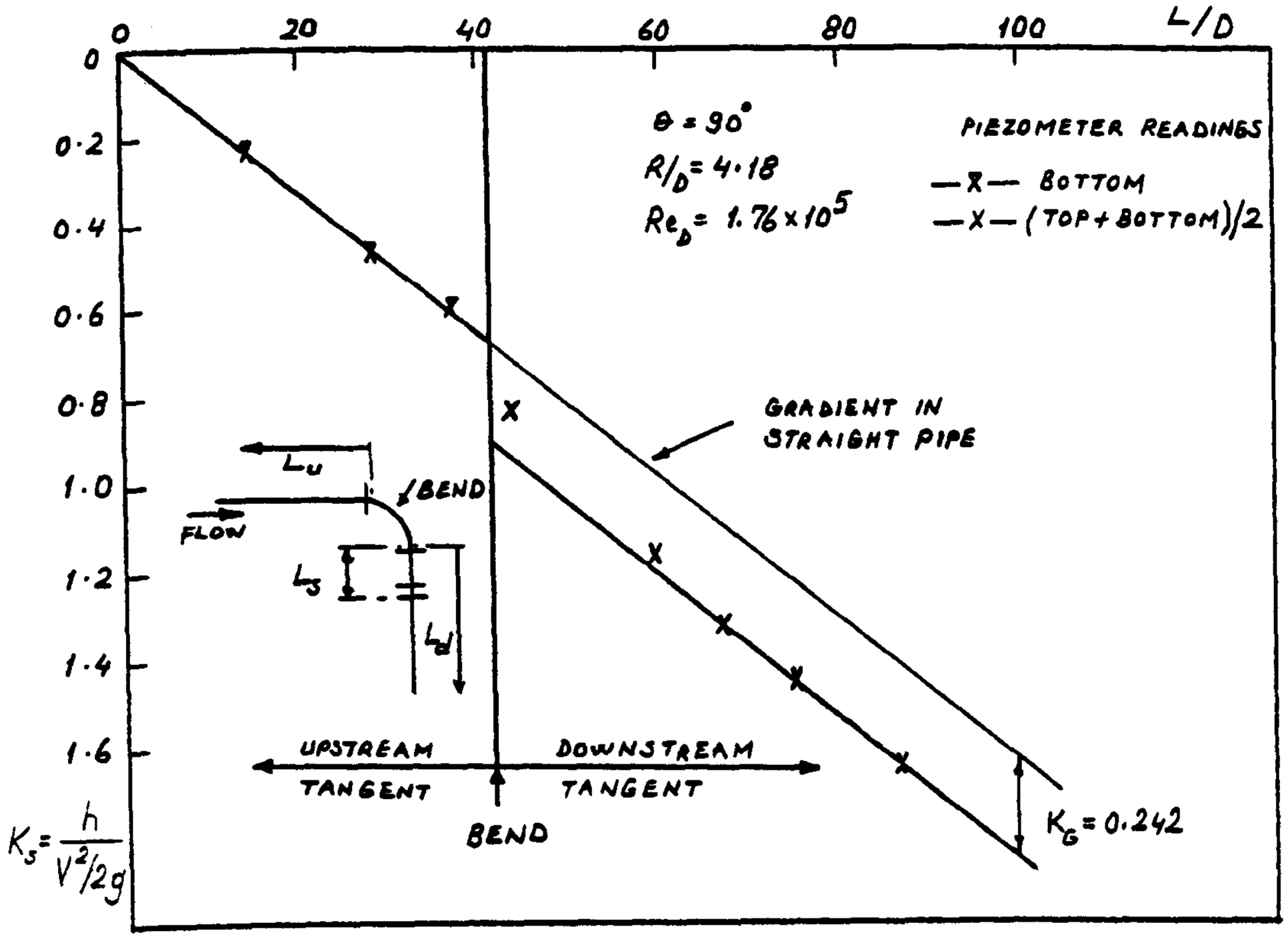

Fig. 4. Typical system head loss coefficient versus axial length

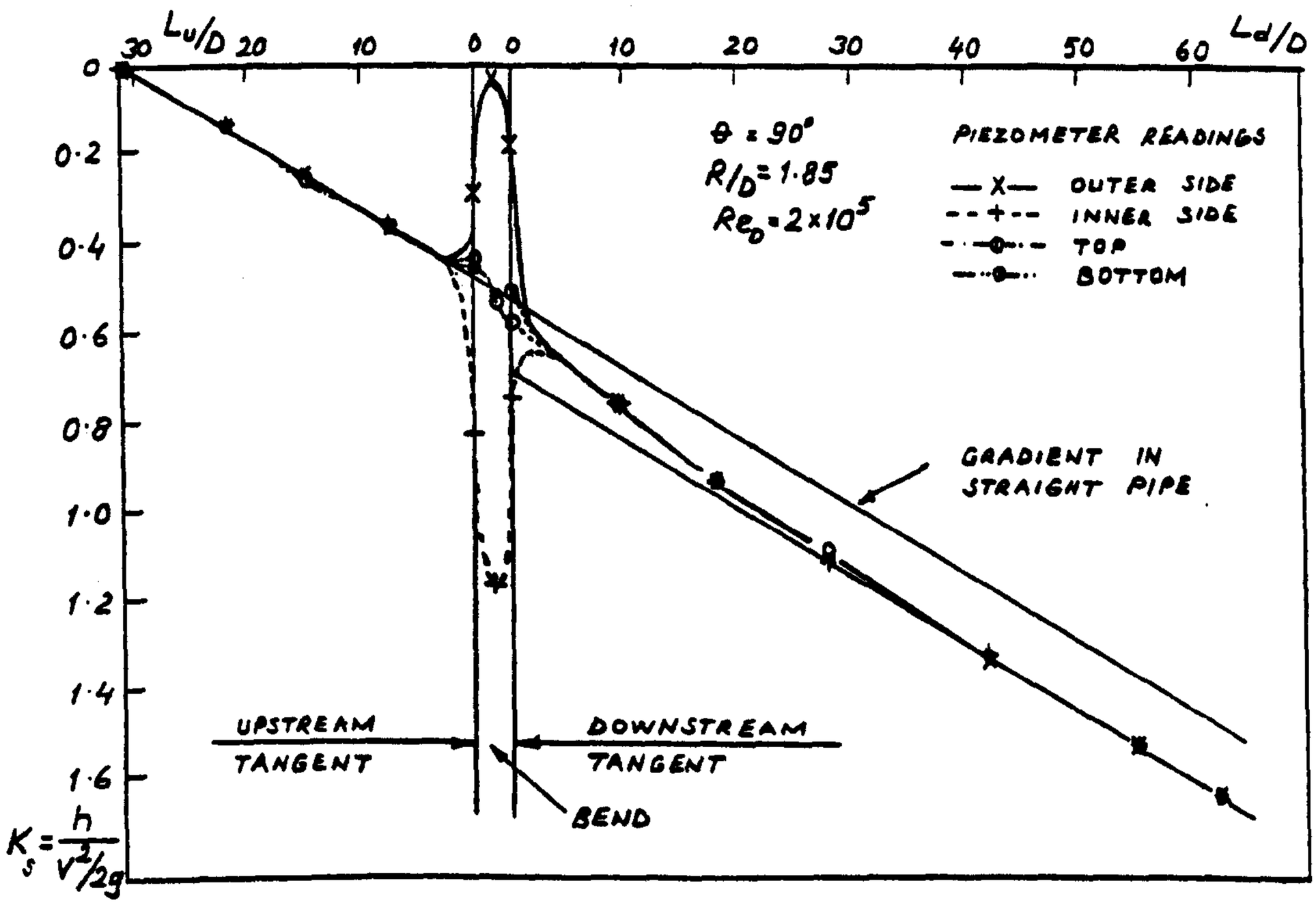

Fig. 5. Typical pressure distribution around a bend with long tangents, from Itō (1960)

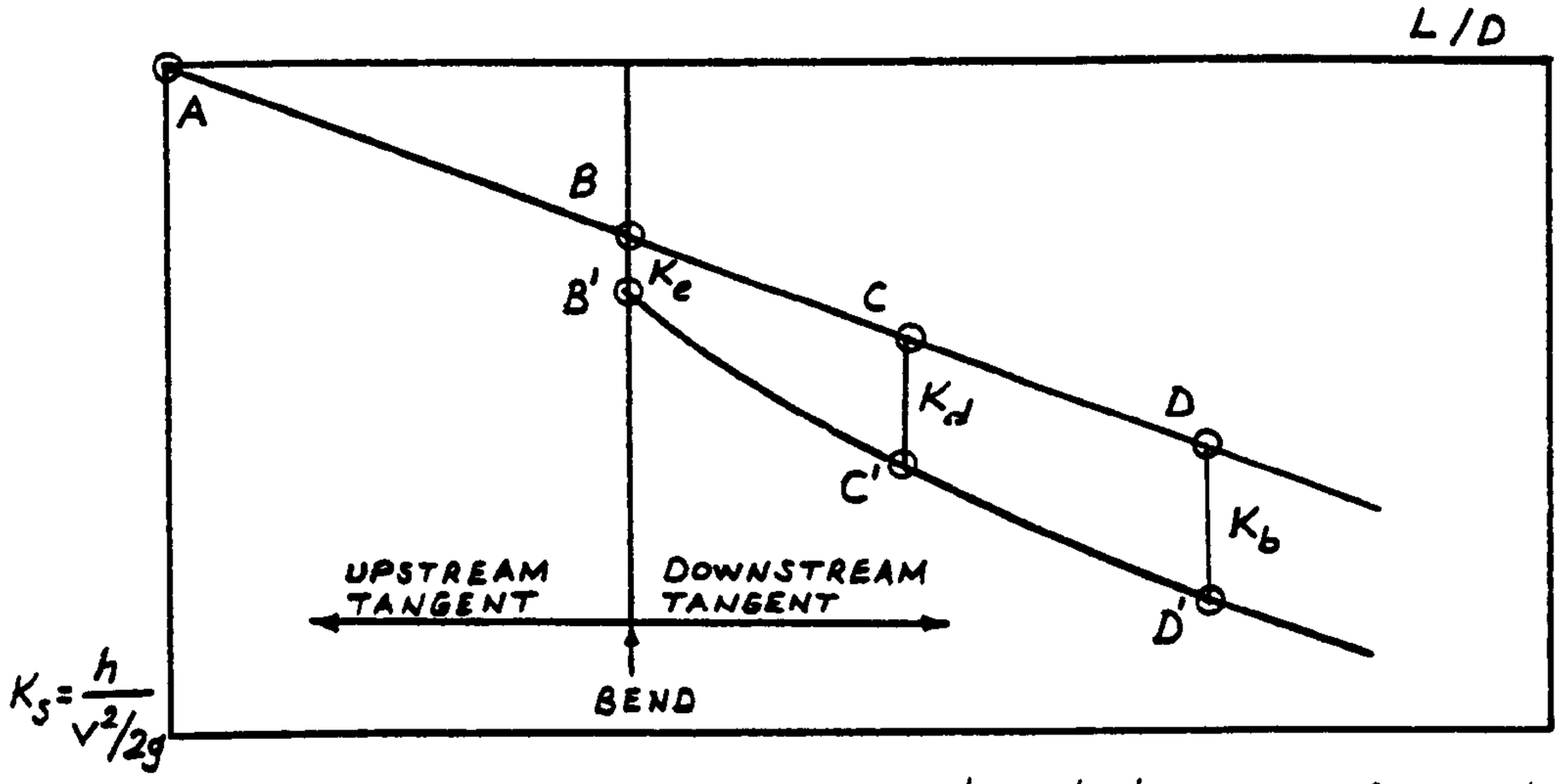

Fig. 6. Definition of bend head loss coefficient

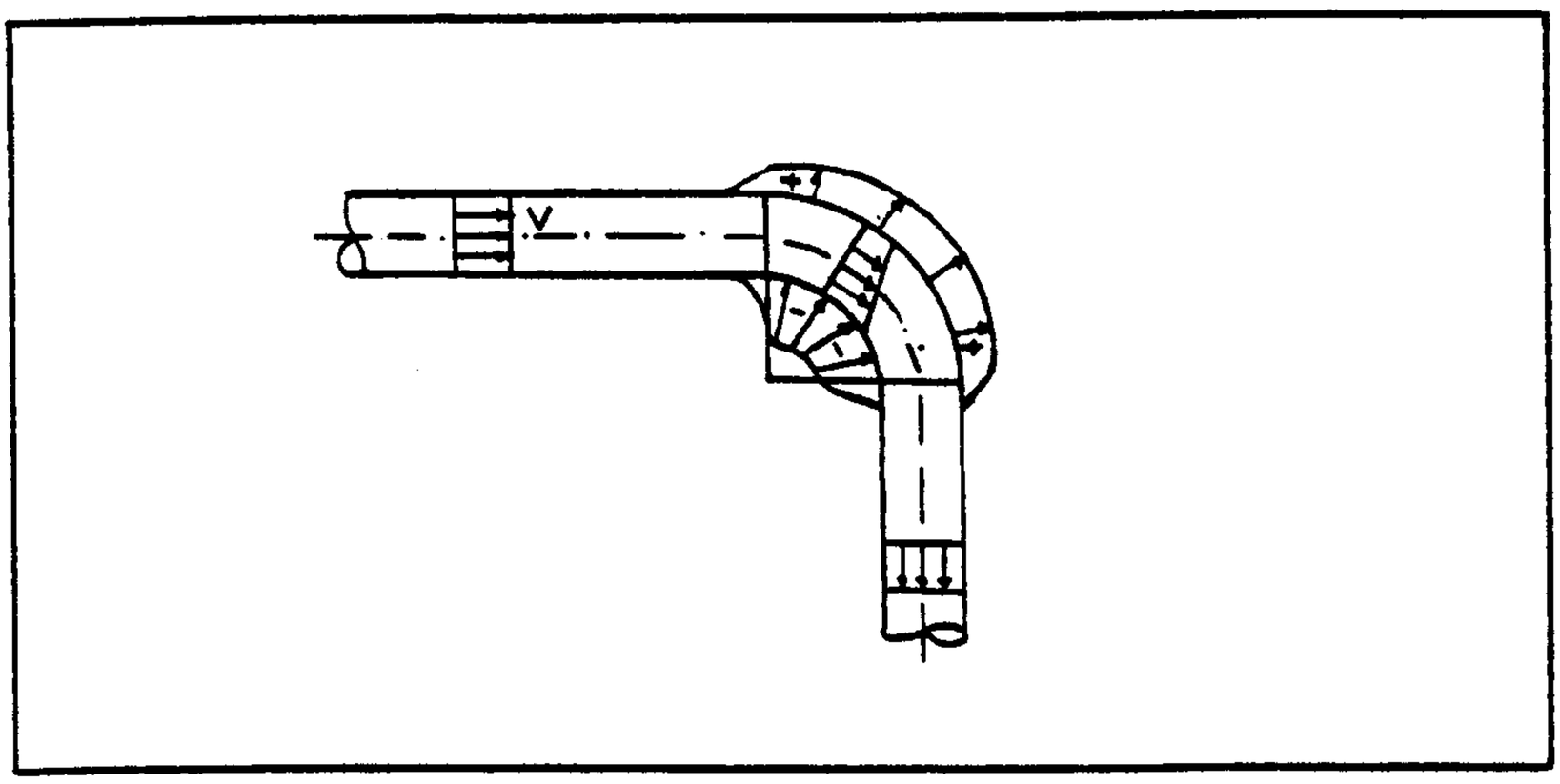

Fig. 7. Flow of an ideal incompressible fluid through a bend (vR = constant)

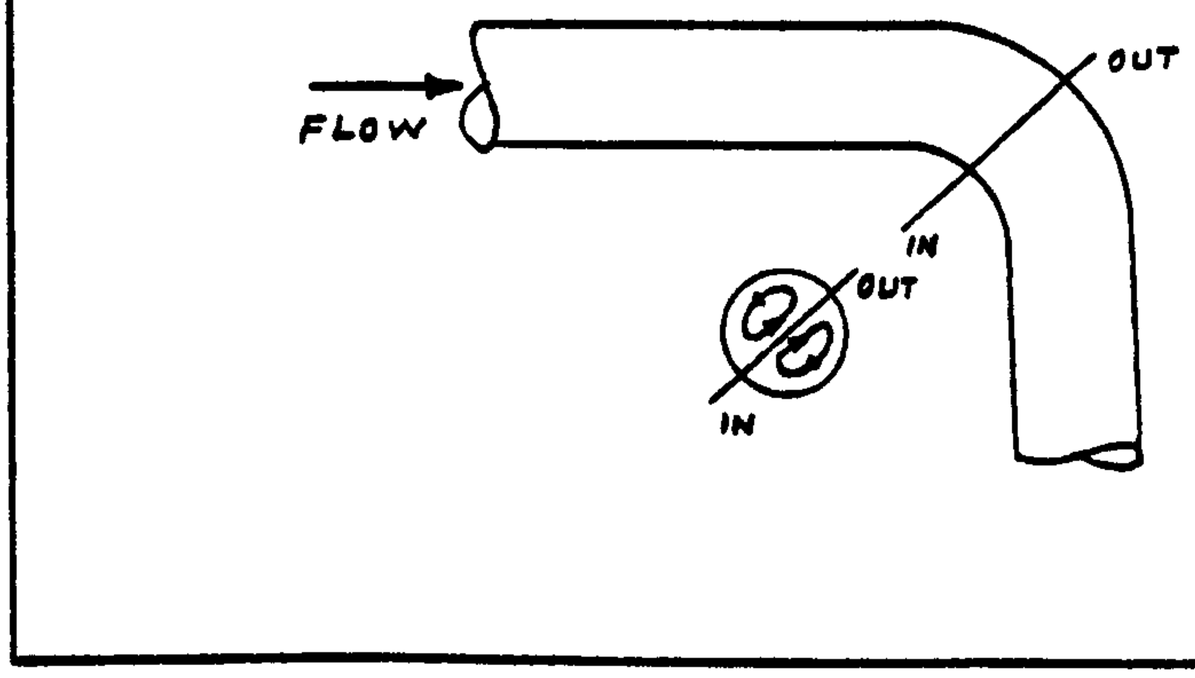

Fig. 8. Secondary flow in a bend

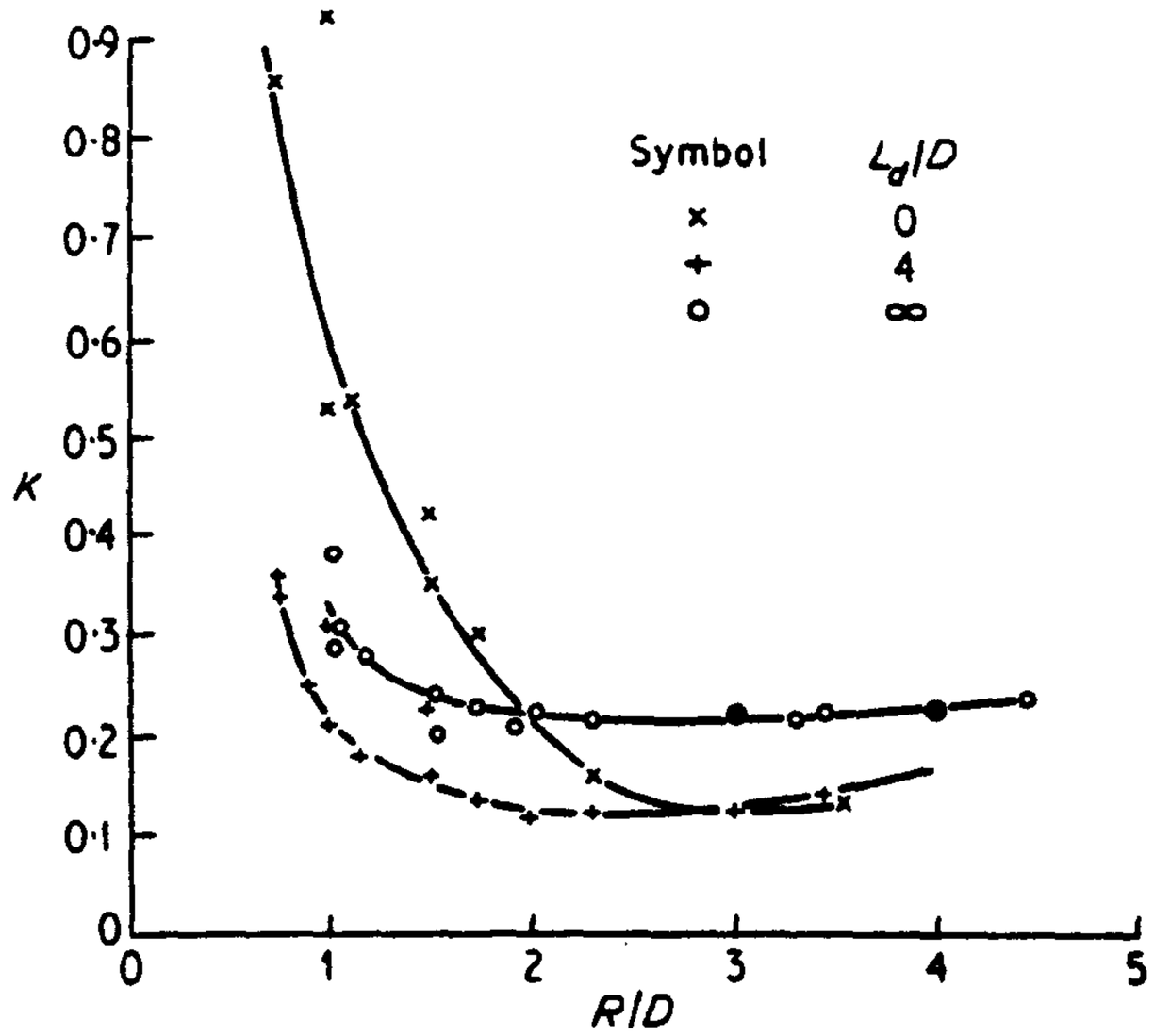

Fig. 9. Effect of length of downstream tangent on the performance of circular-arc bends, $Re_D = 10^5$, from Ward-Smith (1976)

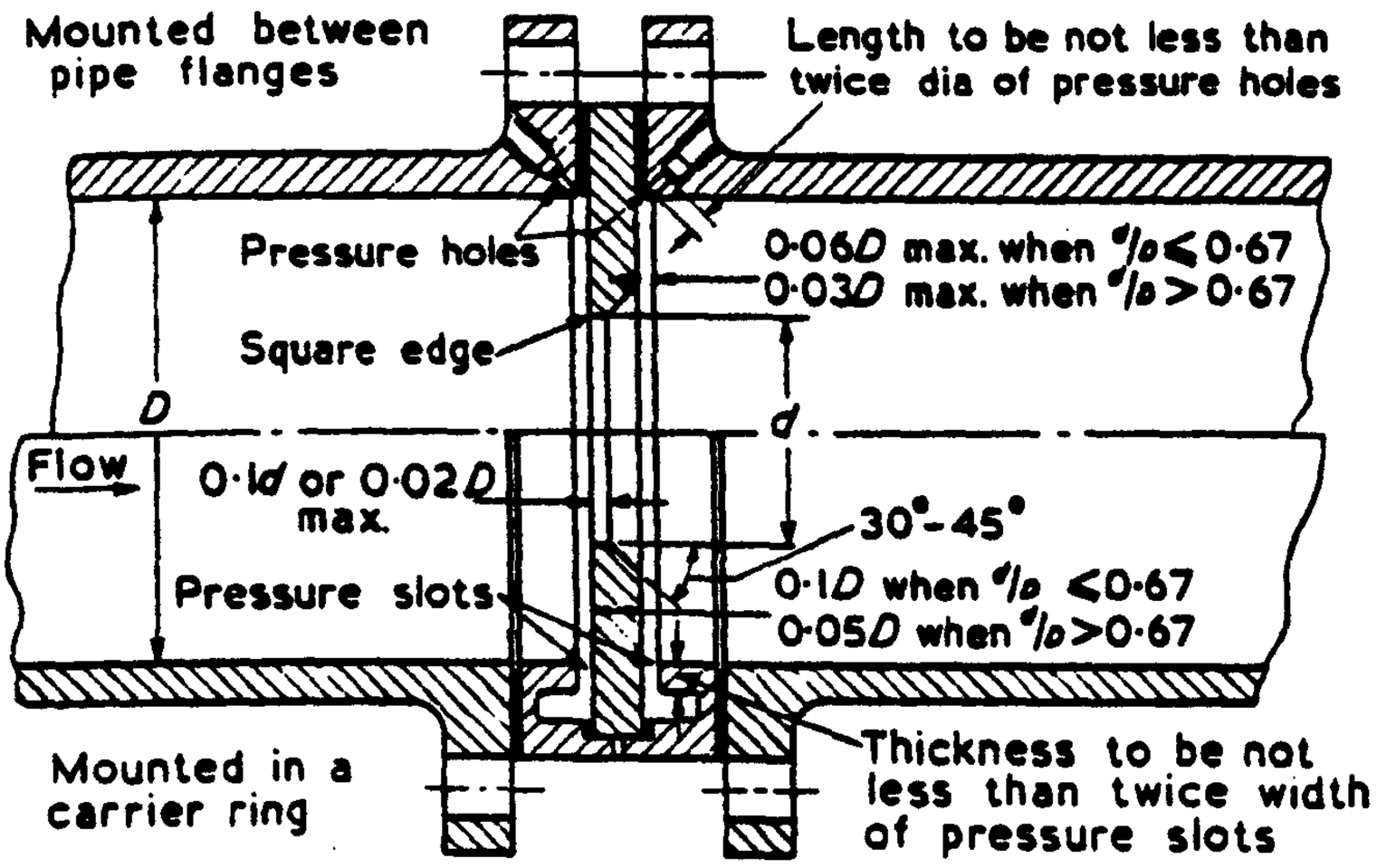

Fig. 10. A standard single-hole orifice plate with corner tappings, from B.S. 1042 (1964)

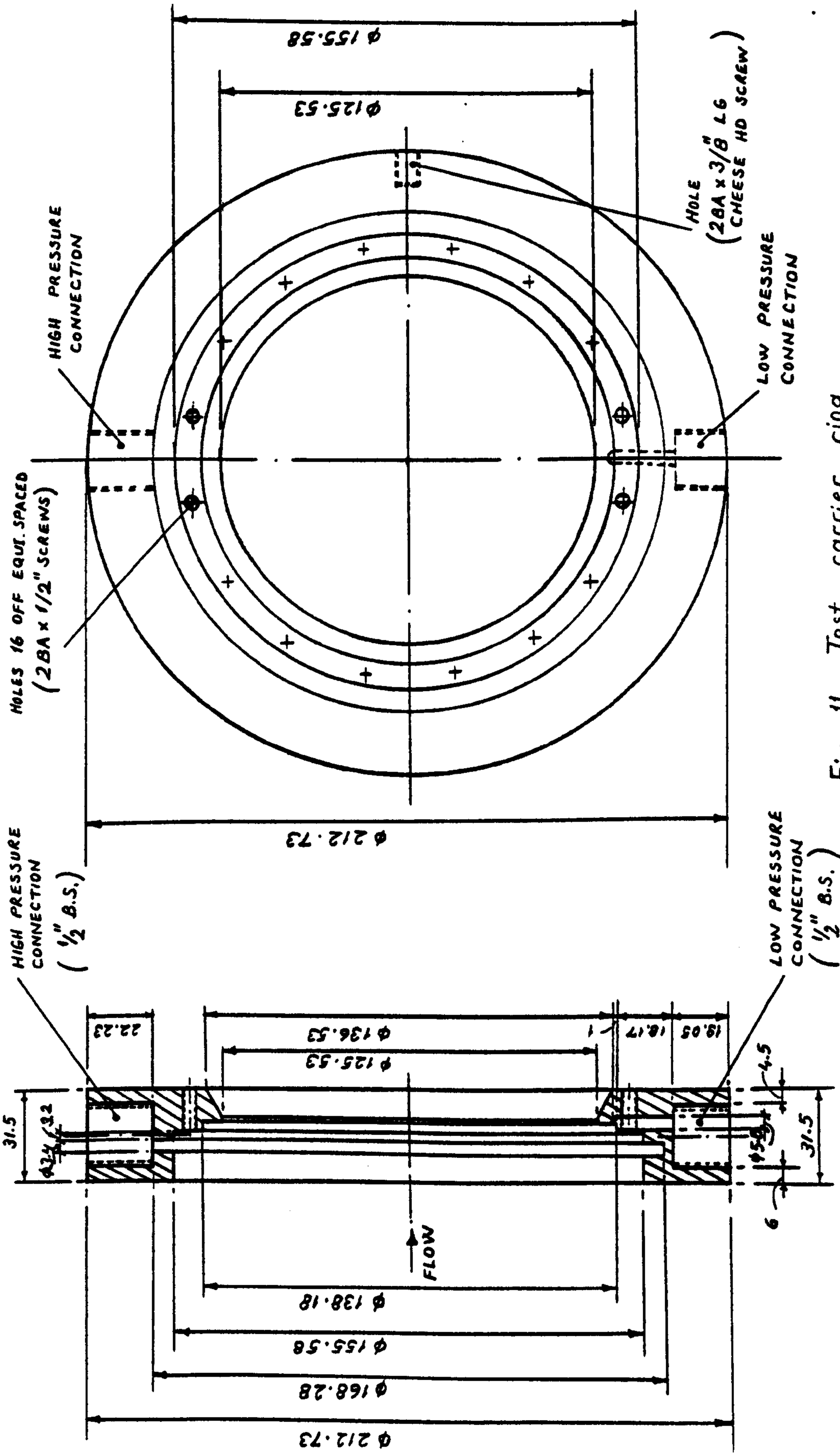

Fig. 11. Test carrier ring

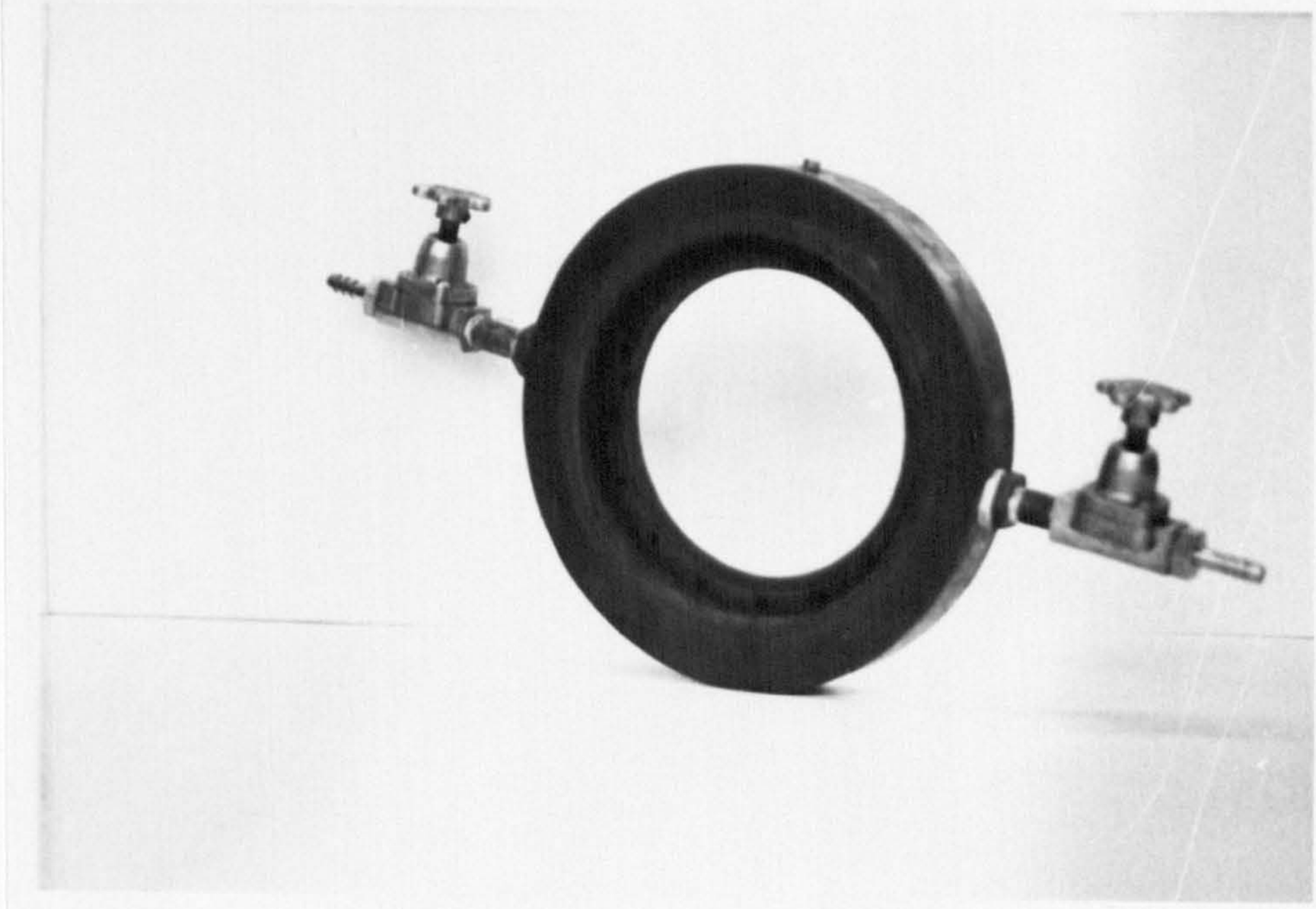

Fig. 12. Test carrier ring

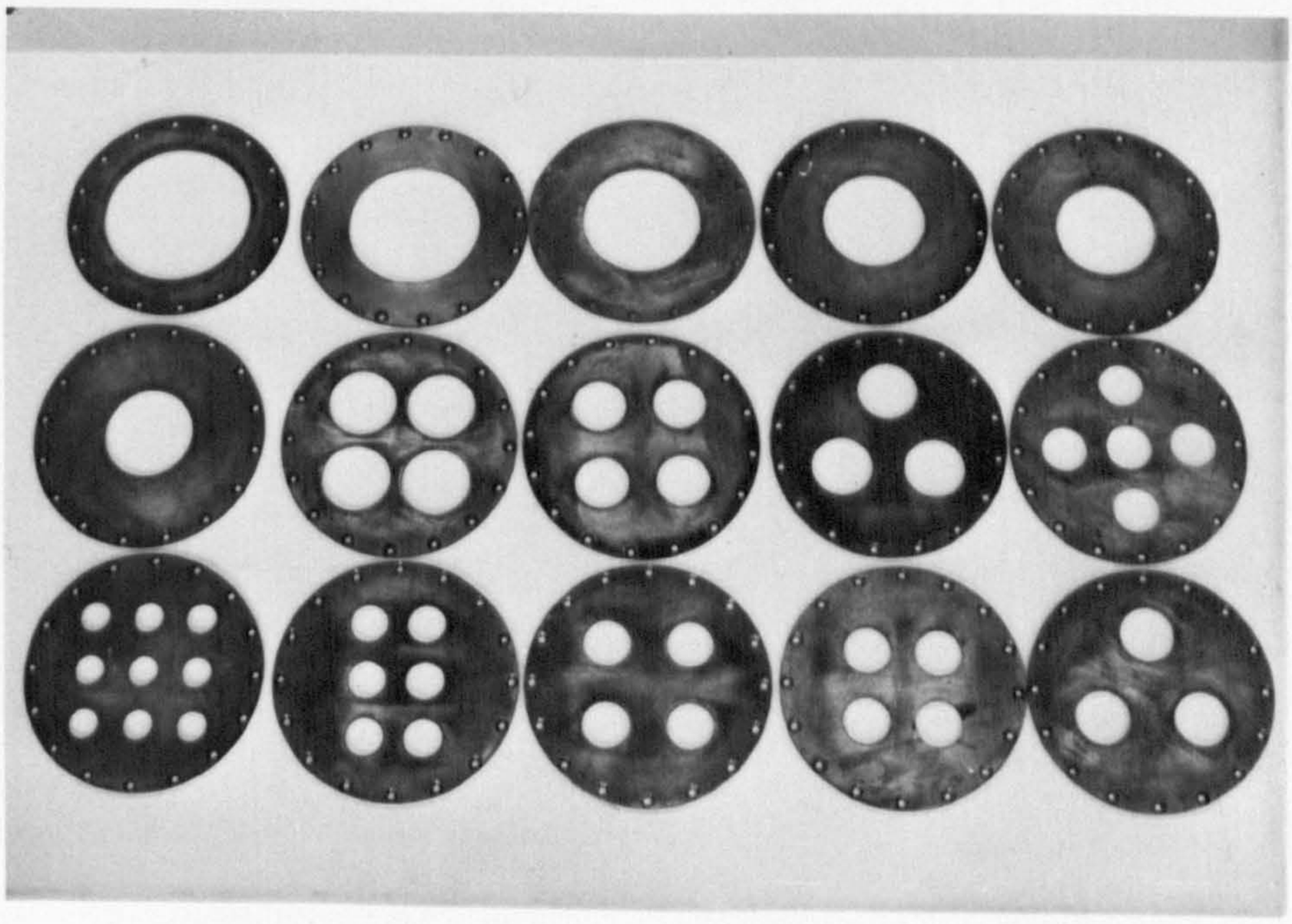

Fig. 13. Single-hole and multi-hole orifice plates tested

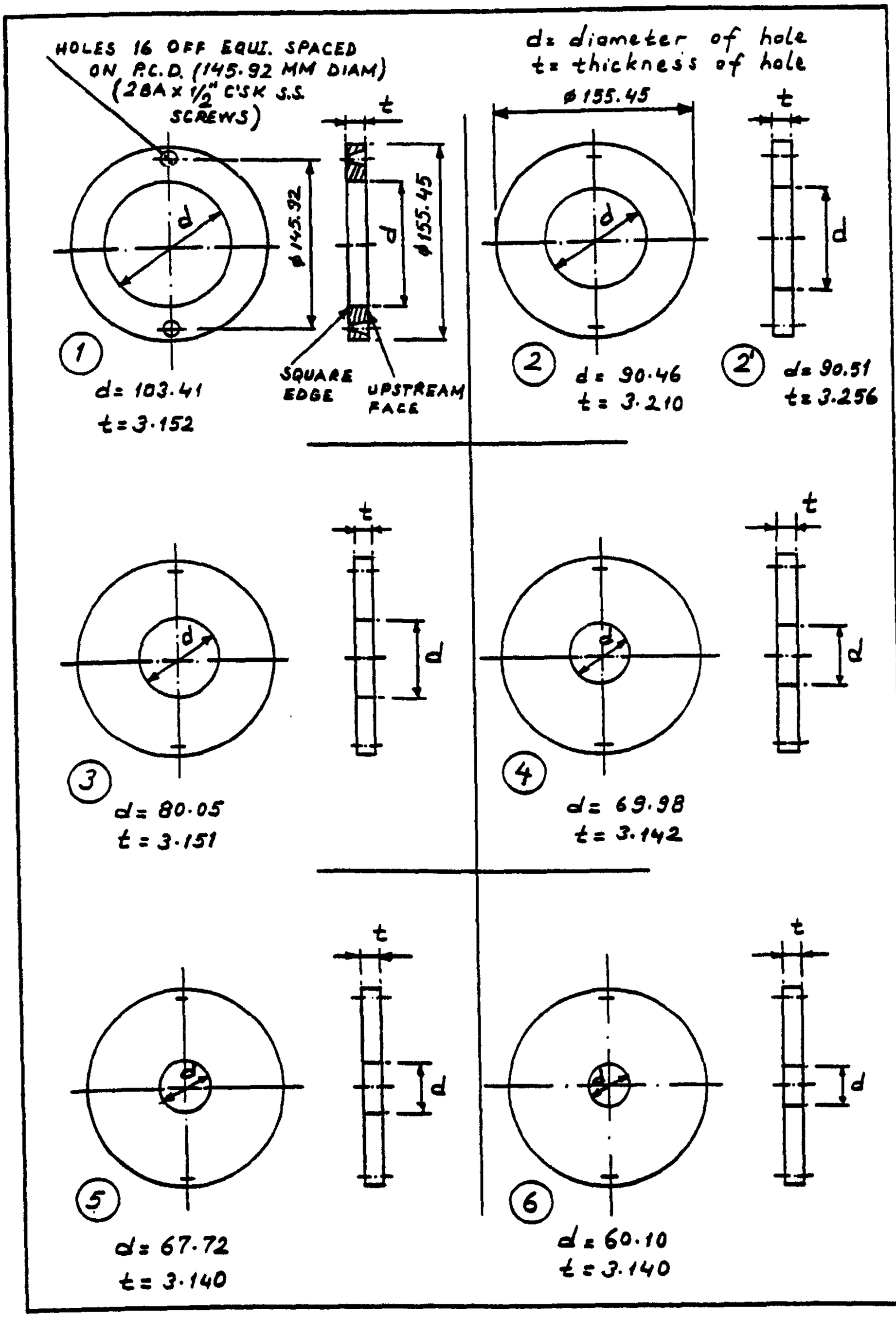

Fig. 14. Geometry of the single-hole orifice plates tested

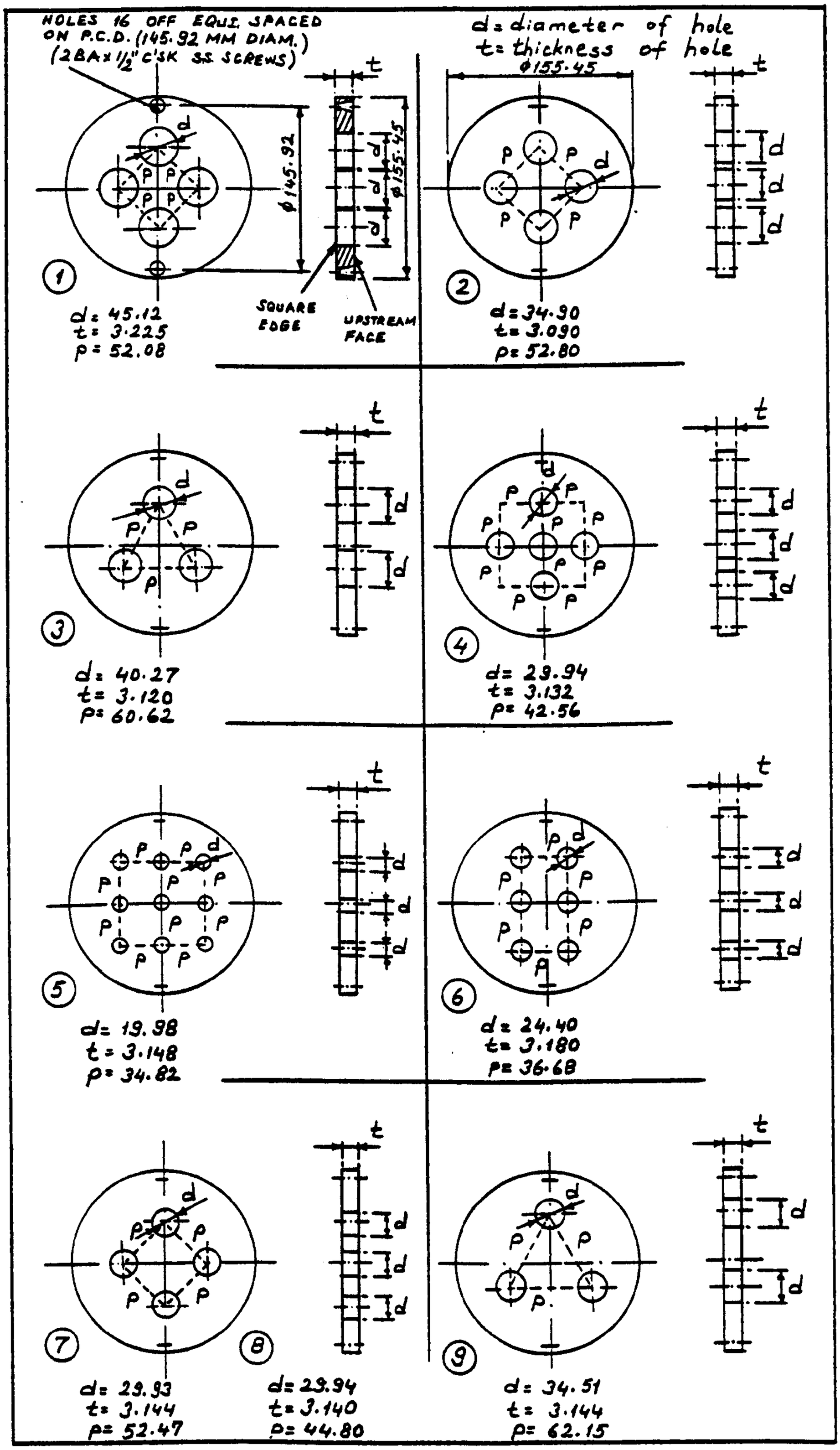

Fig. 15. Geometry of the multi-hole orifice plates tested

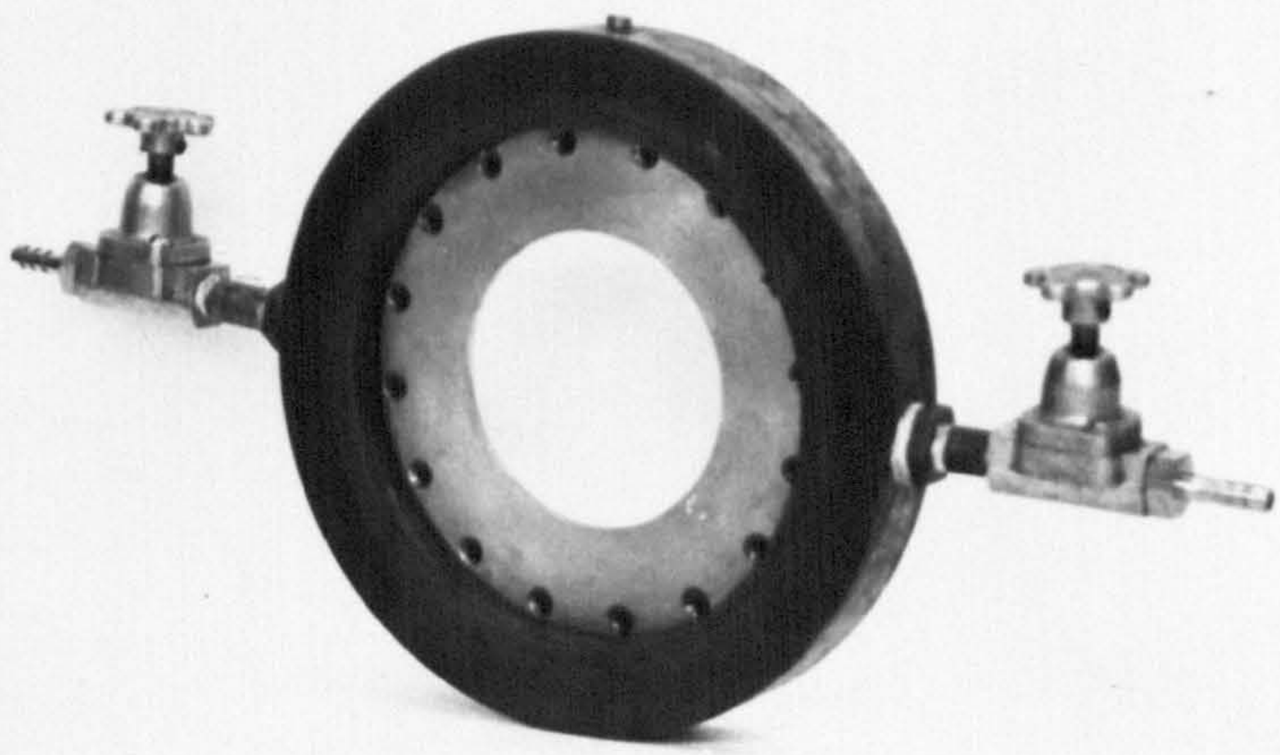

(a)

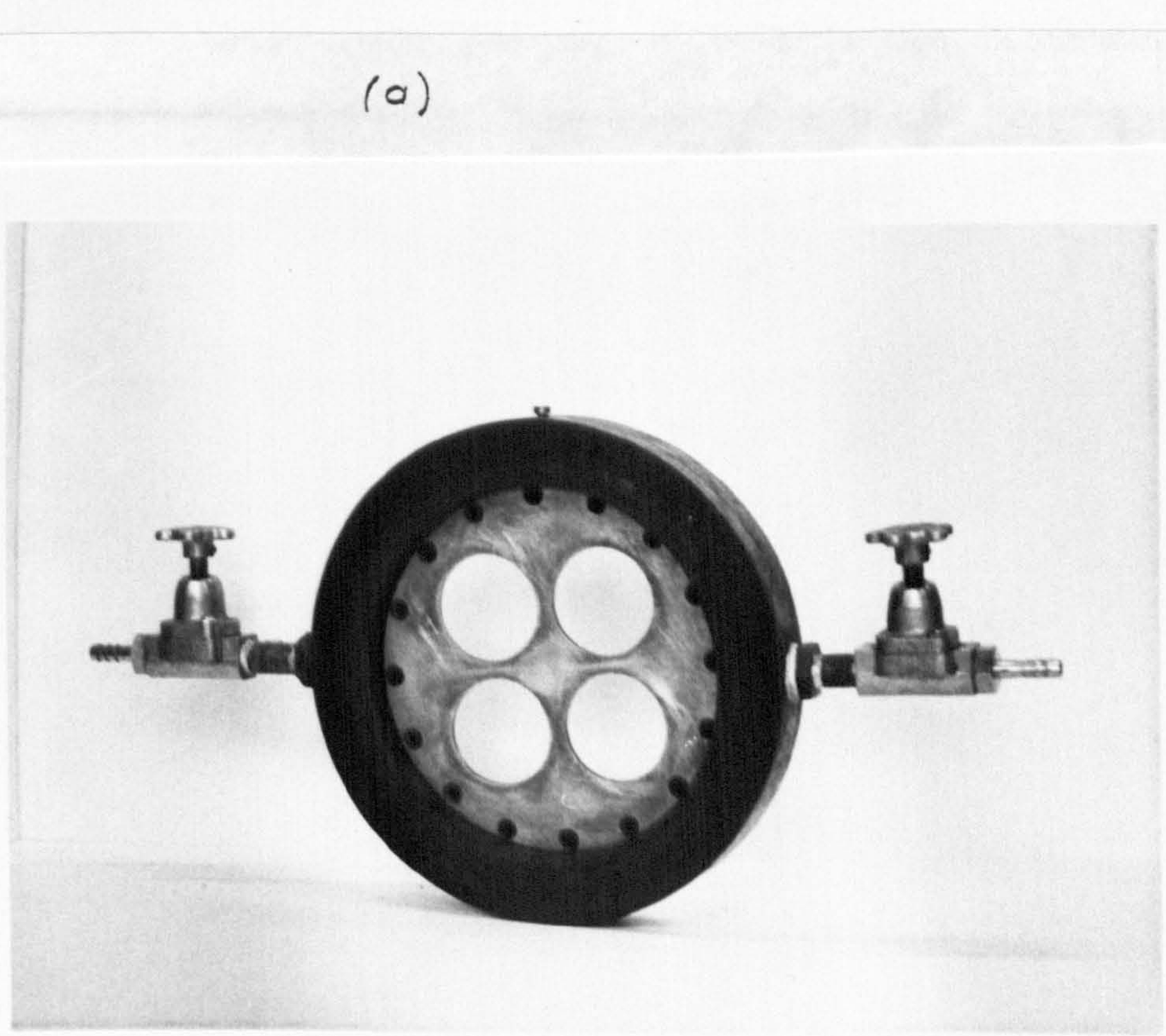

(b)

Fig. 16. An orifice plate fixed into the carrier ring, (a) single-hole orifice plate of $m=0.389$ (b) multi-hole orifice plate of $m=0.387$

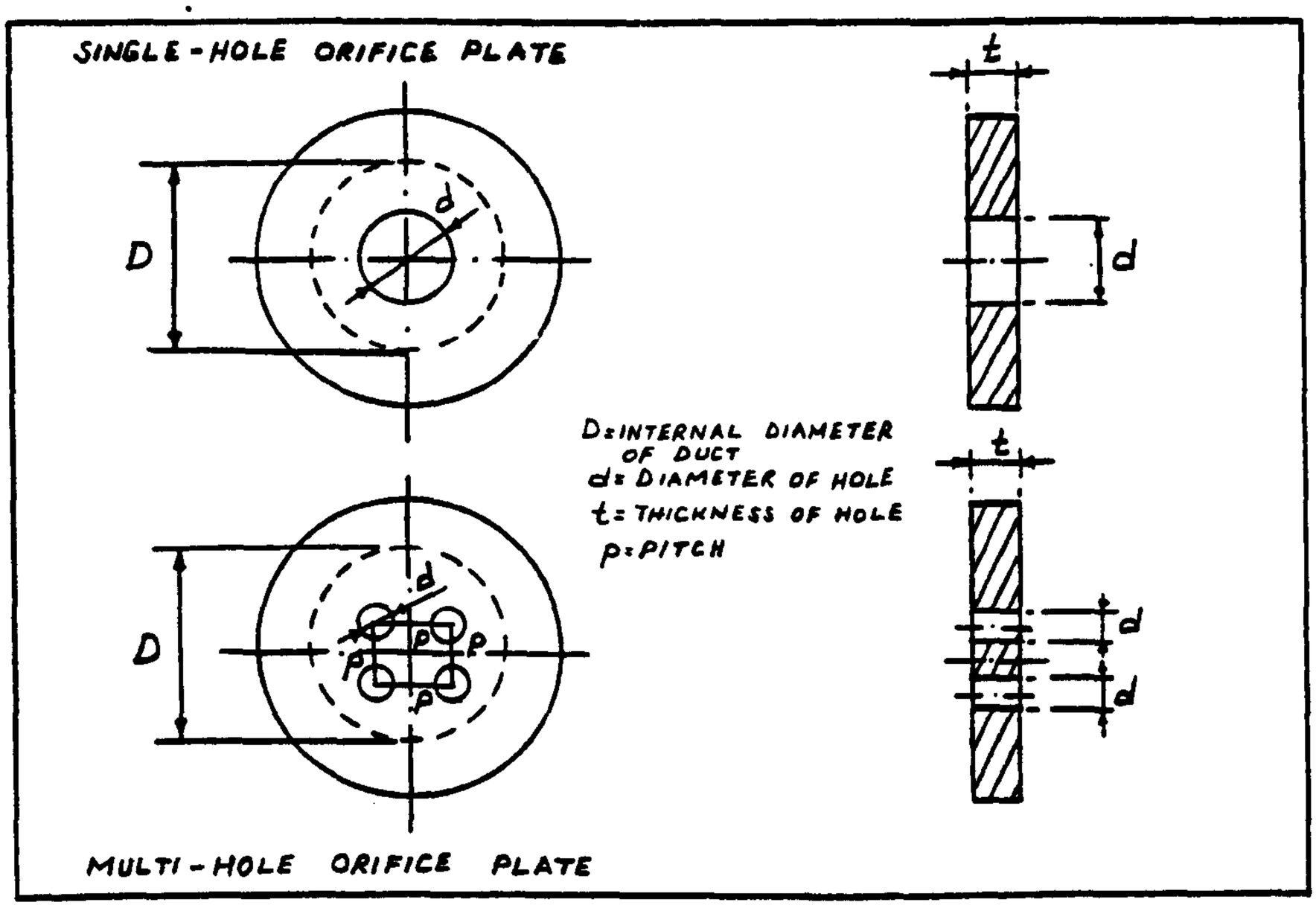

Fig. 17. Definition of orifice plate geometry

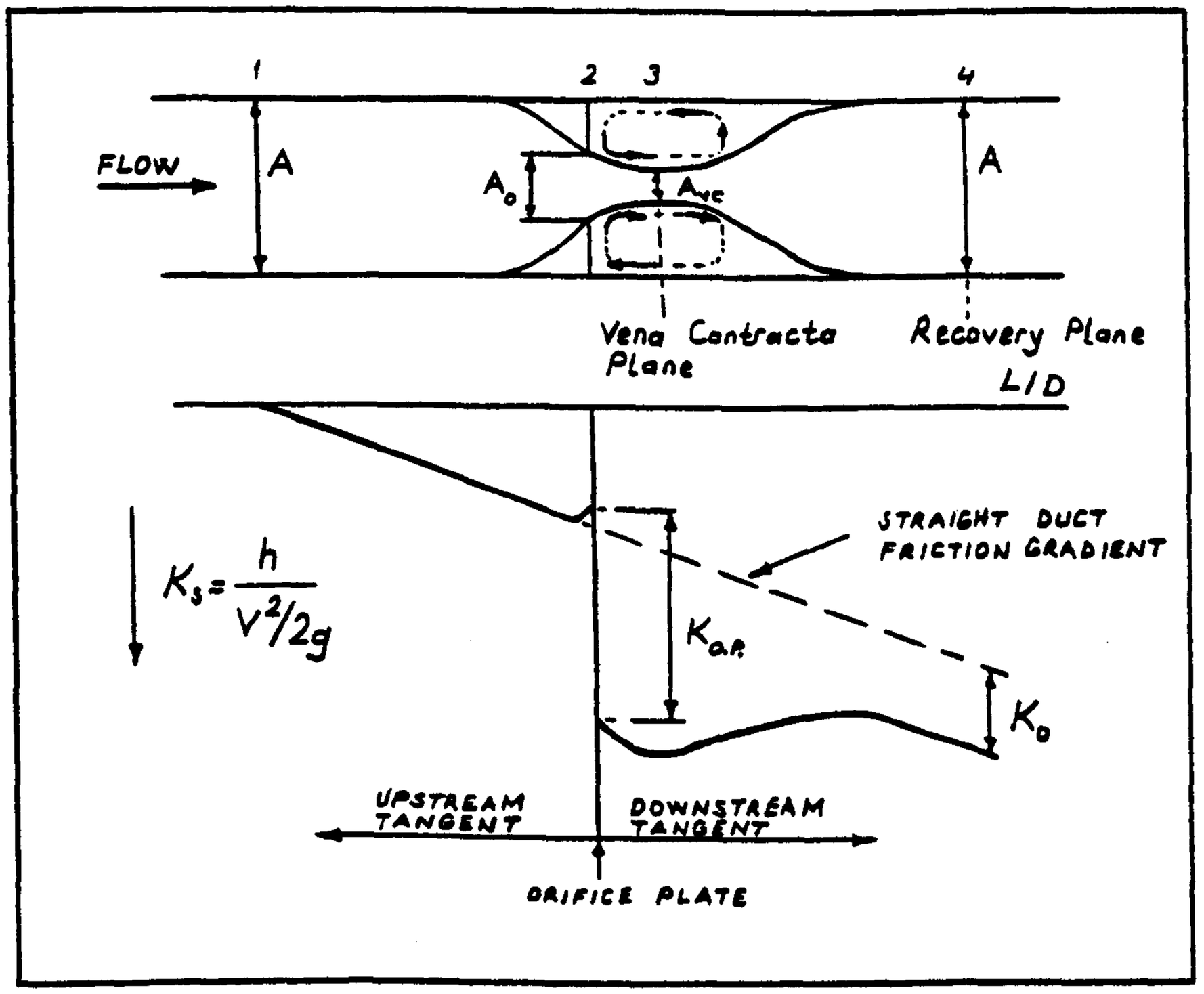

Fig. 18. Characteristics of flow through an orifice plate

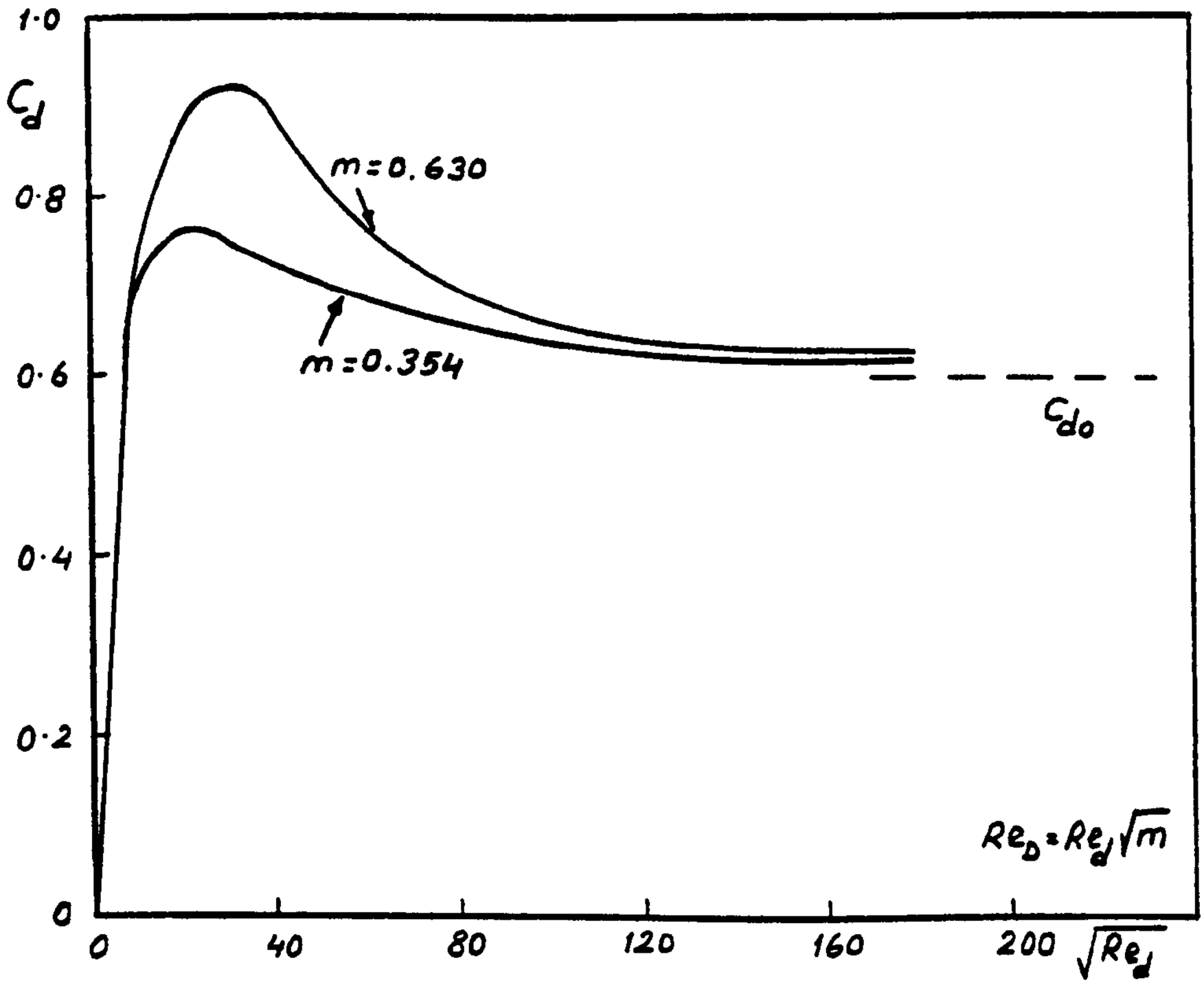

Fig. 19. Variation of C_d with Re_d, from Johansen (1929)

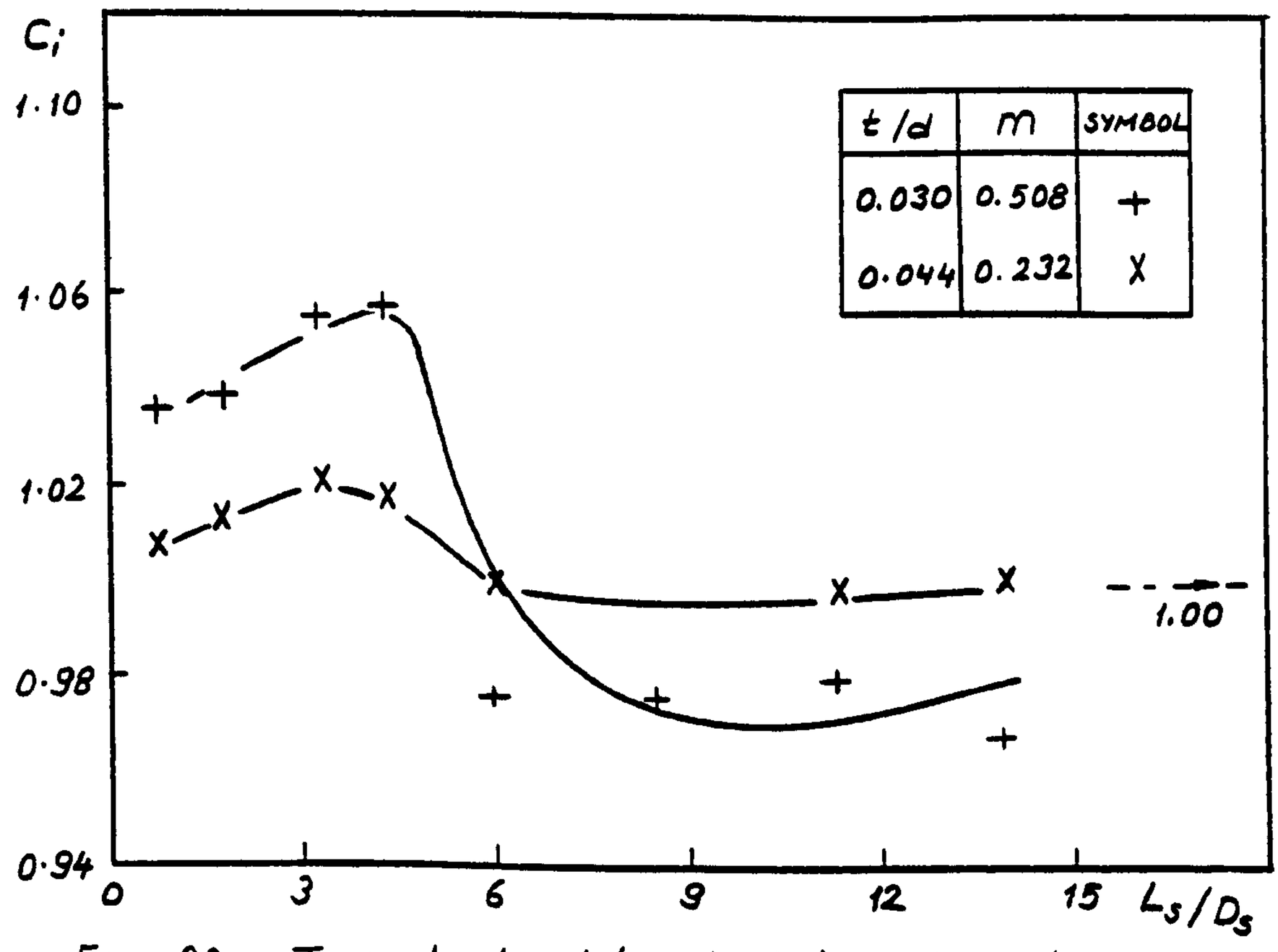

Fig. 20. Typical bend/single-hole orifice plate interaction, PVC bend of R/D = 4.18

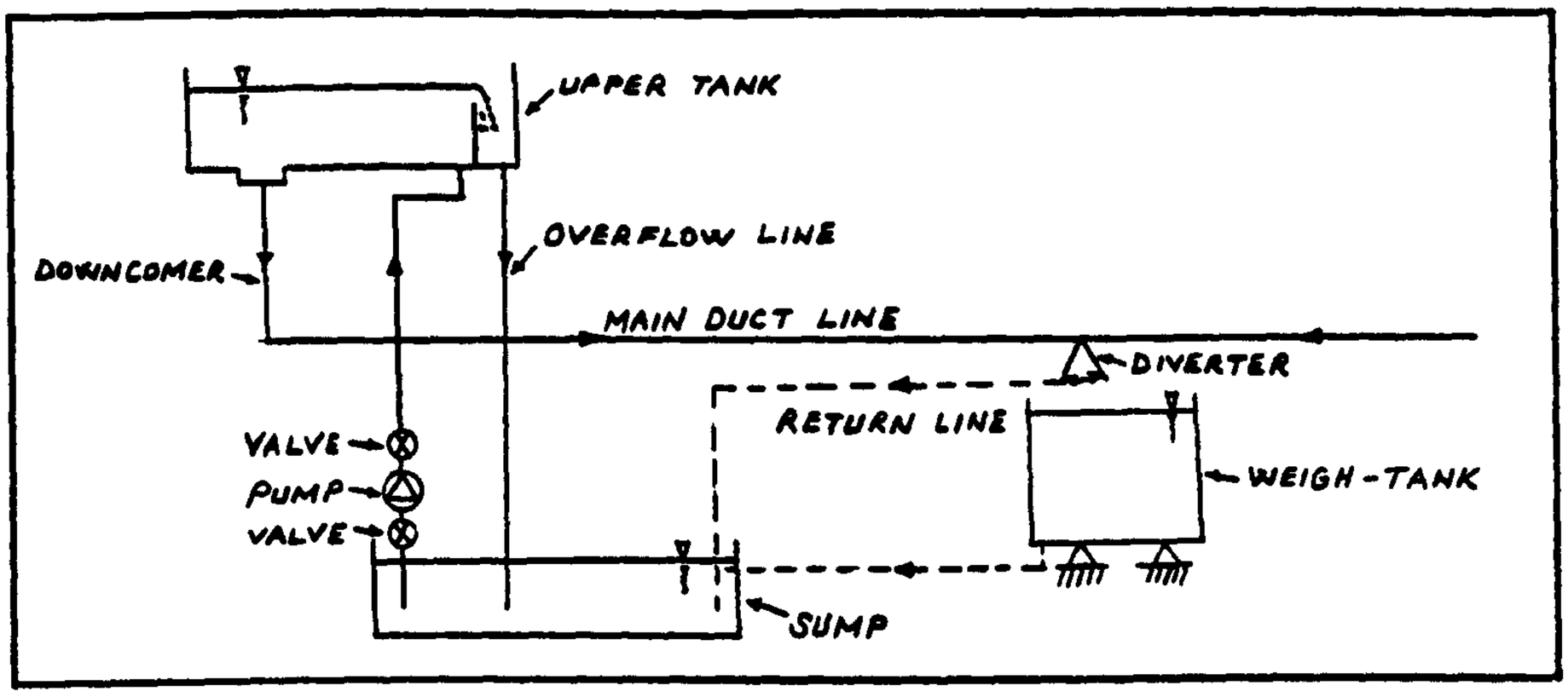

Fig. 21. General arrangement of test rig

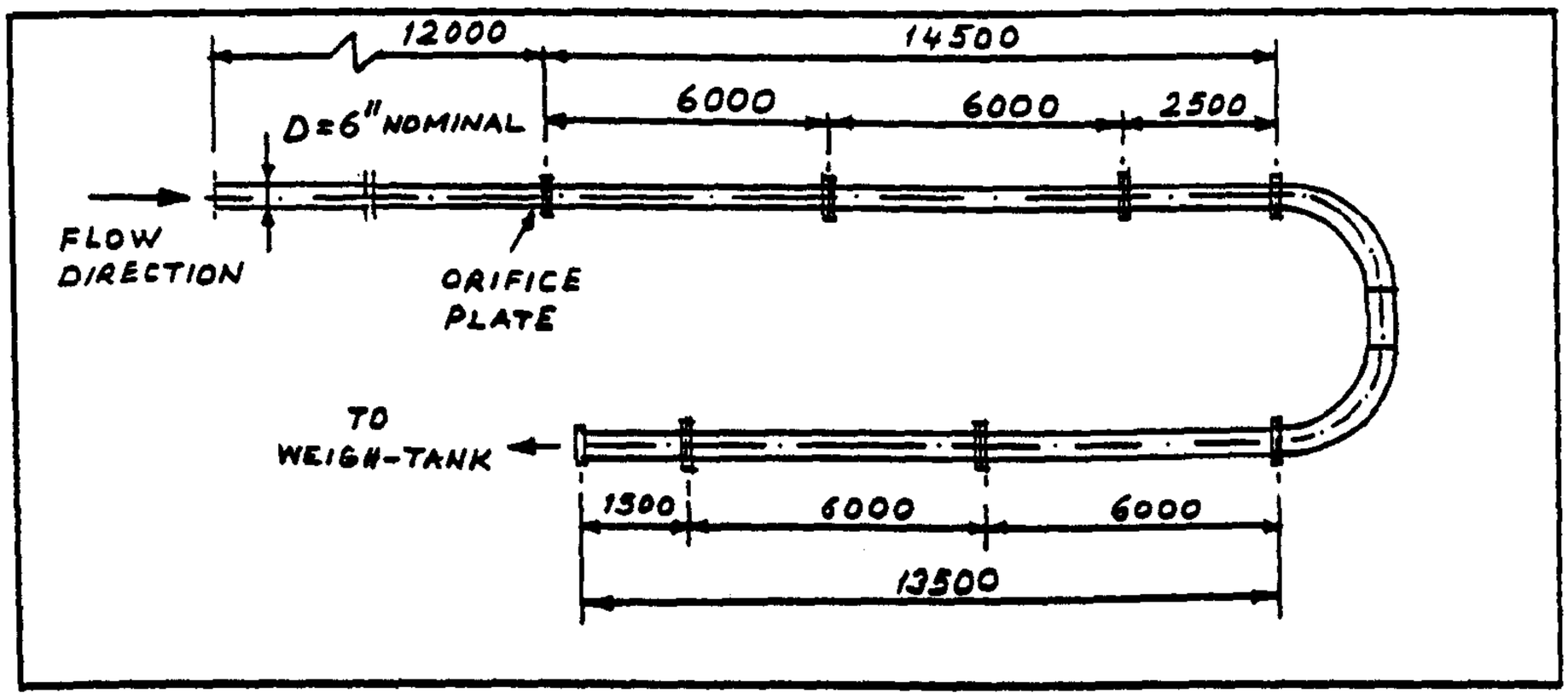

Fig. 22. Configuration of duct work in the laboratory for the preliminary tests (all dimensions are in millimeter)

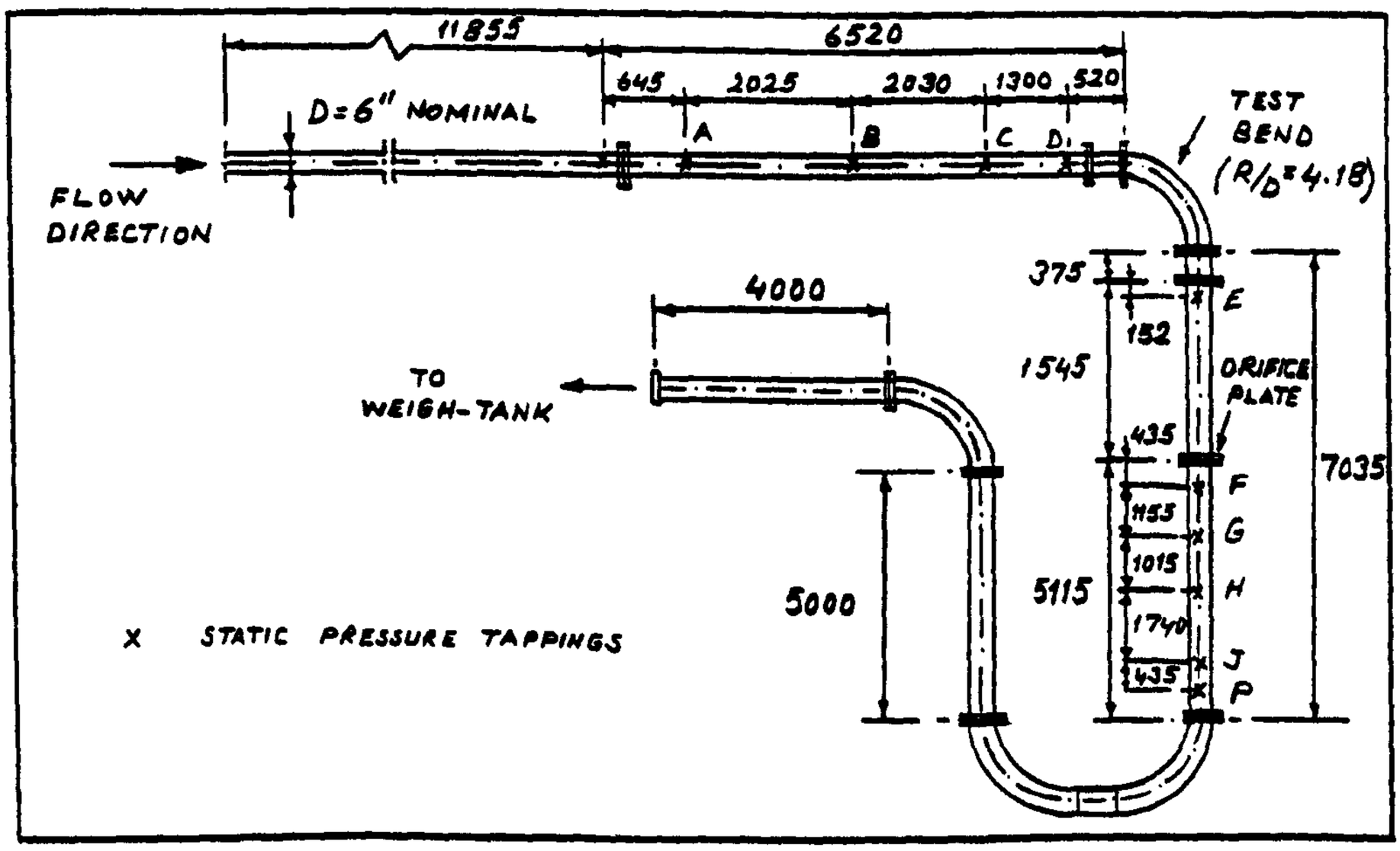

Fig. 23. Typical arrangement for bend/orifice plate combination (all dimensions are in millimeter)

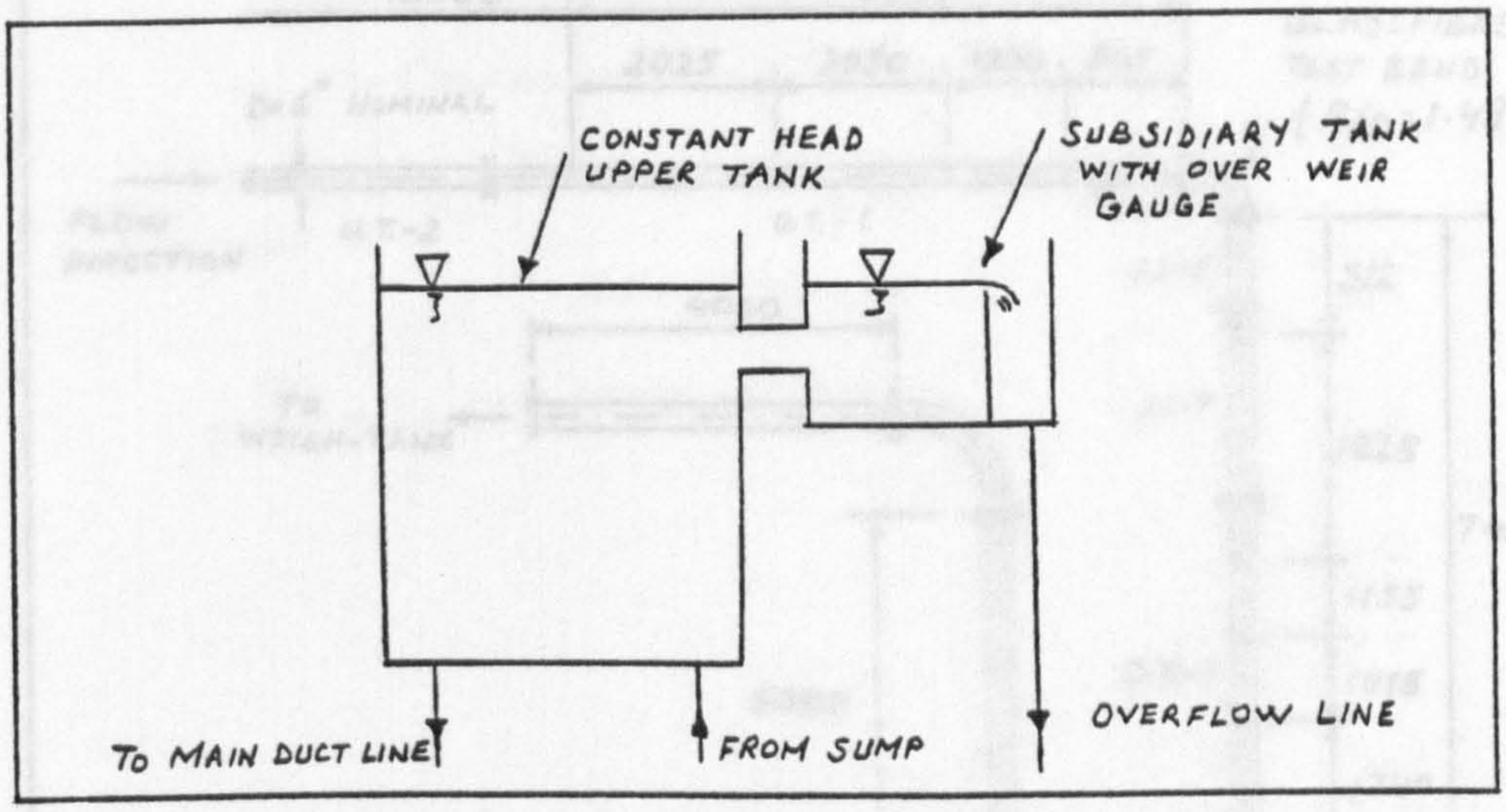

Fig. 24. Upper tank

Fig. 25. Metal flange

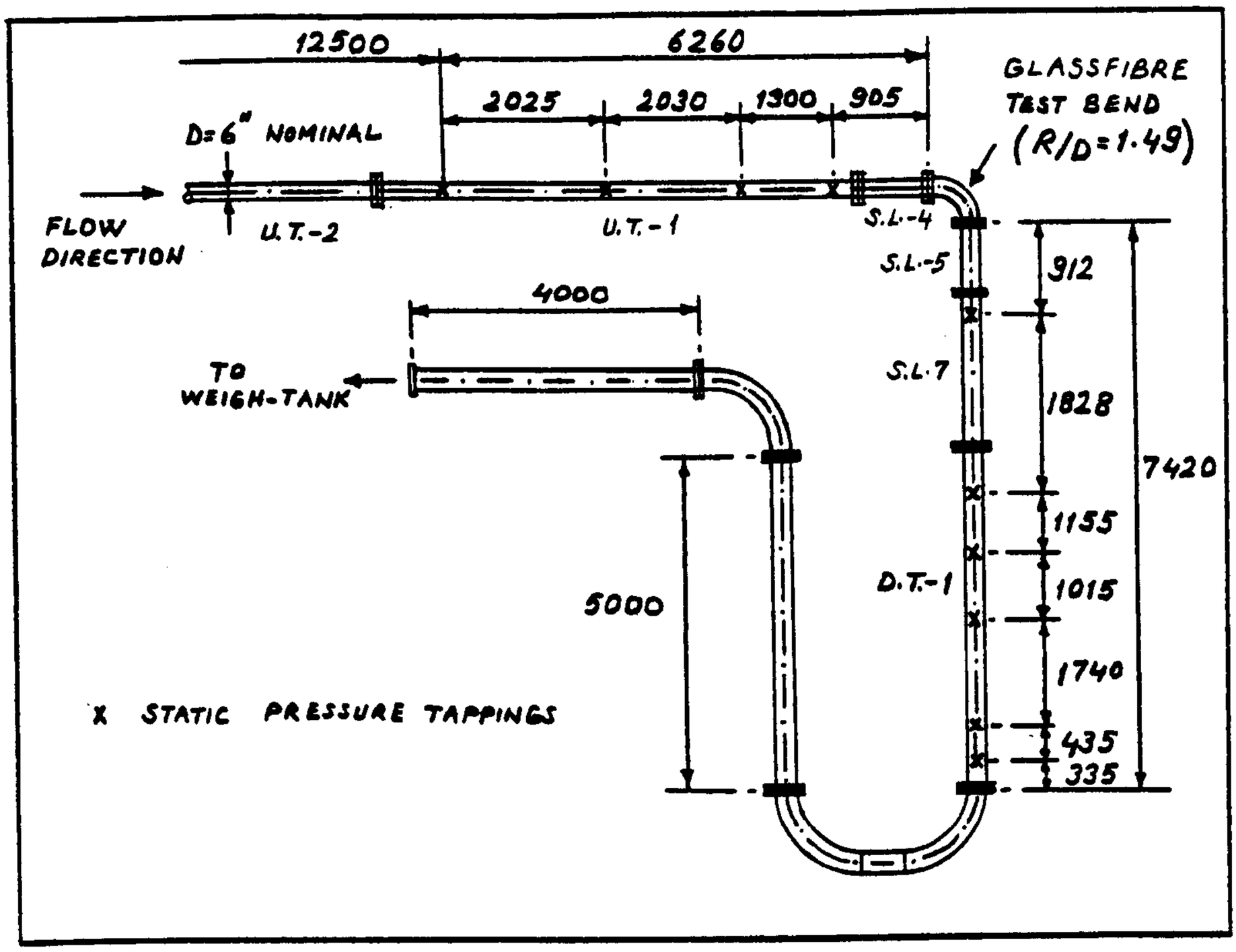

Fig. 26. Diagram of duct line with a test bend ($R/D=1.49$, all dimensions are in millimeter)

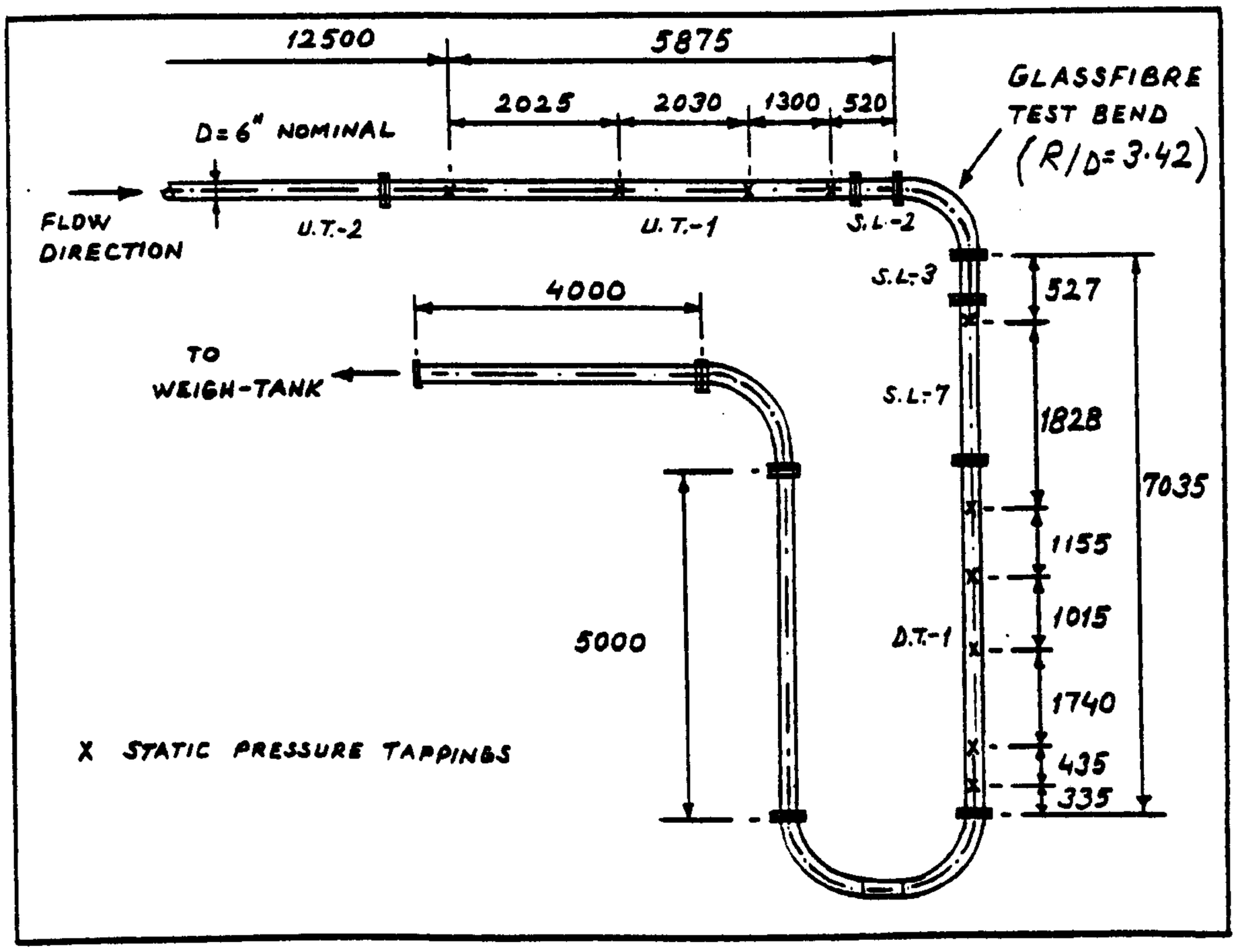

Fig. 27. Diagram of duct line with a test bend ($R/D=3.42$, all dimensions are in millimeter)

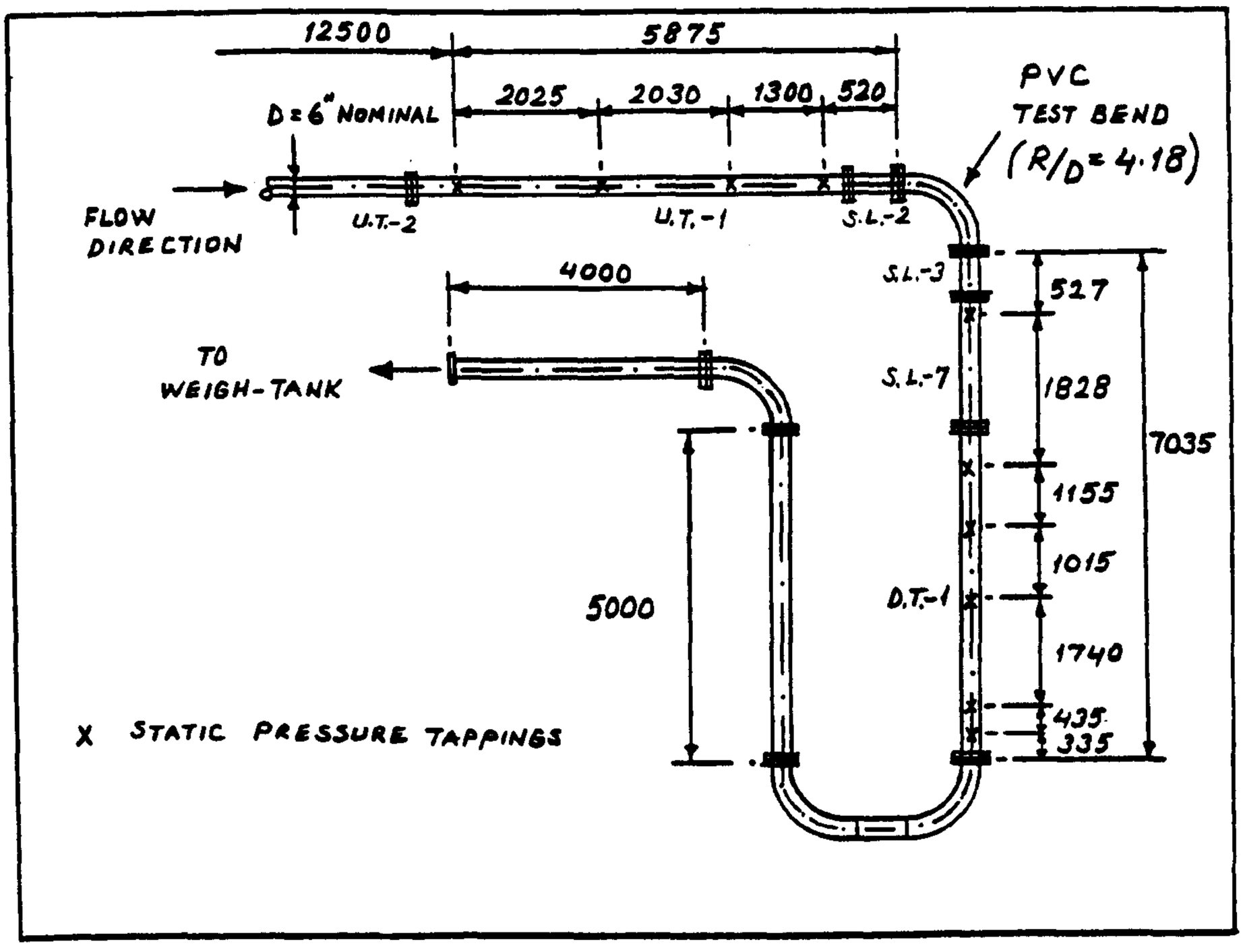

Fig. 28. Diagram of duct line with a test bend (R/D=4.18, all dimensions are in millimeter)

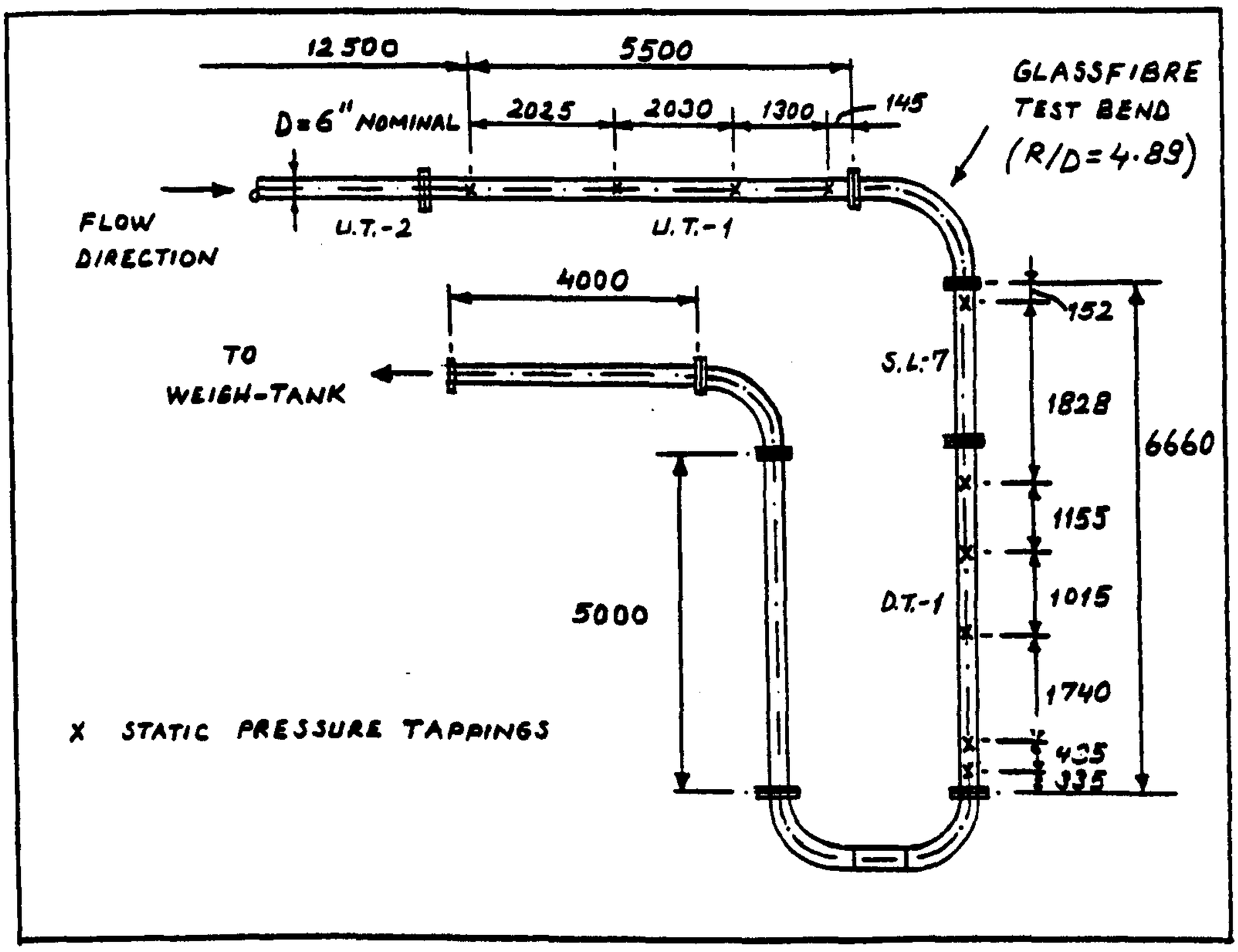

Fig. 29. Diagram of duct line with a test bend (R/D=4.89, all dimensions are in millimeter)

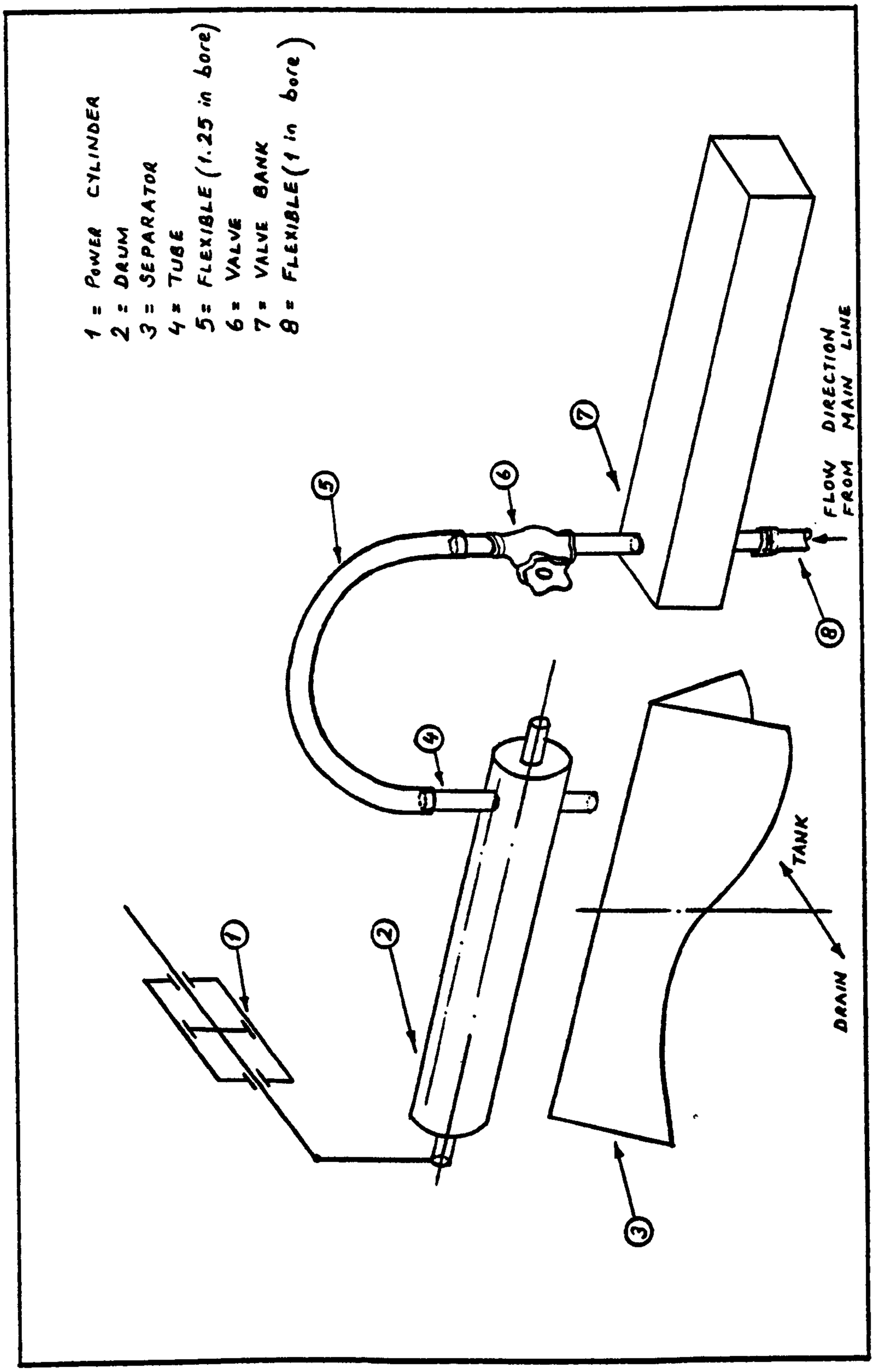

Fig. 30. Diverter (only one of fourteen tubes shown)

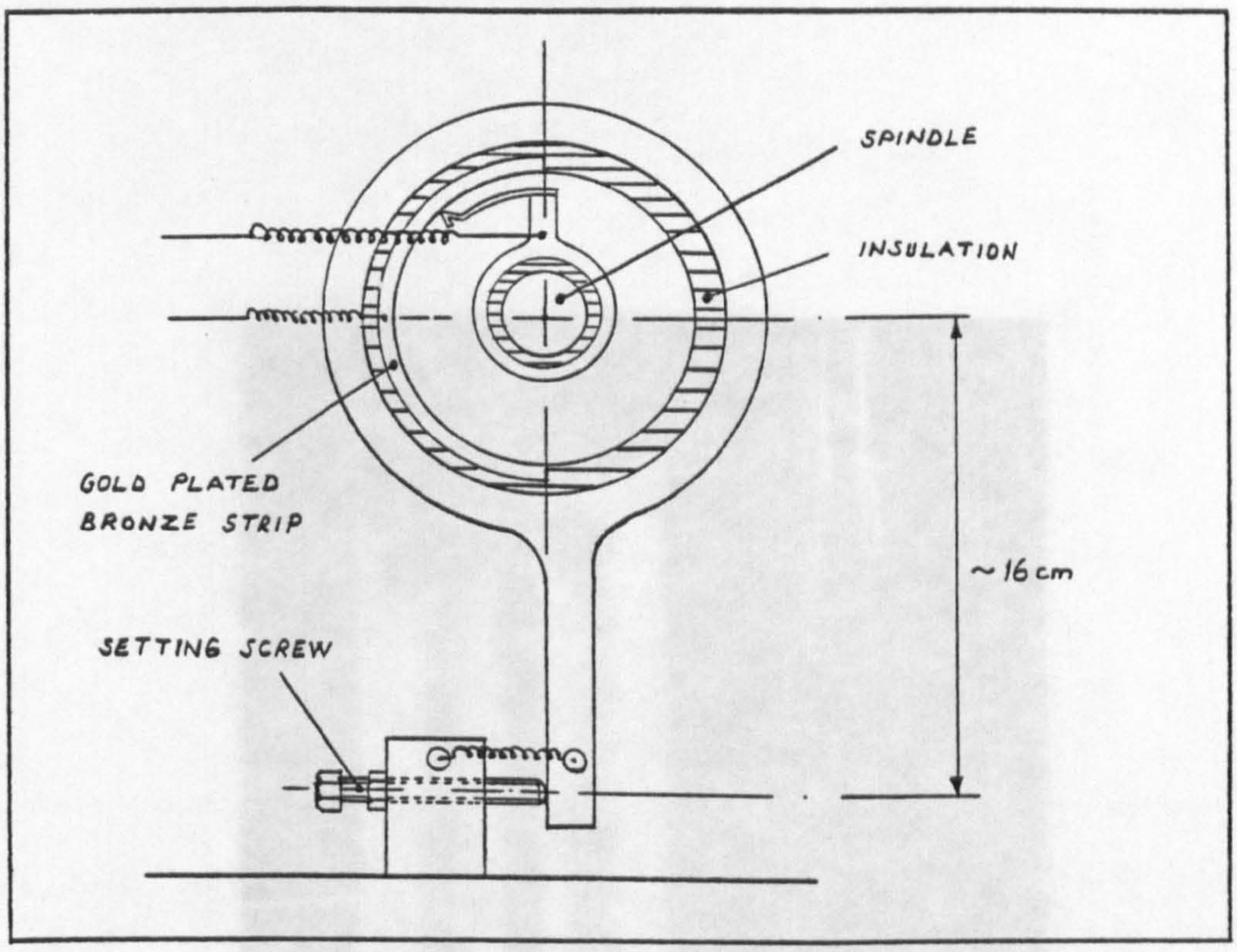

Fig. 31. Switch

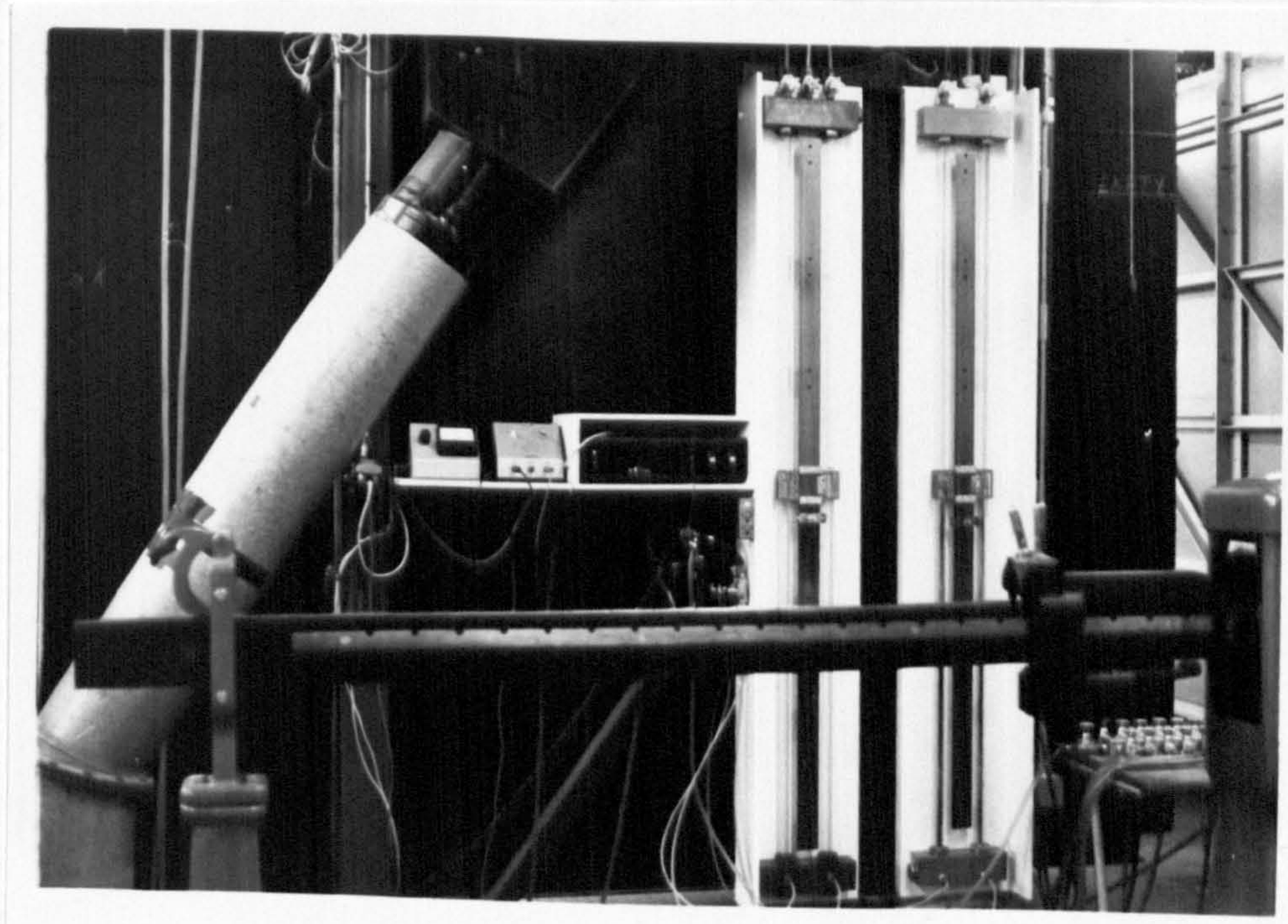

Fig. 32. A view of clock

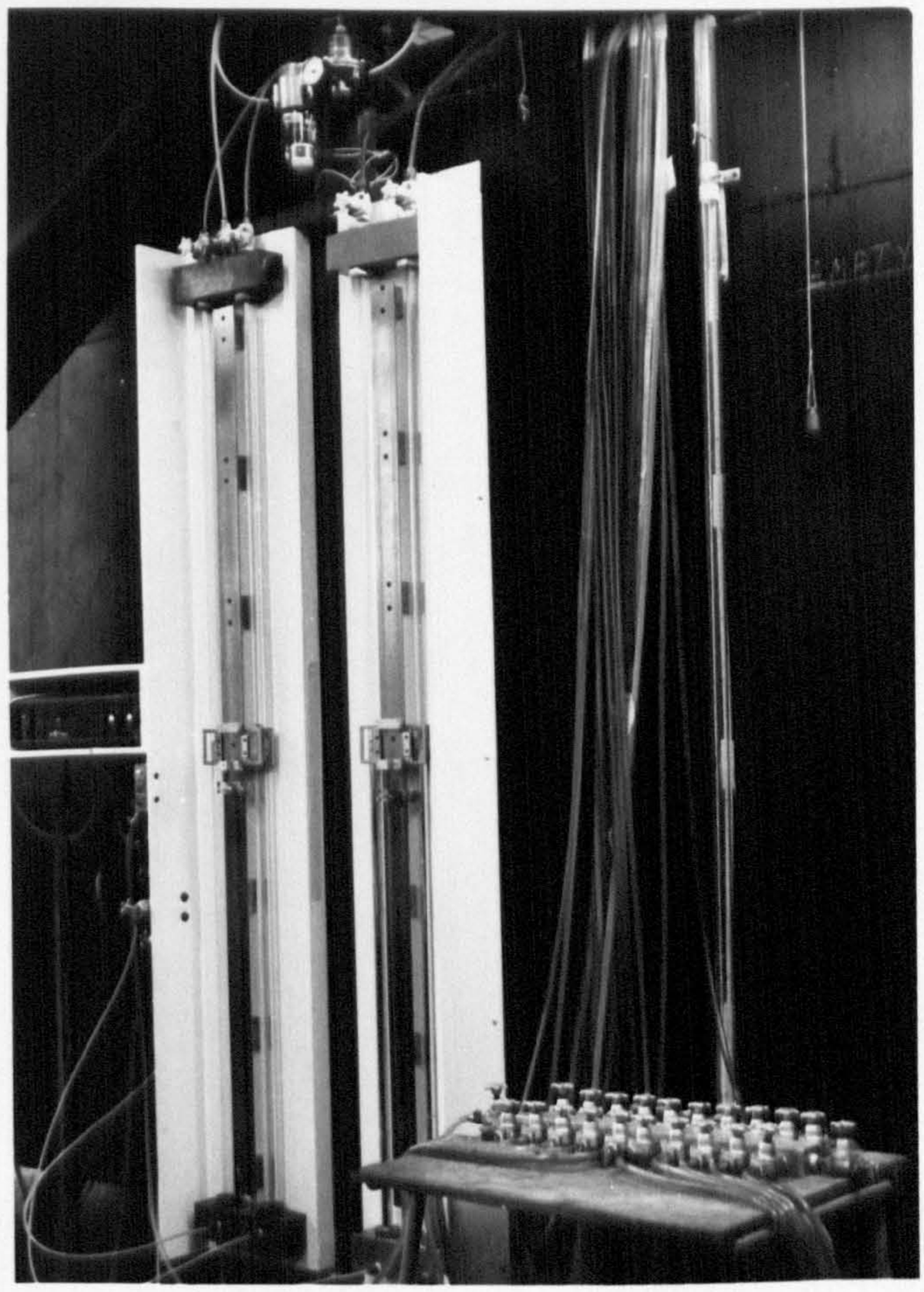

Fig. 33. A view of manometers

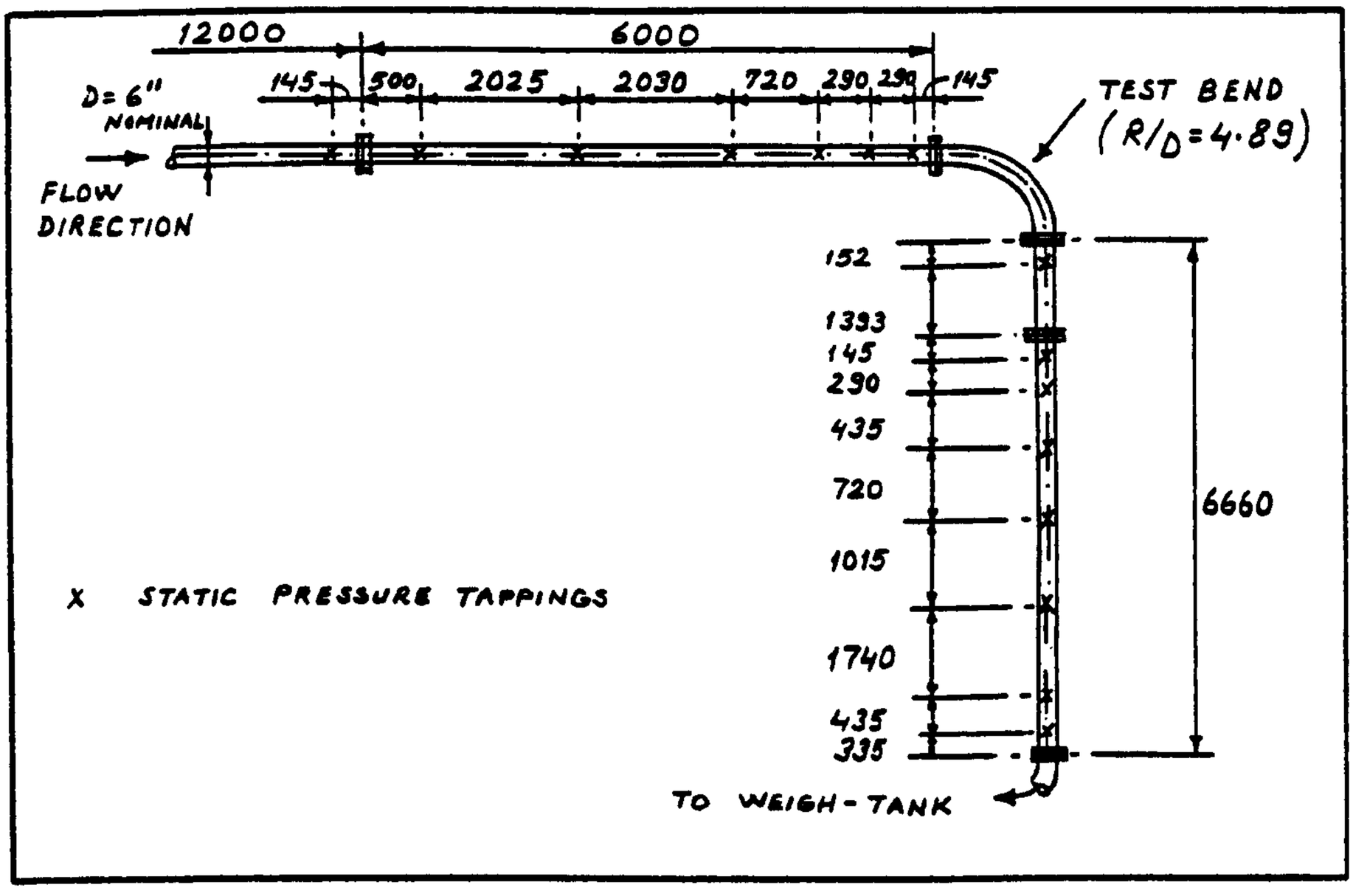

Fig. 34. Location of static pressure tapping connections (all dimensions are in millimeter)

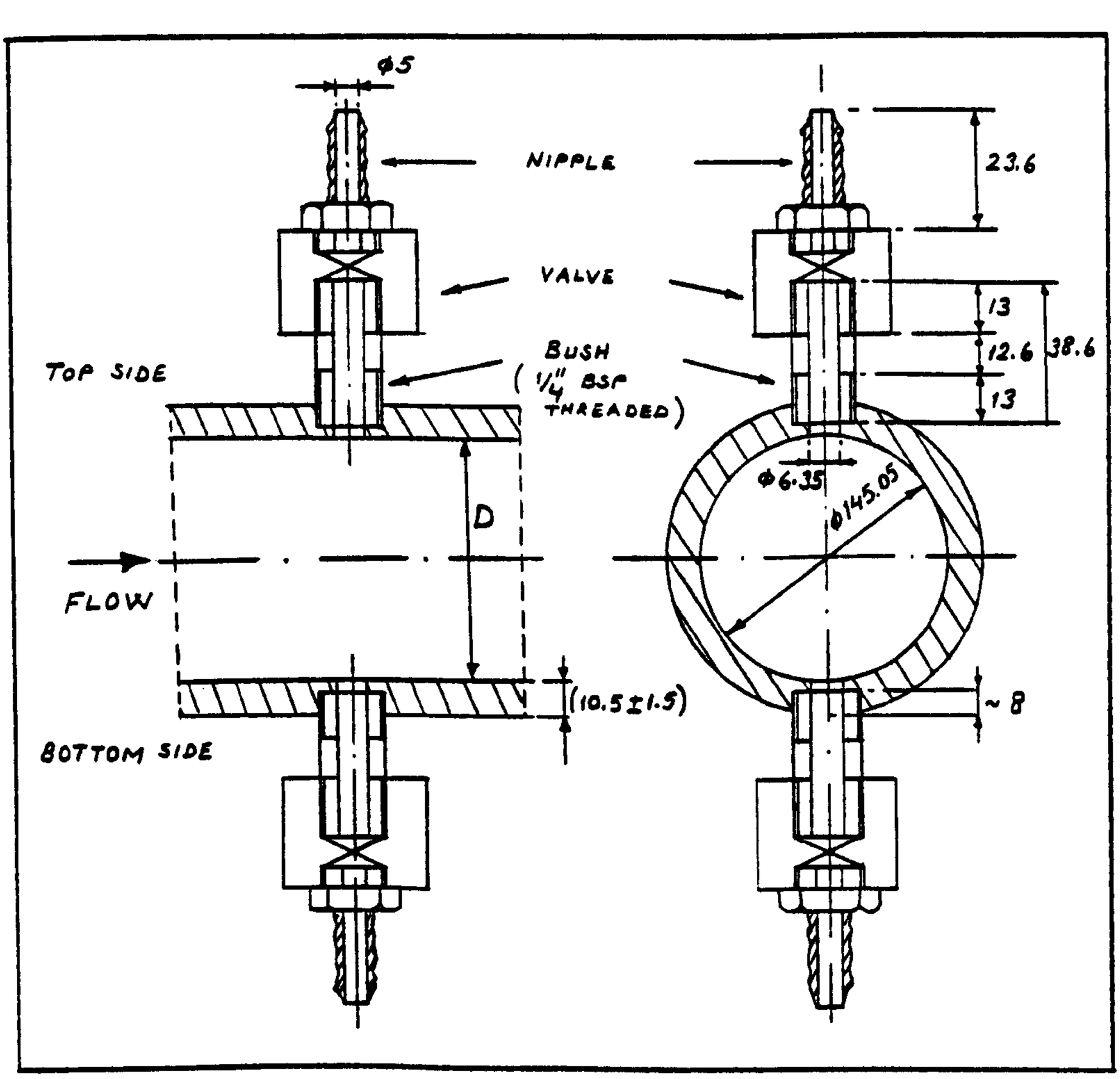

Fig. 35. Static pressure tappings (all dimensions are in millimeter)

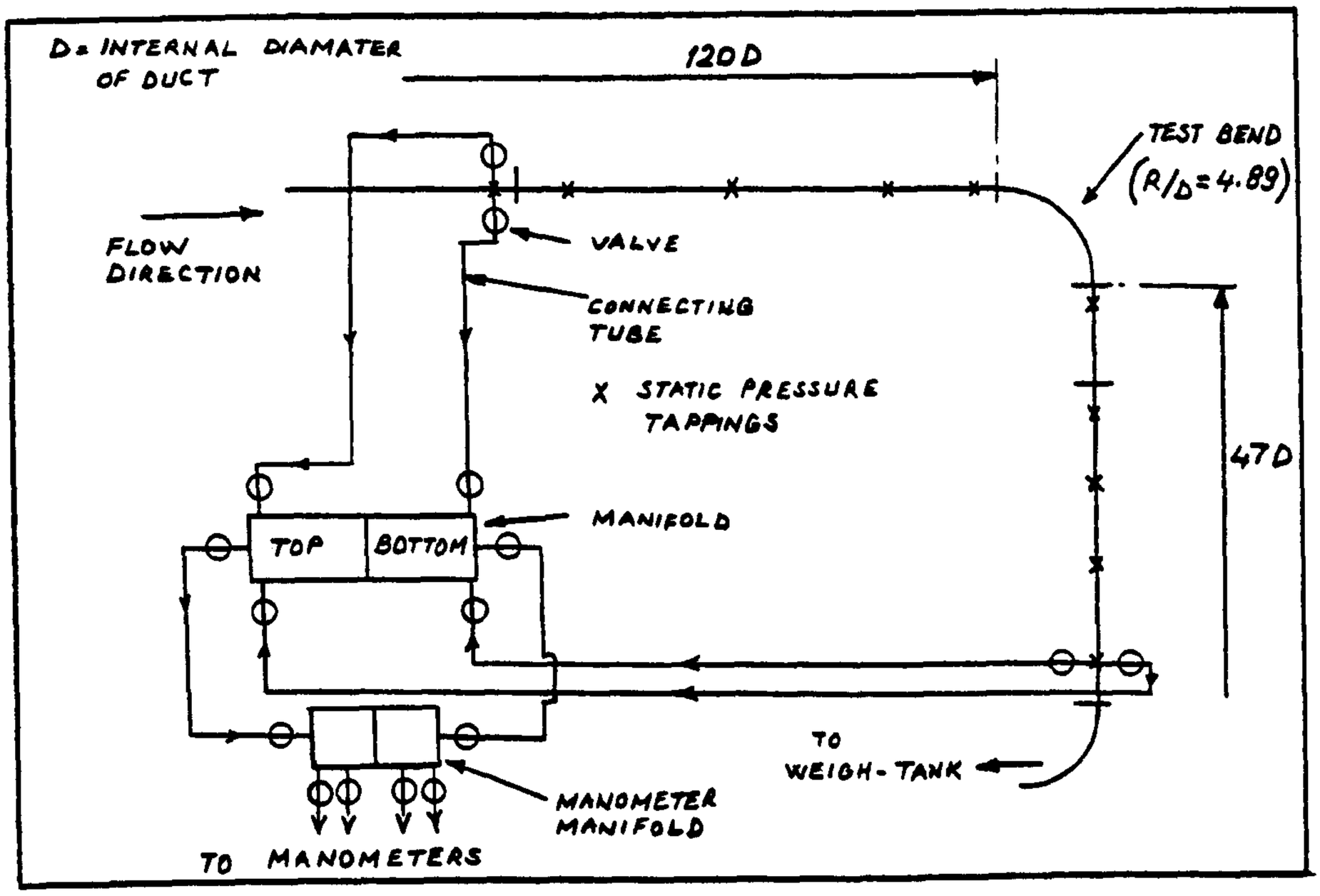

Fig. 36. System of ducting, valves and manifold

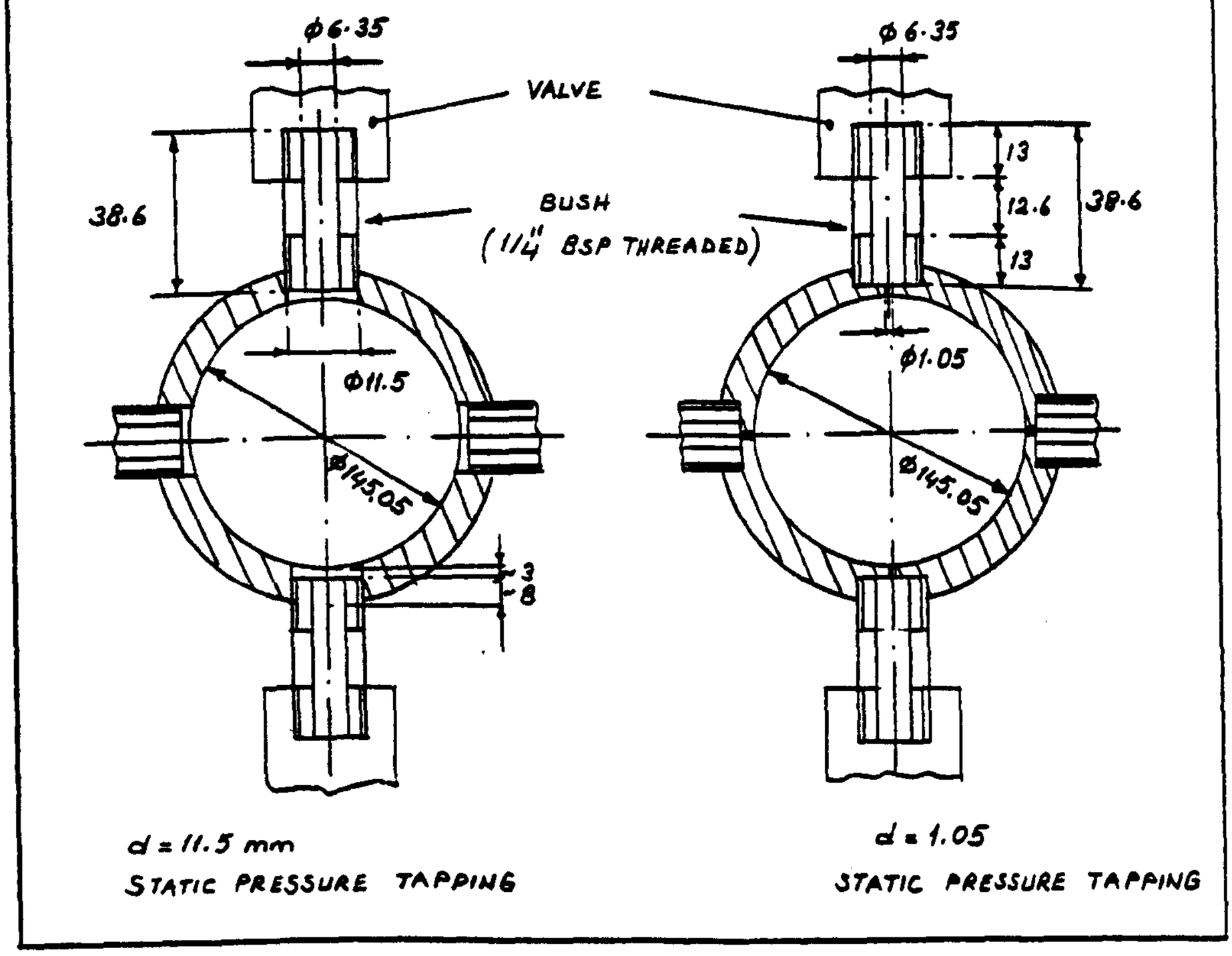

Fig. 37. Static pressure tappings (all dimensions are in millimeter)

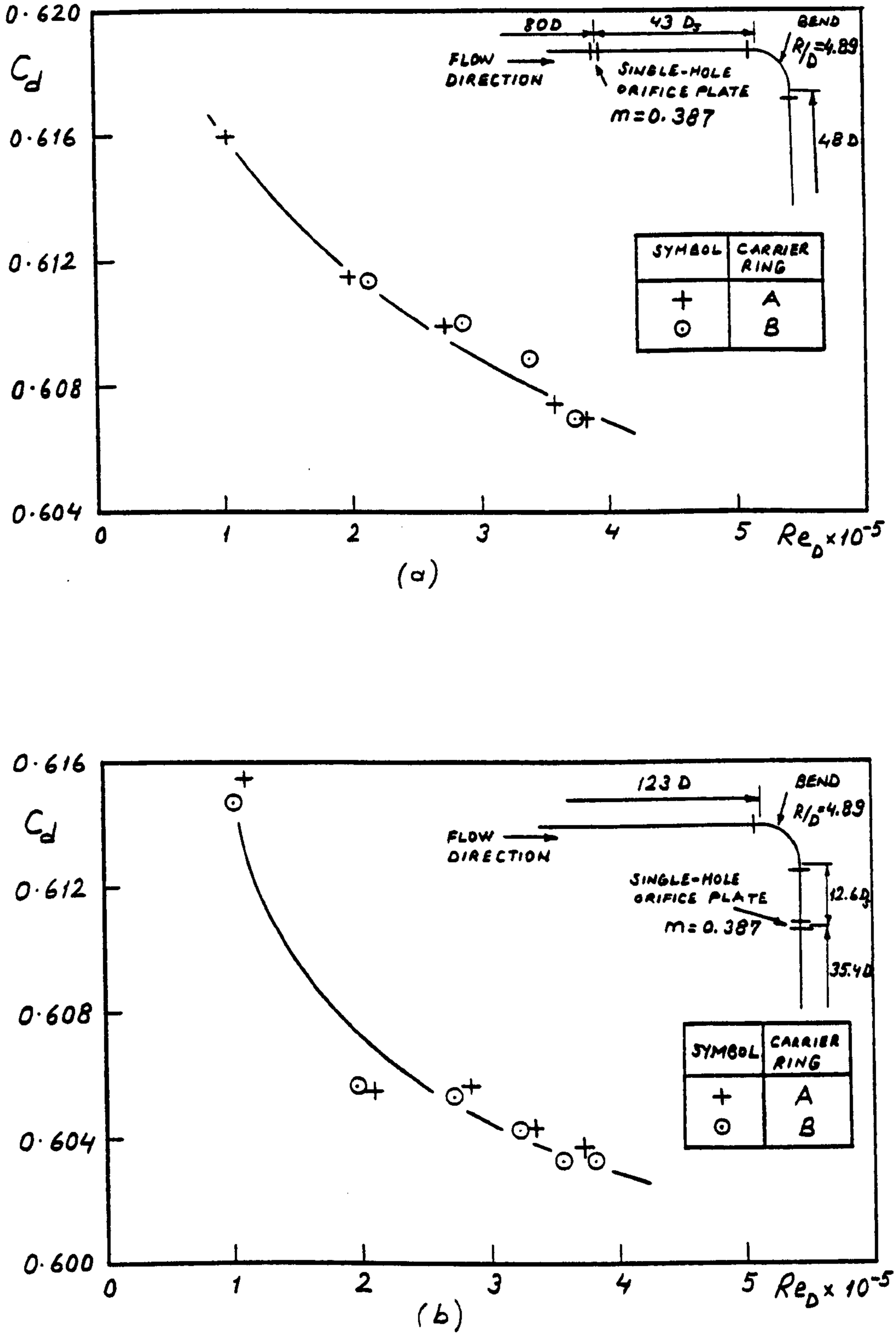

Fig. 38. Comparison of test carrier rings

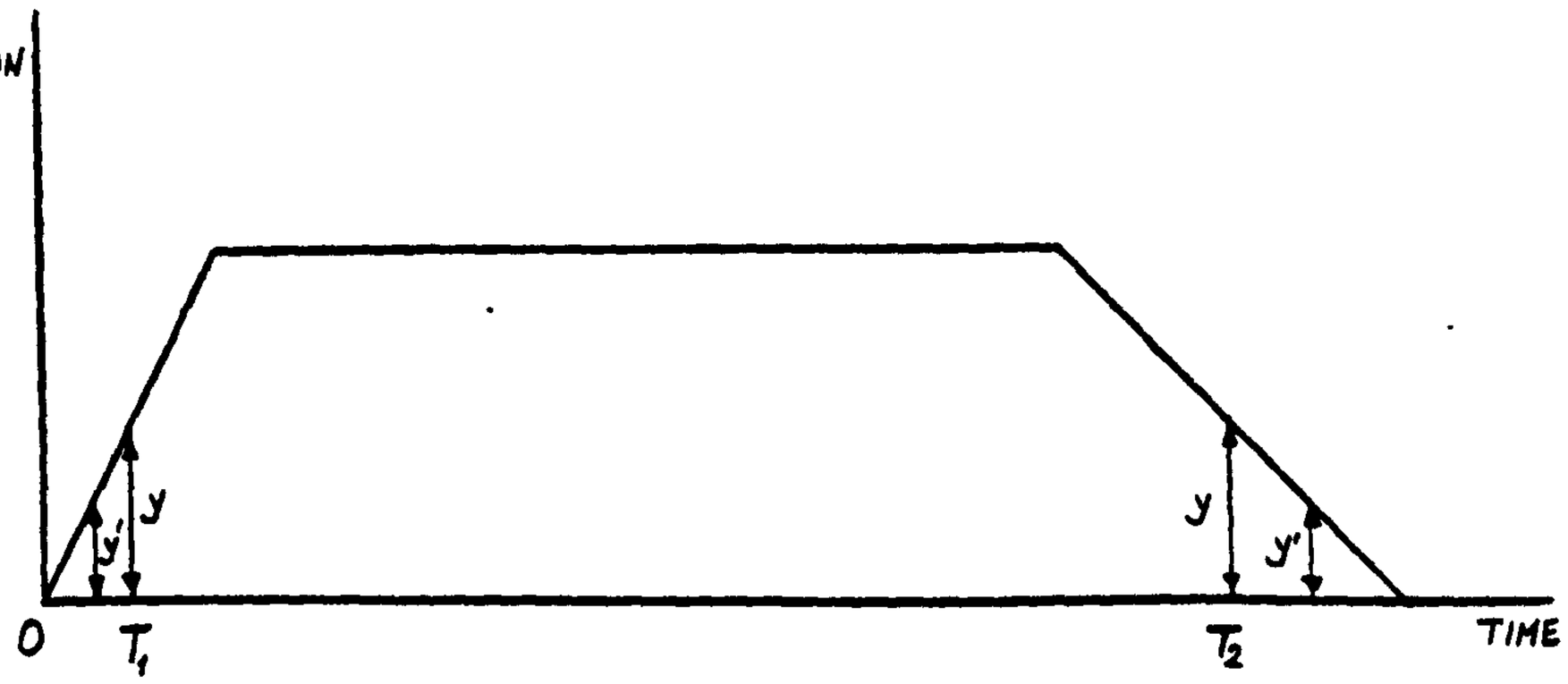

(a)

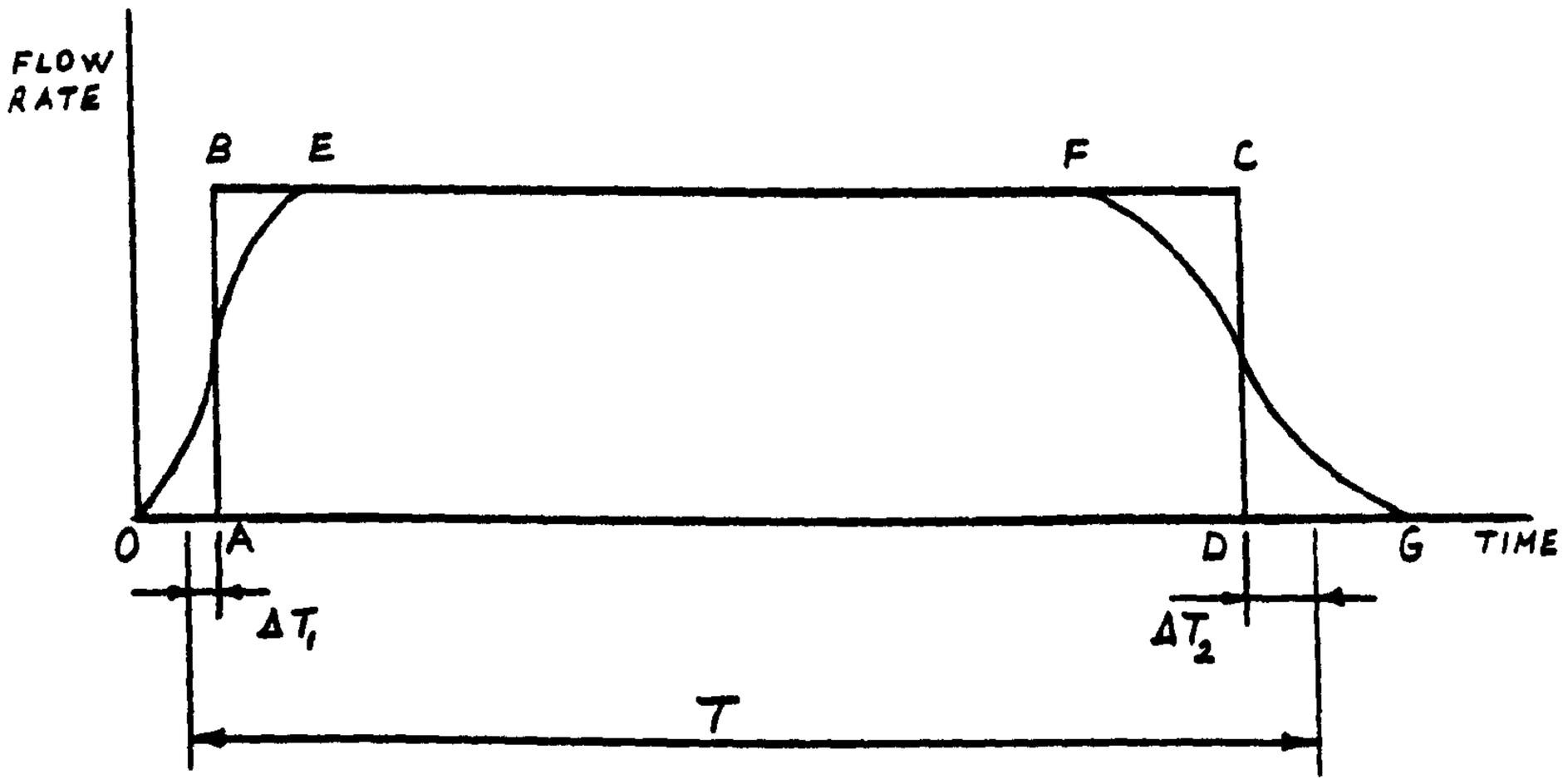

(b)

Fig. 39. Principle of diverter

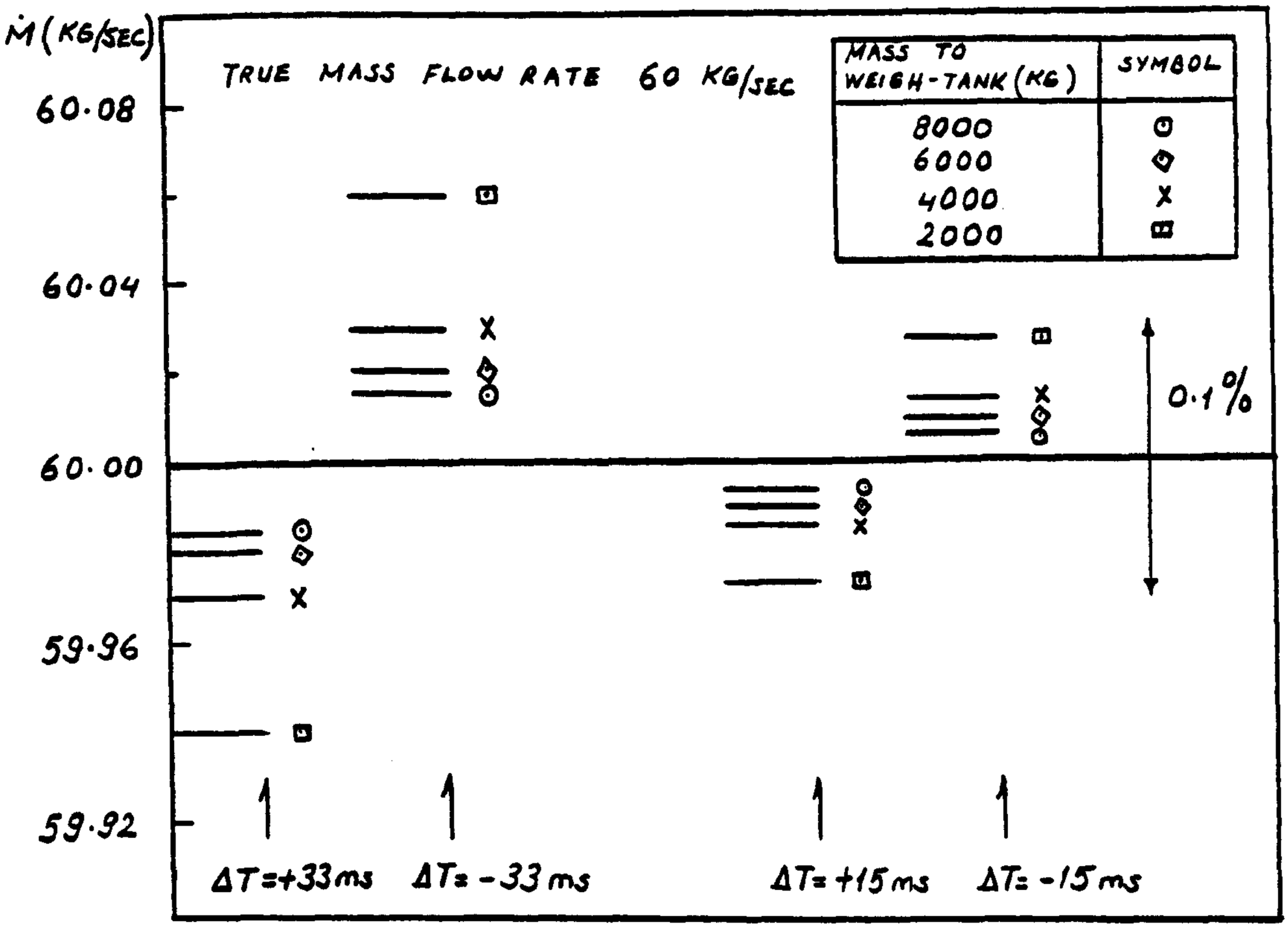

(a)

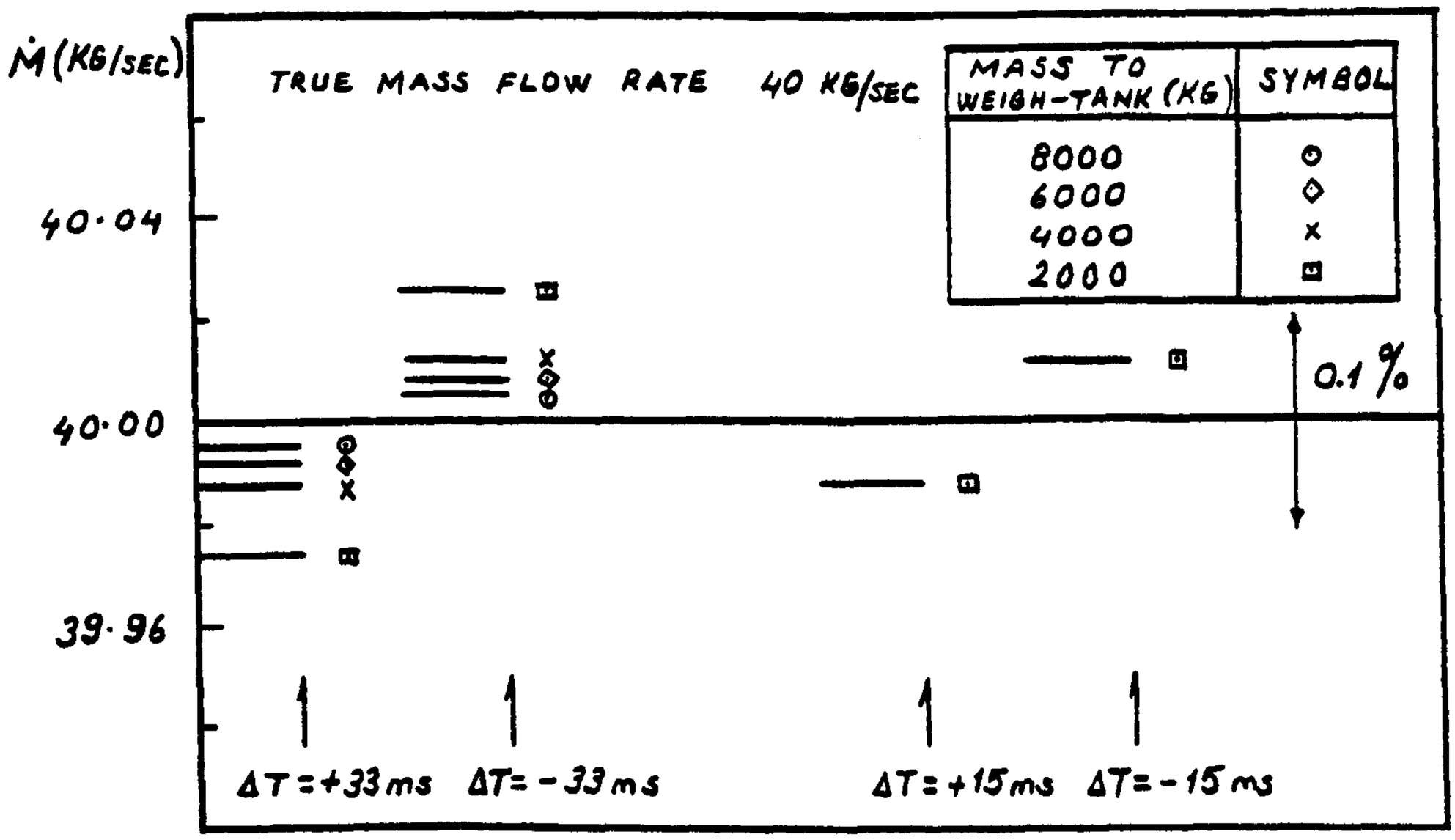

(b)

Fig. 40. Effect of error in setting the switch, from Crook (1974)

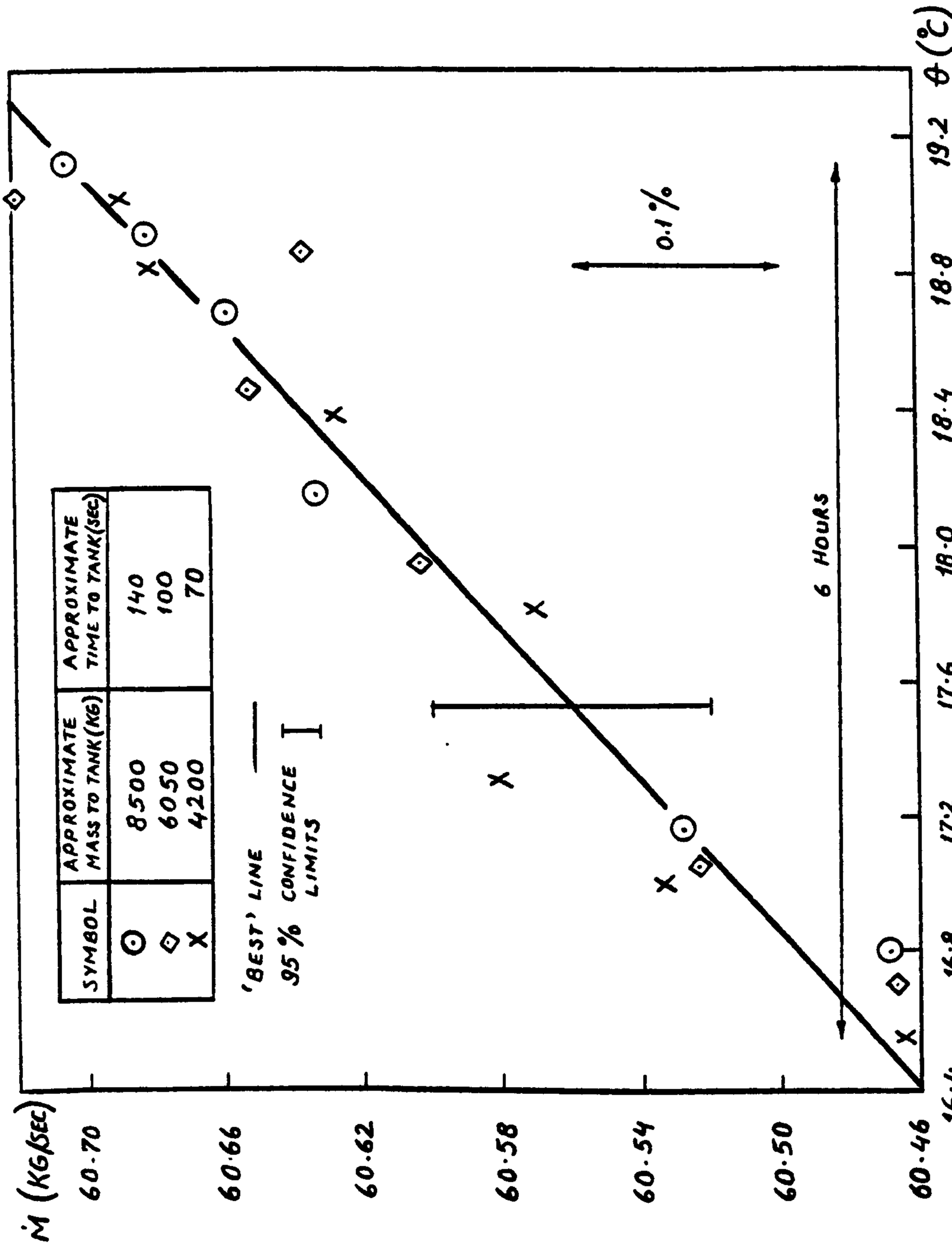

Fig. 41. Effect of temperature of water on the measured mass flow rate, from Crook (1974)

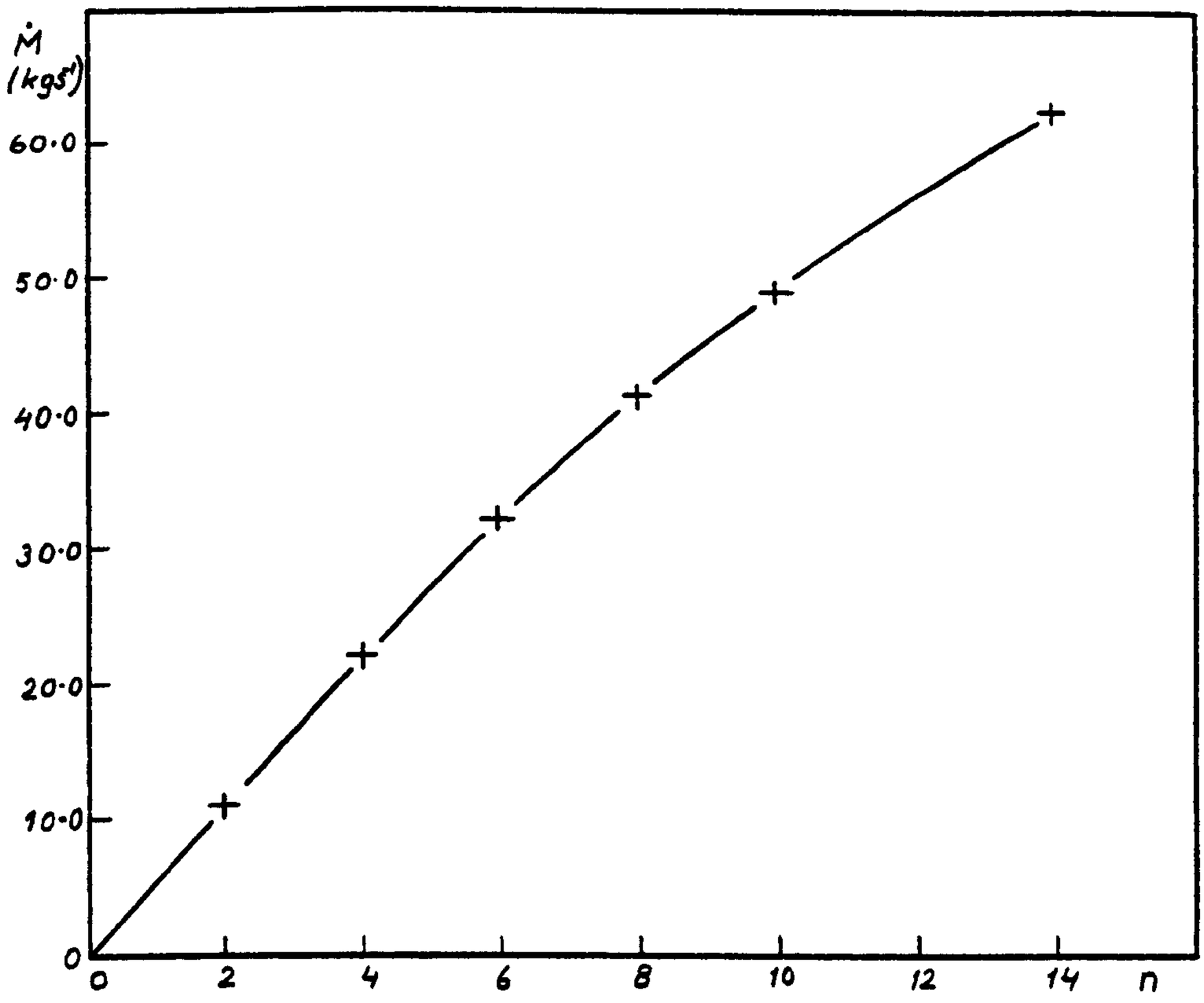

Fig. 42. Mass flow rate as a function of the number of valves open

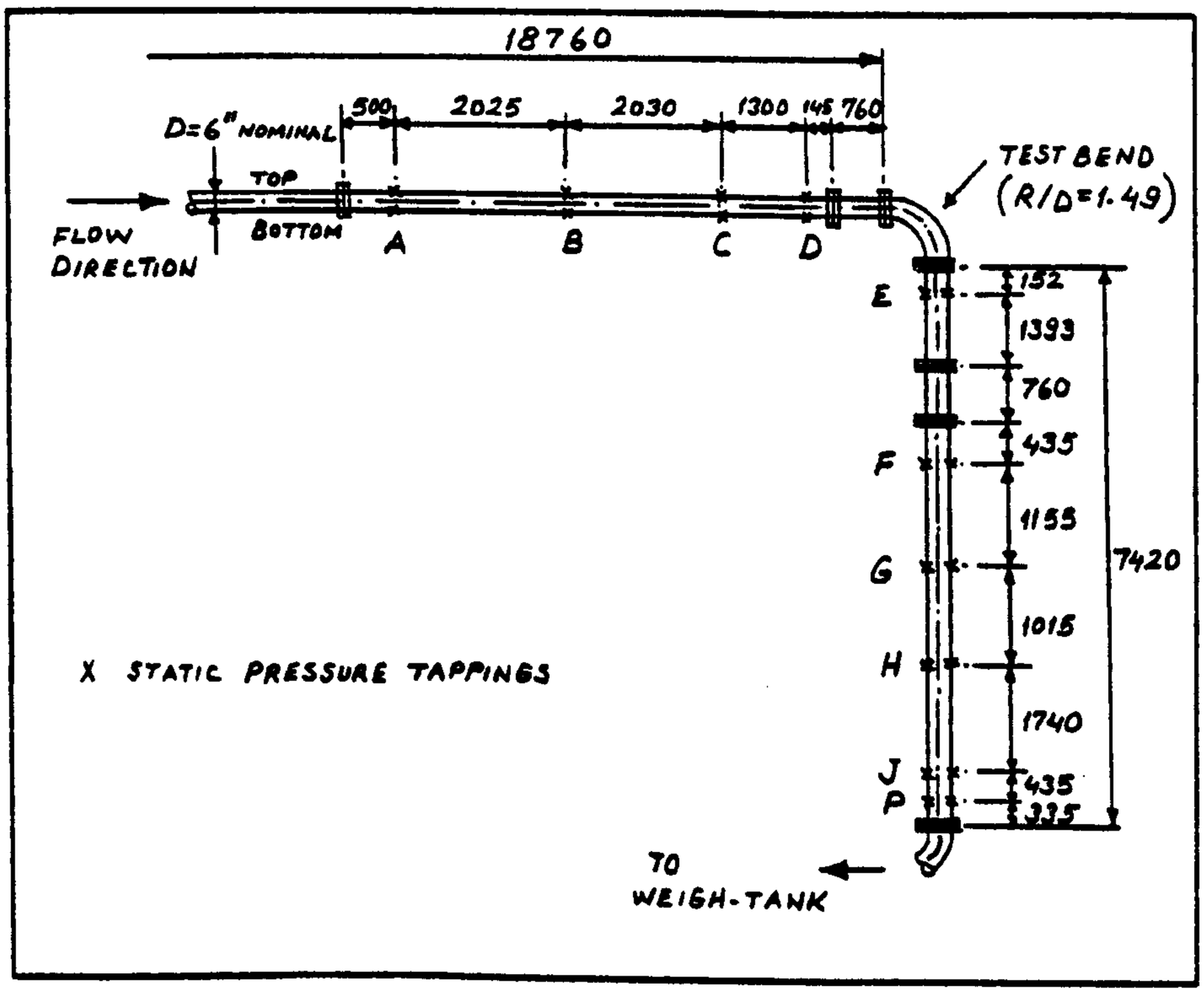

Fig. 43. Location of the static pressure tappings (all dimensions are in millimeter)

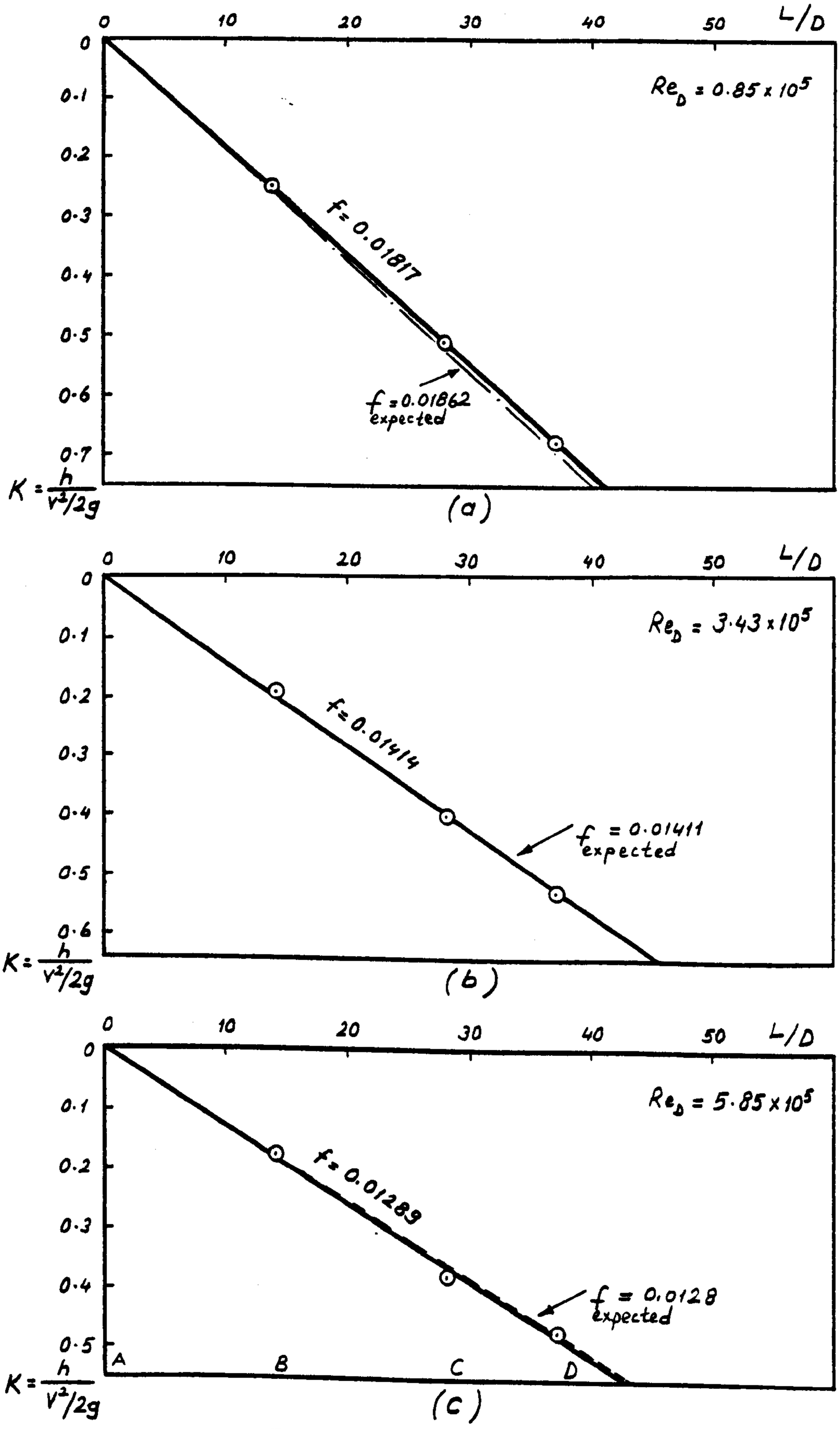

Fig. 44. Friction gradient in a straight duct

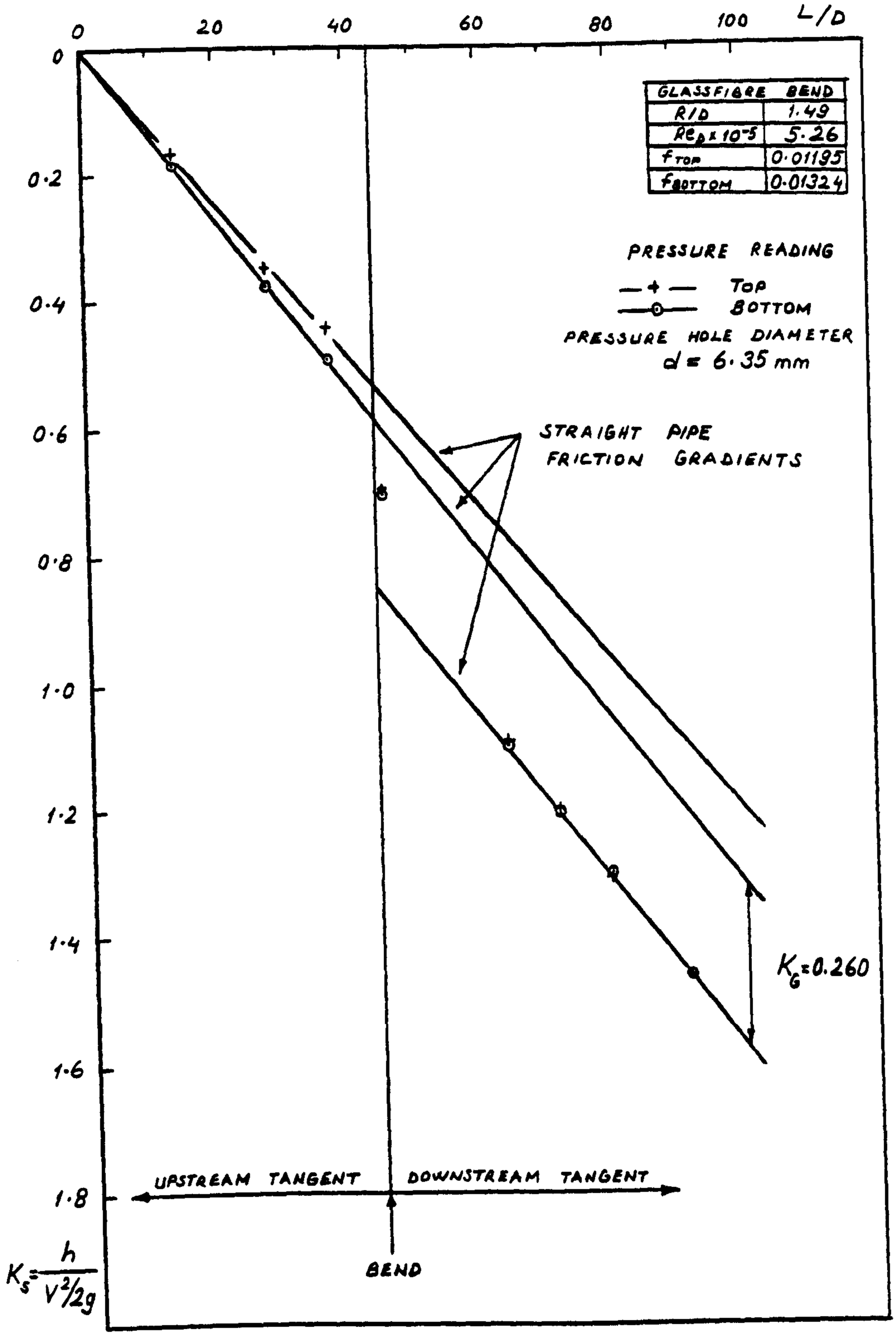

Fig. 45. System head loss measured by top and bottom static pressure tappings

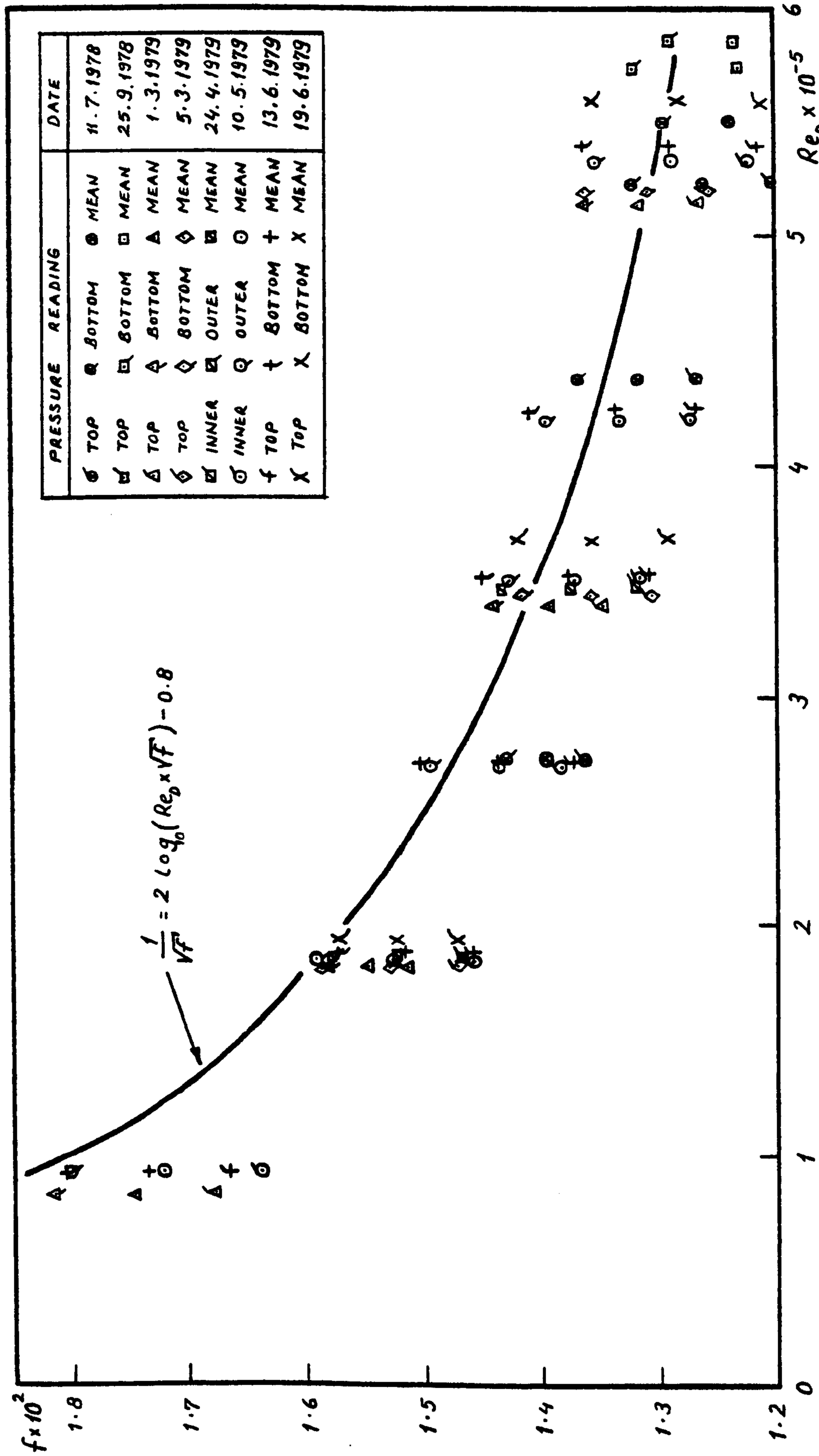

Fig. 46. Variation of f with Re_D

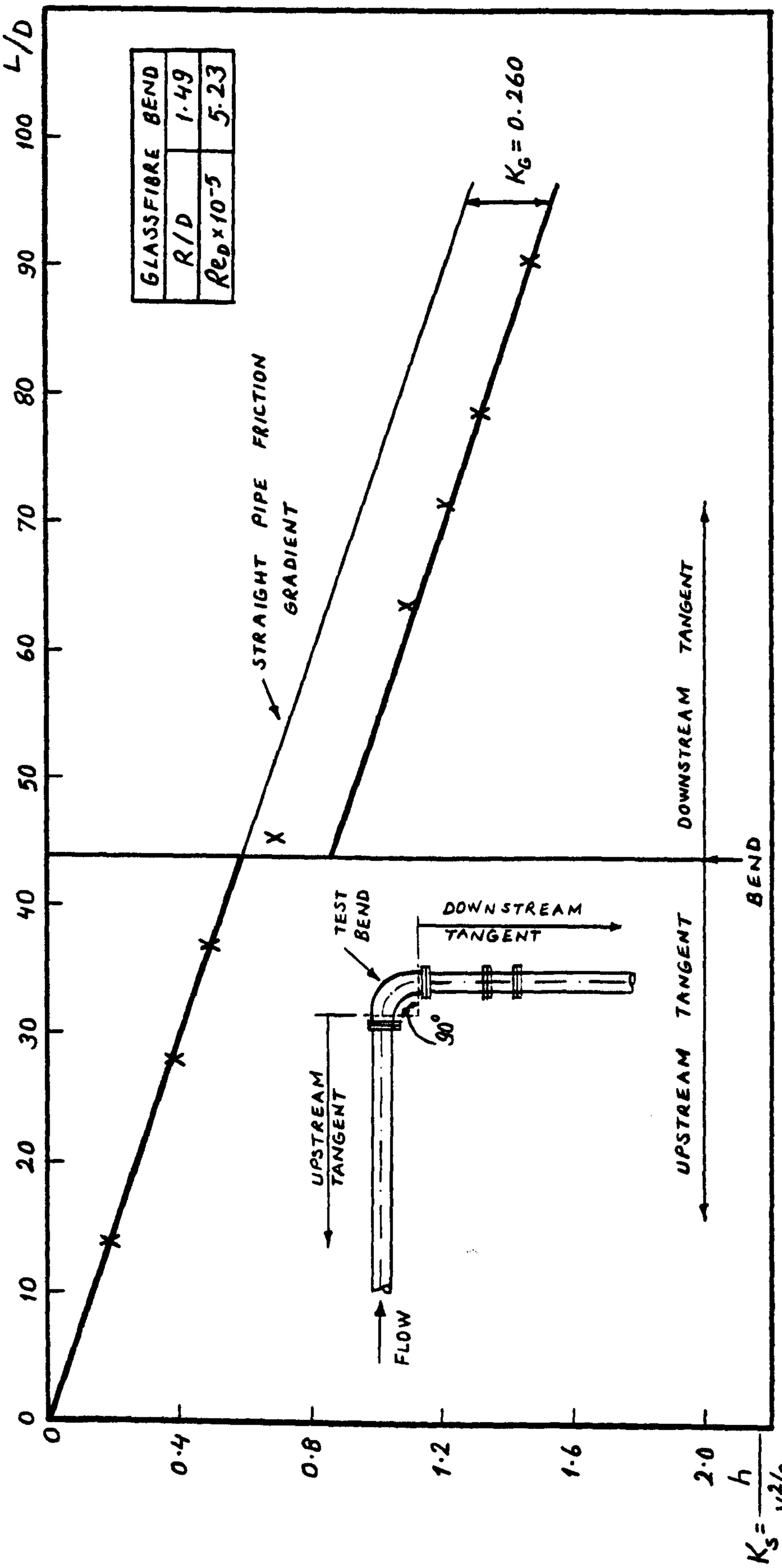

Fig. 47. Typical system head loss coefficient versus axial length

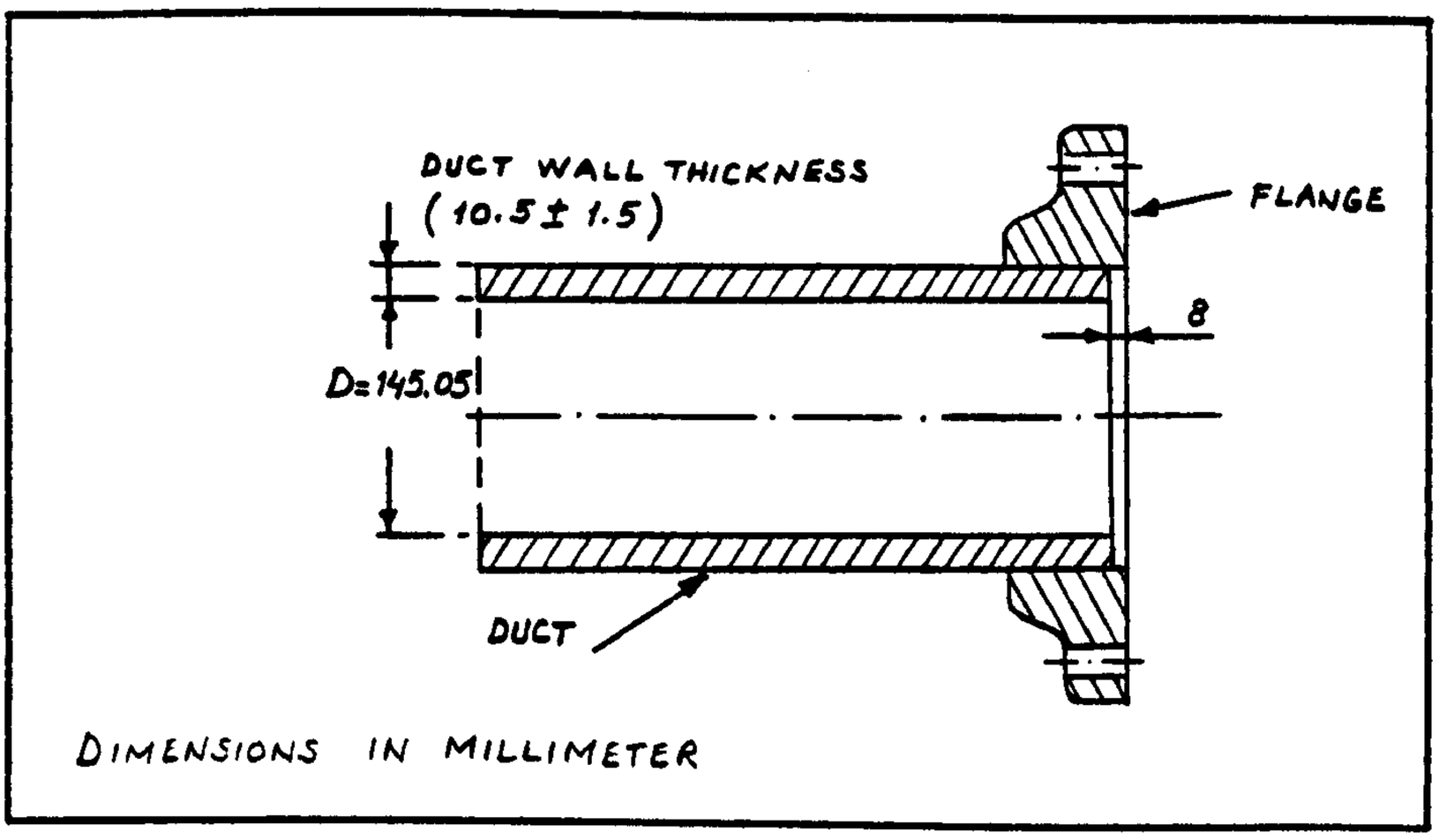

Fig. 48. Connection of flange

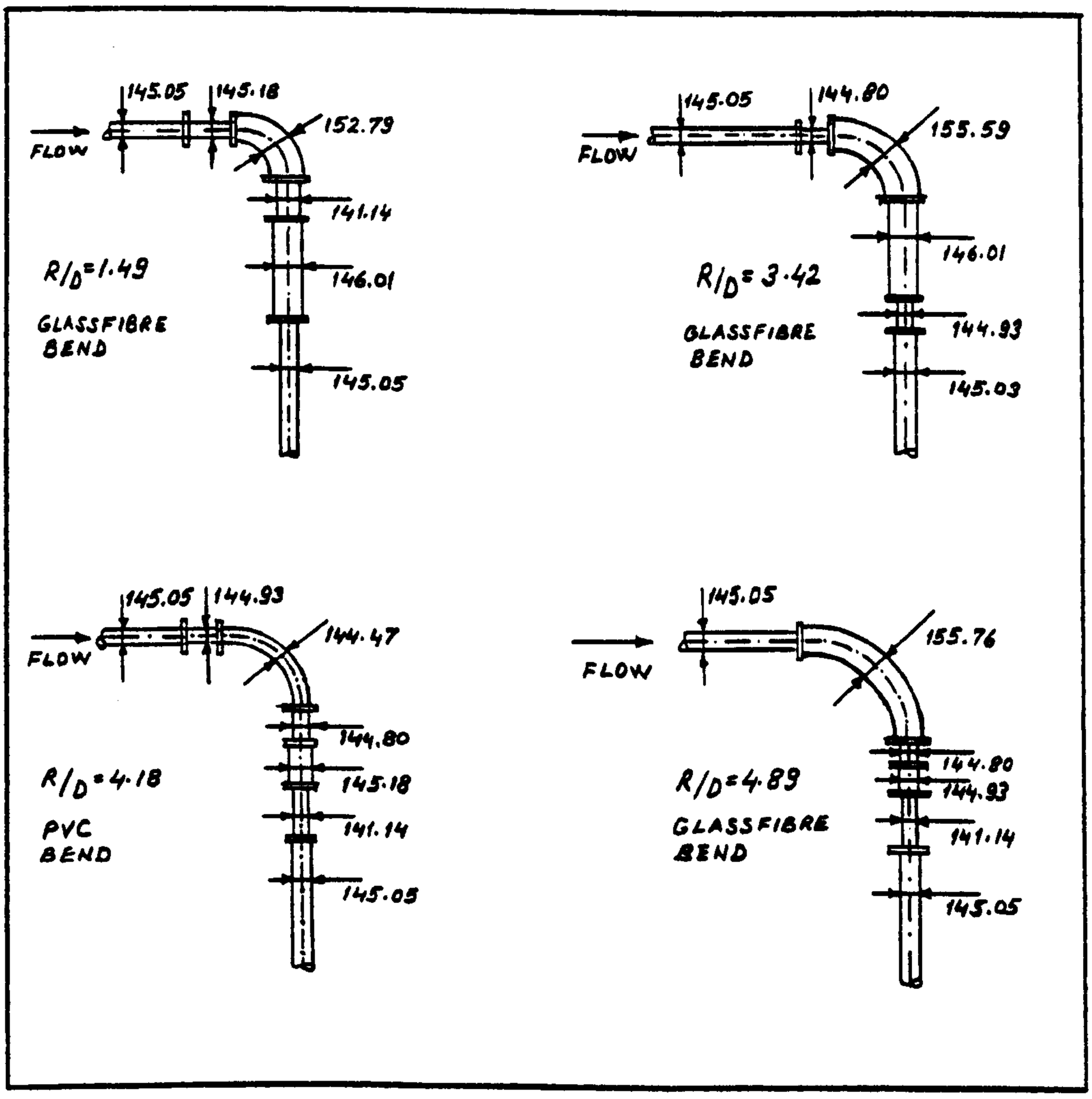

Fig. 49. Arrangements for spacer length

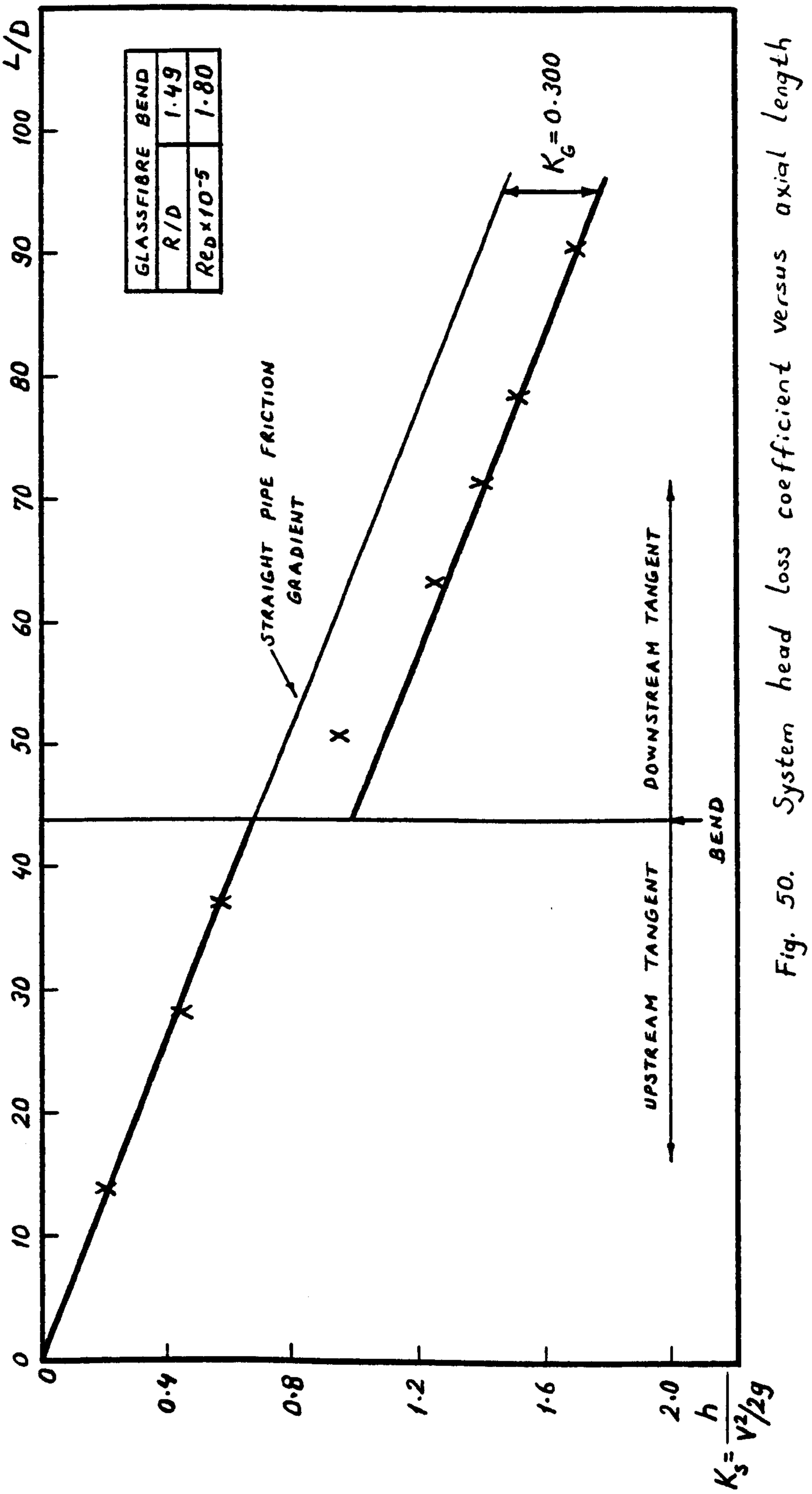
L/D
100
90
80
70
60
50
40
30
20
10
0
GLASSFIBRE BEND
R/D
1.49
1.80
ReD x10-5
KG=0.300
STRAIGHT PIPE FRICTION GRADIENT
UPSTREAM TANGENT
DOWNSTREAM TANGENT
BEND
0
0.4
0.8
1.2
1.6
2.0
Ks= h / V2/2g
System head loss coefficient versus axial length

Fig. 50.

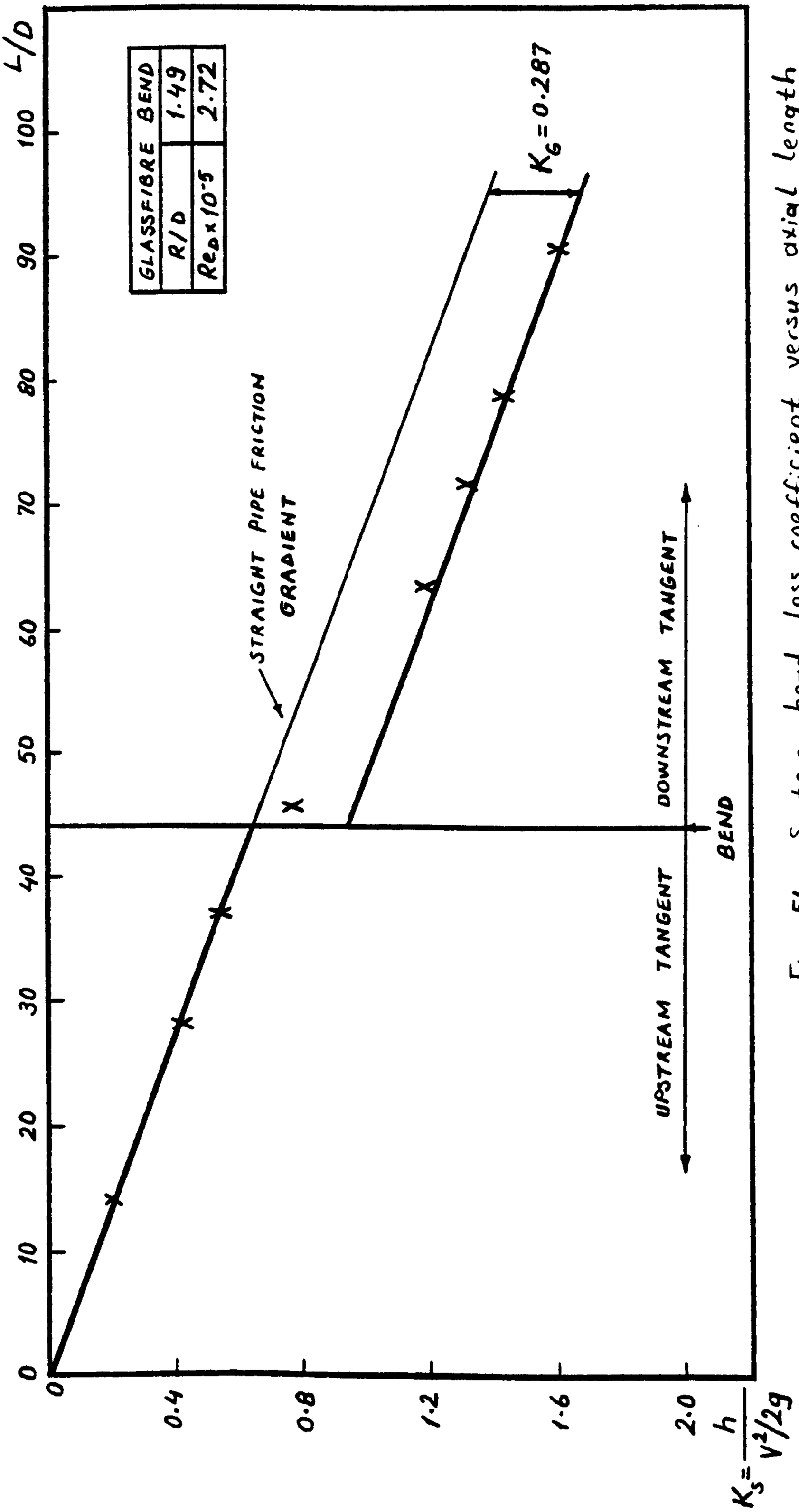

Fig. 51. System head loss coefficient versus axial length

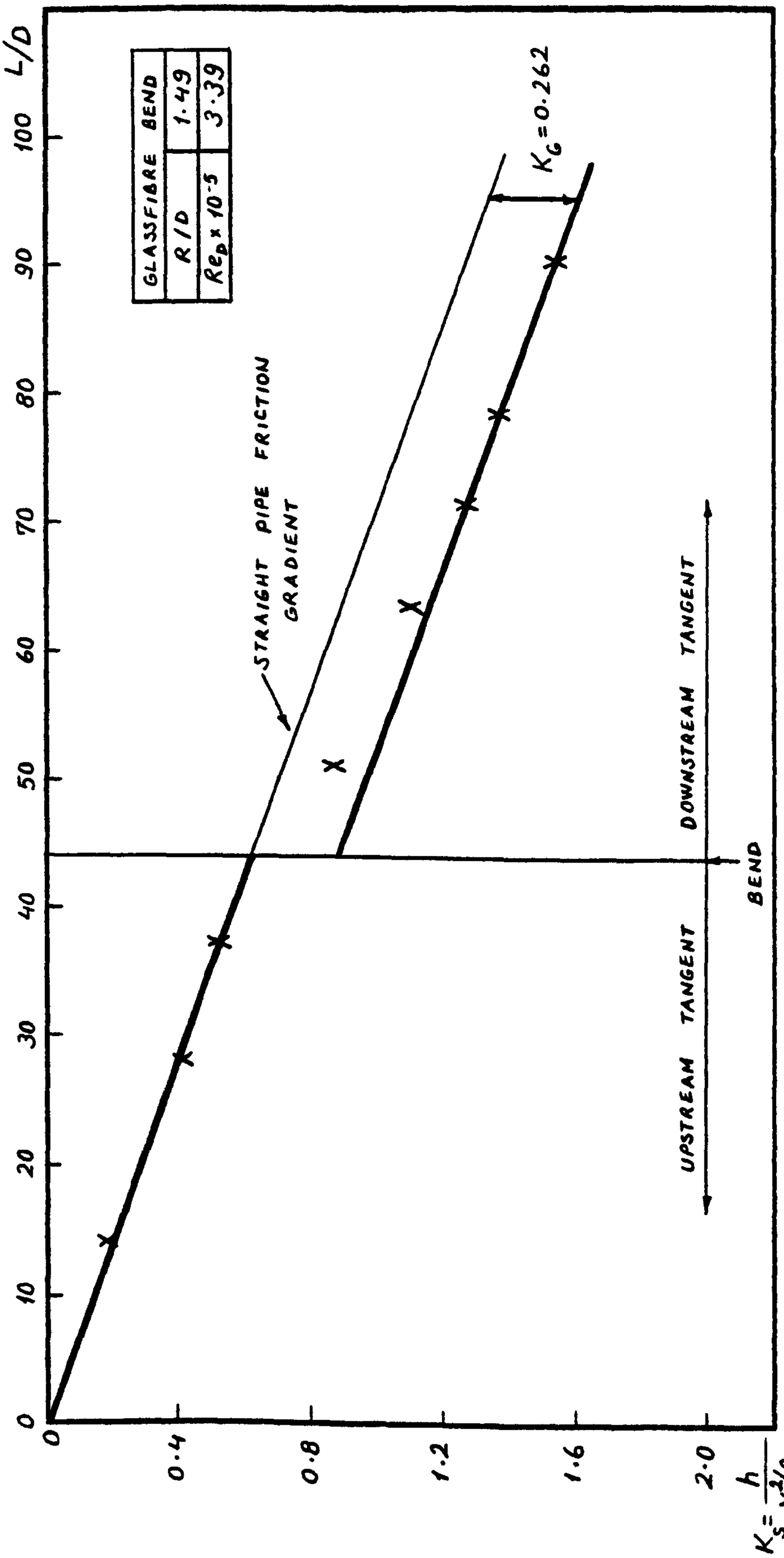

Fig. 52. System head loss coefficient versus axial length

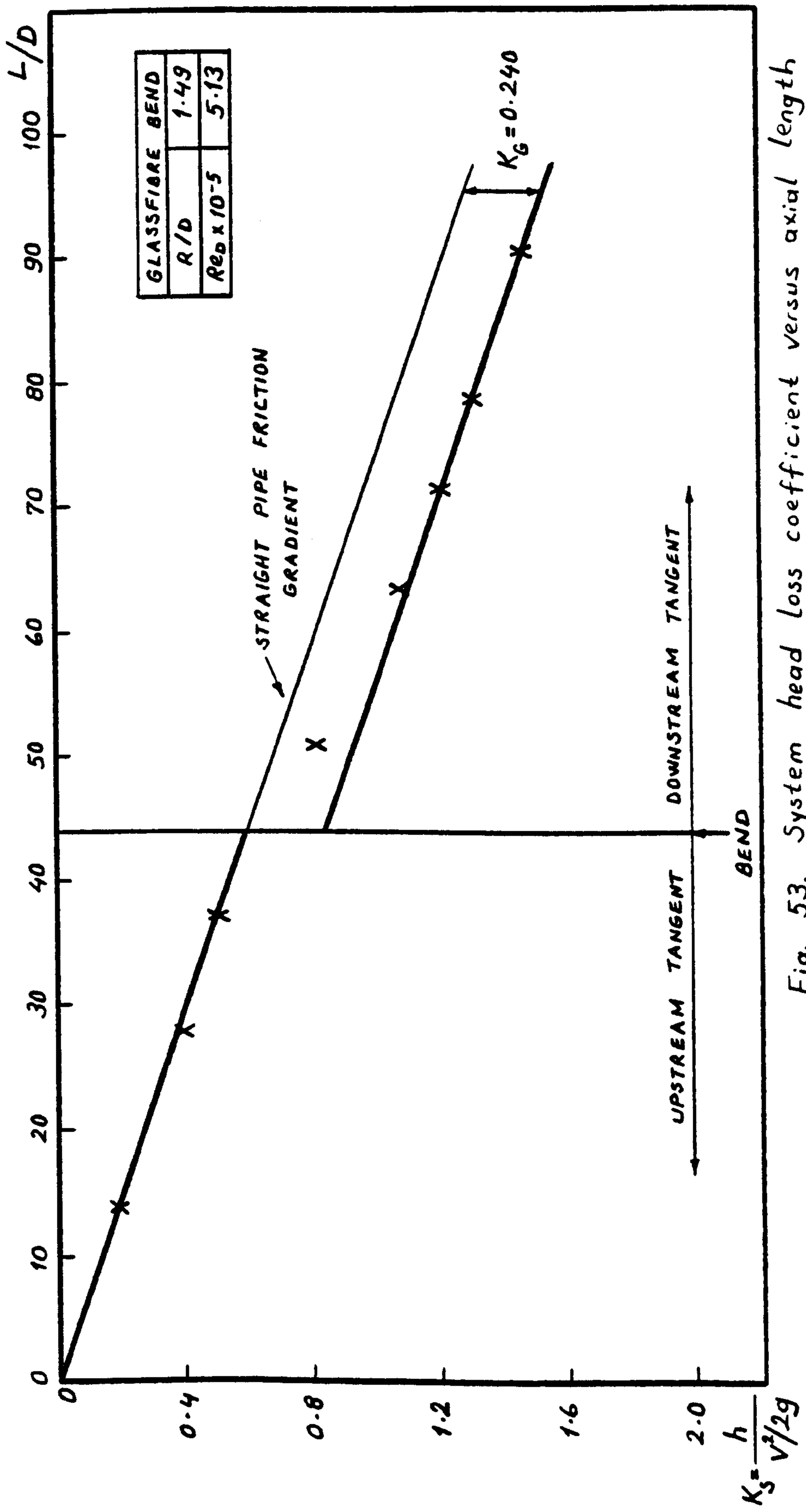
L/D
100
90
80
70
60
50
40
30
20
10
0
GLASSFIBRE BEND
R/D 1.49
ReD x 10-5 5.13
KG = 0.240
STRAIGHT PIPE FRICTION GRADIENT
UPSTREAM TANGENT
BEND
DOWNSTREAM TANGENT
0
0.4
0.8
1.2
1.6
2.0
K3 = h / V²/2g
Fig. 53. System head loss coefficient versus axial length

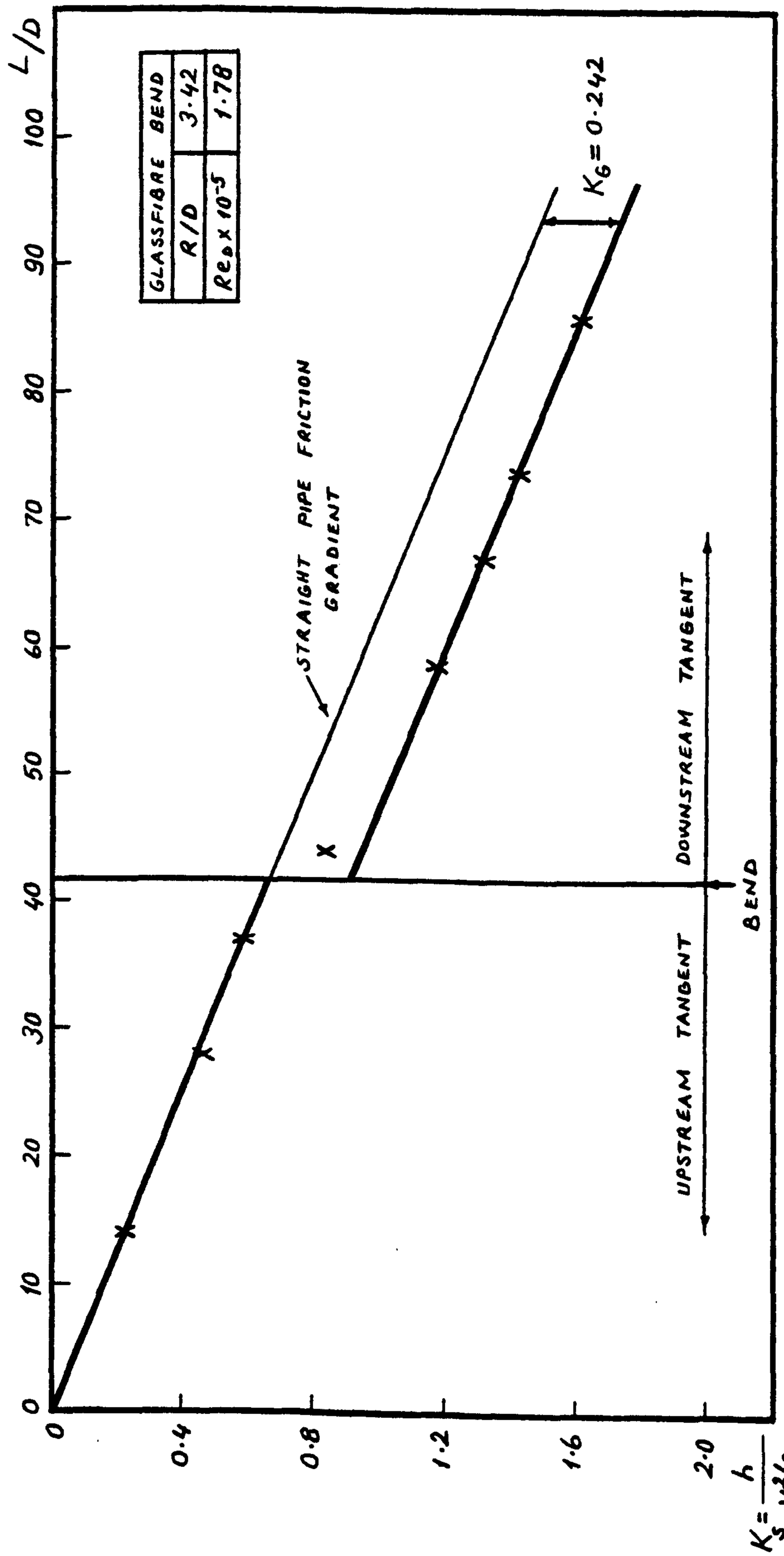

Fig. 54. System head loss coefficient versus axial length

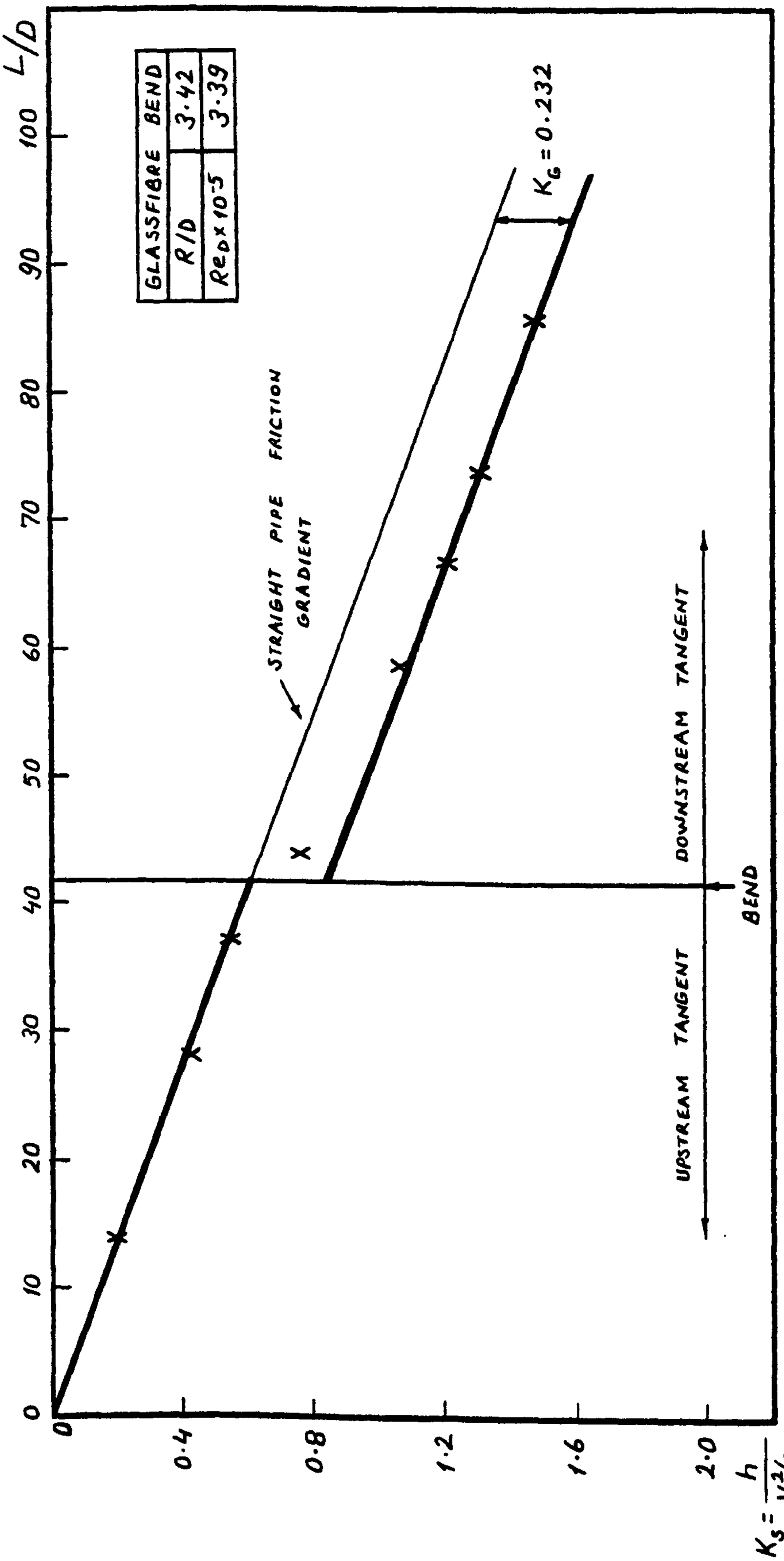

Fig. 55. System head loss coefficient versus axial length

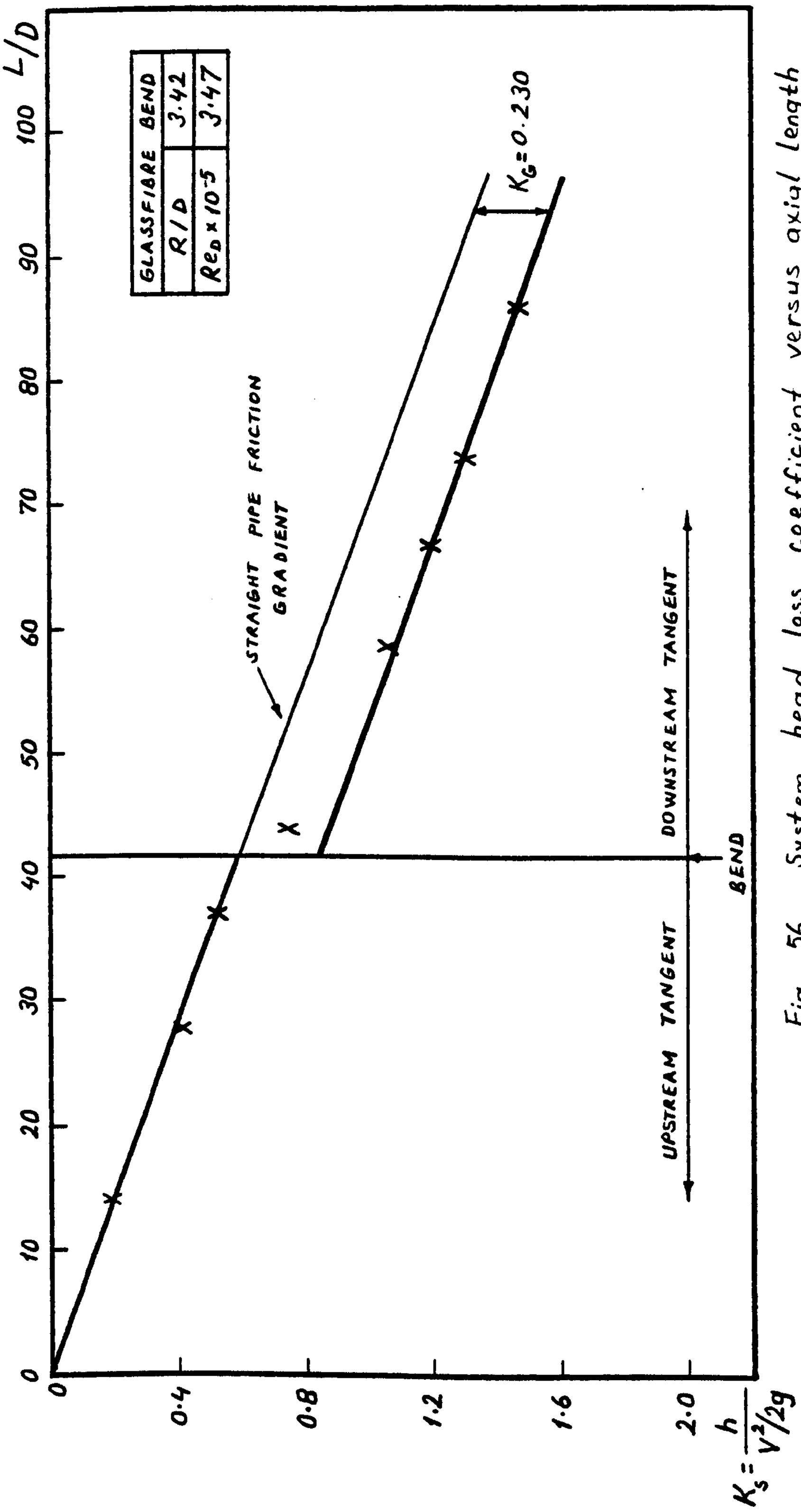

Fig. 56. System head loss coefficient versus axial length

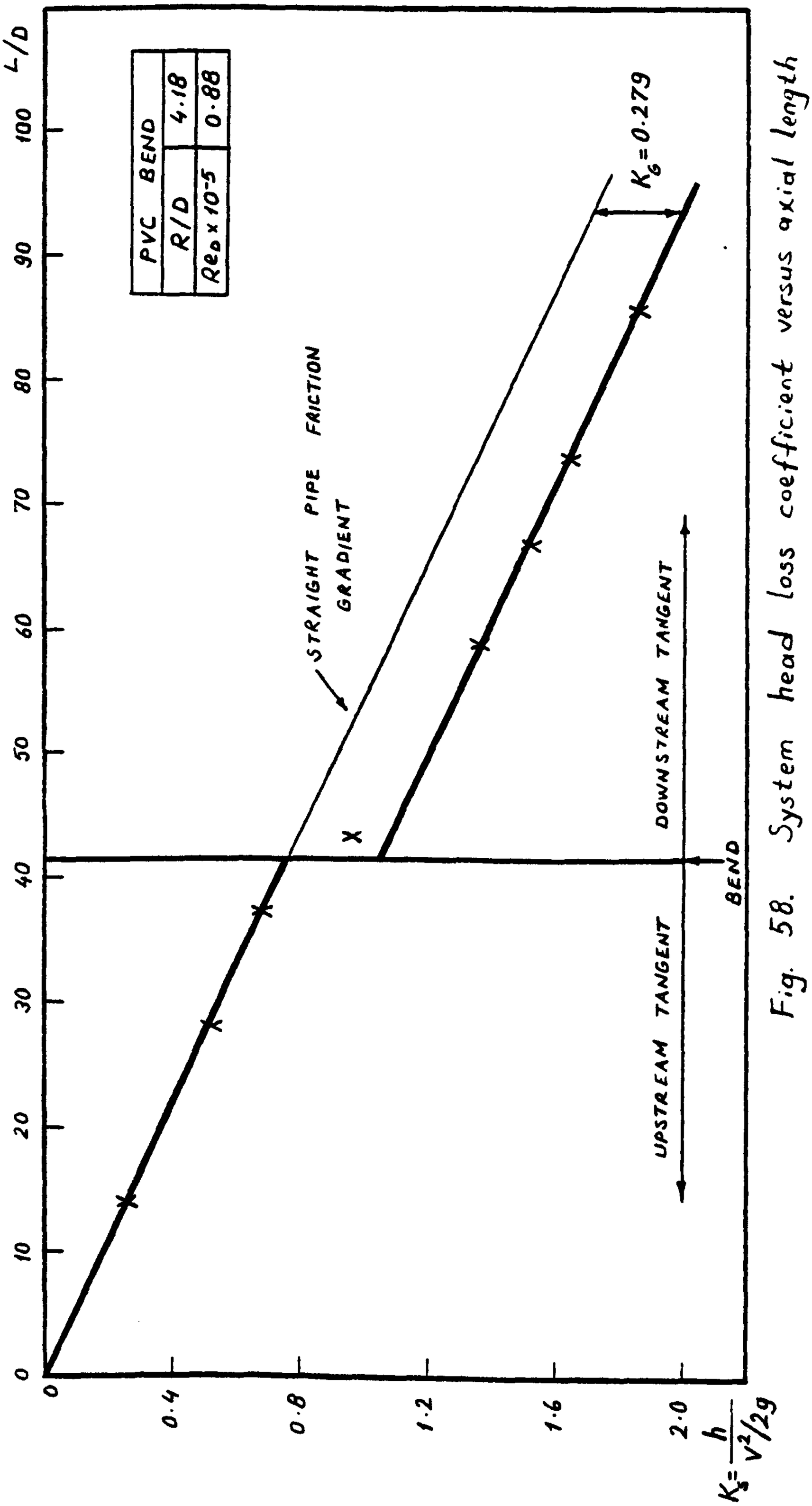

Fig. 58. System head loss coefficient versus axial length

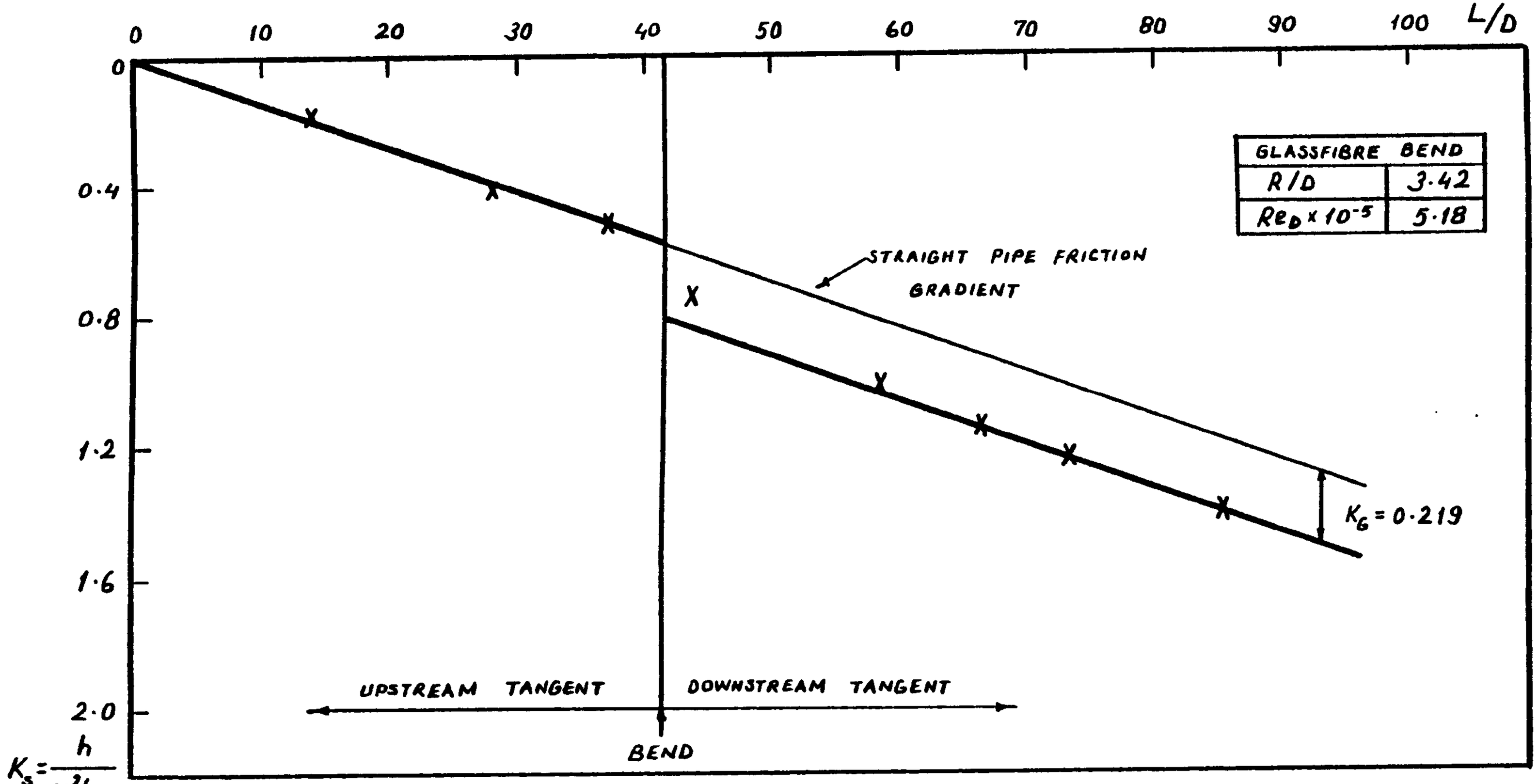

Fig. 57. System head loss coefficient versus axial length

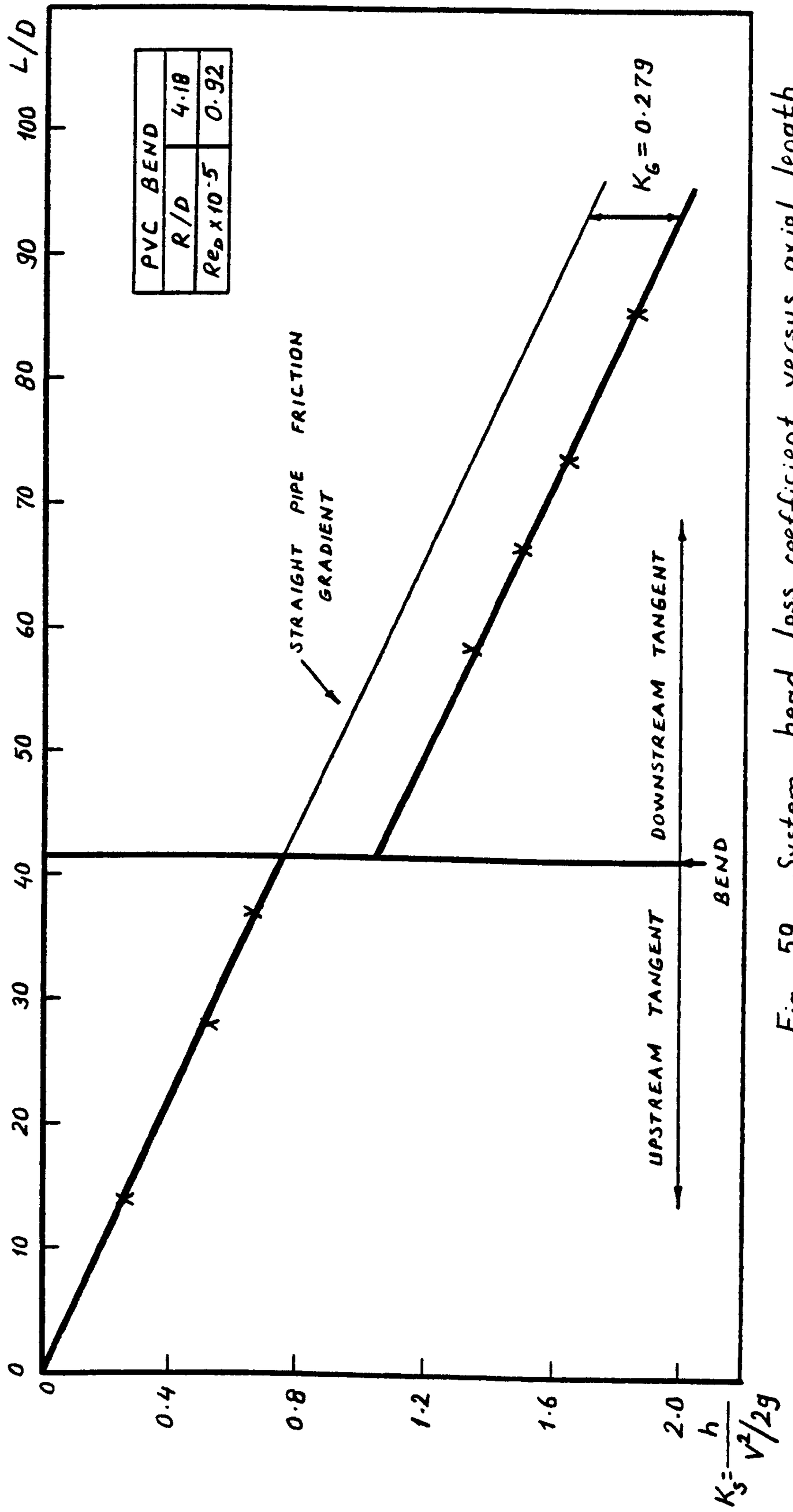

Fig. 59. System head loss coefficient versus axial length

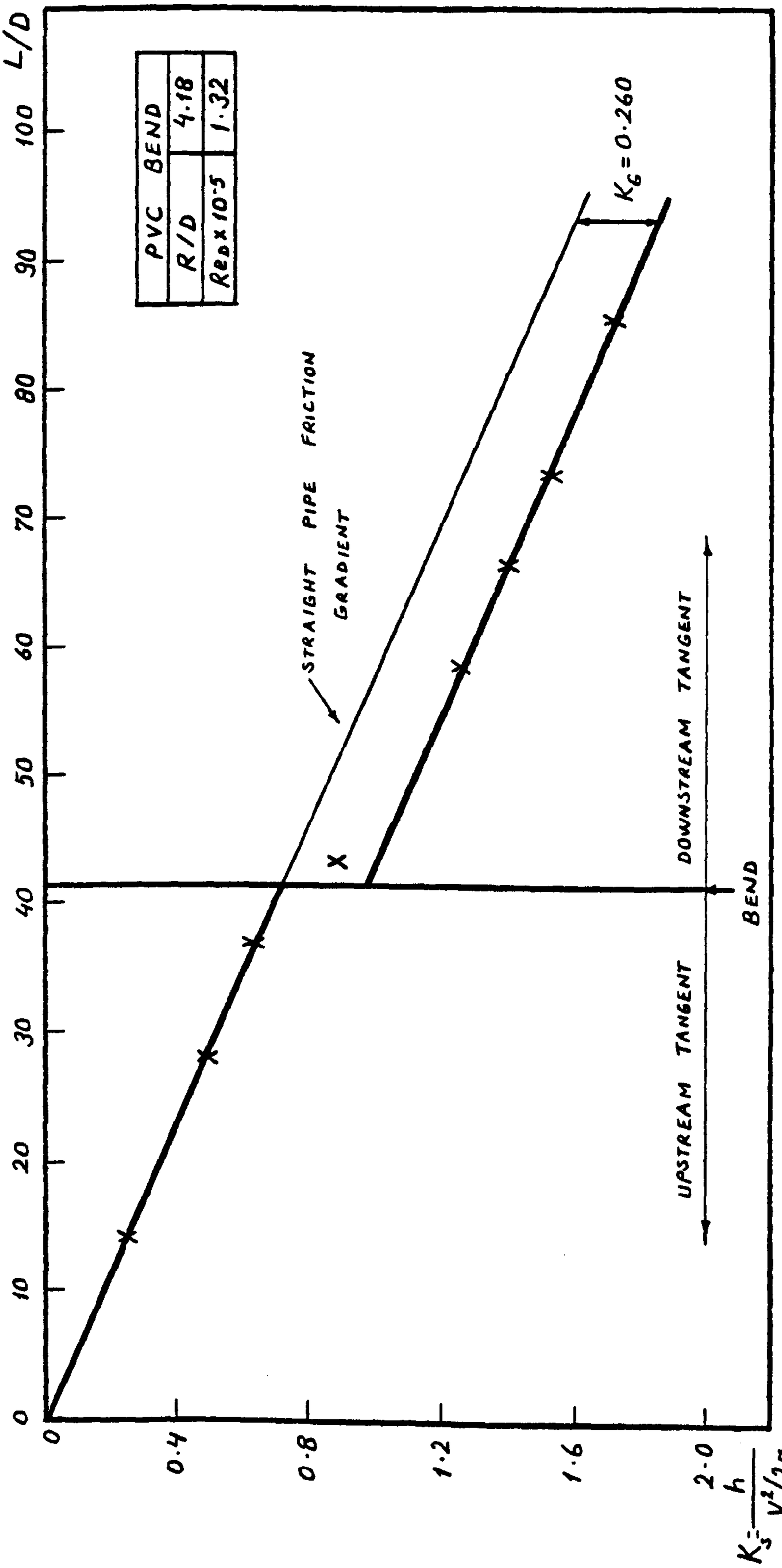

Fig. 60. System head loss coefficient versus axial length

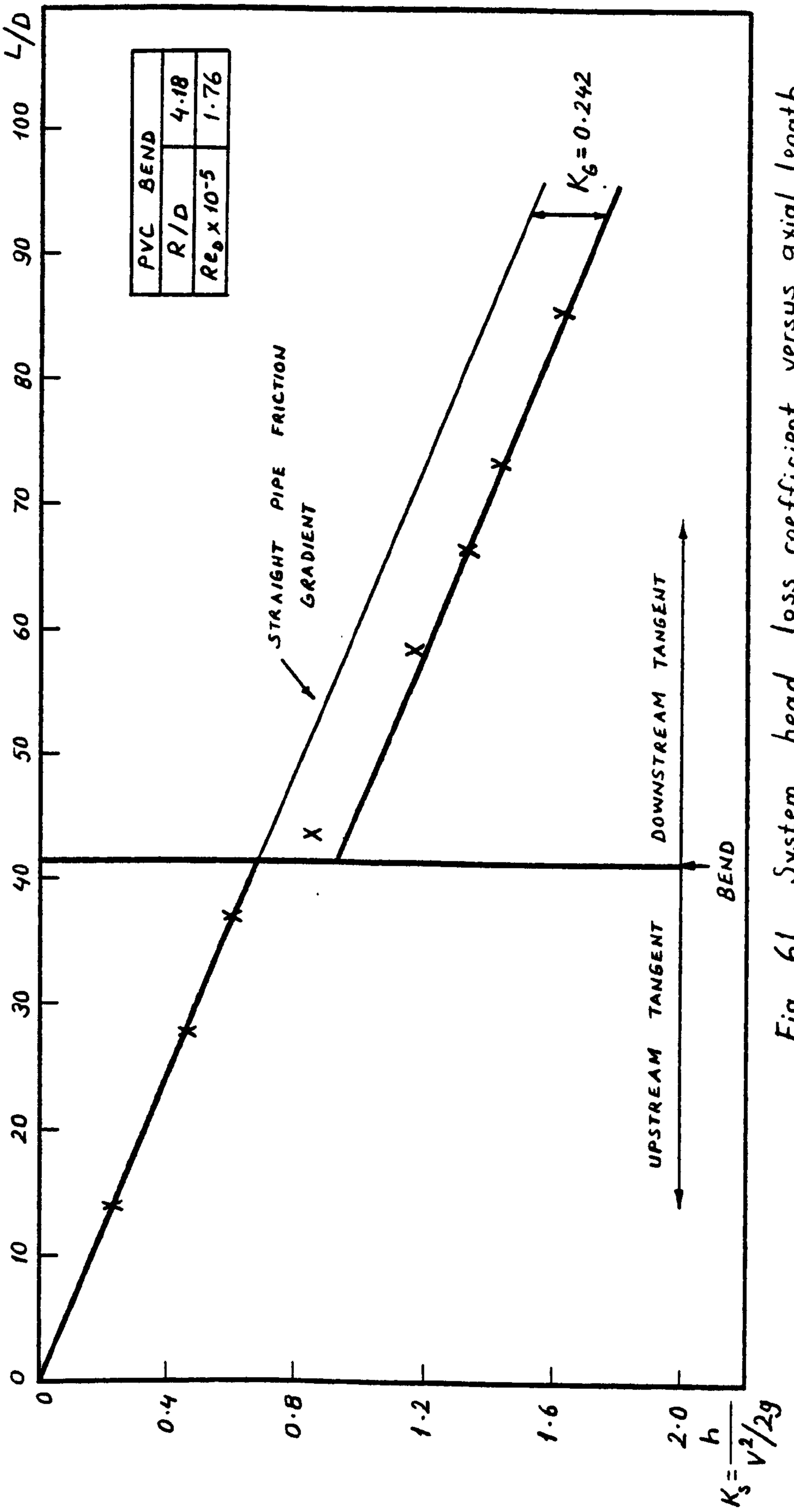

Fig. 61. System head loss coefficient versus axial length

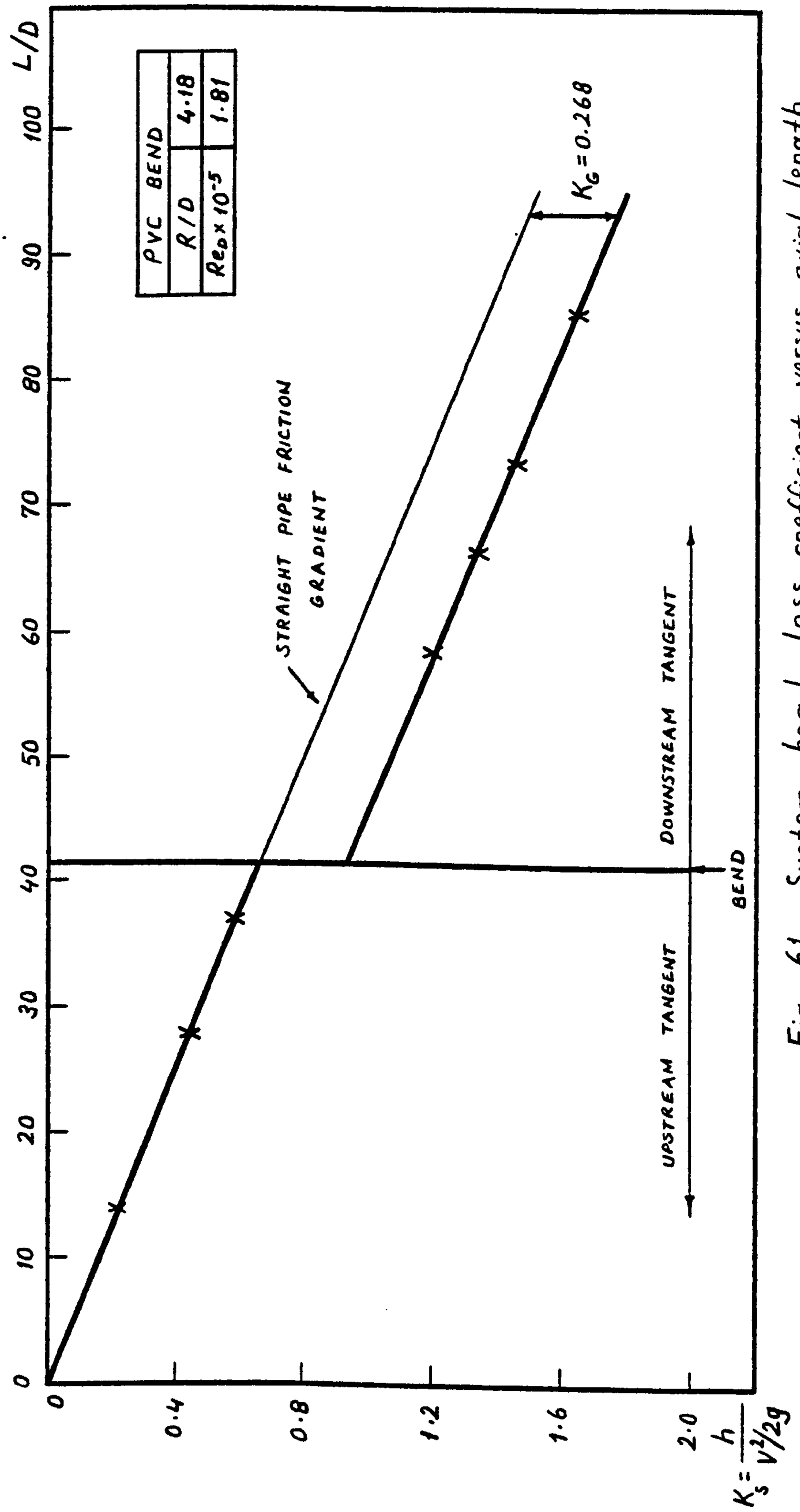

Fig. 61. System head Loss coefficient versus axial length

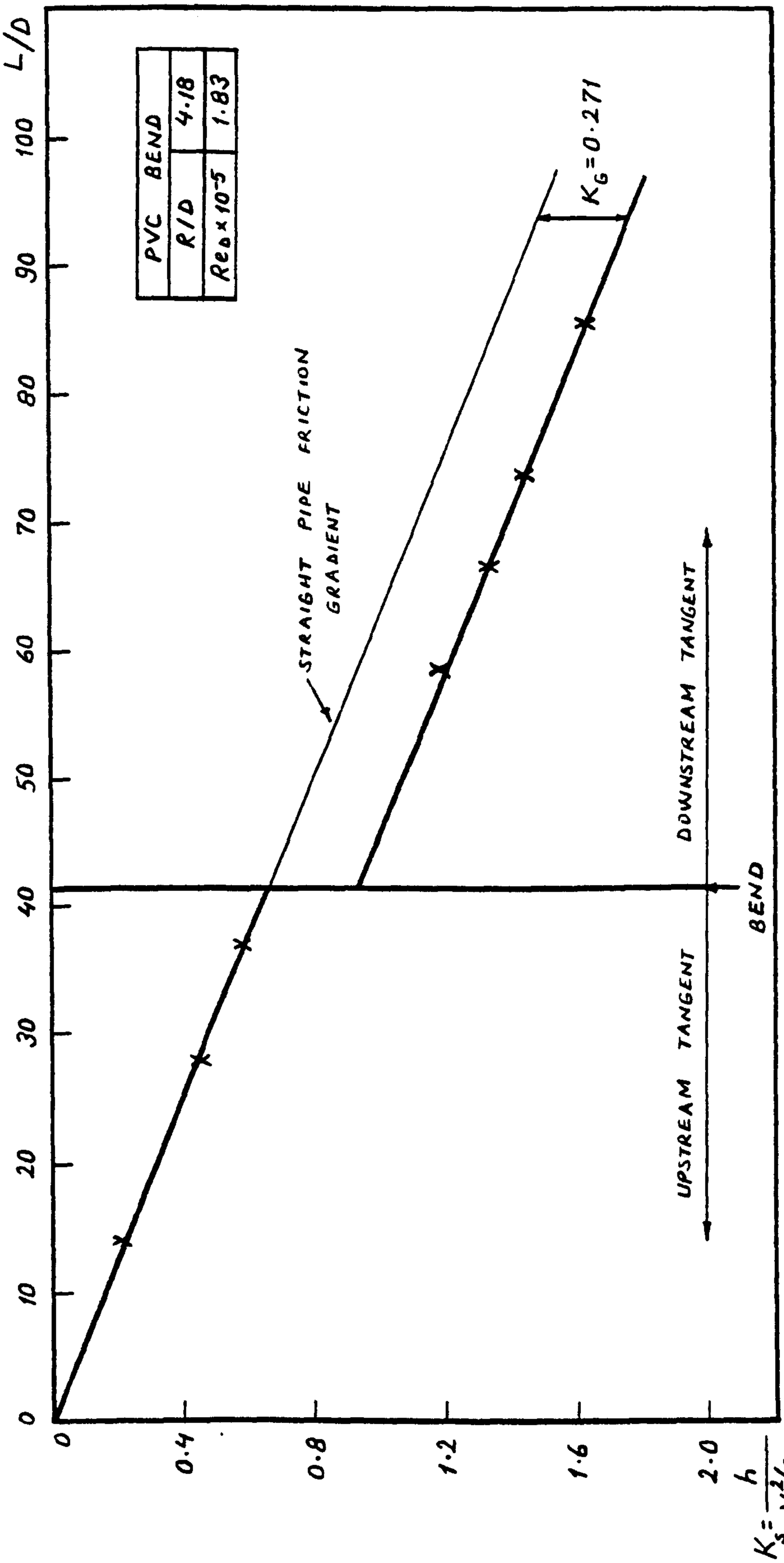

Fig. 63. System head loss coefficient versus

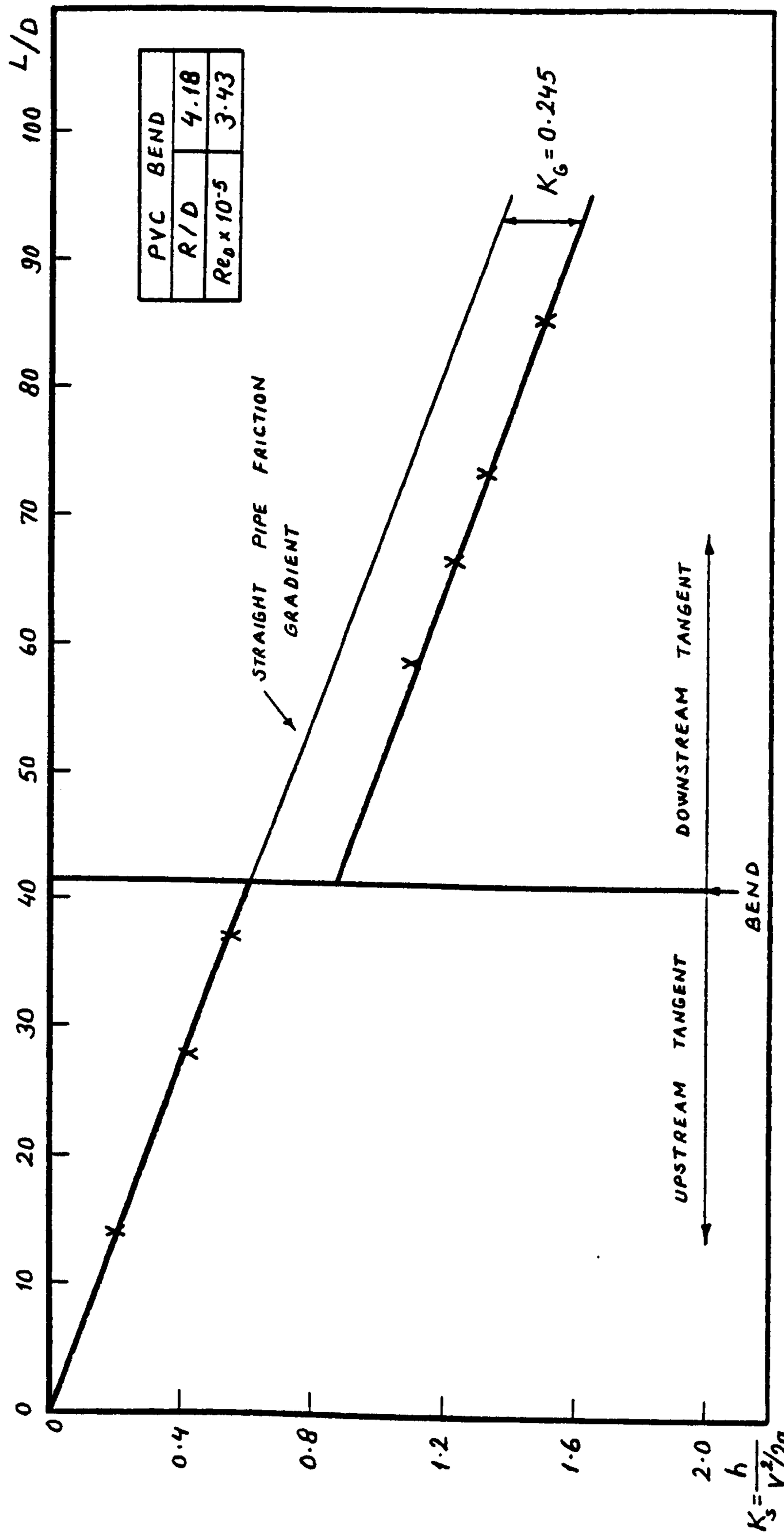

Fig. 64. System head

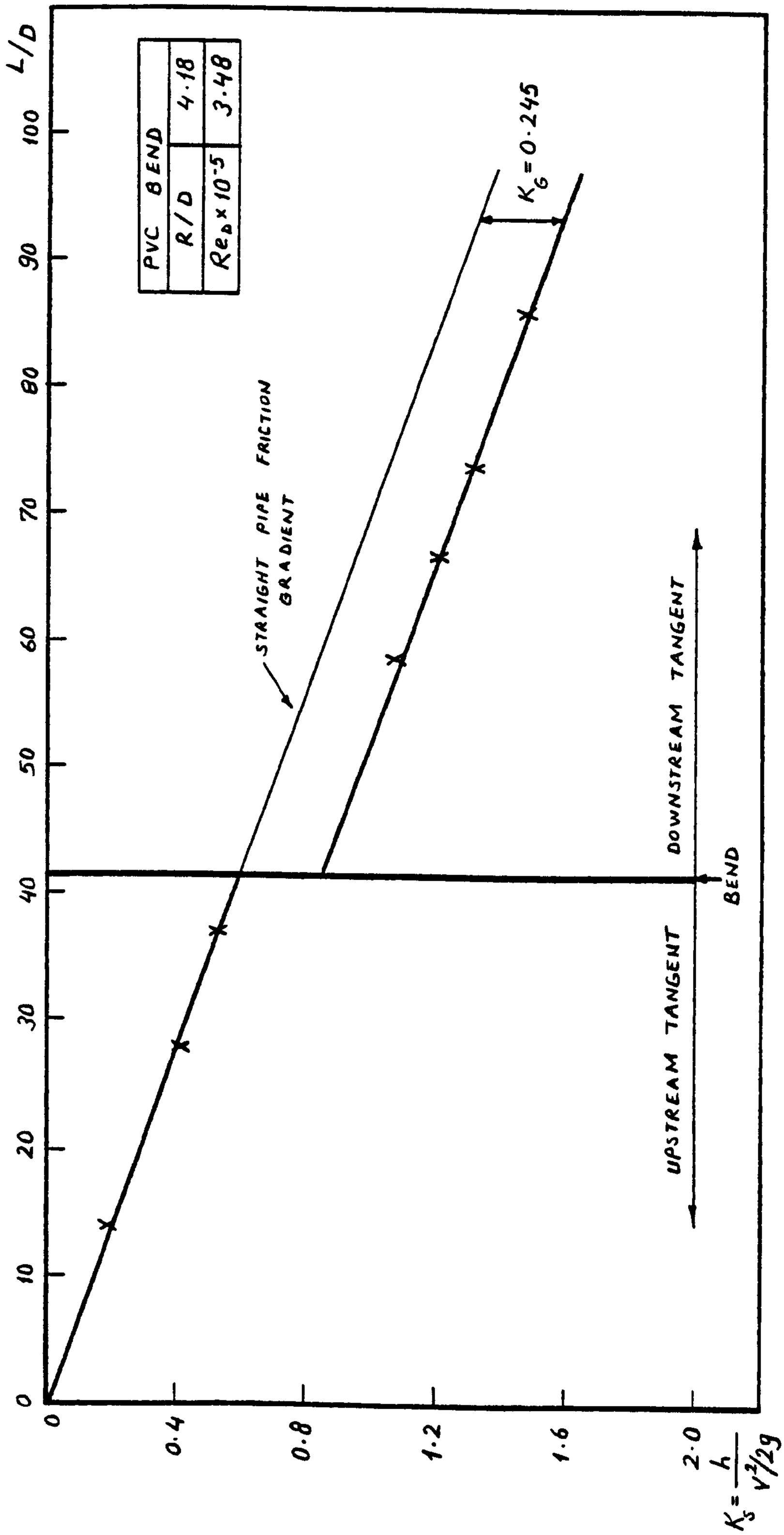

Fig. 65. System head loss coefficient versus axial length

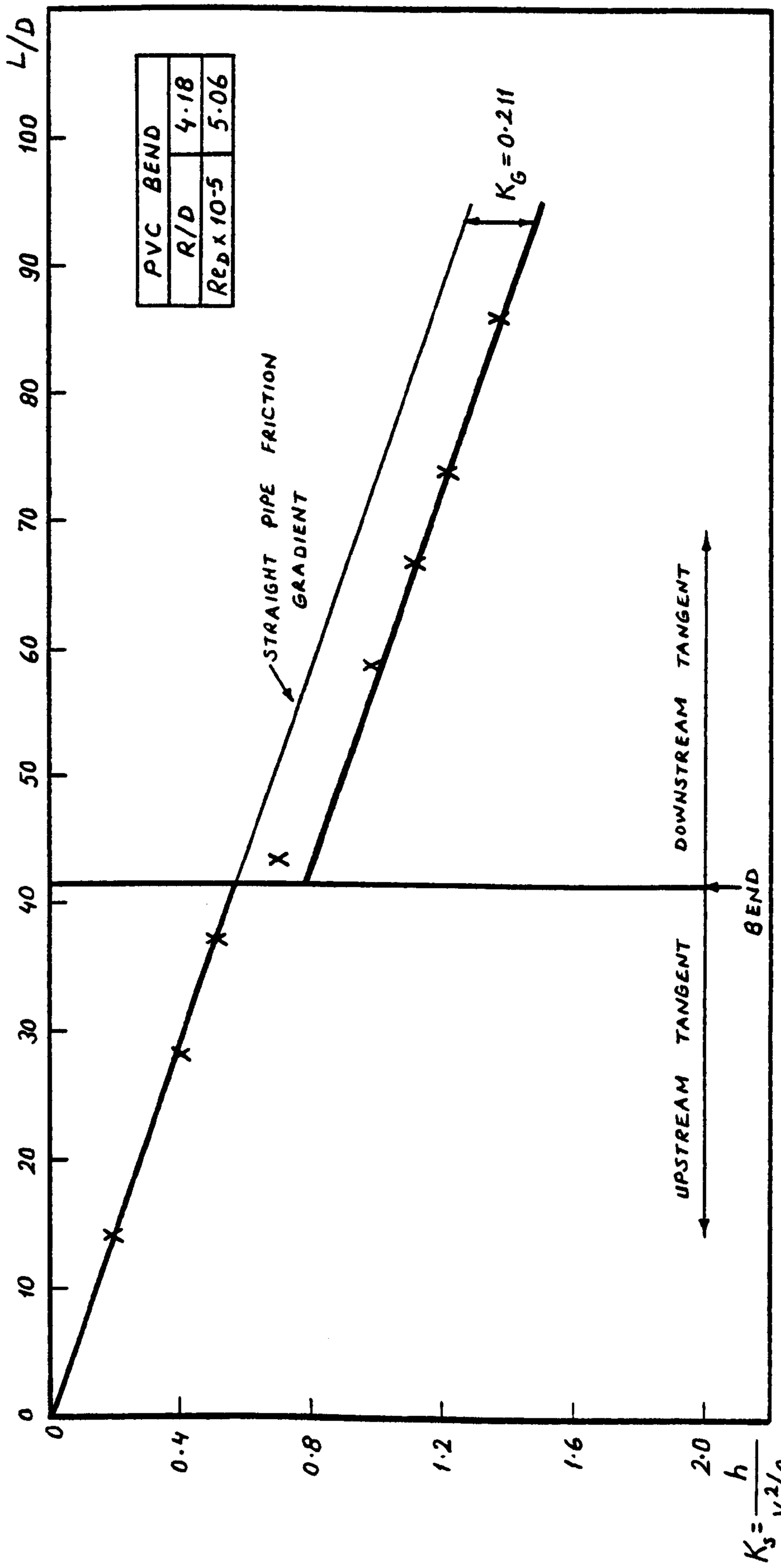

Fig. 66. System head loss coefficient versus axial length

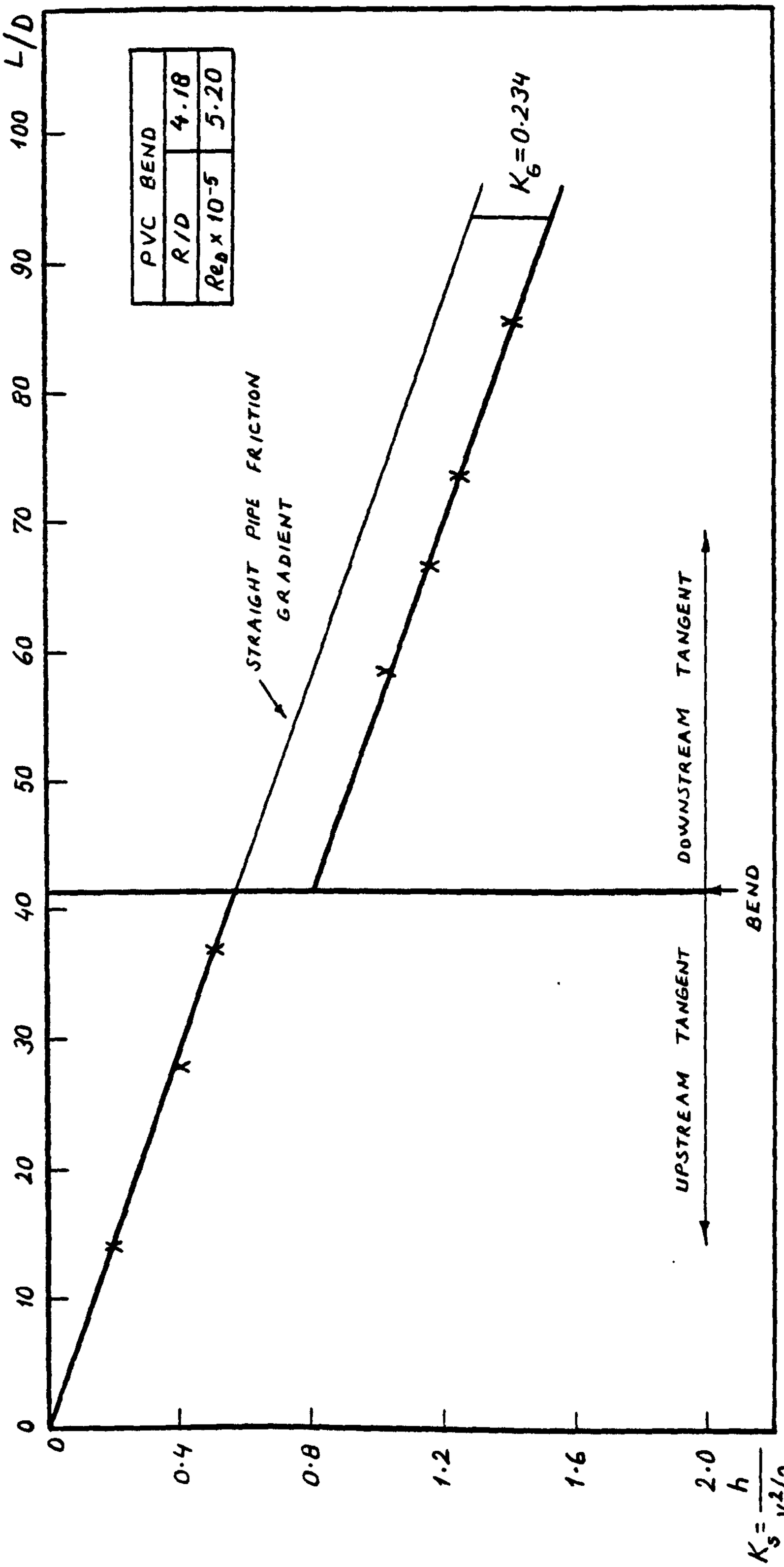

Fig. 67. System head Loss coefficient versus axial length

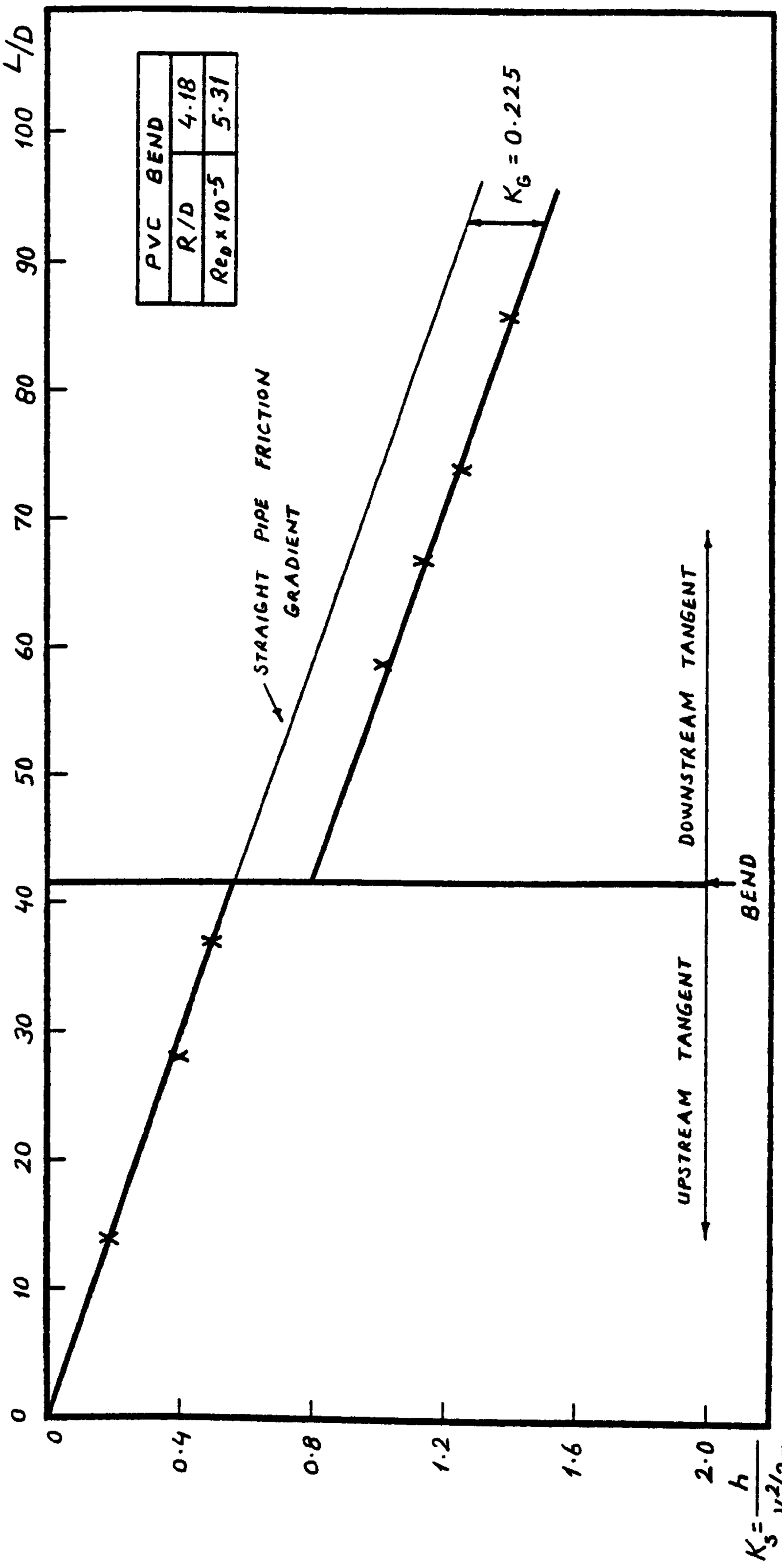

Fig. 68. System head loss coefficient versus axial length

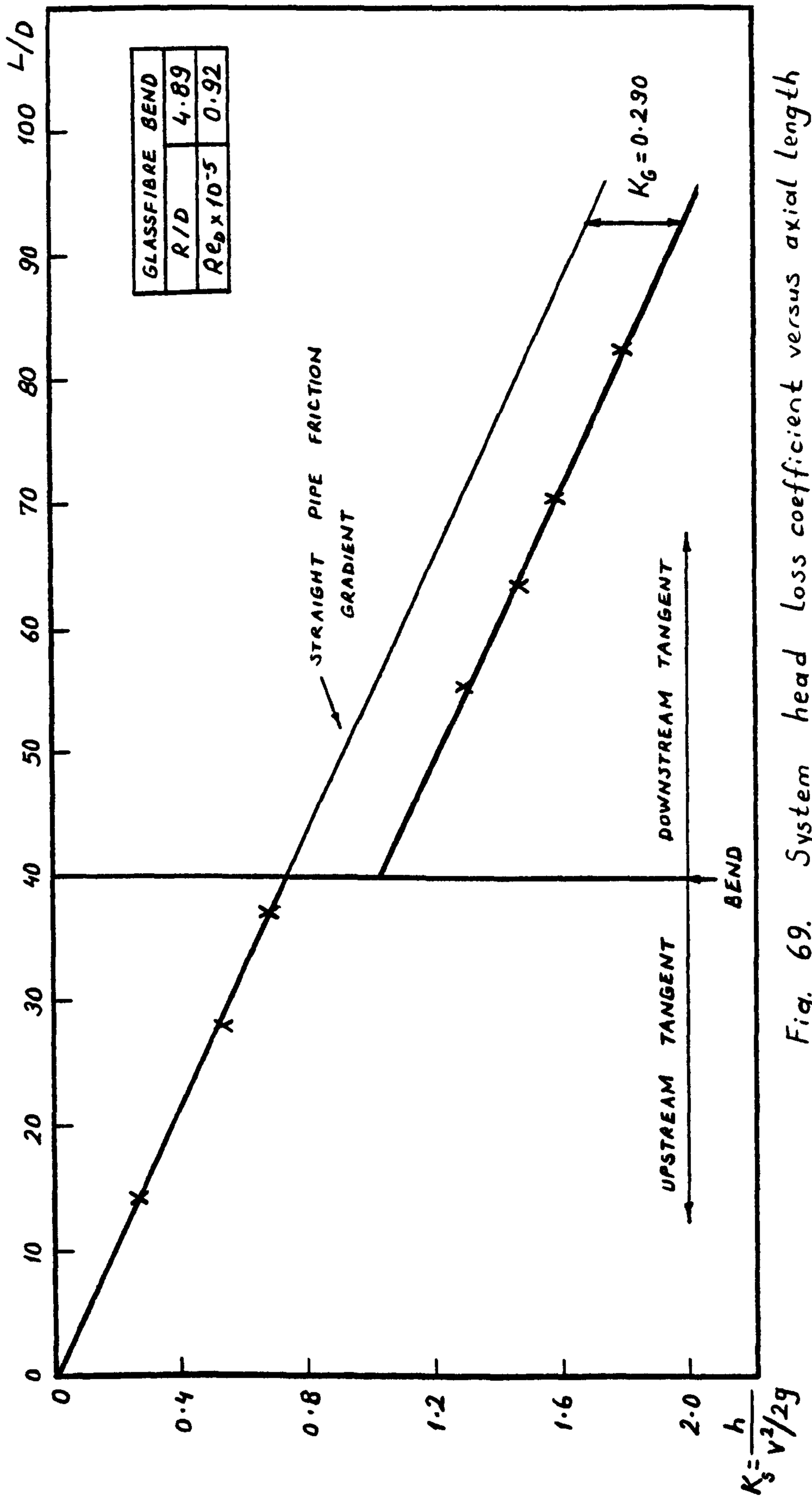

Fig. 69. System head loss coefficient versus axial length

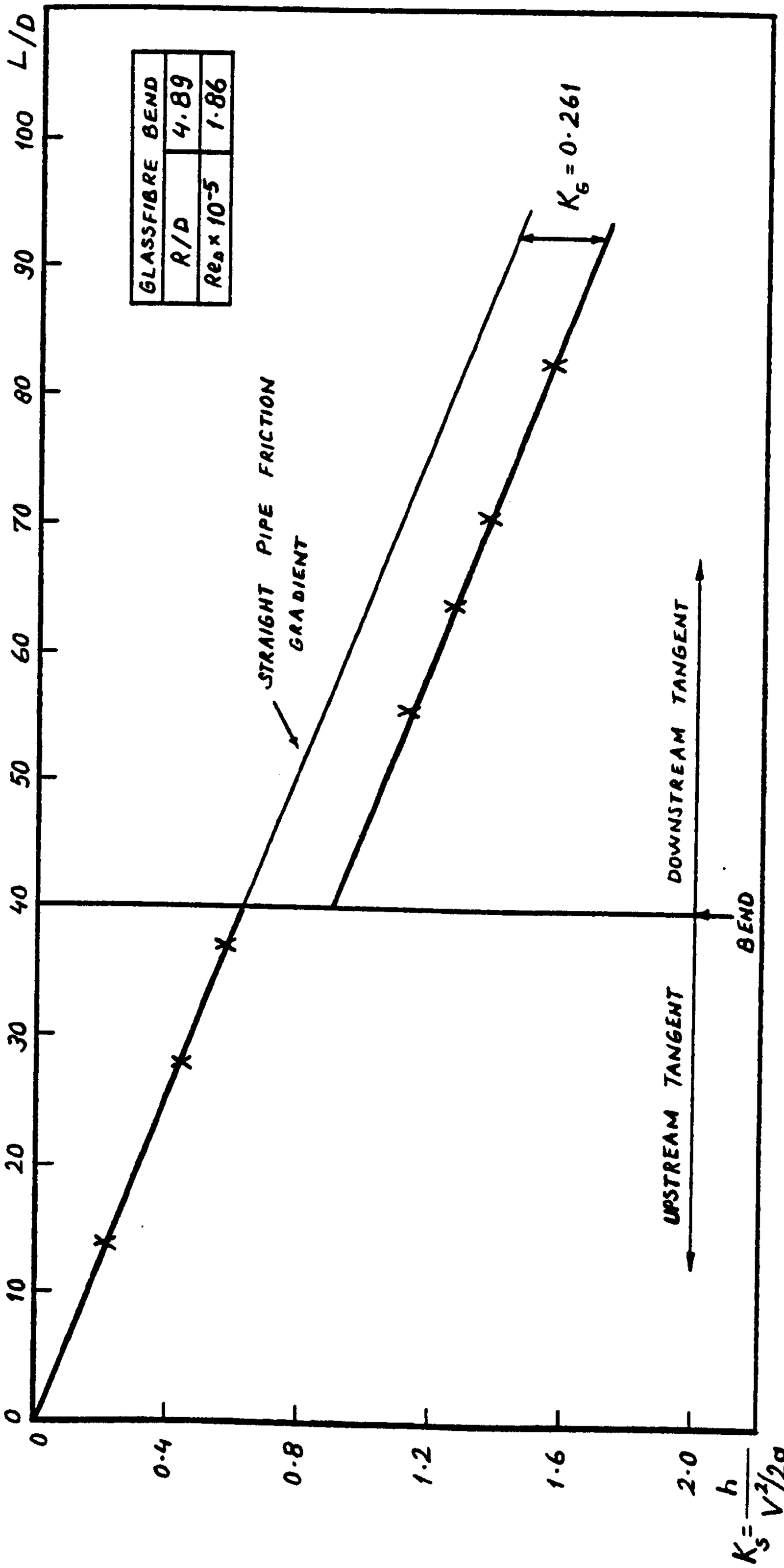

Fig. 70. System

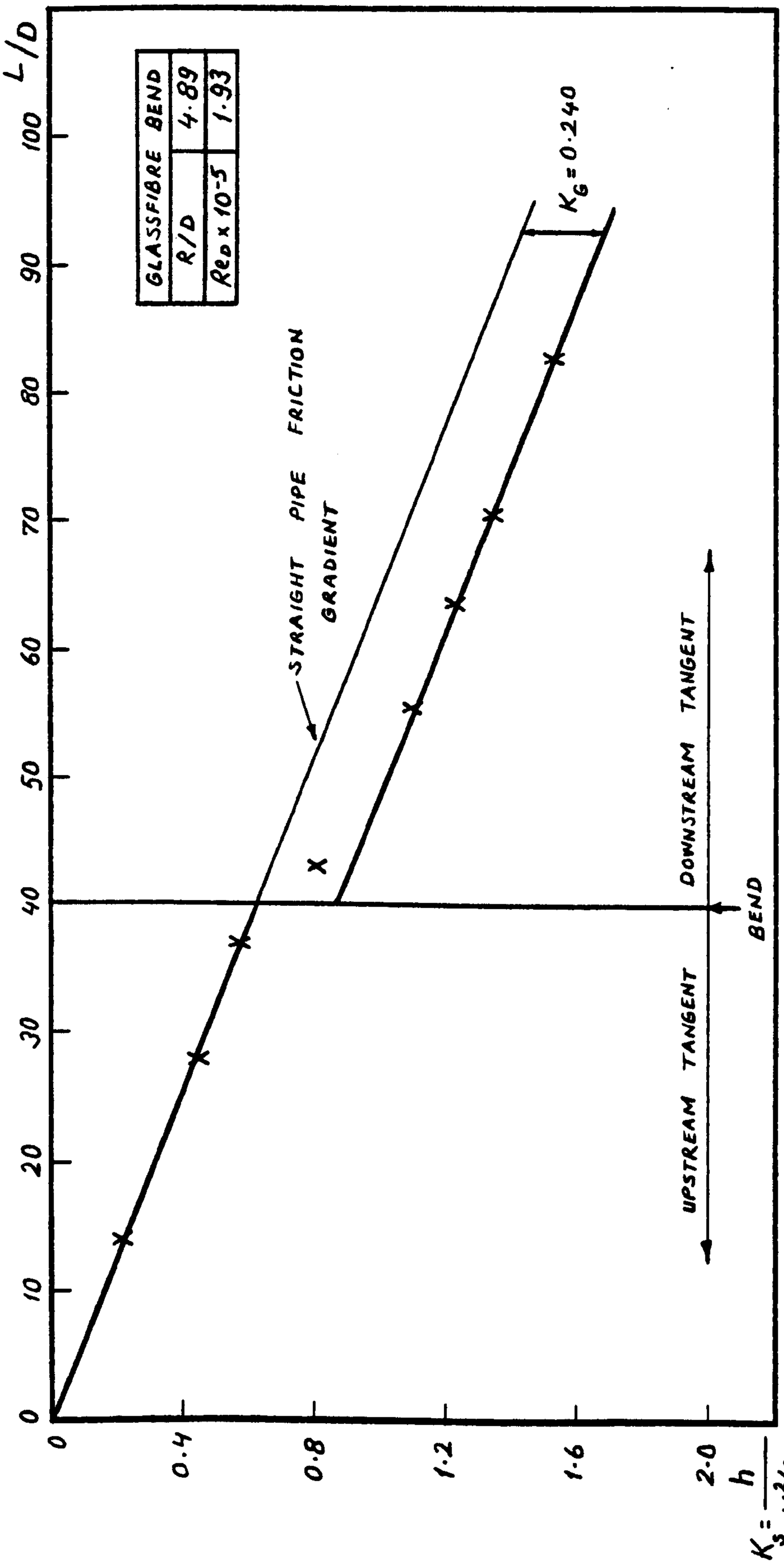

Fig. 71. System head loss coefficient versus axial length

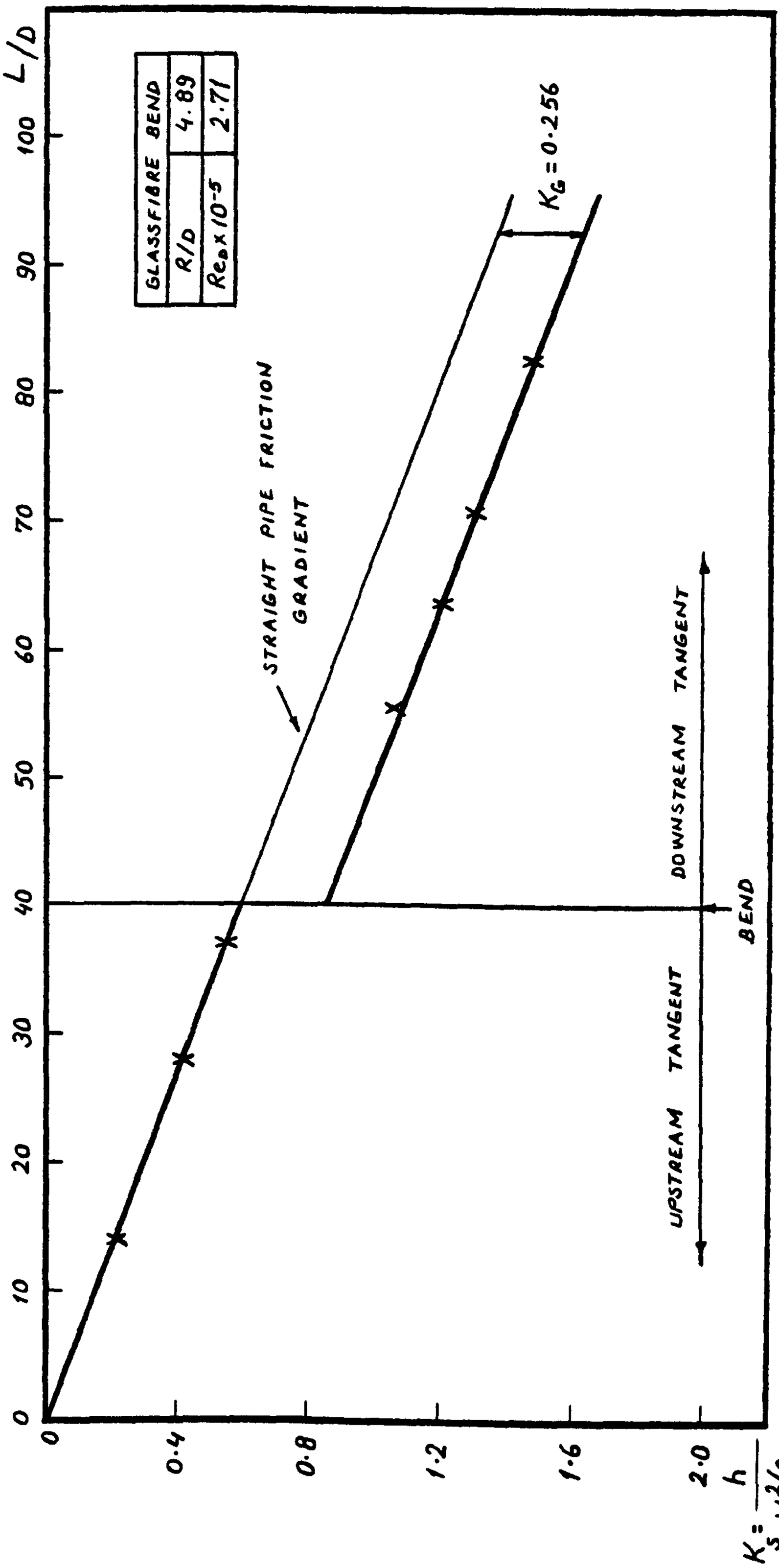

Fig. 72. System head loss coefficient versus axial length

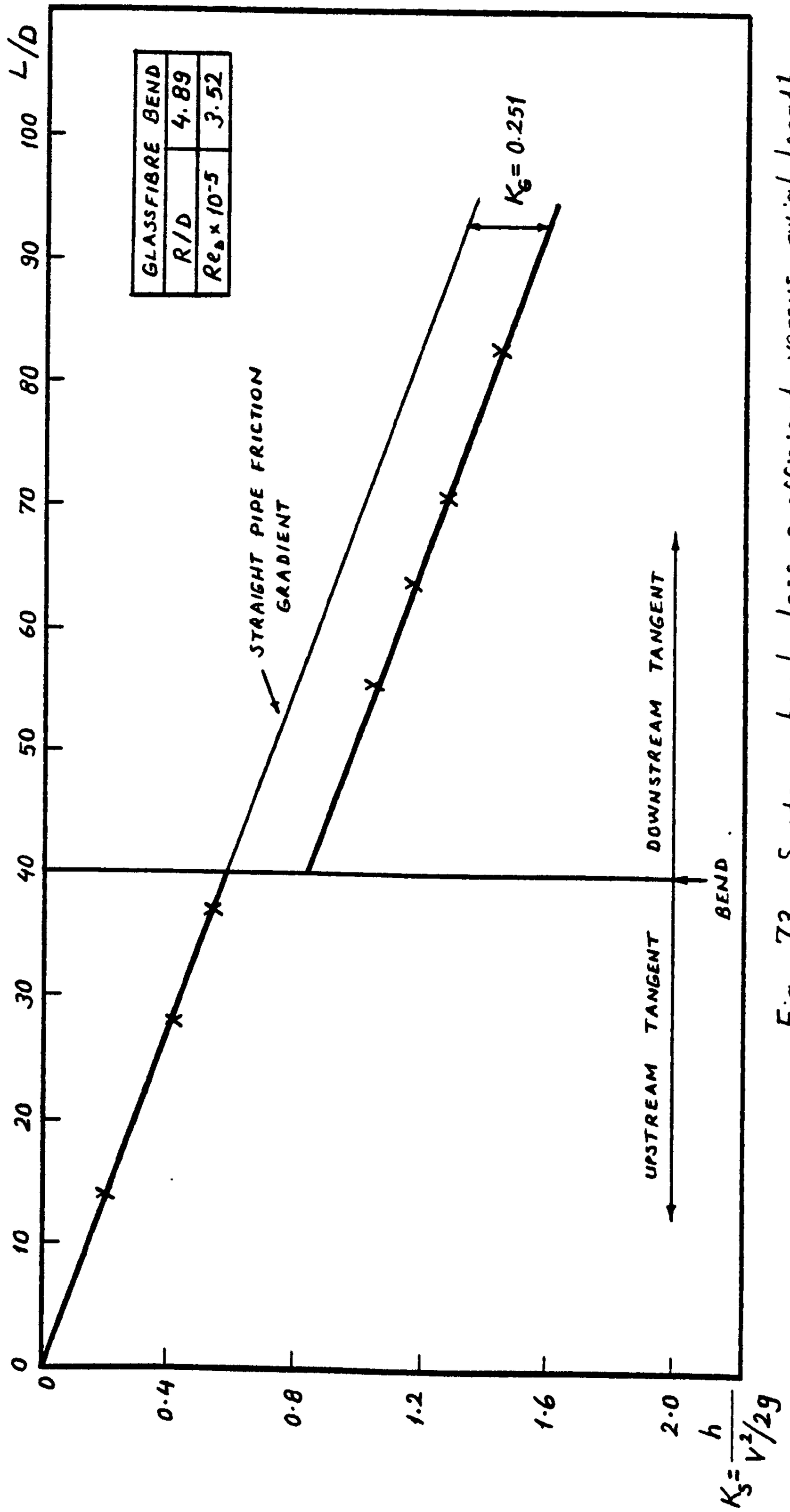

Fig. 73. System head Loss coefficient versus axial length

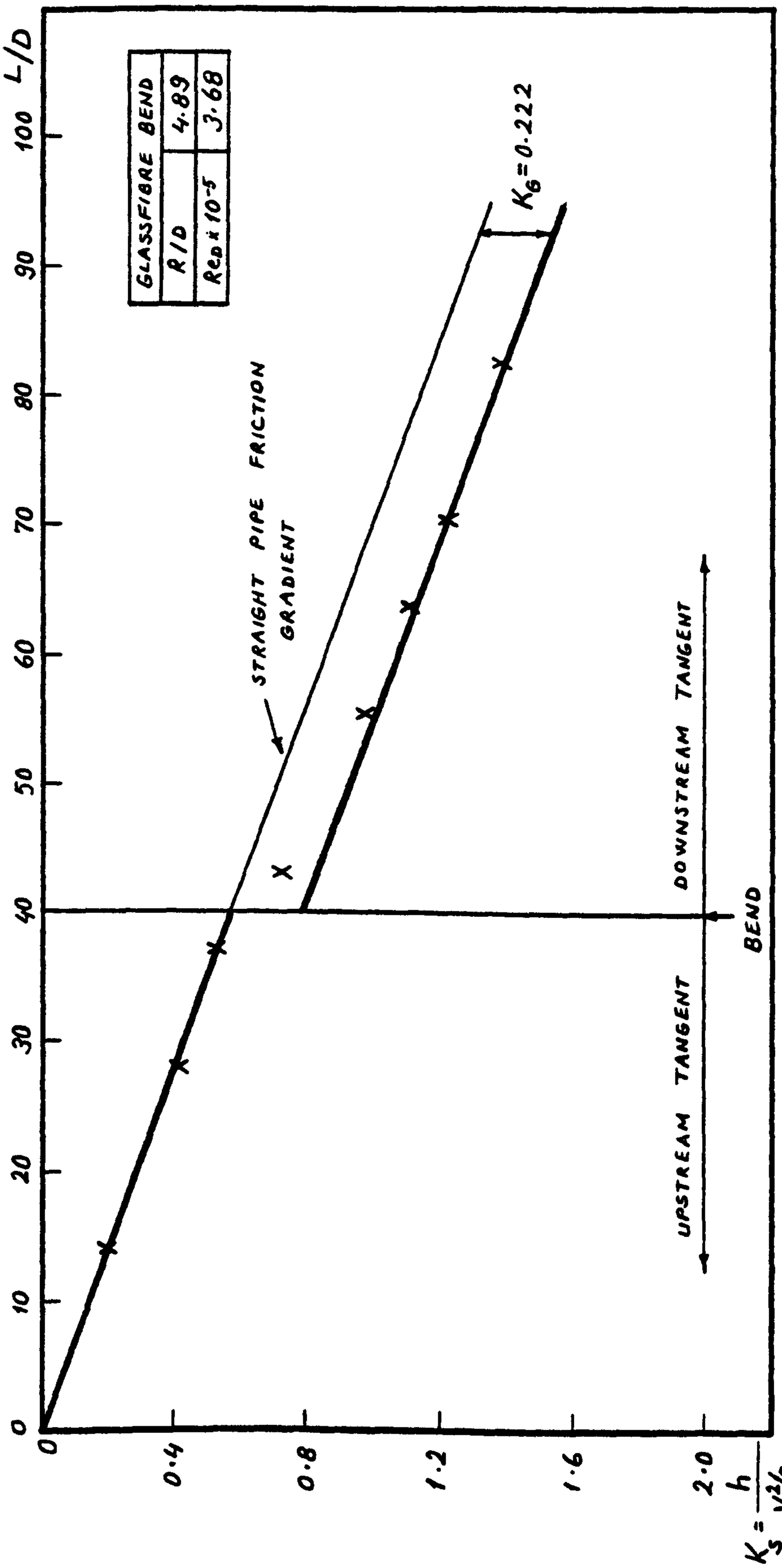

Fig. 74. System head loss coefficient versus axial length.

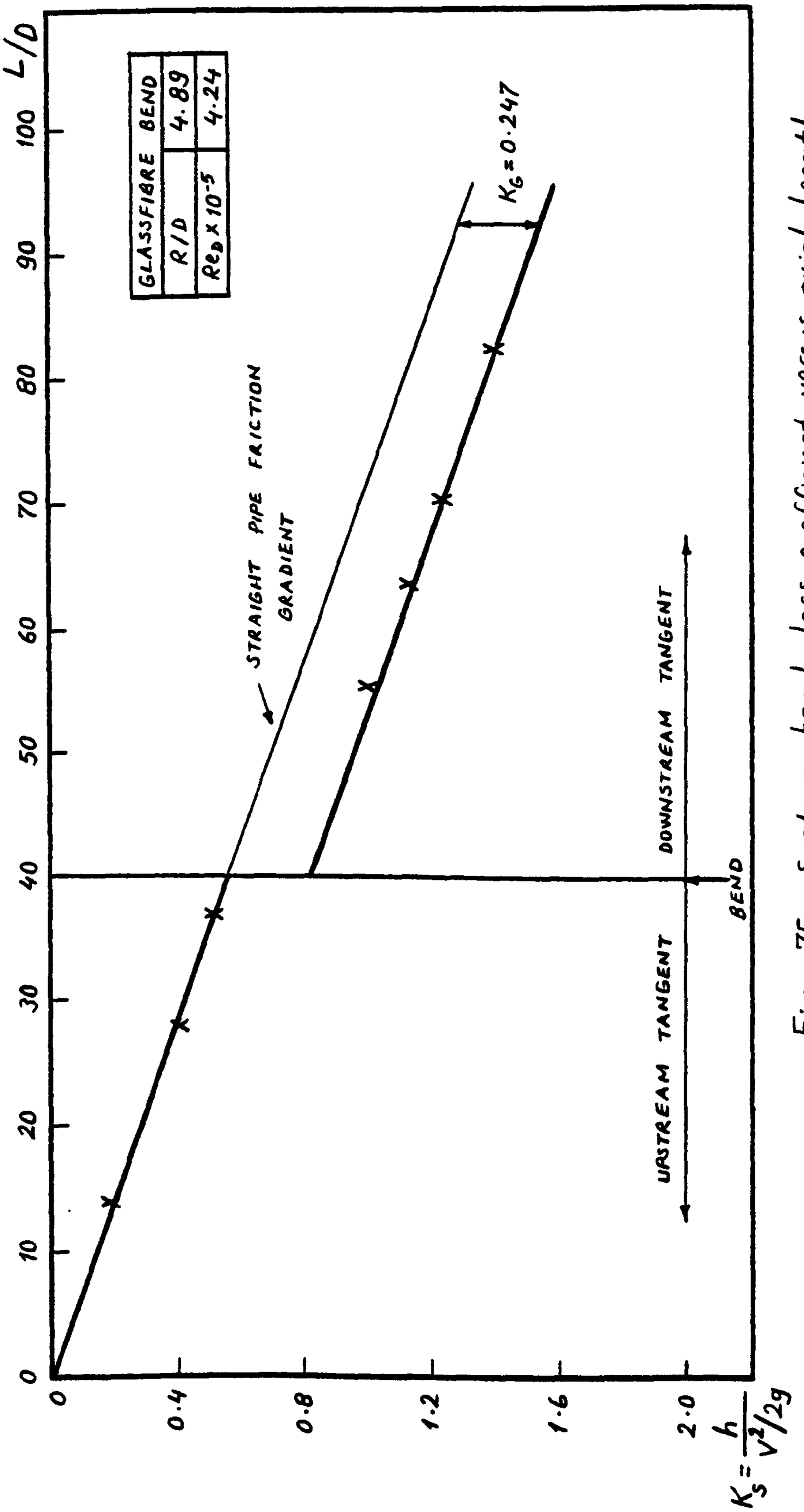

Fig. 75. System head loss coefficient versus axial length

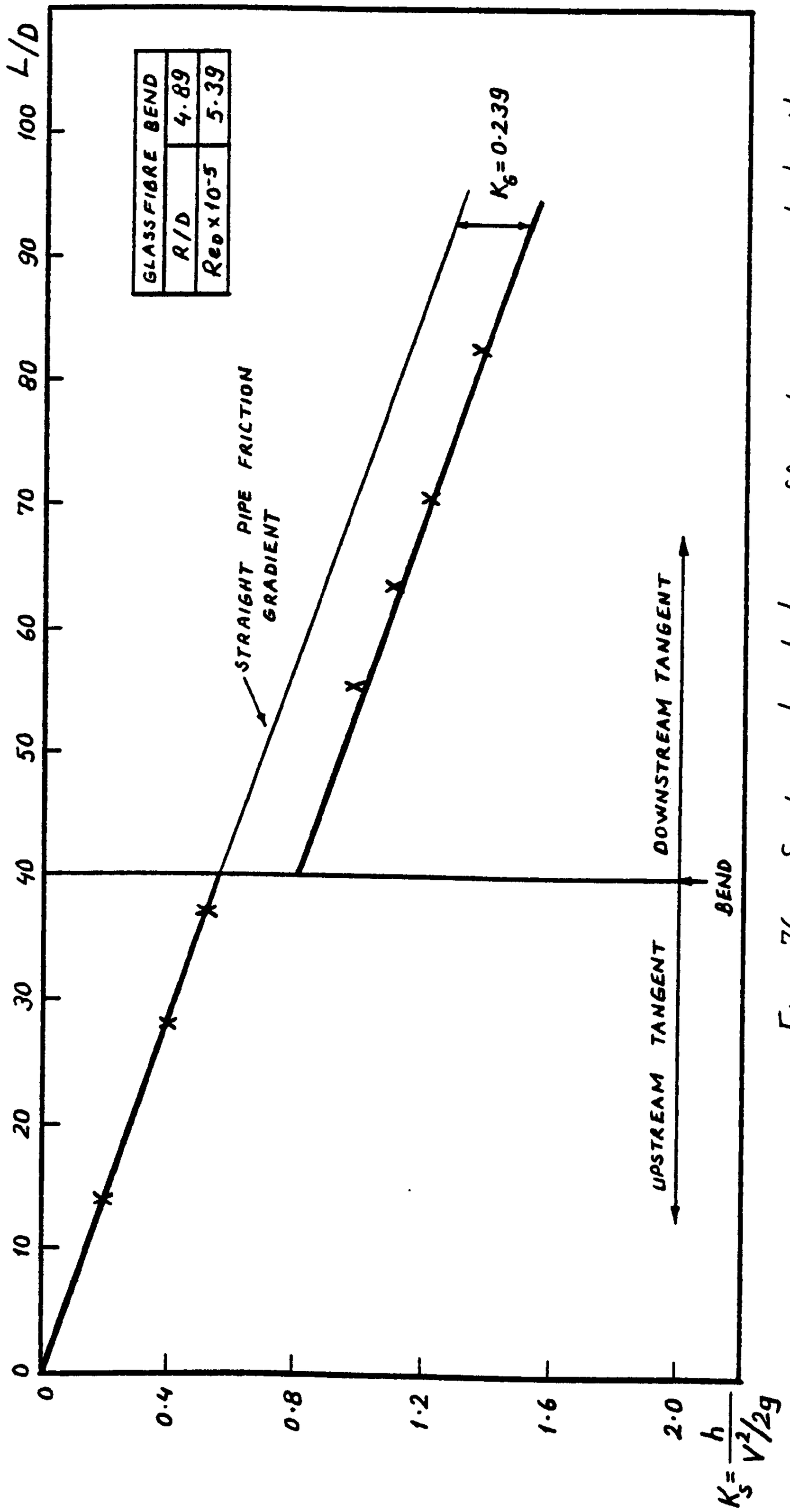

Fig. 76. System head loss coefficient versus axial length

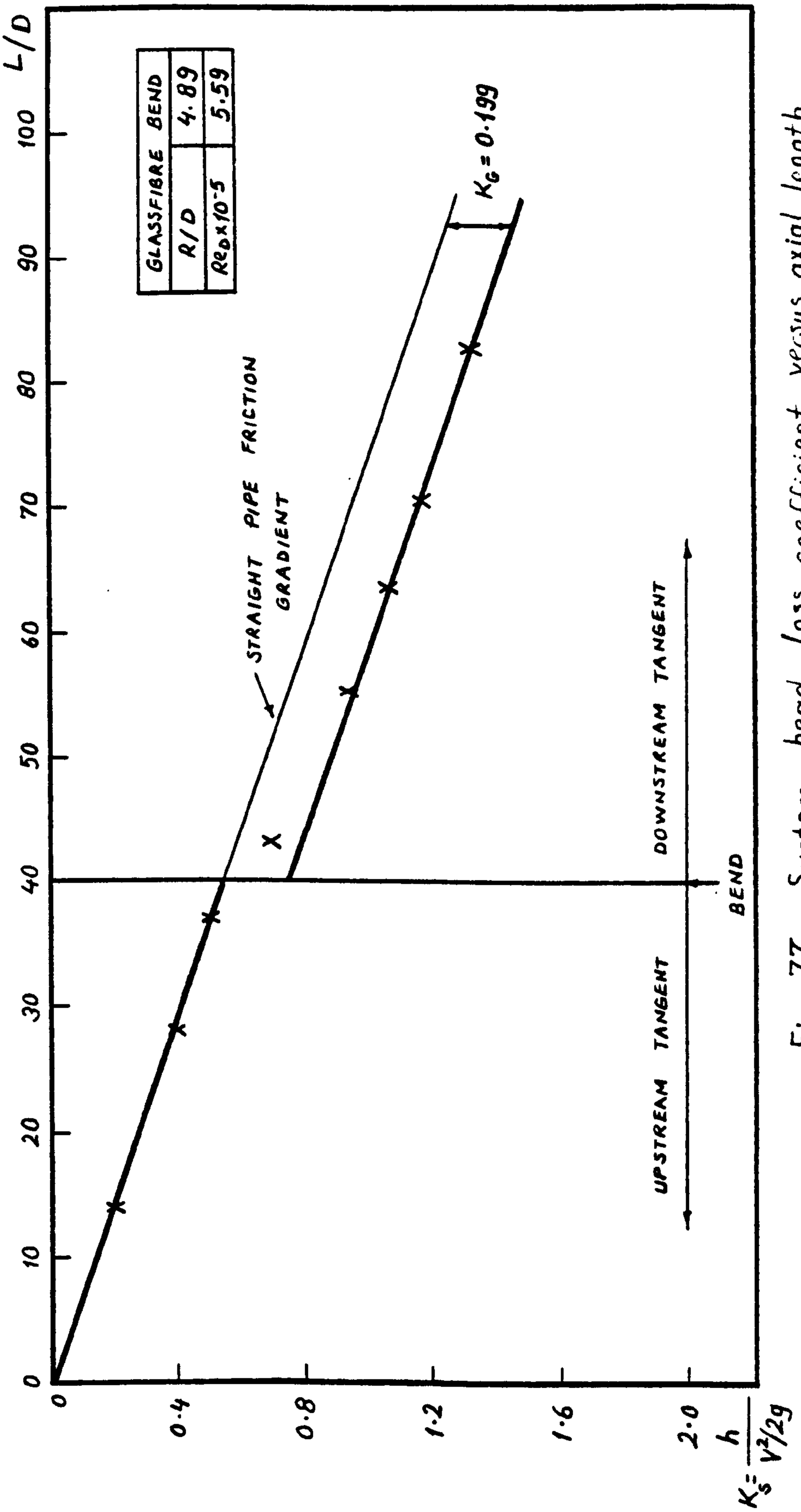

Fig. 77. System head loss coefficient versus axial length

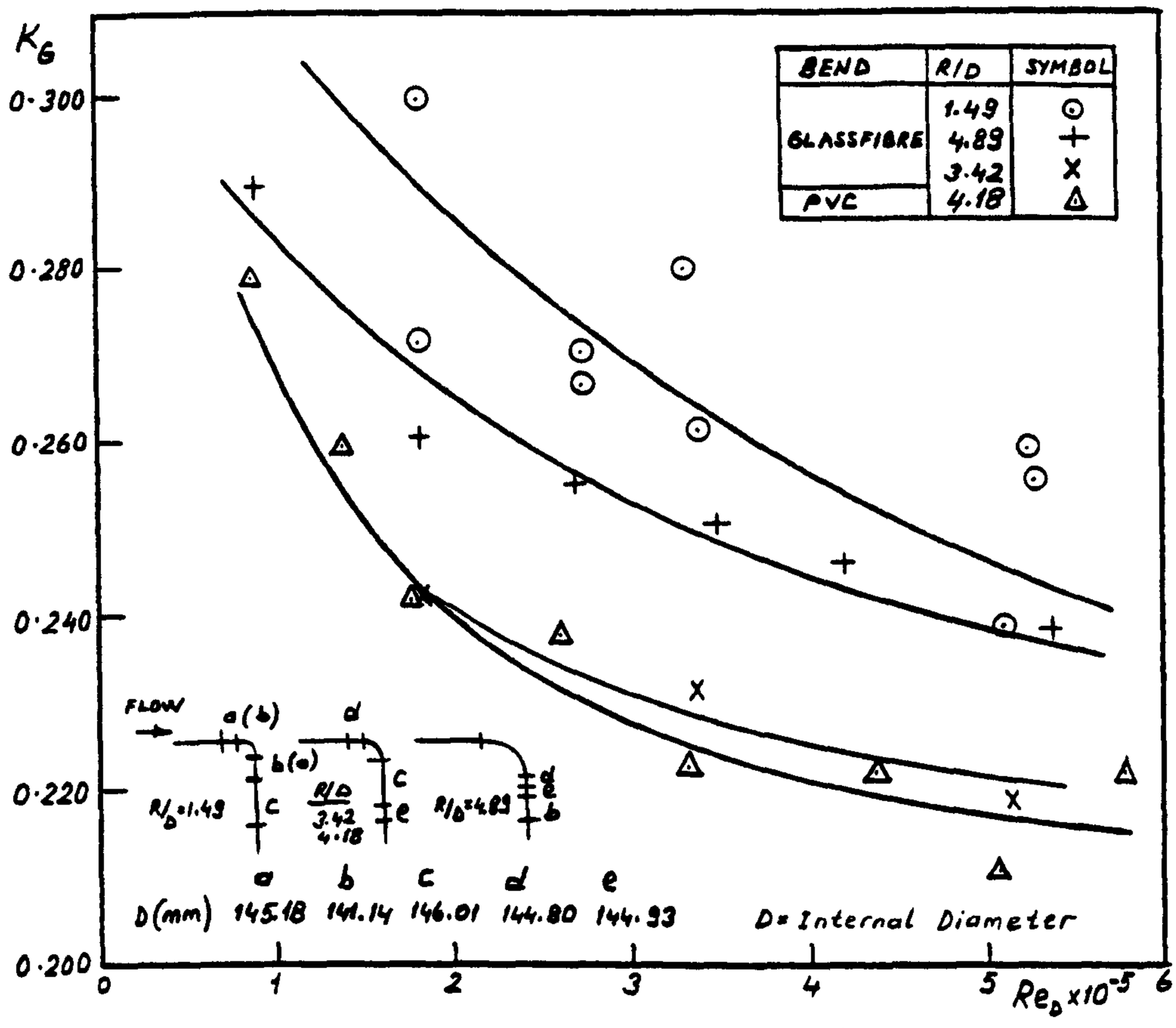

Fig. 78. Variation of gross bend head loss coefficient with Reynolds number

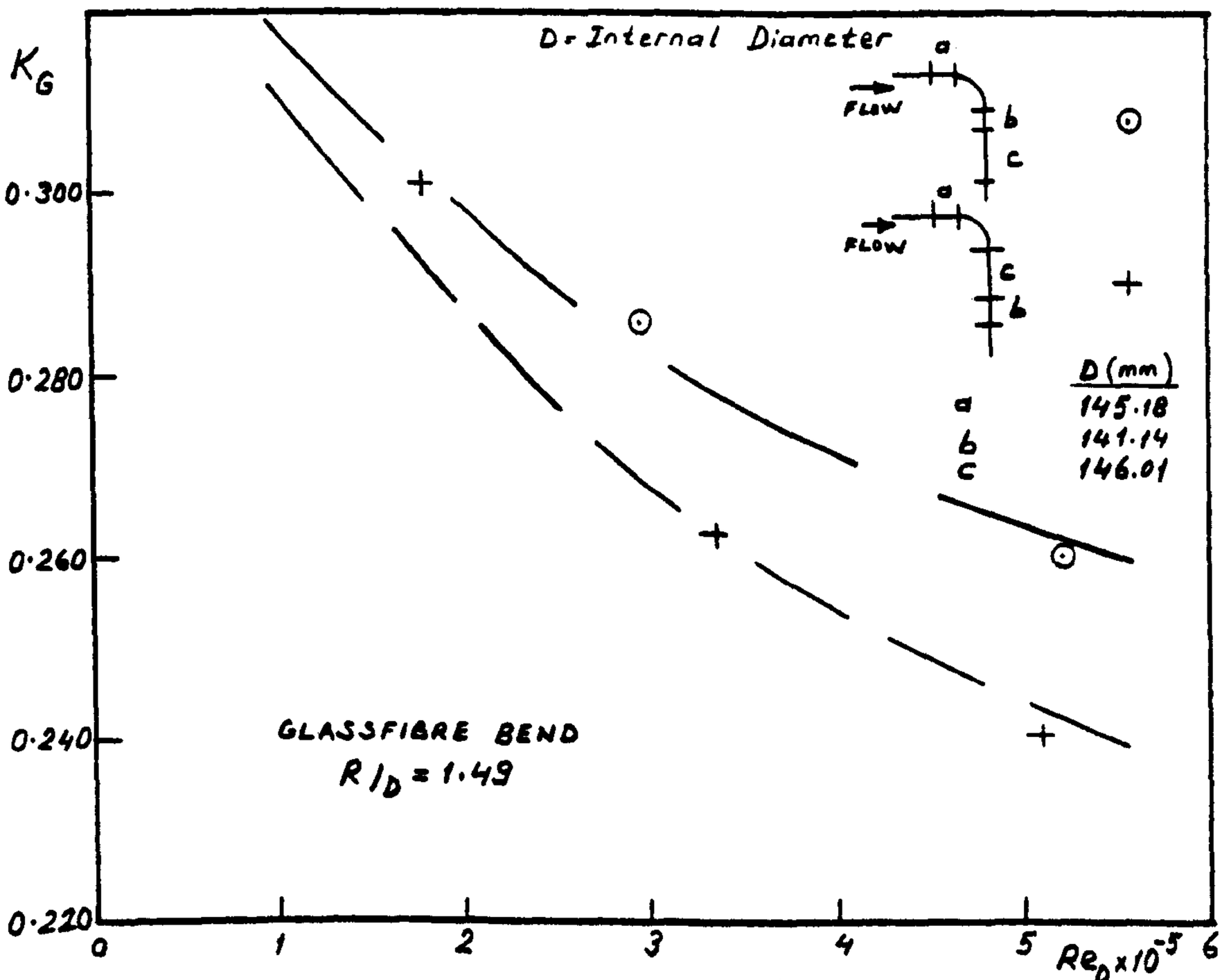

Fig. 79. Effect of various short lengths of various duct diameters on K_G

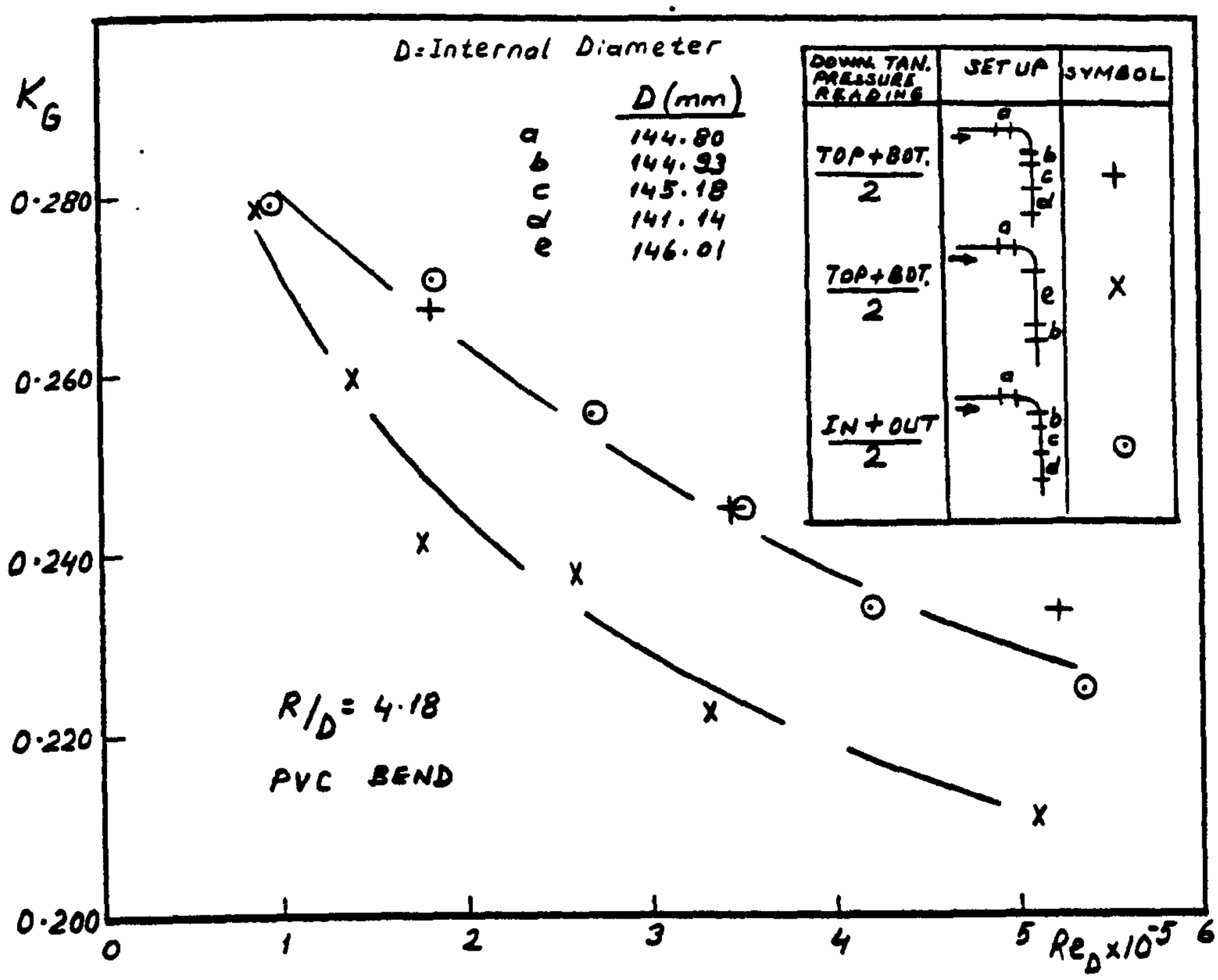

Fig. 80. Effect of various short lengths of various duct diameters on K_G

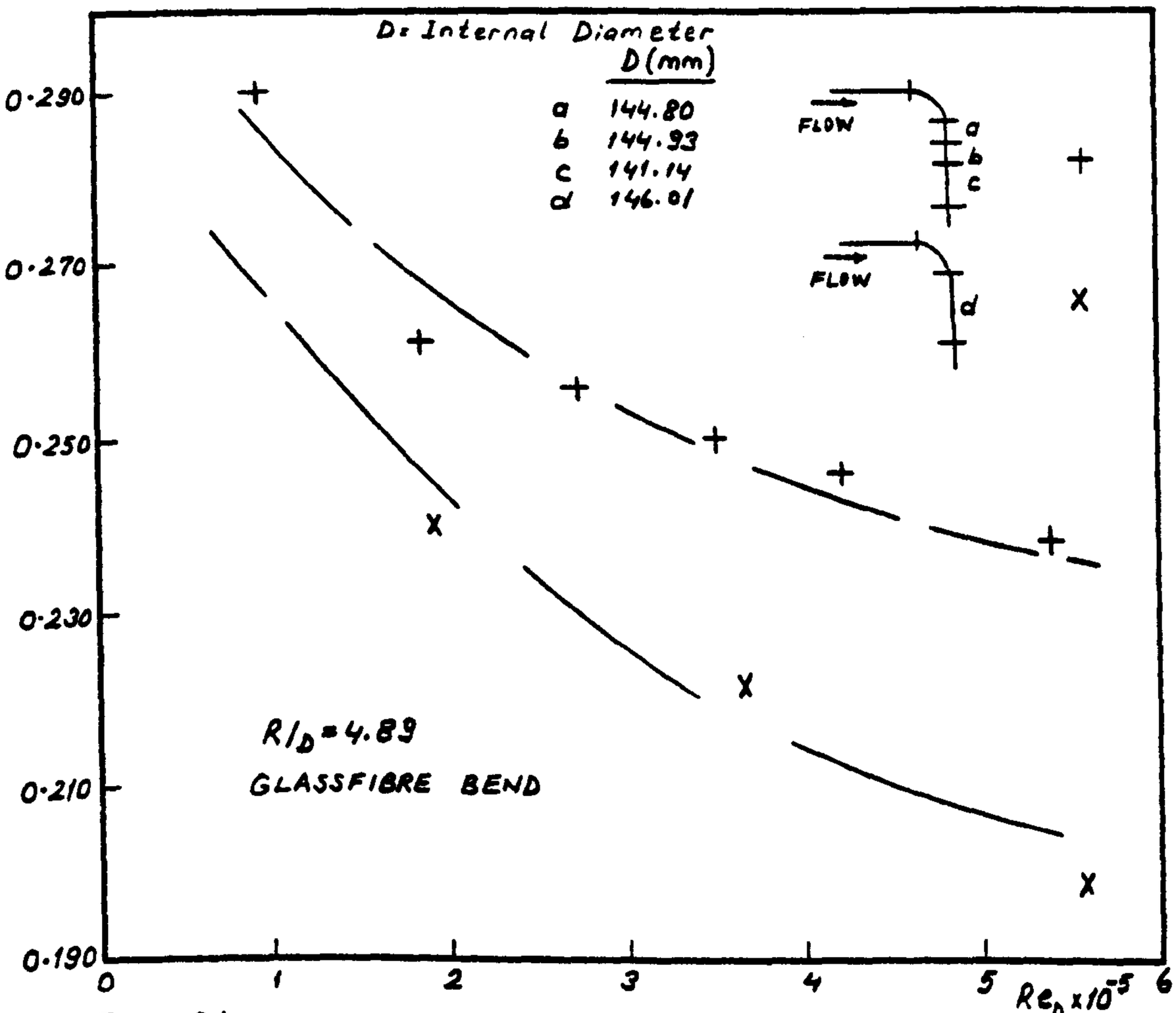

Fig. 81. Effect of various short lengths of various duct diameters on K_G

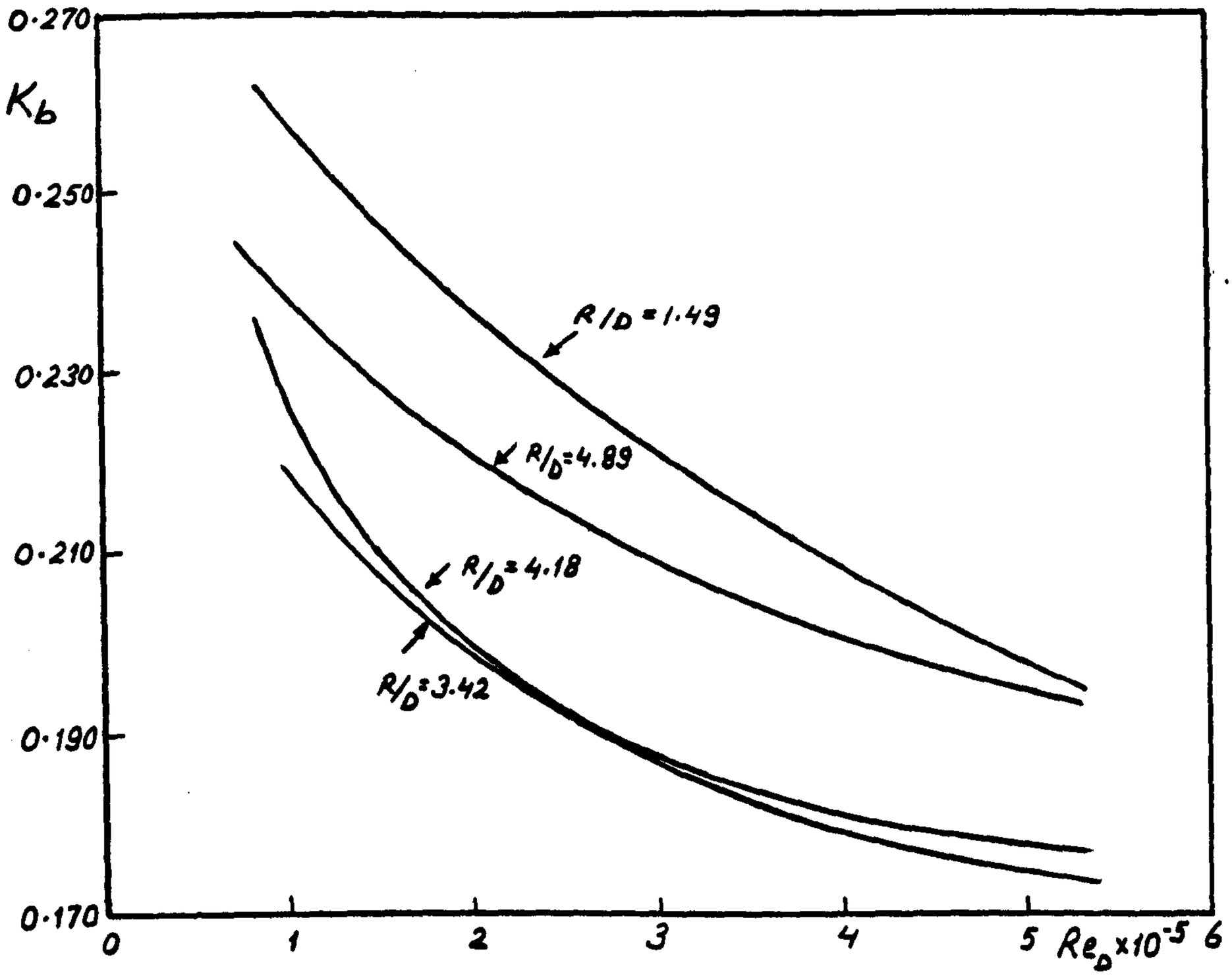

Fig. 82. Variation of bend head loss coefficient with Reynolds number

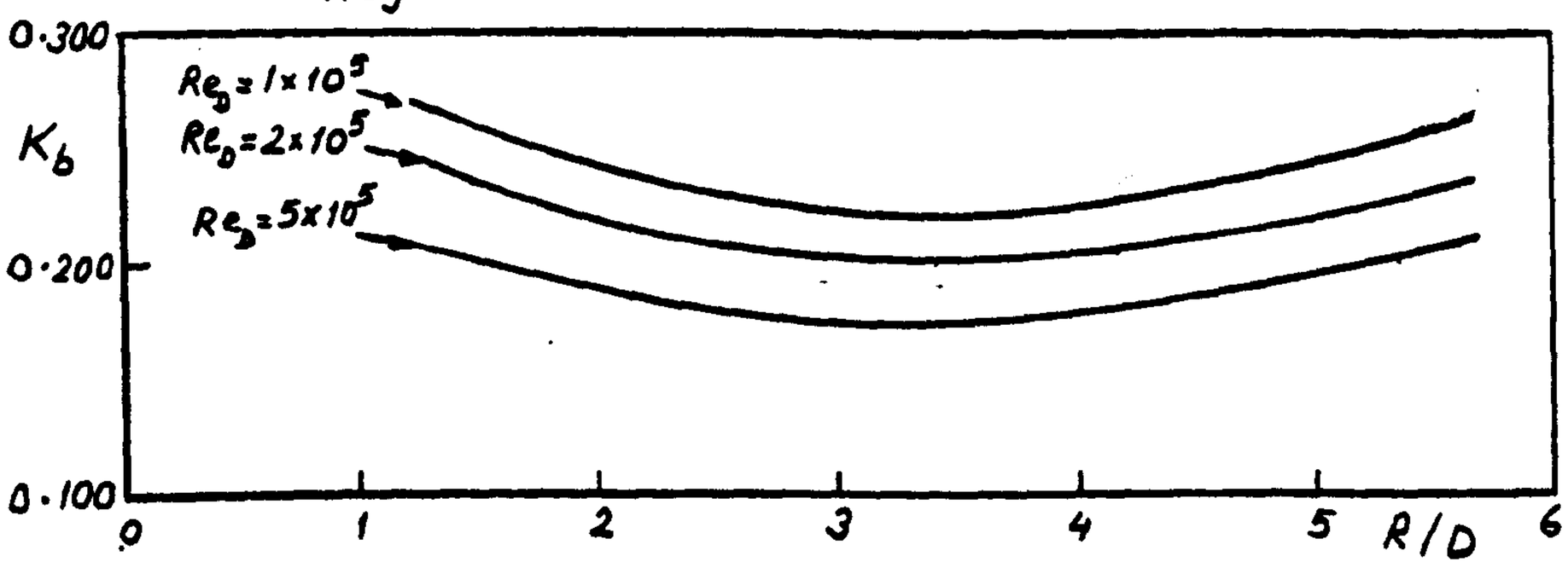

Fig. 83. Variation of bend head loss coefficient with radius ratio

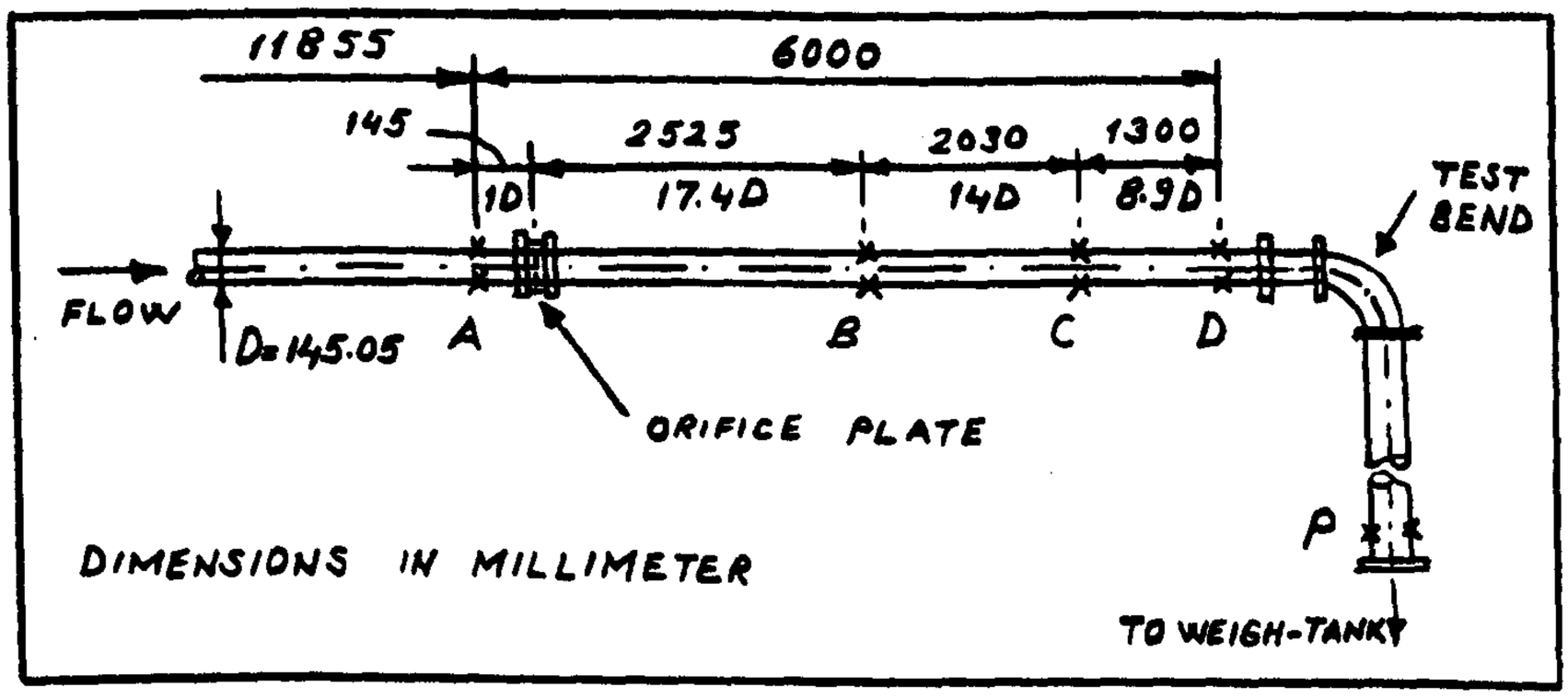

Fig. 84. Location of static pressure tappings

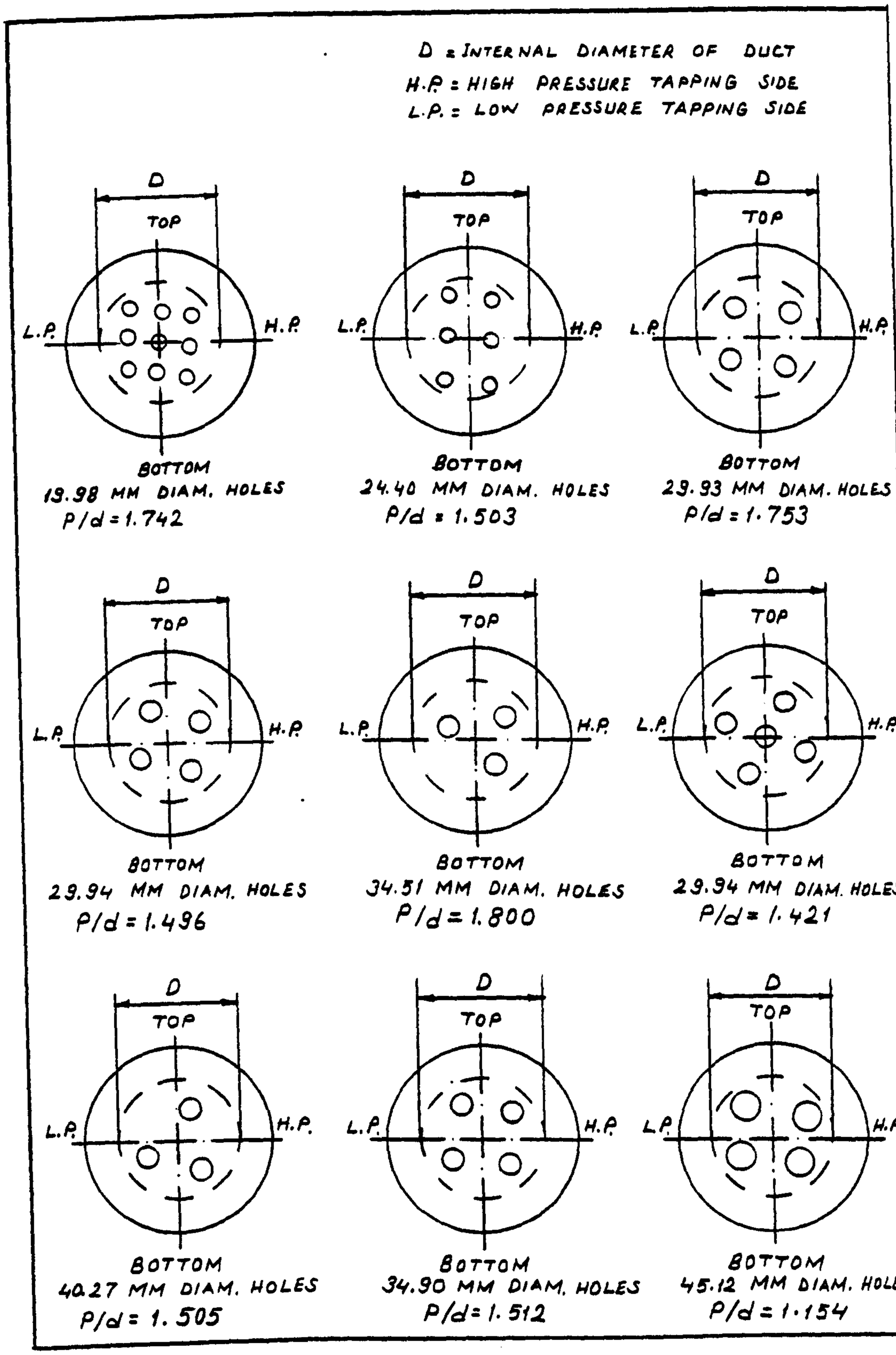

Fig. 85. Position of multi-hole orifice plates fixed into the carrier ring

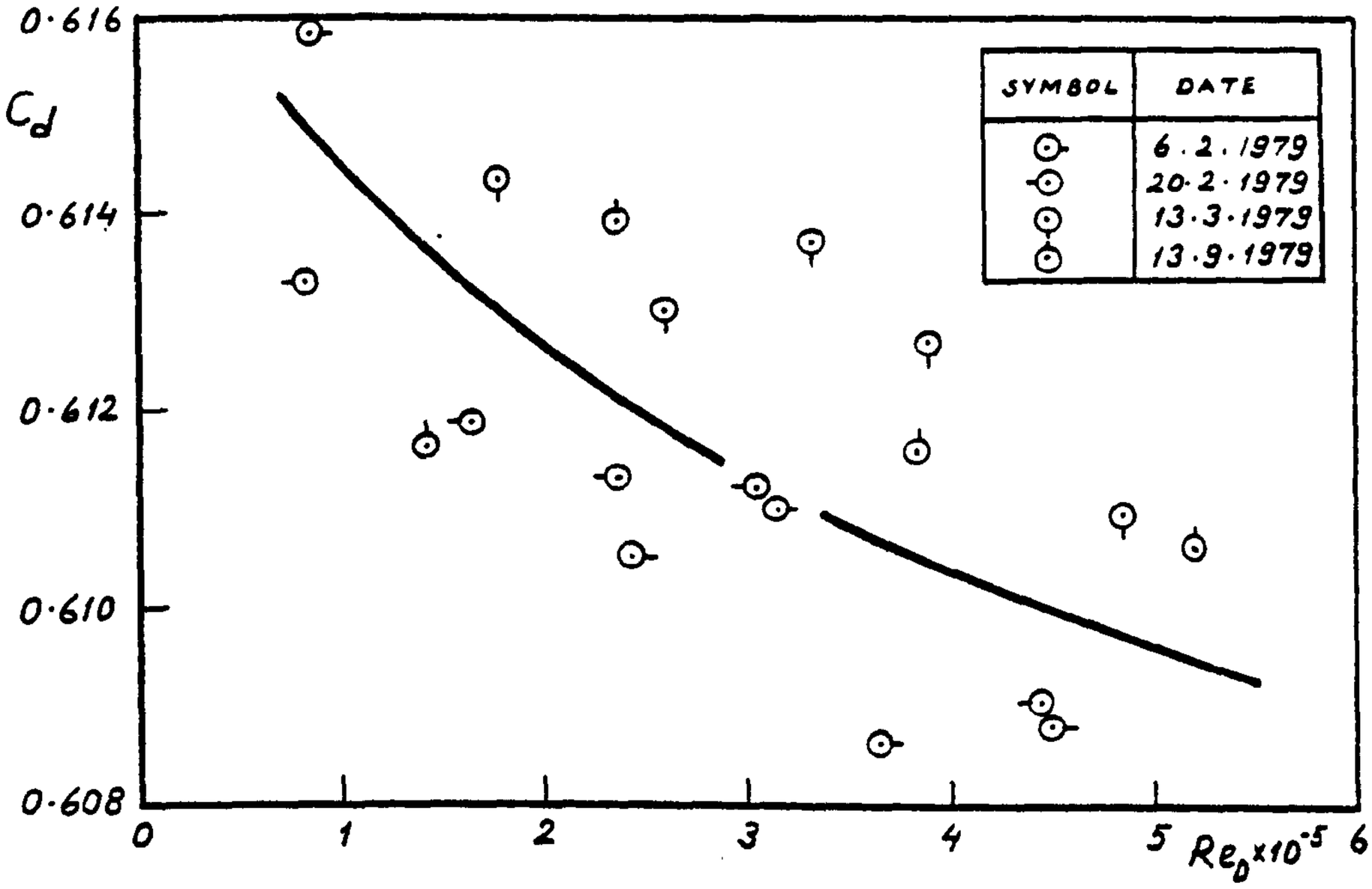

Fig. 86. Variation of discharge coefficient with Reynolds number, single-hole orifice plate of m = 0.508

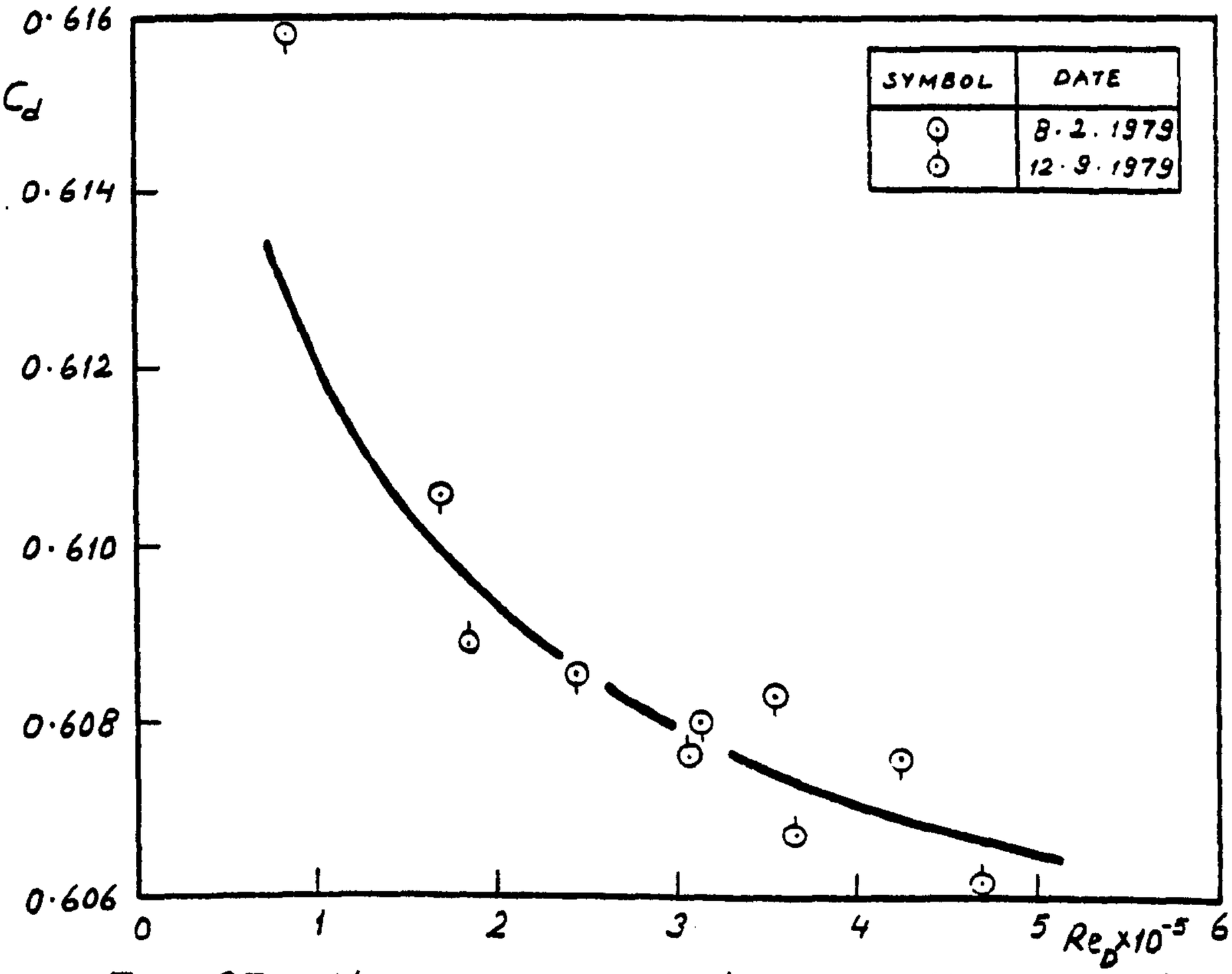

Fig. 87. Variation of discharge coefficient with Reynolds number, single-hole orifice plate of m = 0.389

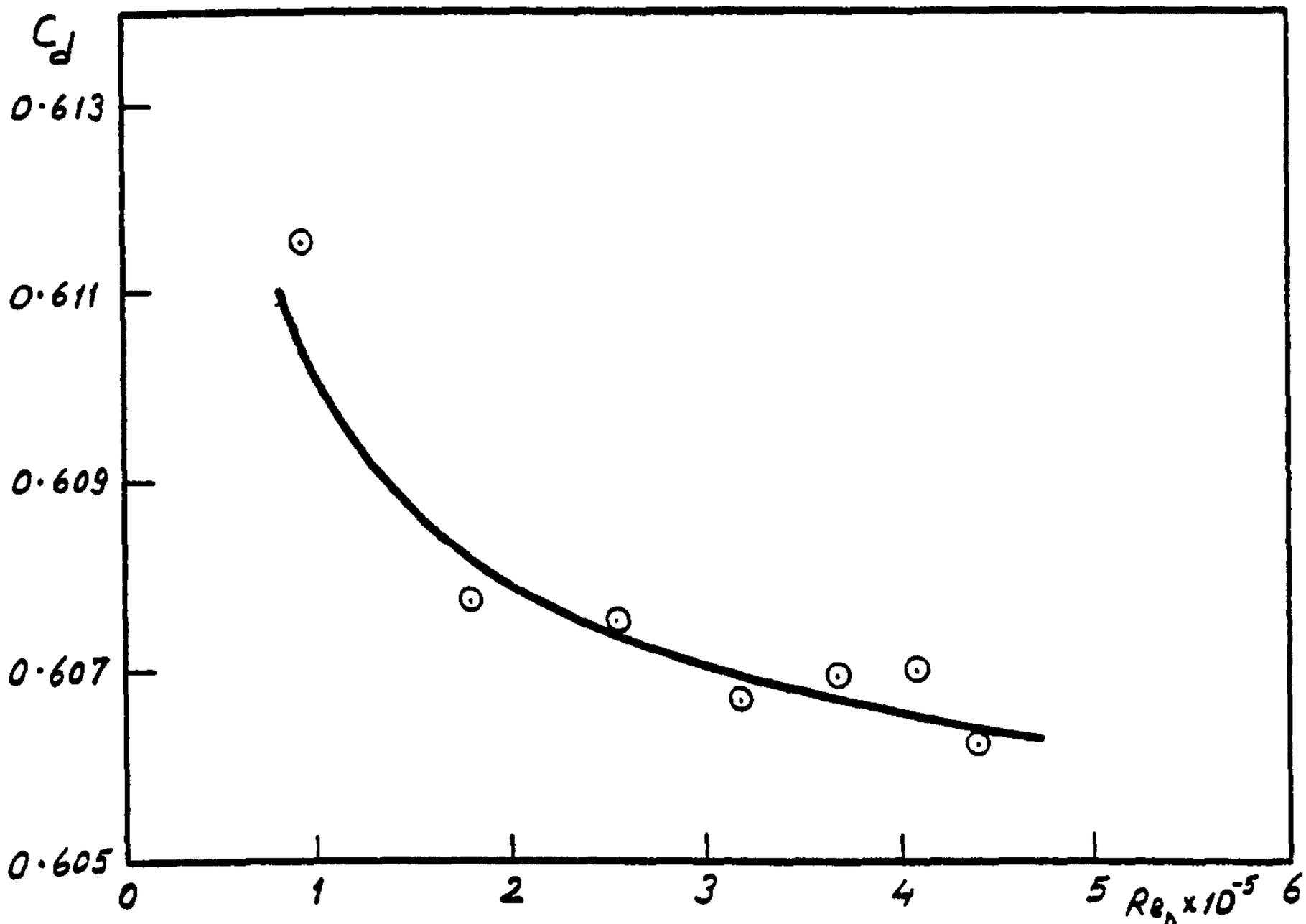

Fig. 88. Variation of discharge coefficient with Reynolds number, single-hole orifice plate of $m = 0.386$

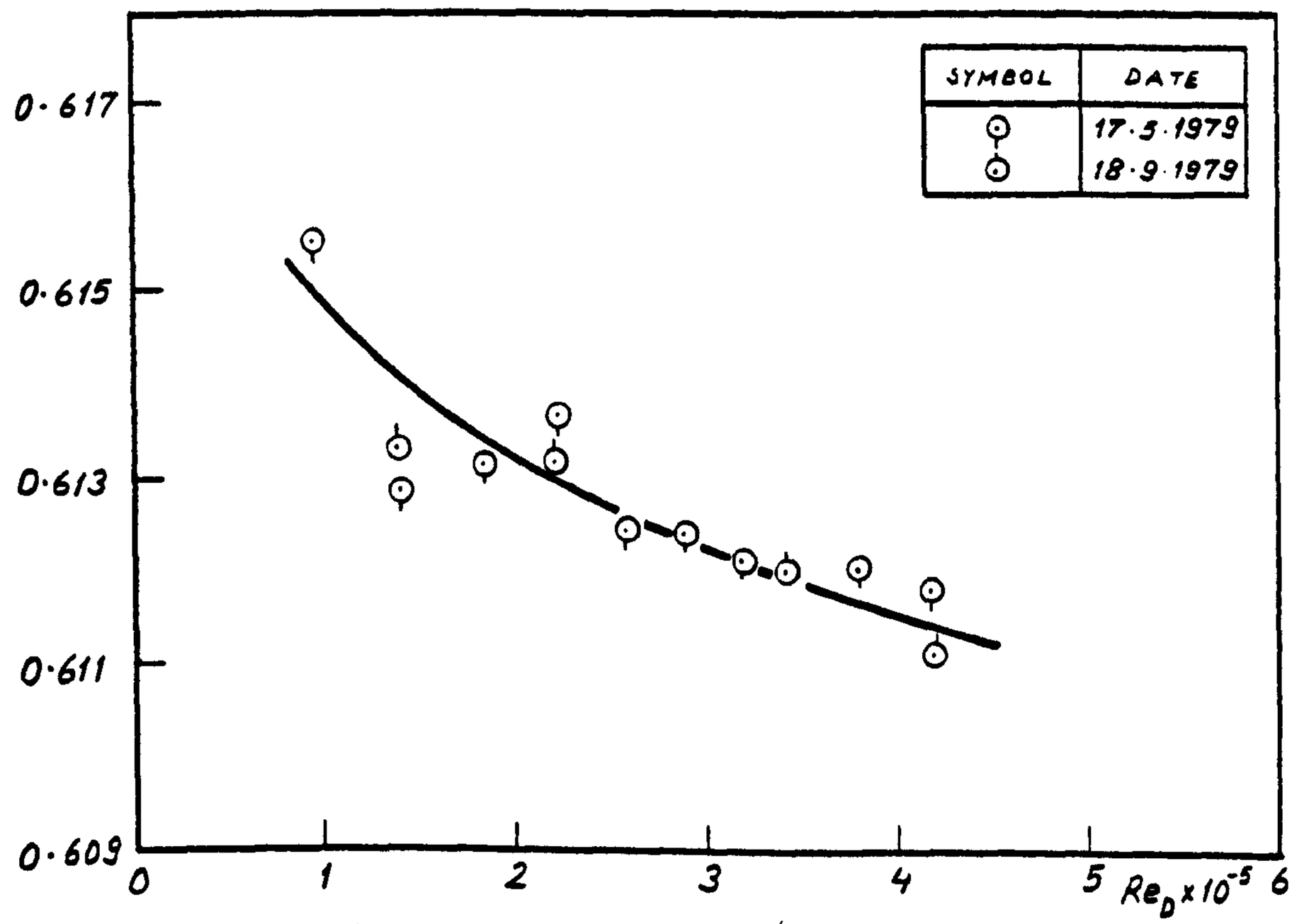

Fig. 89. Variation of discharge coefficient with Reynolds number, single-hole orifice plate of $m = 0.304$

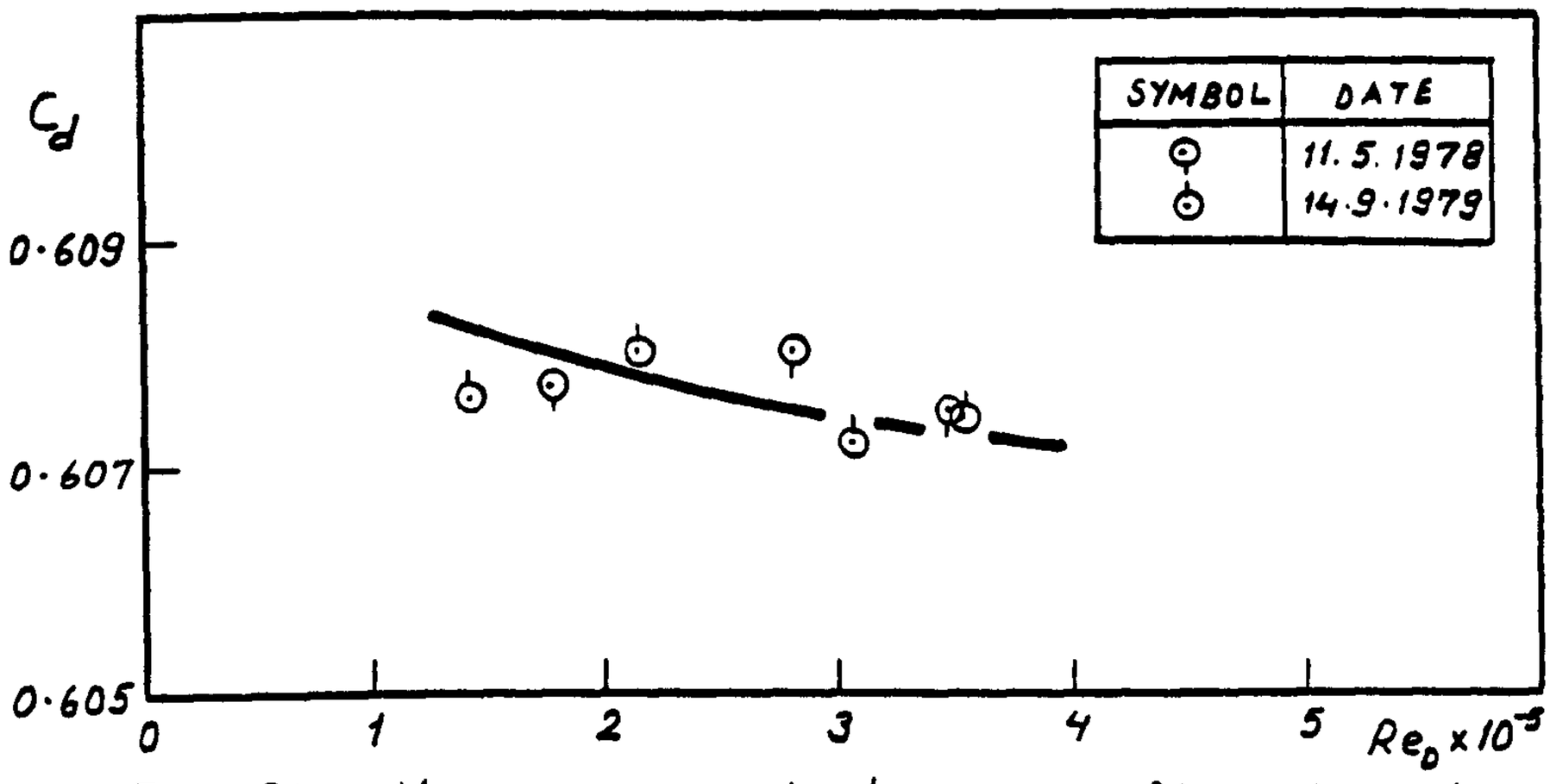

Fig. 90. Variation of discharge coefficient with Reynolds number, single-hole orifice plate of m = 0.232

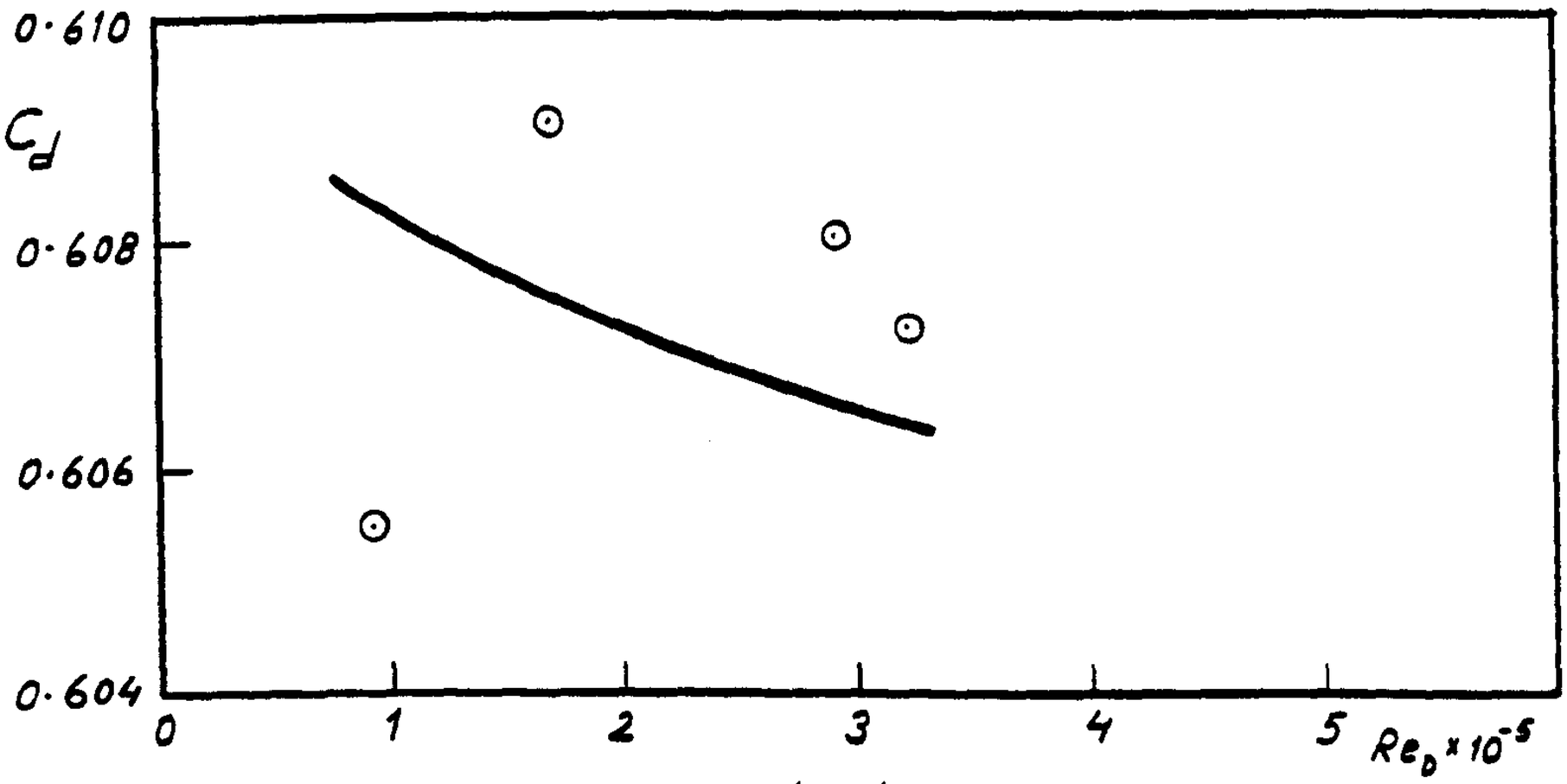

Fig. 91. Variation of discharge coefficient with Reynolds number, single-hole orifice plate of m = 0.218

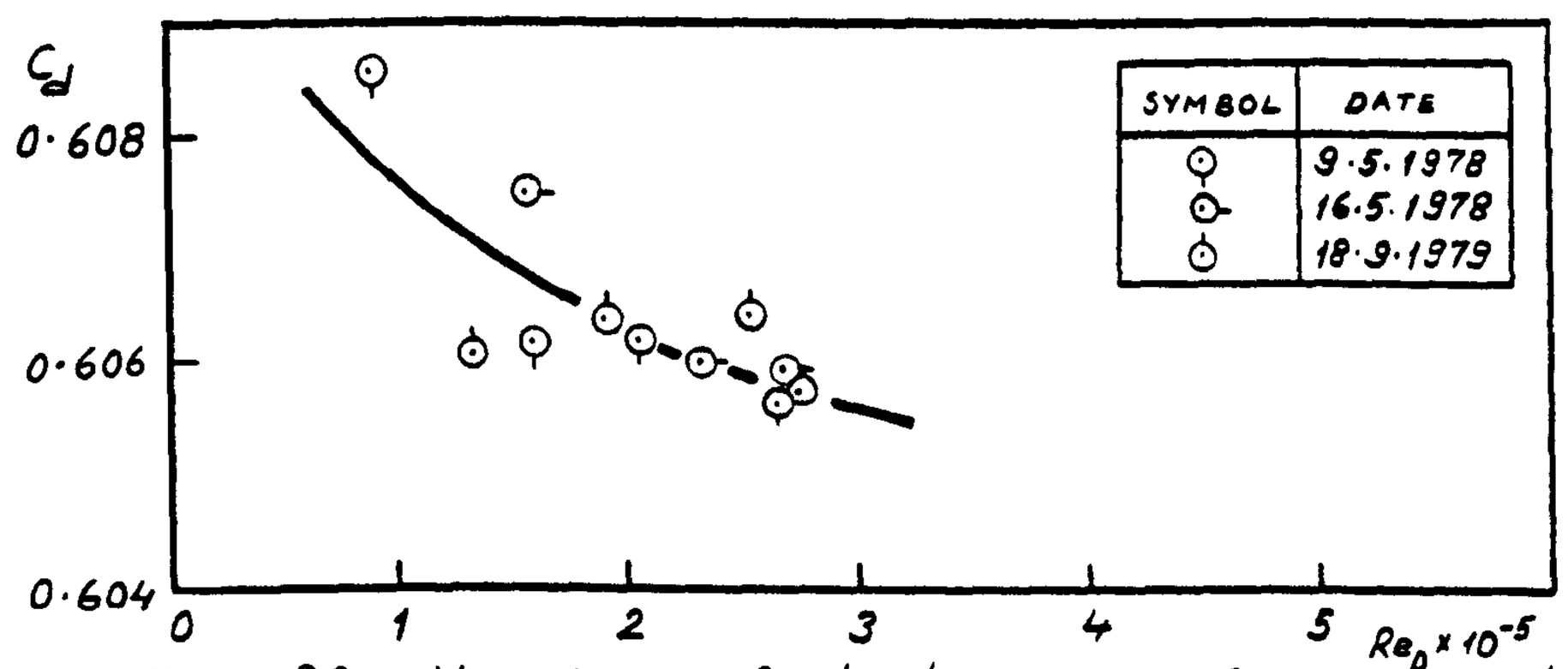

Fig. 92. Variation of discharge coefficient with Reynolds number, single-hole orifice plate of m = 0.171

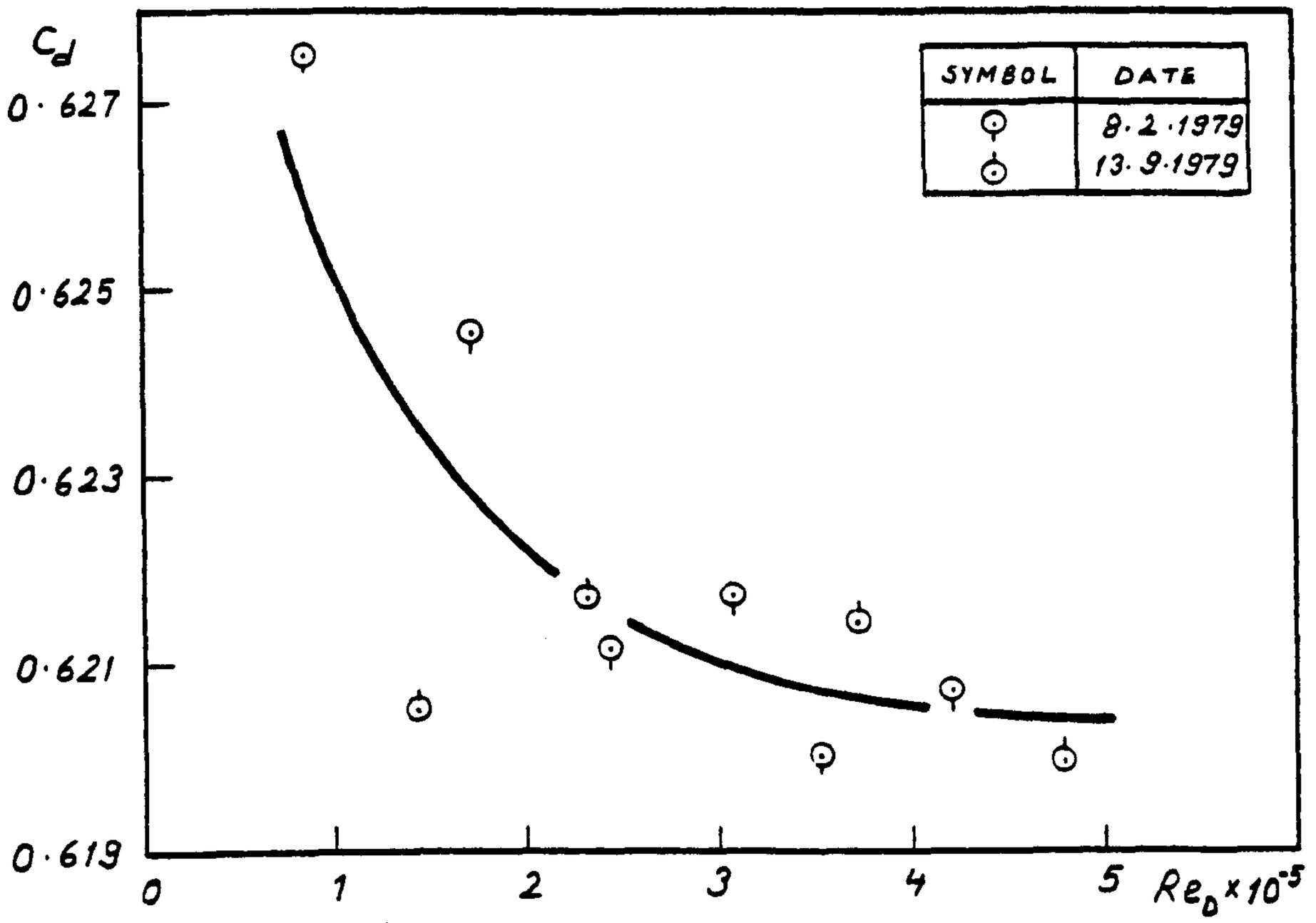

Fig. 93. Variation of discharge coefficient with Reynolds number, multi-hole orifice plate of $m = 0.387$, $p/d = 1.154$, $N = 4$

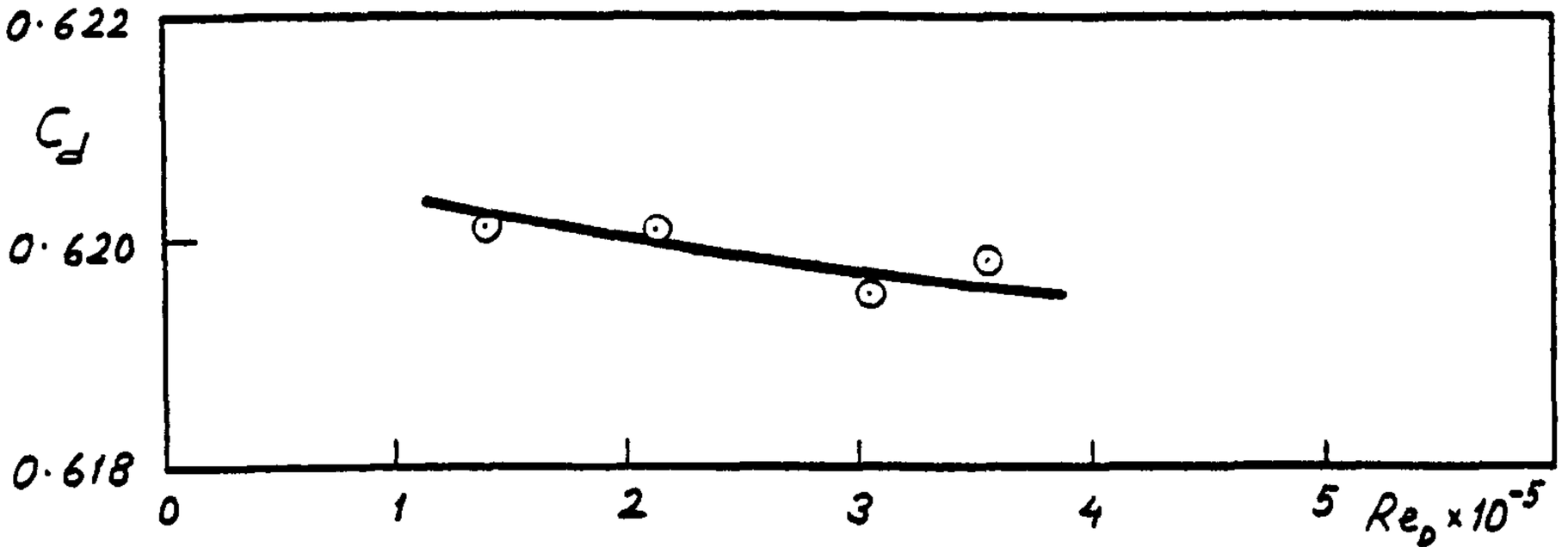

Fig. 94. Variation of discharge coefficient with Reynolds number, multi-hole orifice plate of $m = 0.231$, $p/d = 1.512$, $N = 4$

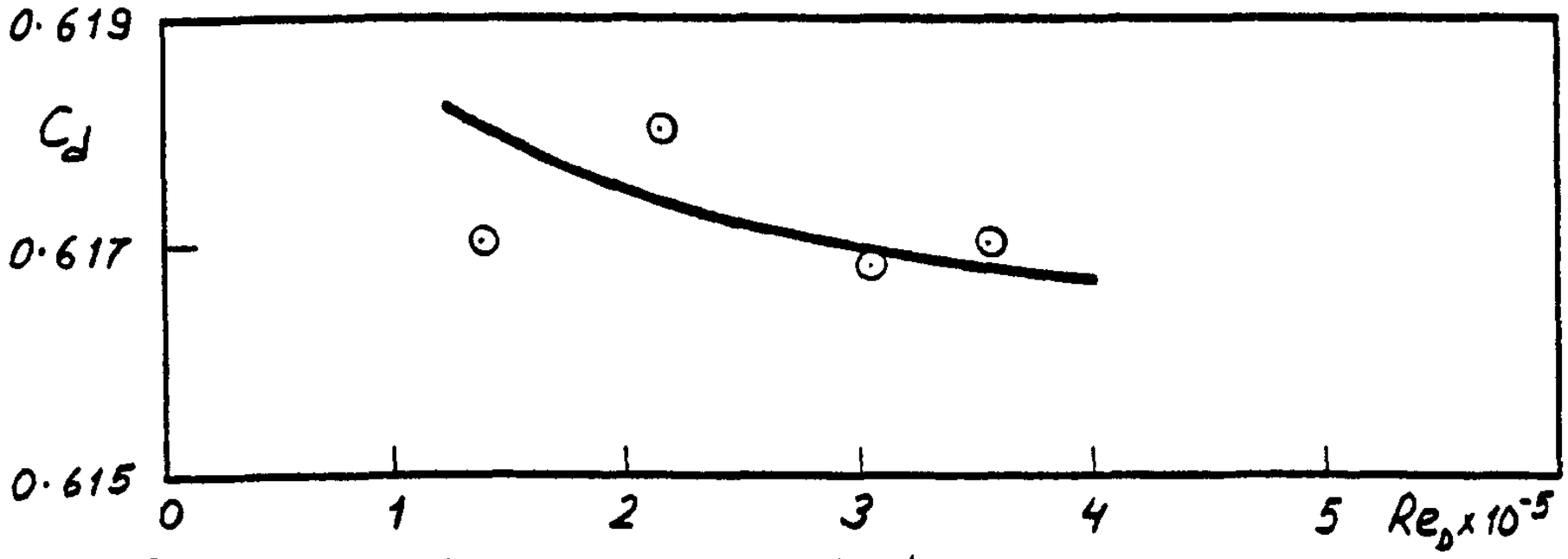

Fig. 95. Variation of discharge coefficient with Reynolds number, multi-hole orifice plate of $m = 0.231$, $p/d = 1.505$, $N = 3$

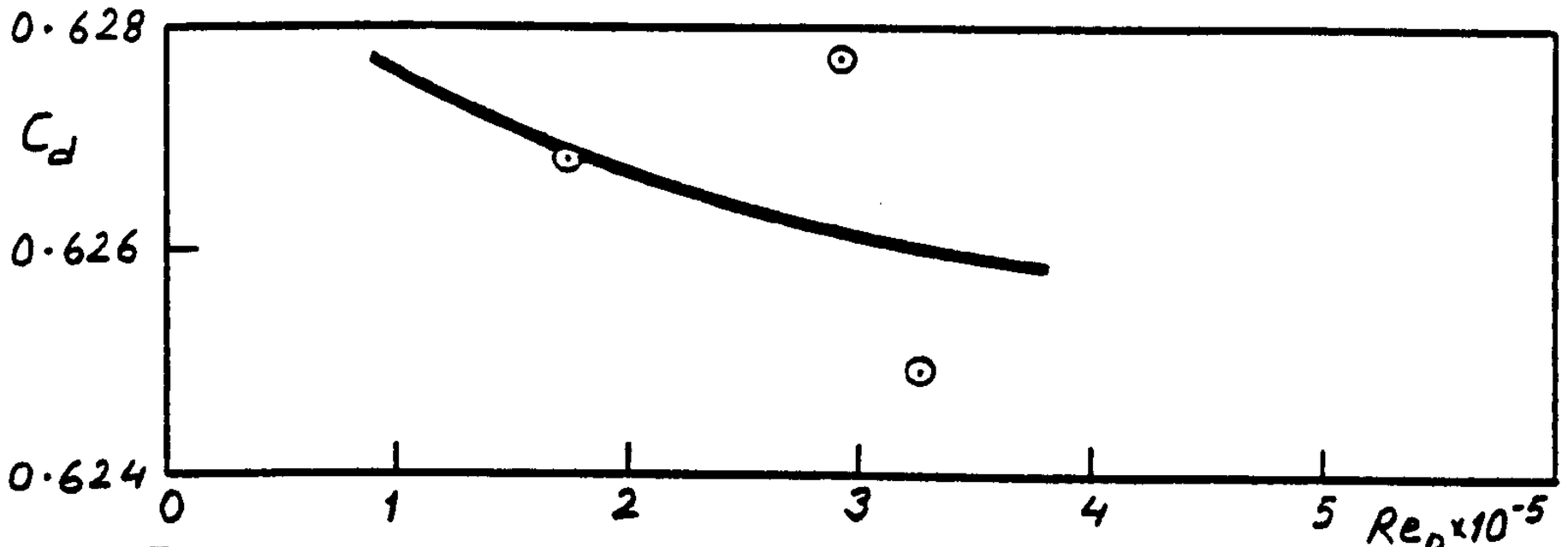

Fig. 96. Variation of discharge coefficient with Reynolds number, multi-hole orifice plate of $m = 0.213$, $p/d = 1.421$, $N = 5$

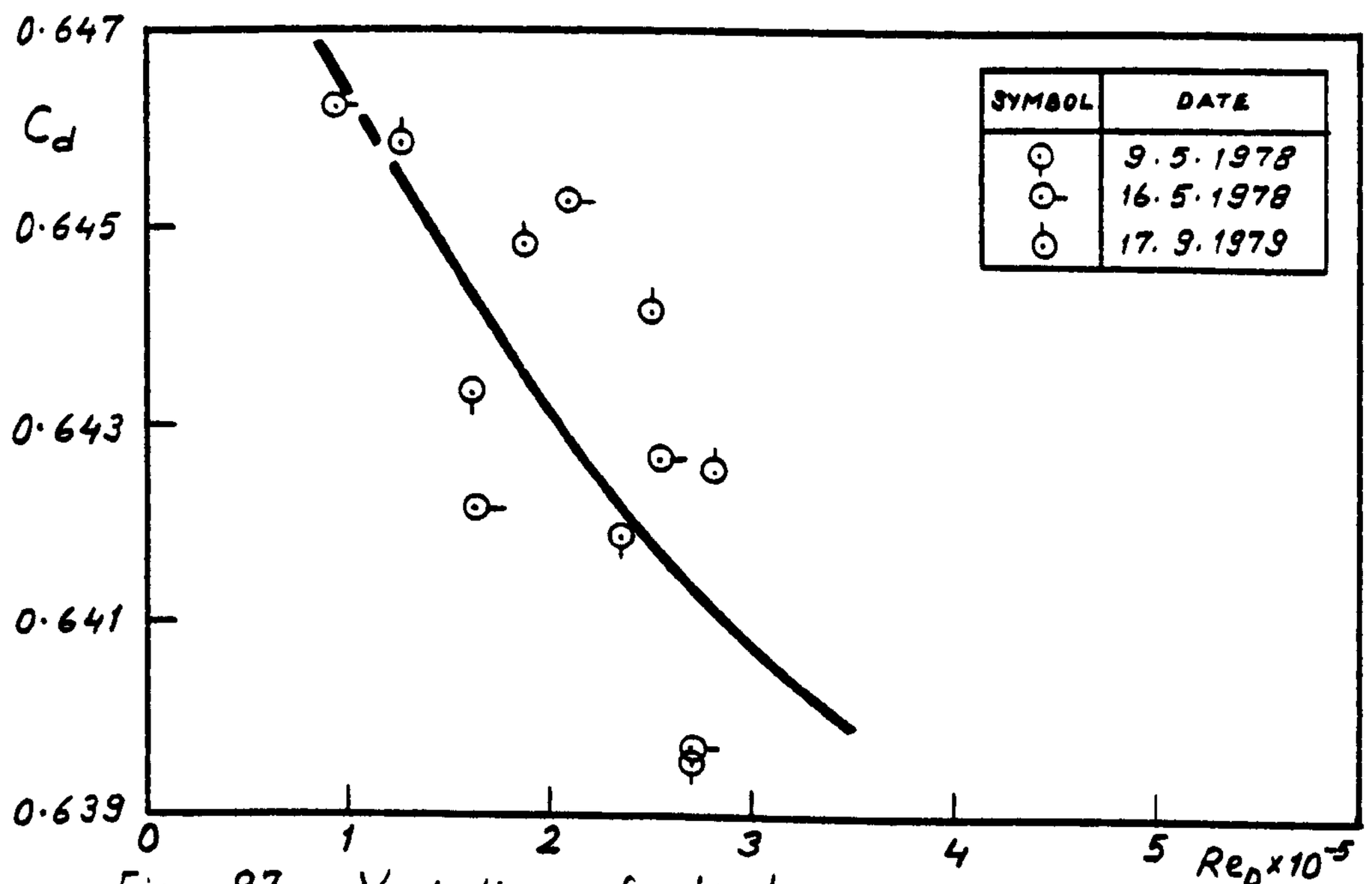

Fig. 97. Variation of discharge coefficient with Reynolds number, multi-hole orifice plate of $m = 0.171$, $p/d = 1.742$, $N = 9$

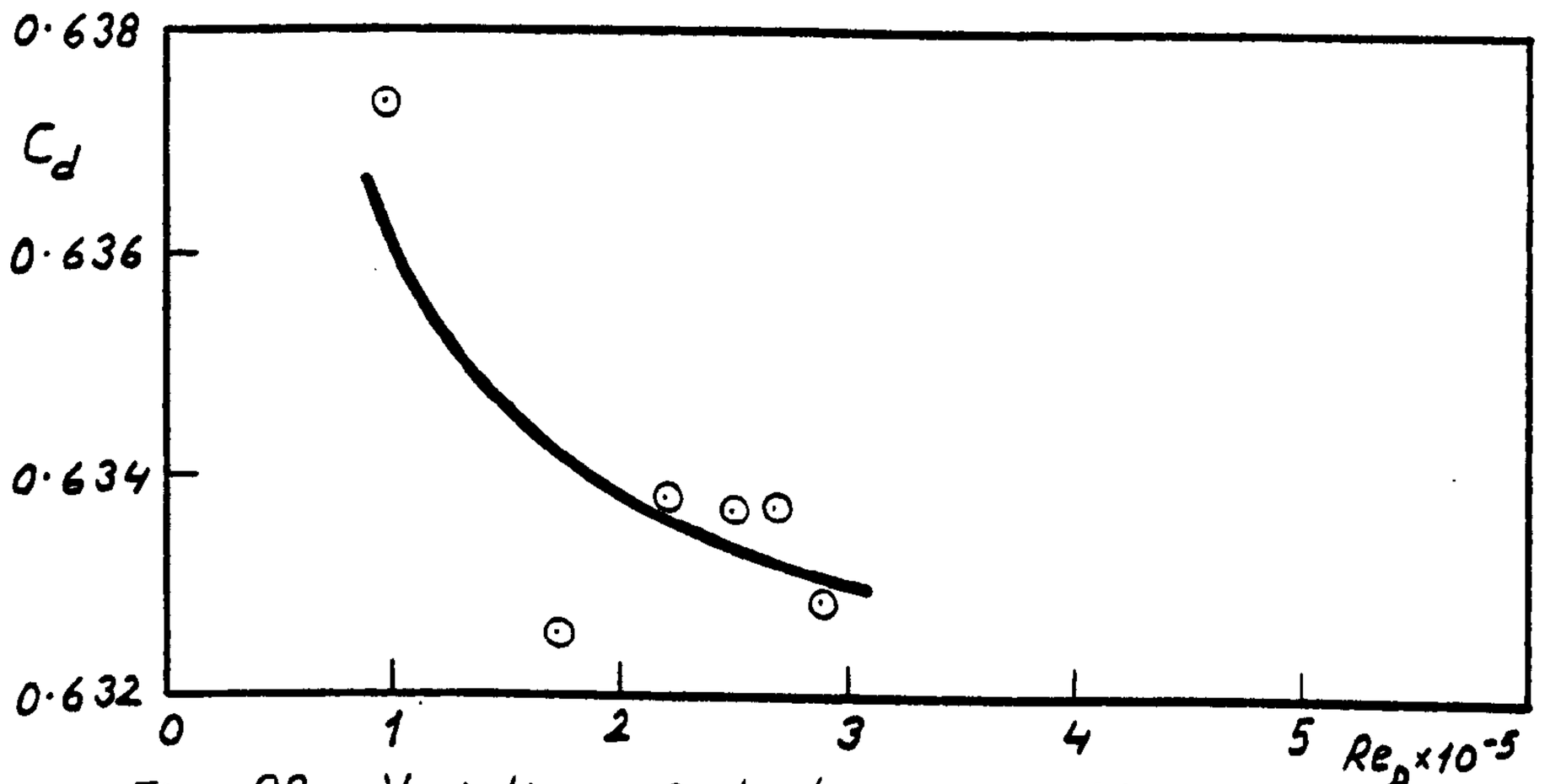

Fig. 98. Variation of discharge coefficient with Reynolds number, multi-hole orifice plate of $m = 0.170$, $p/d = 1.503$, $N = 6$

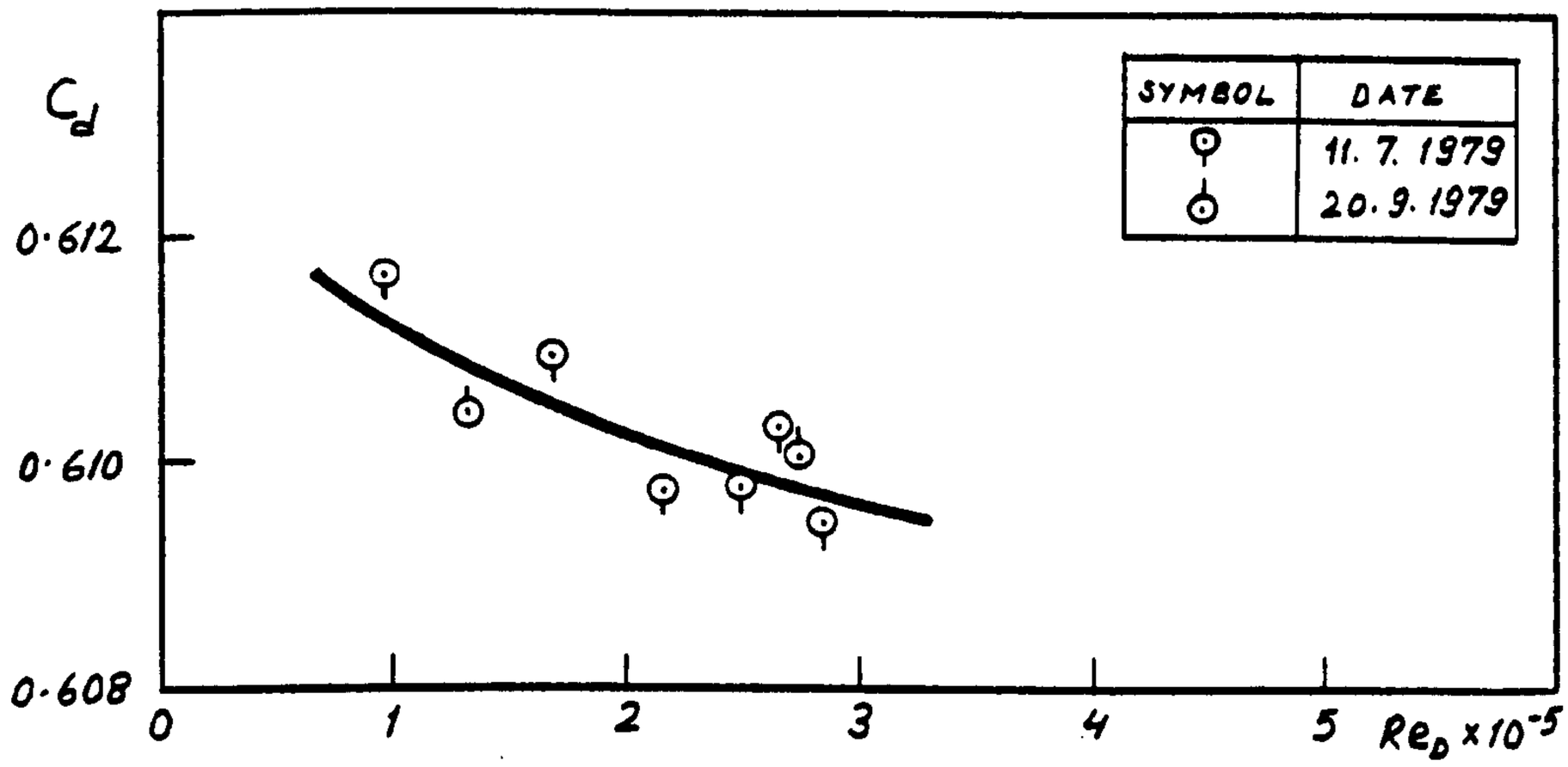

Fig. 99. Variation of discharge coefficient with Reynolds number, multi-hole orifice plate of $m = 0.170$, $p/d = 1.800$, $N = 3$

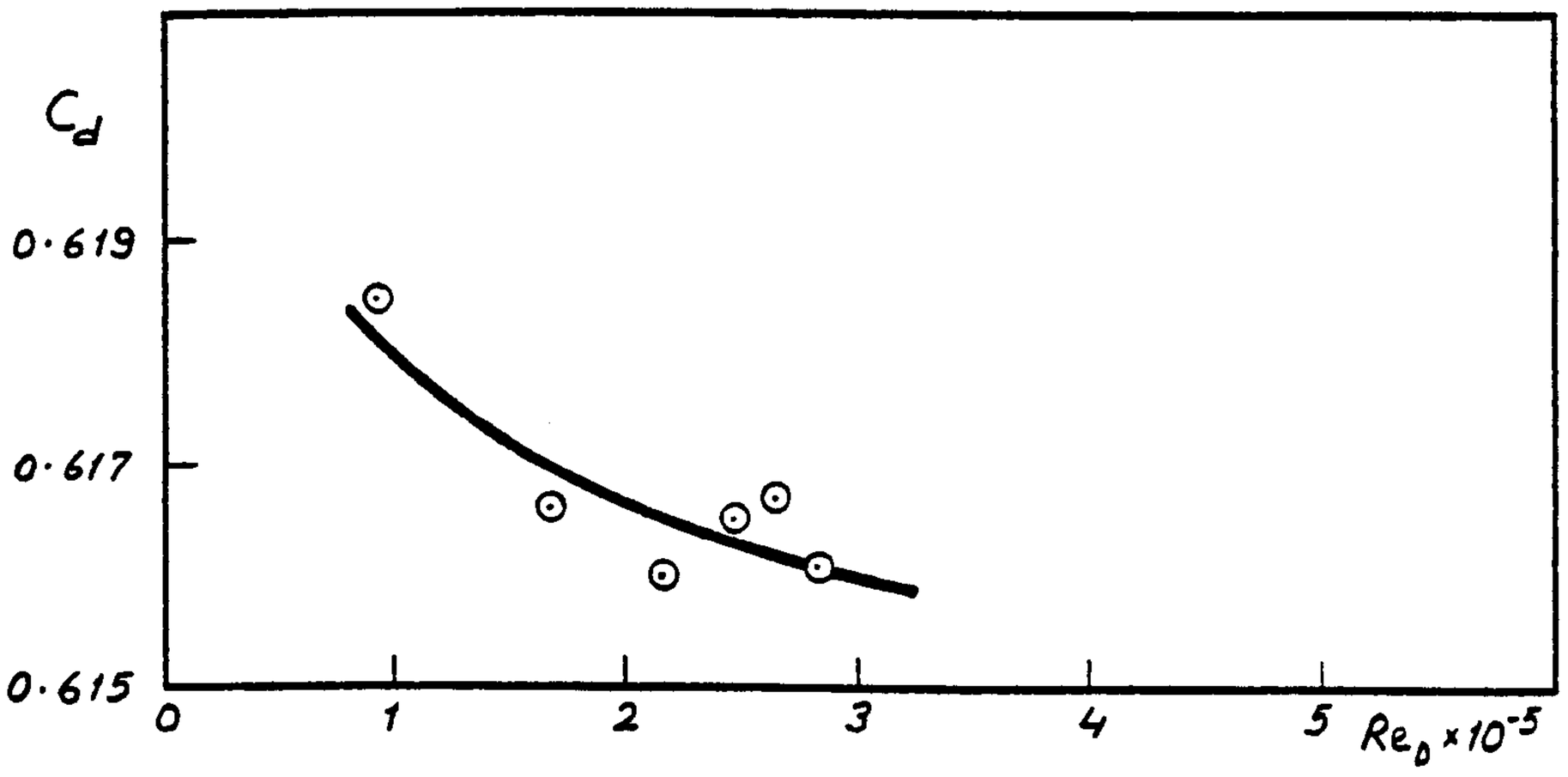

Fig. 100. Variation of discharge coefficient with Reynolds number, multi-hole orifice plate of $m = 0.170$, $p/d = 1.753$, $N = 4$

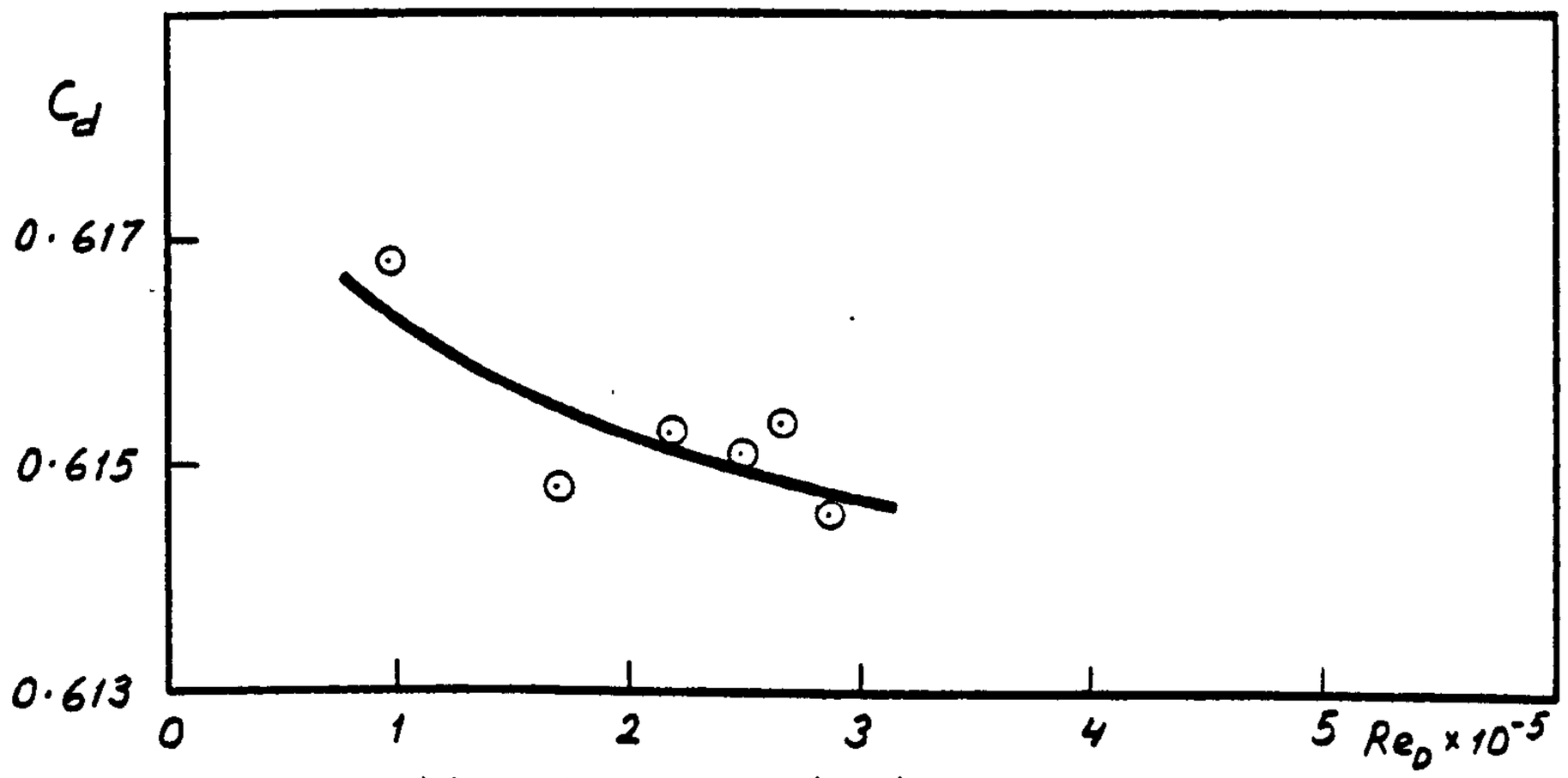

Fig. 101. Variation of discharge coefficient with Reynolds number, multi-hole orifice plate of $m = 0.170$, $p/d = 1.496$, $N = 4$

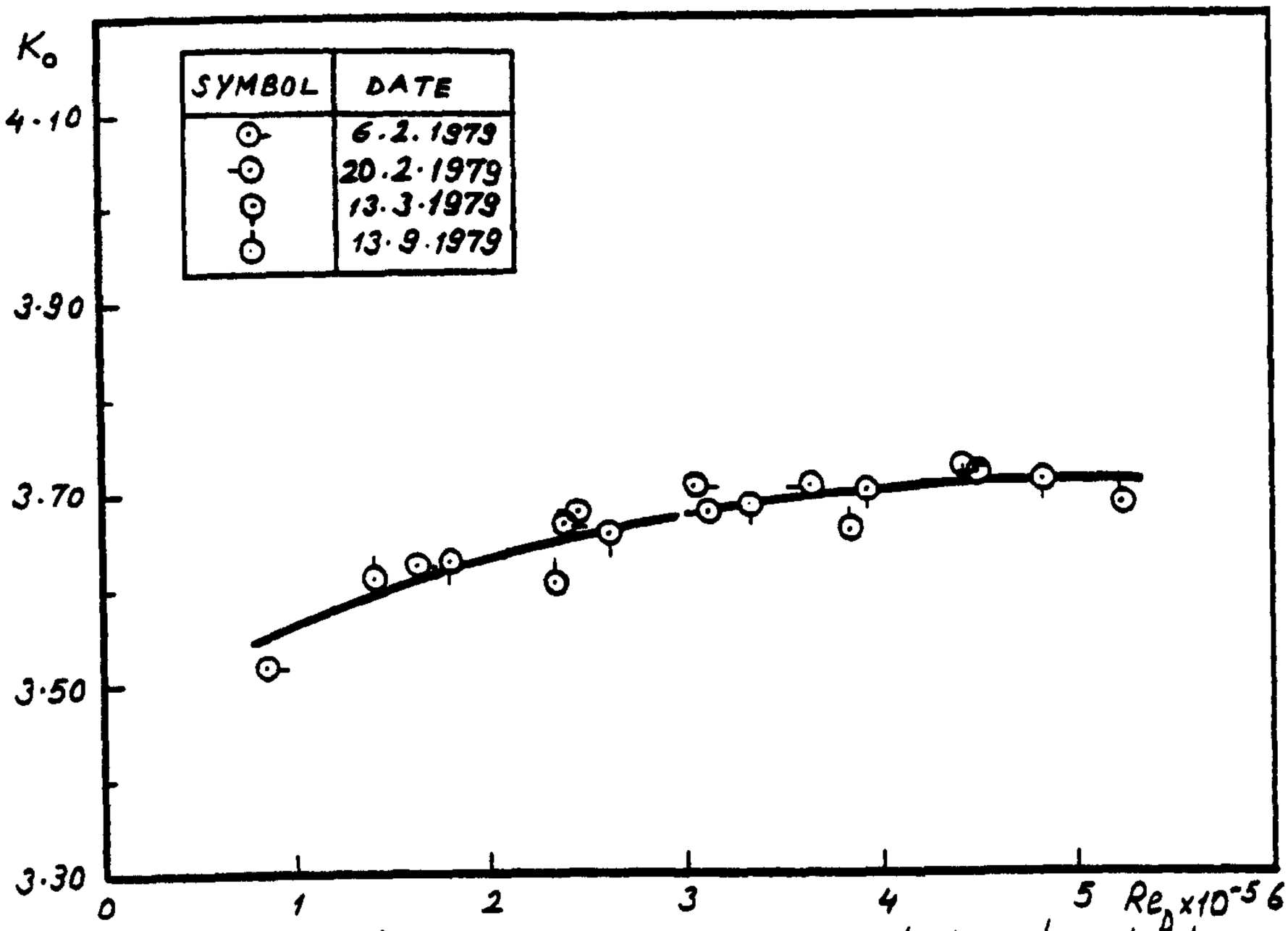

Fig. 102. Variation of orifice plate head loss coefficient with Reynolds number, single-hole orifice plate of m=0.508

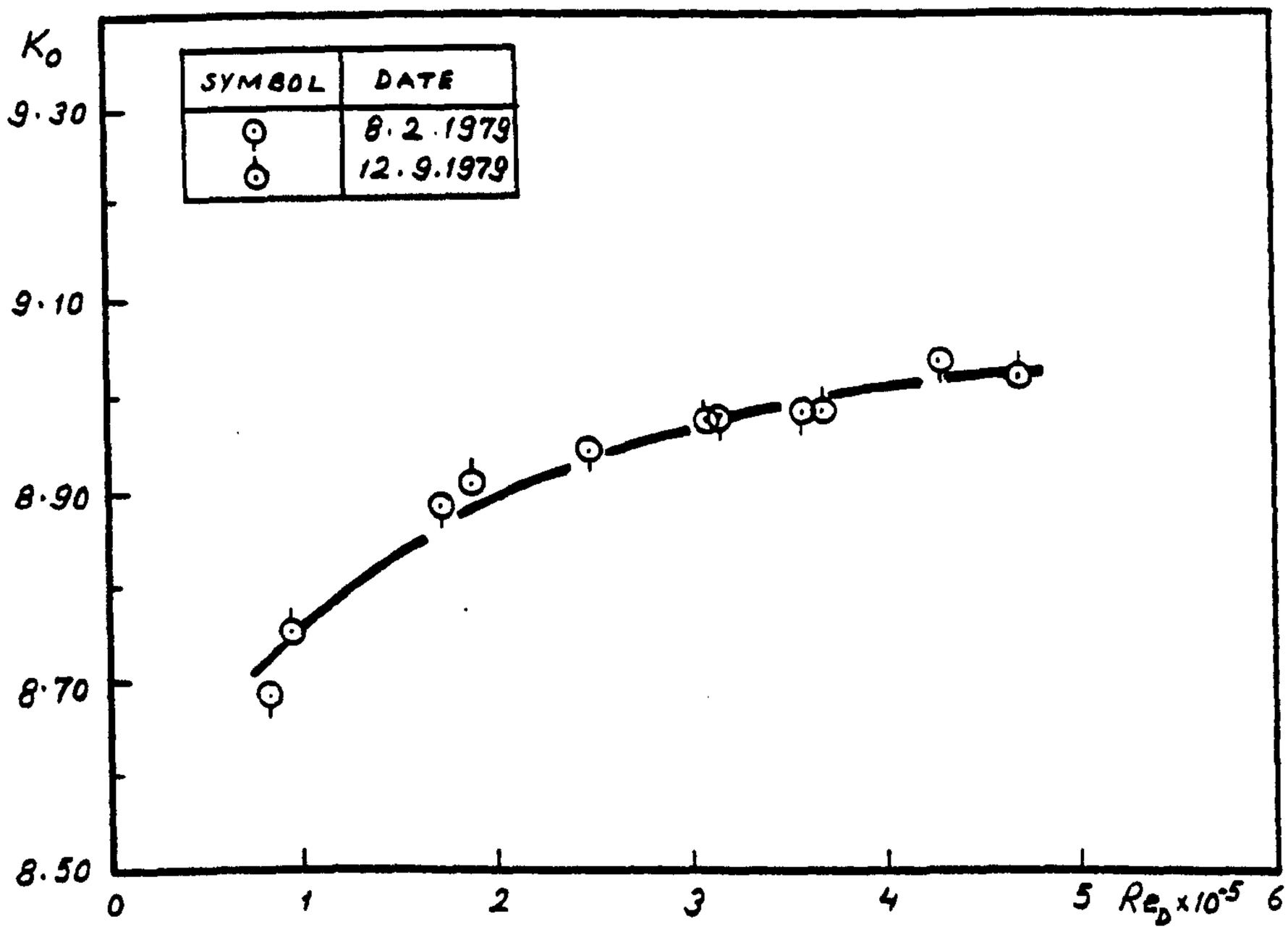

Fig. 103. Variation of orifice plate head loss coefficient with Reynolds number, single-hole orifice plate of m=0.389

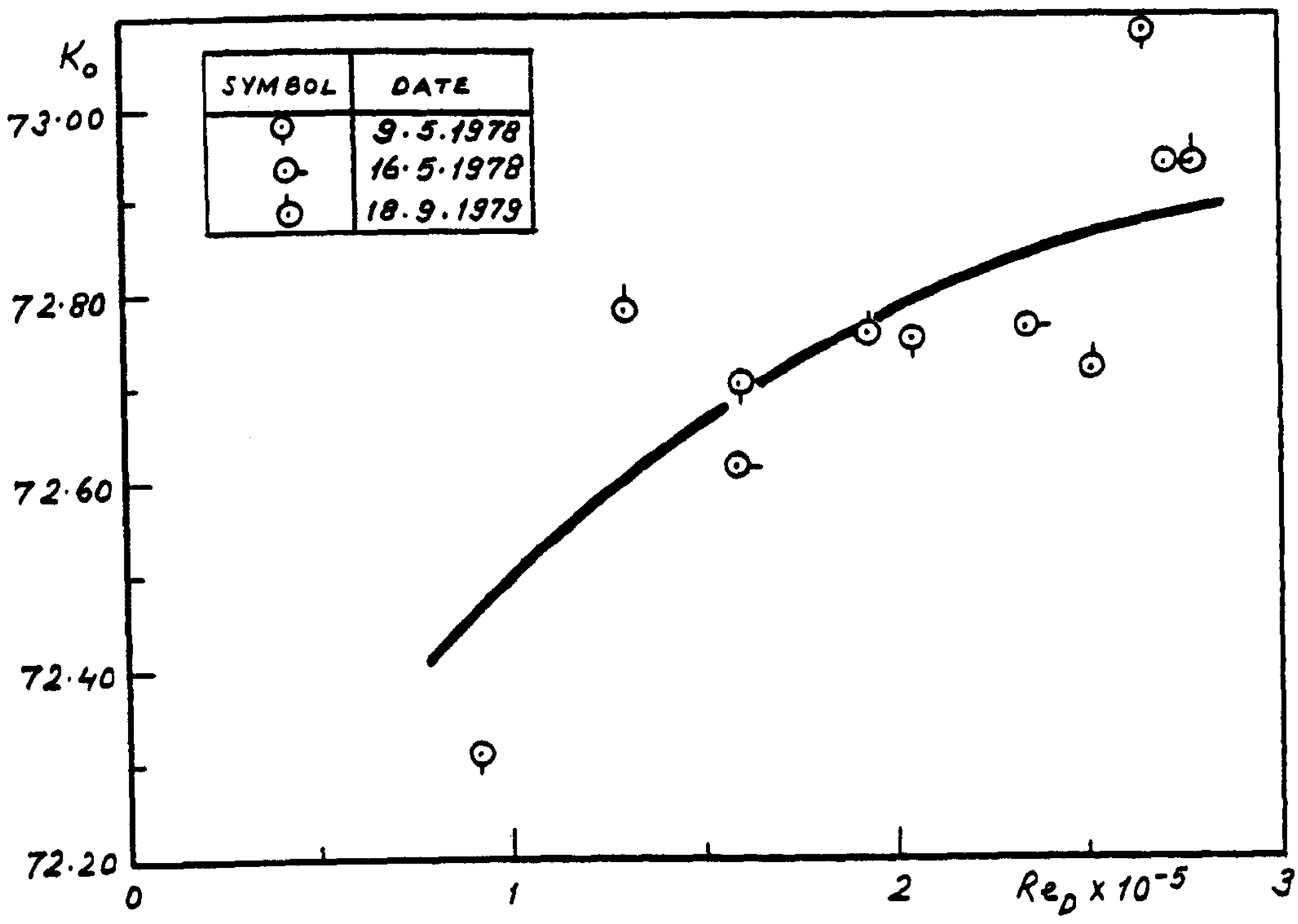

Fig. 106a. Variation of orifice plate head loss coefficient with Reynolds number, single-hole orifice plate of $m = 0.171$

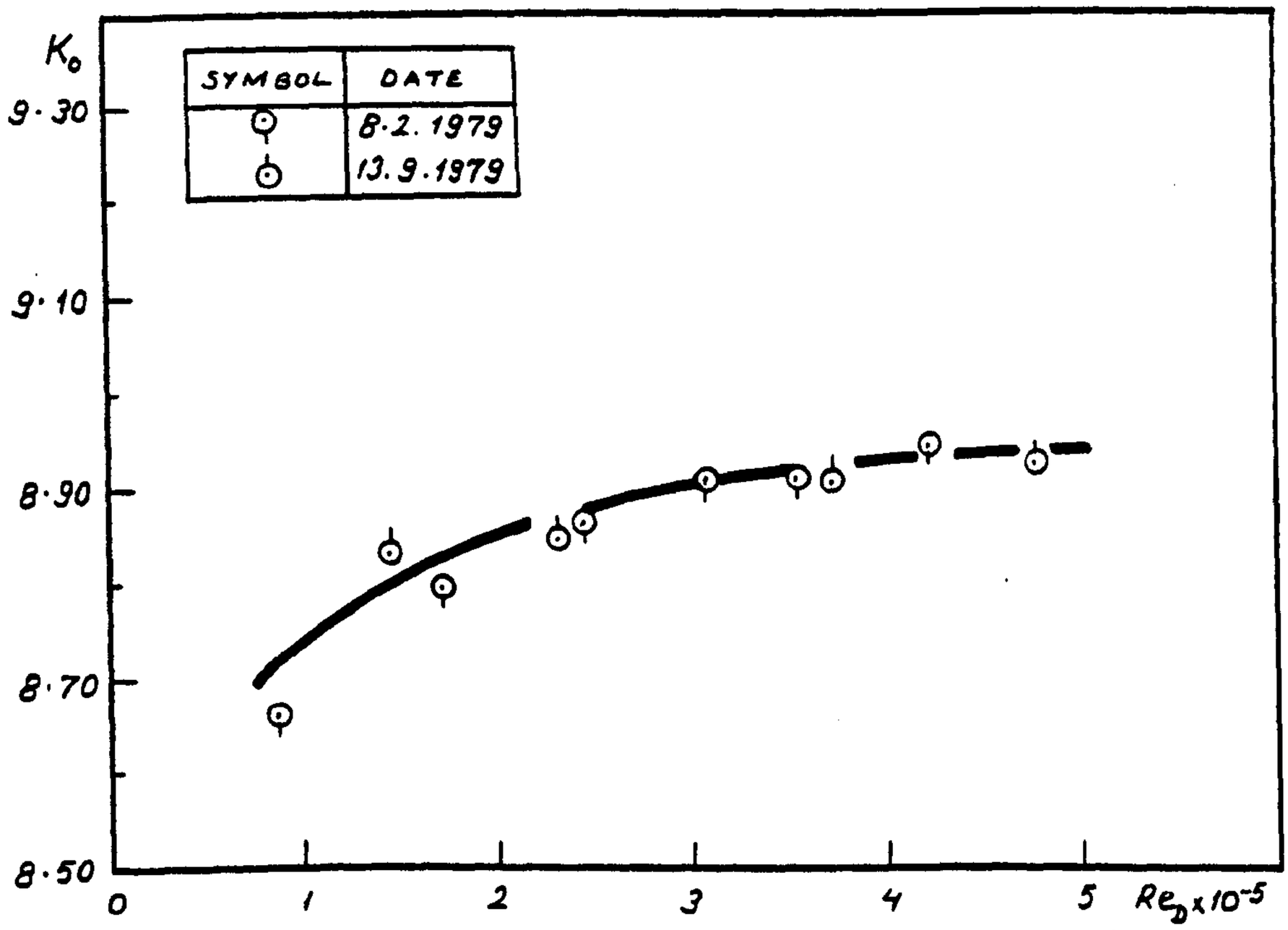

Fig. 107. Variation of orifice plate head loss coefficient with Reynolds number, multi-hole orifice plate of $m = 0.387$, $p/d = 1.154$, $N = 4$

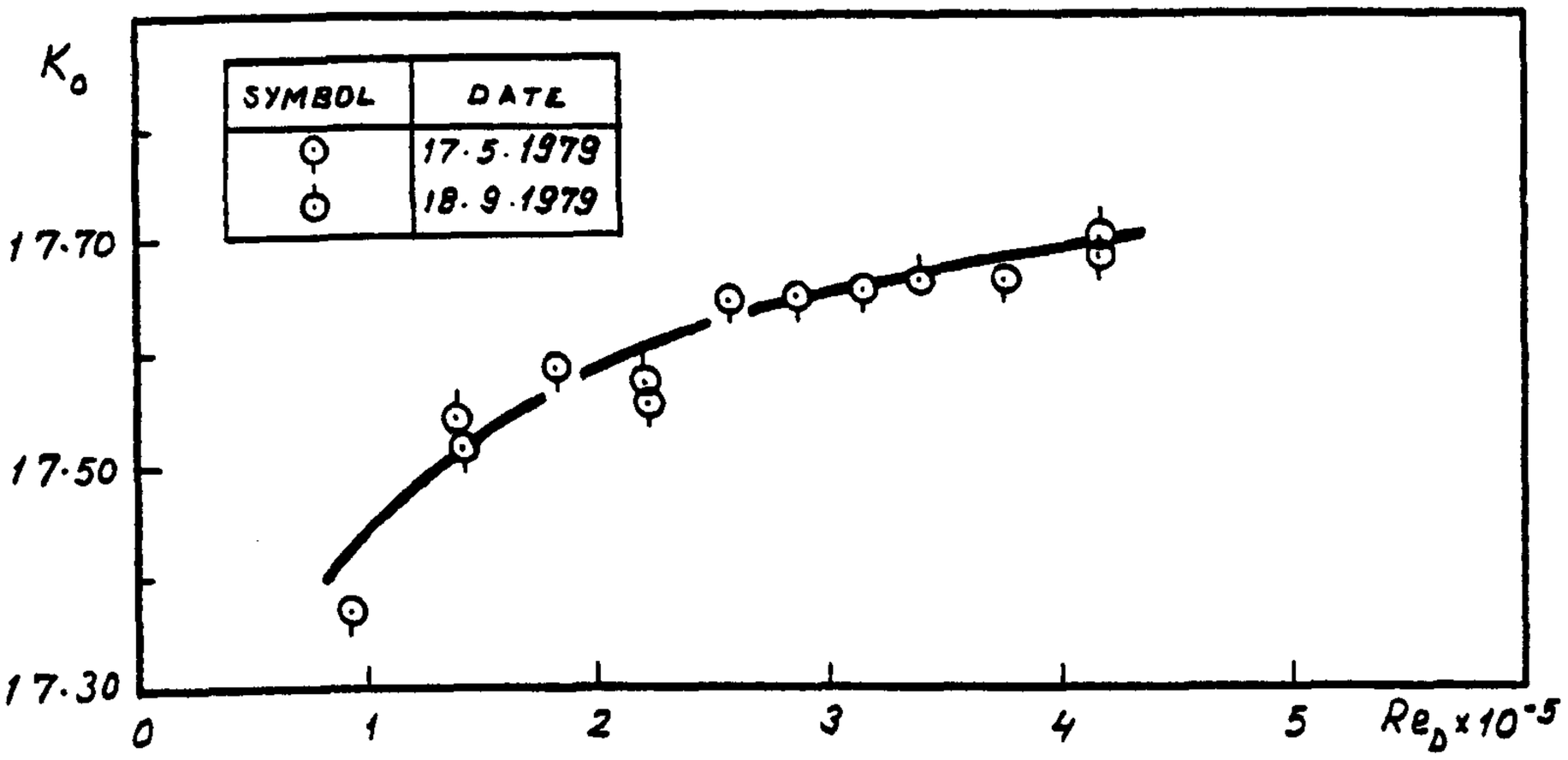

Fig. 104. Variation of orifice plate head loss coefficient with Reynolds number, single-hole orifice plate of $m = 0.304$

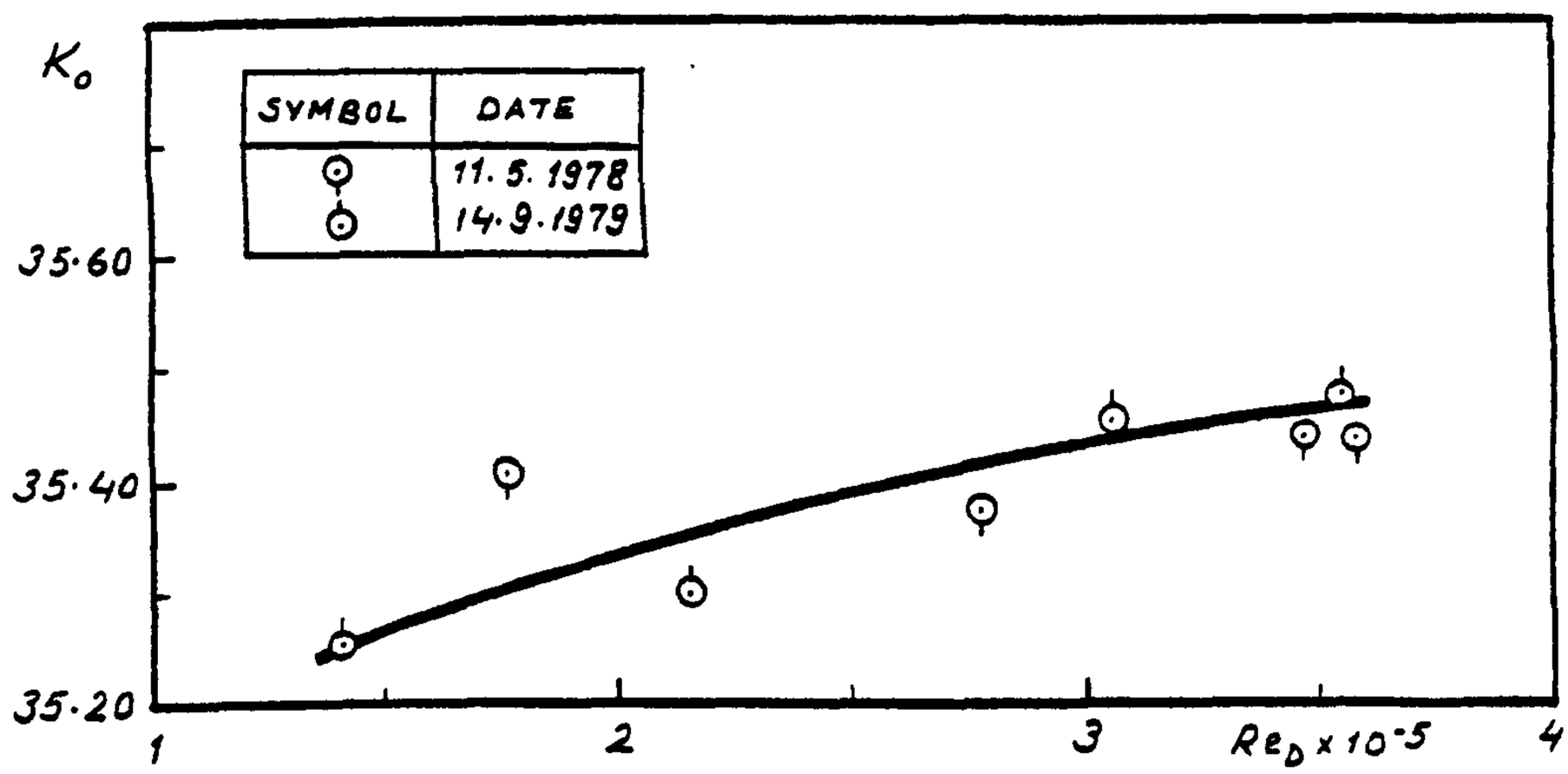

Fig. 105. Variation of orifice plate head loss coefficient with Reynolds number, single-hole orifice plate of $m = 0.232$

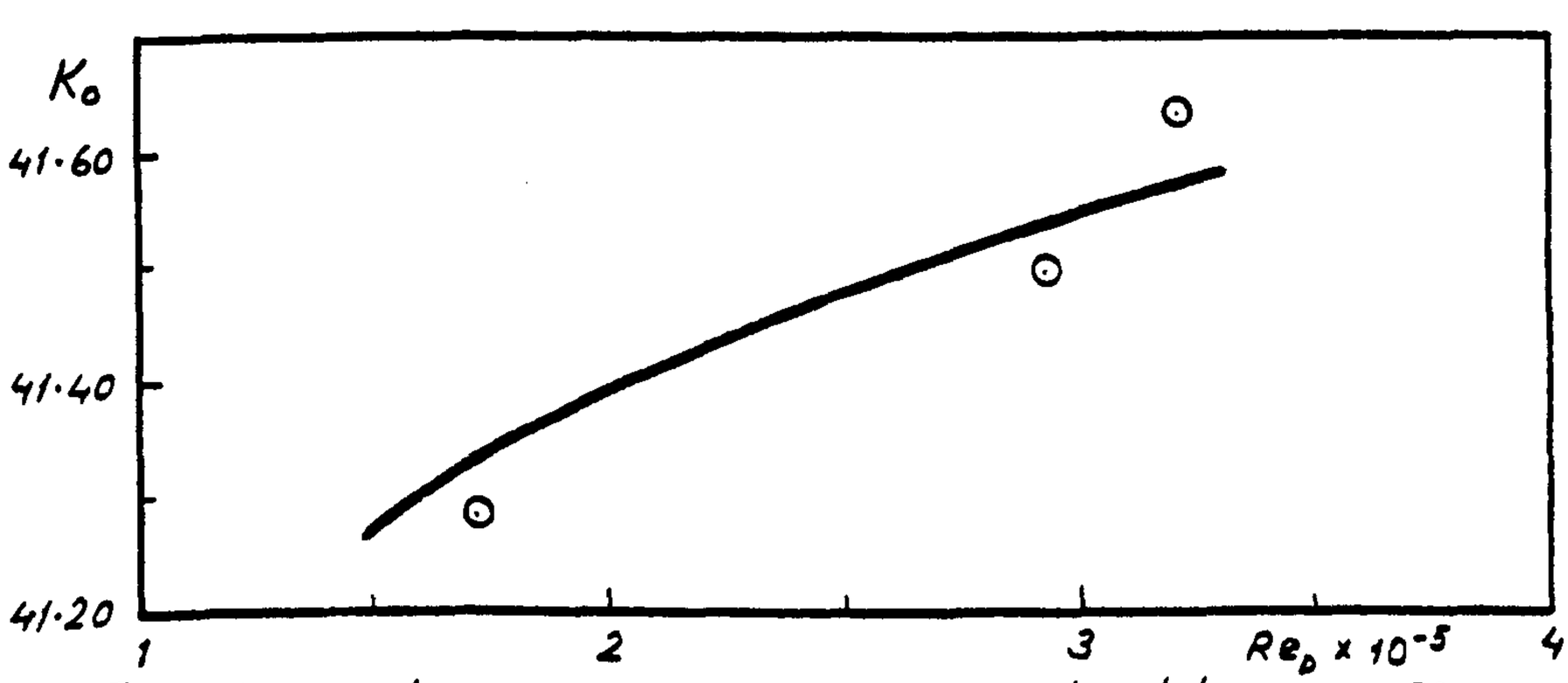

Fig. 106. Variation of orifice plate head loss coefficient with Reynolds number, single-hole orifice plate of $m = 0.218$

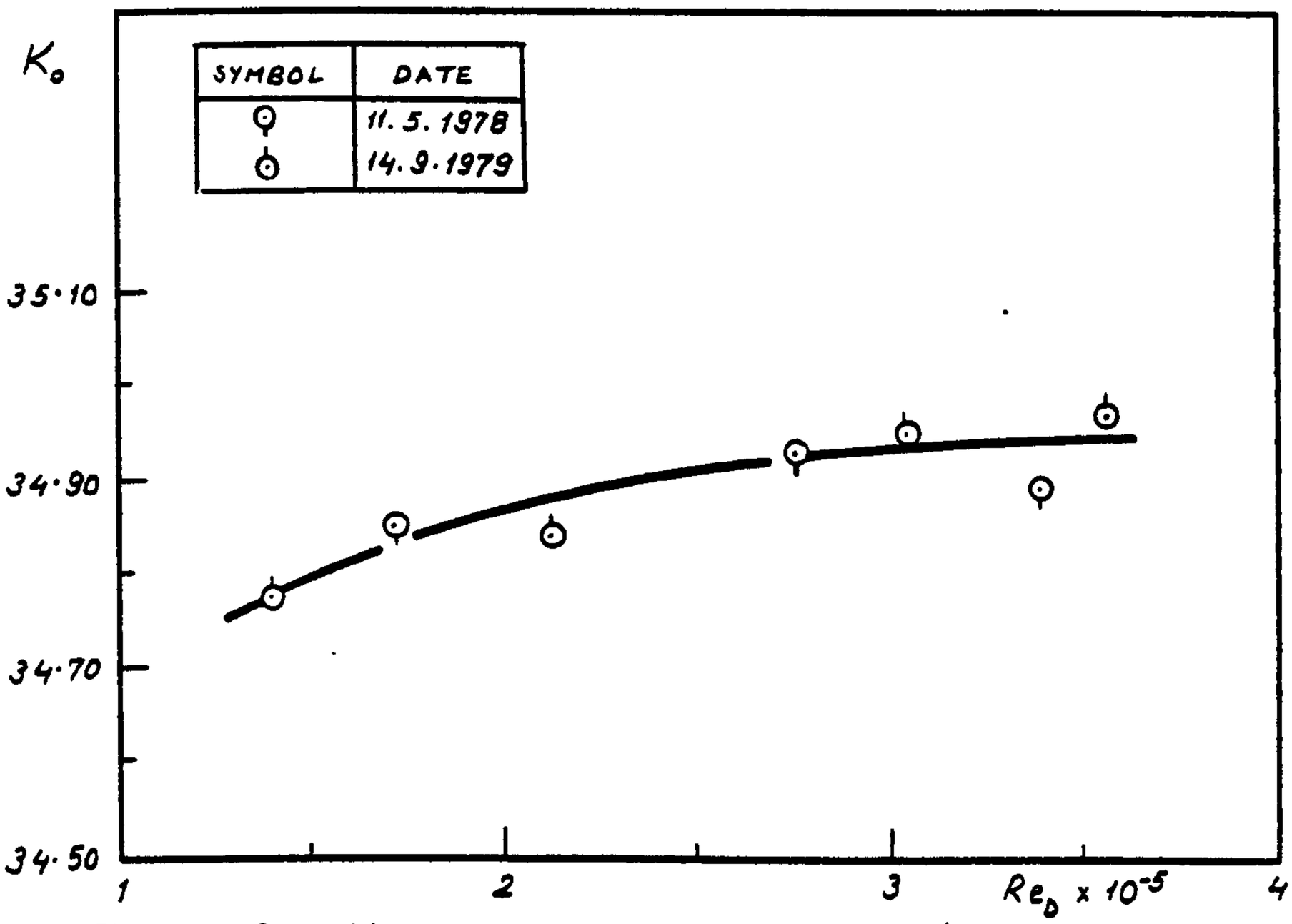

Fig. 108. Variation of orifice plate head loss coefficient with Reynolds number, multi-hole orifice plate of $m = 0.231$, $p/d = 1.512$, $N = 4$

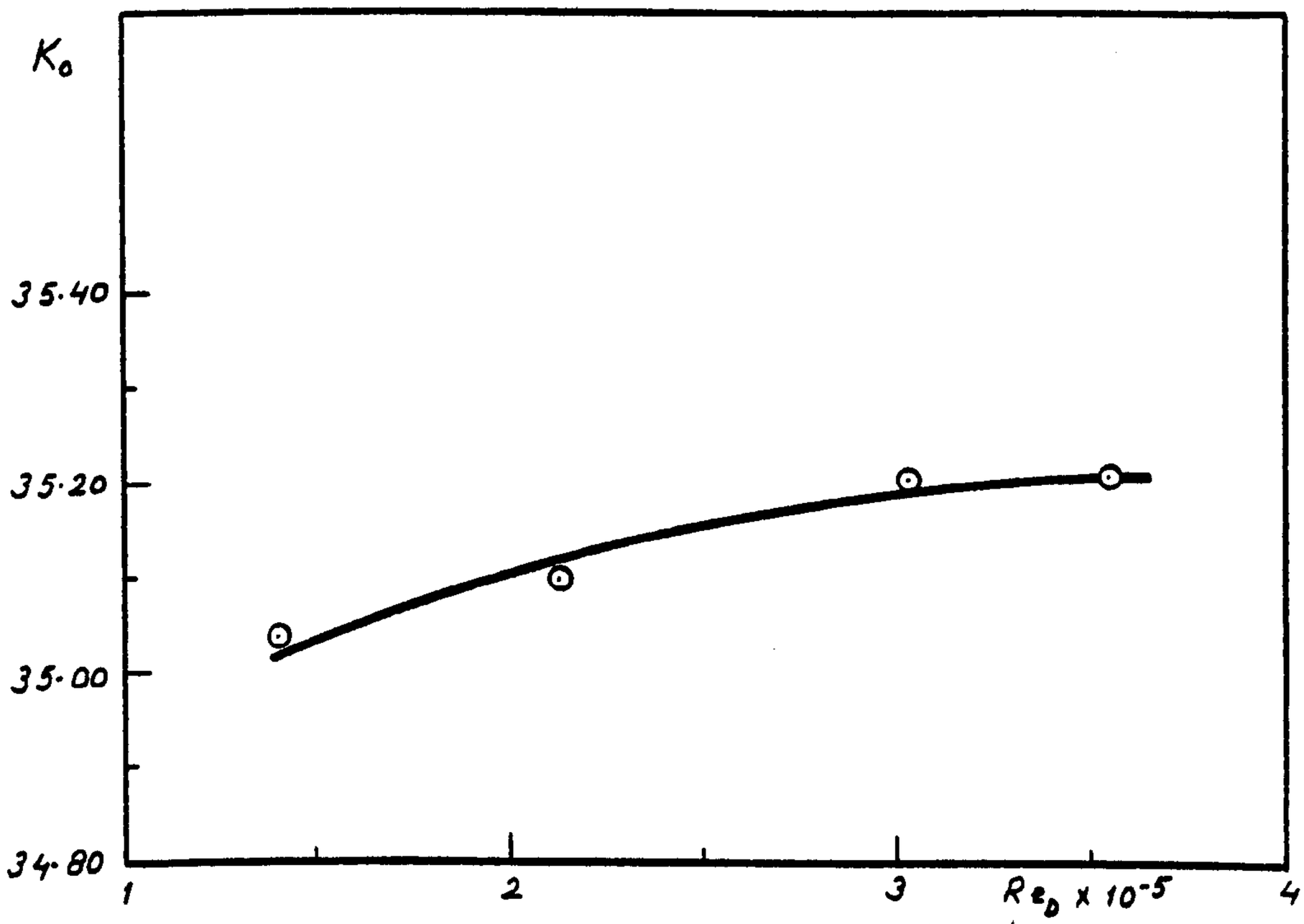

Fig. 109. Variation of orifice plate head loss coefficient with Reynolds number, multi-hole orifice plate of $m = 0.231$, $p/d = 1.505$, $N = 3$

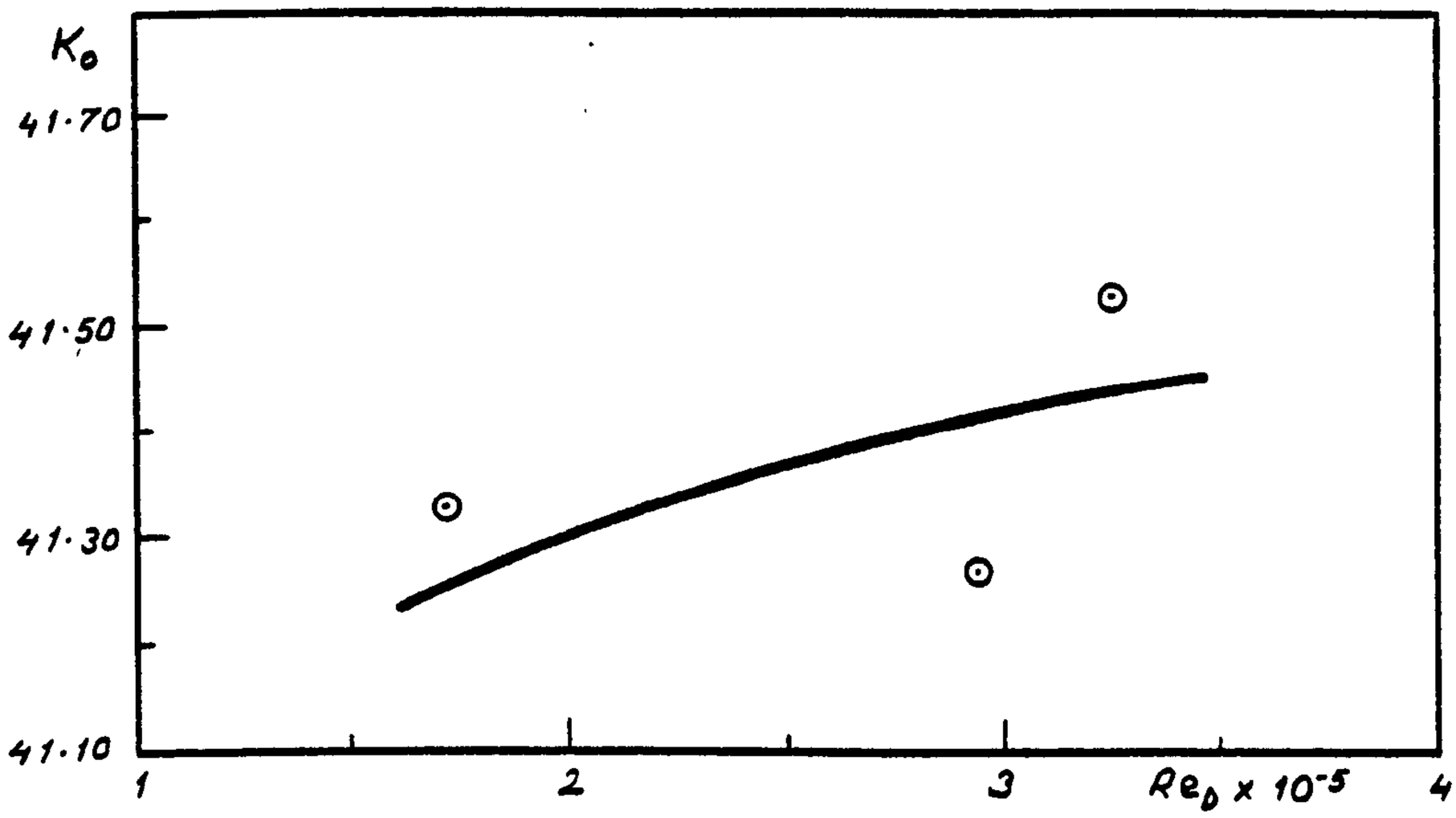

Fig. 110. Variation of orifice plate head loss coefficient with Reynolds number, multi-hole orifice plate of $m = 0.213$, $p/d = 1.421$, $N = 5$

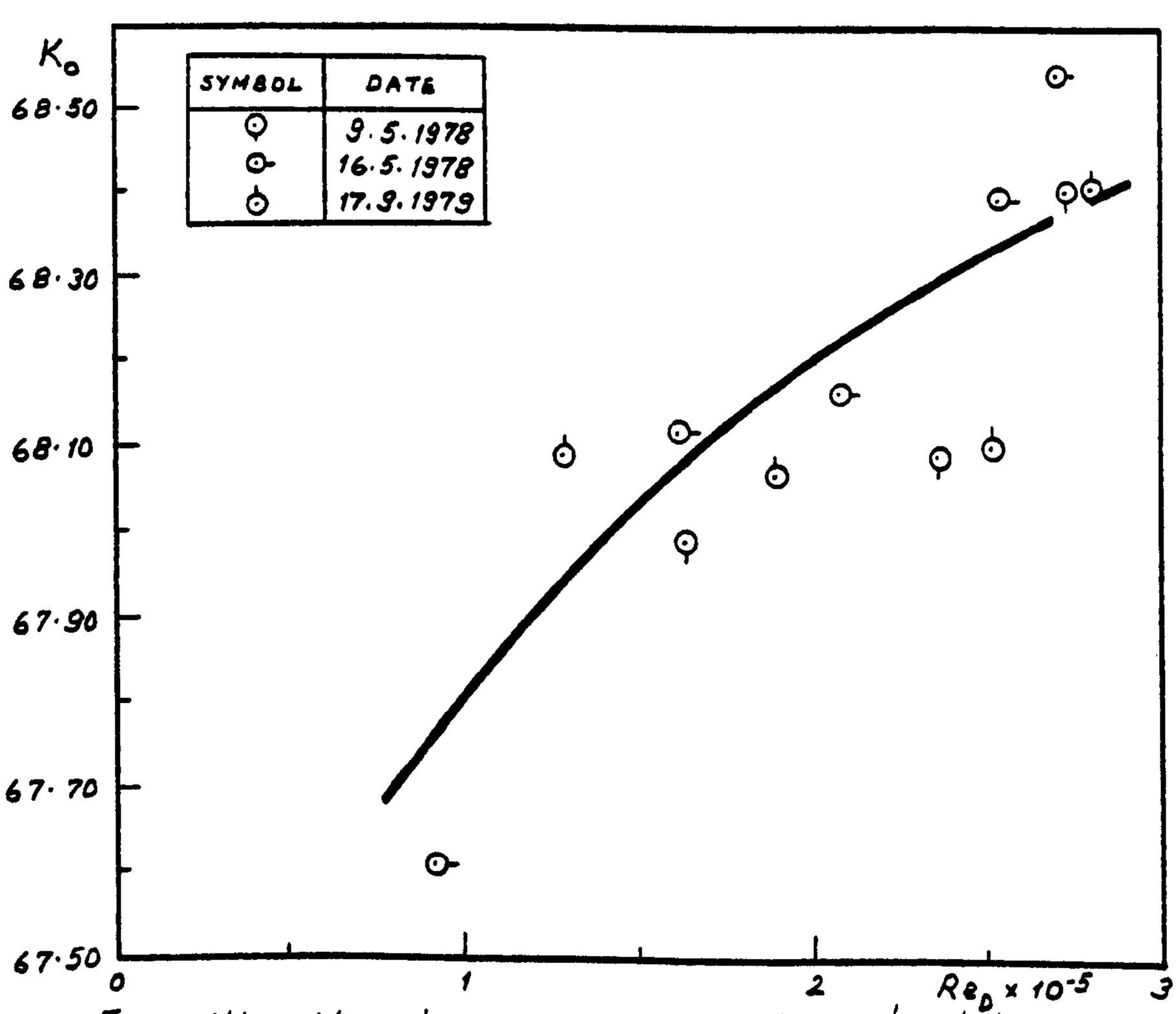

Fig. 111. Variation of orifice plate head loss coefficient with Reynolds number, multi-hole orifice plate of $m = 0.171$, $p/d = 1.742$, $N = 9$

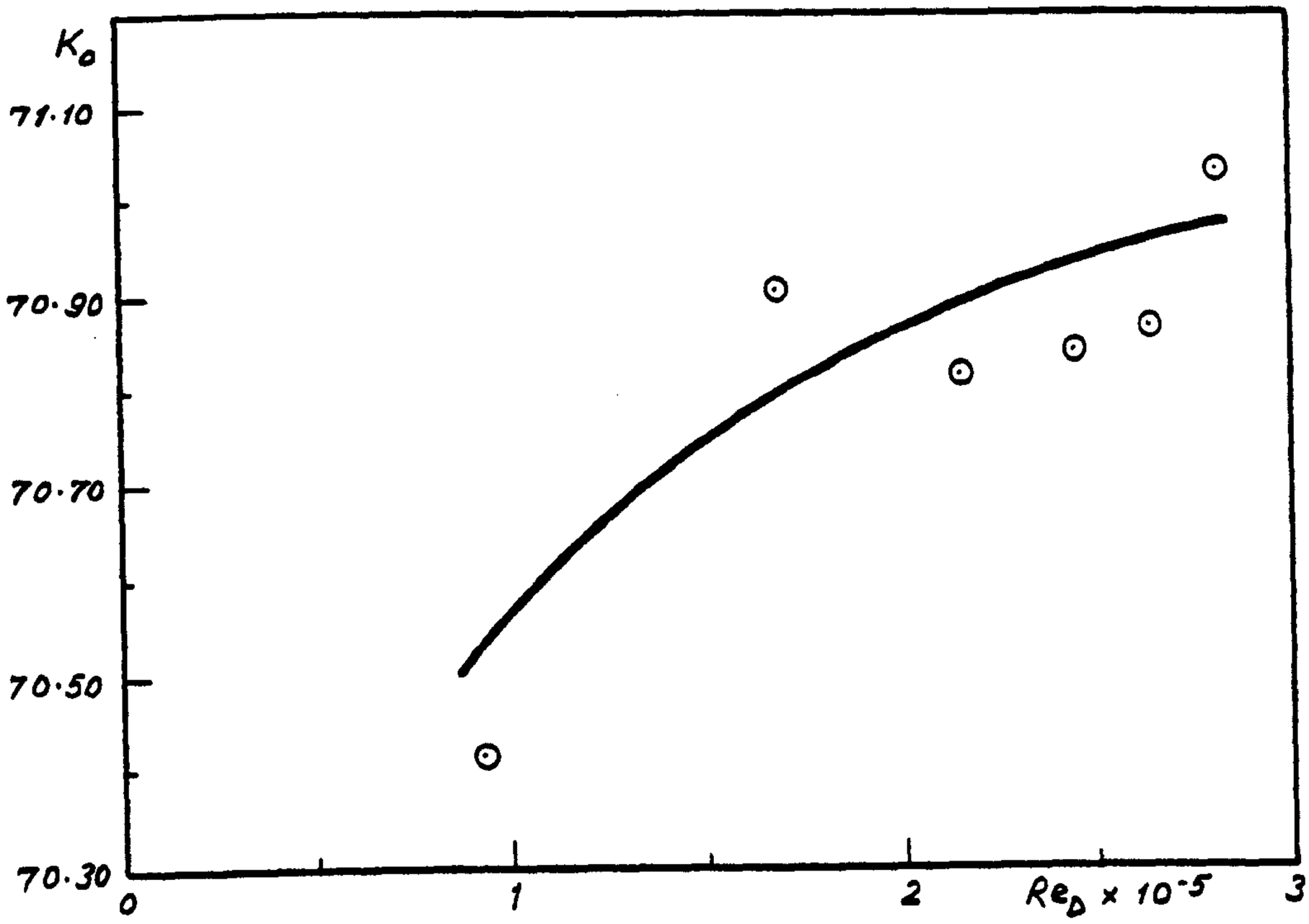

Fig. 112. Variation of orifice plate head loss coefficient with Reynolds number, multi-hole orifice plate of m=0.170, p/d=1.503, N=6

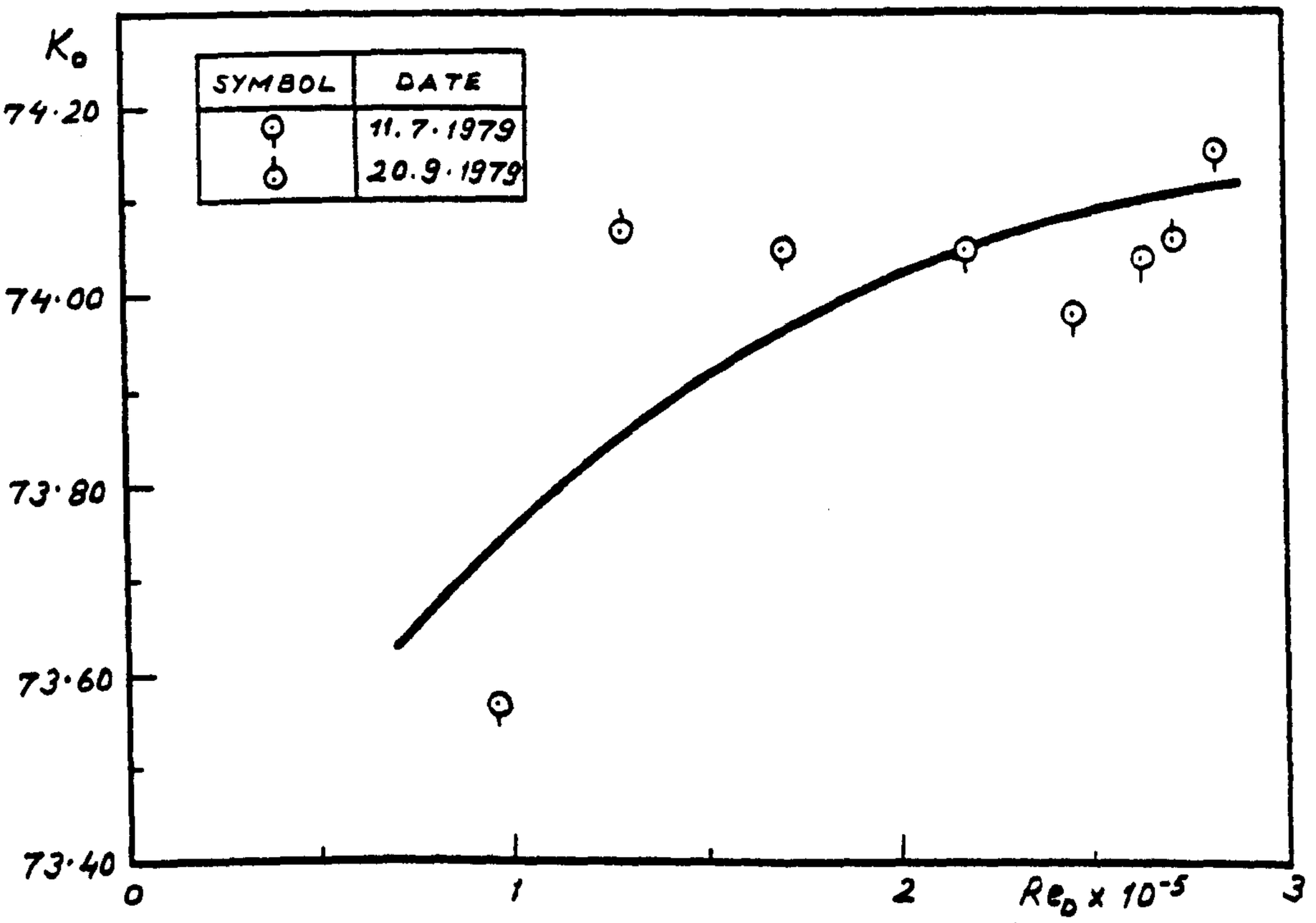

Fig. 113. Variation of orifice plate head loss coefficient with Reynolds number, multi-hole orifice plate of m=0.170, p/d=1.800, N=3

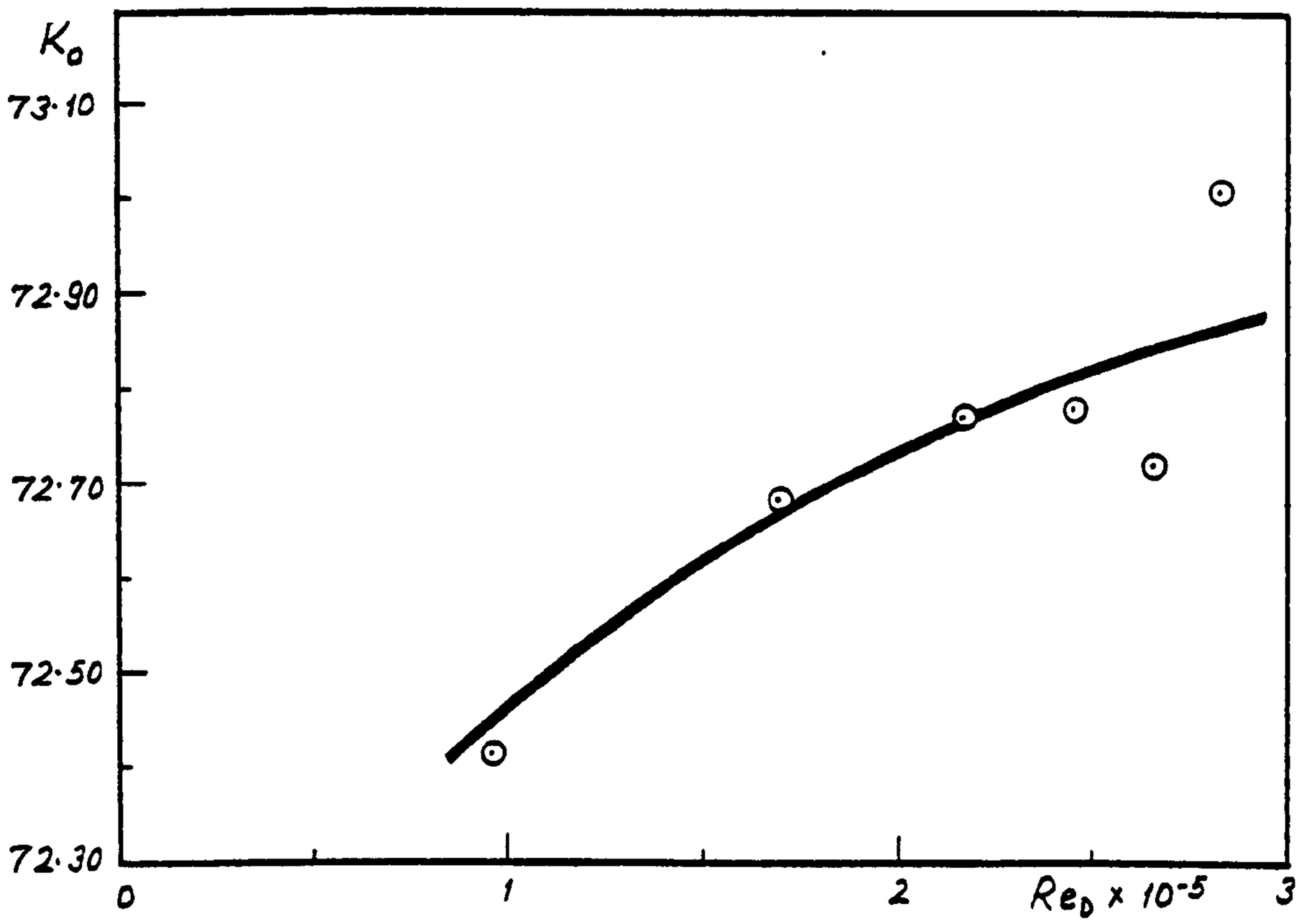

Fig. 114. Variation of orifice plate head loss coefficient with Reynolds number, multi-hole orifice plate of $m = 0.170$, $p/d = 1.496$, $N = 4$

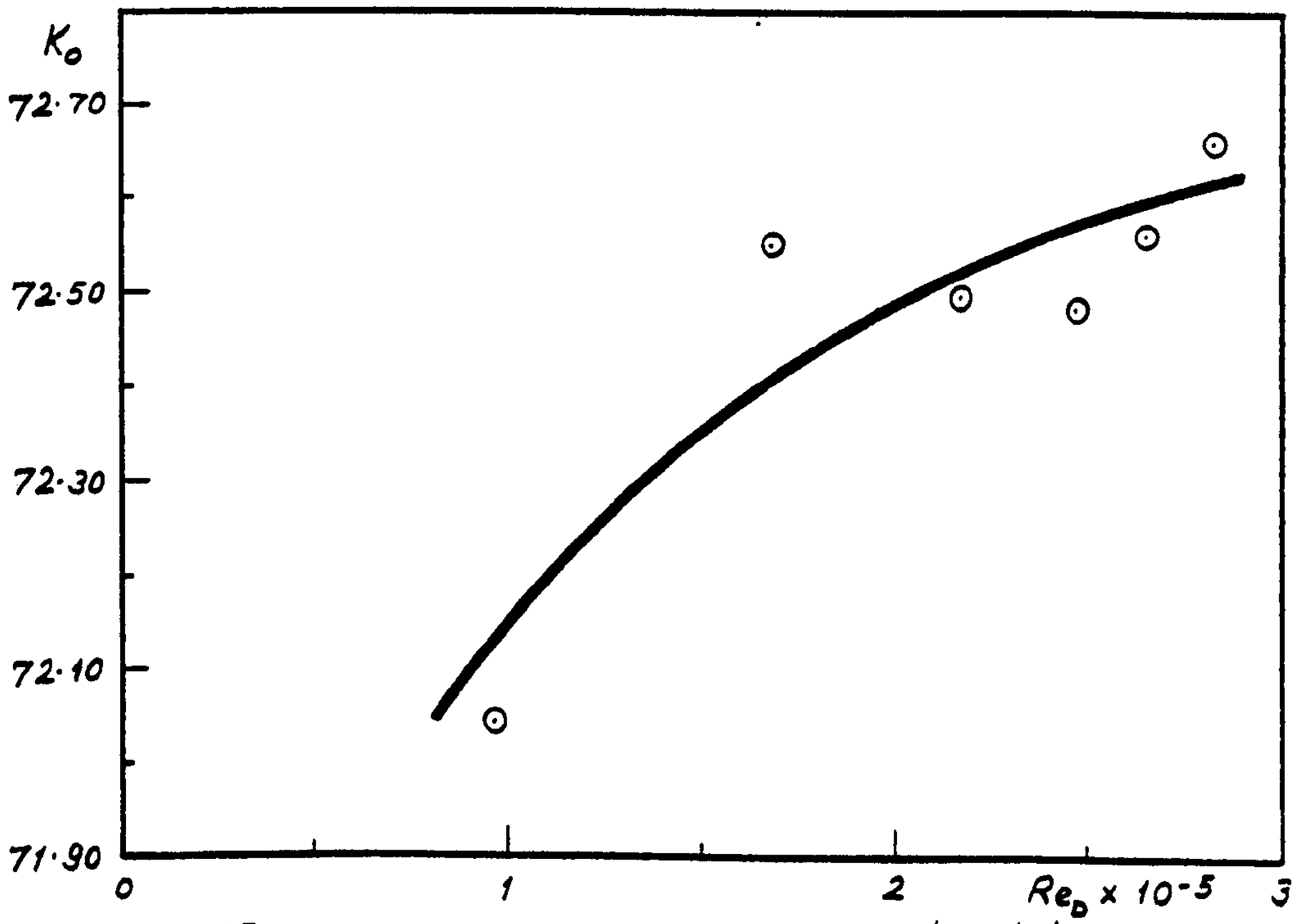

Fig. 115. Variation of orifice plate head loss coefficient with Reynolds number, multi-hole orifice plate of $m = 0.170$, $p/d = 1.753$, $N = 4$

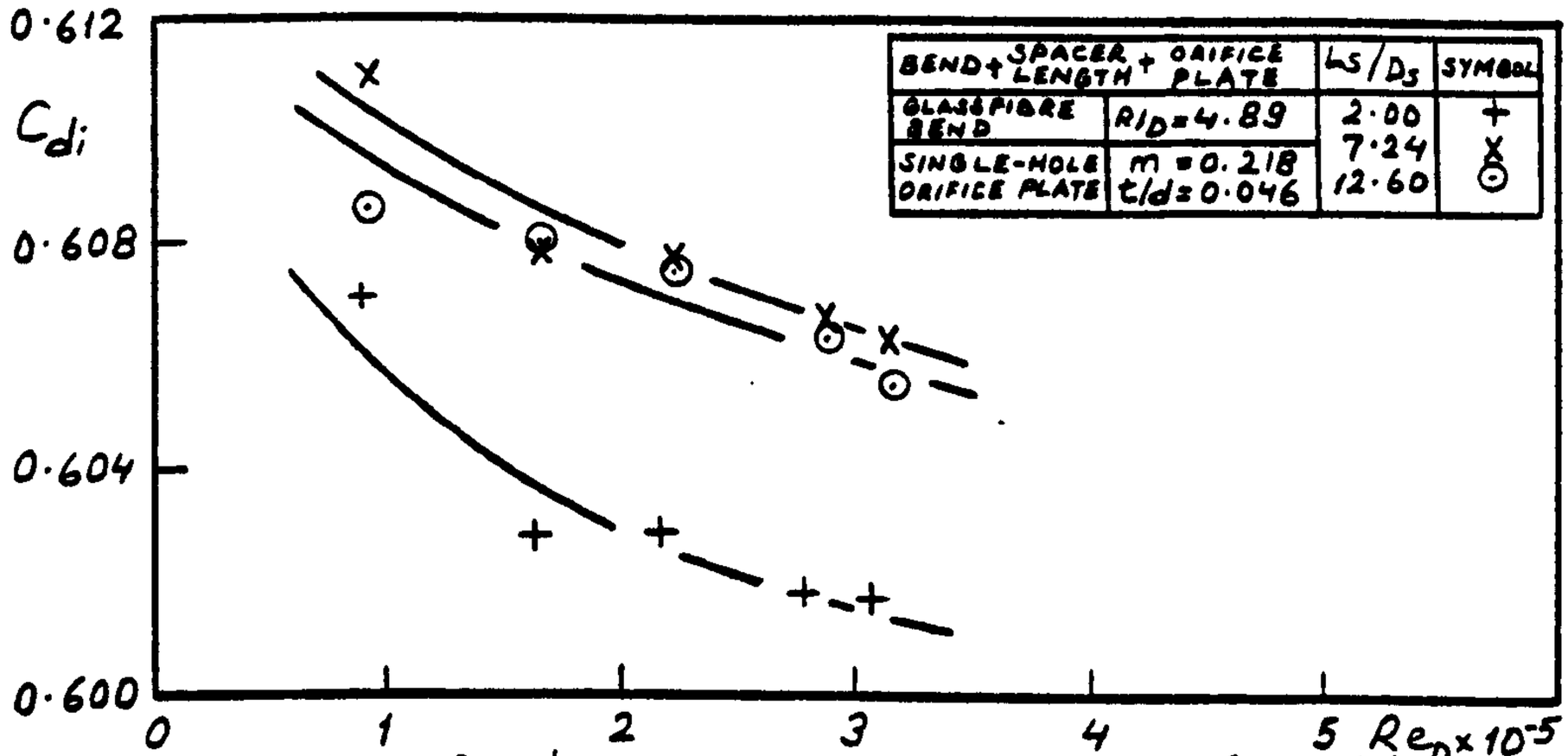

Fig. 116. Discharge coefficient versus Reynolds number for an orifice plate in combination

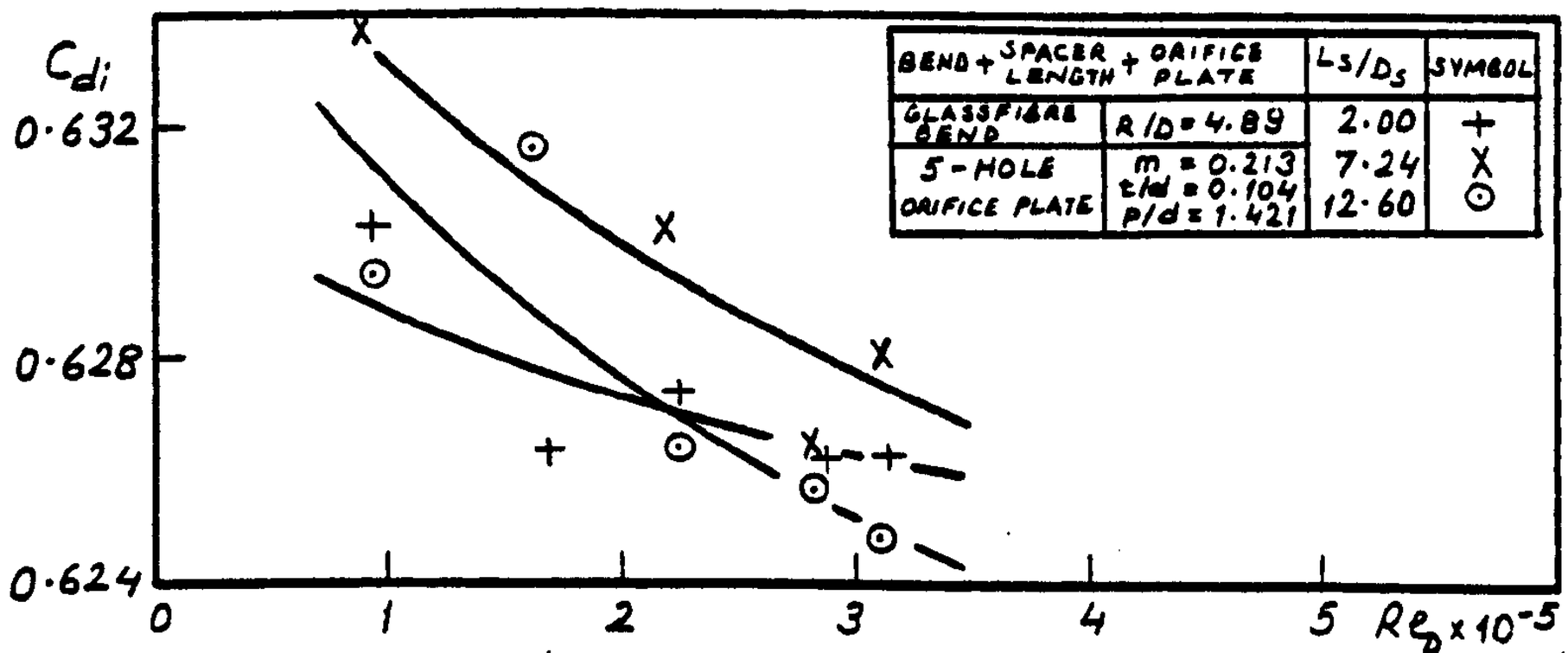

Fig. 117. Discharge coefficient versus Reynolds number for an orifice plate in combination

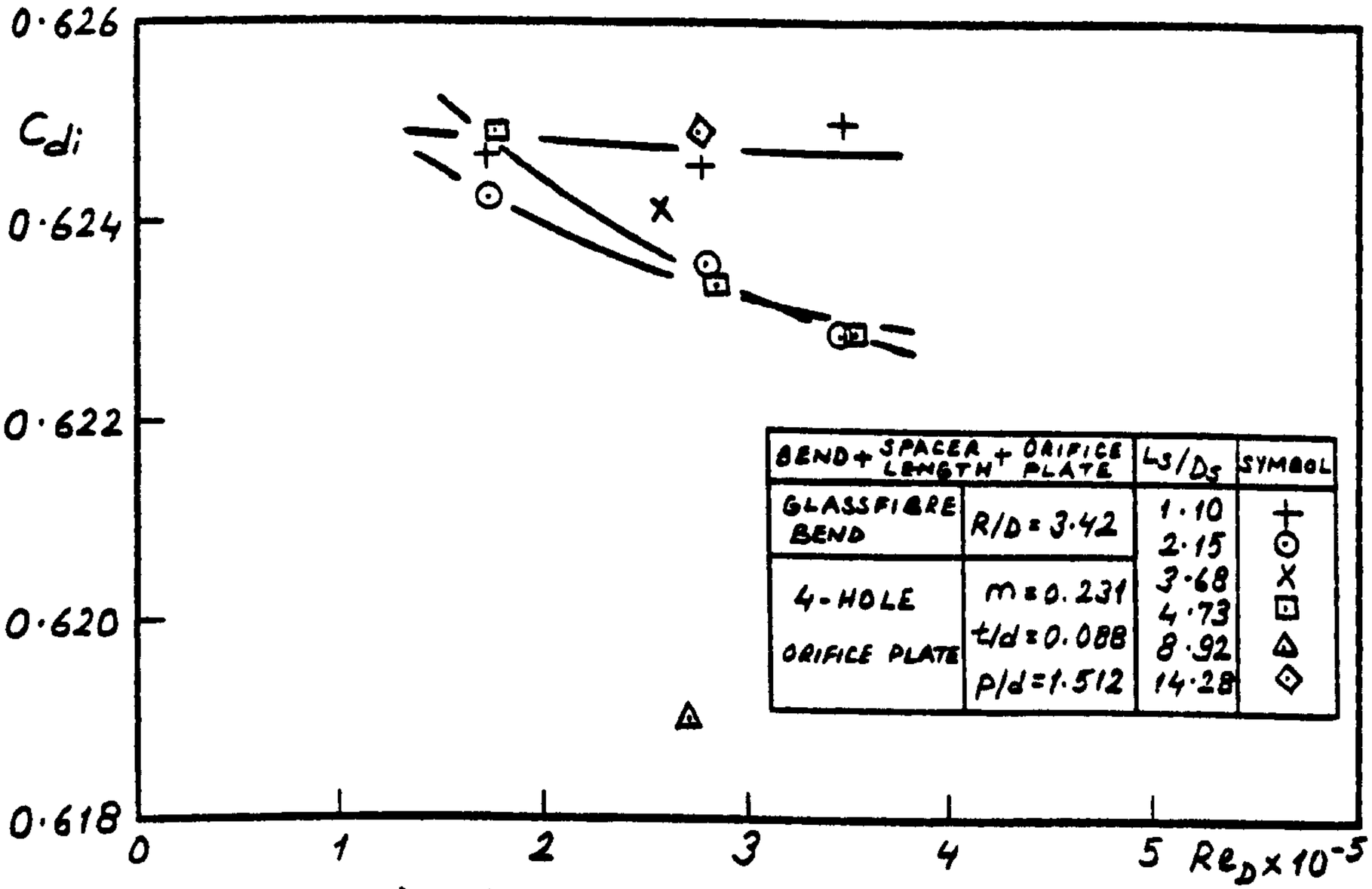

Fig. 118. Discharge coefficient versus Reynolds number for an orifice plate in combination

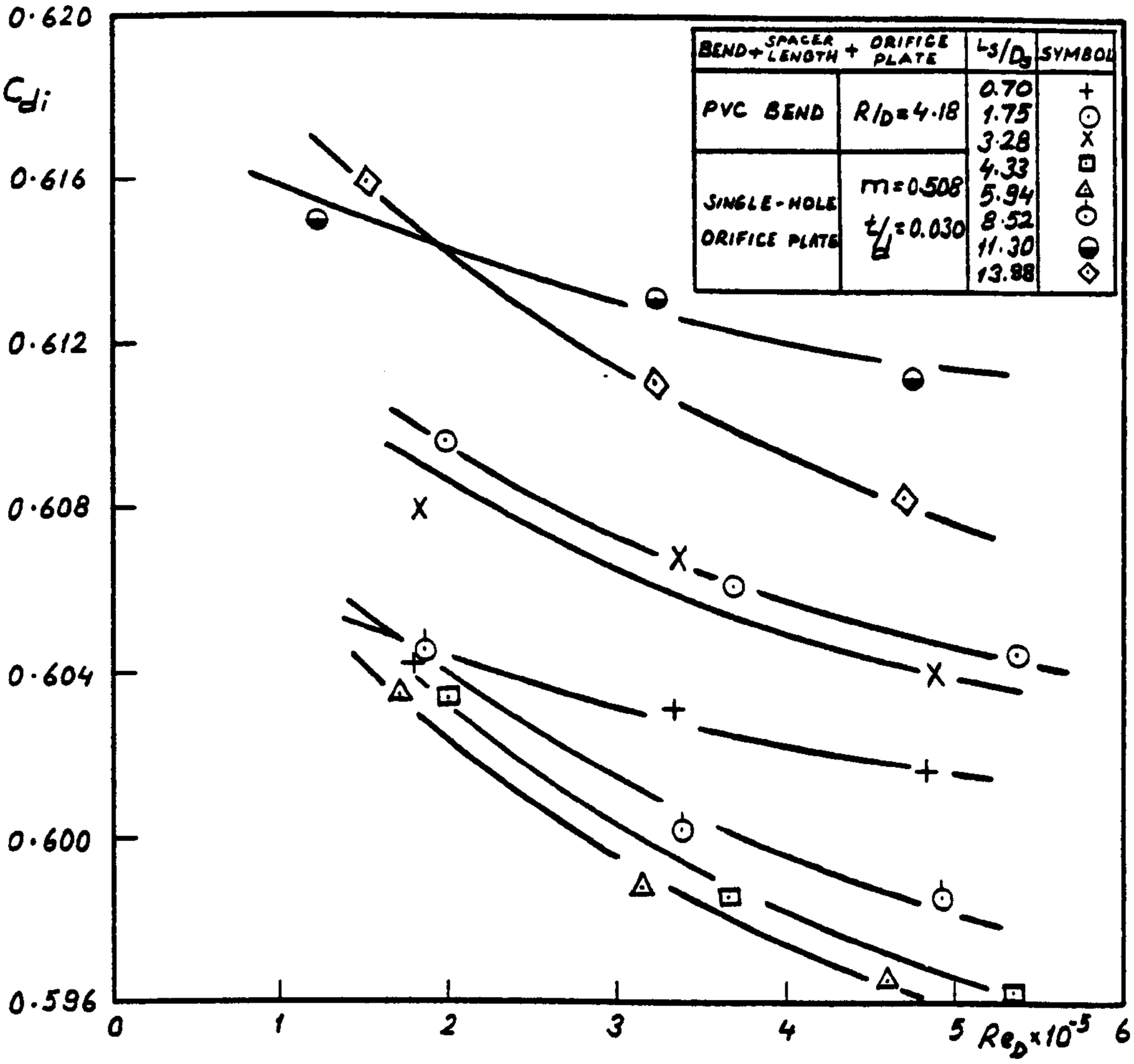

Fig. 119. Discharge coefficient versus Reynolds number for an orifice plate in combination

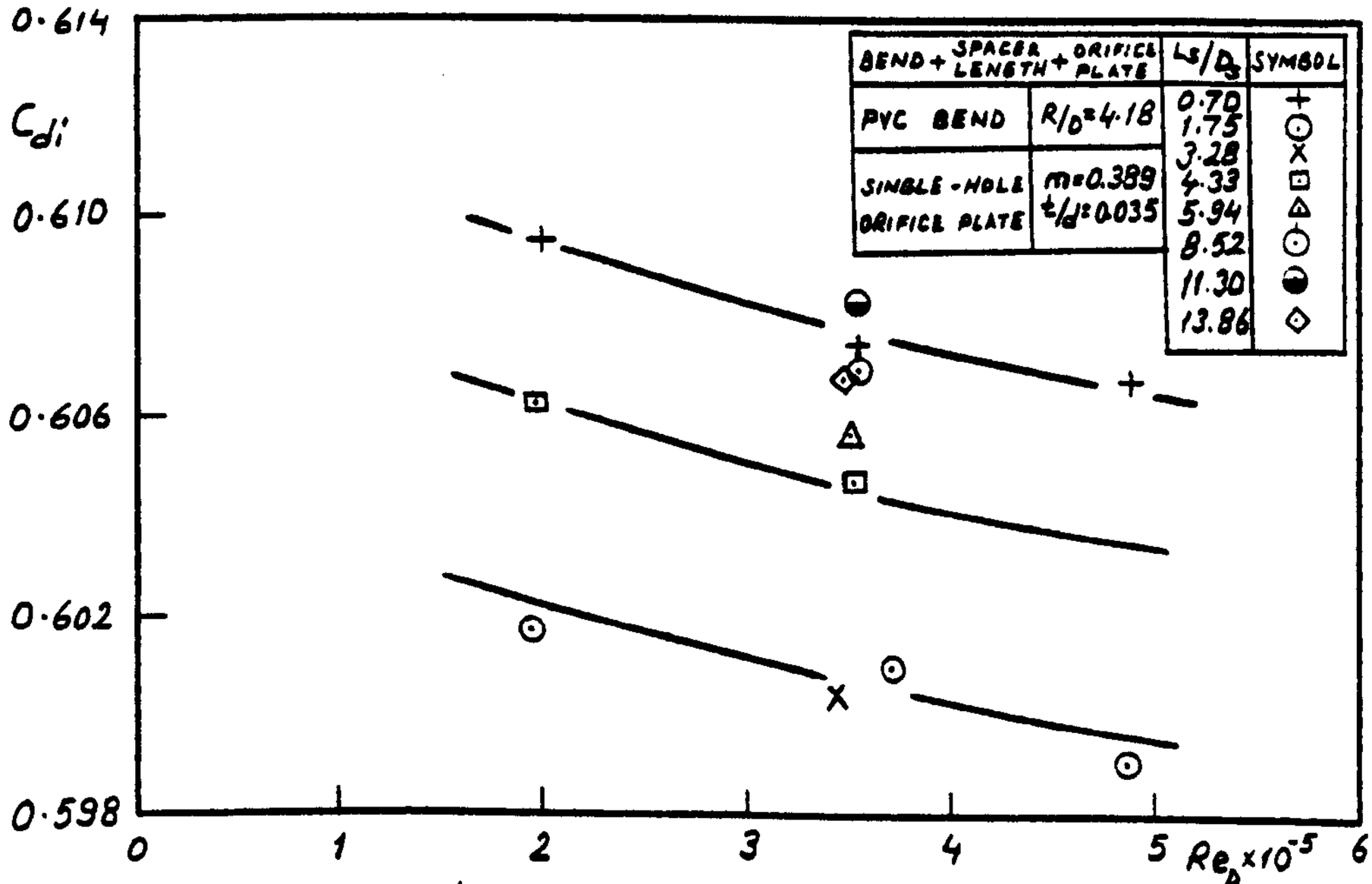

Fig. 120. Discharge coefficient versus Reynolds number for an orifice plate in combination

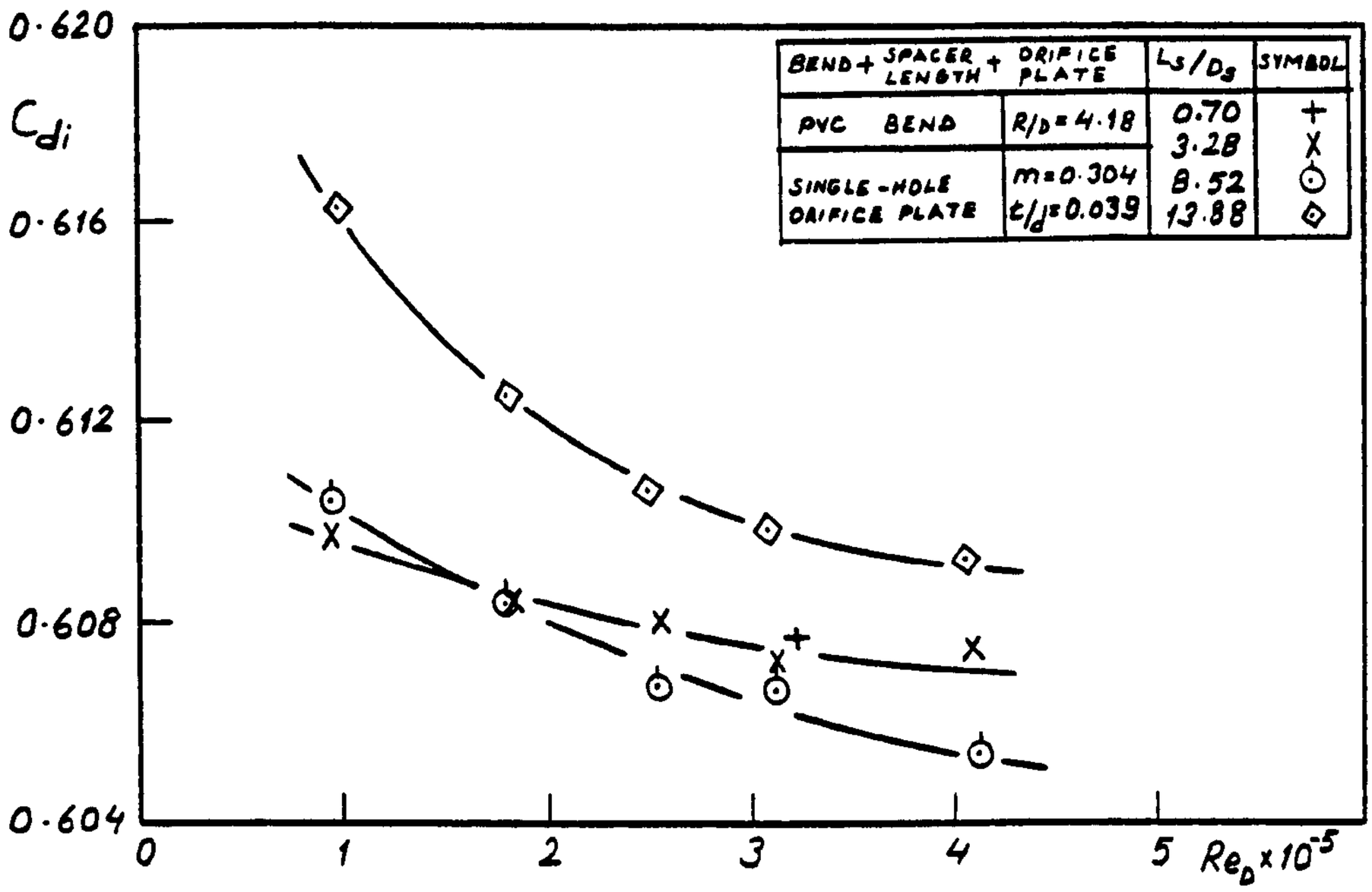

Fig. 121. Discharge coefficient versus Reynolds number for an orifice plate in combination

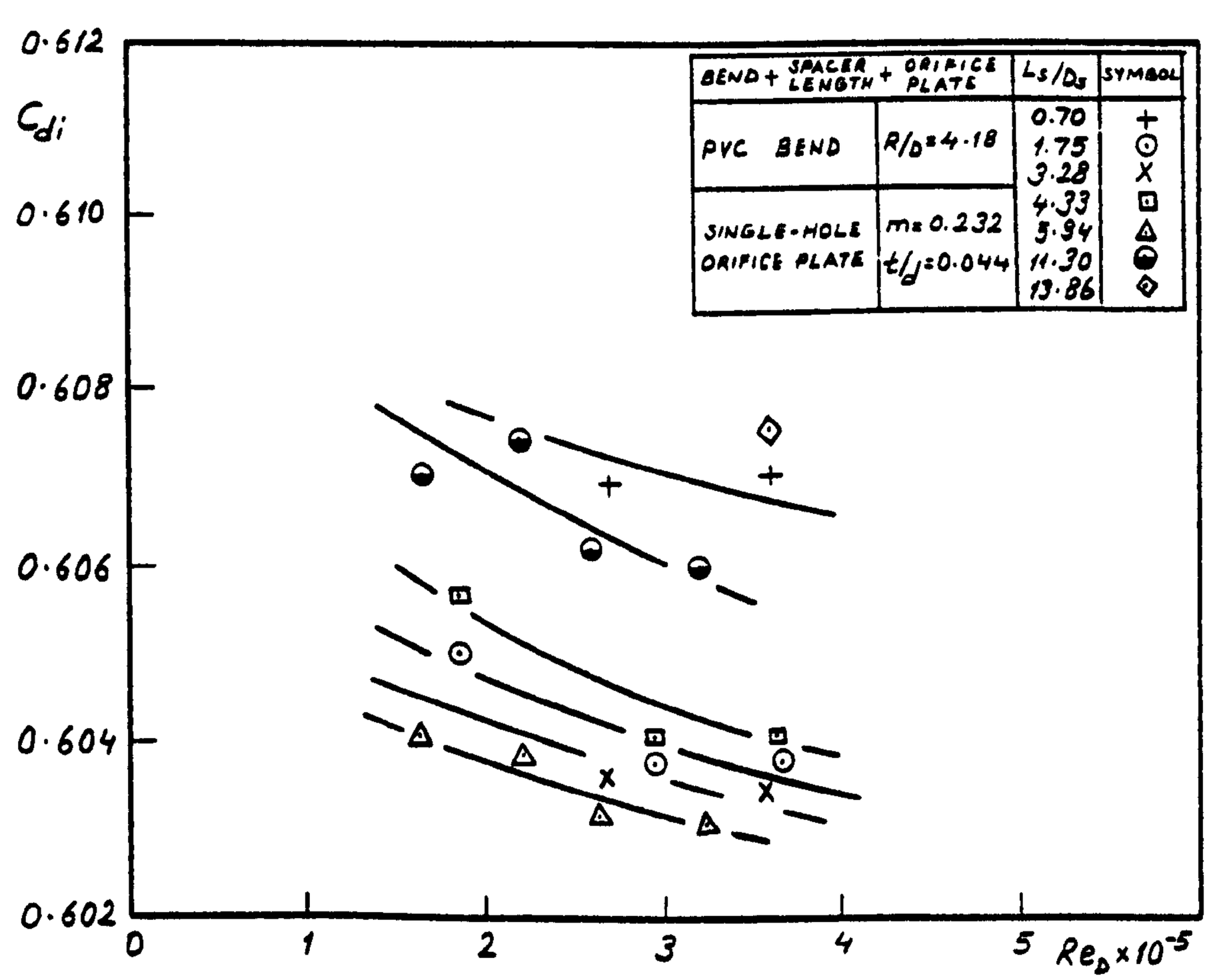

Fig. 122. Discharge coefficient versus Reynolds number for an orifice plate in combination

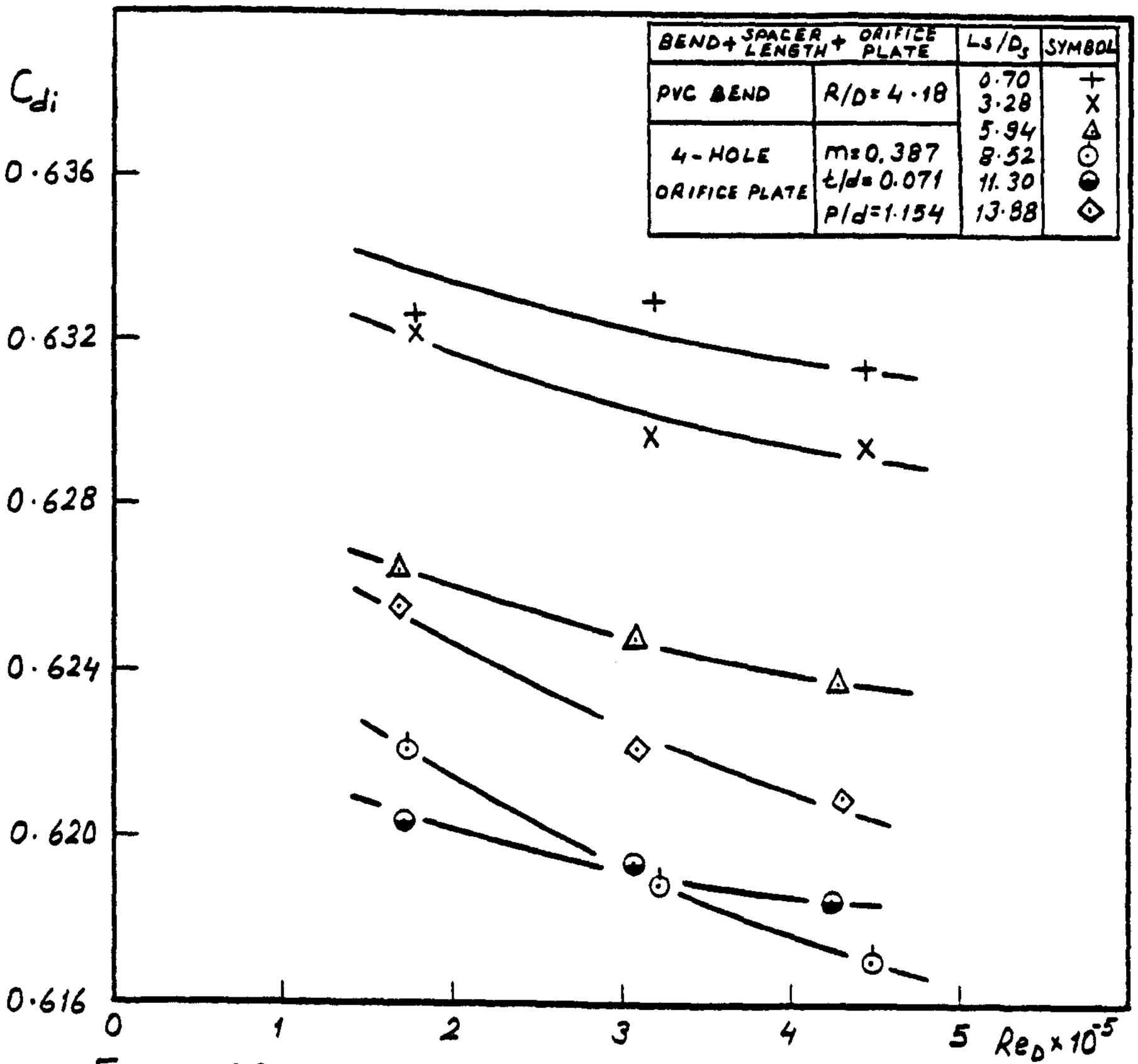

Fig. 123. Discharge coefficient versus Reynolds number for an orifice plate in combination

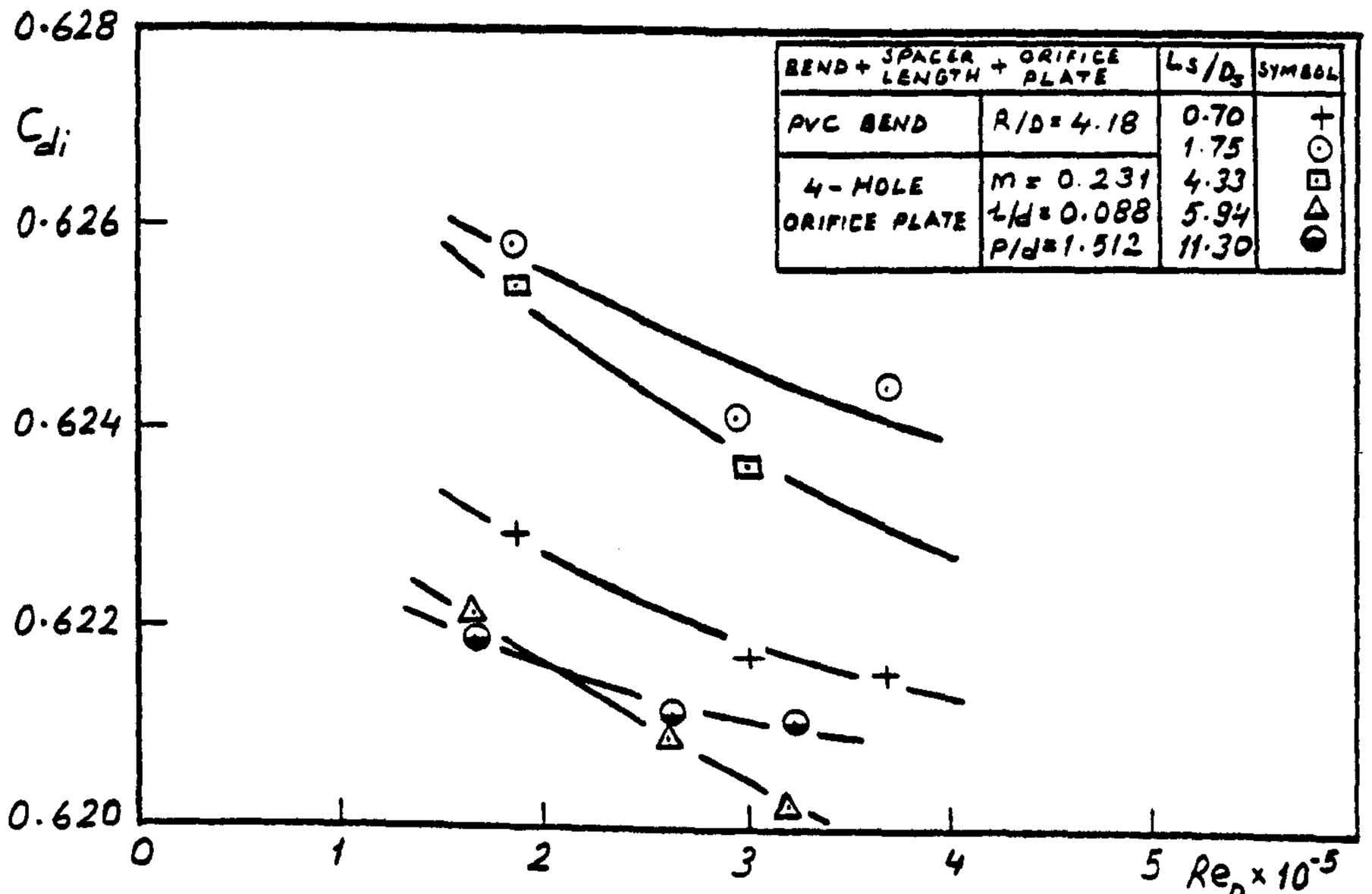

Fig. 124. Discharge coefficient versus Reynolds number for an orifice plate in combination

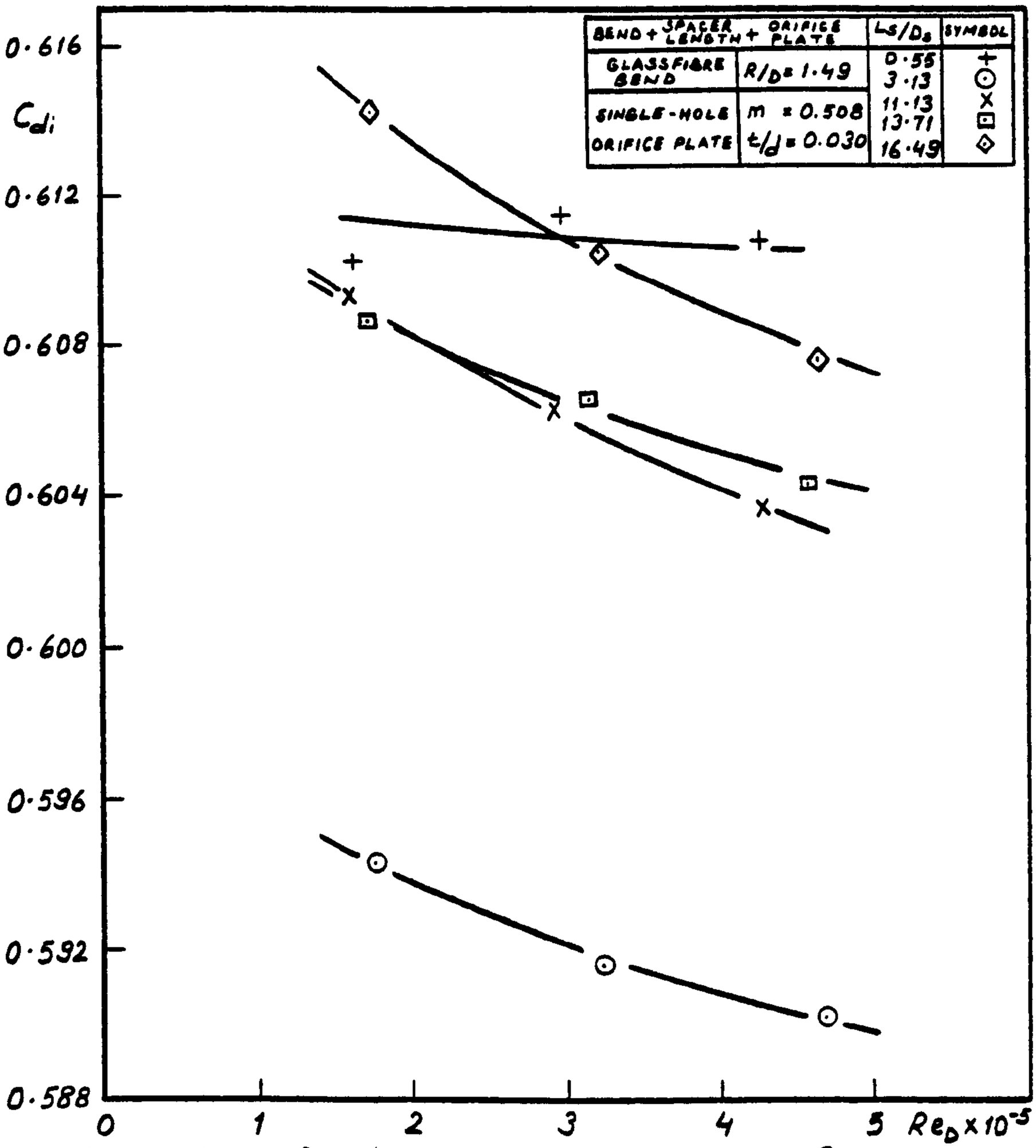

Fig. 125. Discharge coefficient versus Reynolds number for an orifice plate in combination

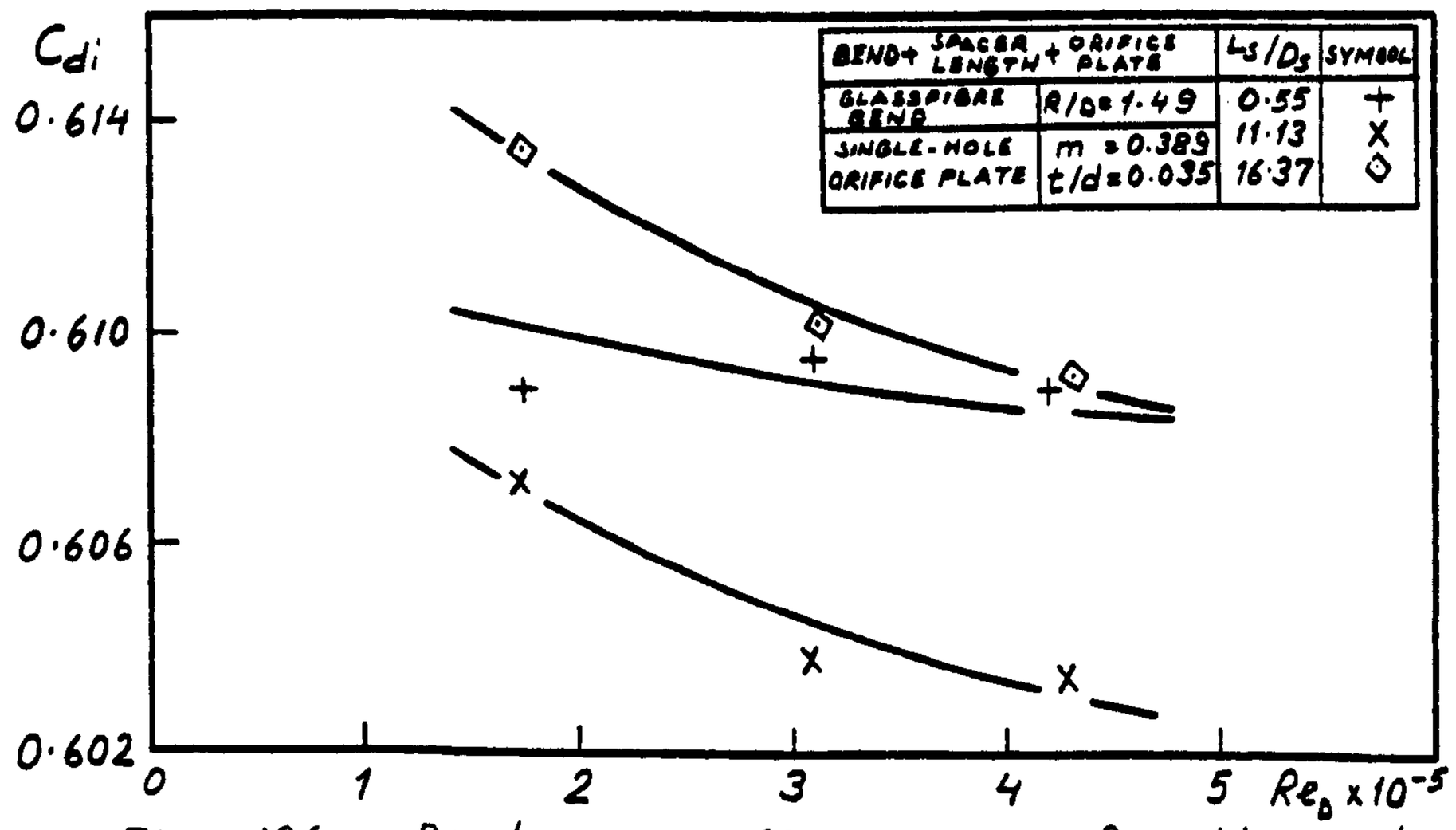

Fig. 126. Discharge coefficient versus Reynolds number for an orifice plate in combination

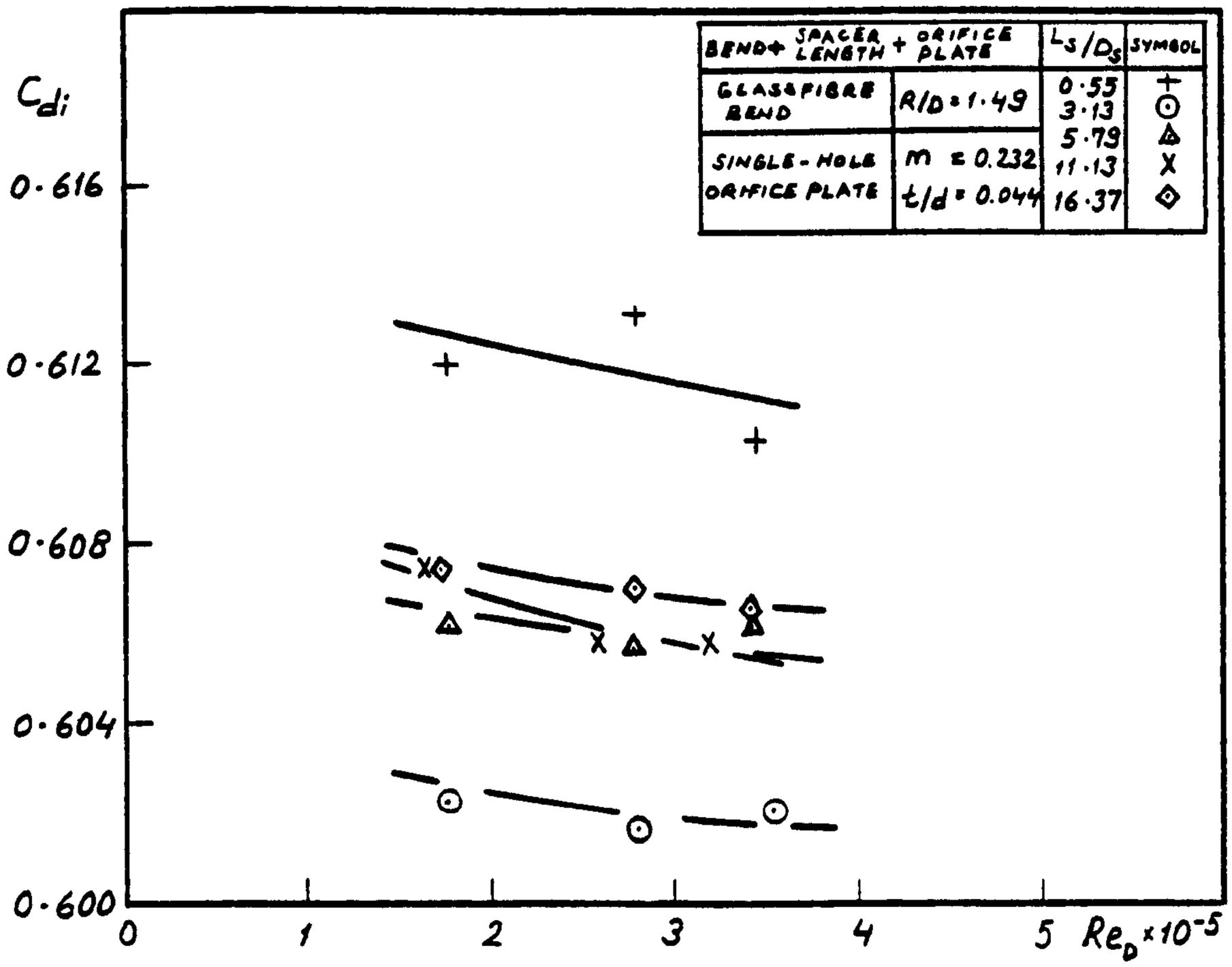

Fig. 127. Discharge coefficient versus Reynolds number for an orifice plate in combination

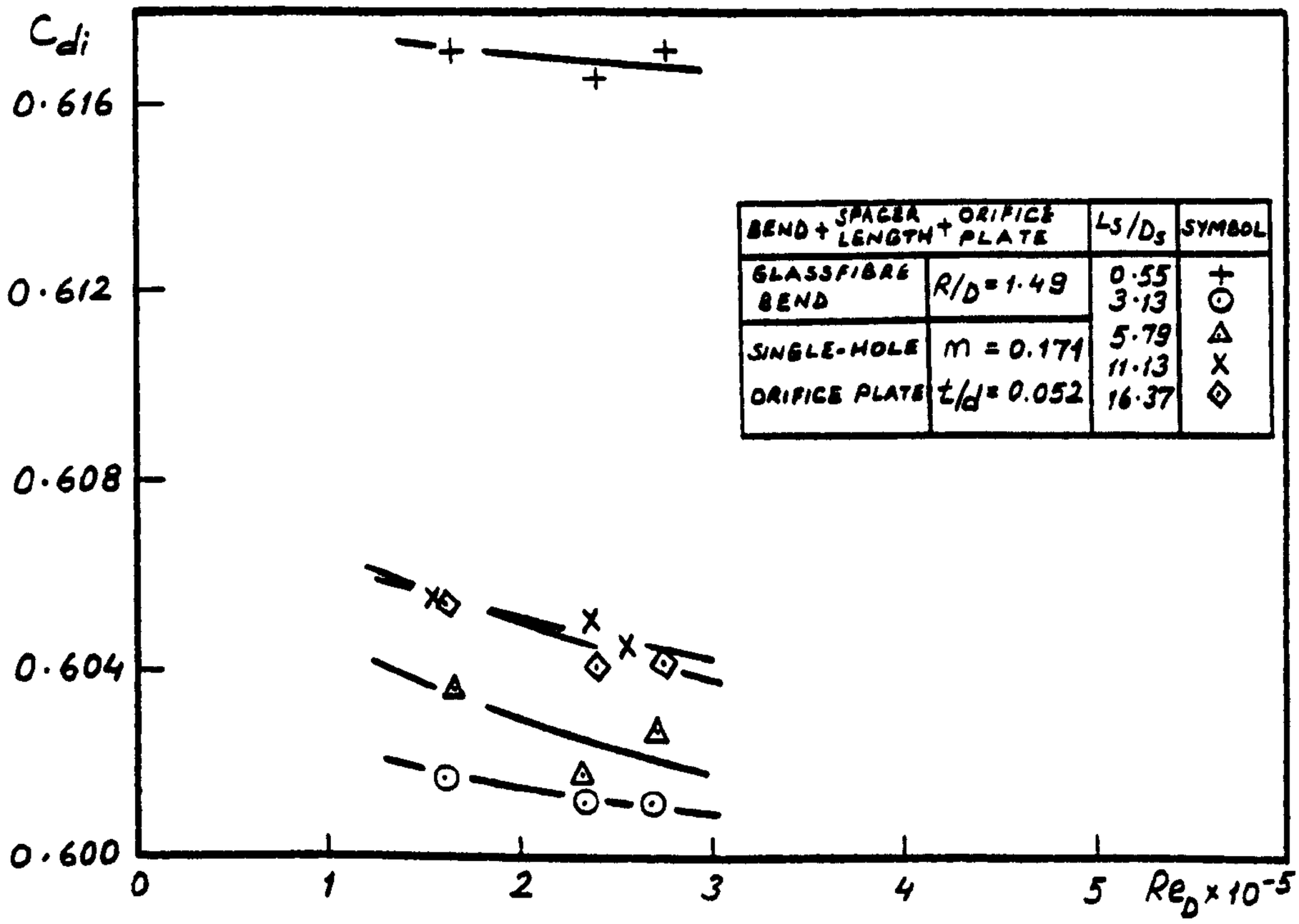

Fig. 128. Discharge coefficient versus Reynolds number for an orifice plate in combination

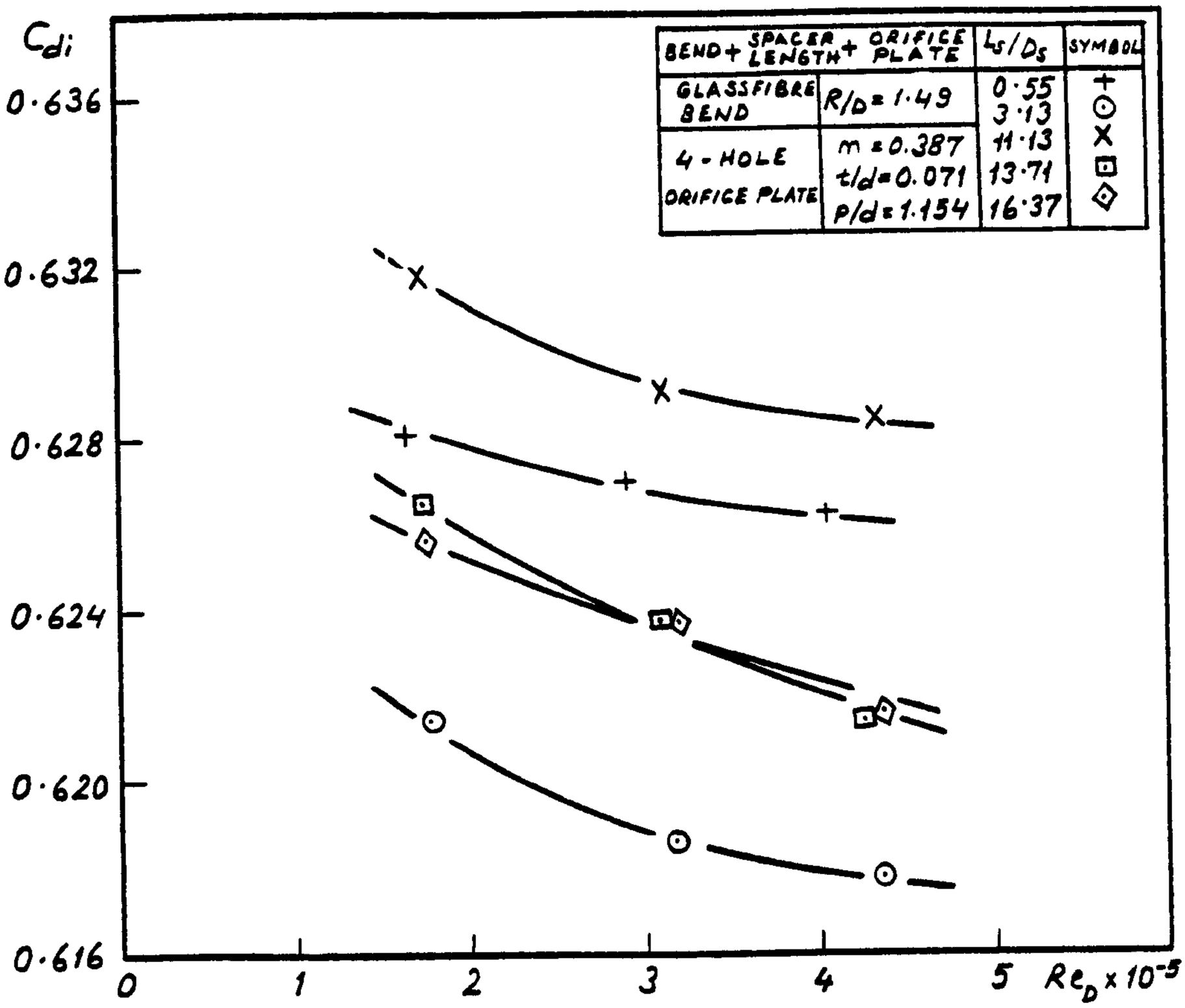

Fig. 129. Discharge coefficient versus Reynolds number for an orifice plate in combination

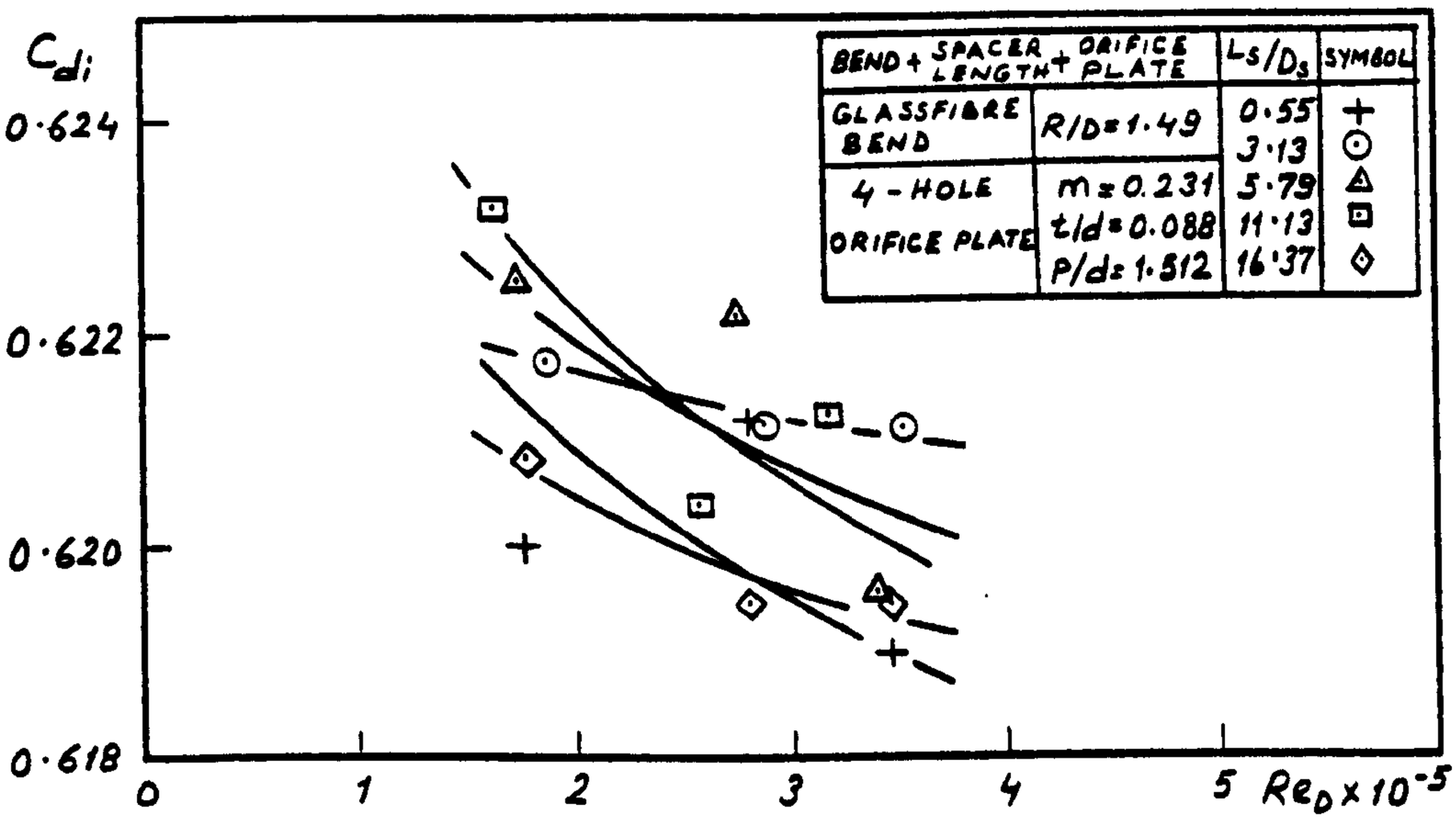

Fig. 130. Discharge coefficient versus Reynolds number for an orifice plate in combination

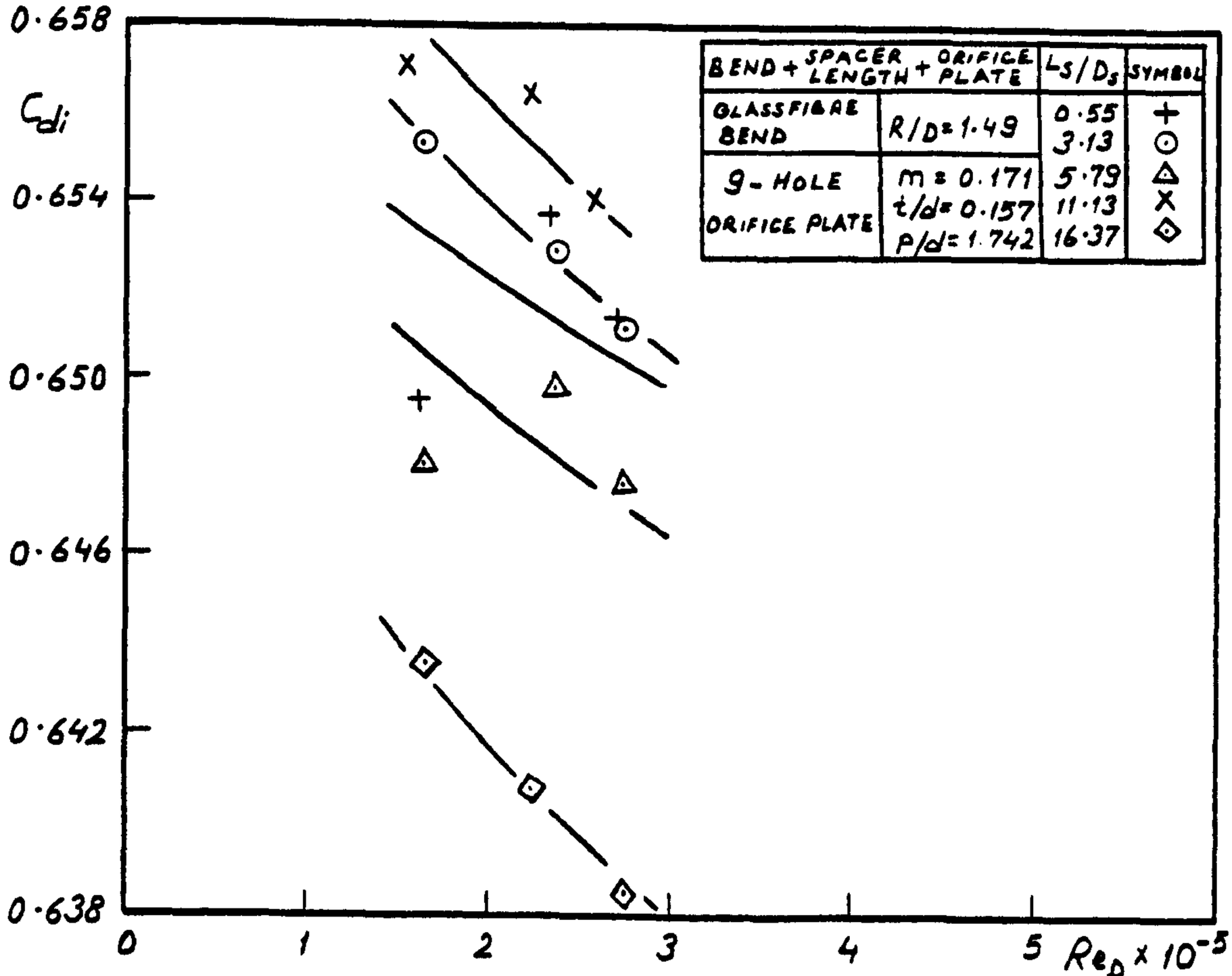

Fig. 131. Discharge coefficient versus Reynolds number for an orifice plate in combination

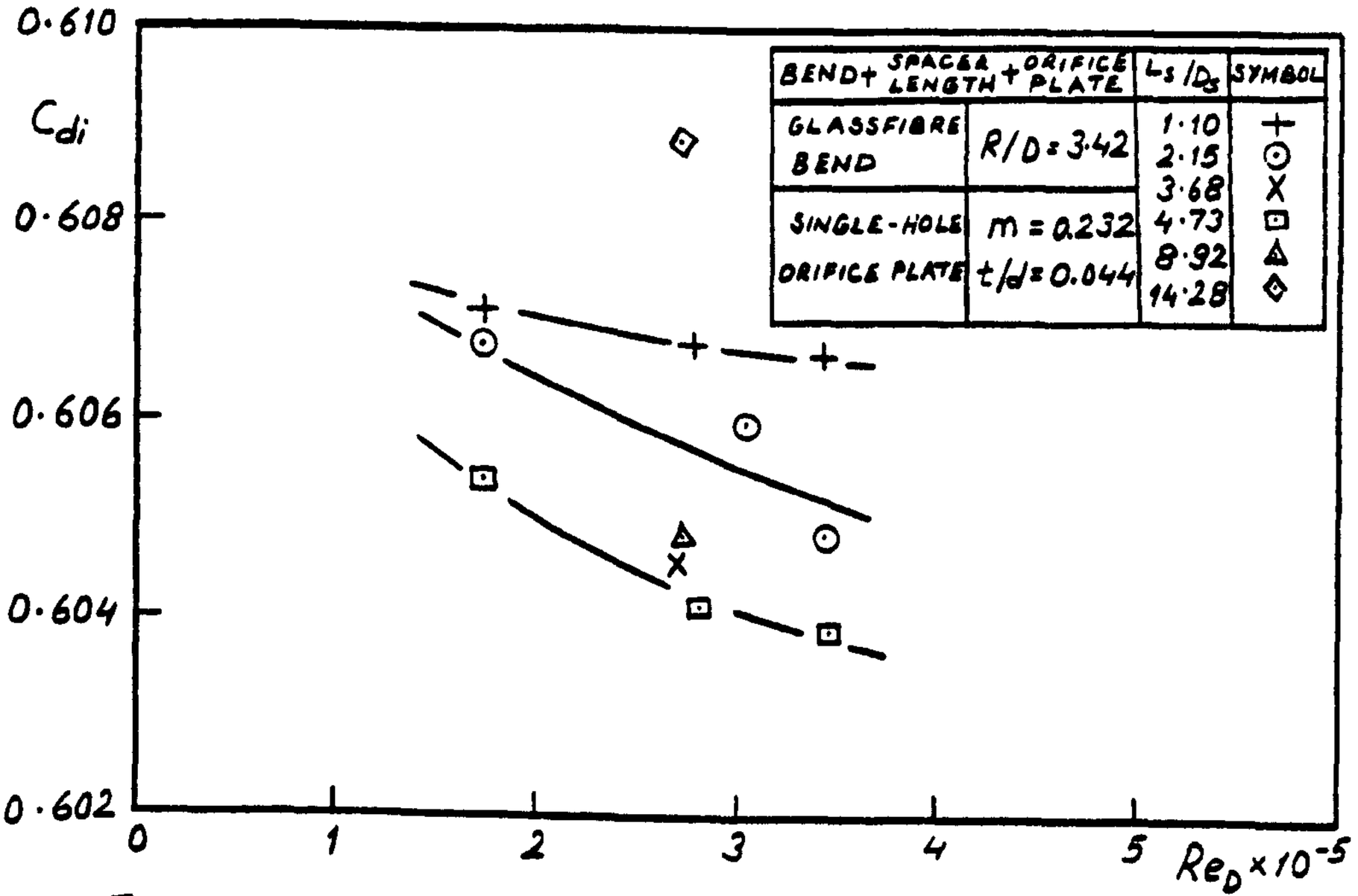

Fig. 132. Discharge coefficient versus Reynolds number for an orifice plate in combination

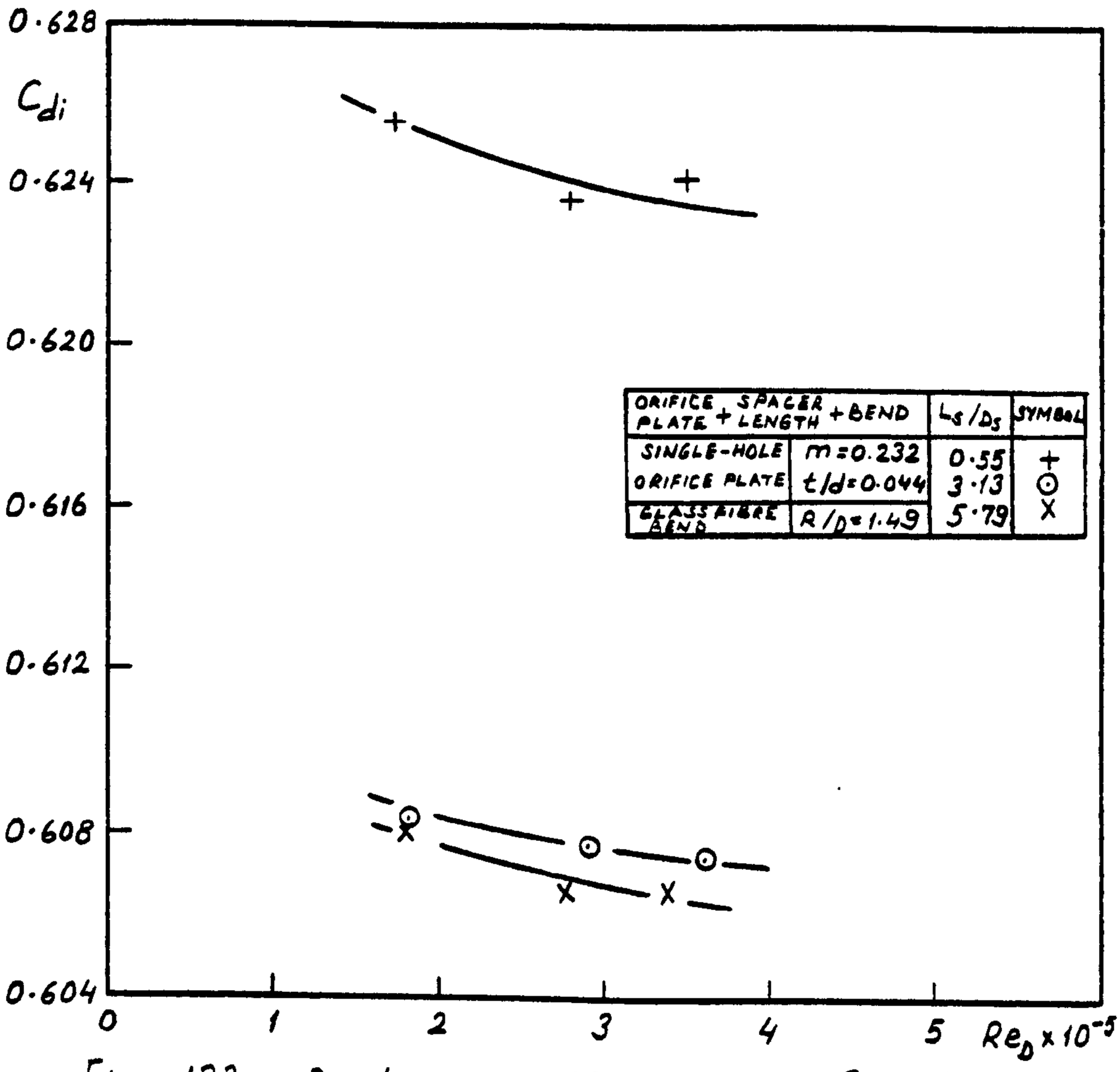

Fig. 133. Discharge coefficient versus Reynolds number for an orifice plate in combination

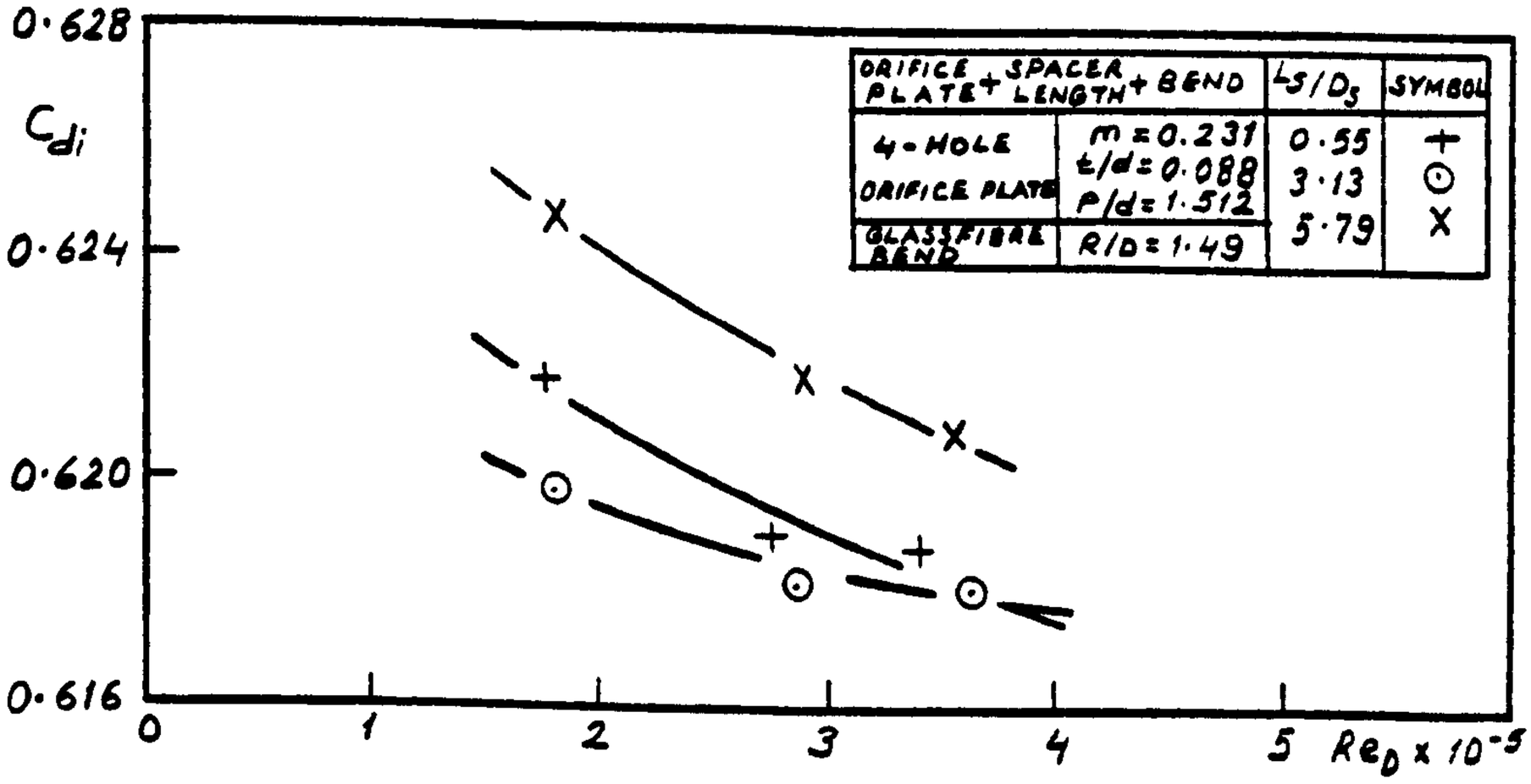

Fig. 134. Discharge coefficient versus Reynolds number for an orifice plate in combination

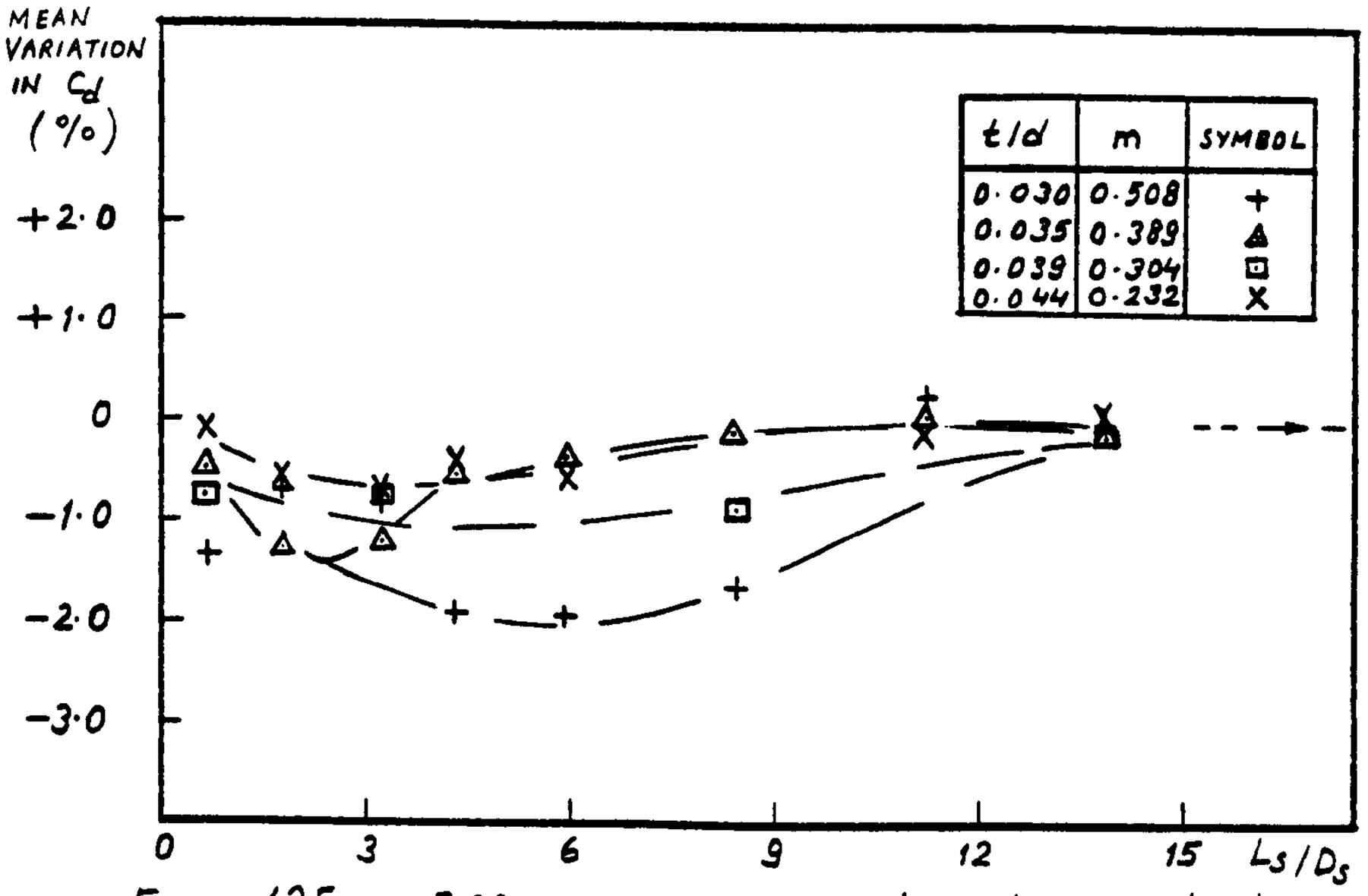

Fig. 135. Effect of spacer length on discharge coefficient (PVC bend of R/D = 4·18 upstream of various single-hole orifice plates)

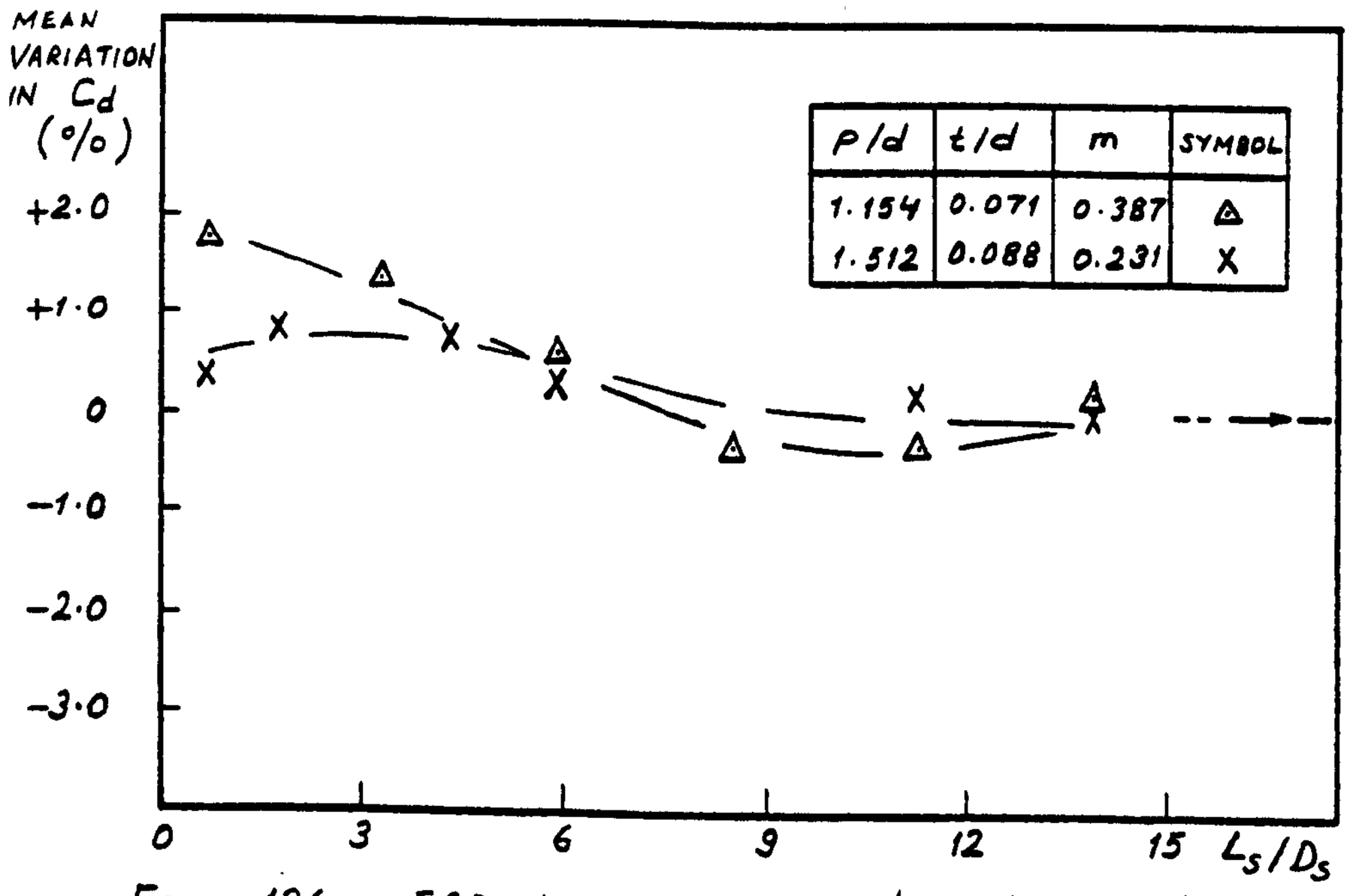

Fig. 136. Effect of spacer length on discharge coefficient (PVC bend of R/D = 4·18 upstream of various multi-hole orifice plates)

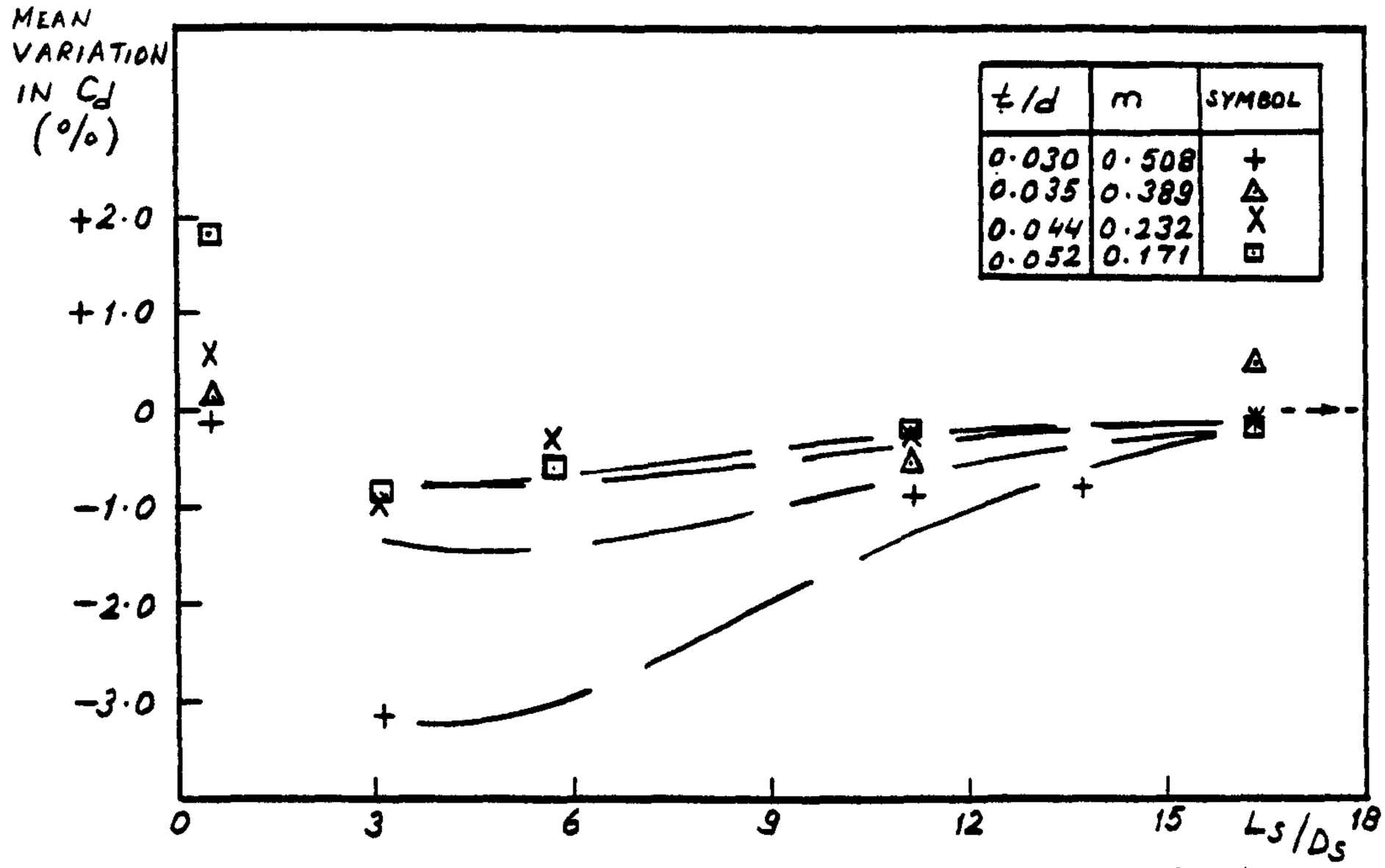

Fig. 137. Effect of spacer length on discharge coefficient (glassfibre bend of R/D=1.49 upstream of various single-hole orifice plates)

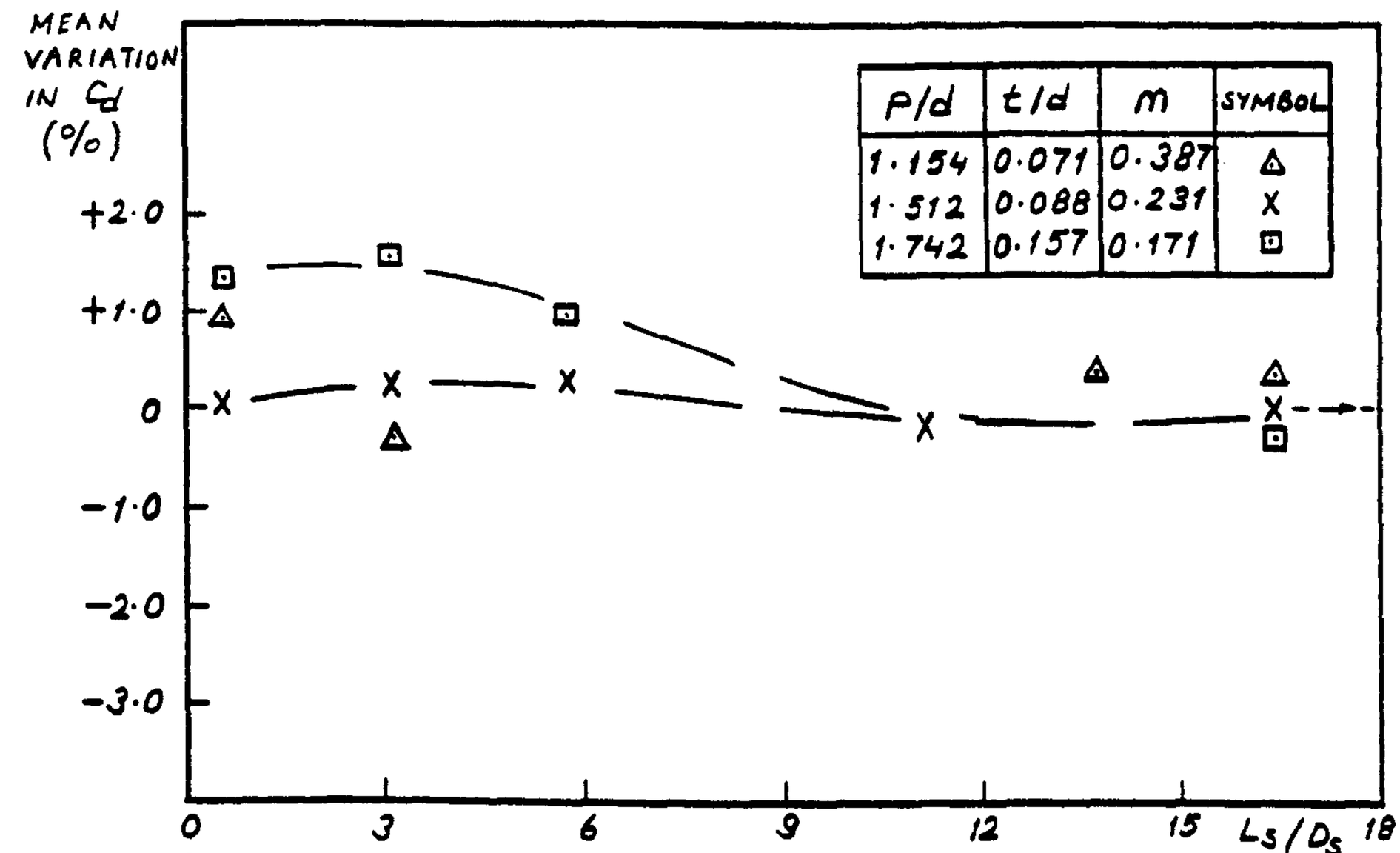

Fig. 138. Effect of spacer length on discharge coefficient (glassfibre bend of R/D=1.49 upstream of various multi-hole orifice plates)

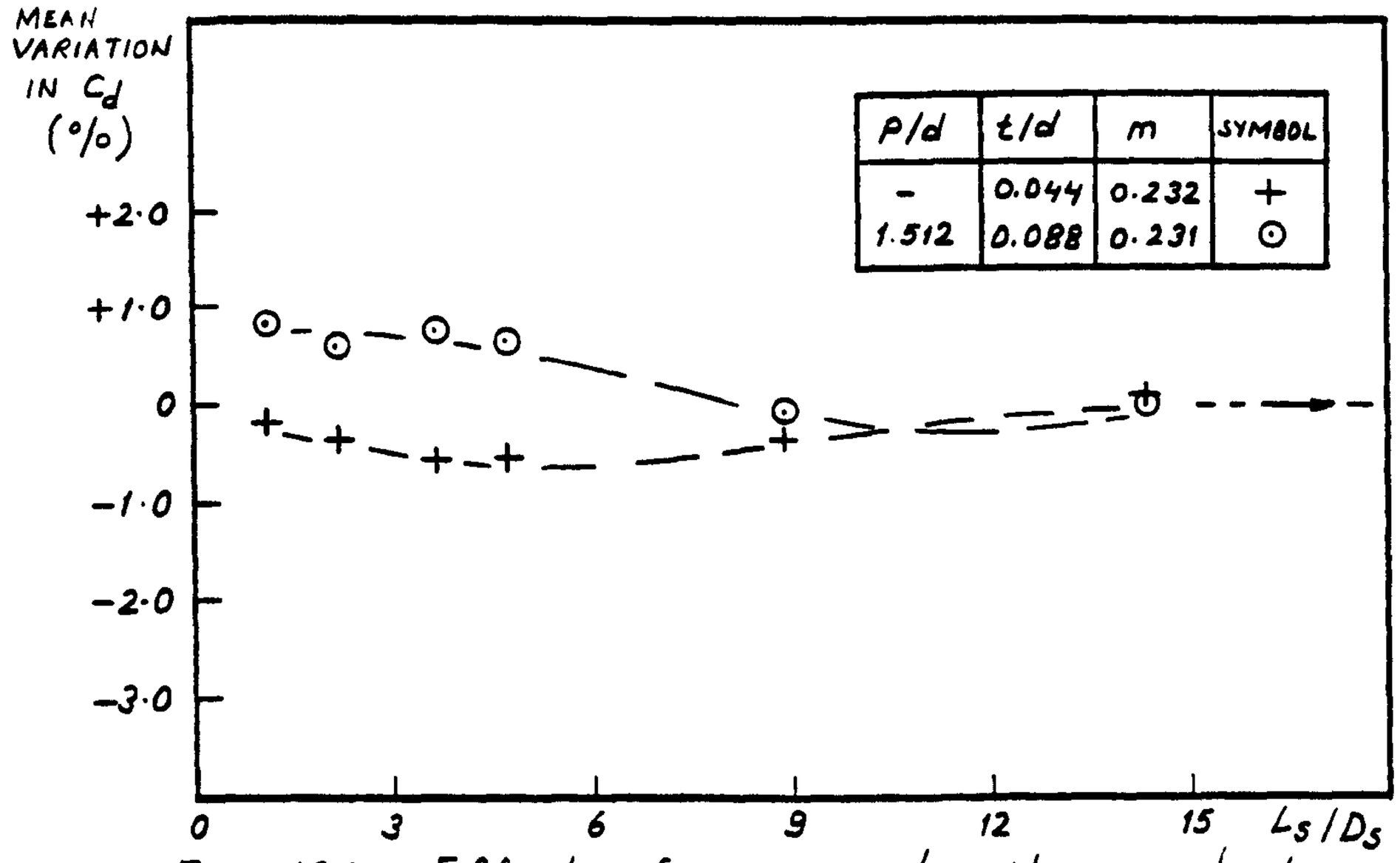

Fig. 139. Effect of spacer length on discharge coefficient (glassfibre bend of $R/D = 3.42$ upstream of various orifice plates)

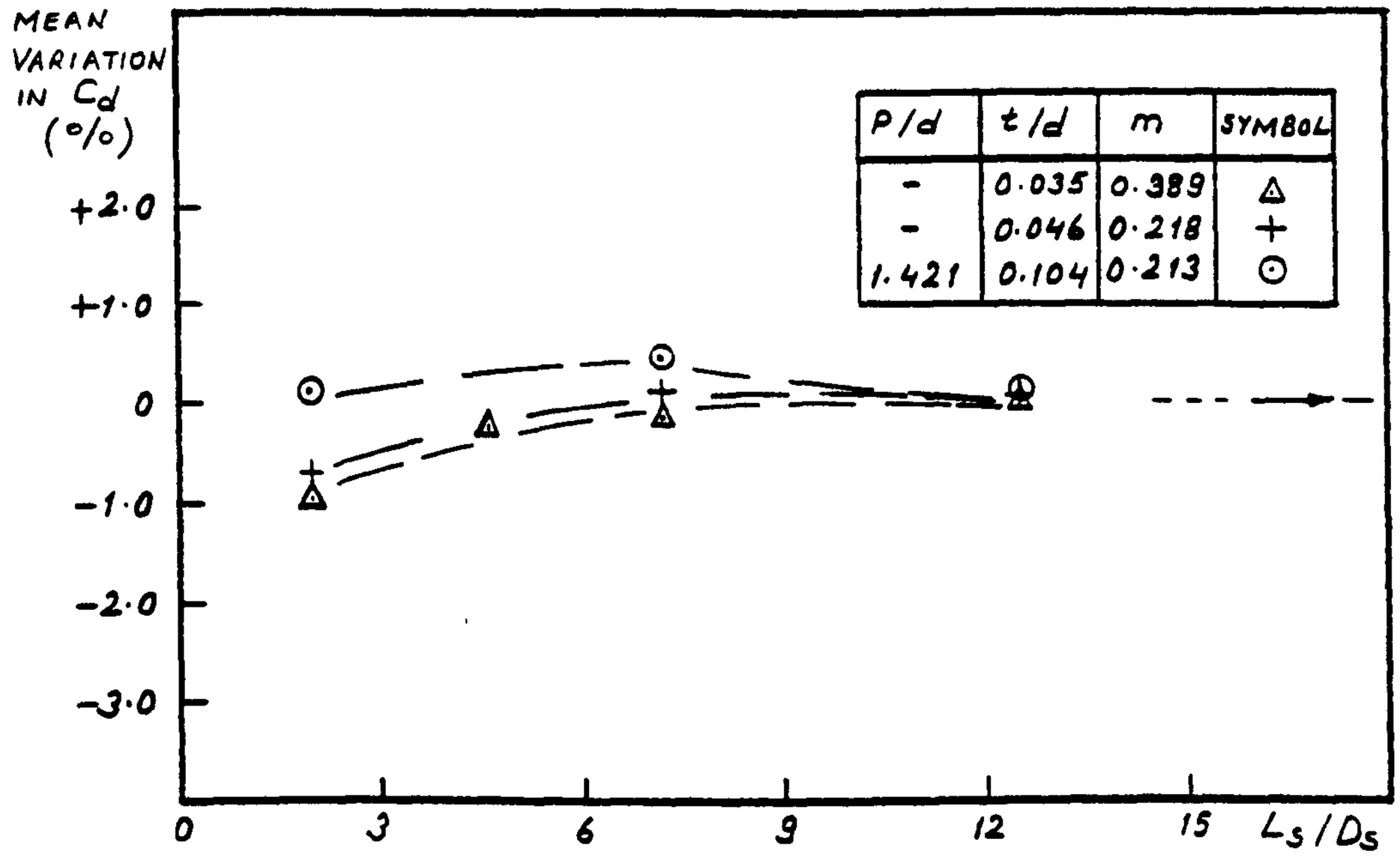

Fig. 140. Effect of spacer length on discharge coefficient (glassfibre bend of $R/D = 4.89$ upstream of various orifice plates)

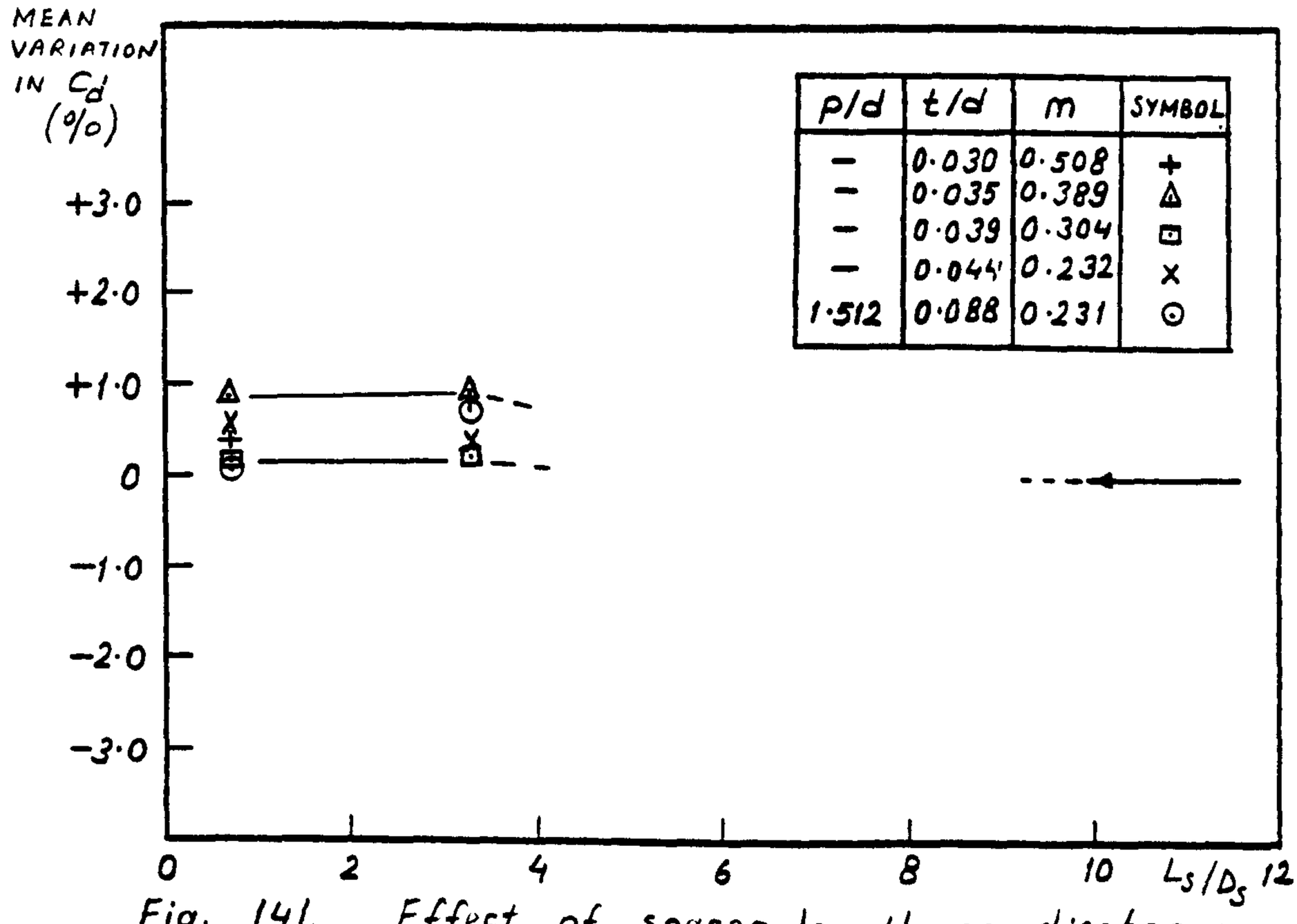

Fig. 141. Effect of spacer length on discharge coefficient (PVC bend of R/D = 4.18 downstream of various orifice plates)

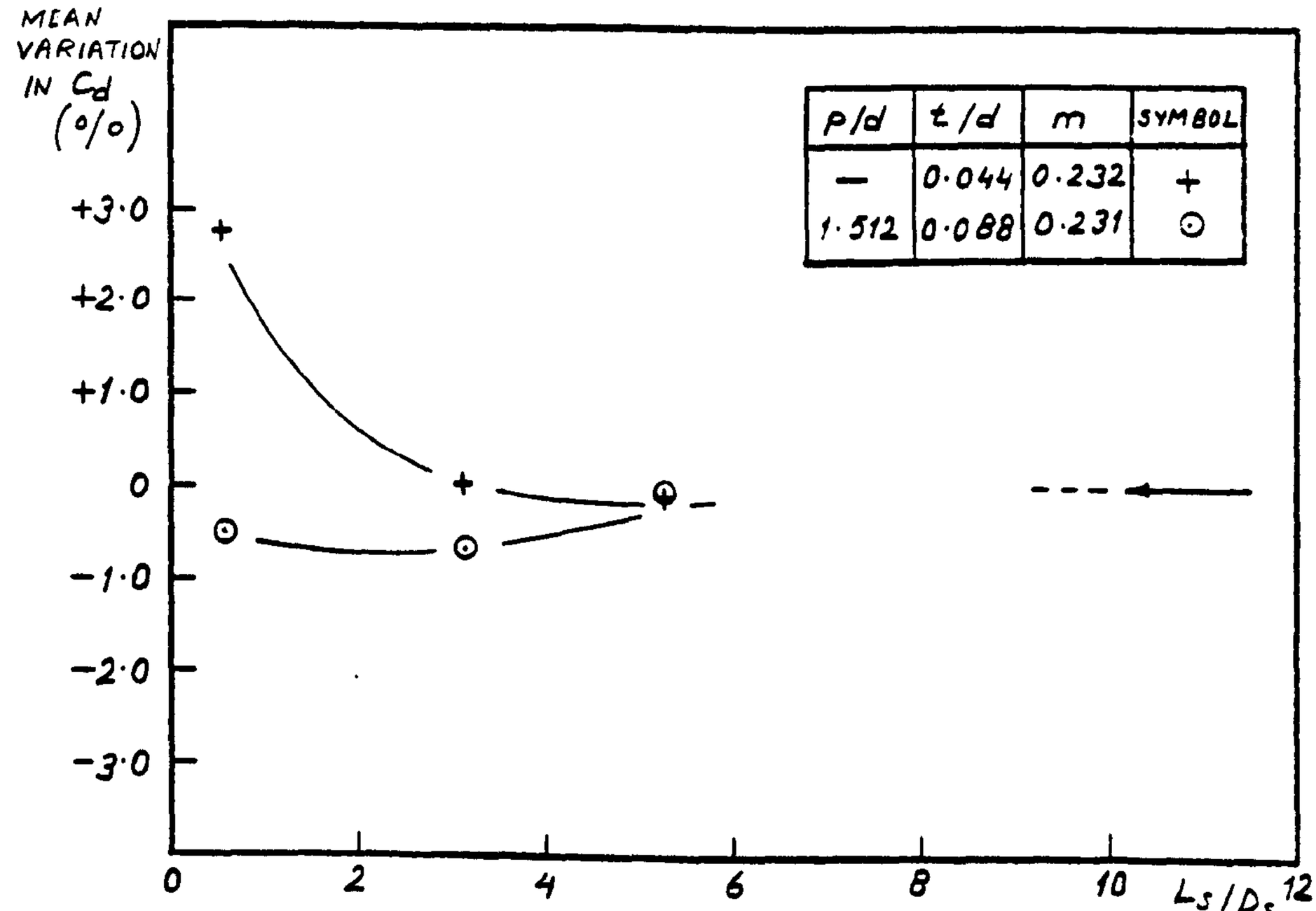

Fig. 142. Effect of spacer length on discharge coefficient (glassfibre bend of R/D = 1.49 downstream of various orifice plates)

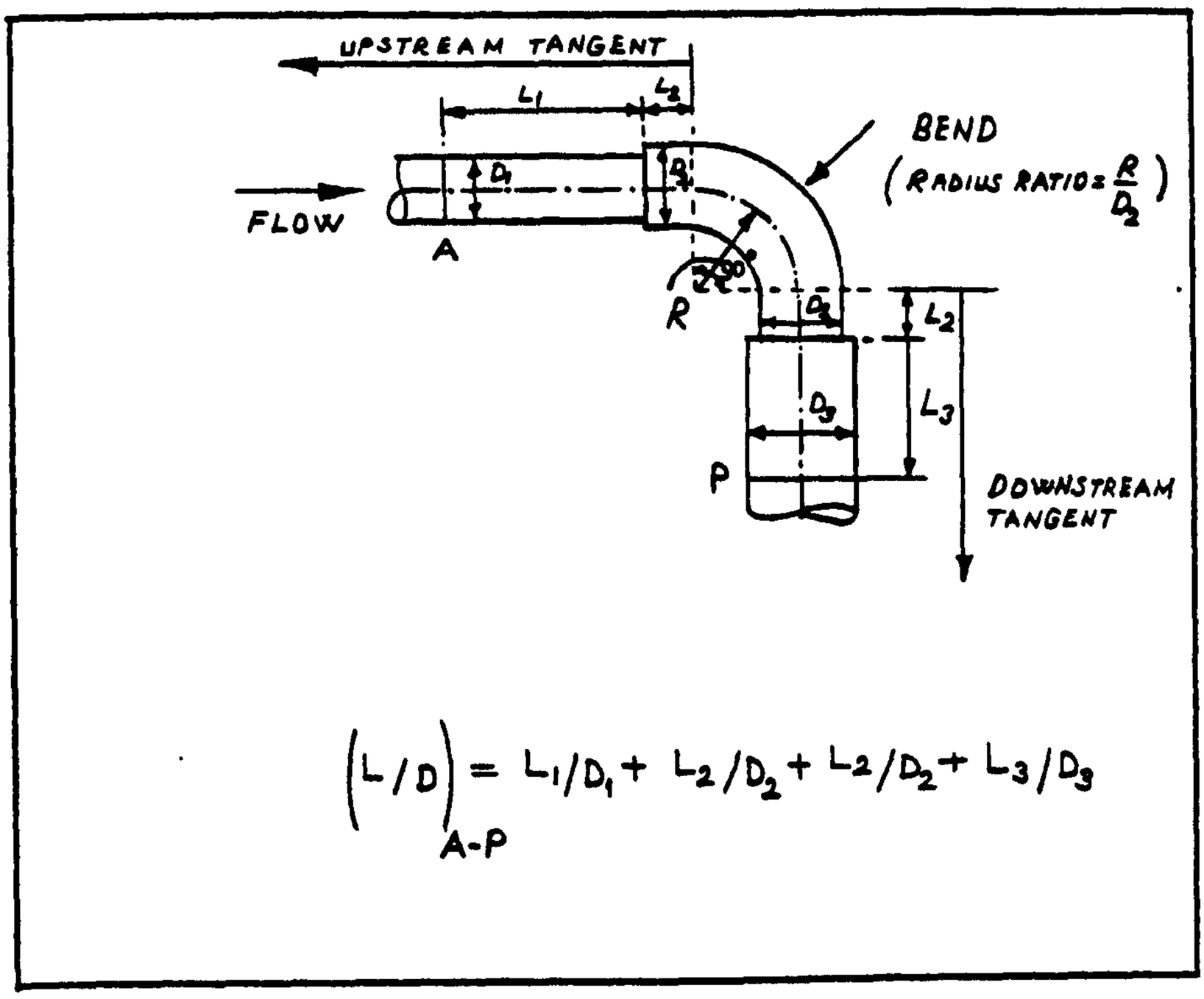

(a)

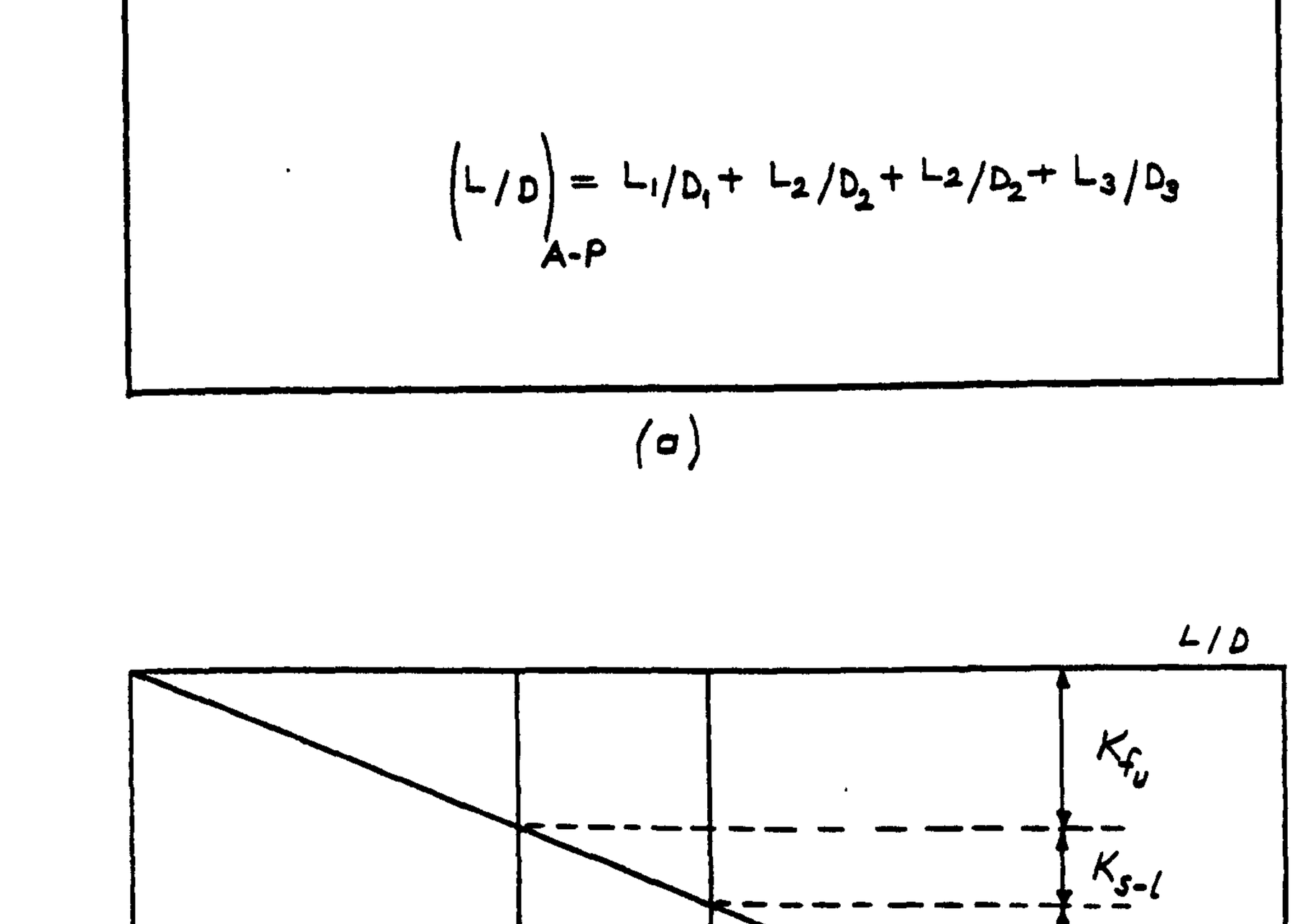

(b)

Fig. 143a. Reckoning of axial length
143b. Plotting of system head loss coefficient

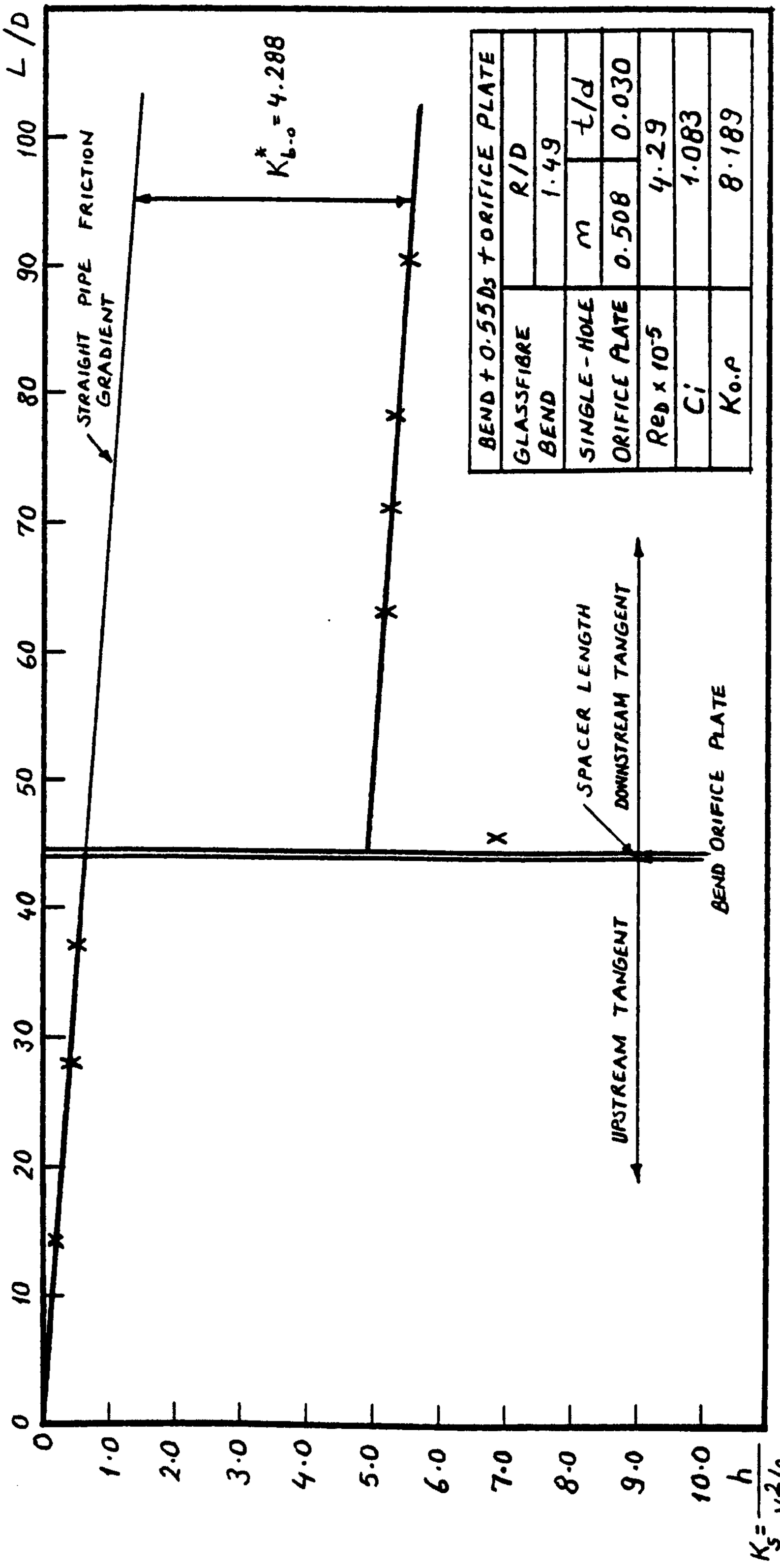

Fig. 144. Variation of system head loss coefficient with axial length

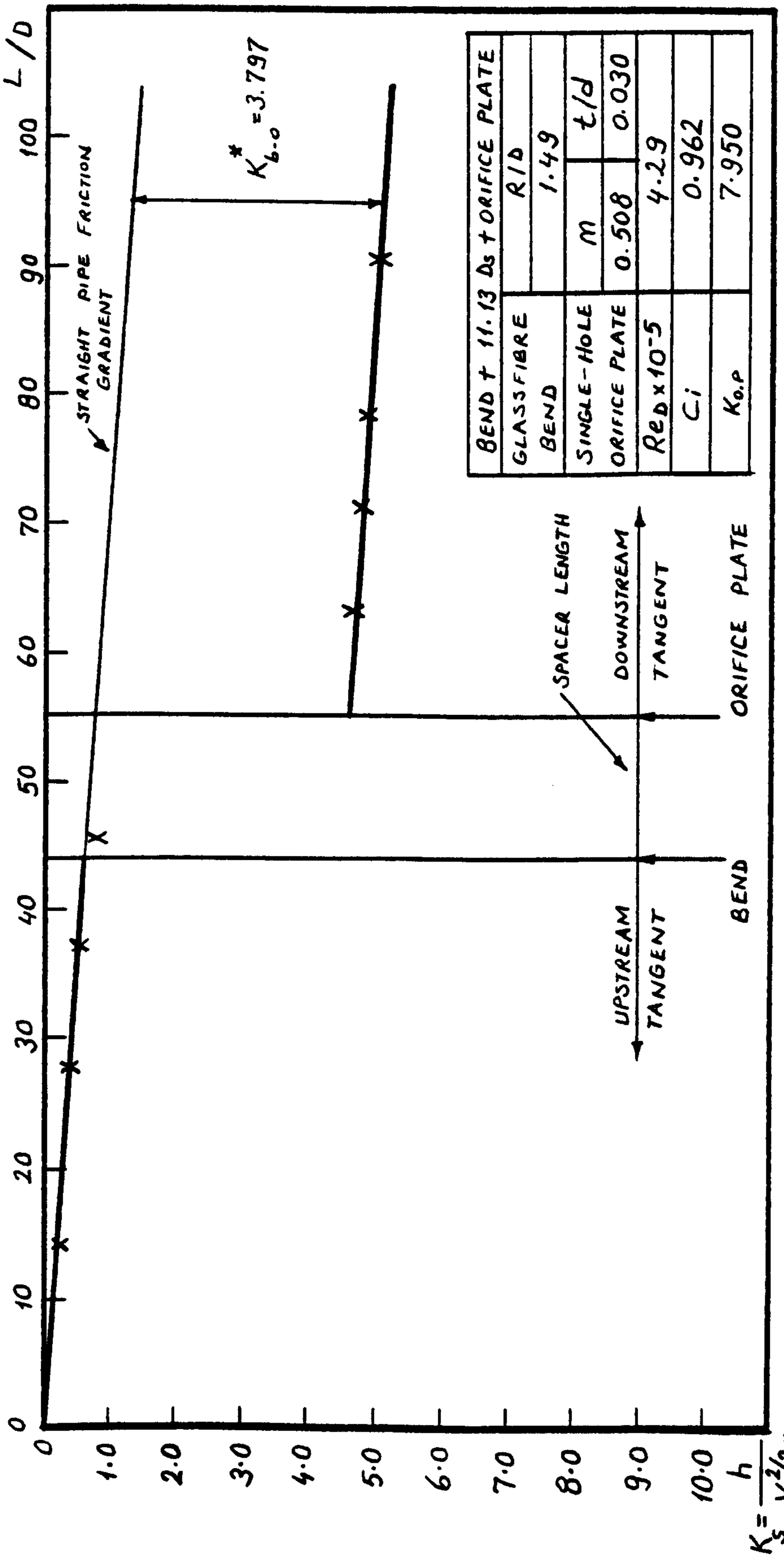

Variation of system head loss coefficient with axial length

Fig. 145.

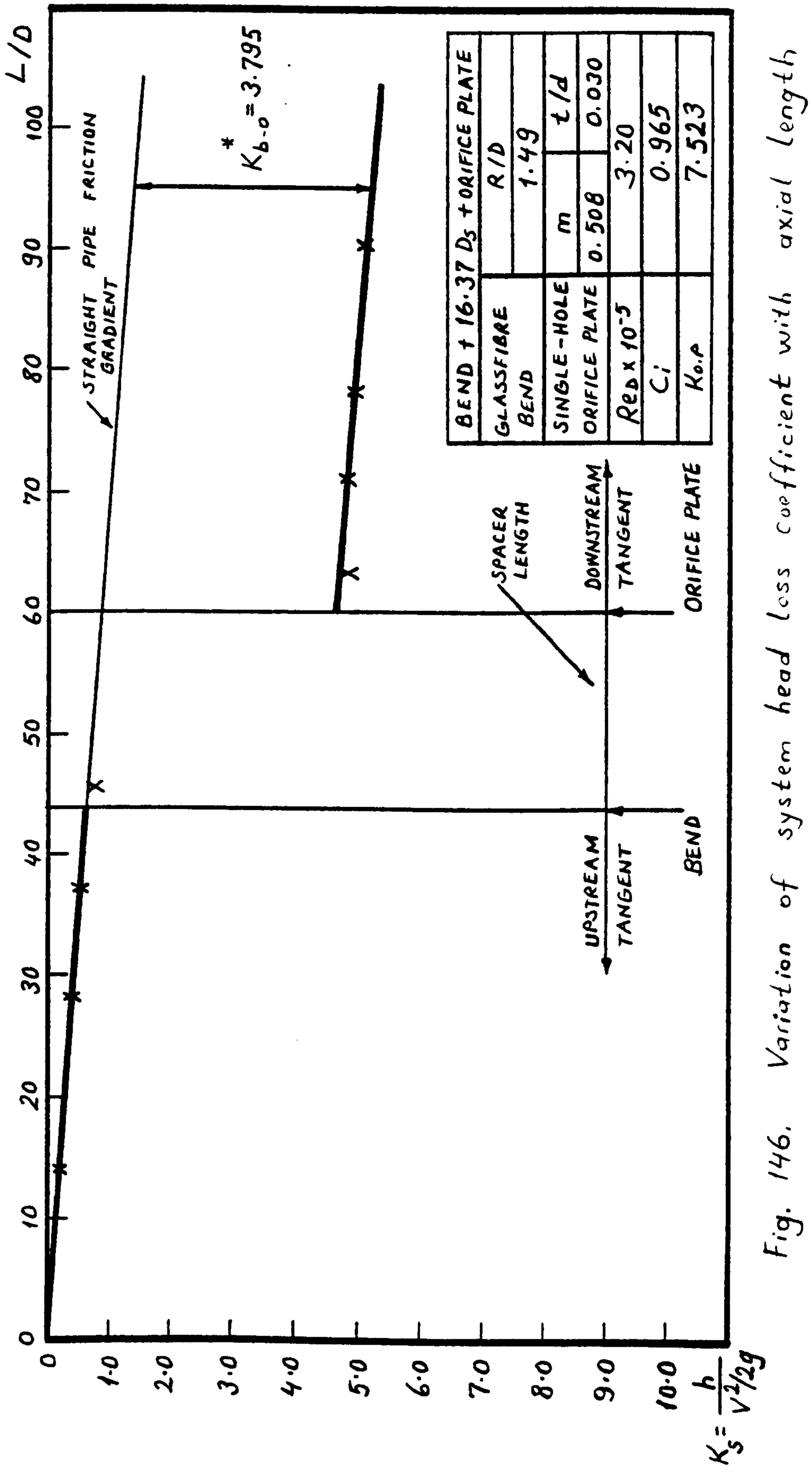

Fig. 1146. Variation of system head loss coefficient with axial length

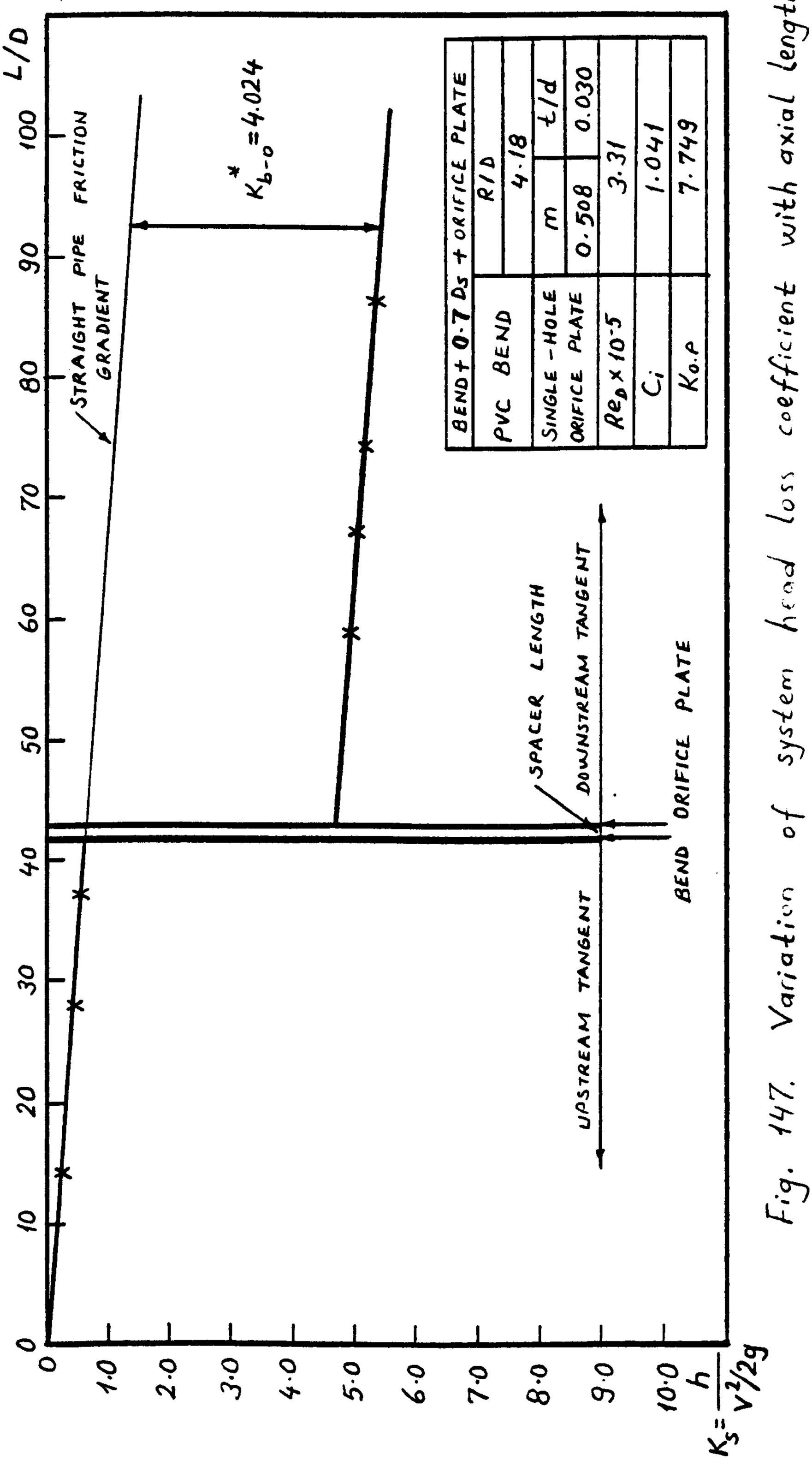

Fig. 147. Variation of system head loss coefficient with axial length

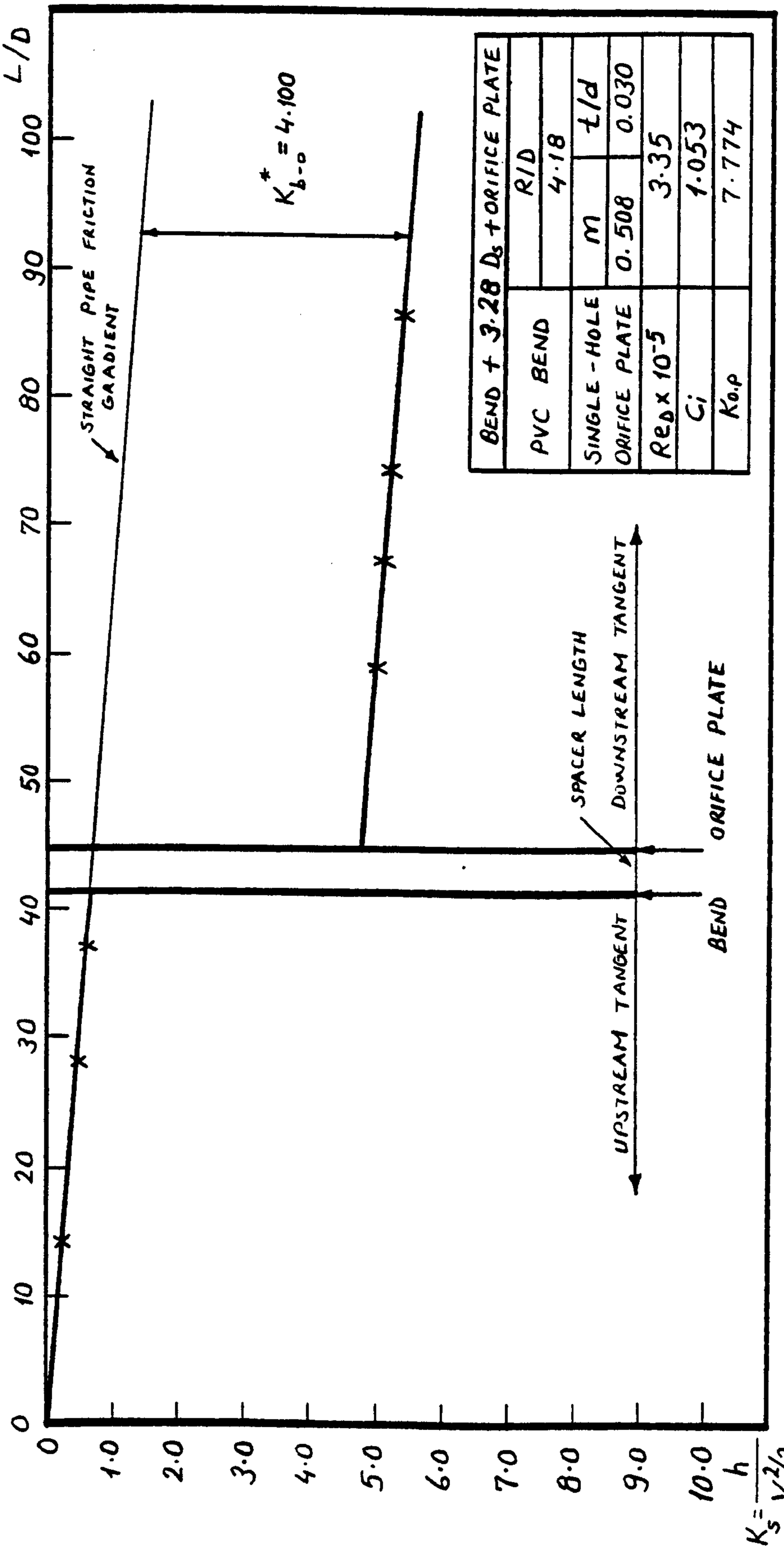

Fig. 148. Variation of system head loss coefficient with axial length

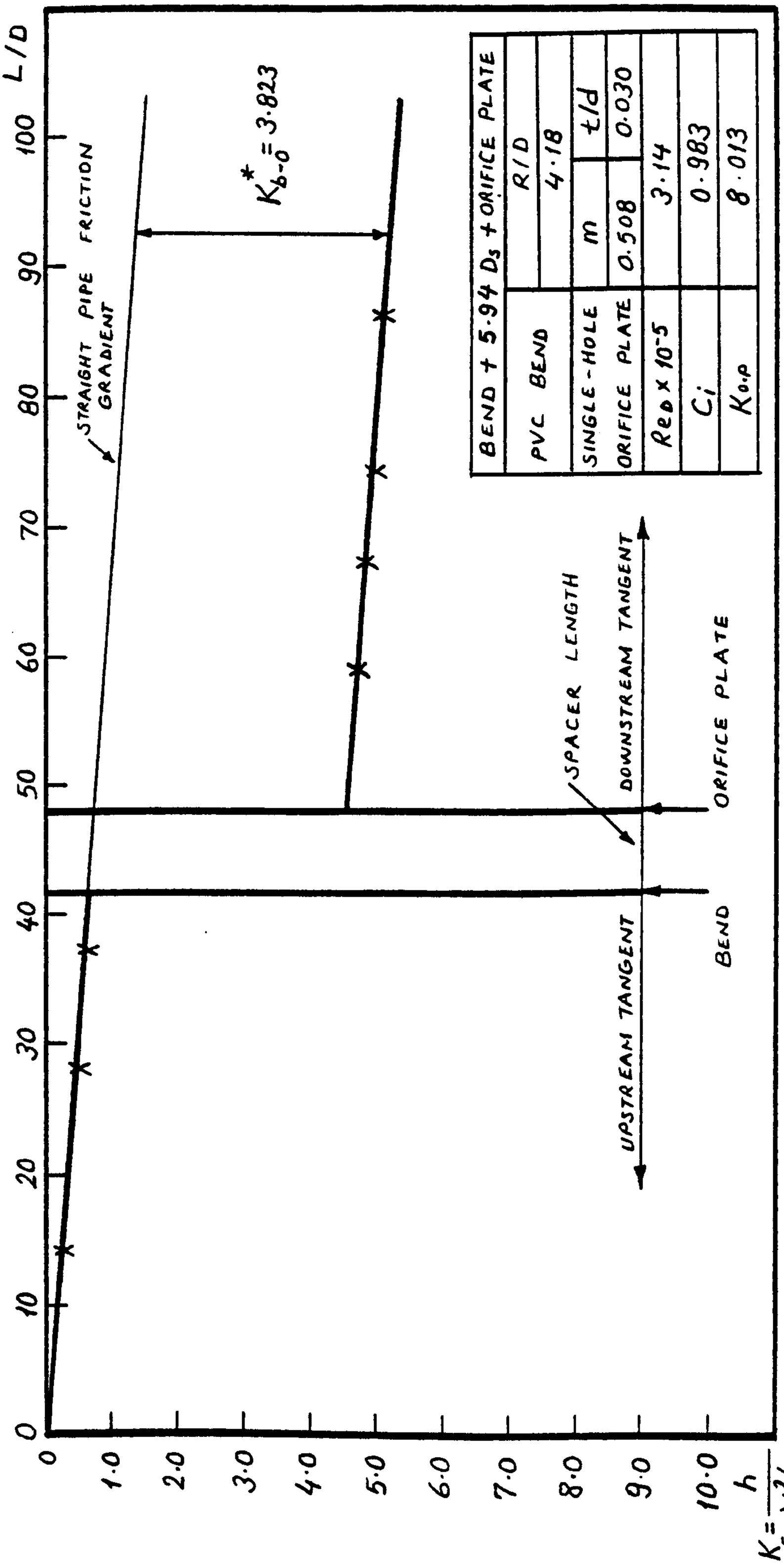

Fig. 149. Variation of system head loss coefficient with

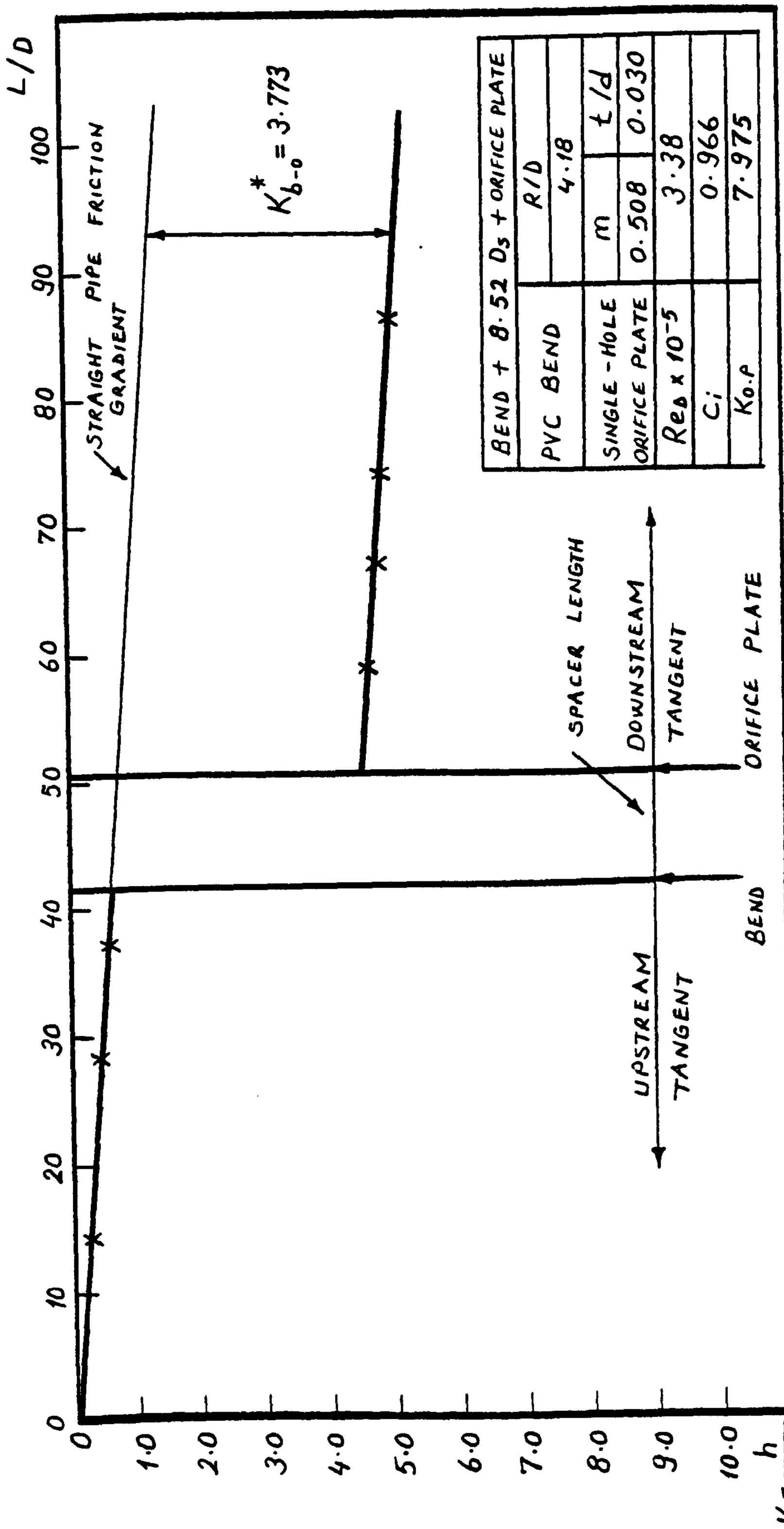

Fig. 150. Variation of system head Loss coefficient with axial length

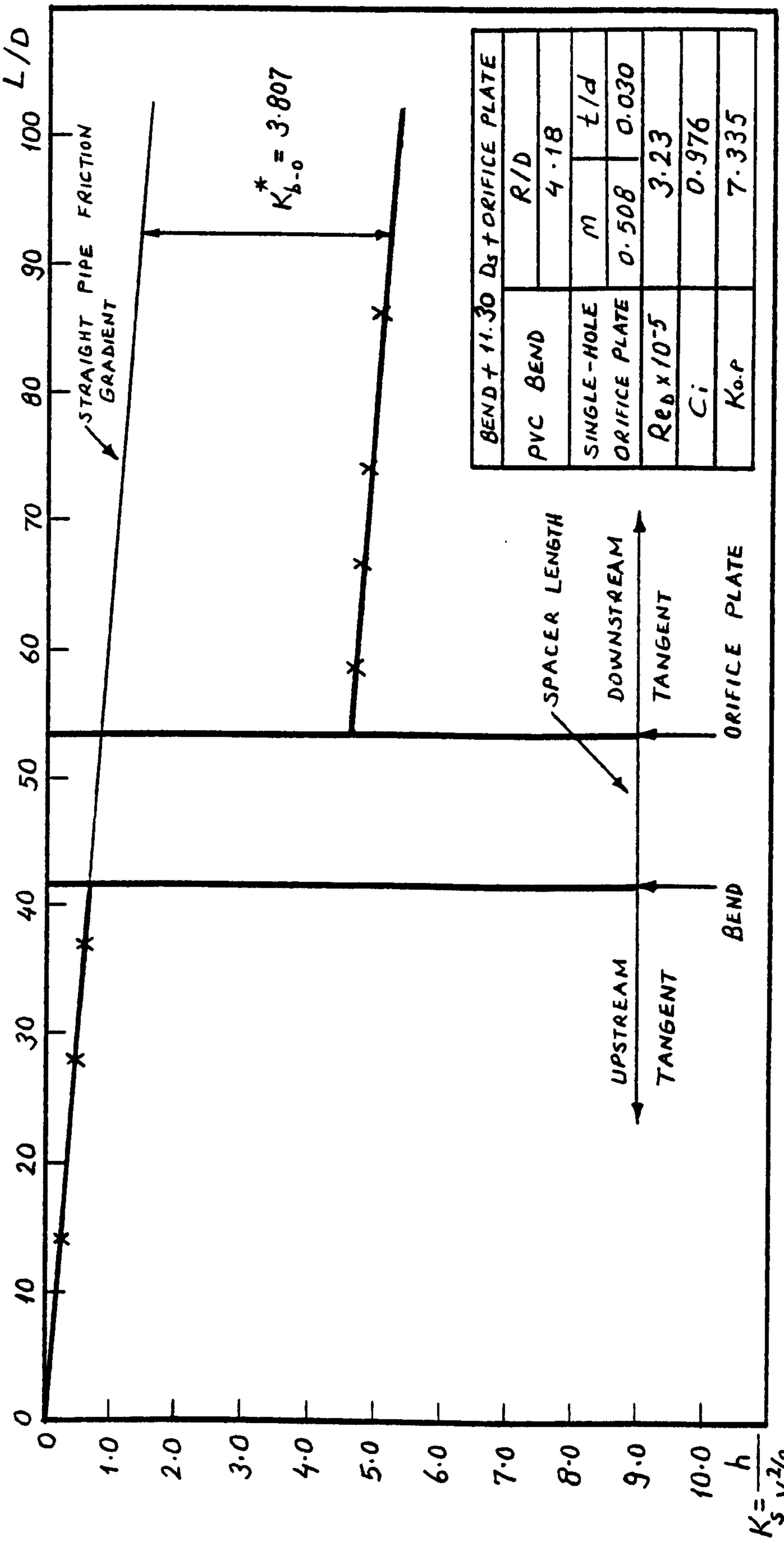

Fig. 151. Variation of system head loss coefficient with axial length

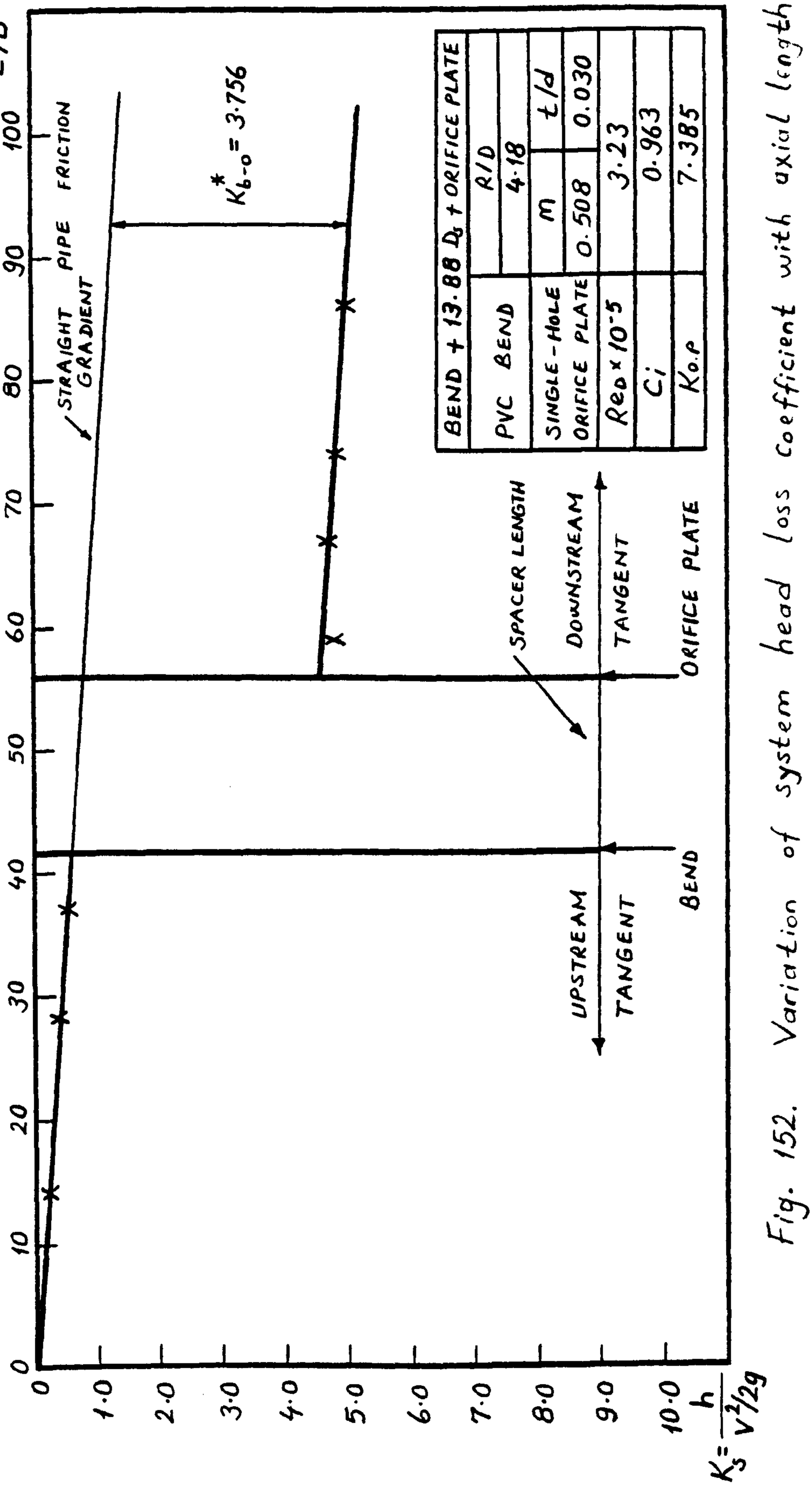

Fig. 152. Variation of system head loss coefficient with

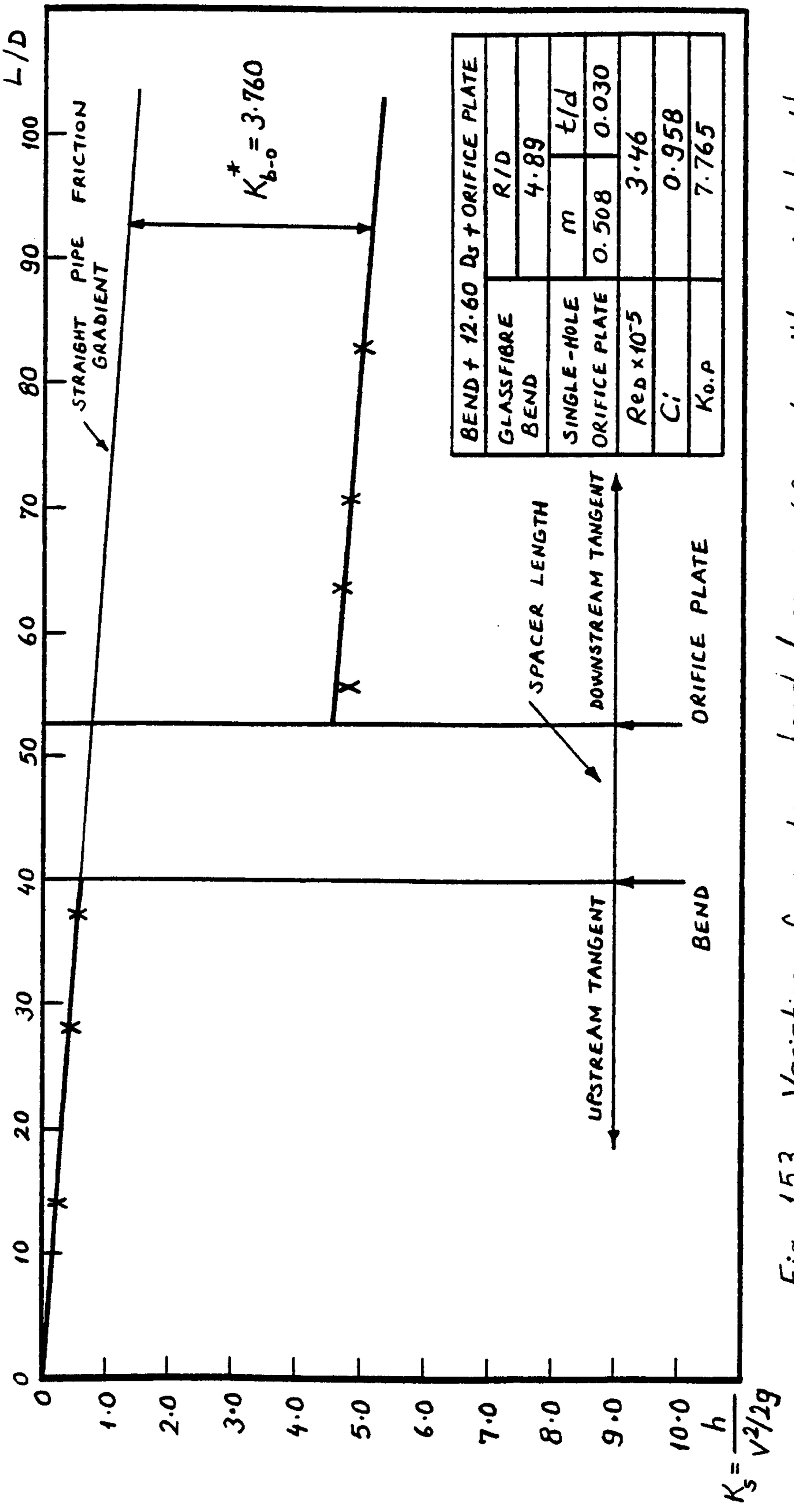

Fig. 153. Variation of system head loss coefficient with axial length

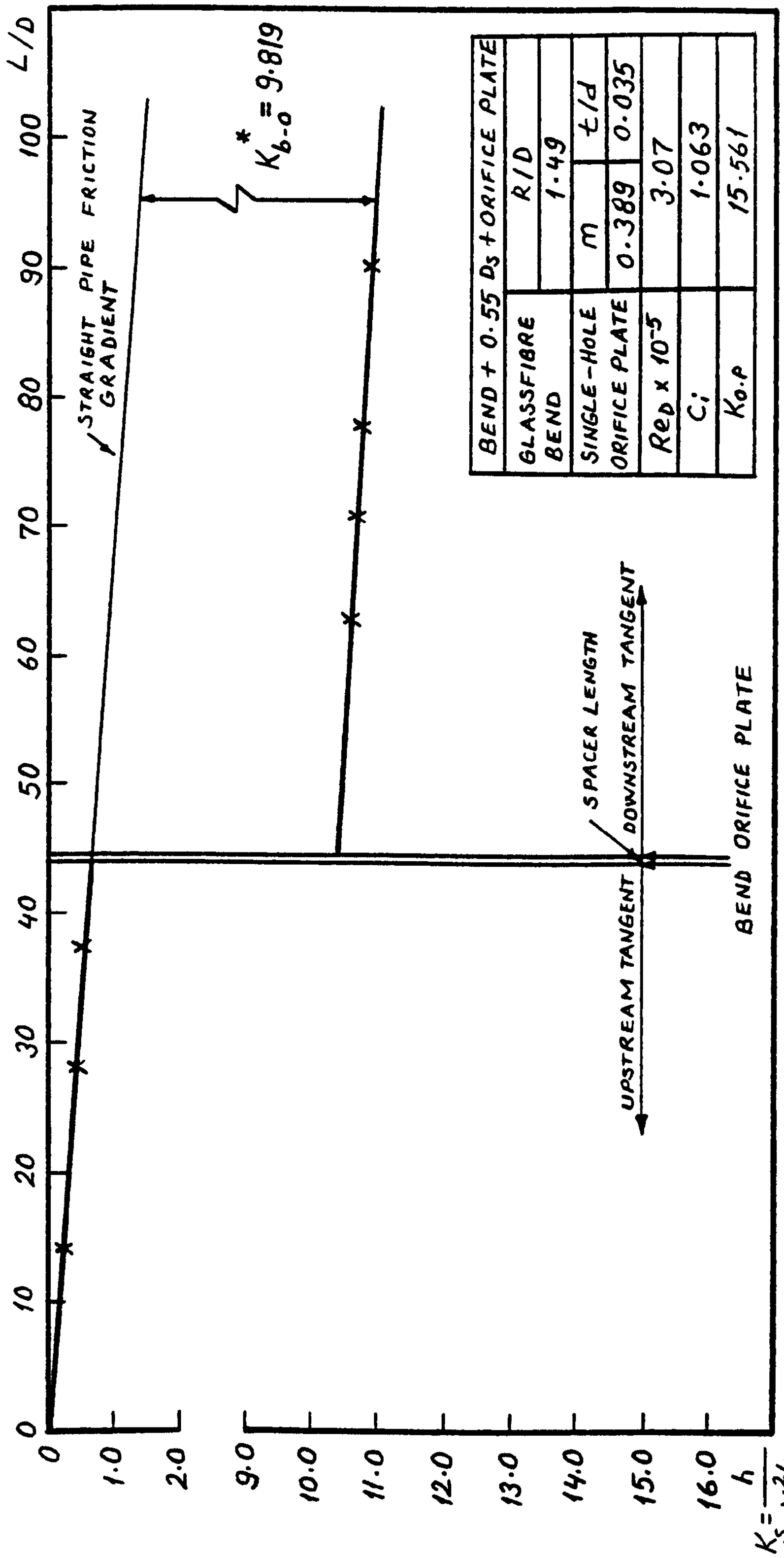

Fig. 154. Variation of system head loss coefficient with axial length

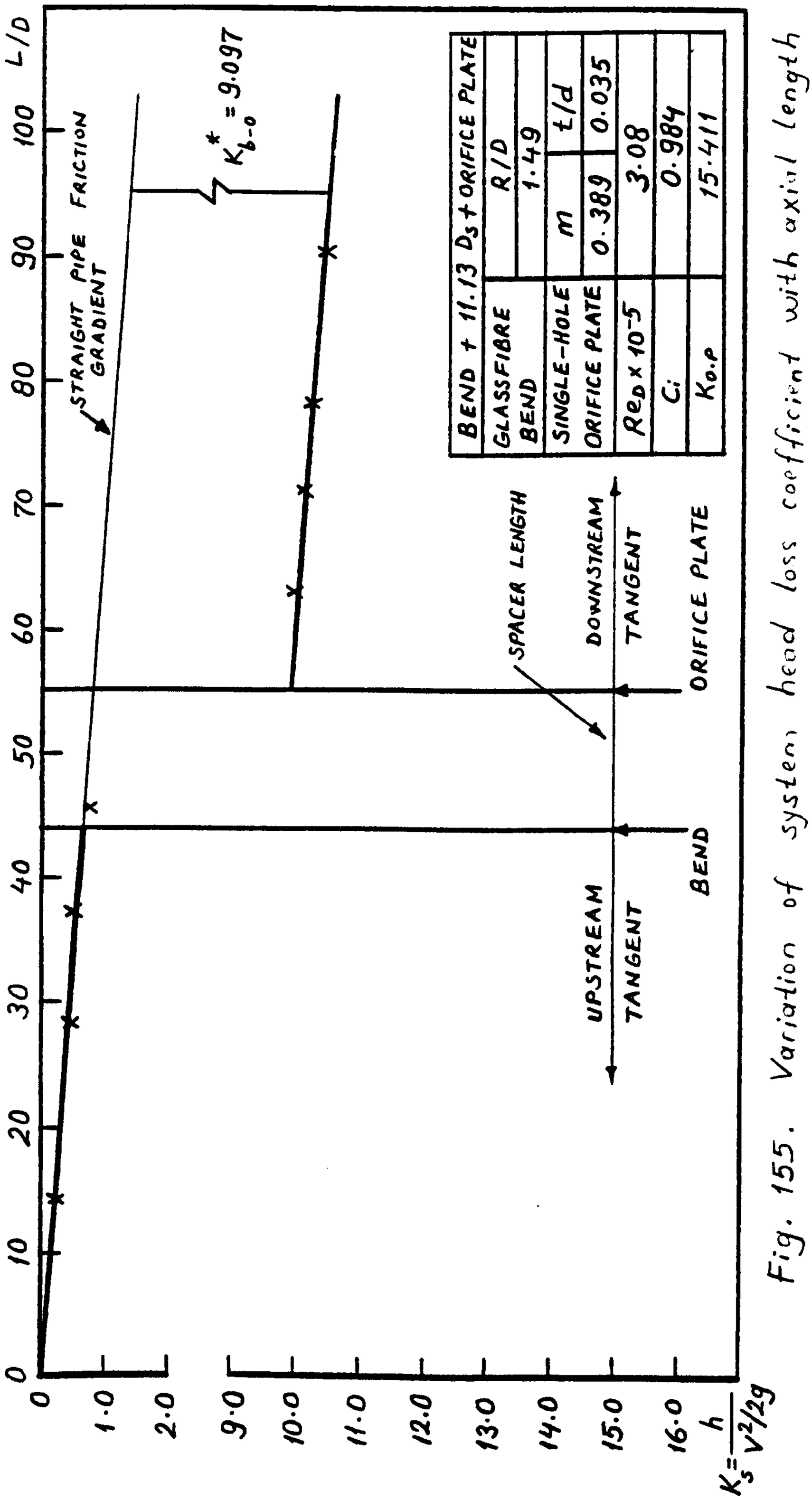

Fig. 155. Variation of system head loss coefficient with axial length

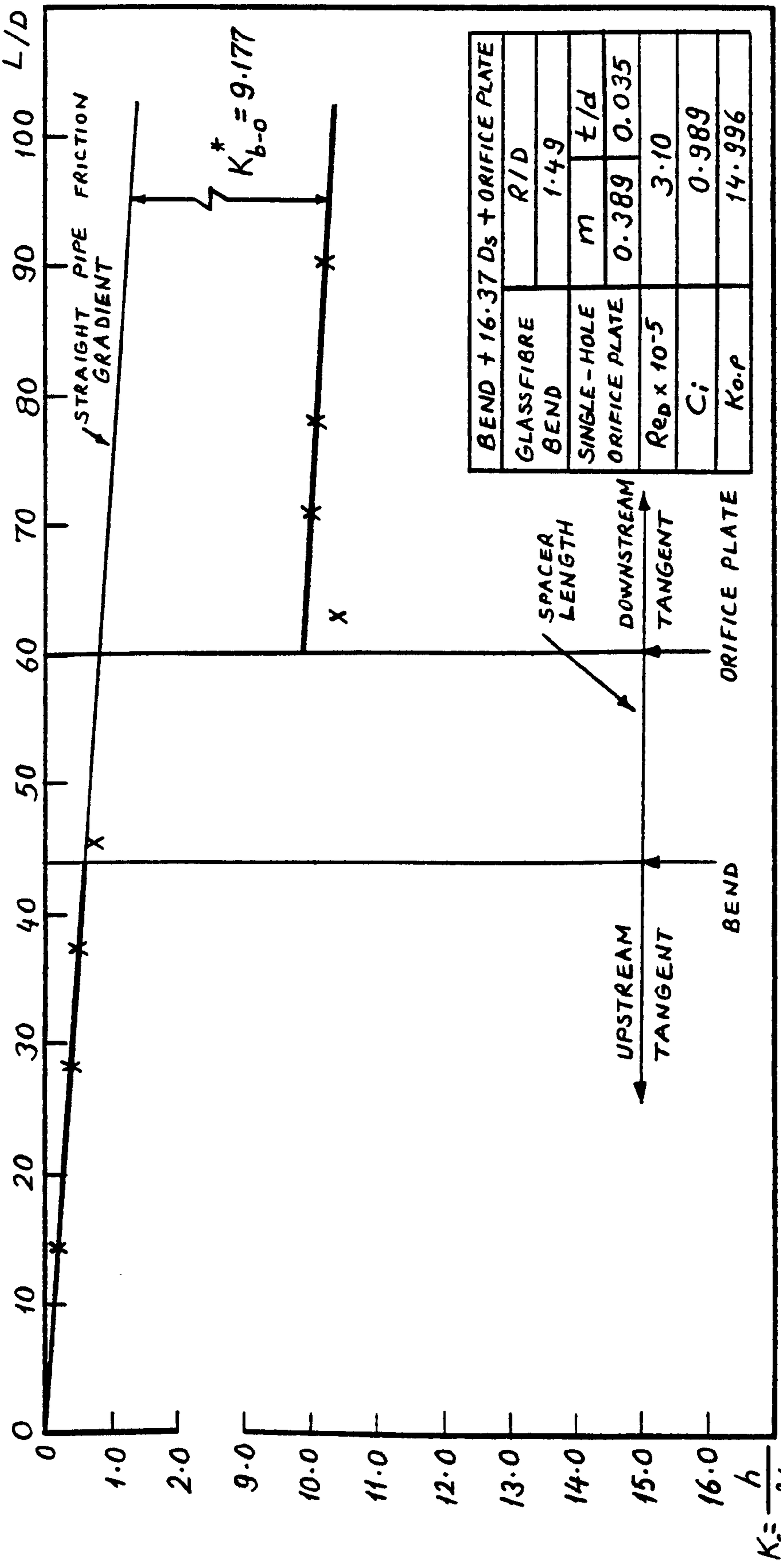

Fig. 156. Variation of system head loss coefficient with axial length

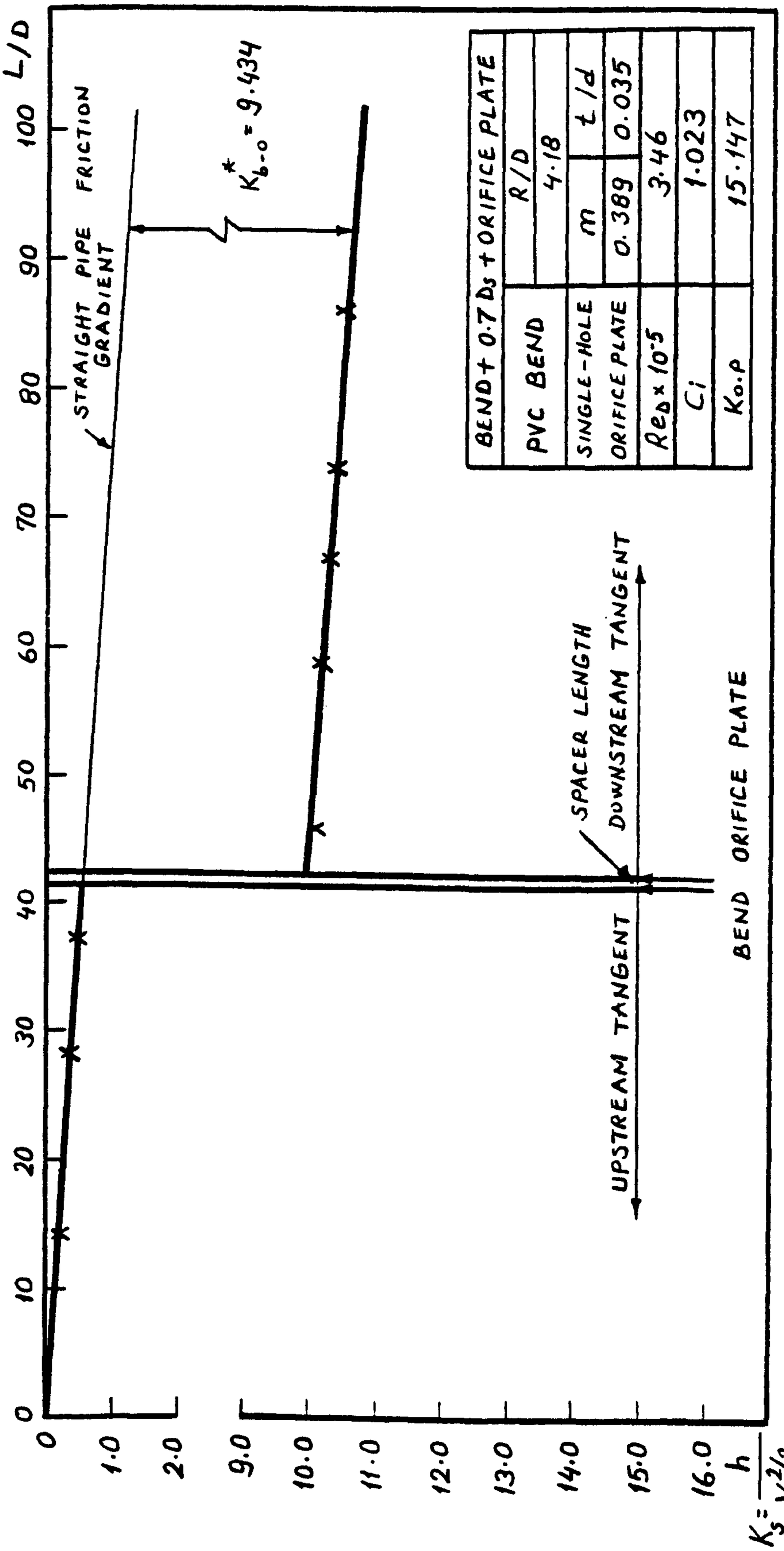

Fig. 157. Variation of system head loss coefficient with axial length

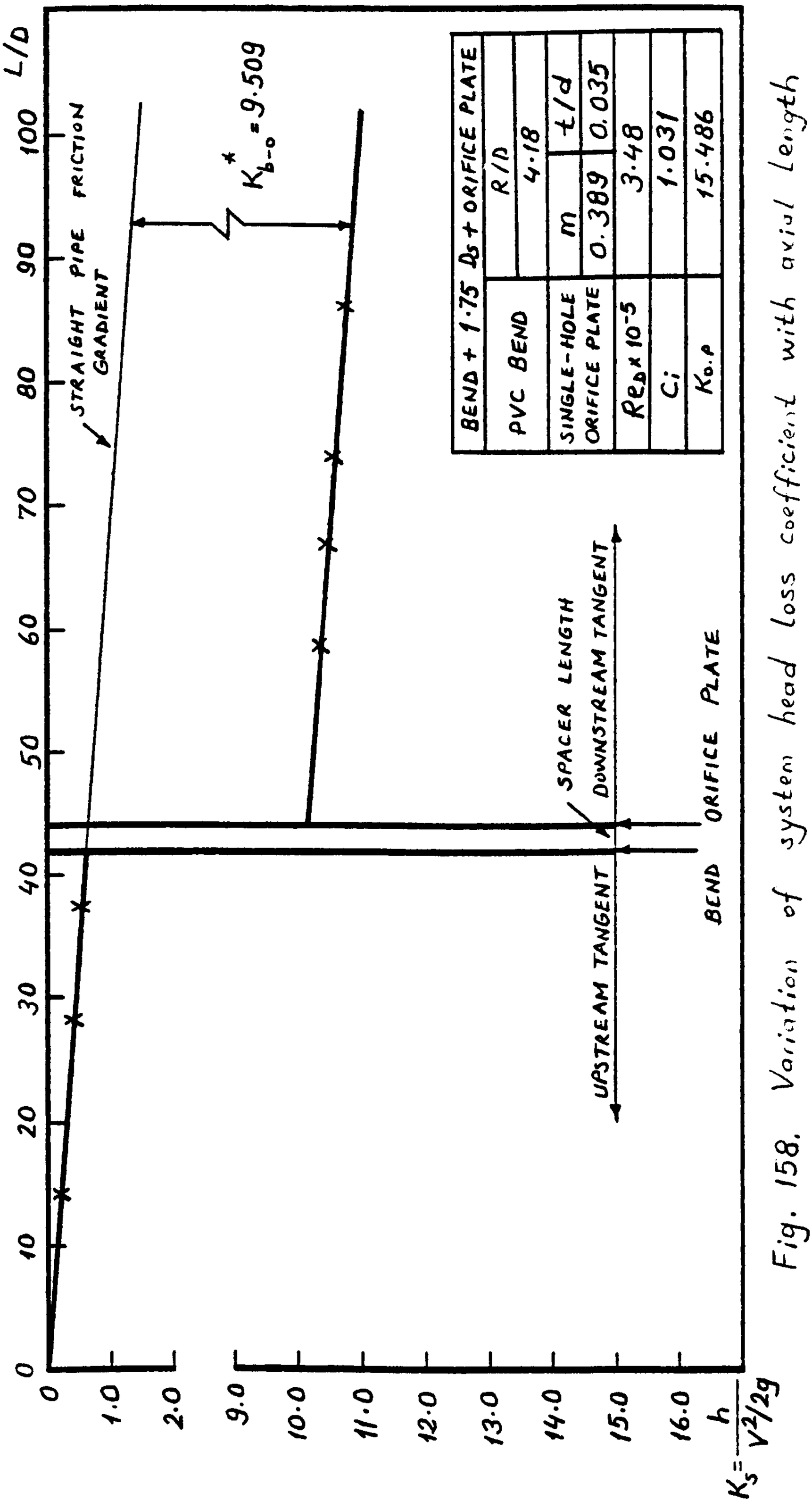

Fig. 158. Variation of system head loss coefficient with

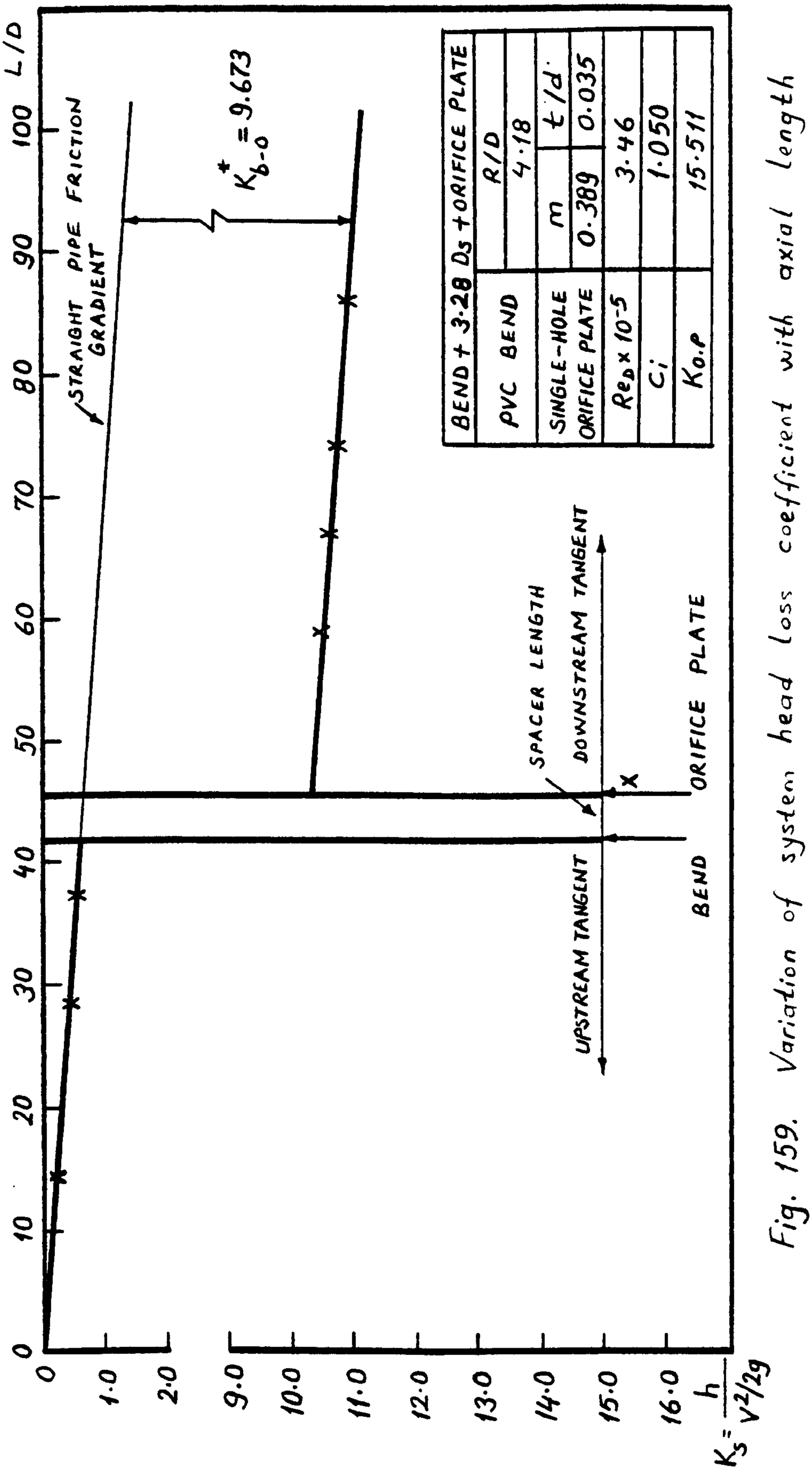

Fig. 159. Variation of system head loss coefficient with axial length

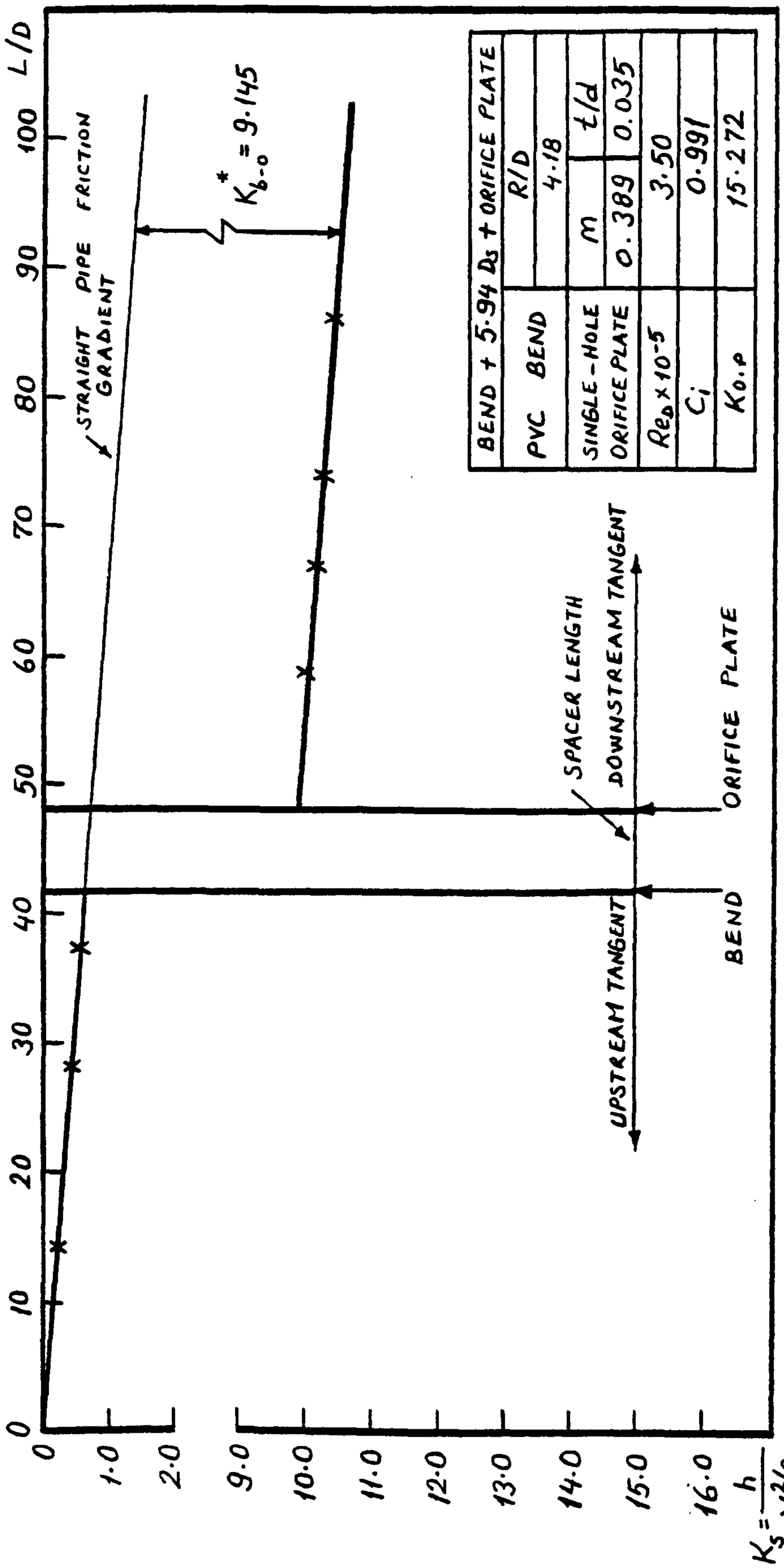

Fig. 160. Variation of system head loss coefficient with axial length

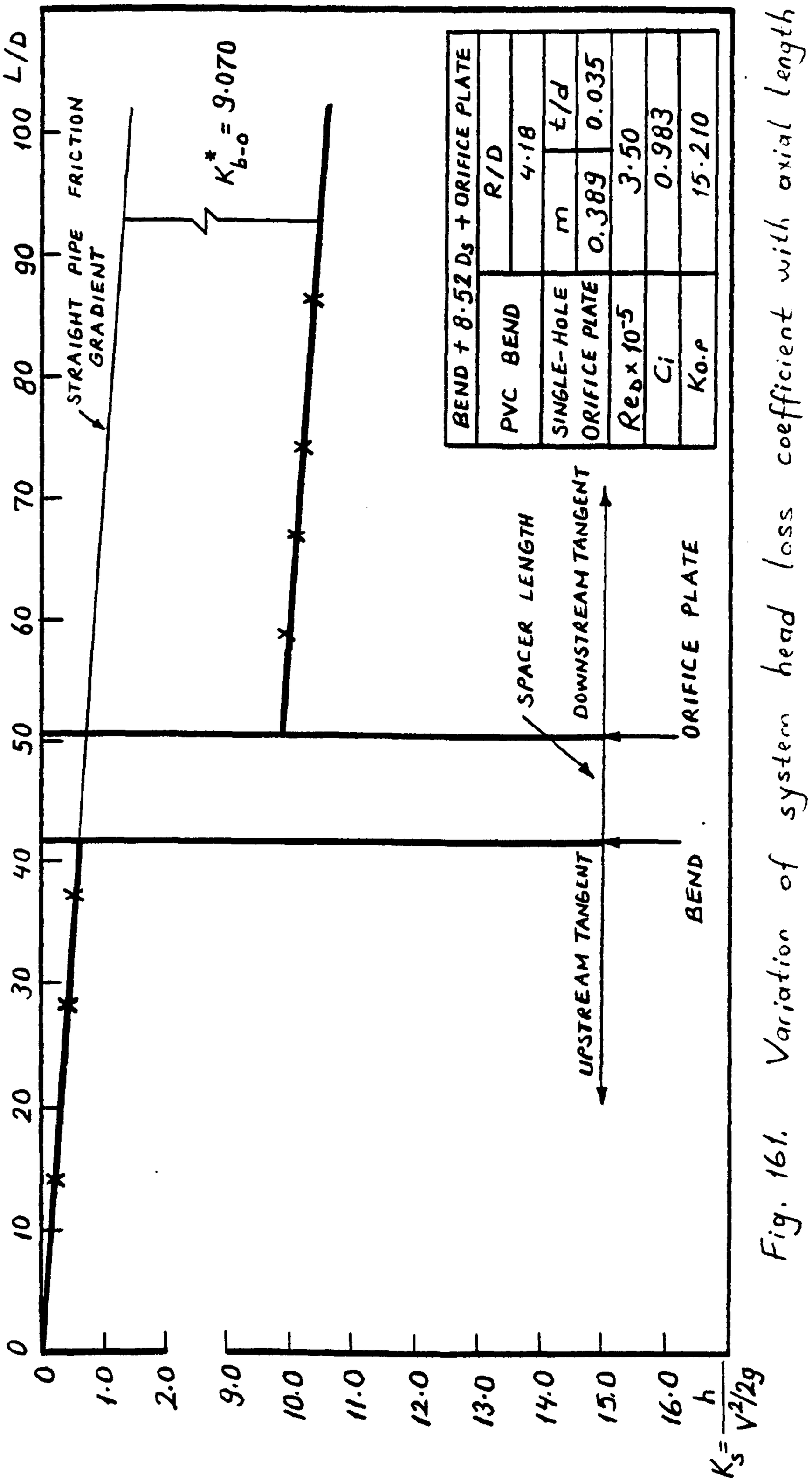

Fig. 161. Variation of system head loss coefficient with axial length

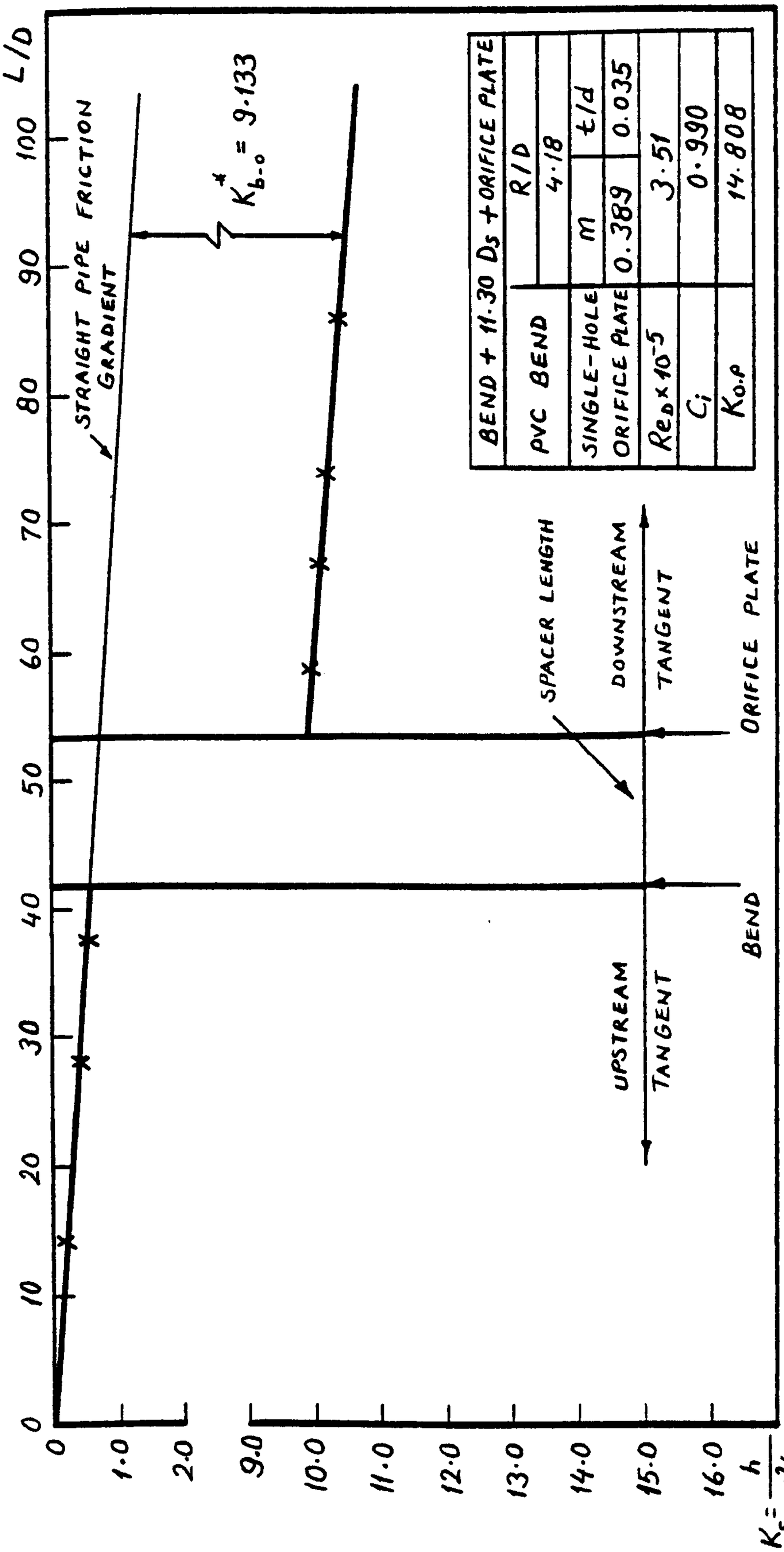

Fig. 162. Variation of system head loss coefficient with axial length

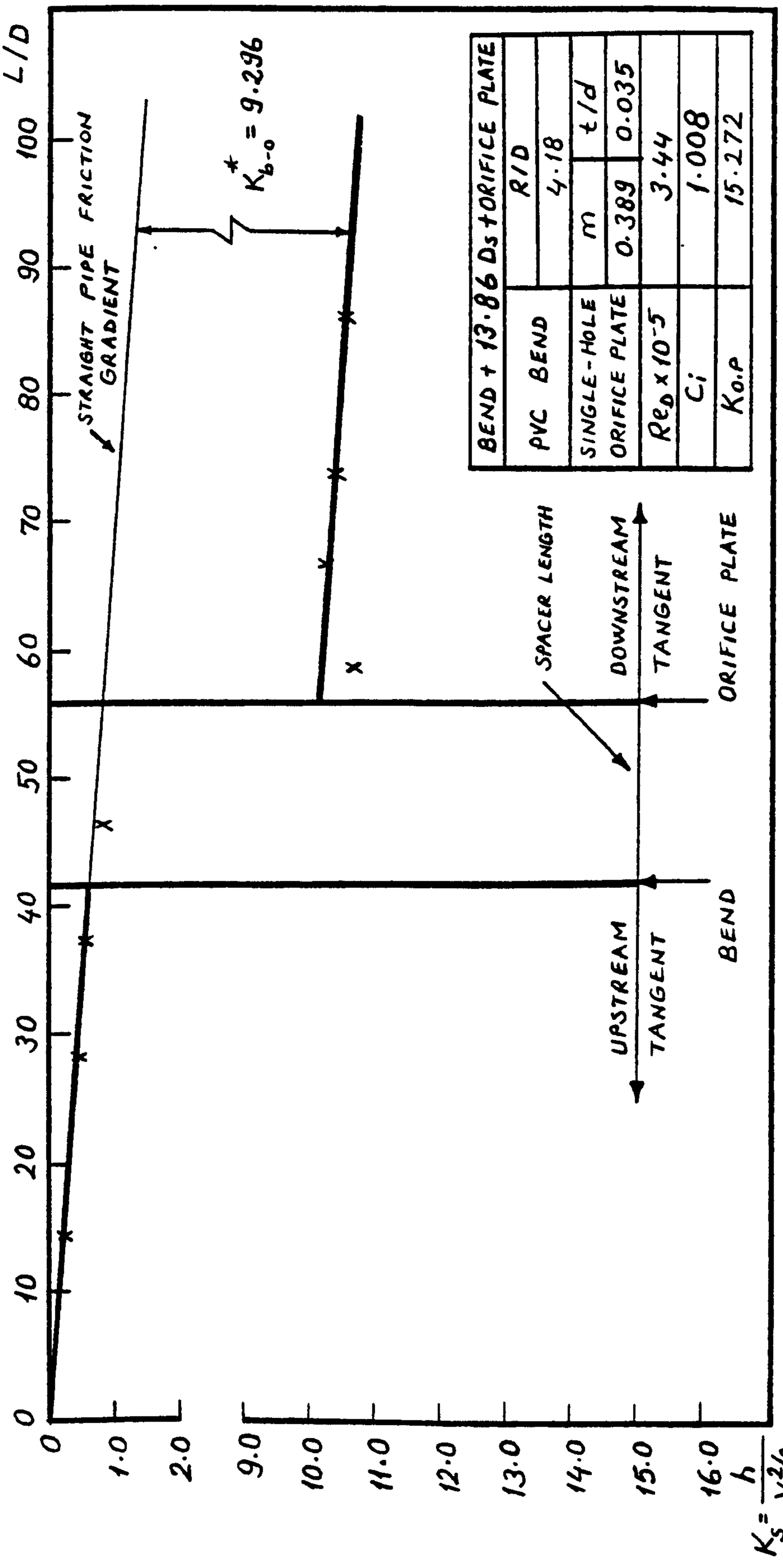

Fig. 163. Variation of system head loss coefficient with axial length

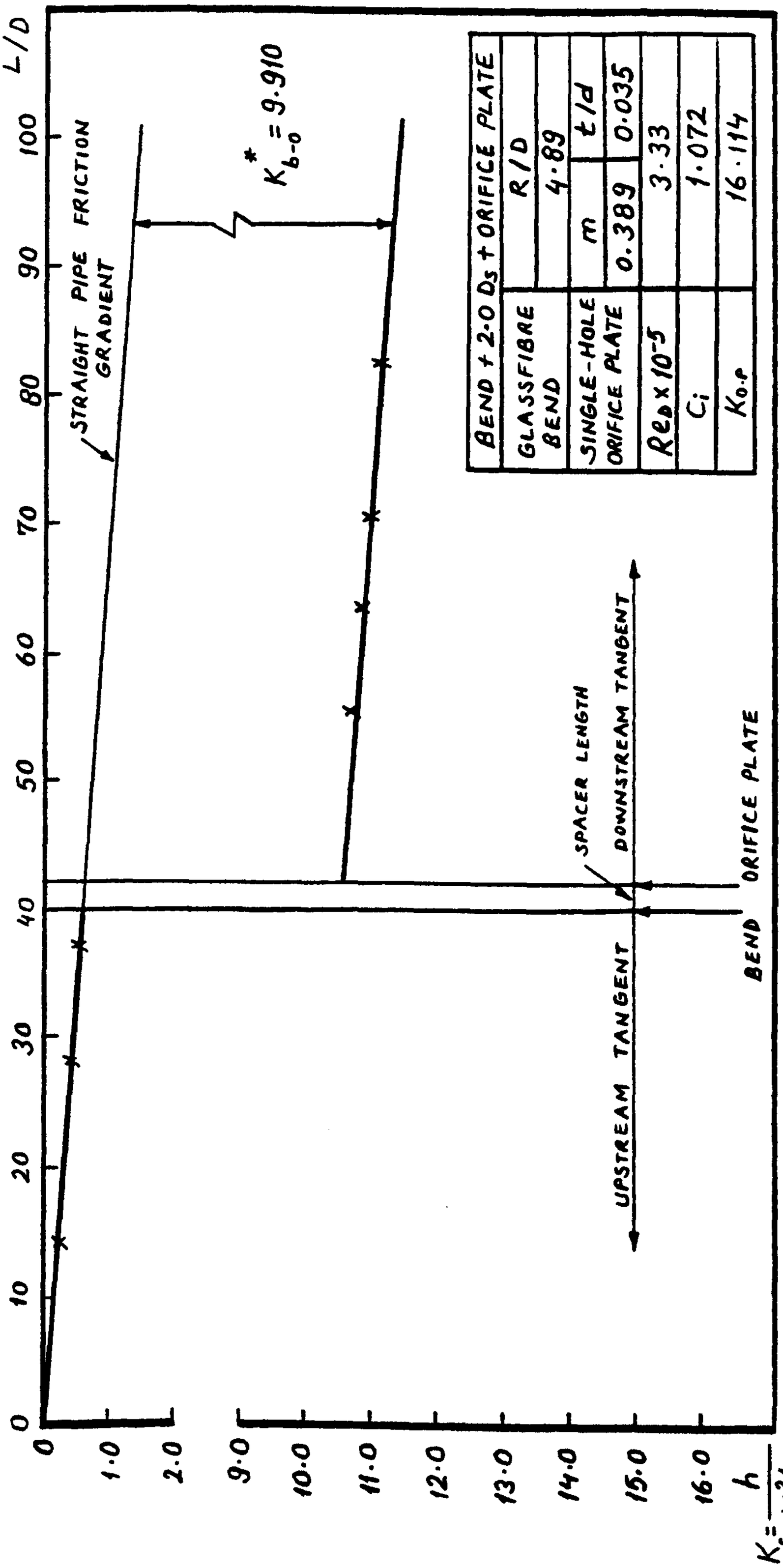

Fig. 164. Variation of system head loss coefficient with axial length

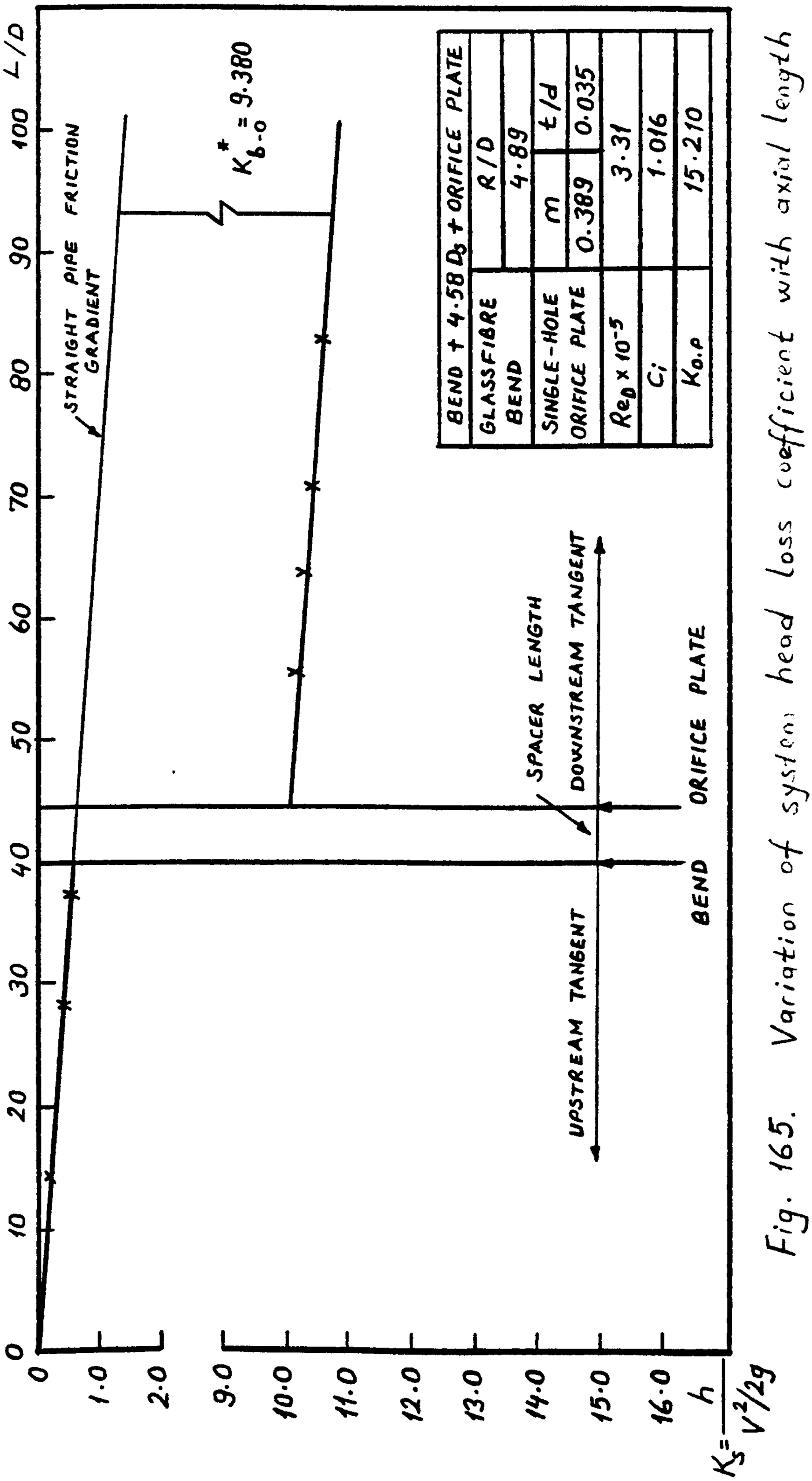

Fig. 165. Variation of system head loss coefficient with axial length

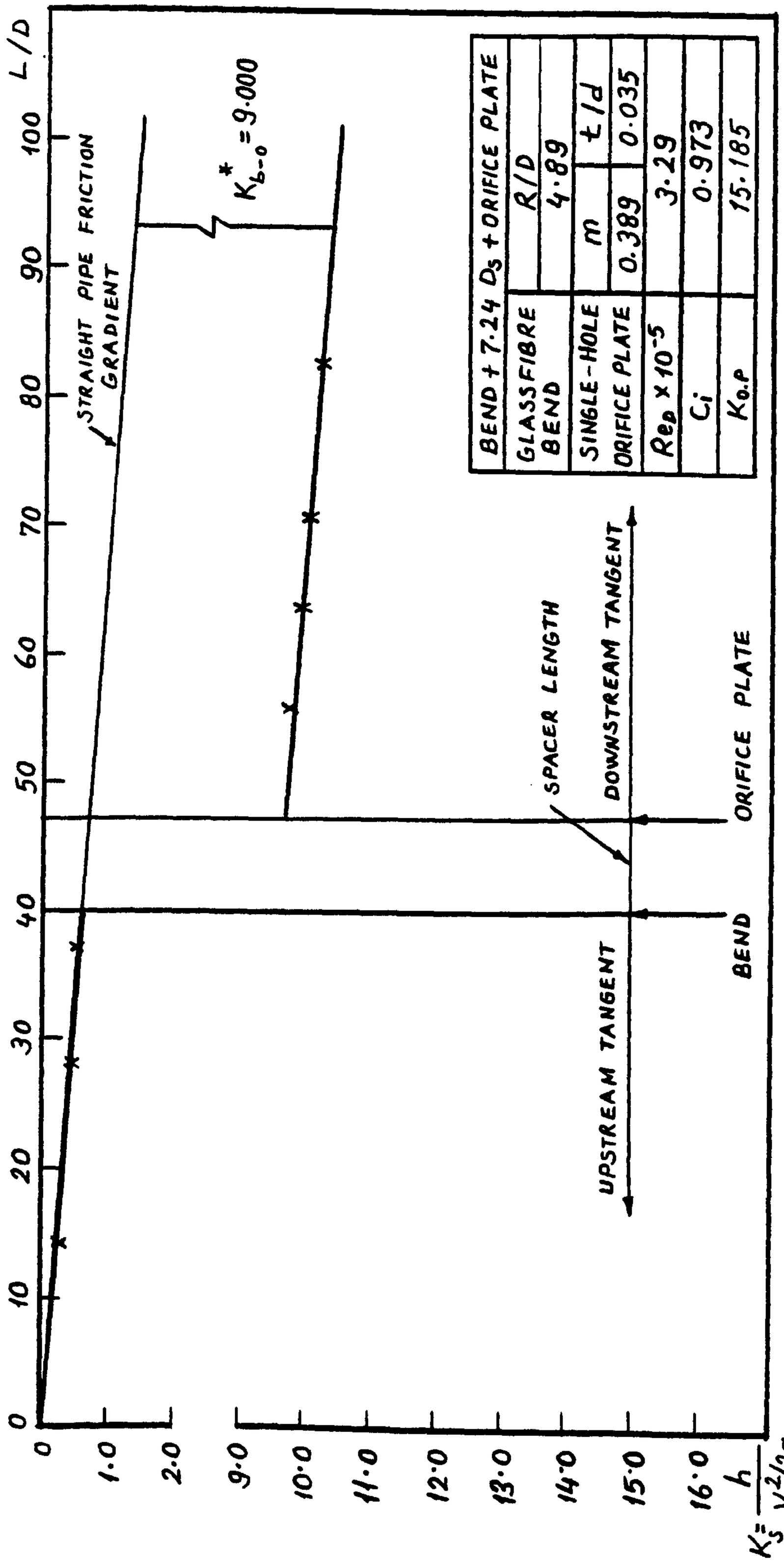

Fig. 166. Variation of system head loss coefficient with

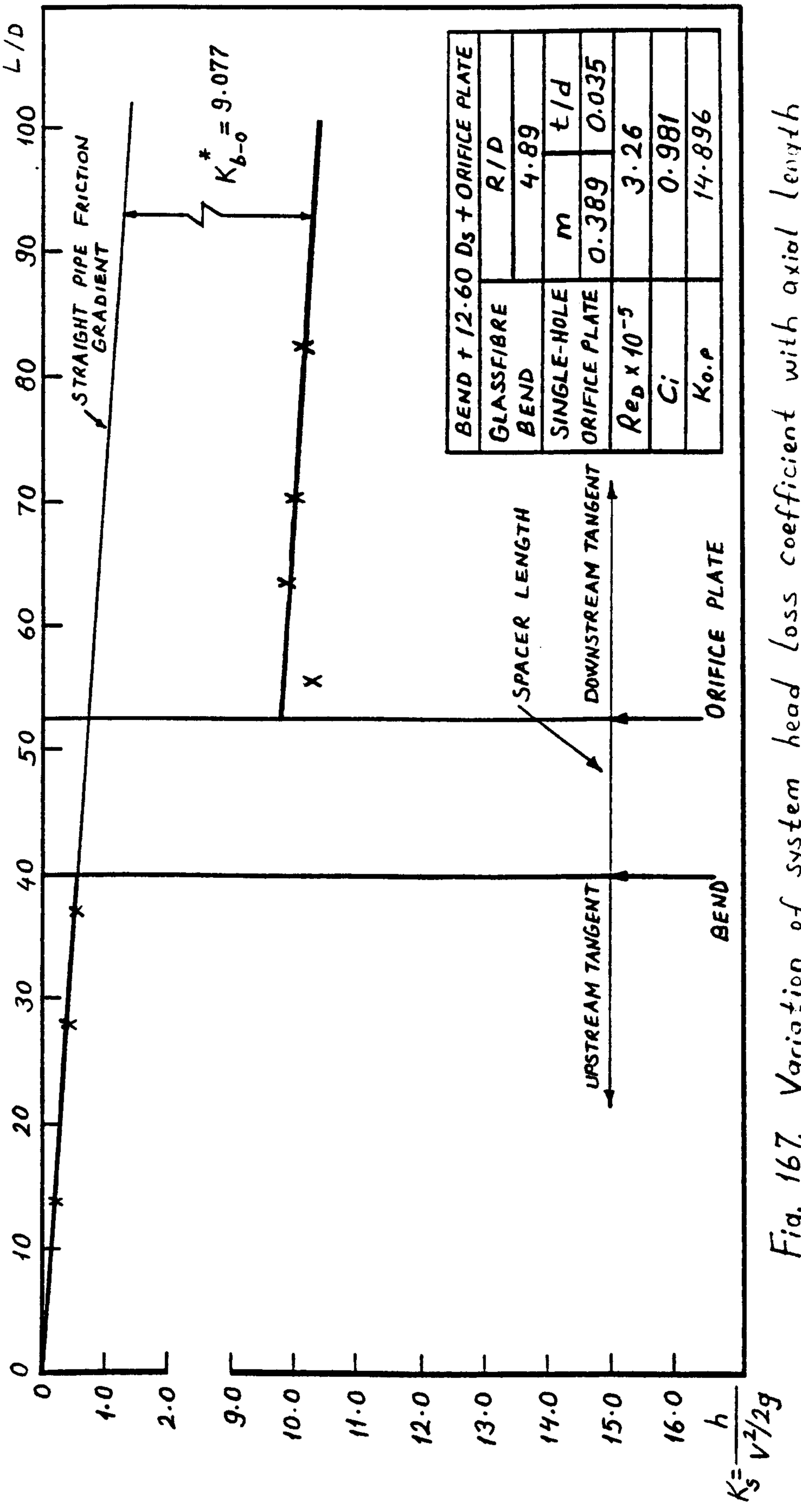

Fig. 167. Variation of system head loss coefficient with axial length

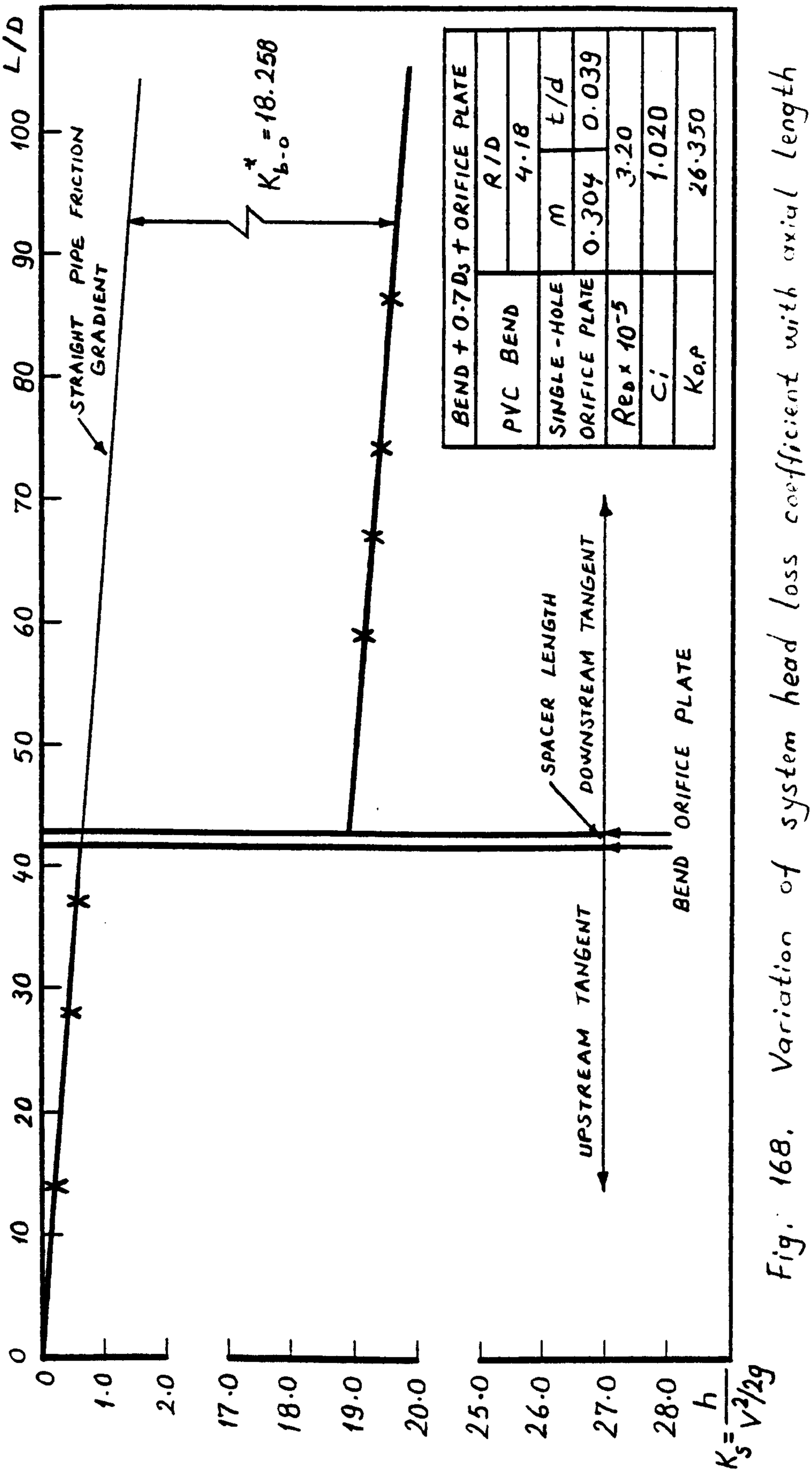

Fig. 168. Variation of system head loss coefficient with axial length

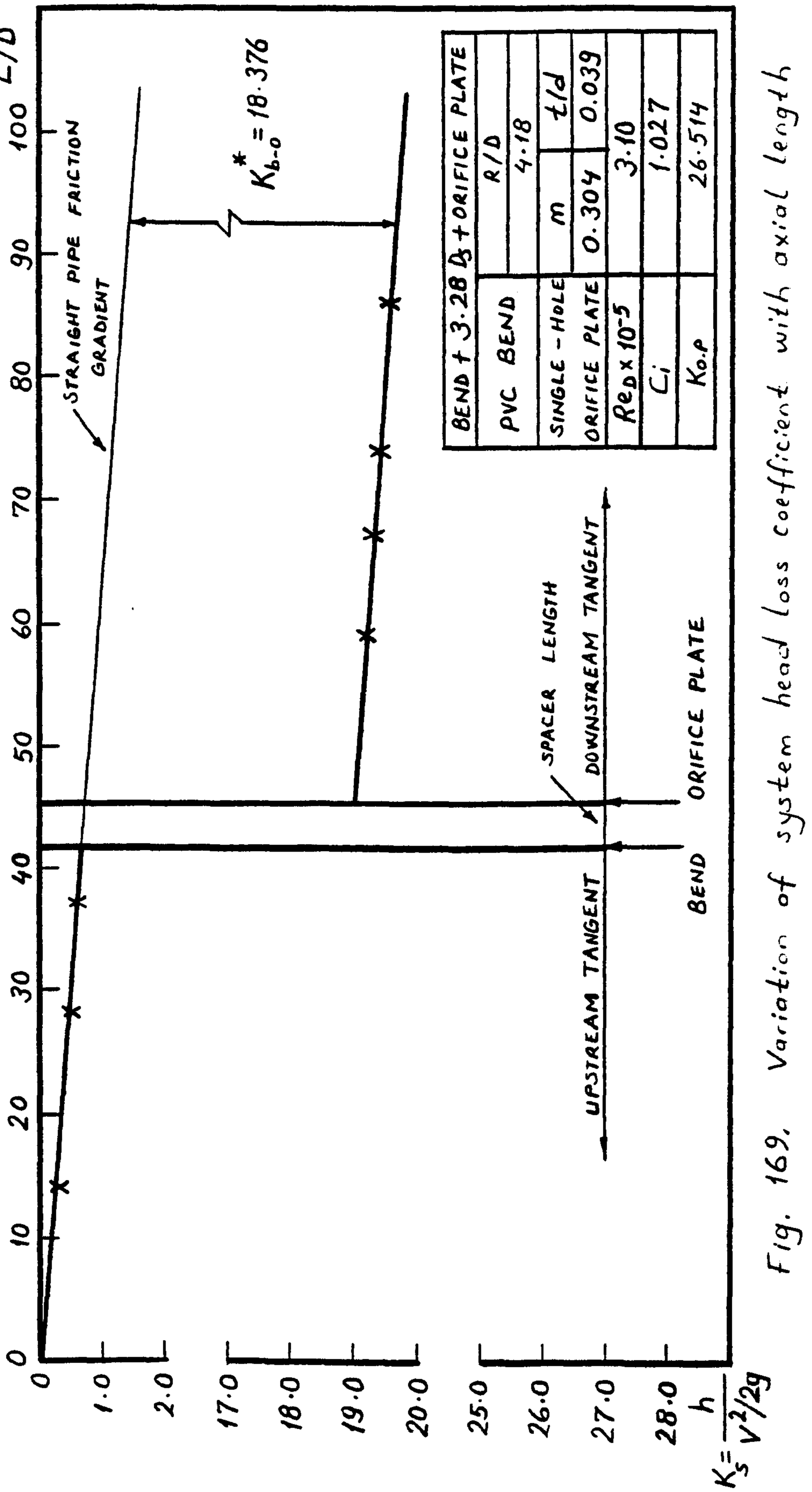

Fig. 169, Variation of system head loss coefficient with

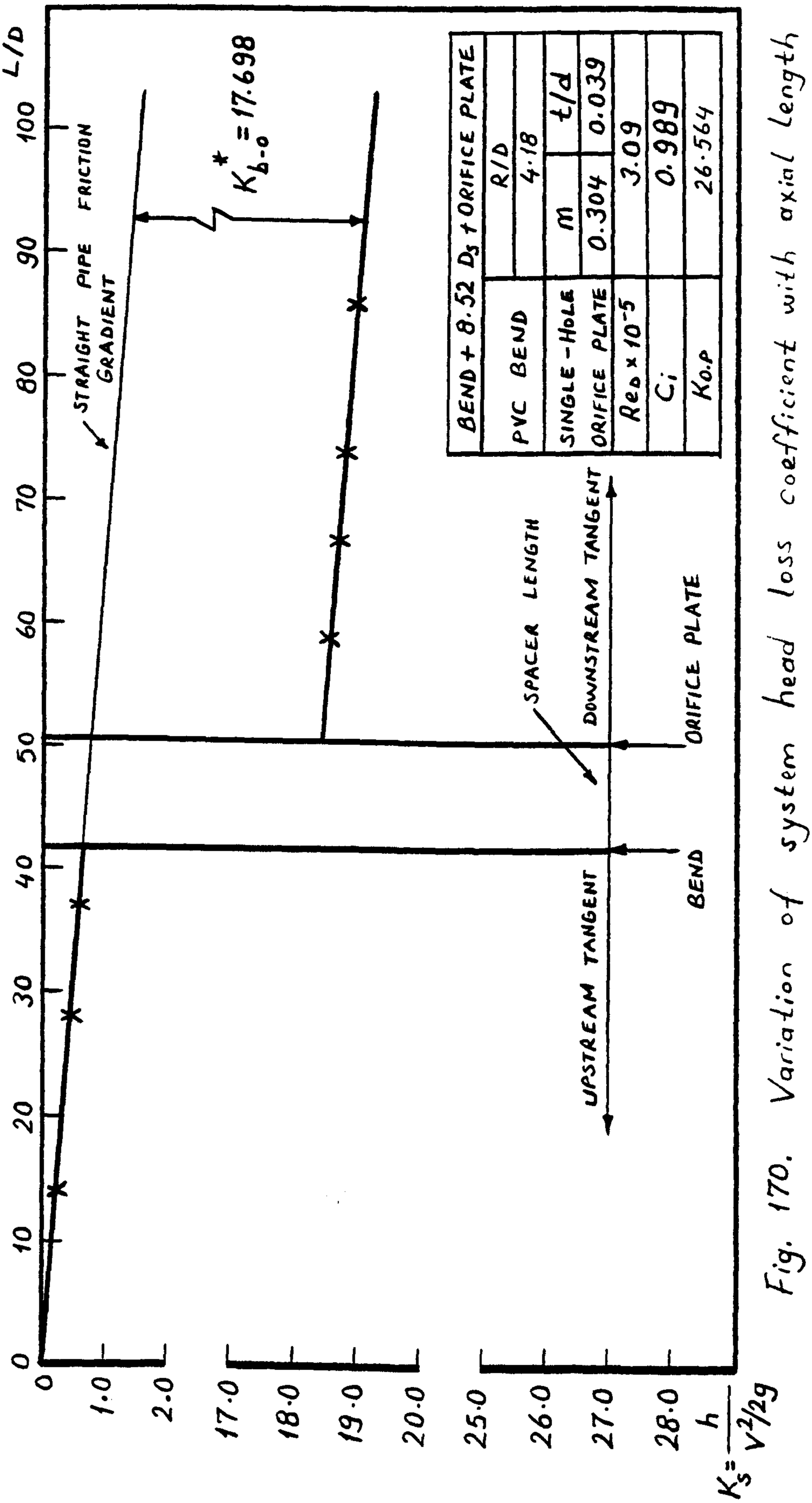

Fig. 170. Variation of system head loss coefficient with

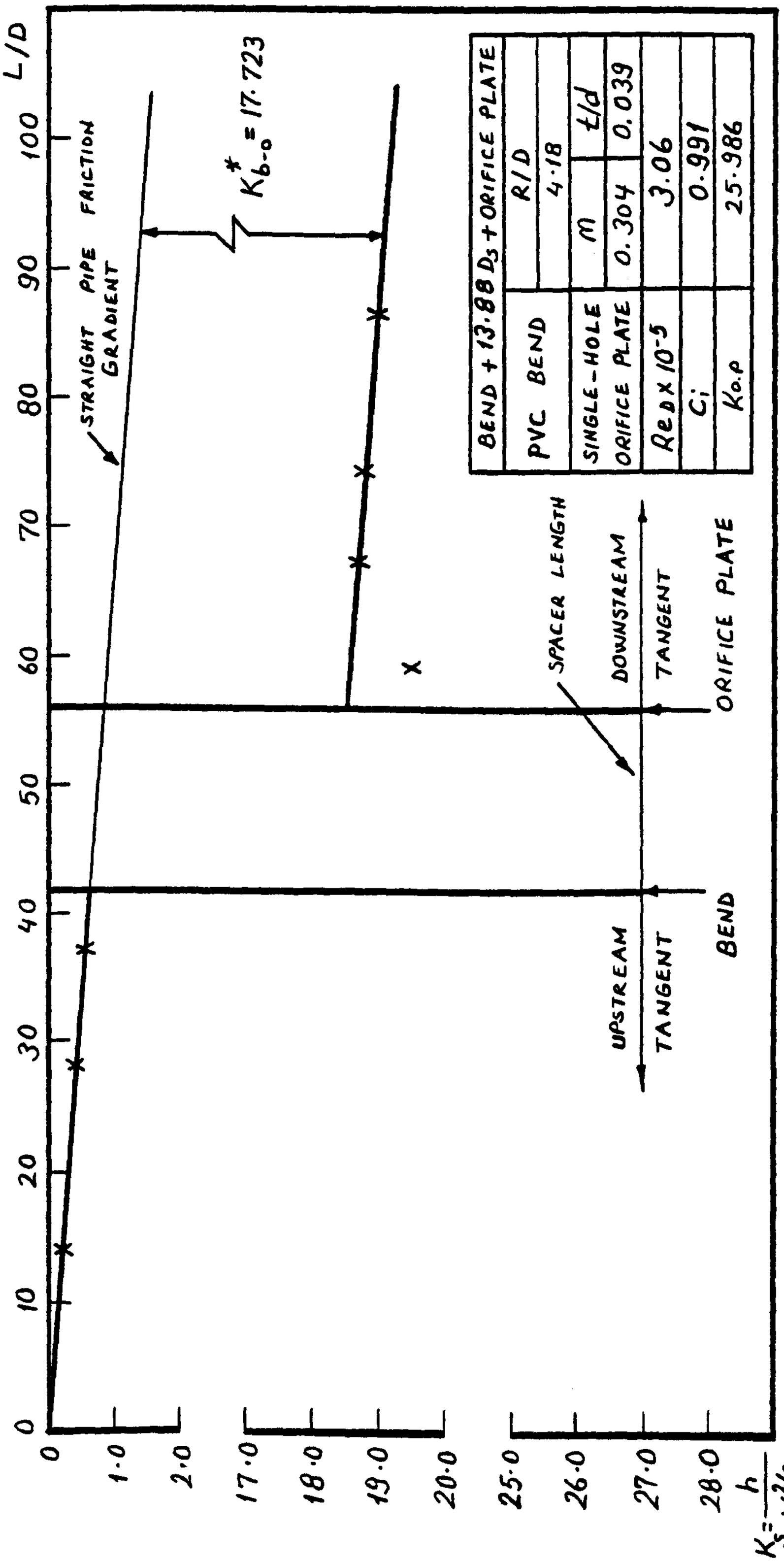

Fig. 171. Variation of system head loss coefficient with axial length

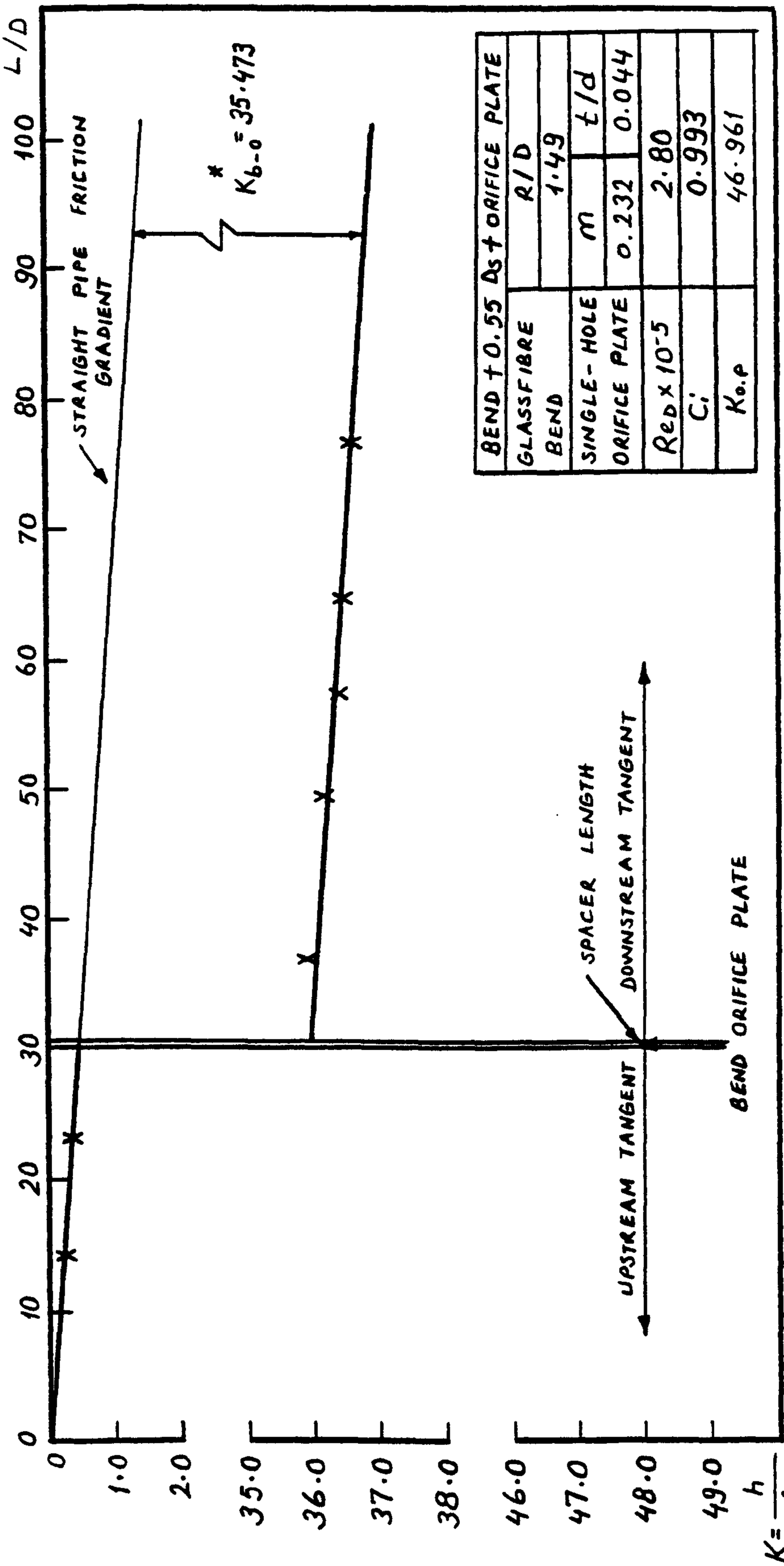

Fig. 172. Variation of system head loss coefficient with axial length

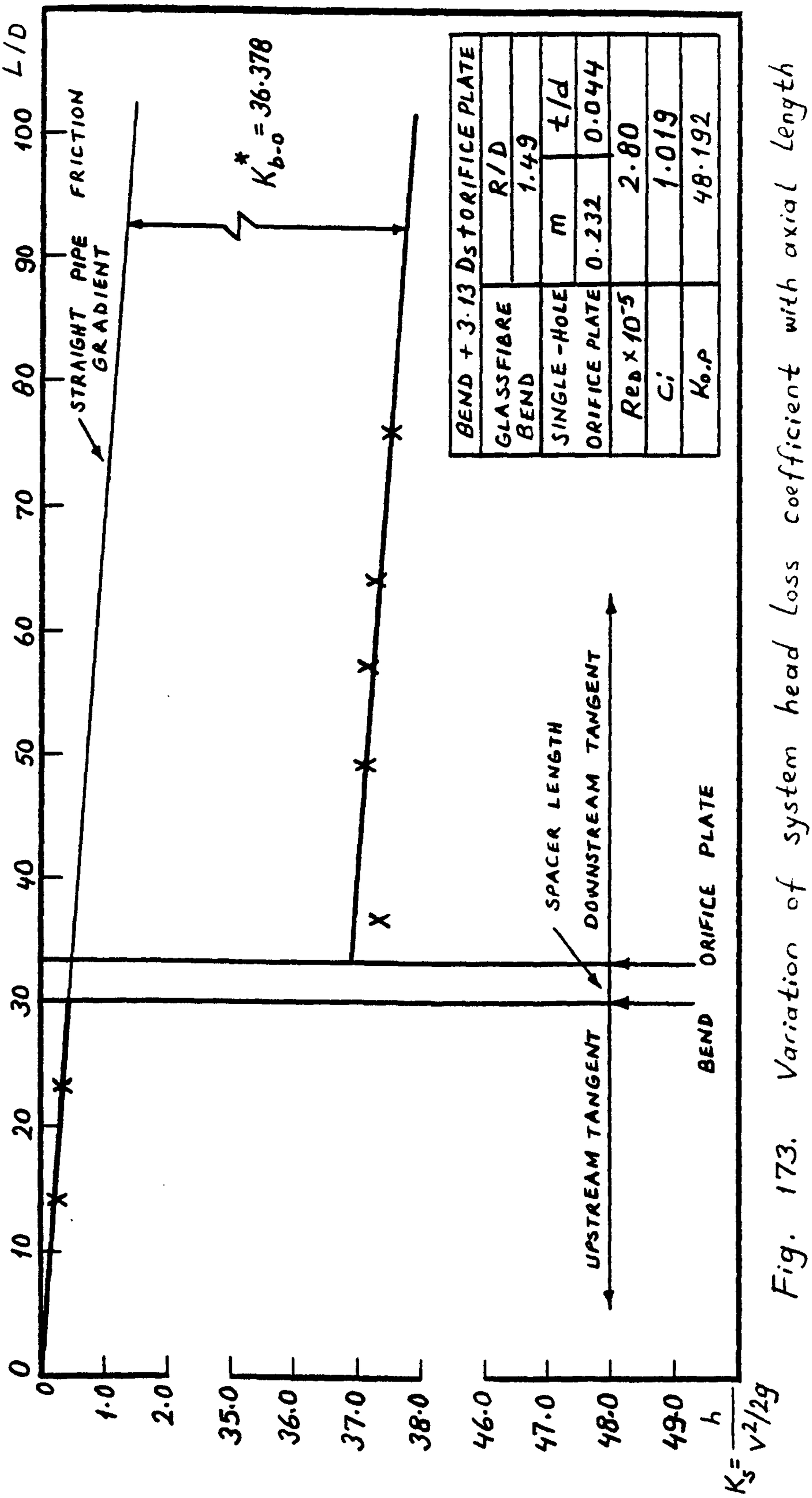

Fig. 173. Variation of system head Loss coefficient with axial Length

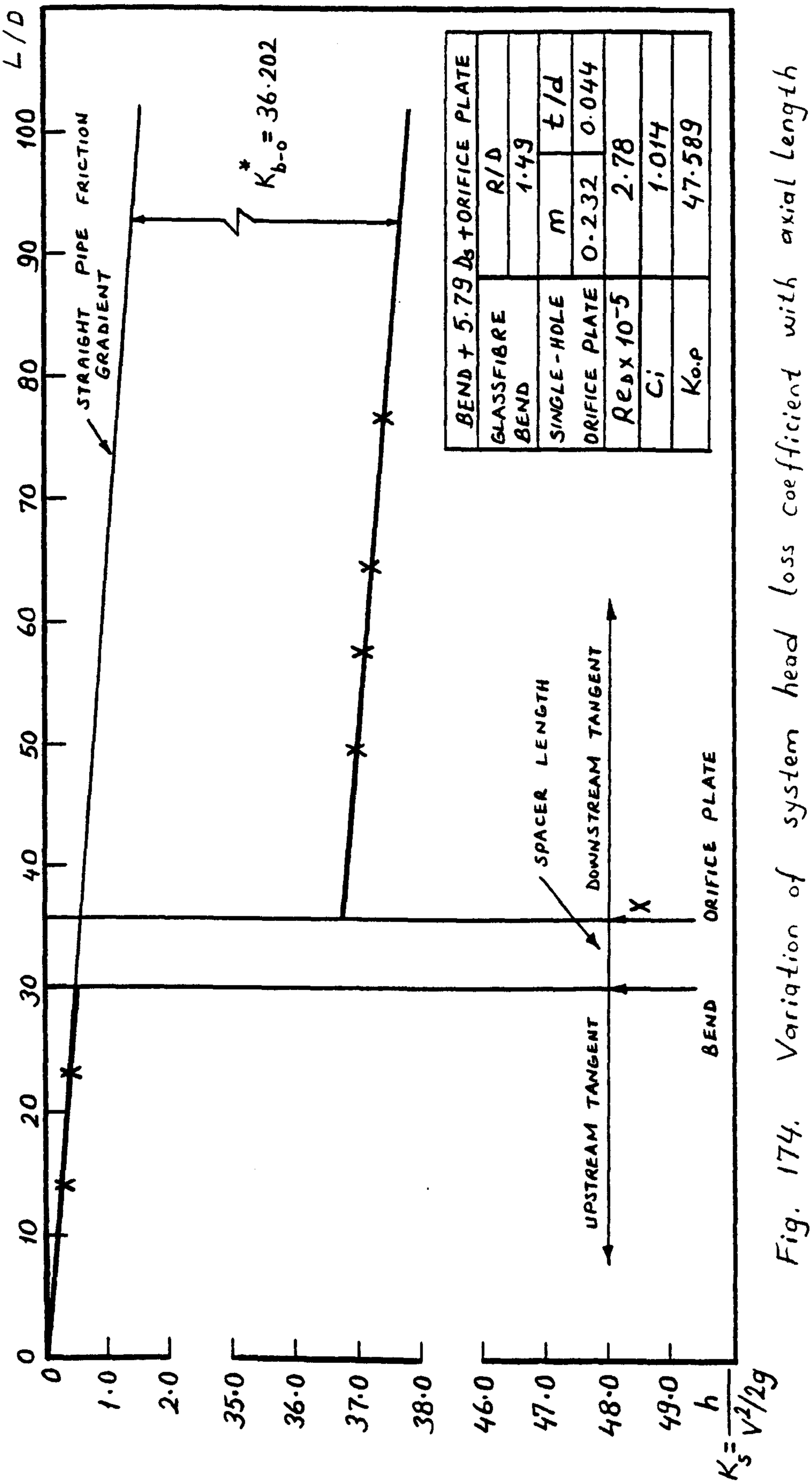

Fig. 174. Variation of system head loss coefficient with axial length

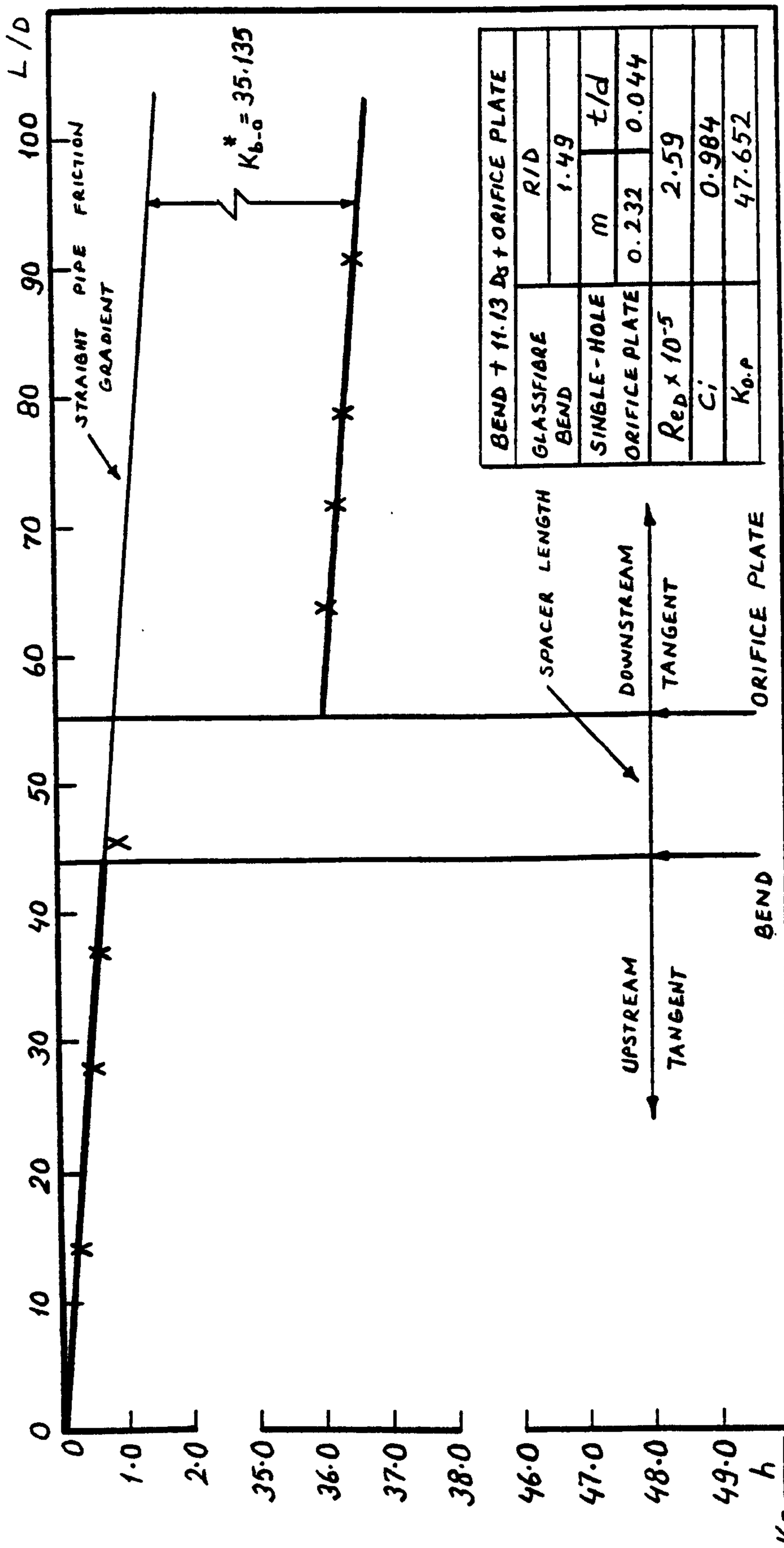

Fig. 175. Variation of system head loss coefficient with axial length

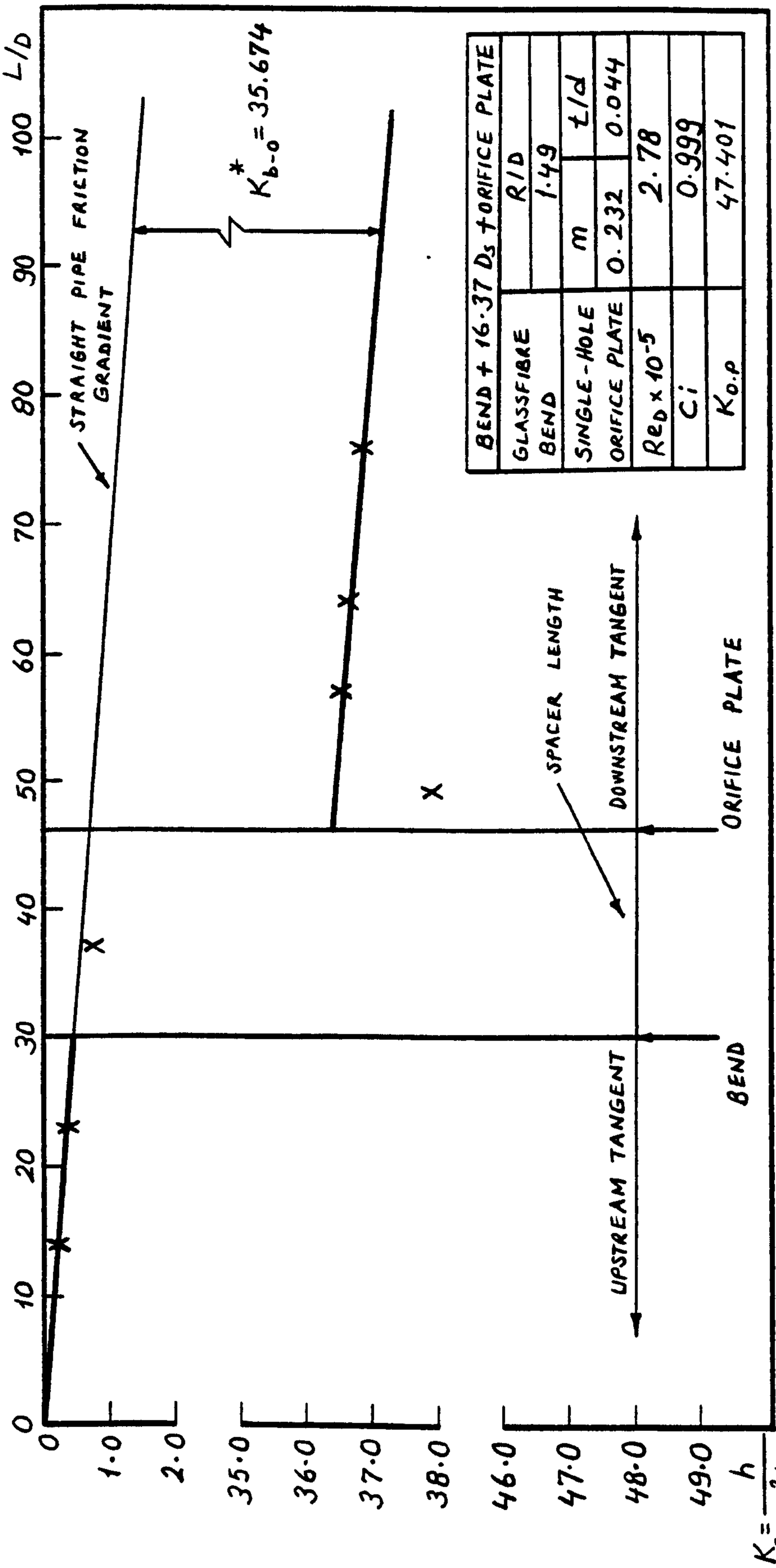

Fig. 176. Variation of system head loss coefficient with axial length

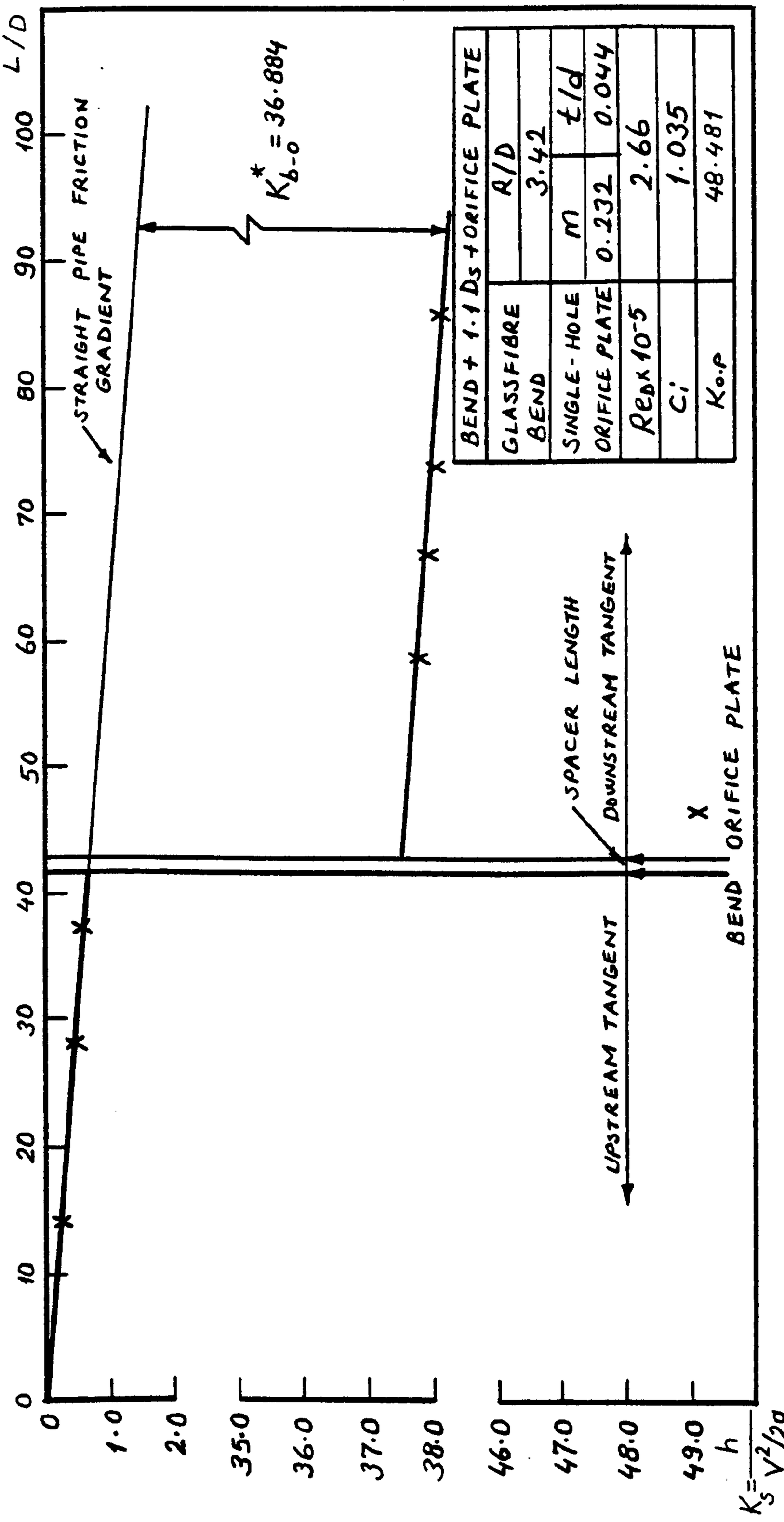

Fig. 177. Variation of system head loss coefficient with axial length

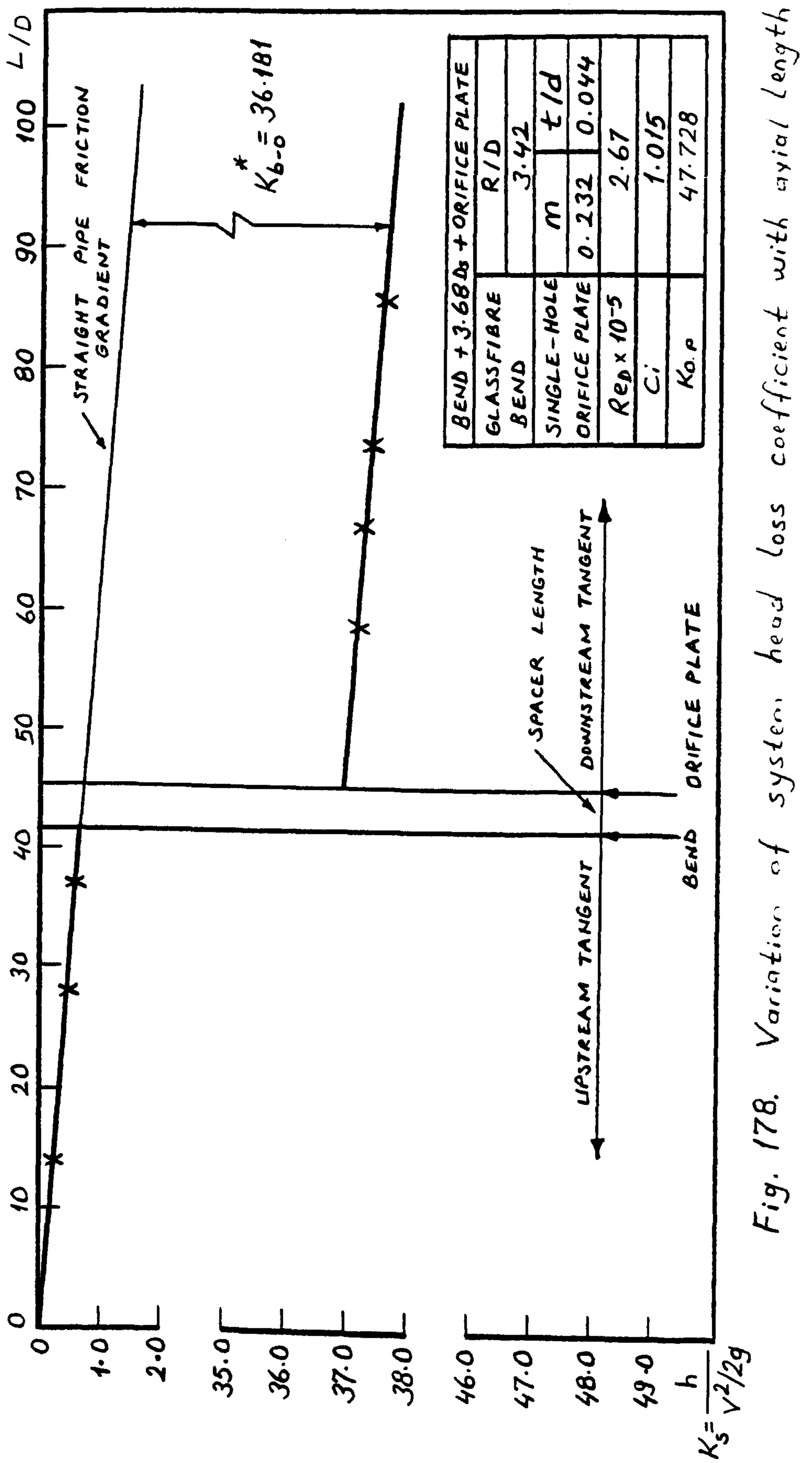

Fig. 178. Variation of system head loss coefficient with axial length

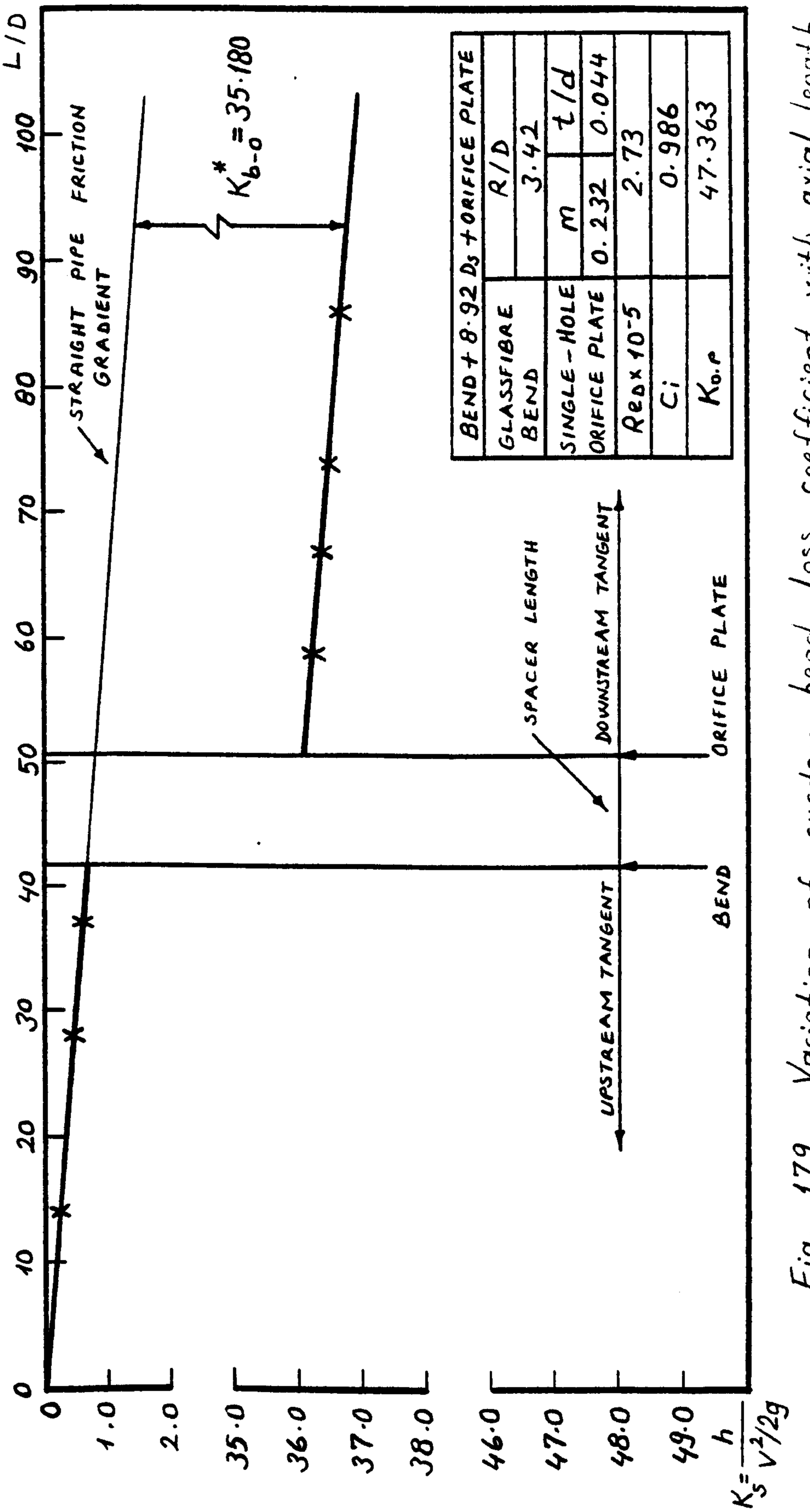

BEND + 8·92 D$_s$ + ORIFICE PLATE	R/D			
GLASSFIBRE BEND	3.42			
SINGLE-HOLE ORIFICE PLATE	m		t/d	
	0.232		0.044	
$Re_D \times 10^{-5}$	2.73			
Ci	0.986			
$K_{o.p}$	47.363			

Fig. 179. Variation of system head loss coefficient with axial length

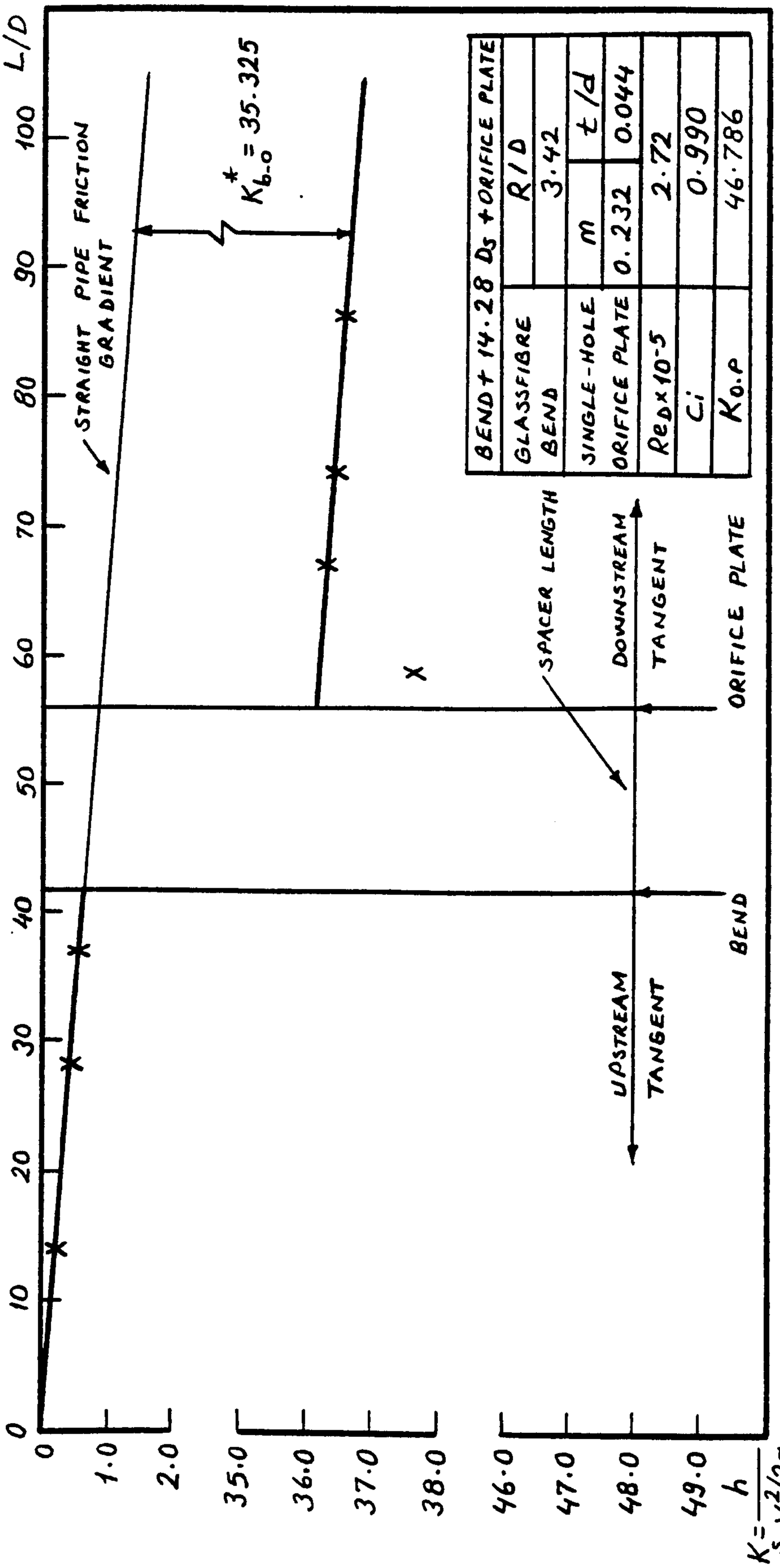

Fig. 180. Variation of system head loss coefficient with axial length

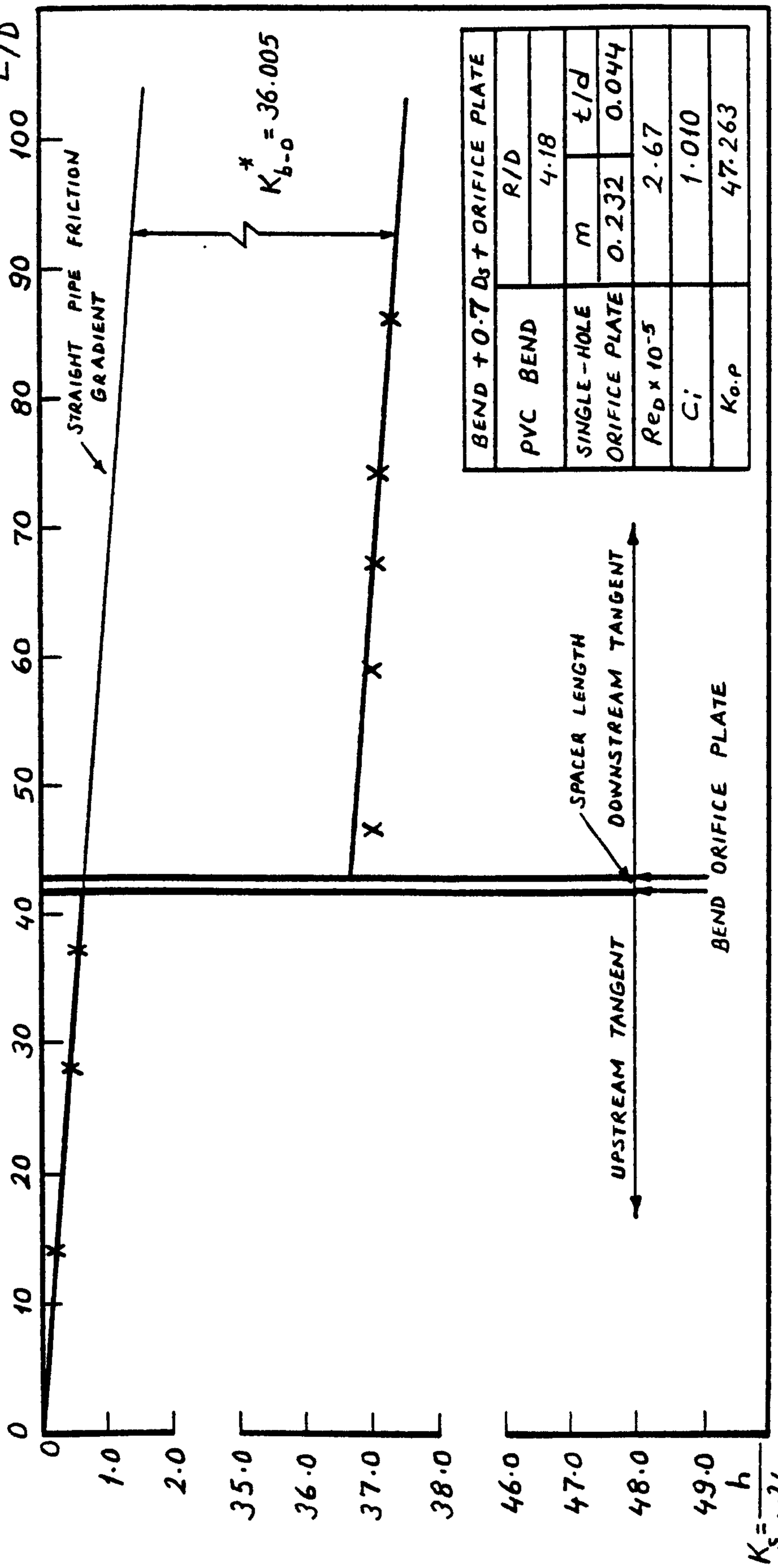

Fig. 181. Variation of system head Loss coefficient with axial length h

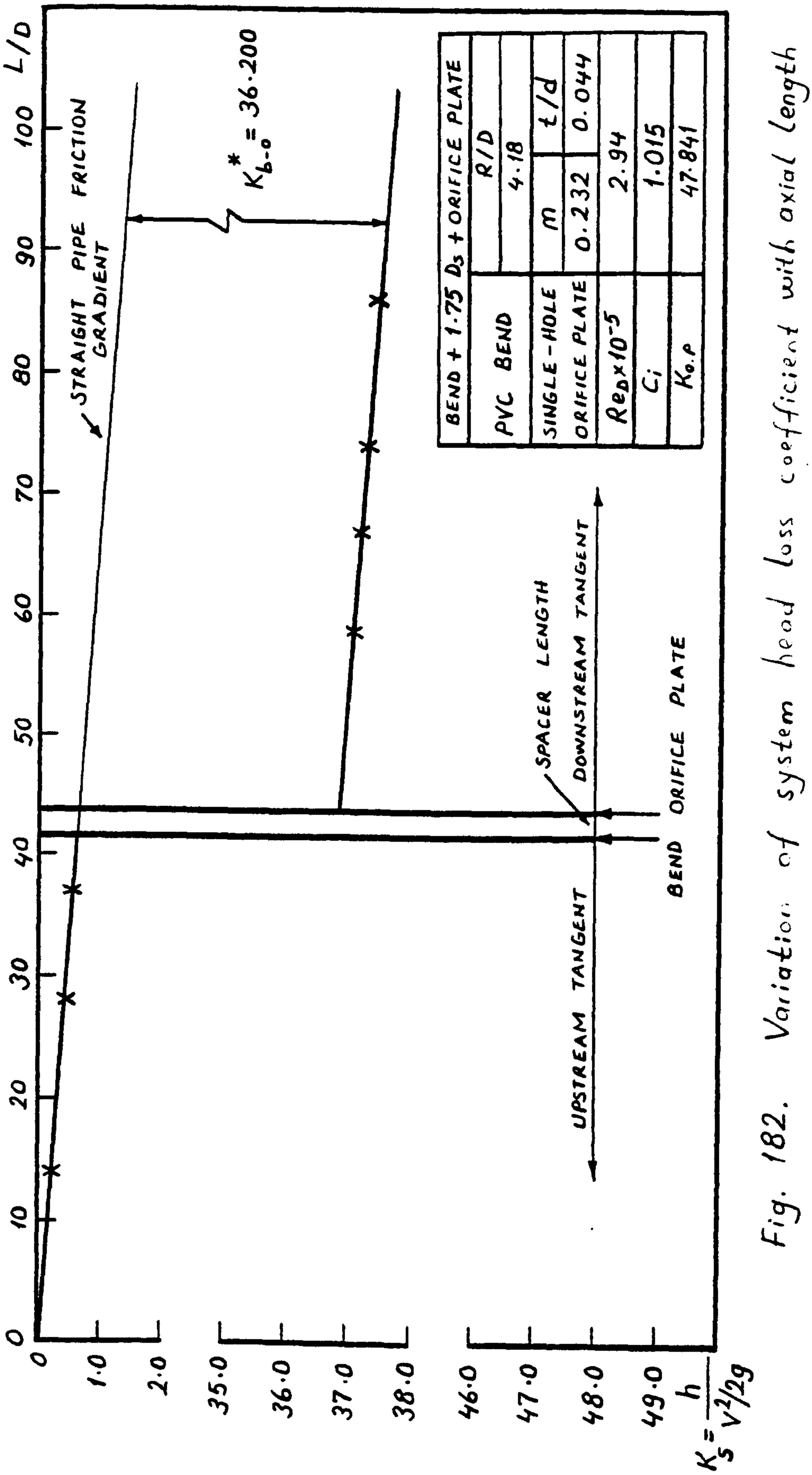

Fig. 182. Variation of system head loss coefficient with axial length

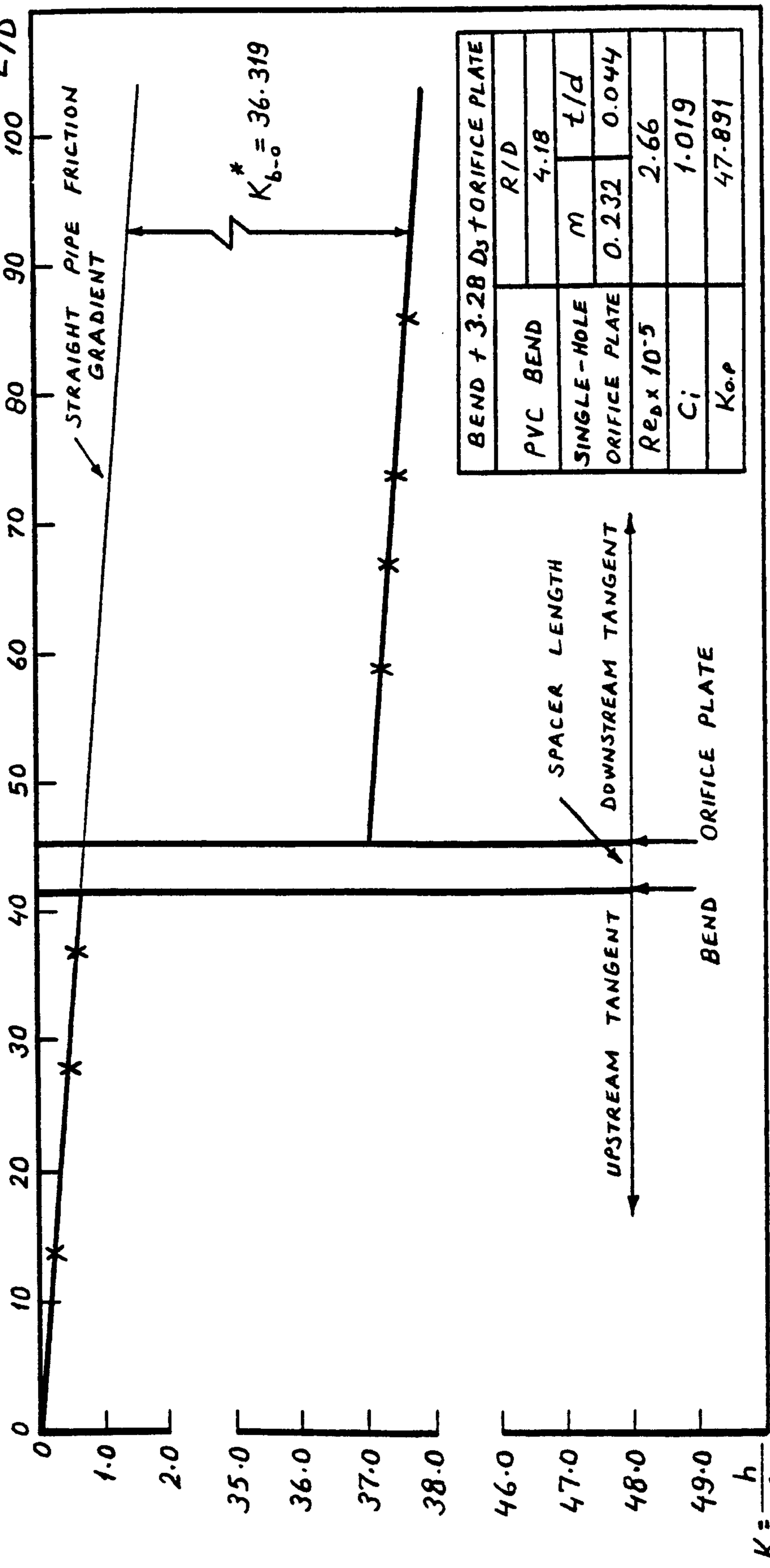

Fig. 183. Variation of system head loss coefficient with axial length

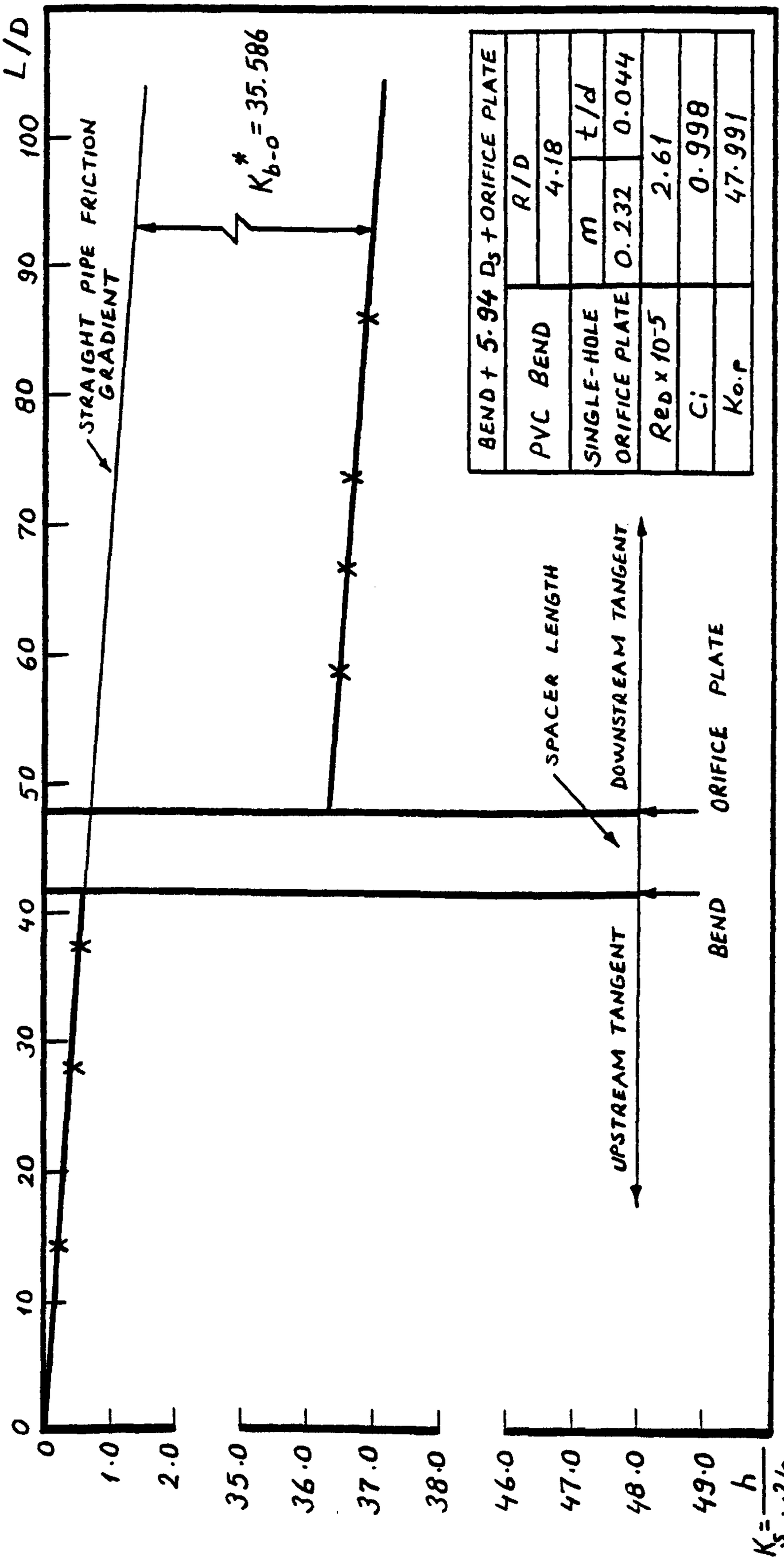

Fig. 184. Variation of system head loss coefficient with axial length

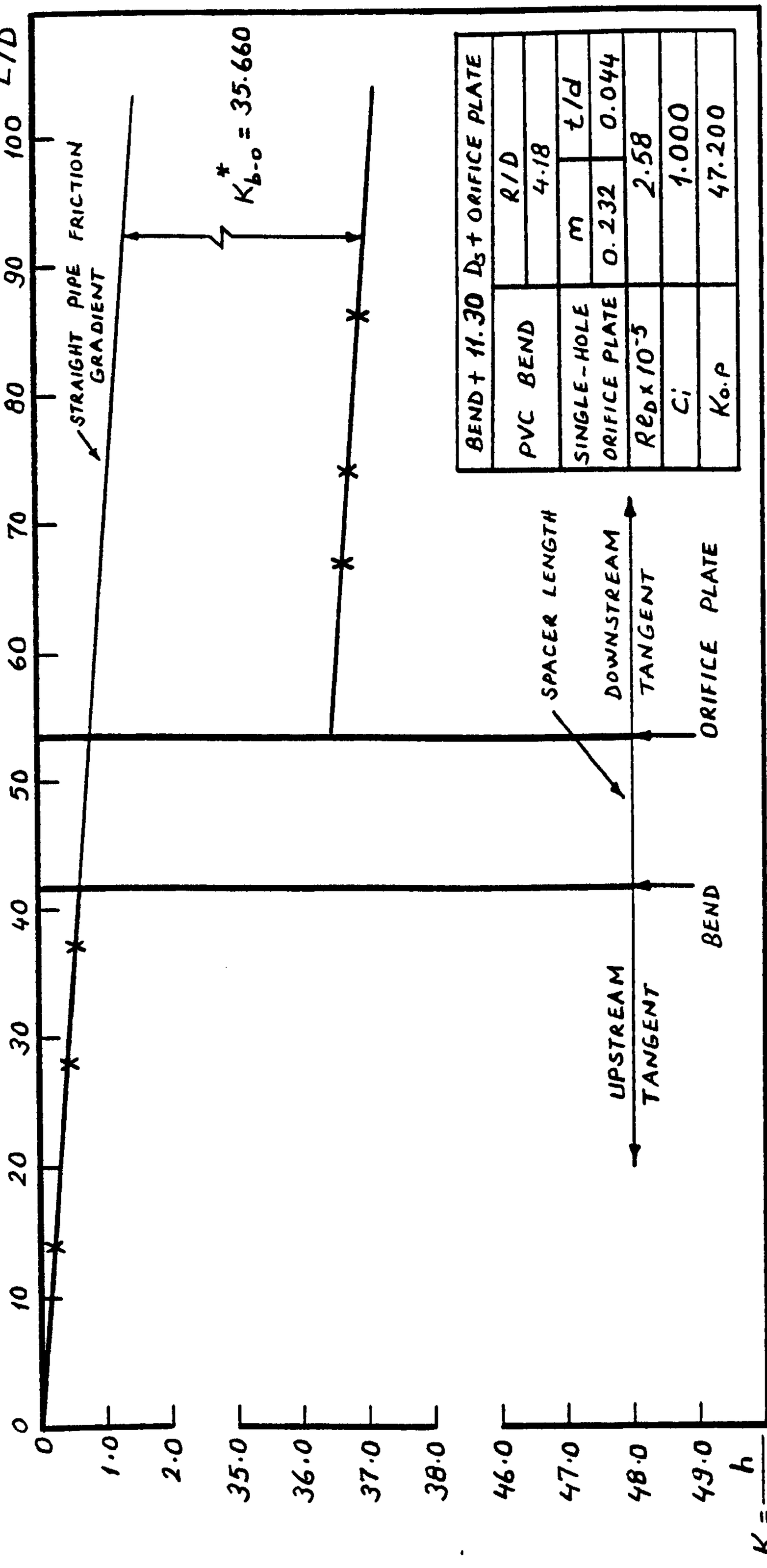

Fig. 185. Variation of system head loss coefficient with axial length

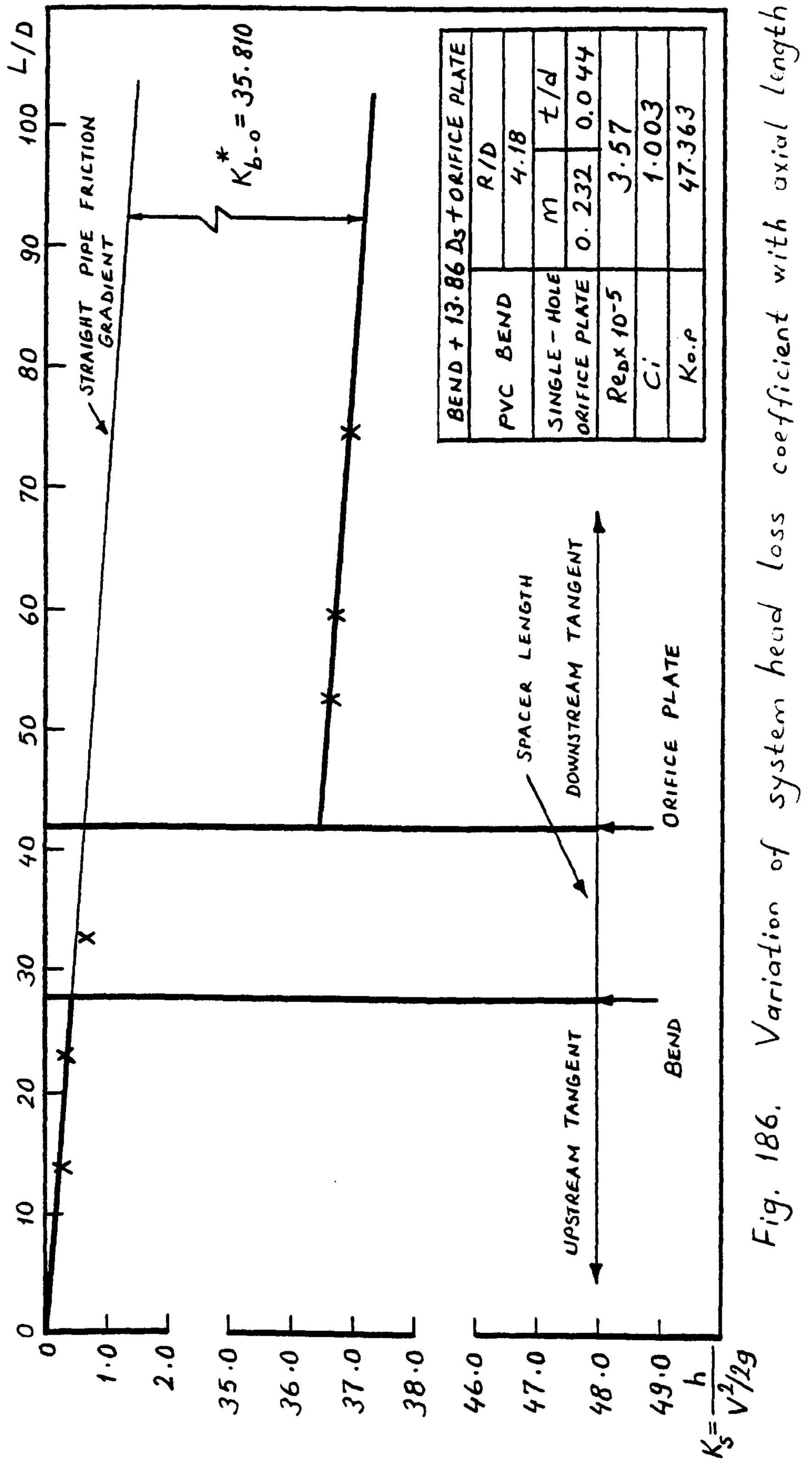

Fig. 186. Variation of system head loss coefficient with axial length

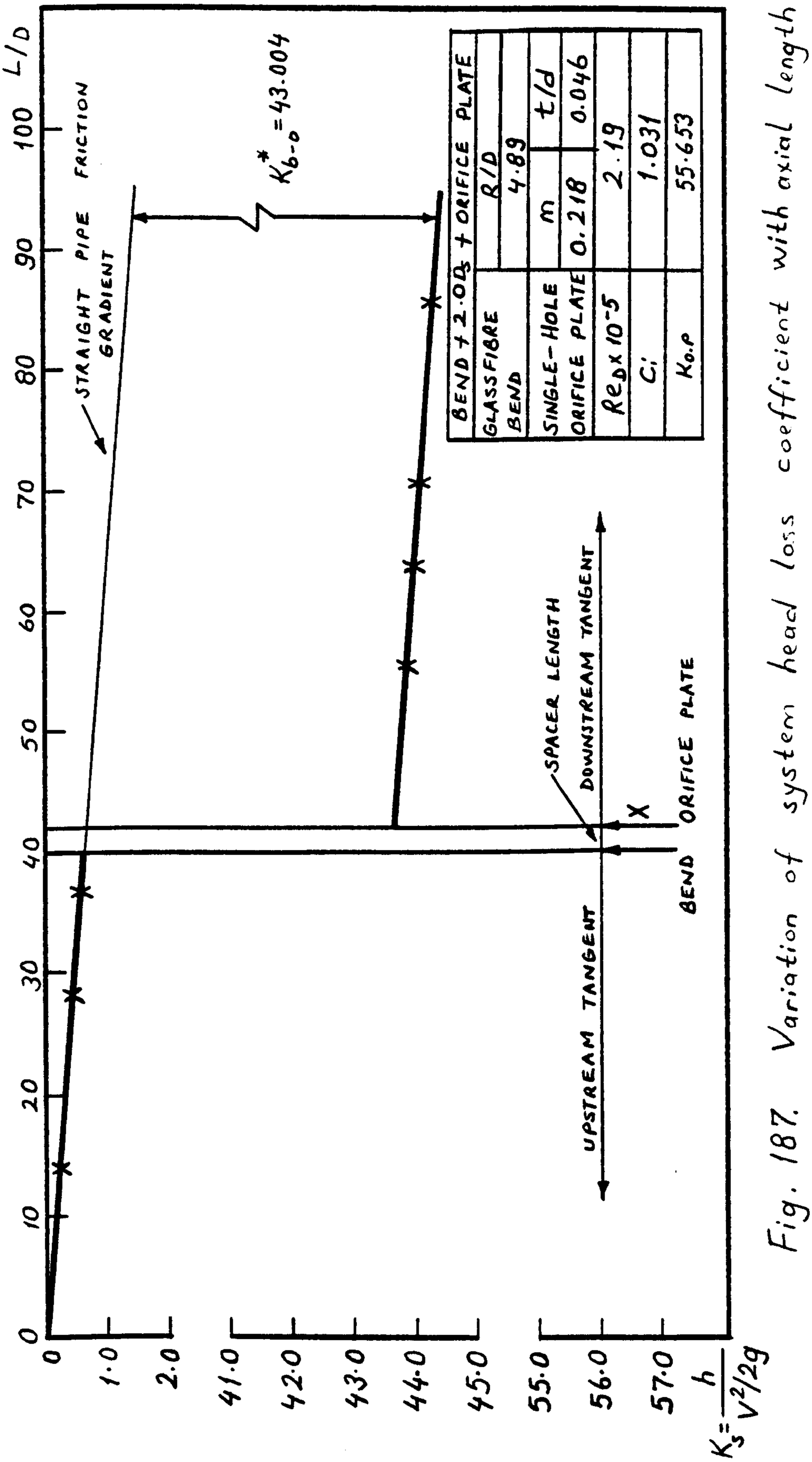

Fig. 187. Variation of system head loss coefficient with axial length

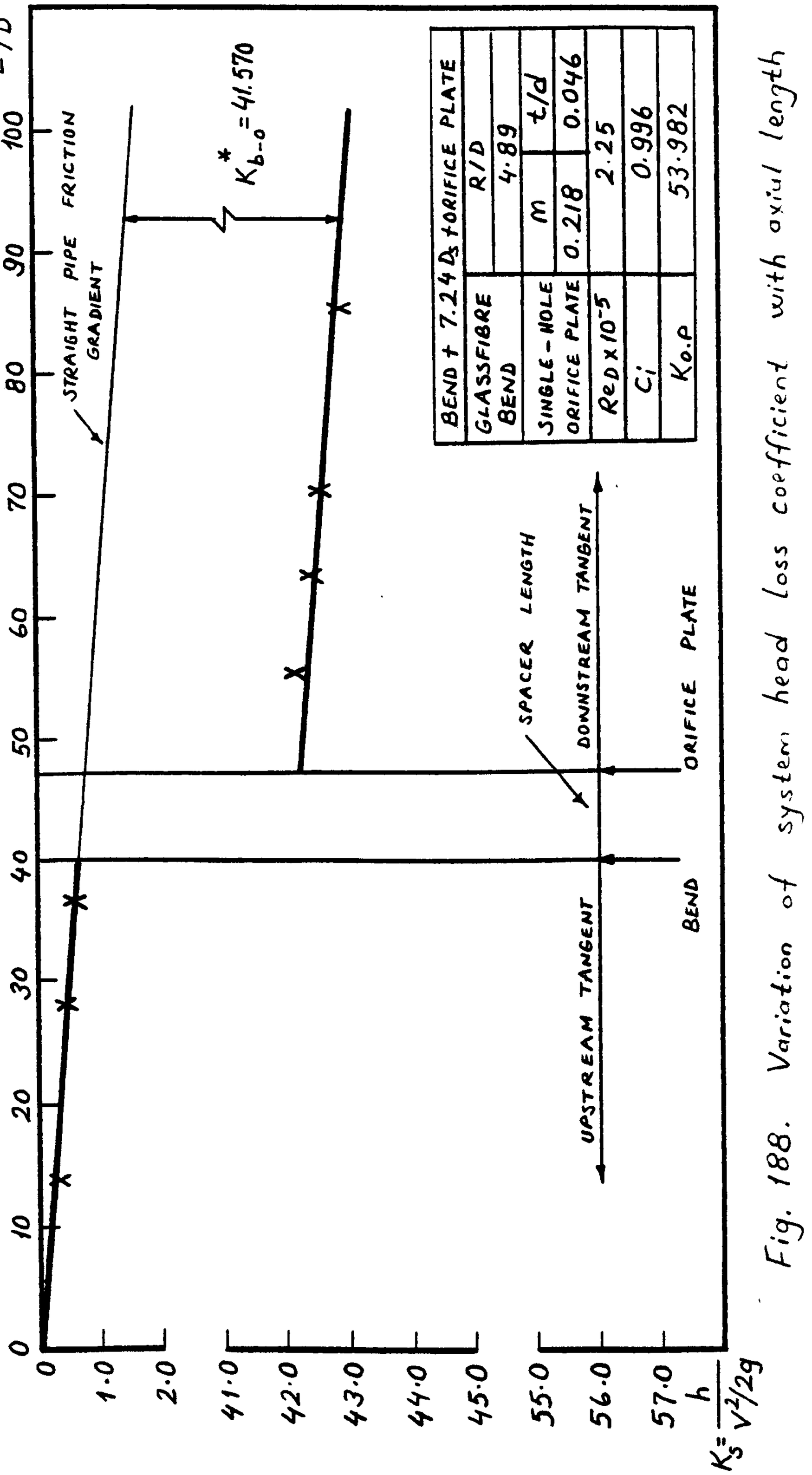

Fig. 188. Variation of system head loss coefficient with axial length

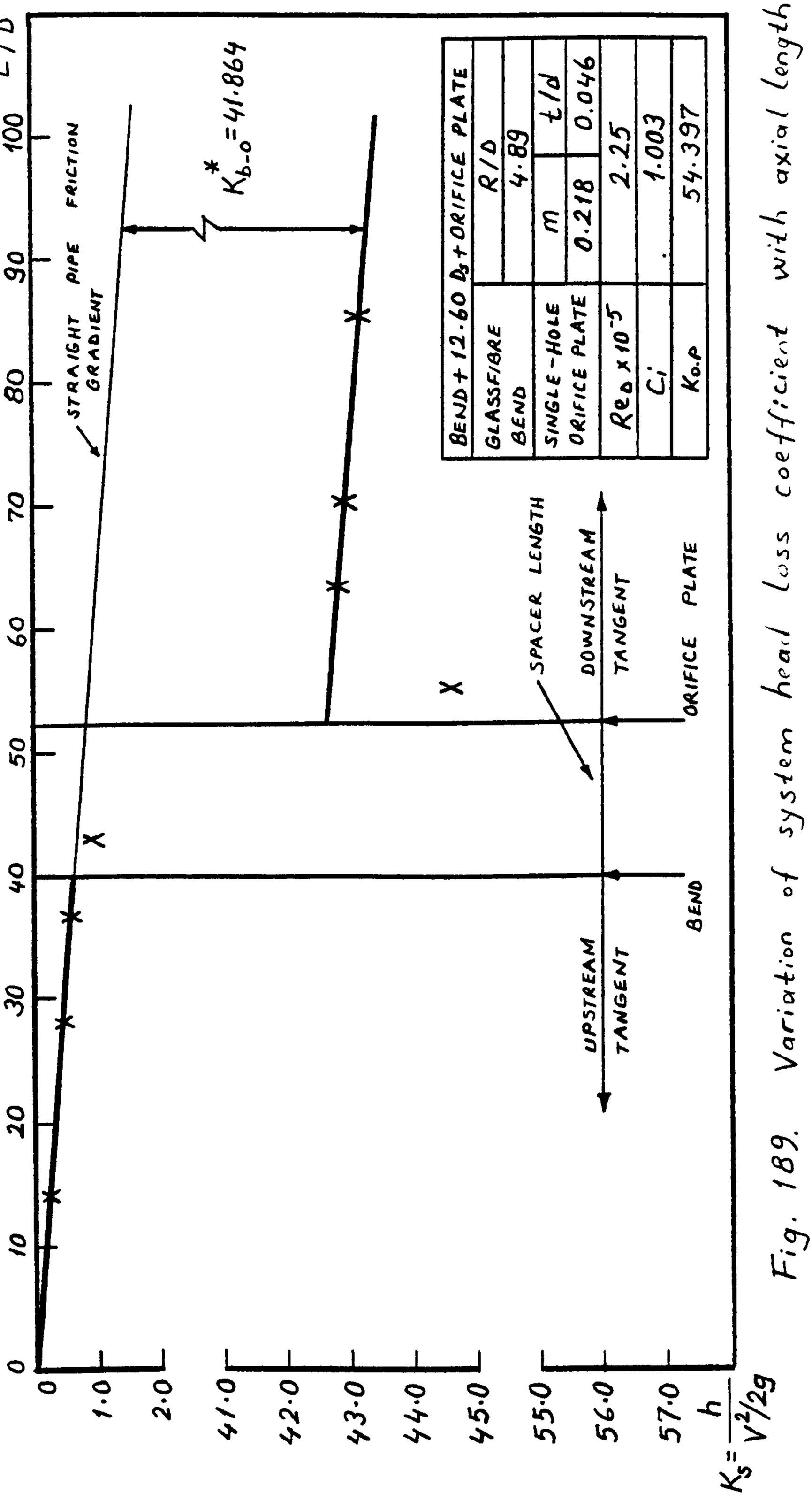

Fig. 189. Variation of system head loss coefficient with axial length

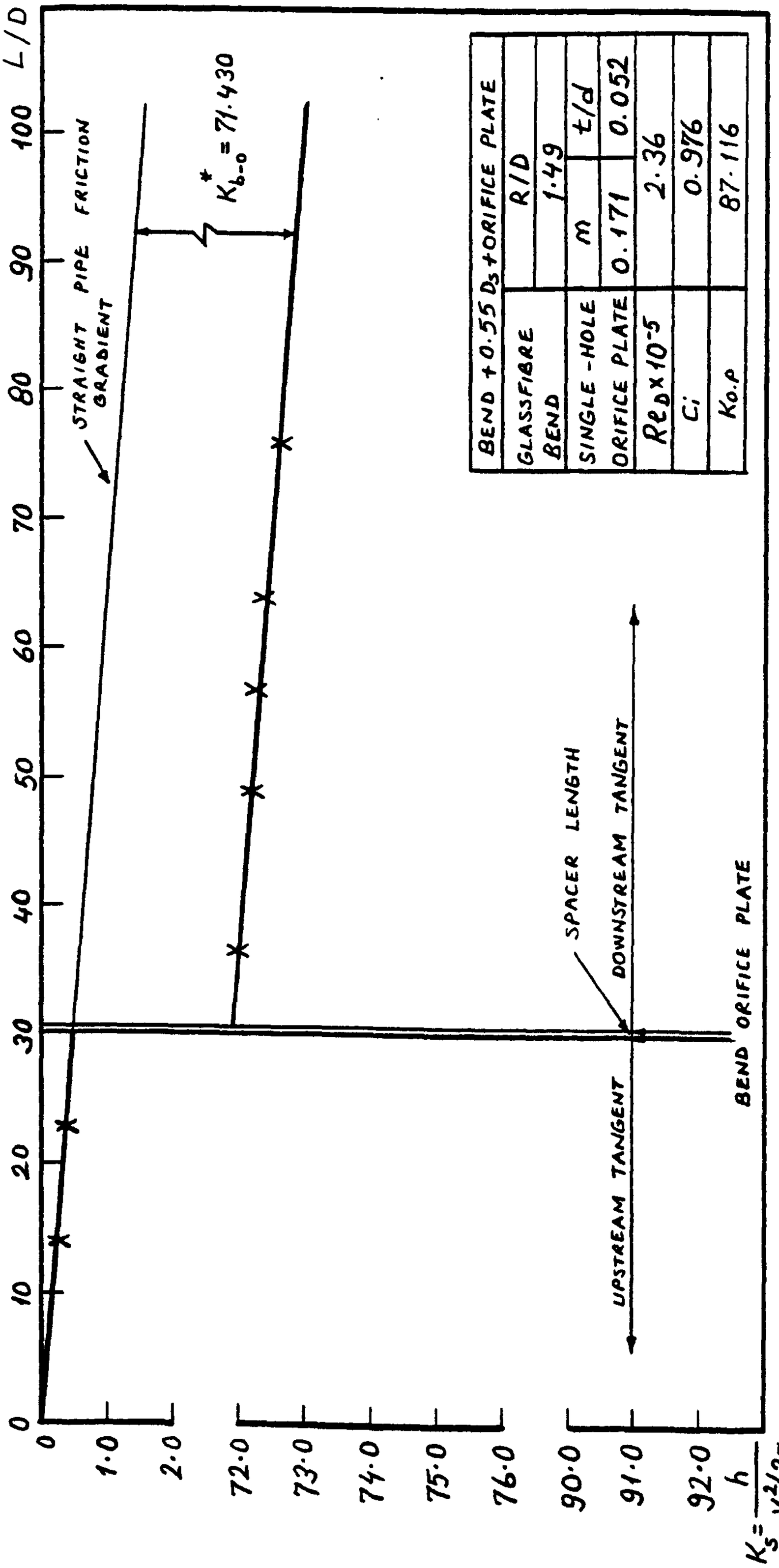

Fig. 190. Variation of system head loss coefficient with axial length

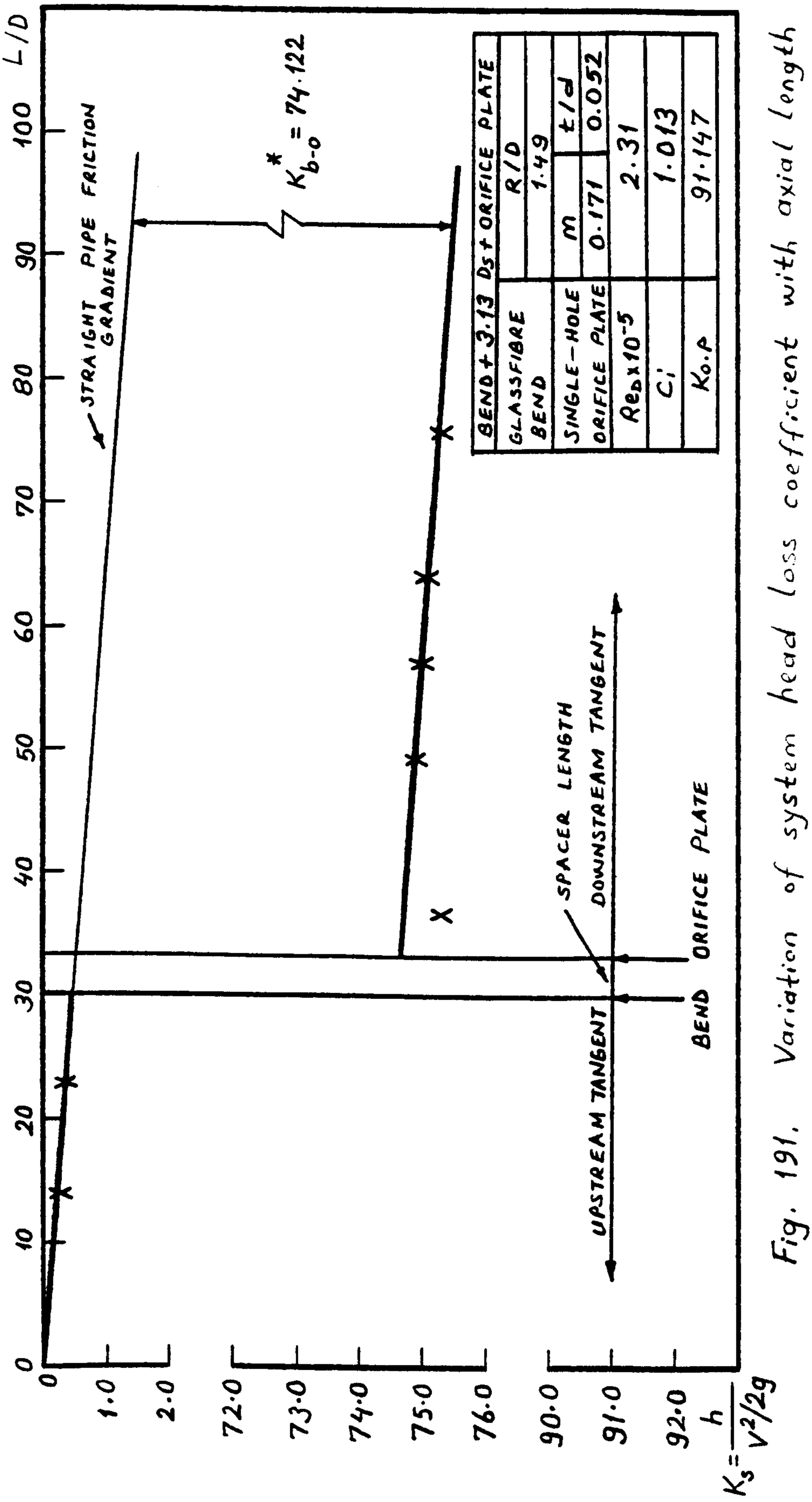

Fig. 191. Variation of system head loss coefficient with axial length

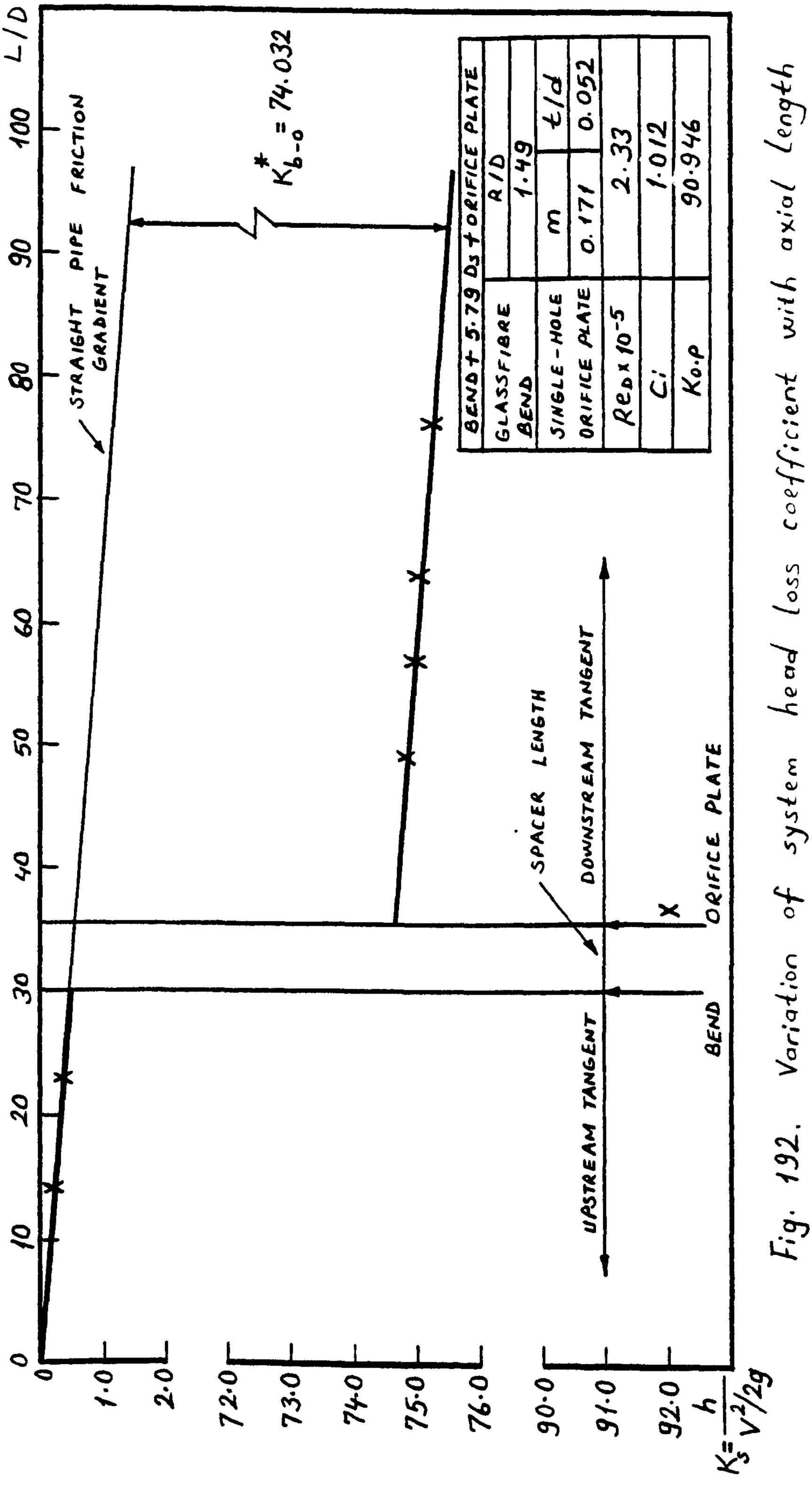

Fig. 192. Variation of system

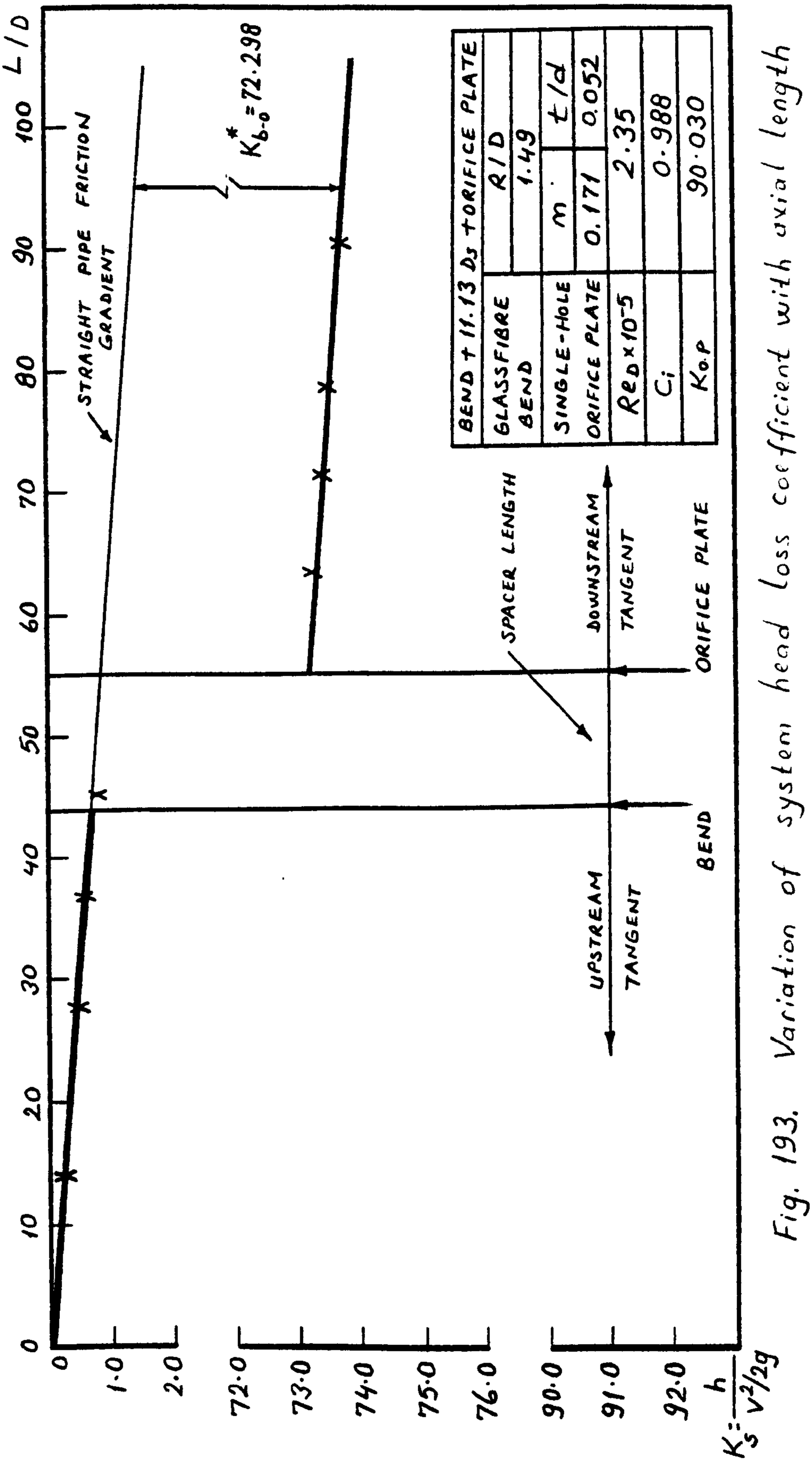

Fig. 193. Variation of system head loss coefficient with axial length

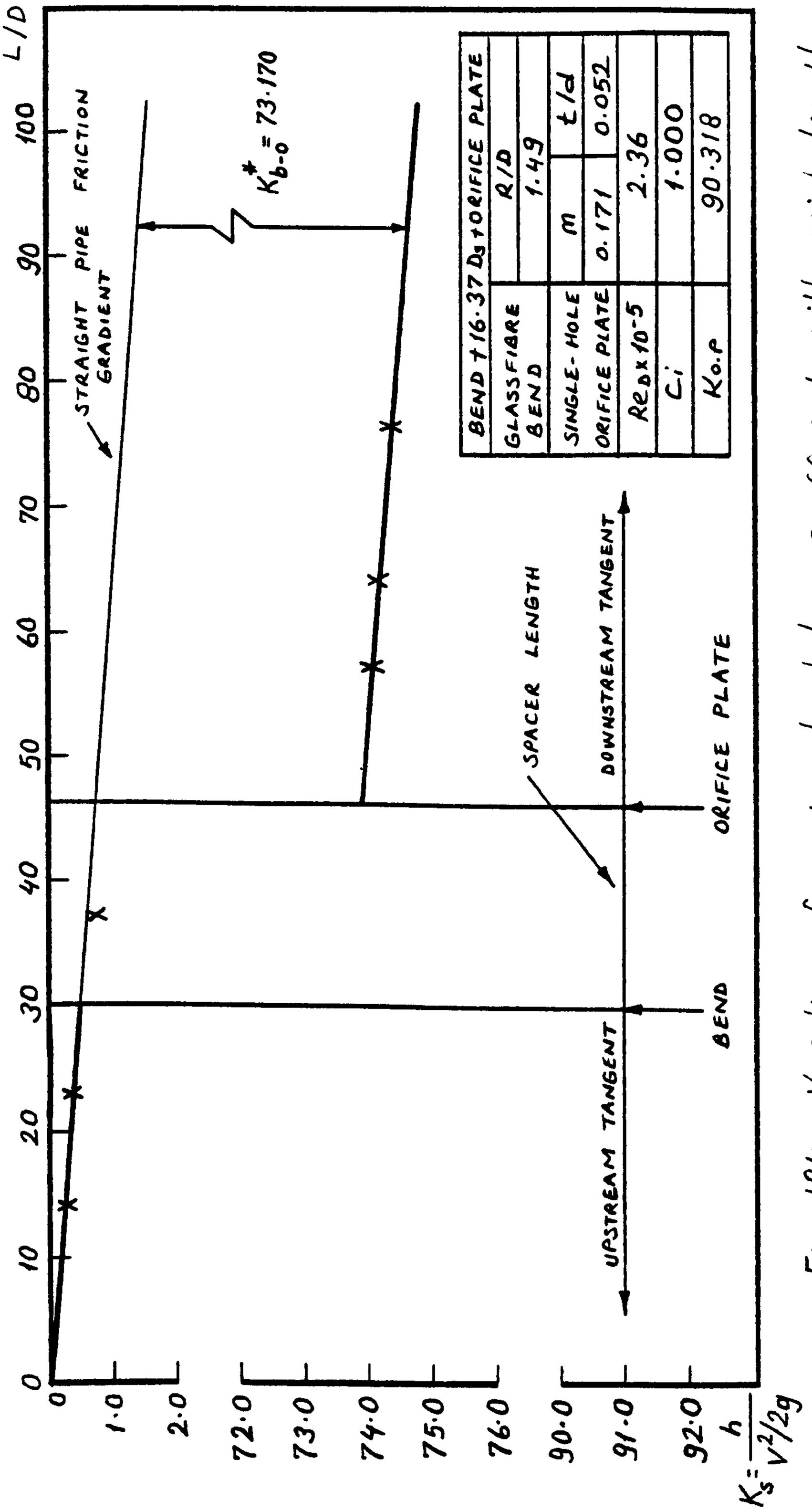

Fig. 194. Variation of system head loss coefficient with axial length

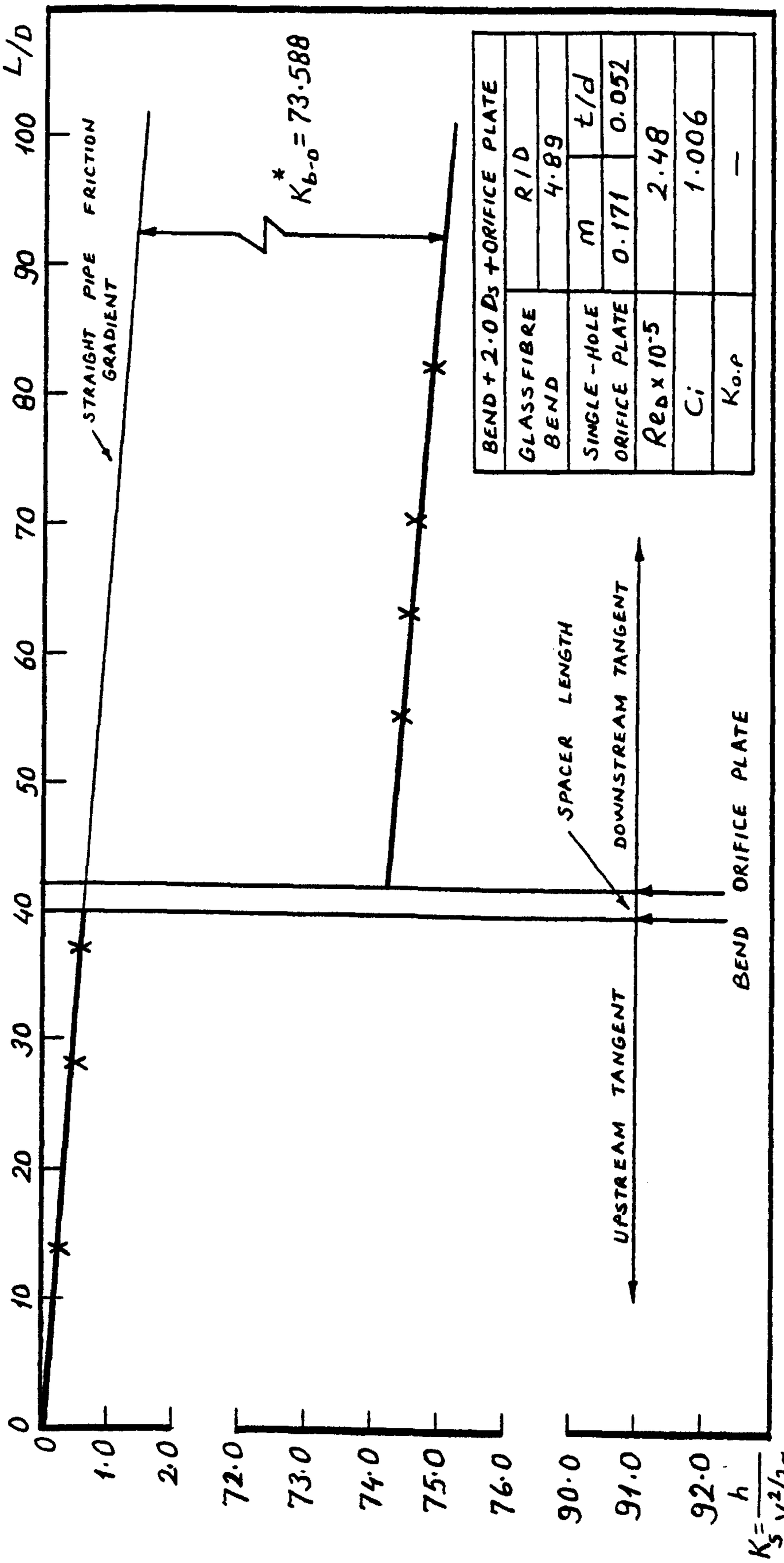

Fig. 195. Variation of system head loss coefficient with axial length

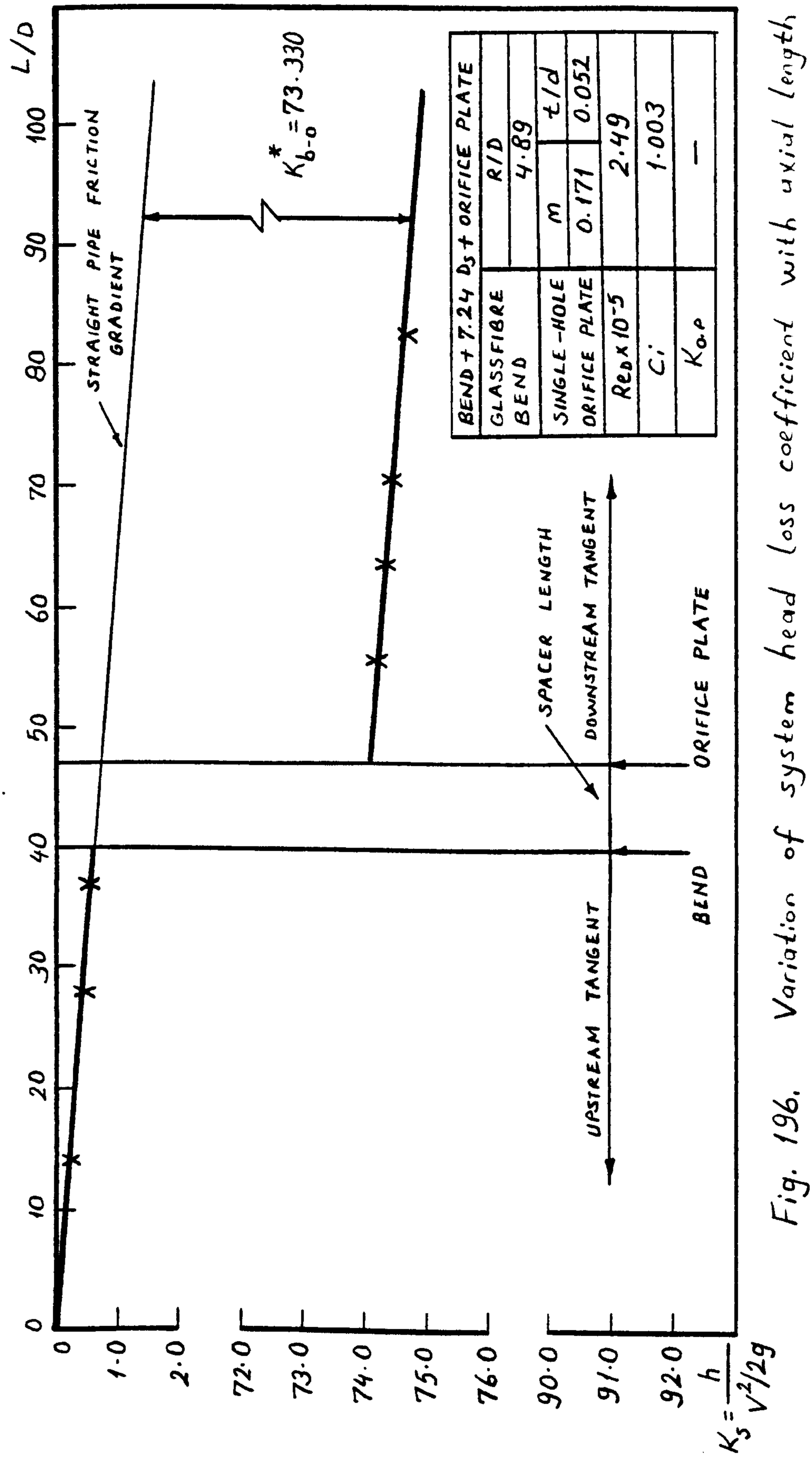

Fig. 196. Variation of system head loss coefficient with axial length

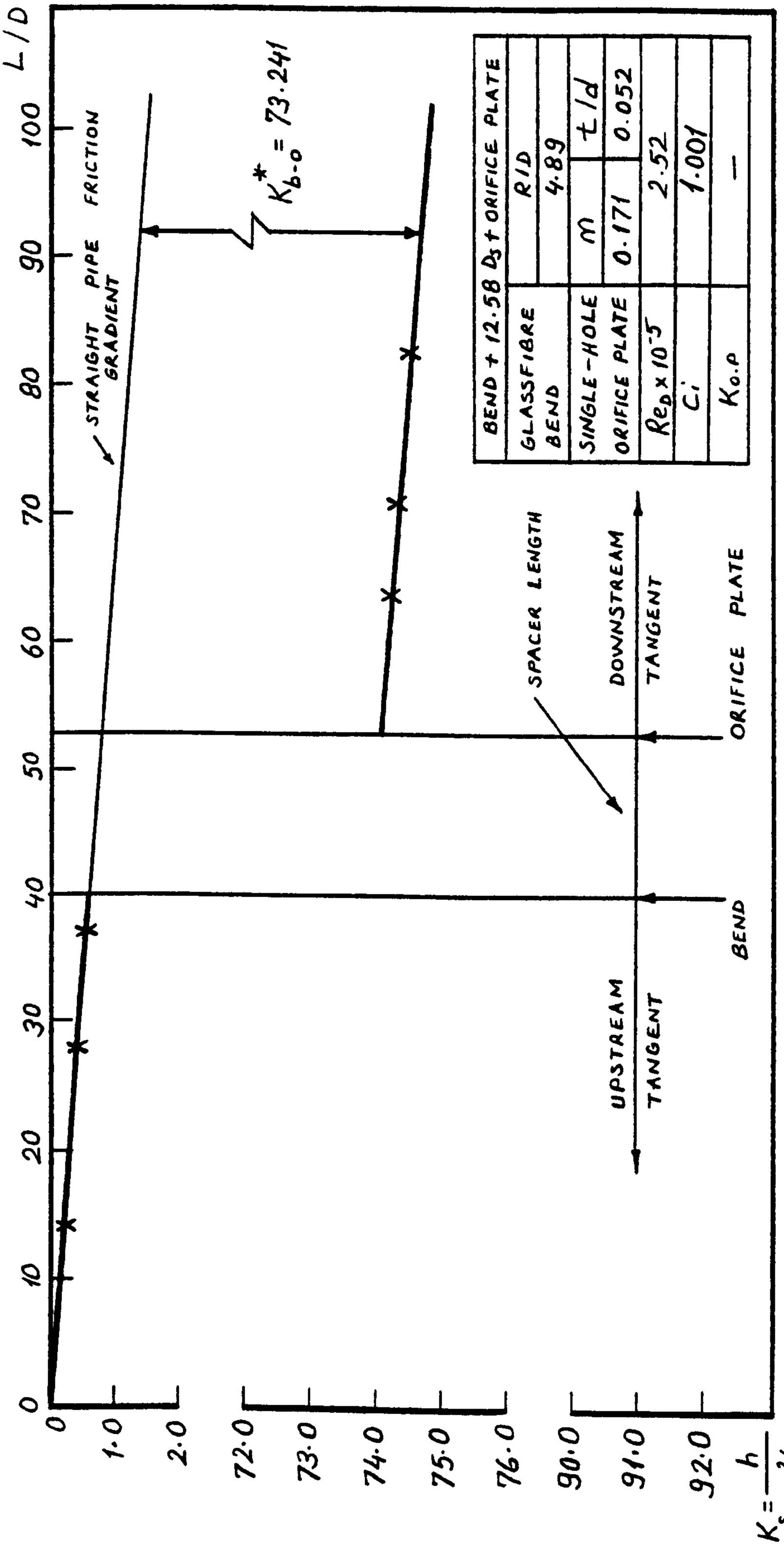

Fig. 197. Variation of system head loss coefficient with axial length

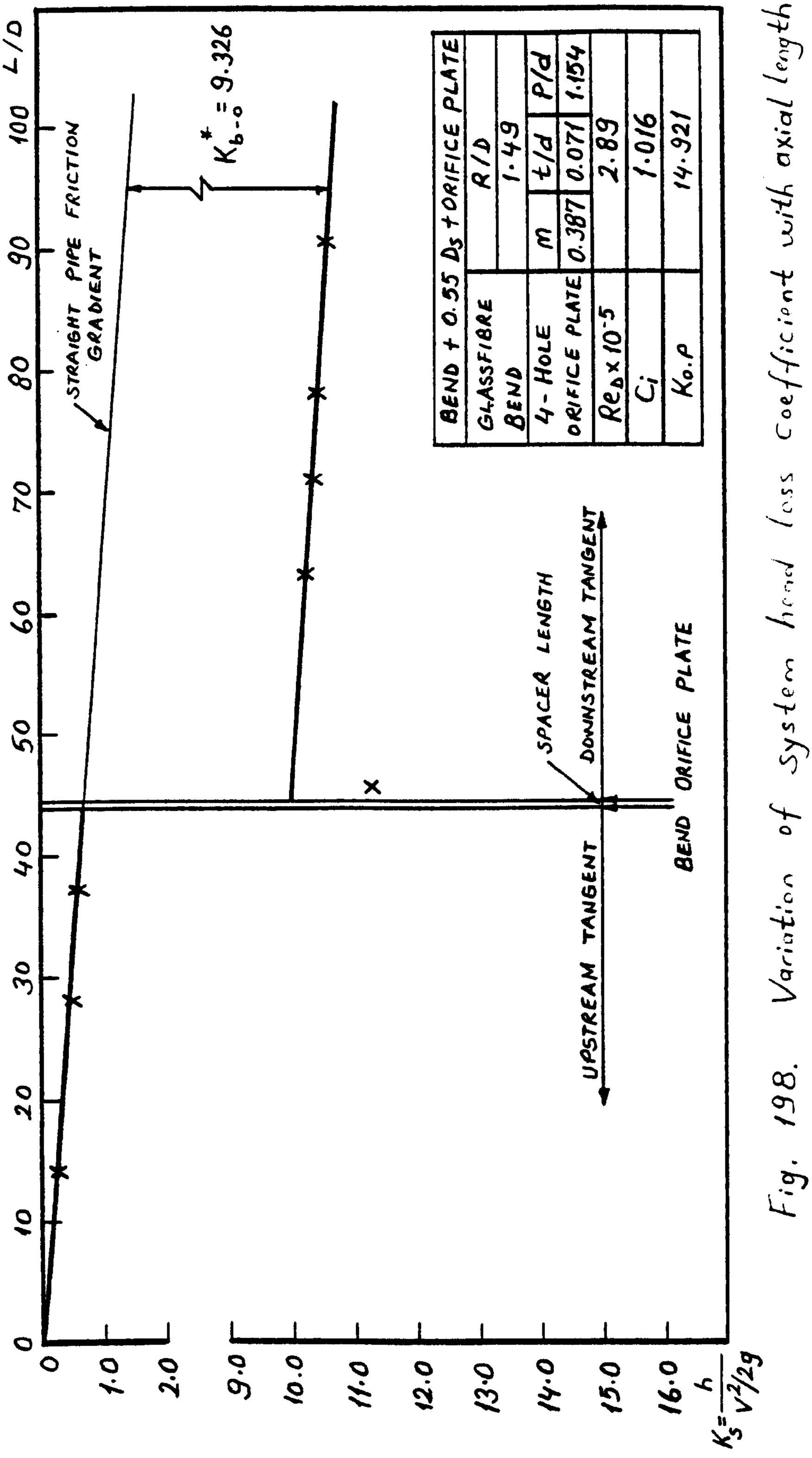

Fig. 198. Variation of System Head loss Coefficient with axial length

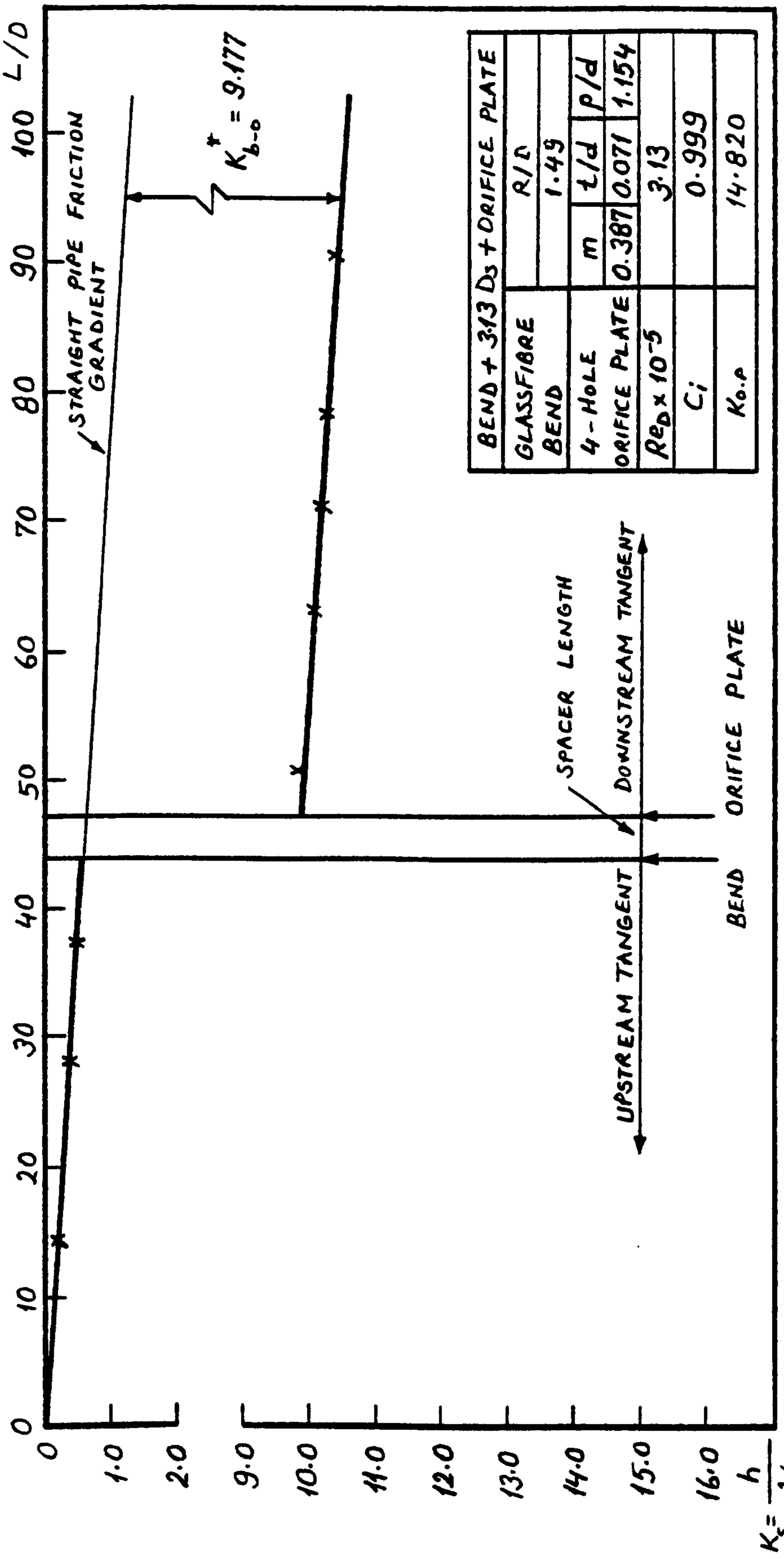

Fig. 199. Variation of system head loss coefficient with axial length

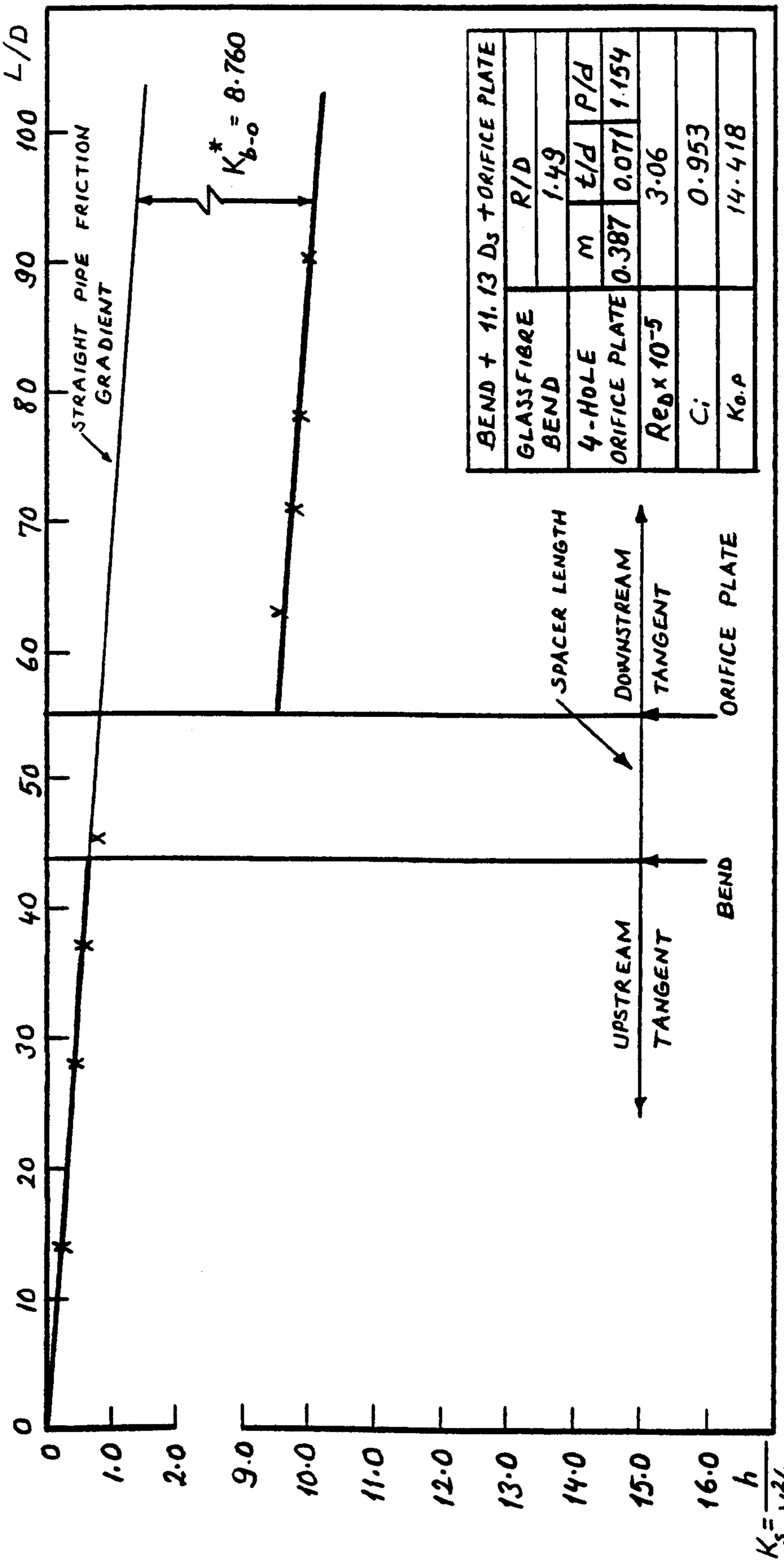

Fig. 200. Variation of system head loss coefficient with axial length

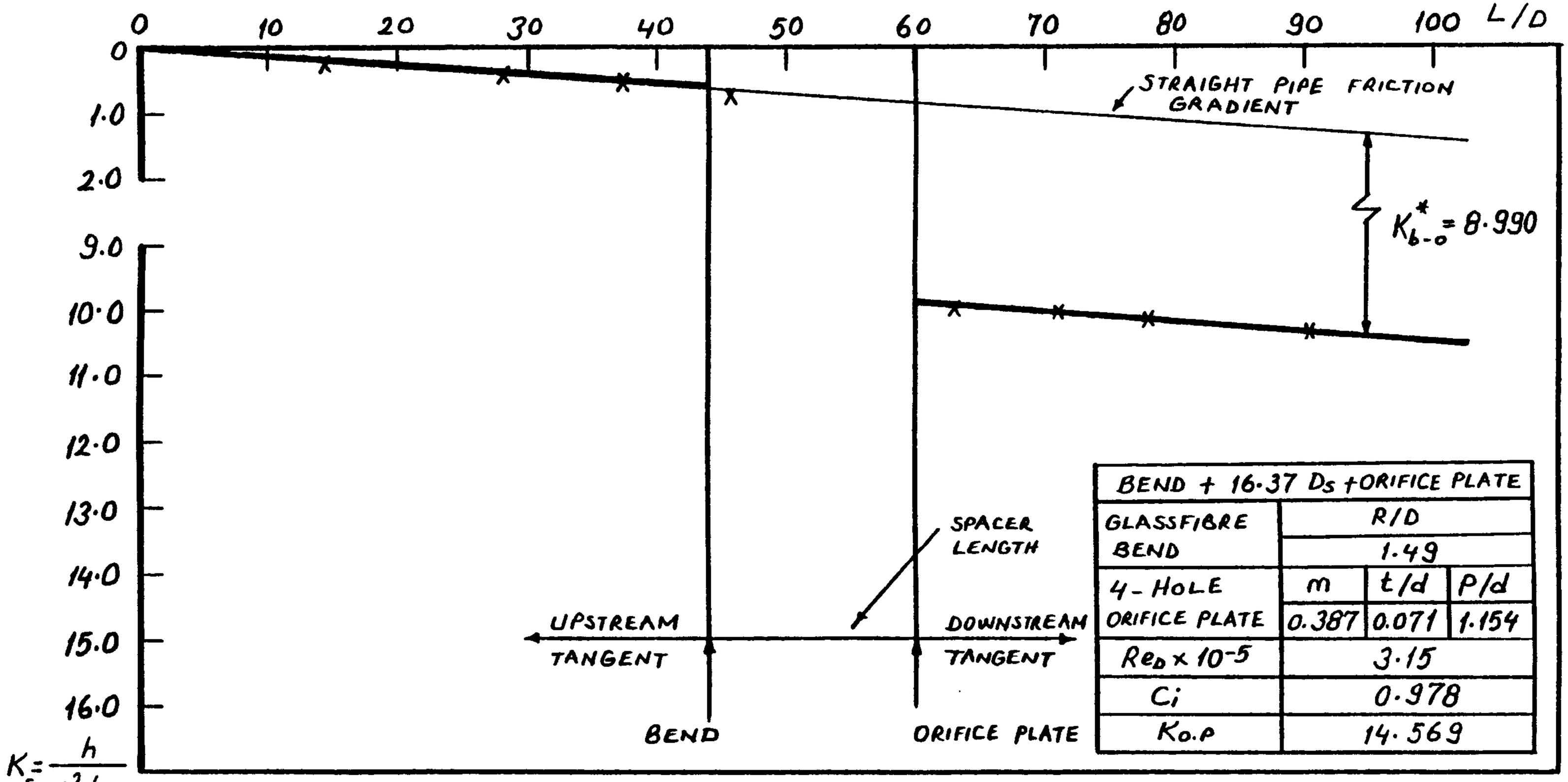

BEND + 16·37 D_s + ORIFICE PLATE			
GLASSFIBRE BEND	R/D		
	1.49		
4-HOLE ORIFICE PLATE	m	t/d	P/d
	0.387	0.071	1.154
$Re_D \times 10^{-5}$	3·15		
C_i	0·978		
$K_{o.p}$	14·569		

Fig. 201. Variation of system head loss coefficient with axial length

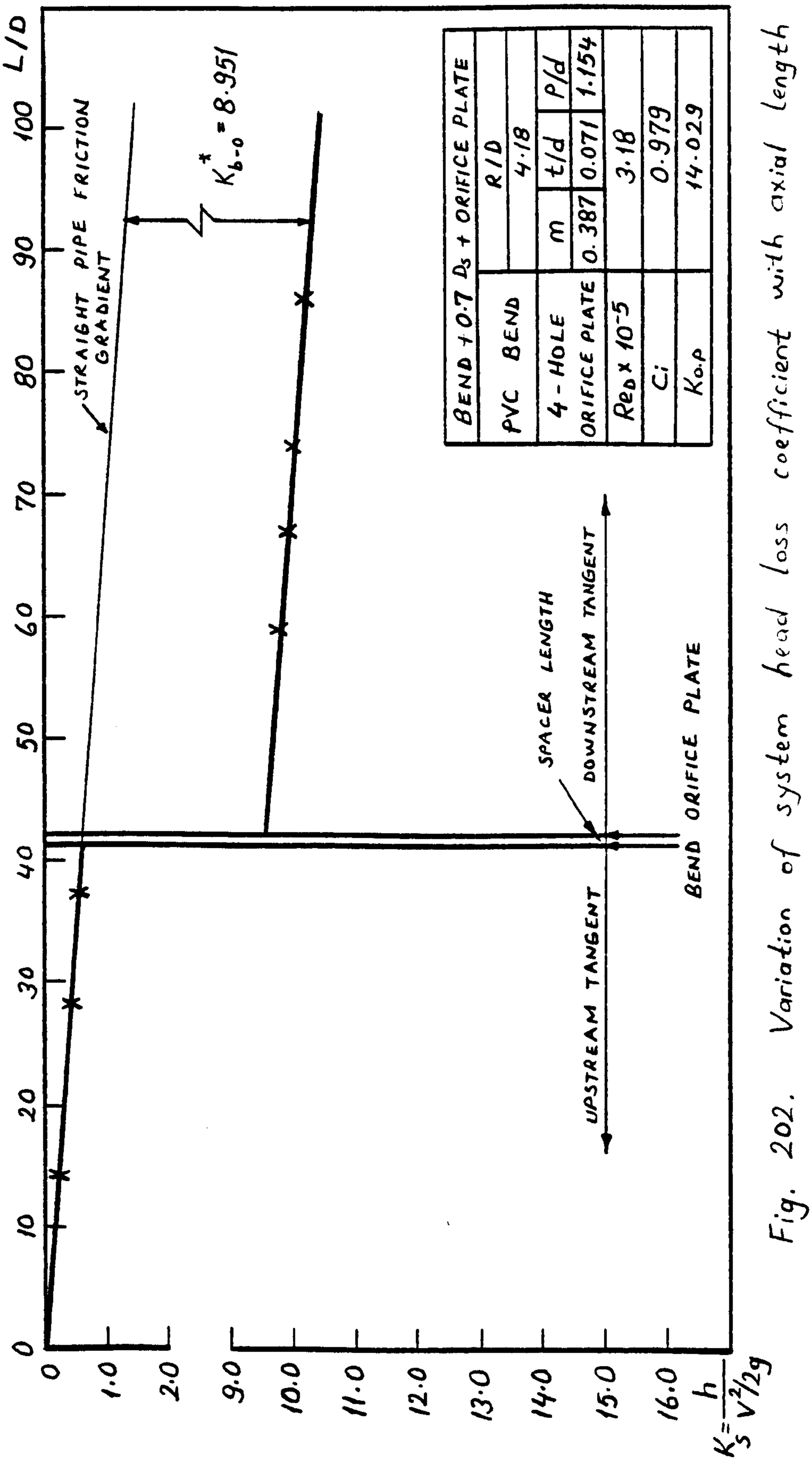

Fig. 202. Variation of system head loss coefficient with axial length

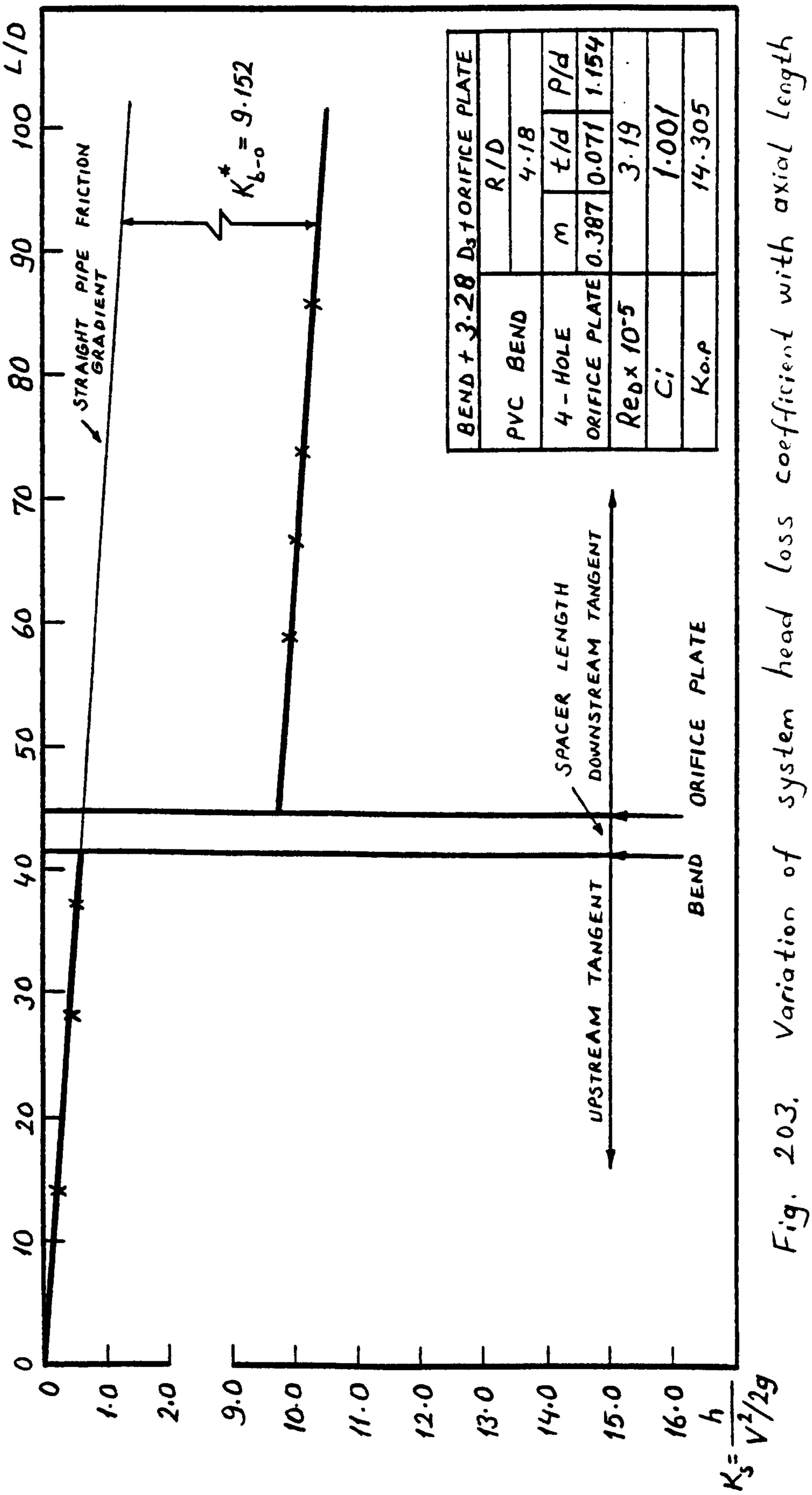

Fig. 203. Variation of system head loss coefficient with axial length

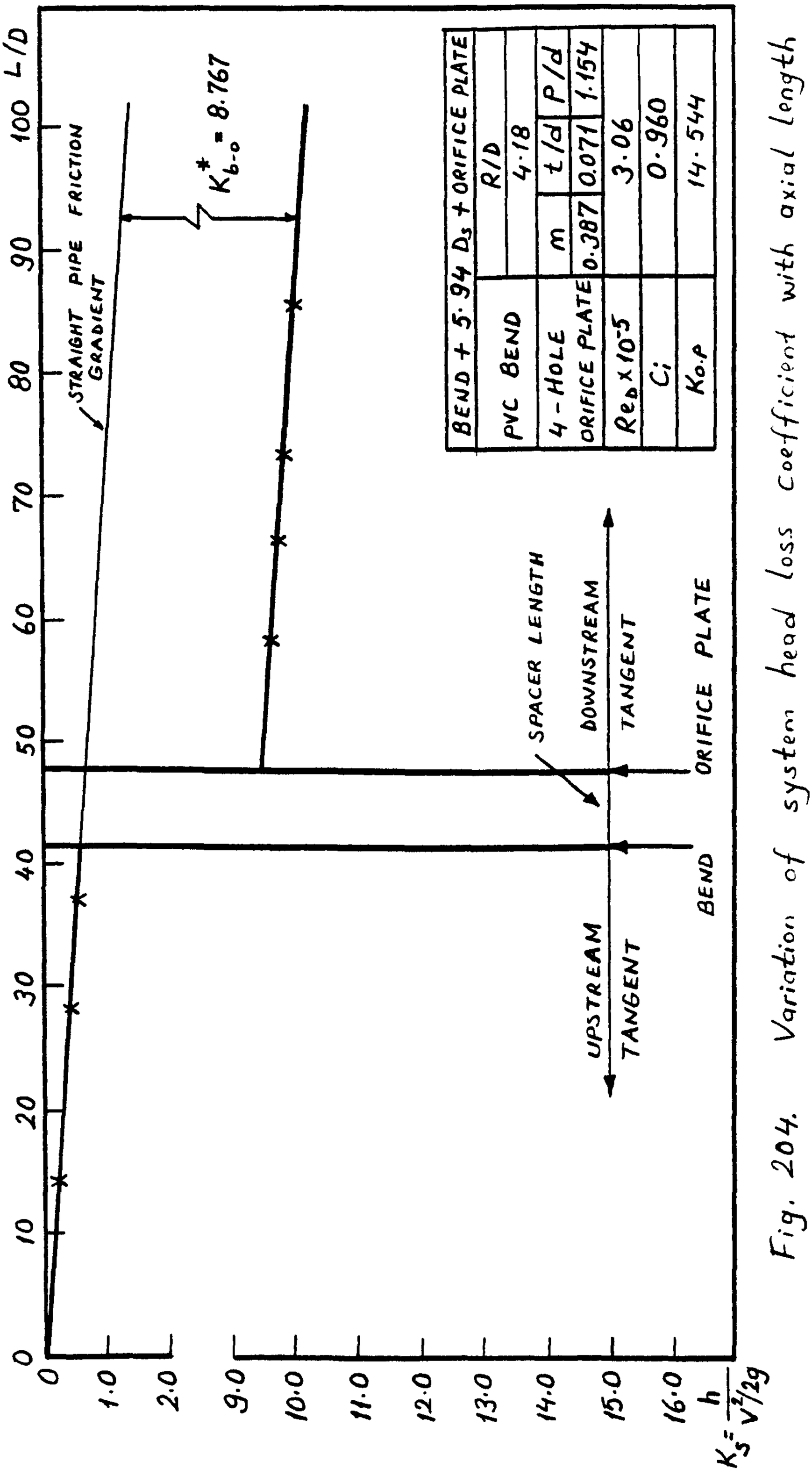

Fig. 204. Variation of system head loss coefficient with axial length

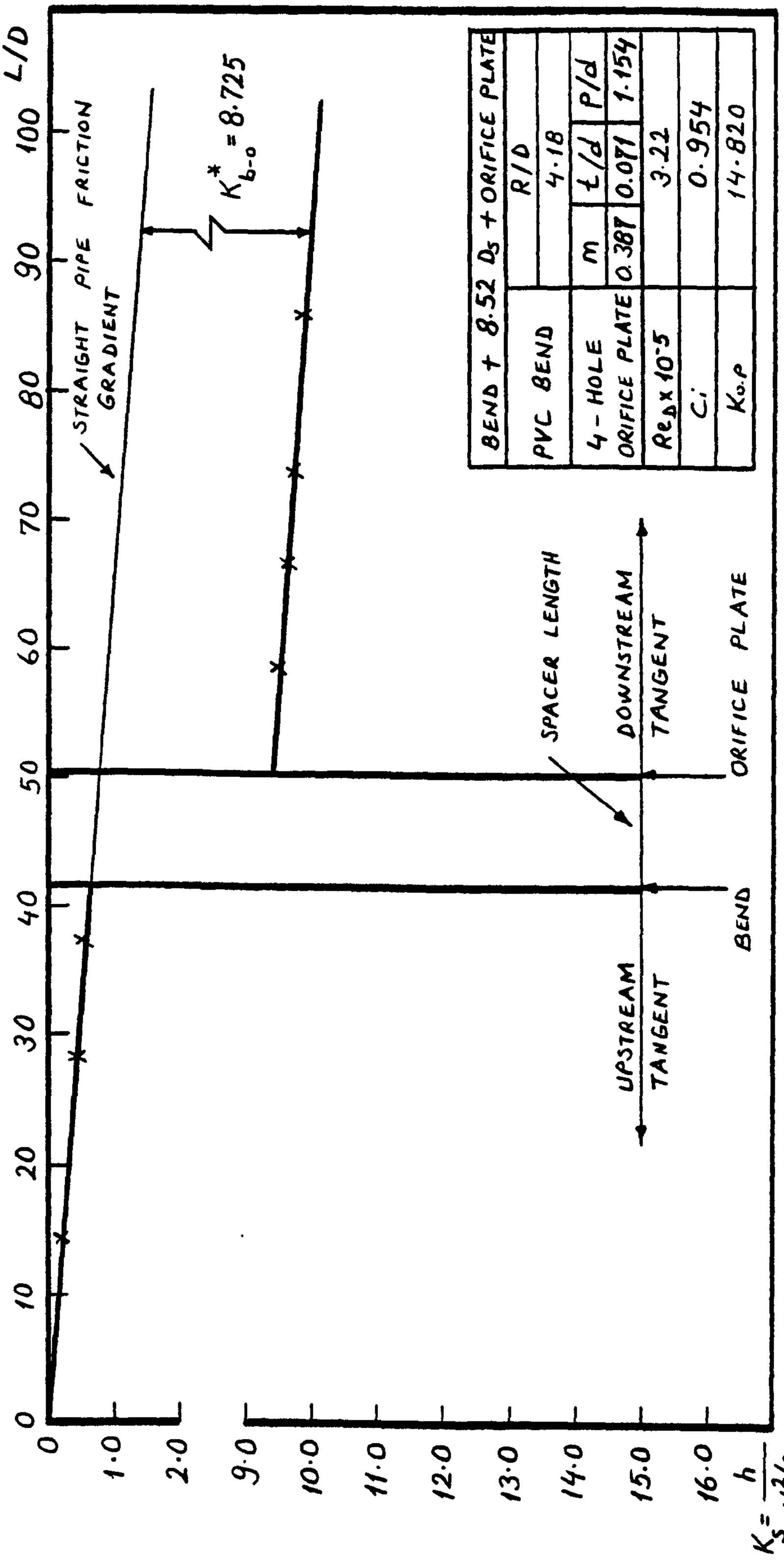

Fig. 205. Variation of system head loss coefficient with

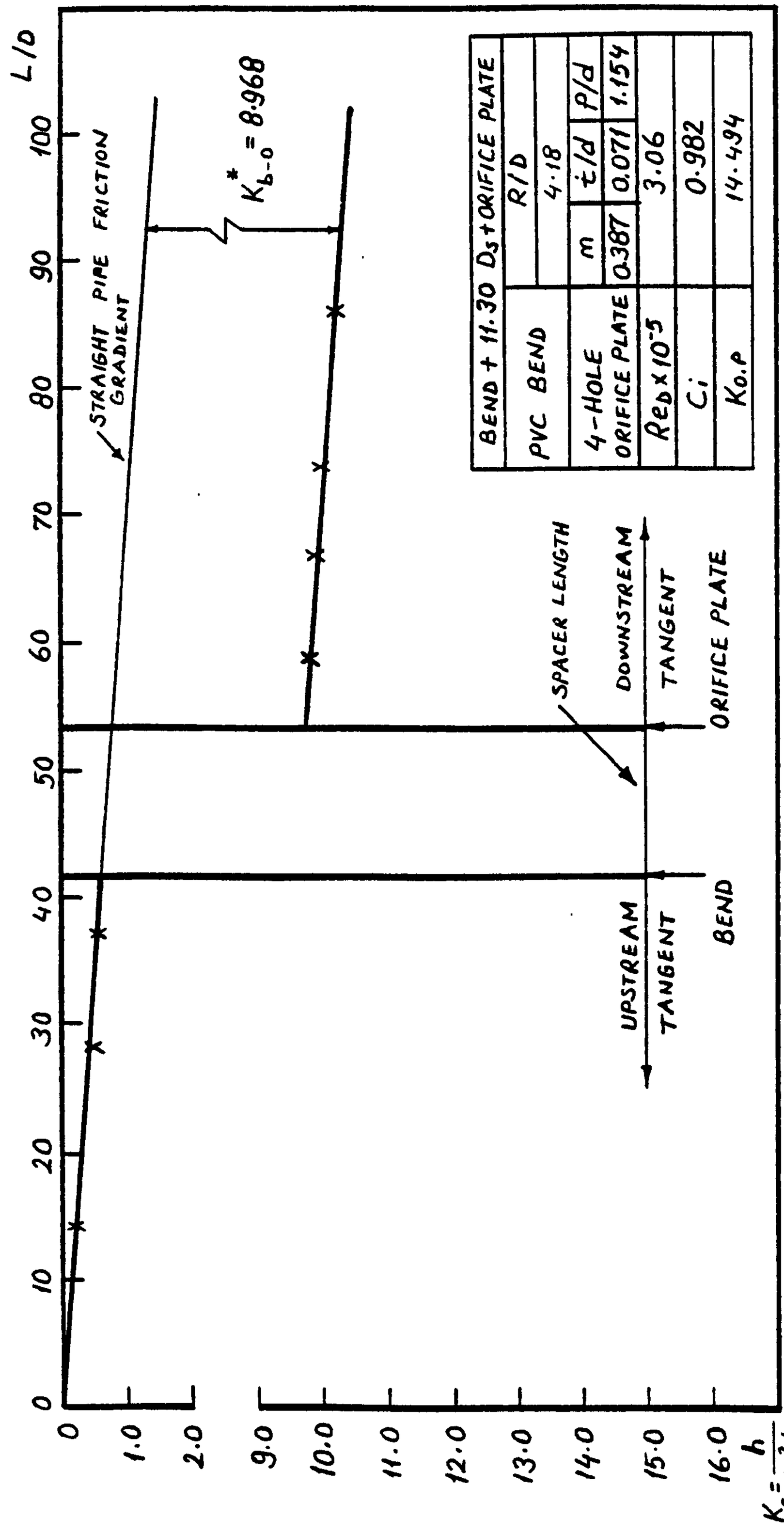

Fig. 206. Variation of system head loss coefficient with axial length

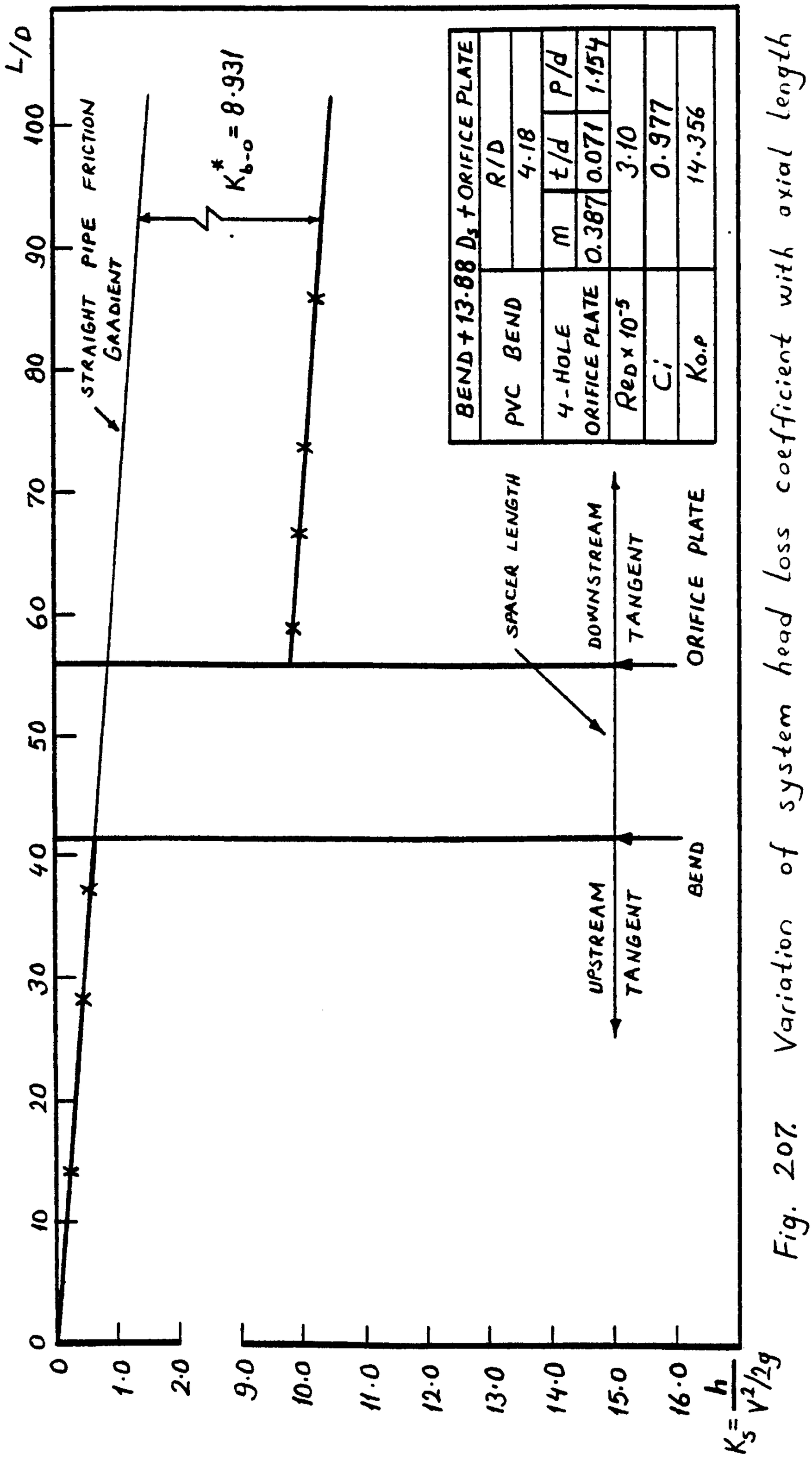

Fig. 207. Variation of system head loss coefficient with axial length

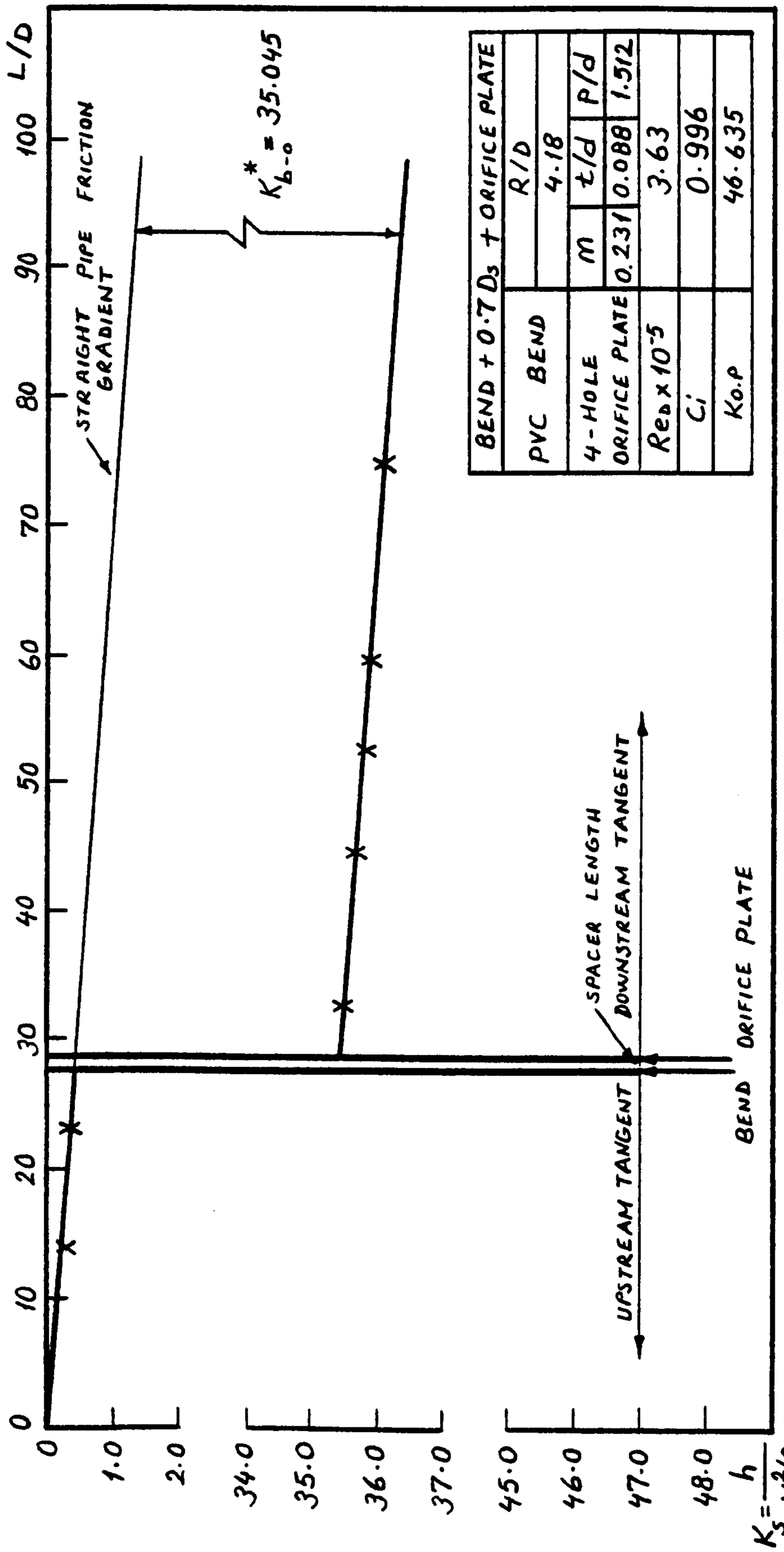

Fig. 208. Variation of system head Loss coefficient with axial length

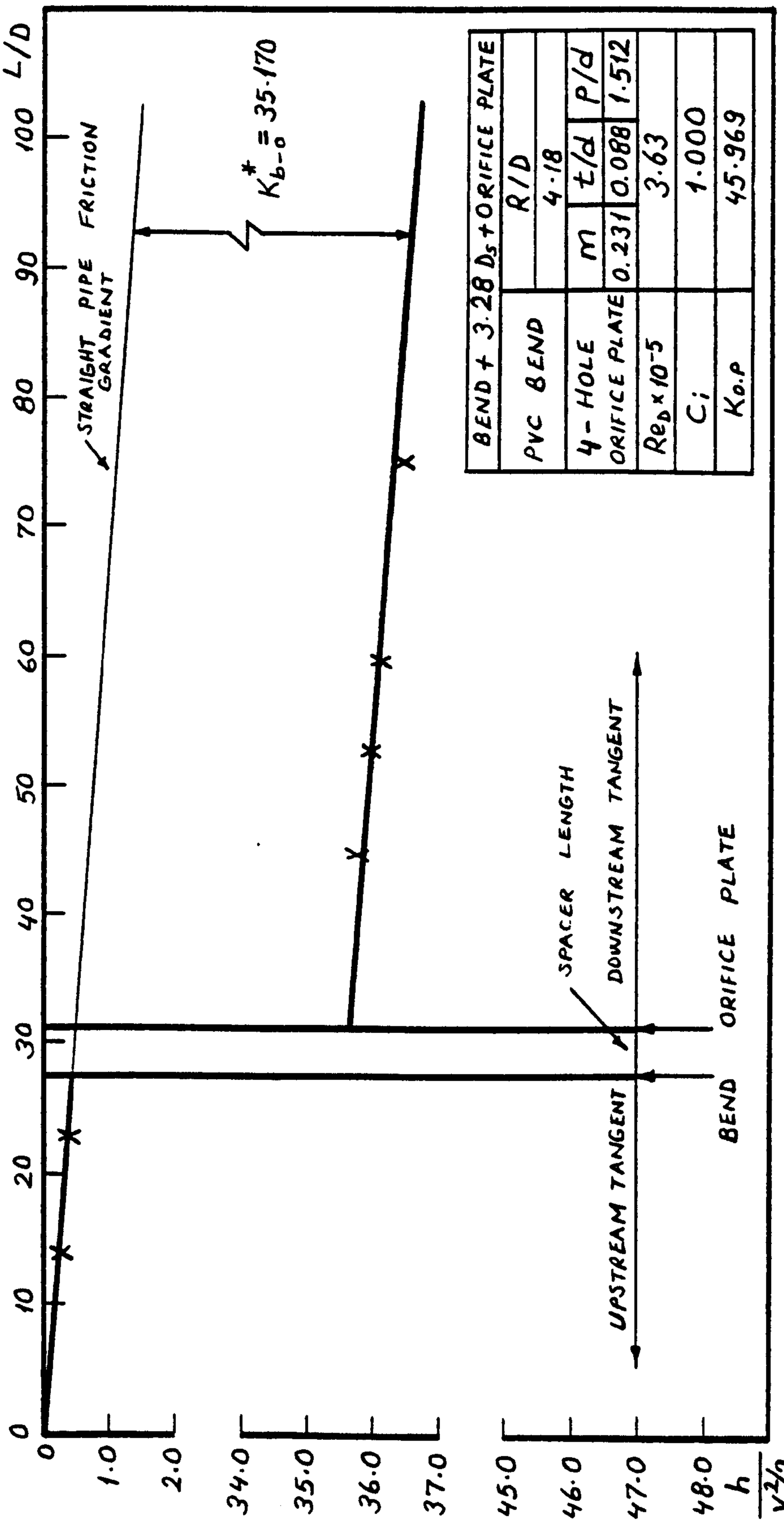

Fig. 209. Variation of system head loss coefficient with axial length

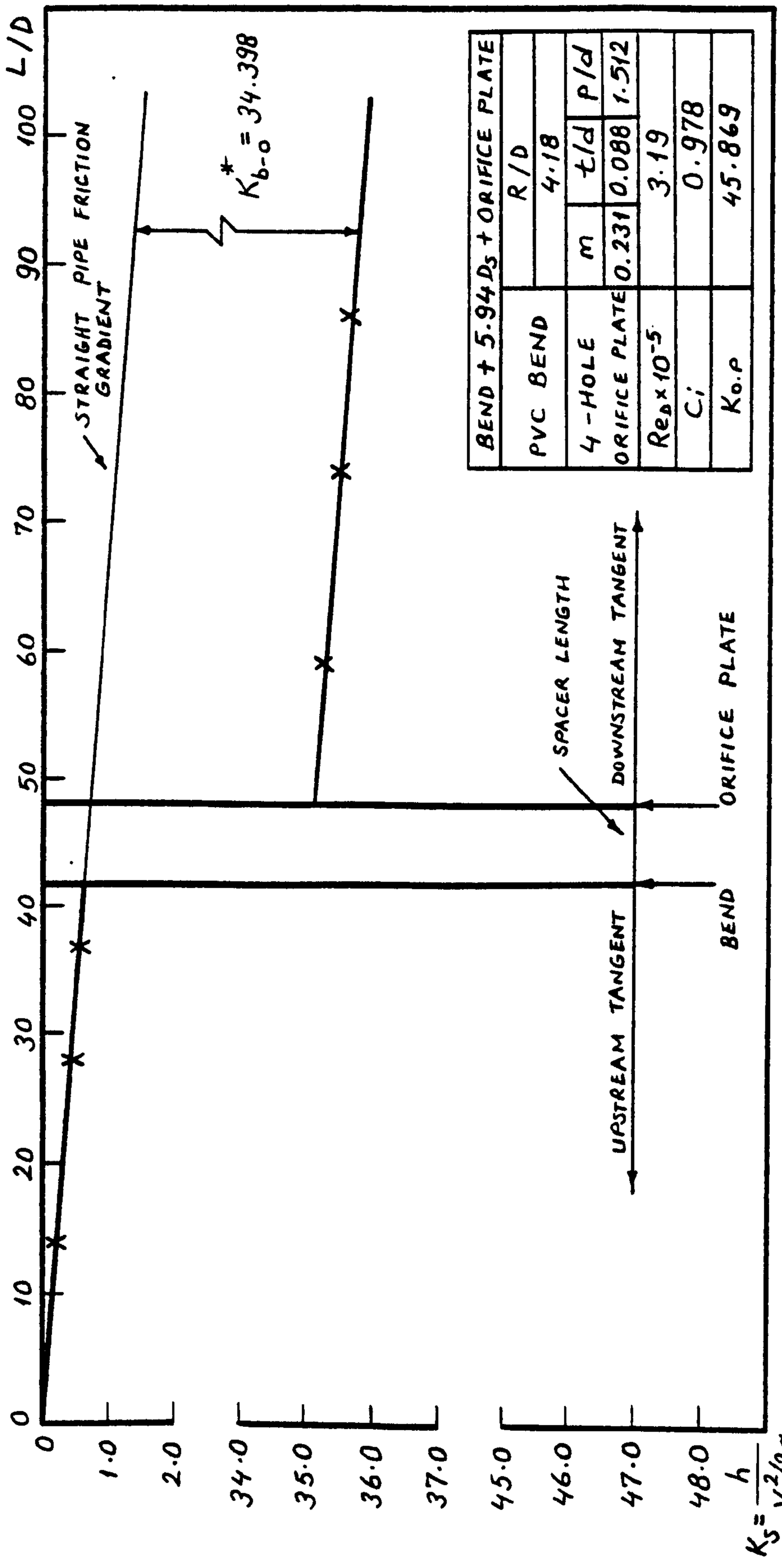

Fig. 210. Variation of system head loss coefficient with axial length

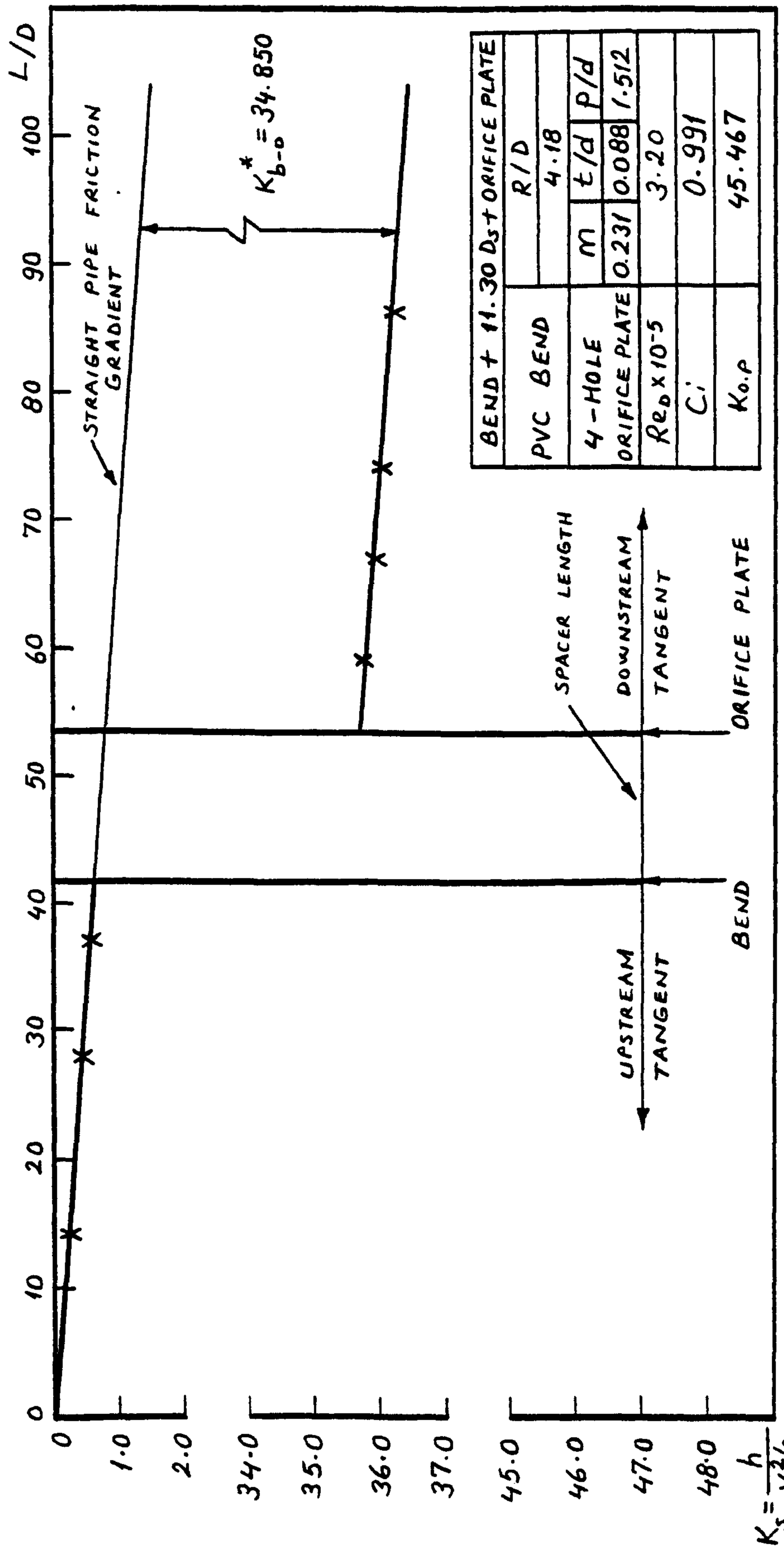

Fig. 211. Variation of system head loss coefficient with axial length

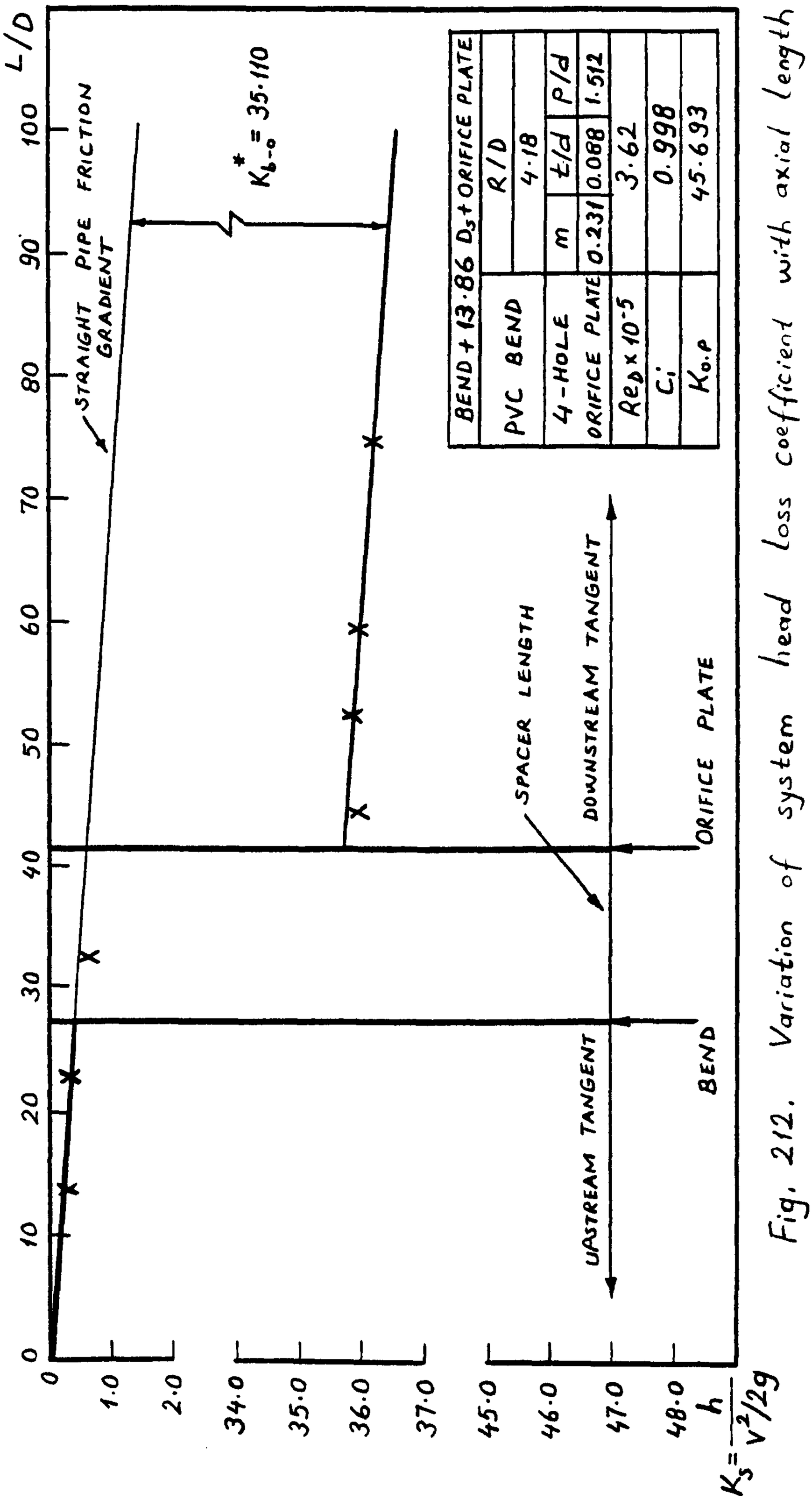

Fig. 212. Variation of system head loss coefficient with axial length

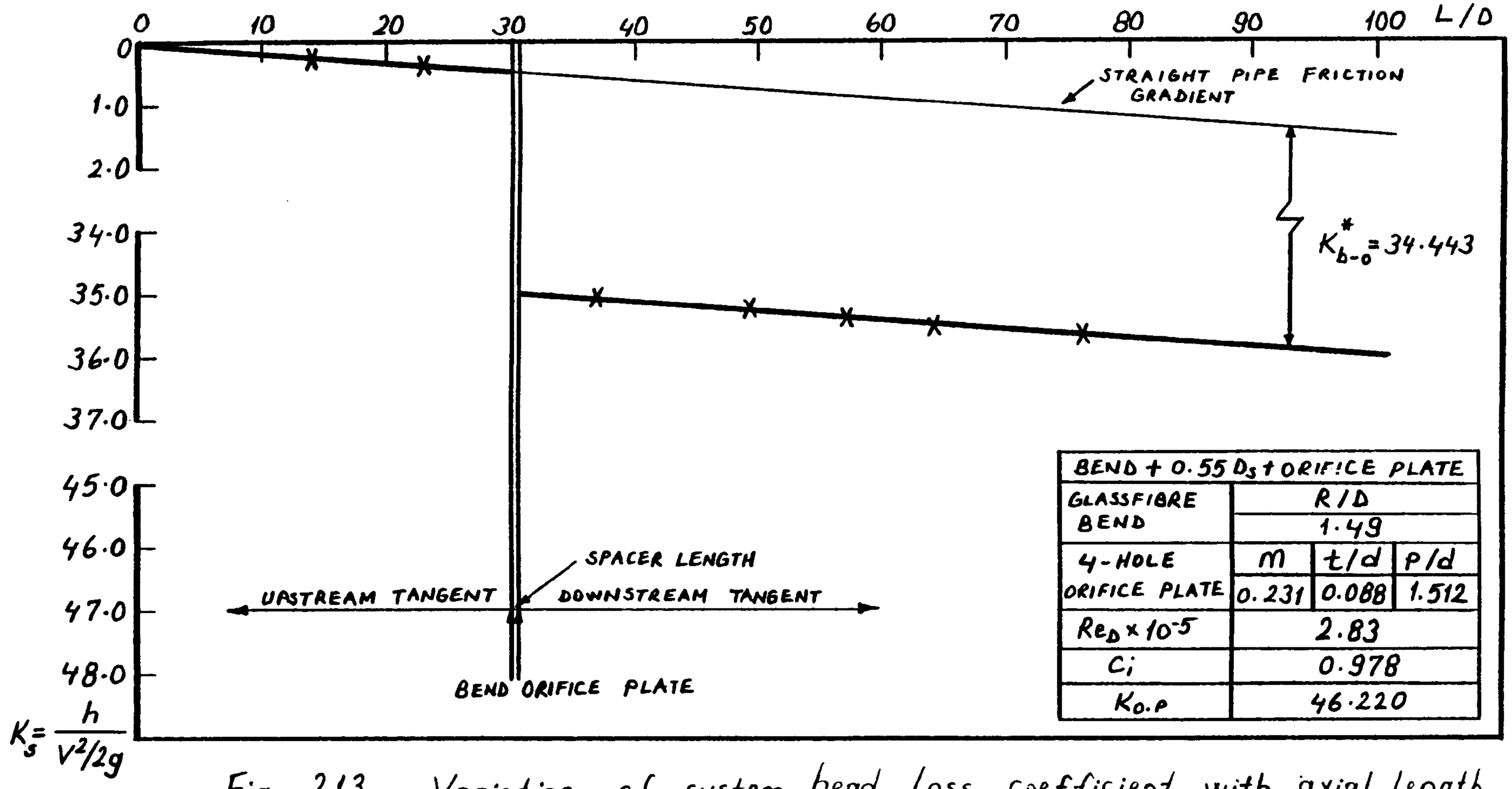

BEND + 0.55 D_s † ORIFICE PLATE			
GLASSFIBRE BEND	R/D		
	1.49		
4-HOLE ORIFICE PLATE	m	t/d	P/d
	0.231	0.088	1.512
$Re_D \times 10^{-5}$	2.83		
C_i	0.978		
$K_{o.p}$	46.220		

Fig. 213. Variation of system head loss coefficient with axial length

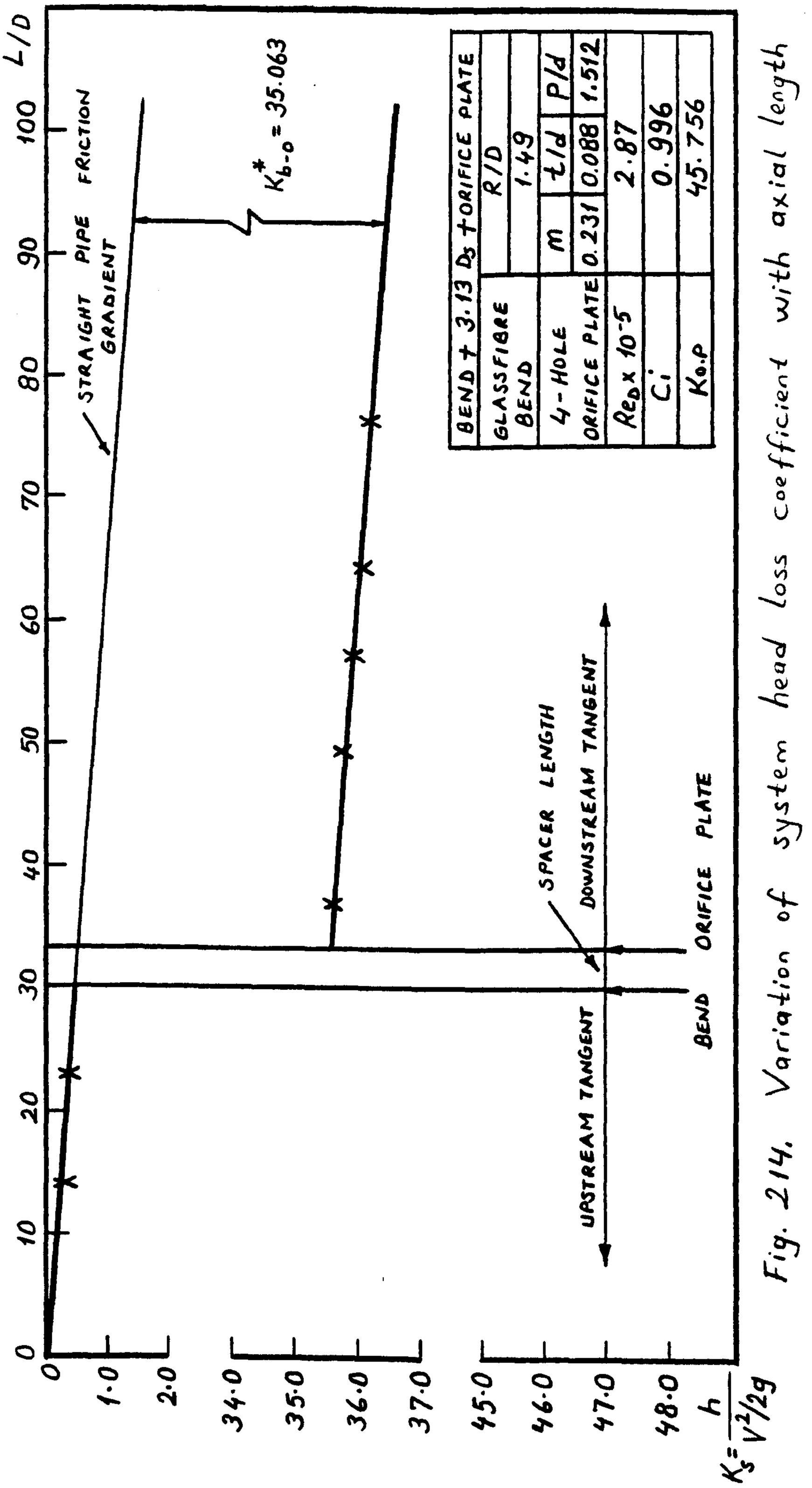

Fig. 214. Variation of system head loss coefficient with axial length

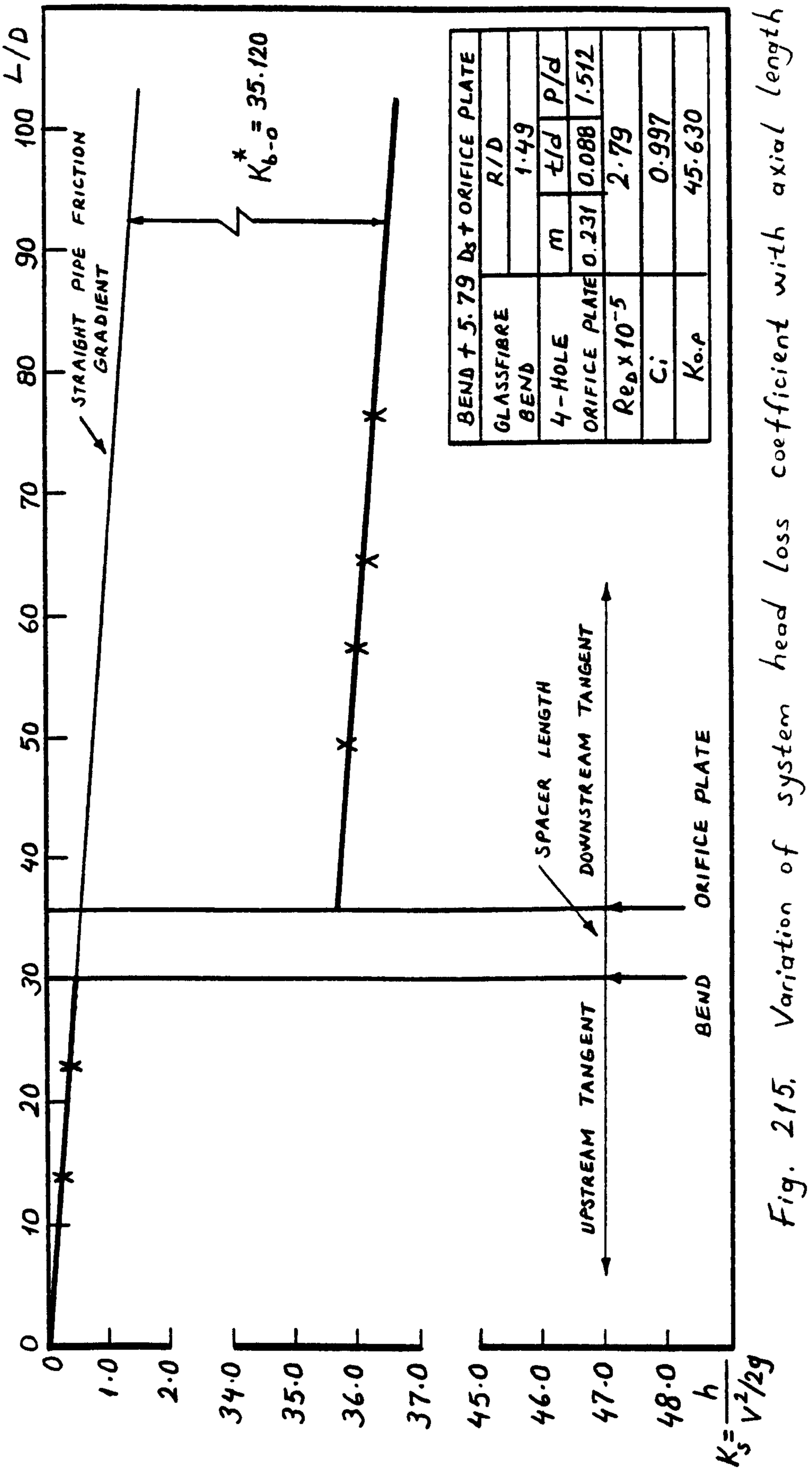

Fig. 215. Variation of system head loss coefficient with axial length

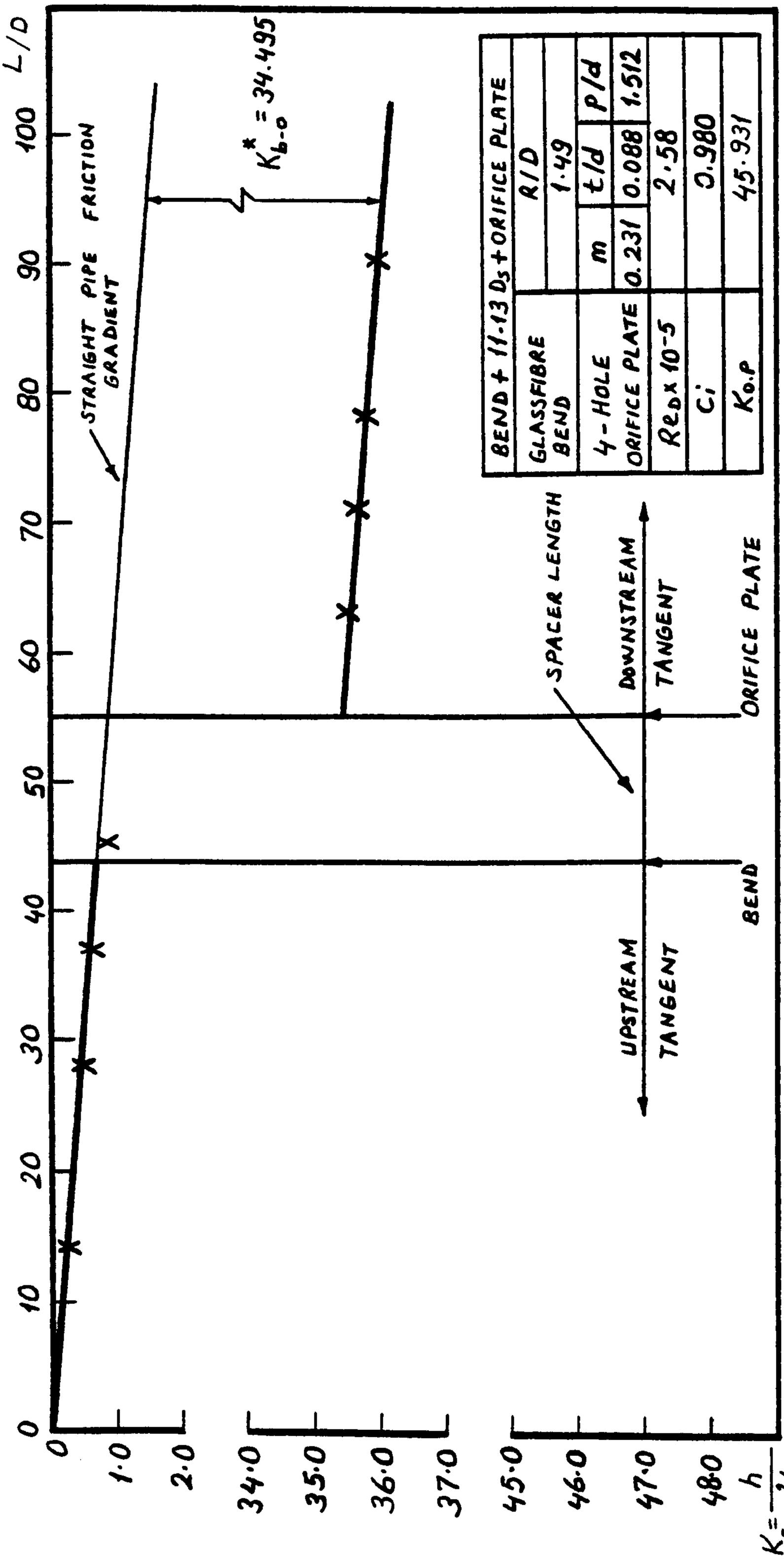

Fig. 216. Variation of system head loss coefficient with axial length

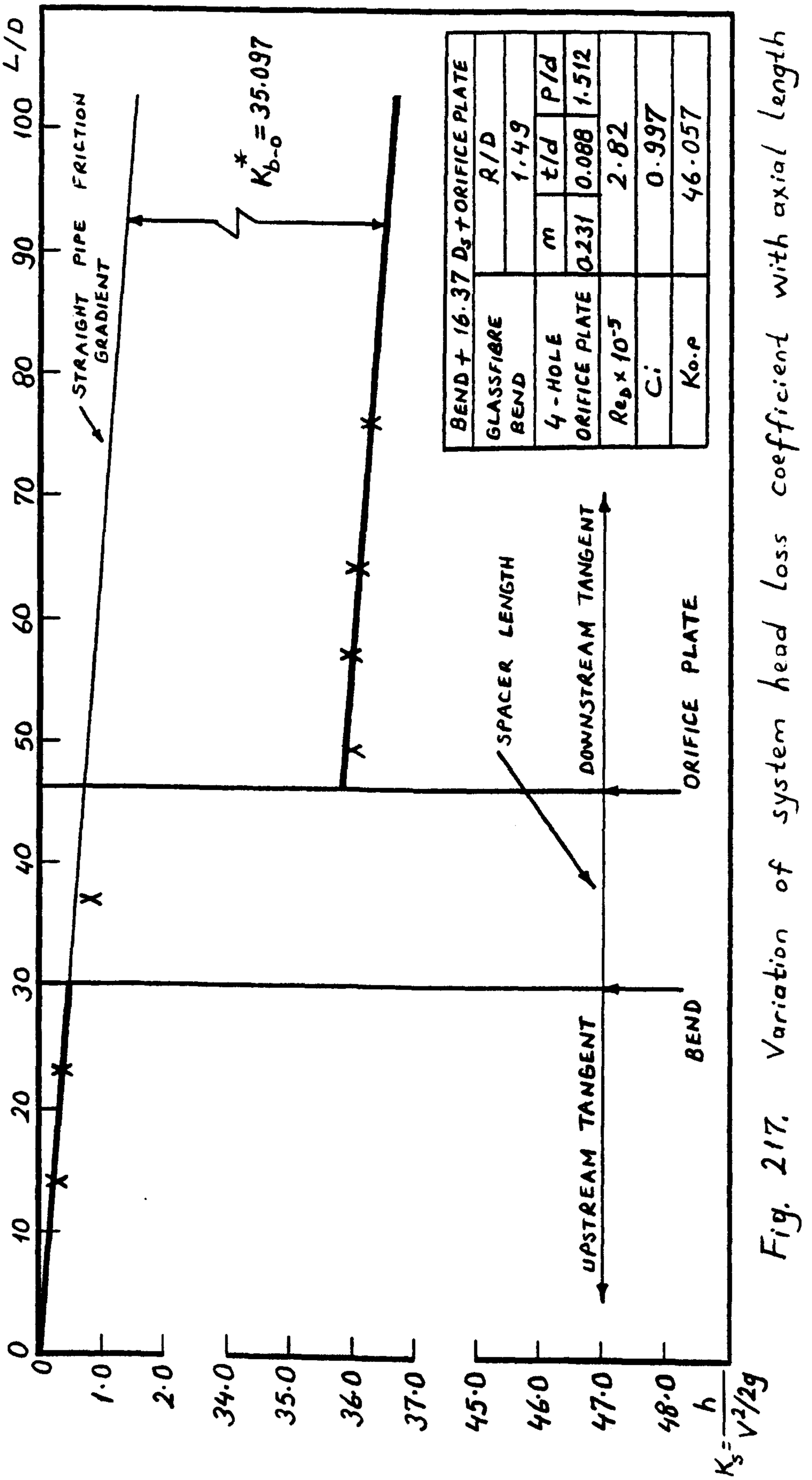

Fig. 217. Variation of system head loss coefficient with axial length

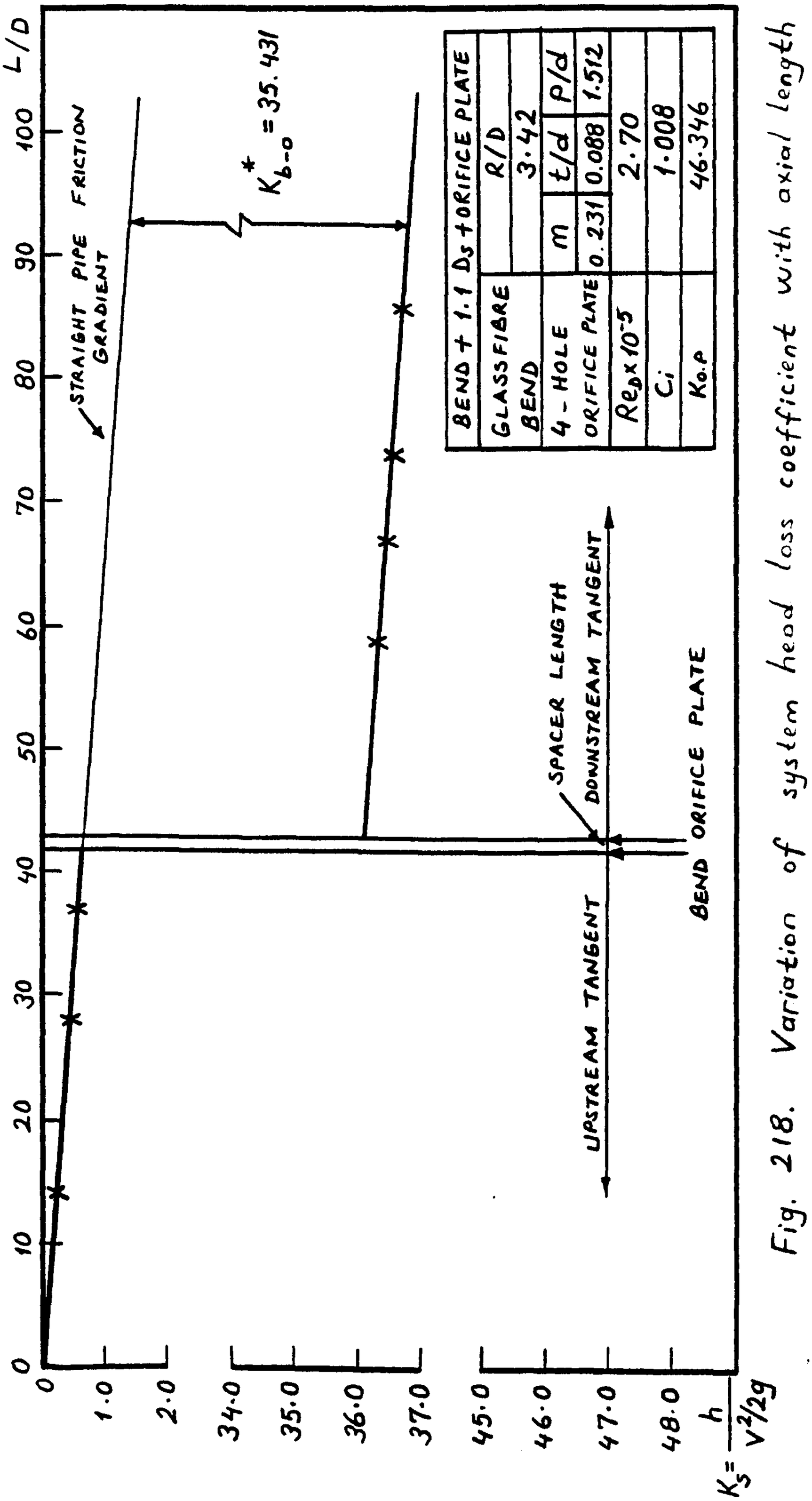

Fig. 218. Variation of system head loss coefficient with axial length

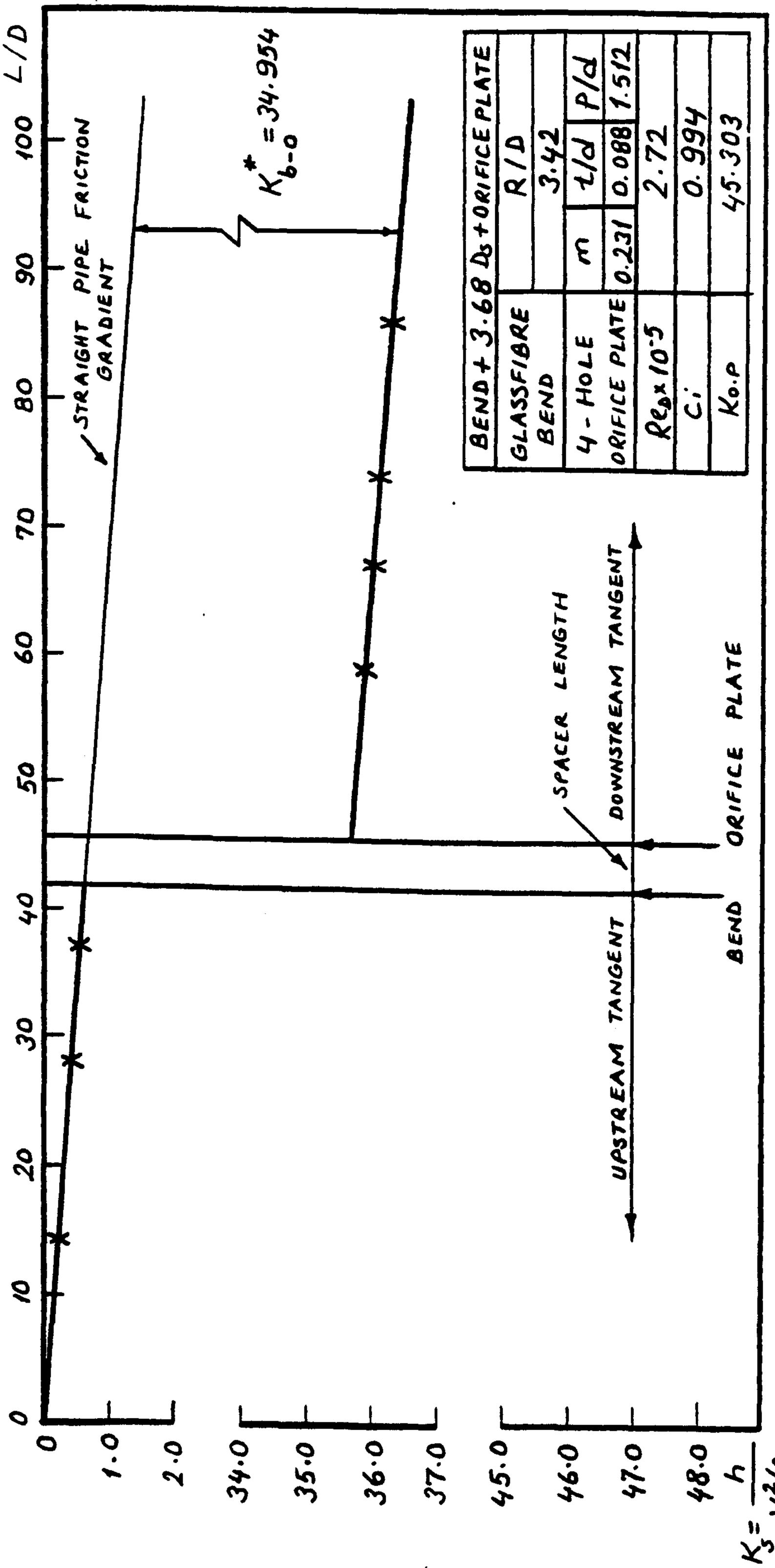

Fig. 219. Variation of system head loss coefficient with axial length

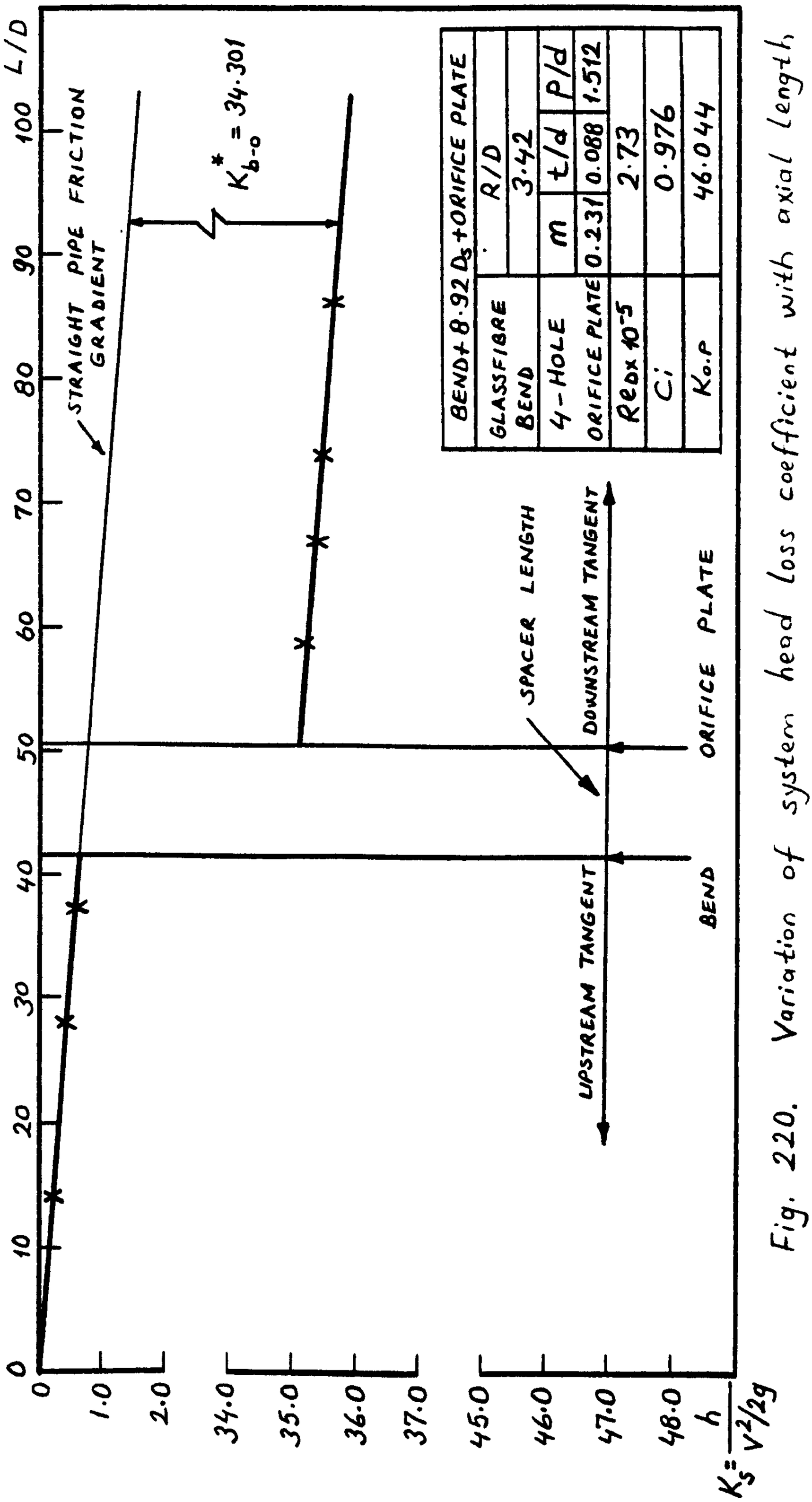

Fig. 220. Variation of system head loss coefficient with axial length

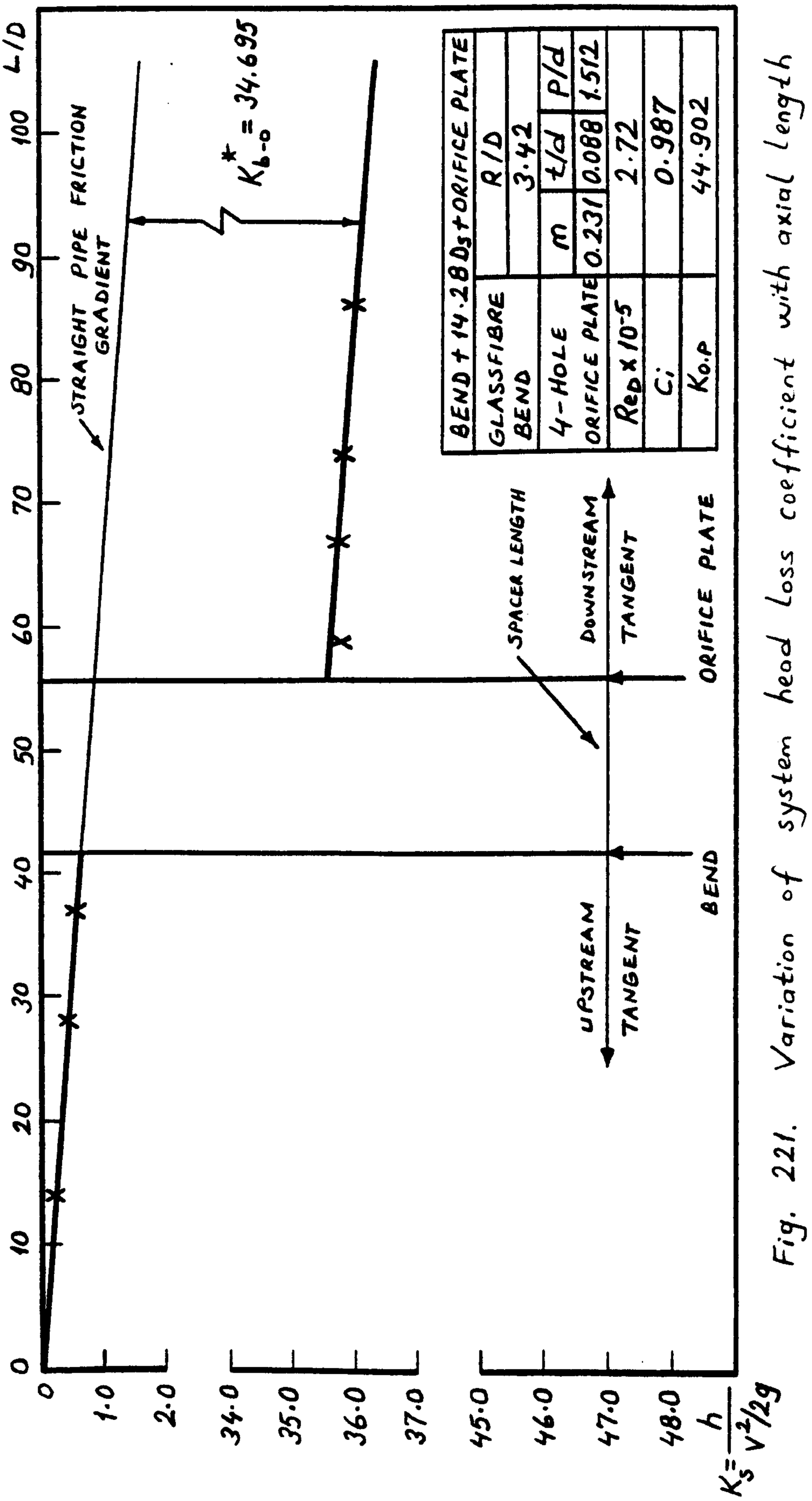

Fig. 221. Variation of system head loss coefficient with axial length

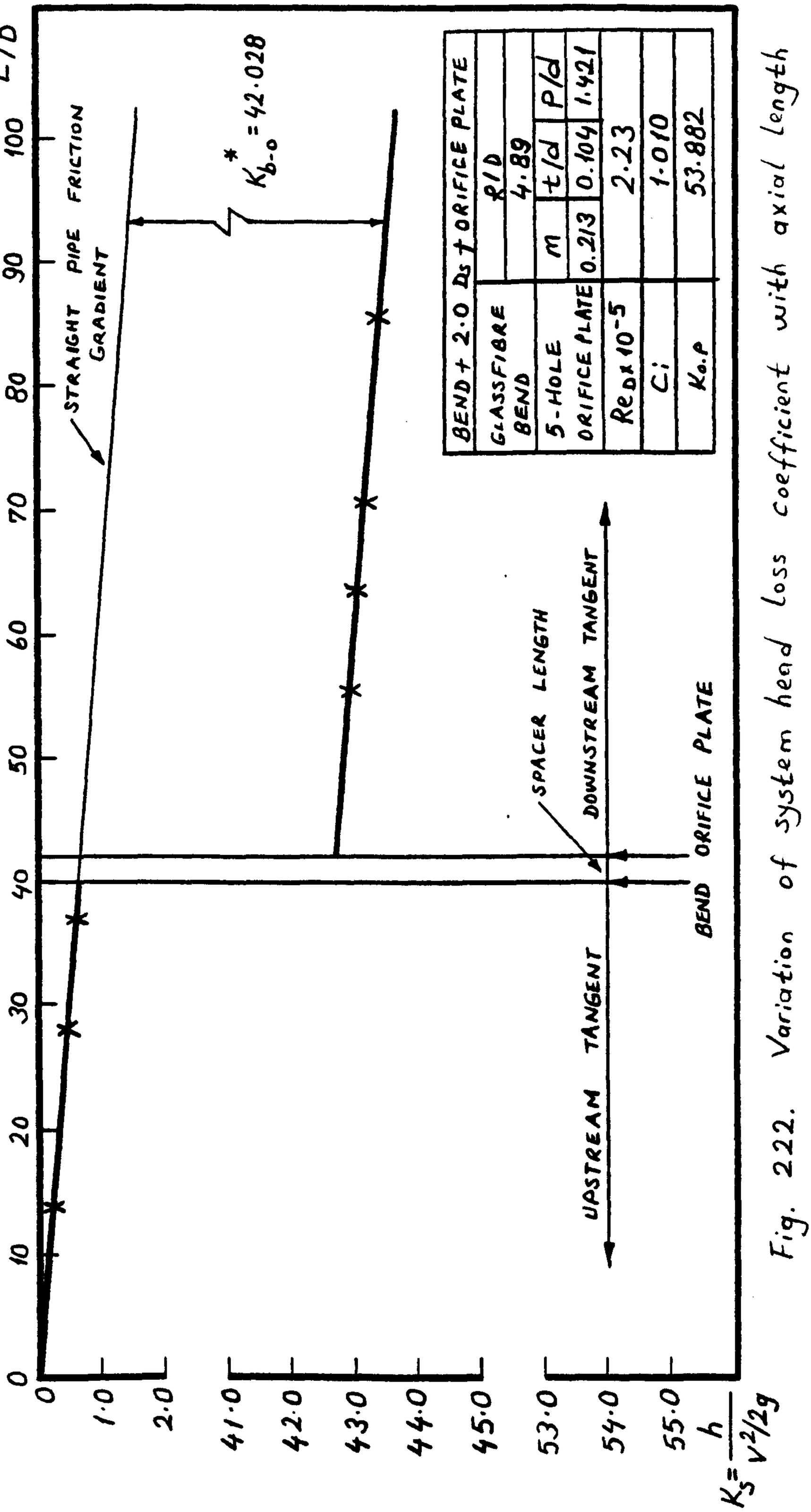

Fig. 222. Variation of system head loss coefficient with axial length

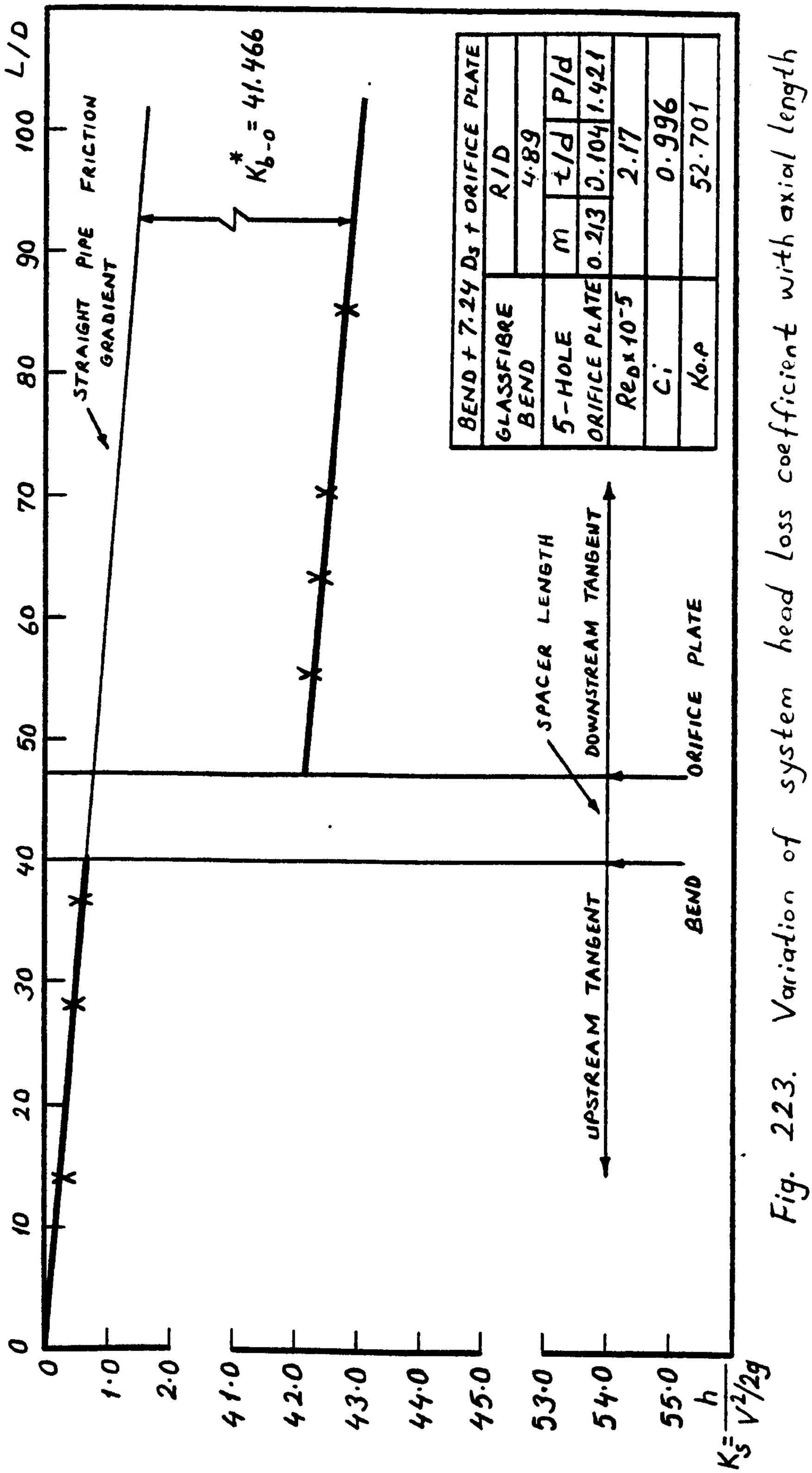

Fig. 223. Variation of system head loss coefficient with ax

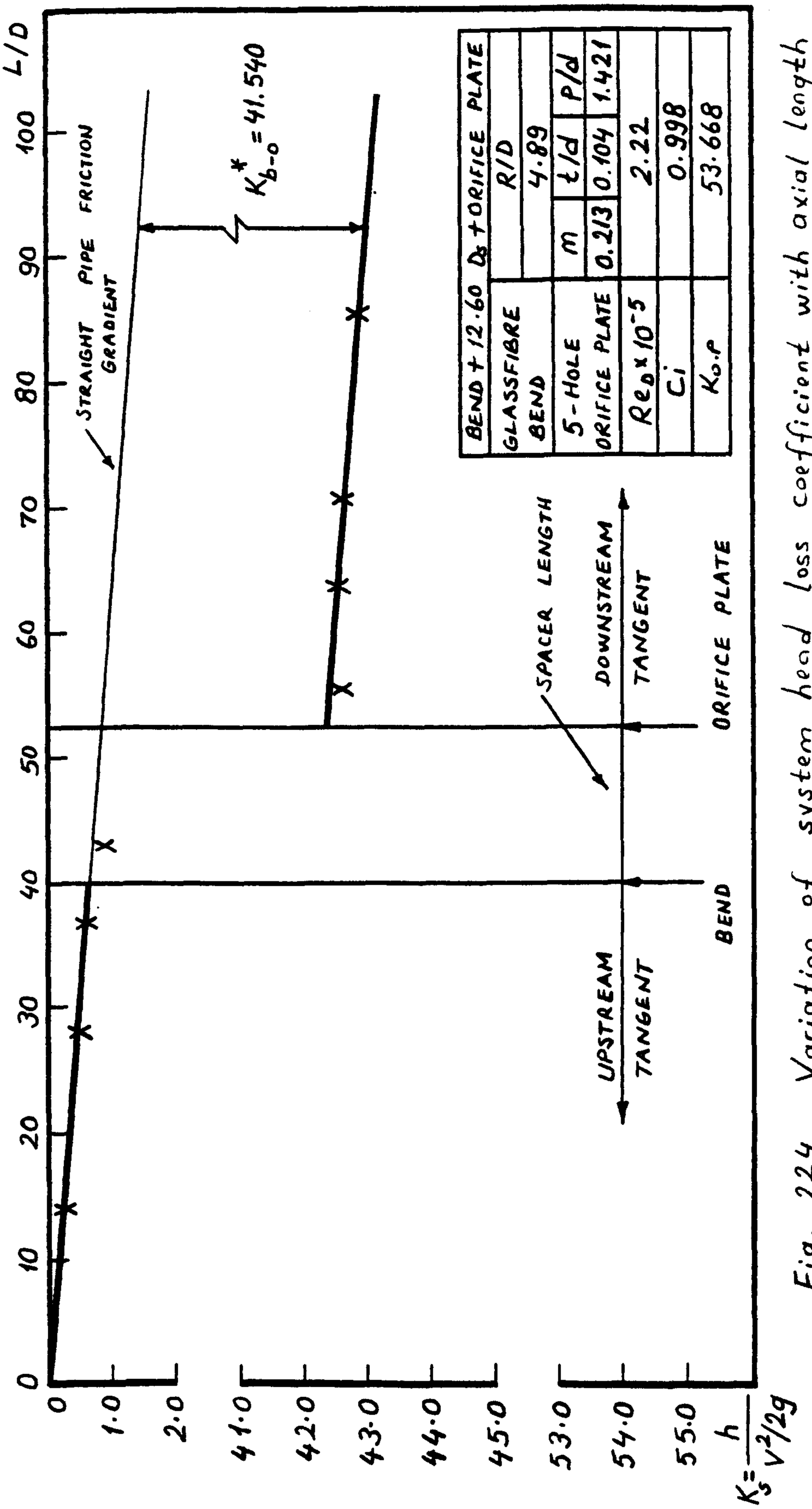

Fig. 224. Variation of system head loss coefficient with axial length

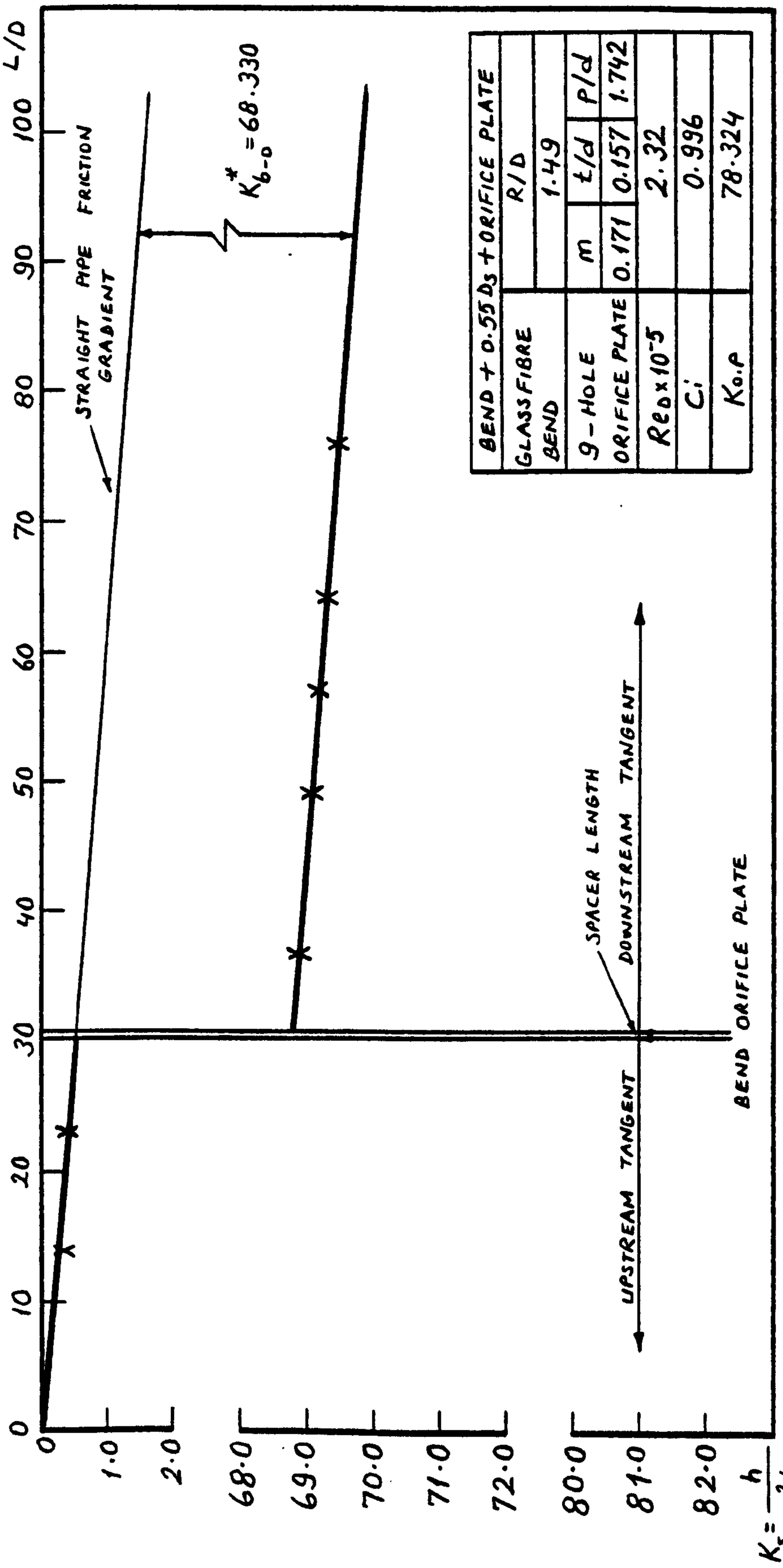

Fig. 225. Variation of System head loss coefficient with axial length

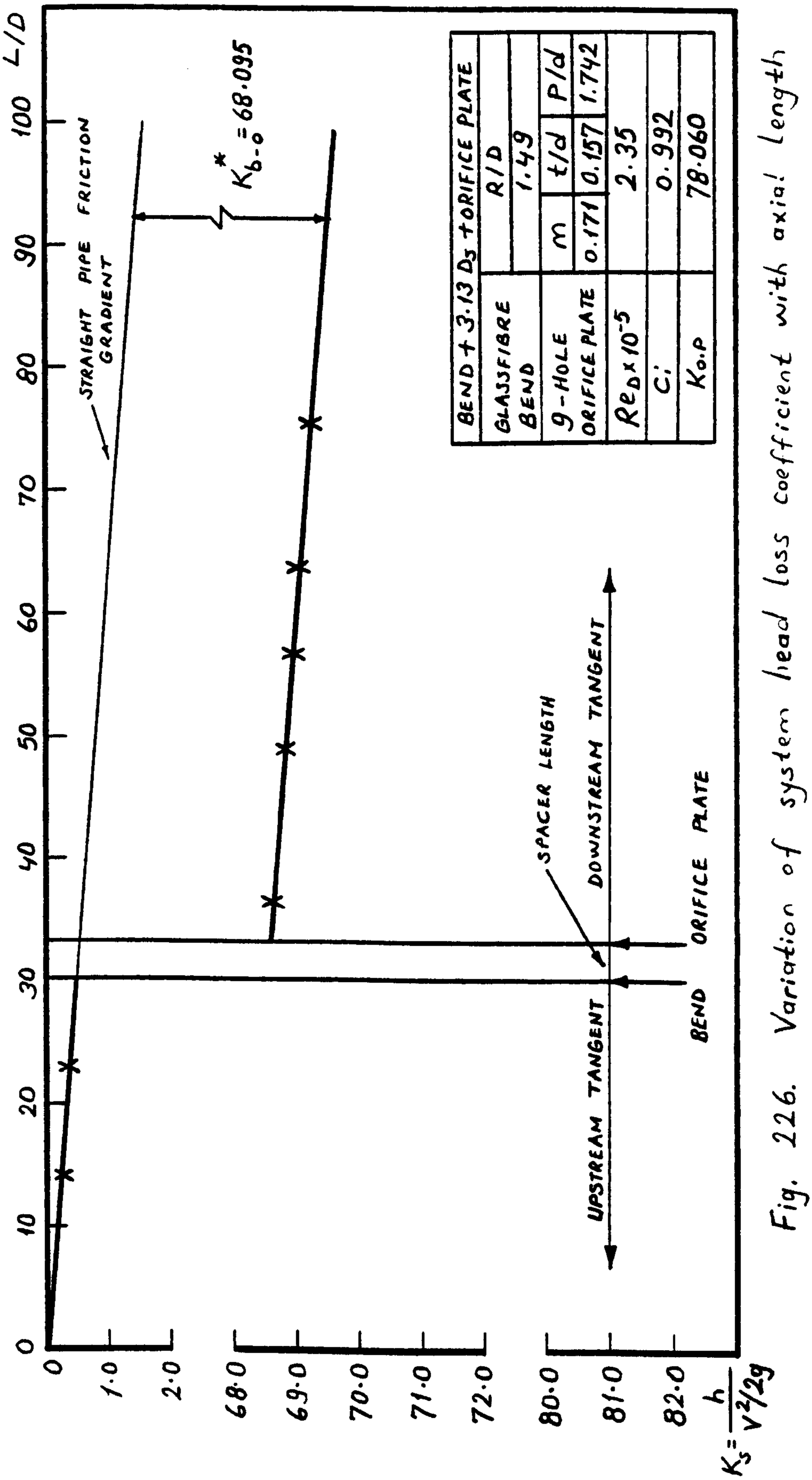

Fig. 226. Variation of system head loss coefficient with axial length

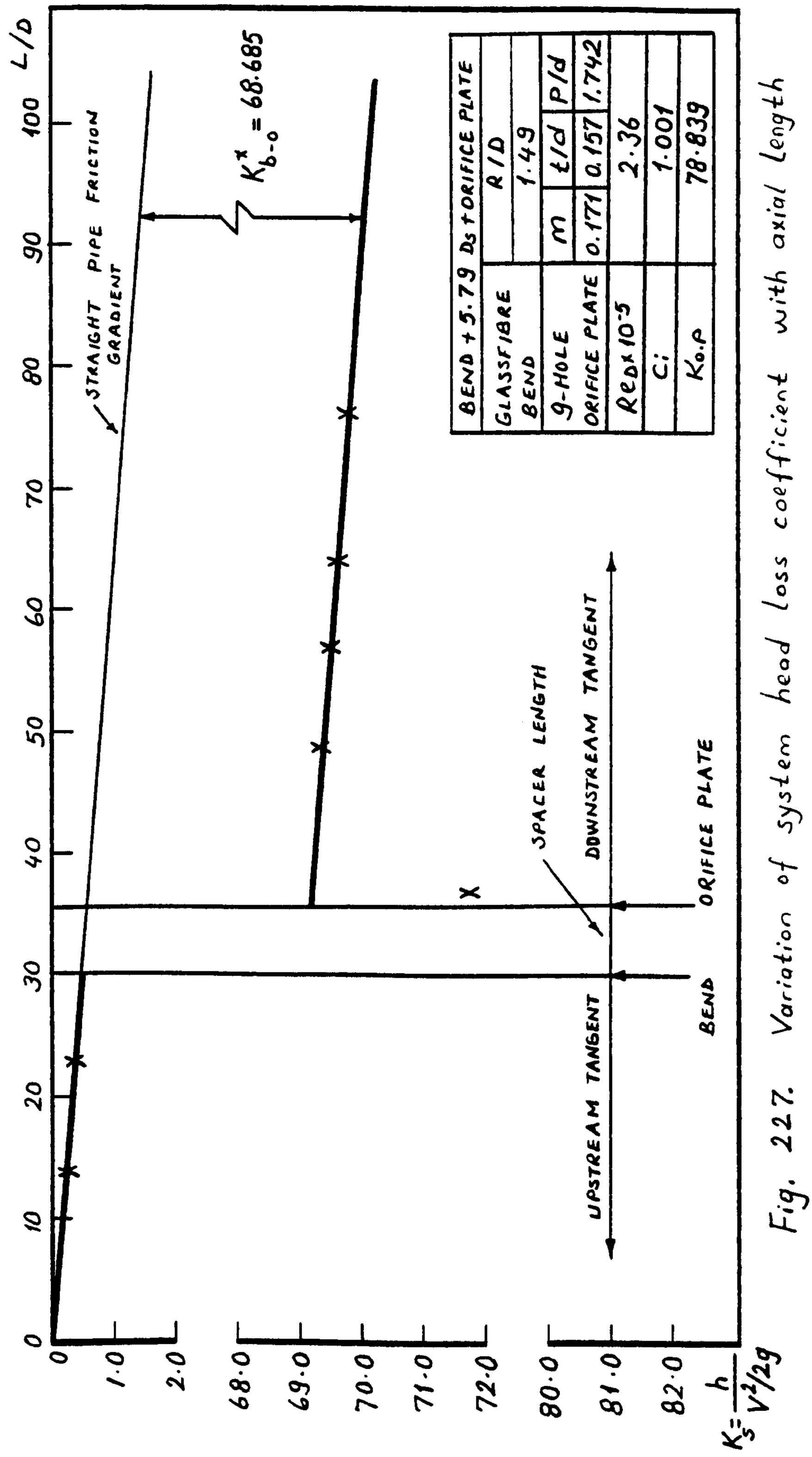
L/D
100
90
80
70
60
50
40
30
20
10
0
STRAIGHT PIPE FRICTION GRADIENT
$K^{*}_{b-o} = 68.685$
BEND + 5.79 DS ORIFICE PLATE
R/D
1.49
GLASSFIBRE BEND
m
0.171
t/d
0.157
P/d
1.742
9-HOLE ORIFICE PLATE
2.36
$Re_{Ds} 10^{-5}$
1.001
Ci
78.839
Ko.p
SPACER LENGTH
DOWNSTREAM TANGENT
ORIFICE PLATE
BEND
UPSTREAM TANGENT
0
1.0
2.0
68.0
69.0
70.0
71.0
72.0
80.0
81.0
82.0
$K_s = \frac{h}{V^2/2g}$
Fig. 227. Variation of system head loss coefficient with axial length

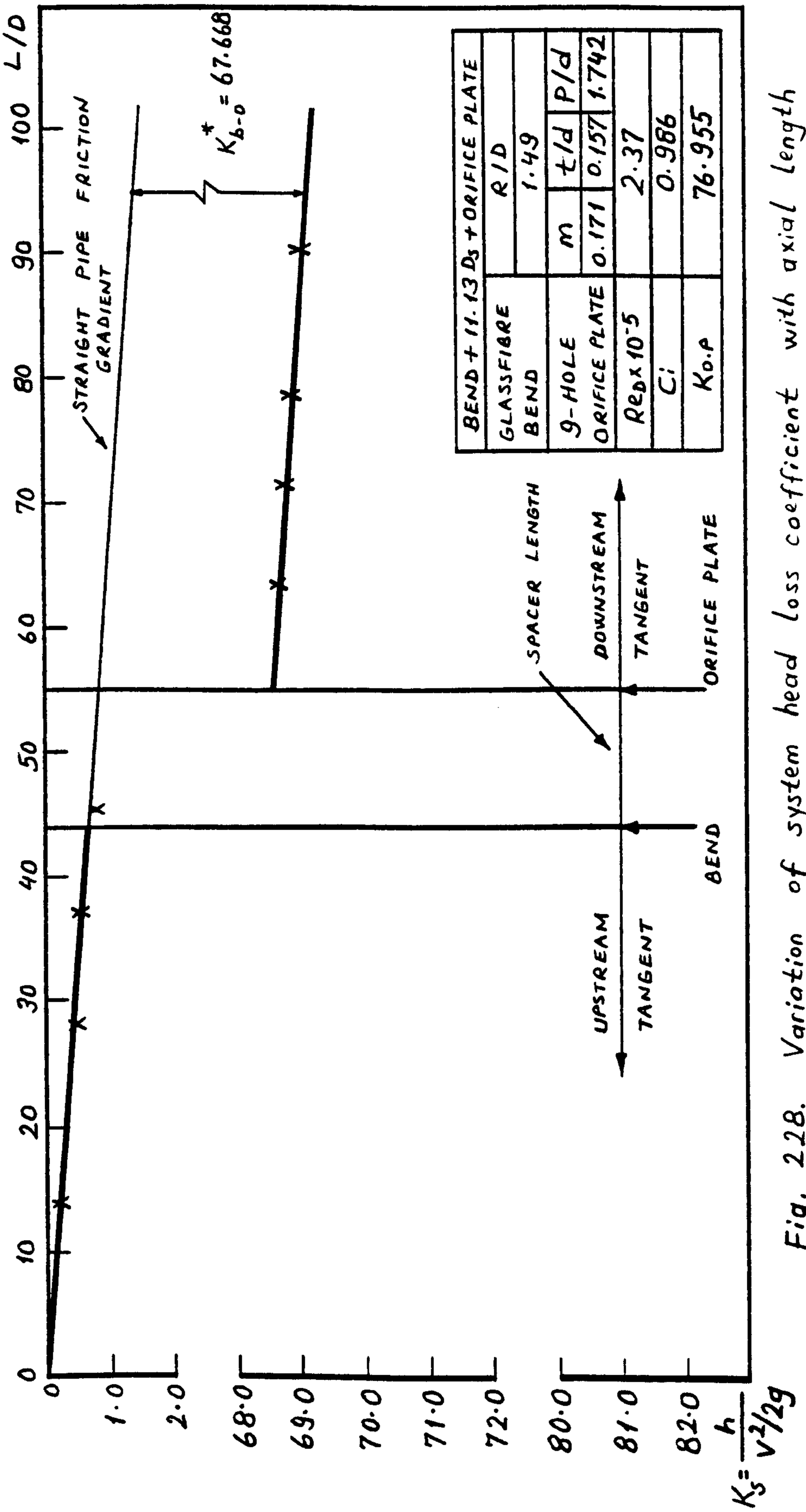

Fig. 228. Variation of system head loss coefficient with axial length

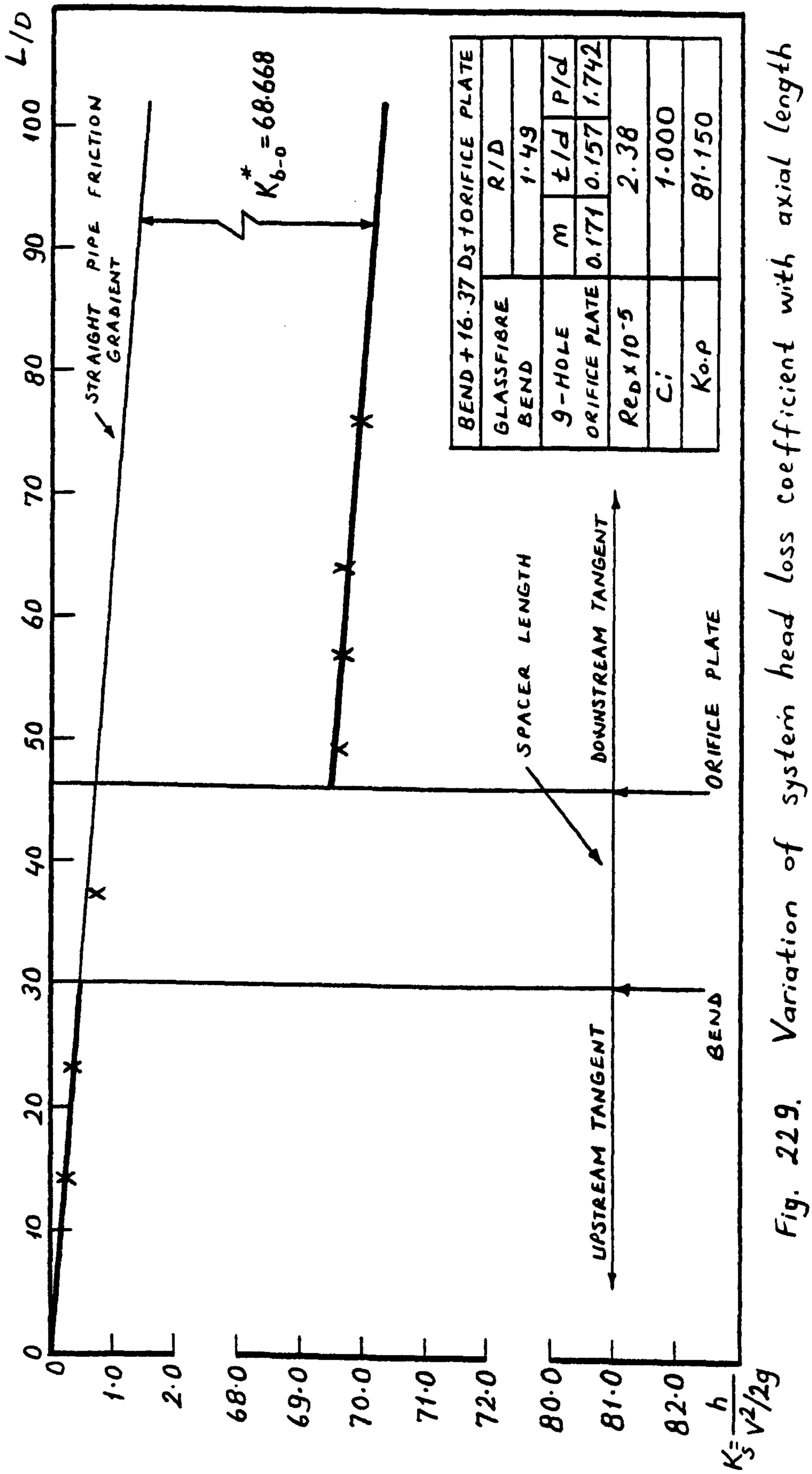

Fig. 229. Variation of system head loss coefficient with axial length

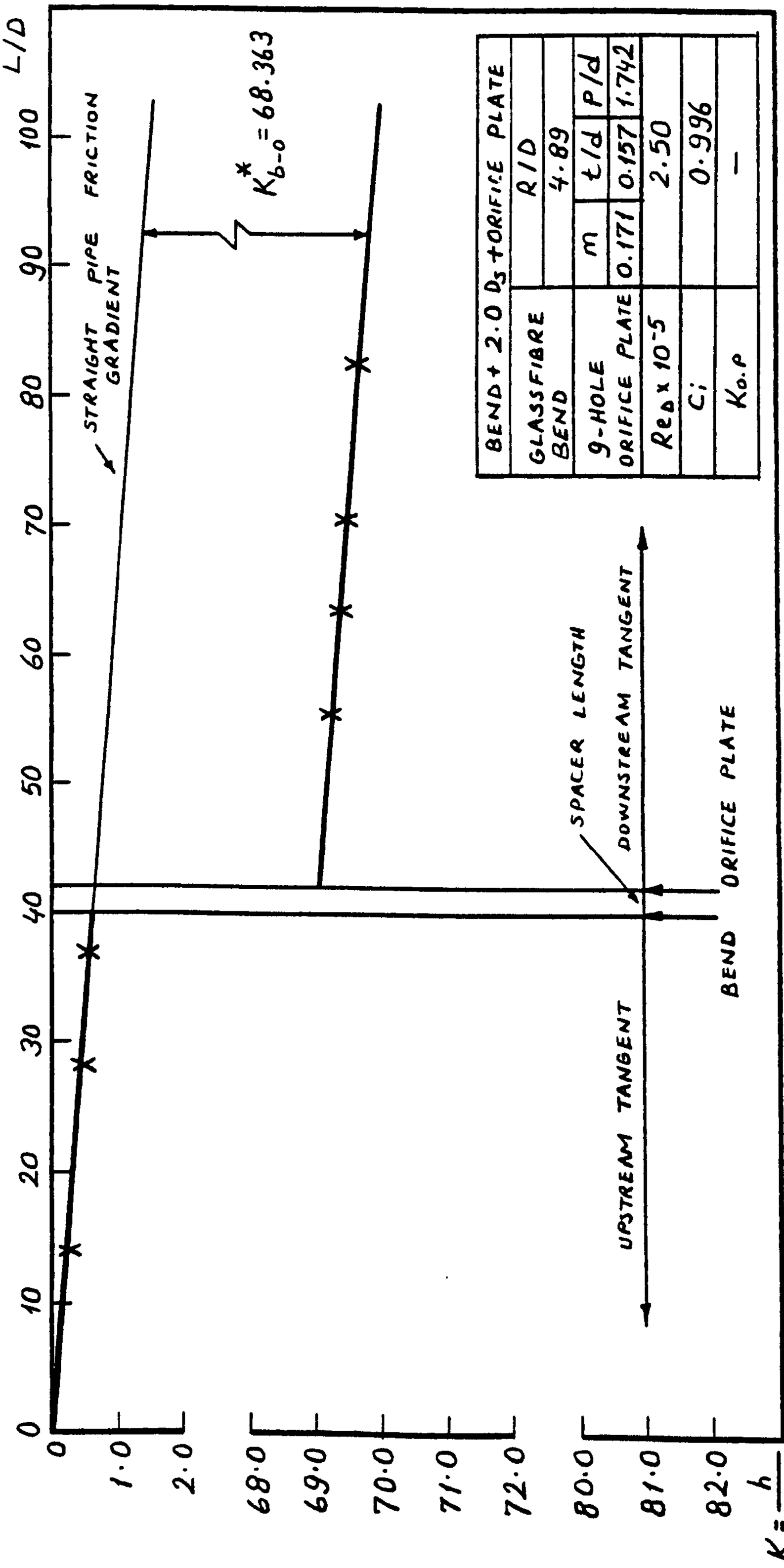

BEND + 2.0 D_3 + ORIFICE PLATE

GLASSFIBRE BEND	R/D			
	4.89		t/d	P/d
9-HOLE ORIFICE PLATE		m	0.171	0.157	1.742
	$Re_D \times 10^{-5}$		2.50		
	C_i		0.996		
	$K_{o.p}$		—		

Fig. 230. Variation of system head Loss coefficient with axial length

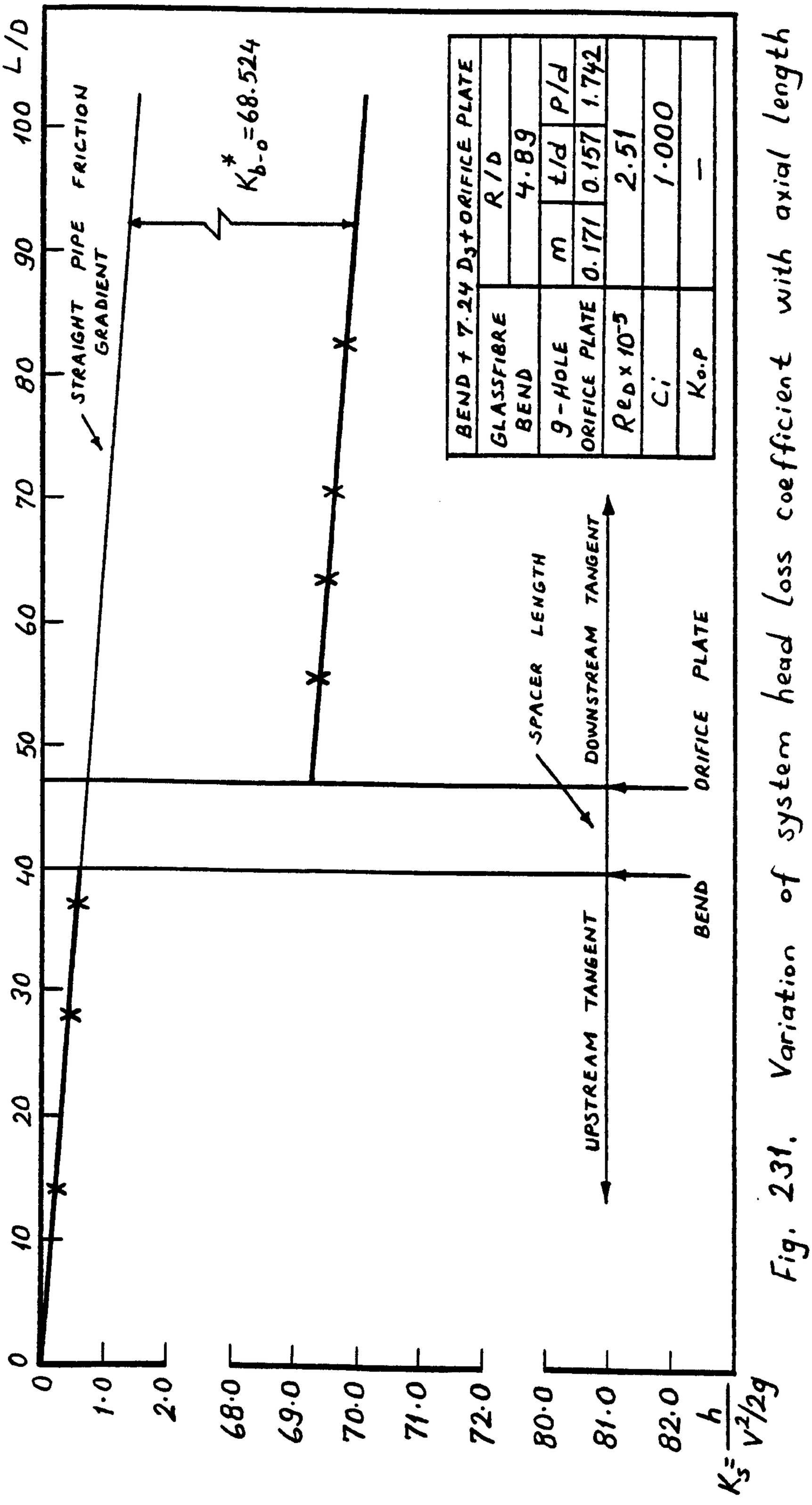

Fig. 231. Variation of system head loss coefficient with axial length

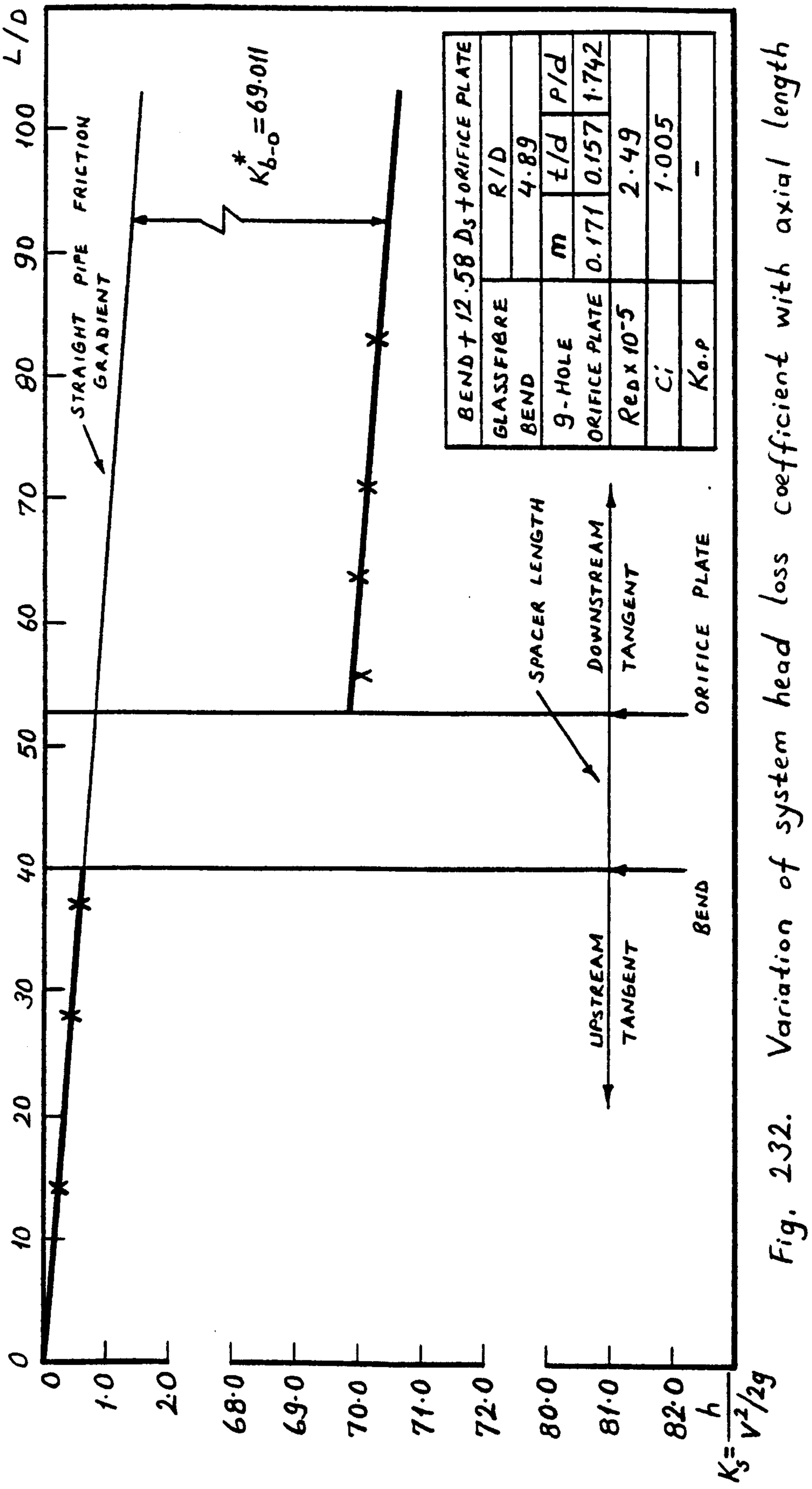

Fig. 2.32. Variation of system head loss coefficient with axial length

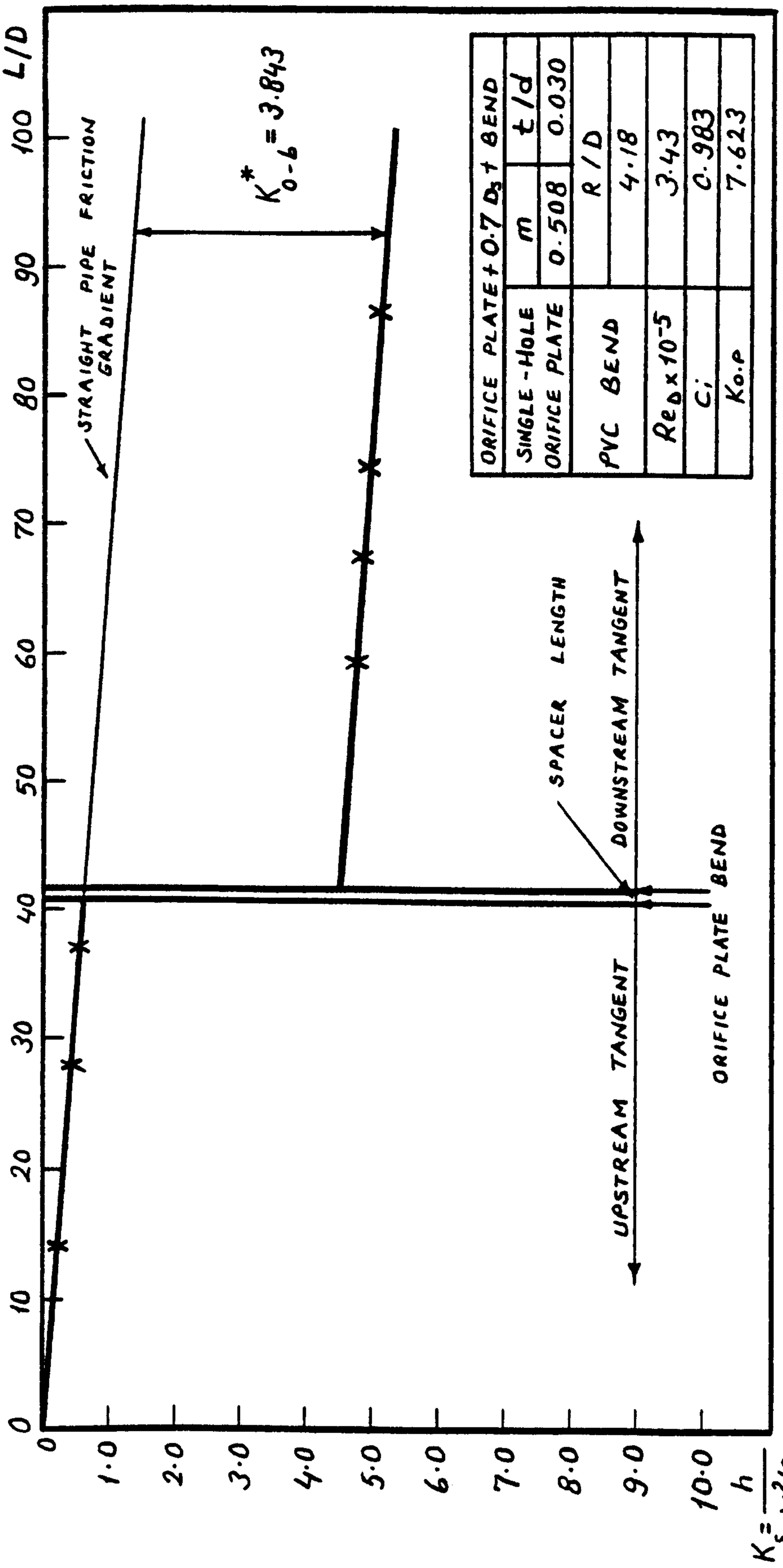

Fig. 233. Variation of system head loss coefficient with axial length

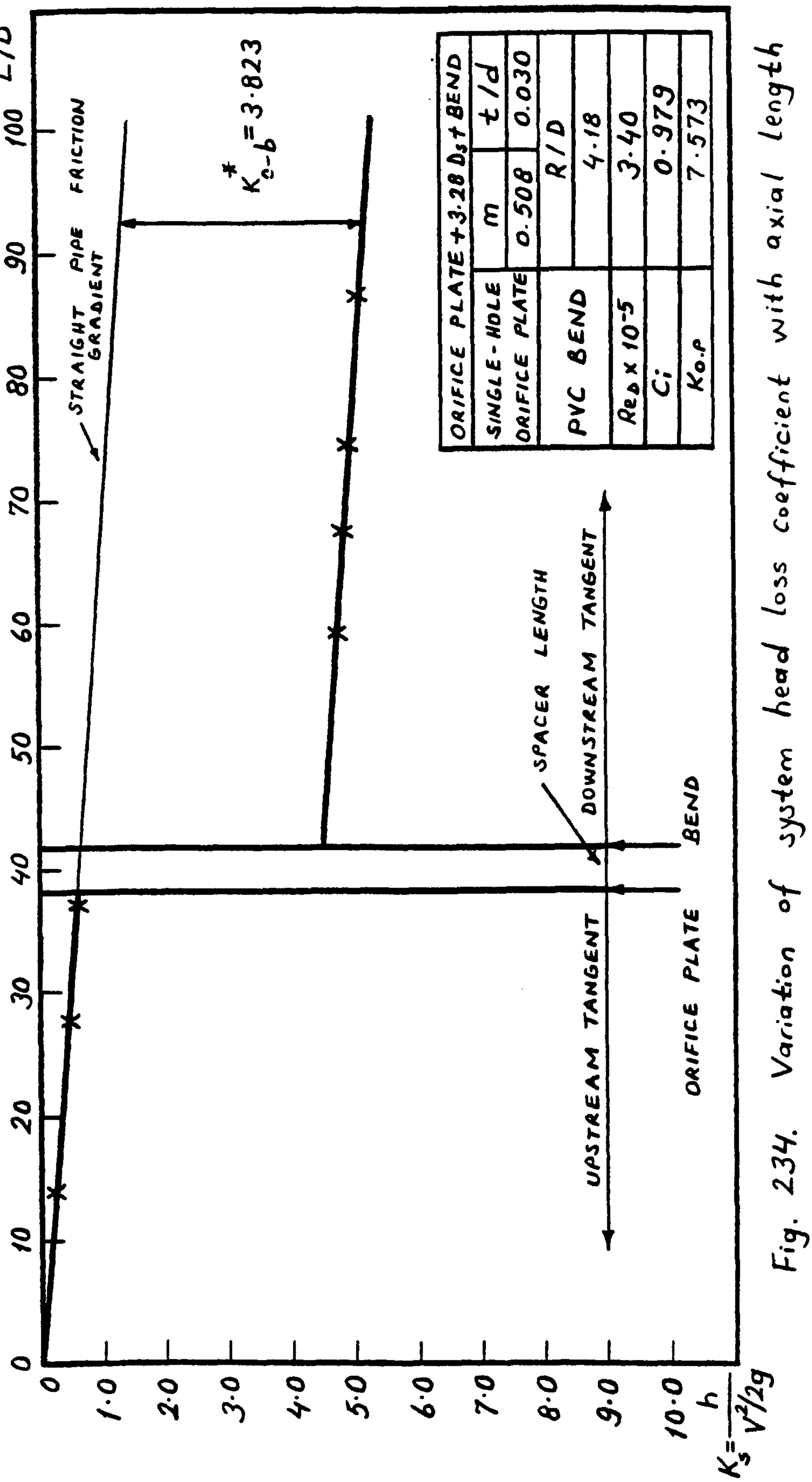

Fig. 234. Variation of system head loss coefficient with axial length

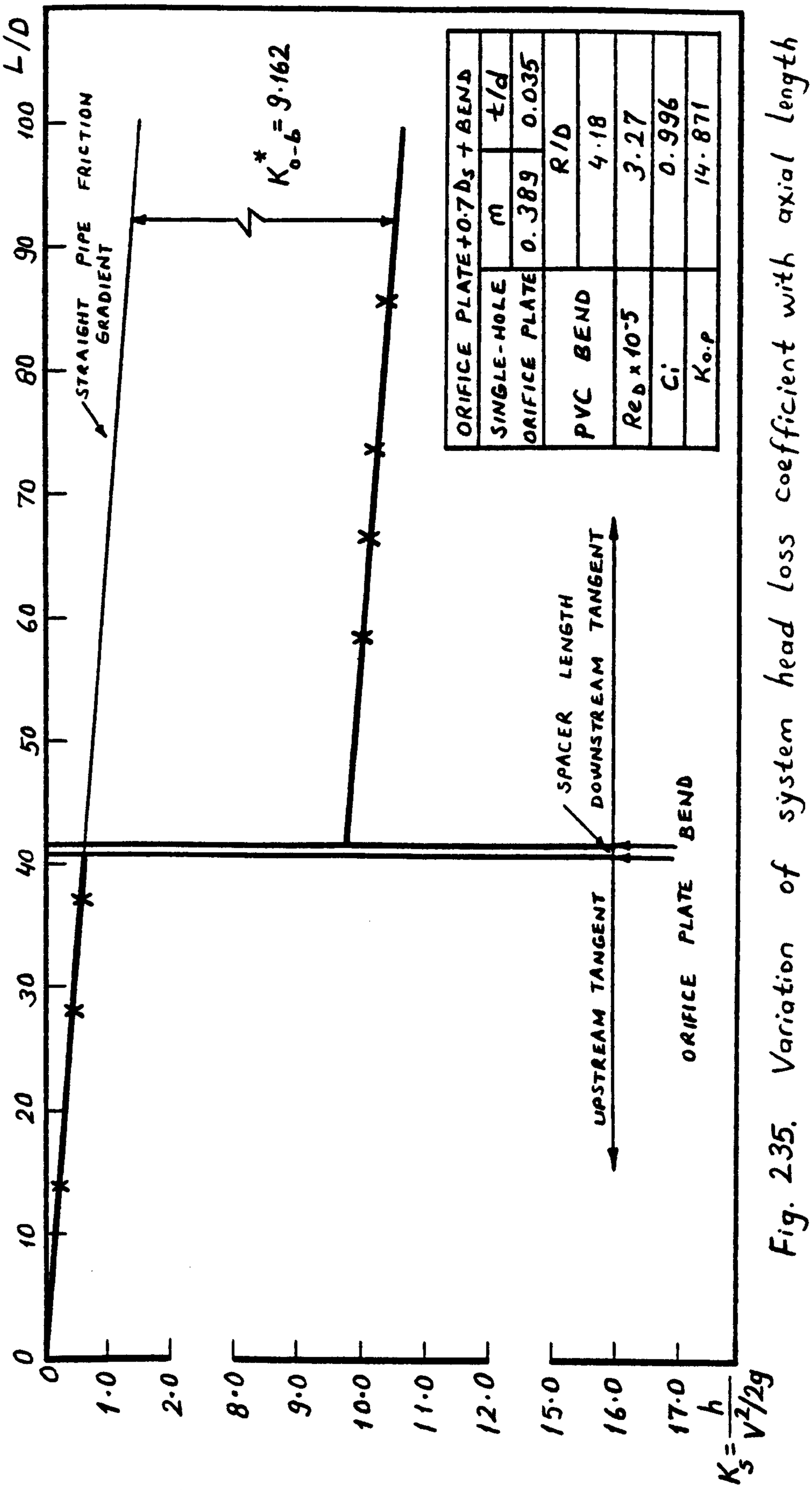

Fig. 235. Variation of system head loss coefficient with

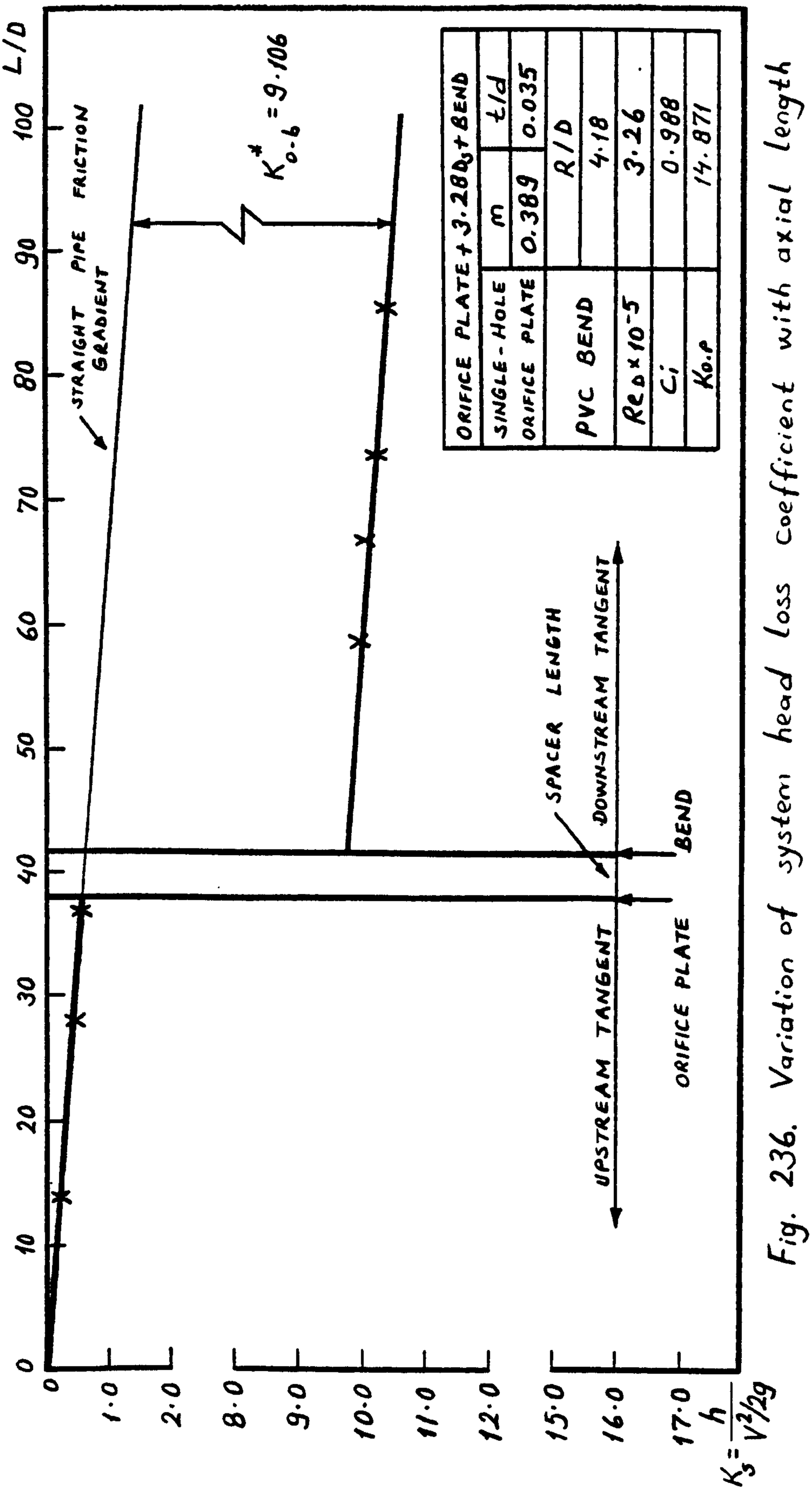

Fig. 236. Variation of system head loss coefficient with axial length

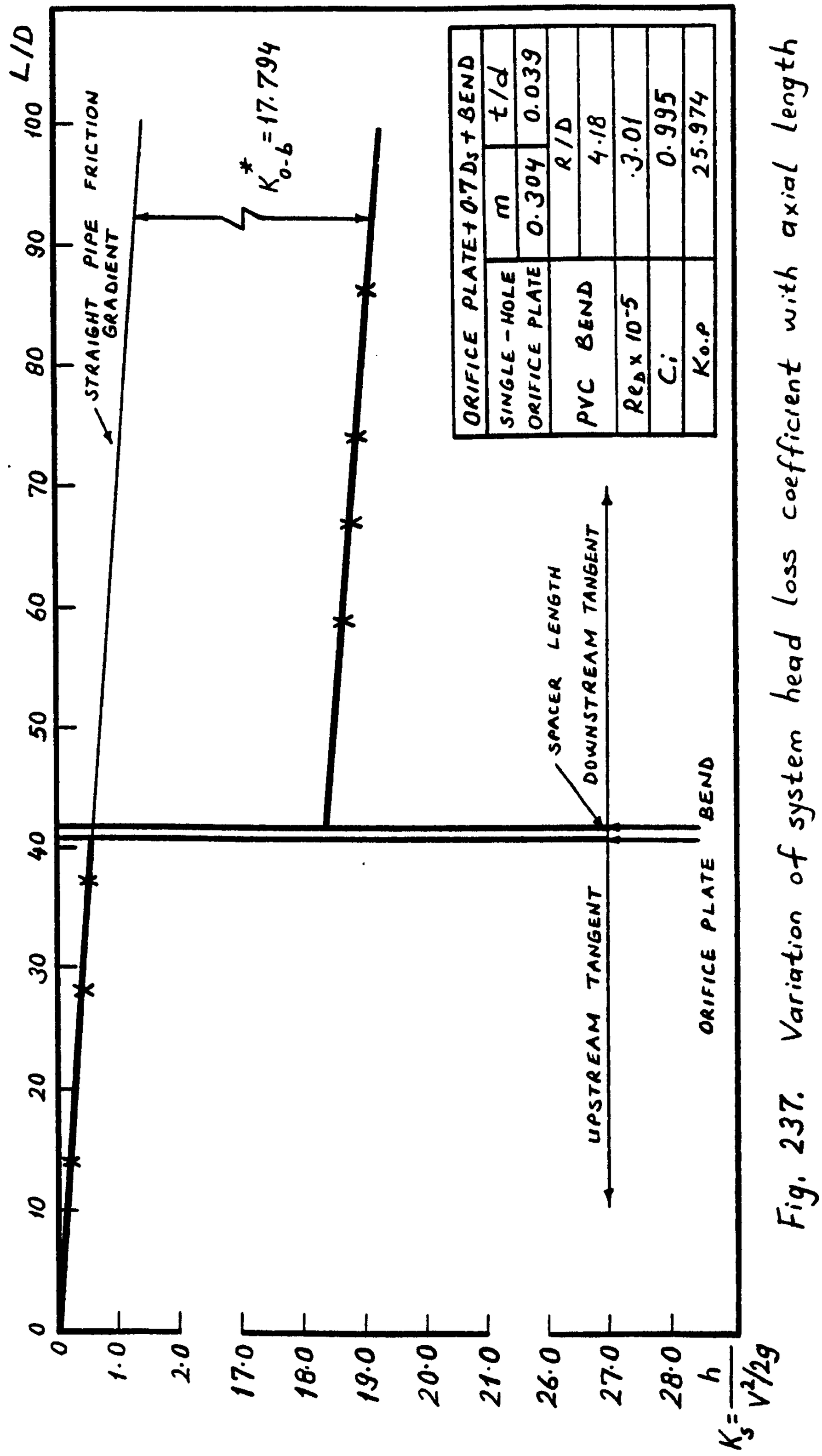

Fig. 237. Variation of system head loss coefficient with axial length

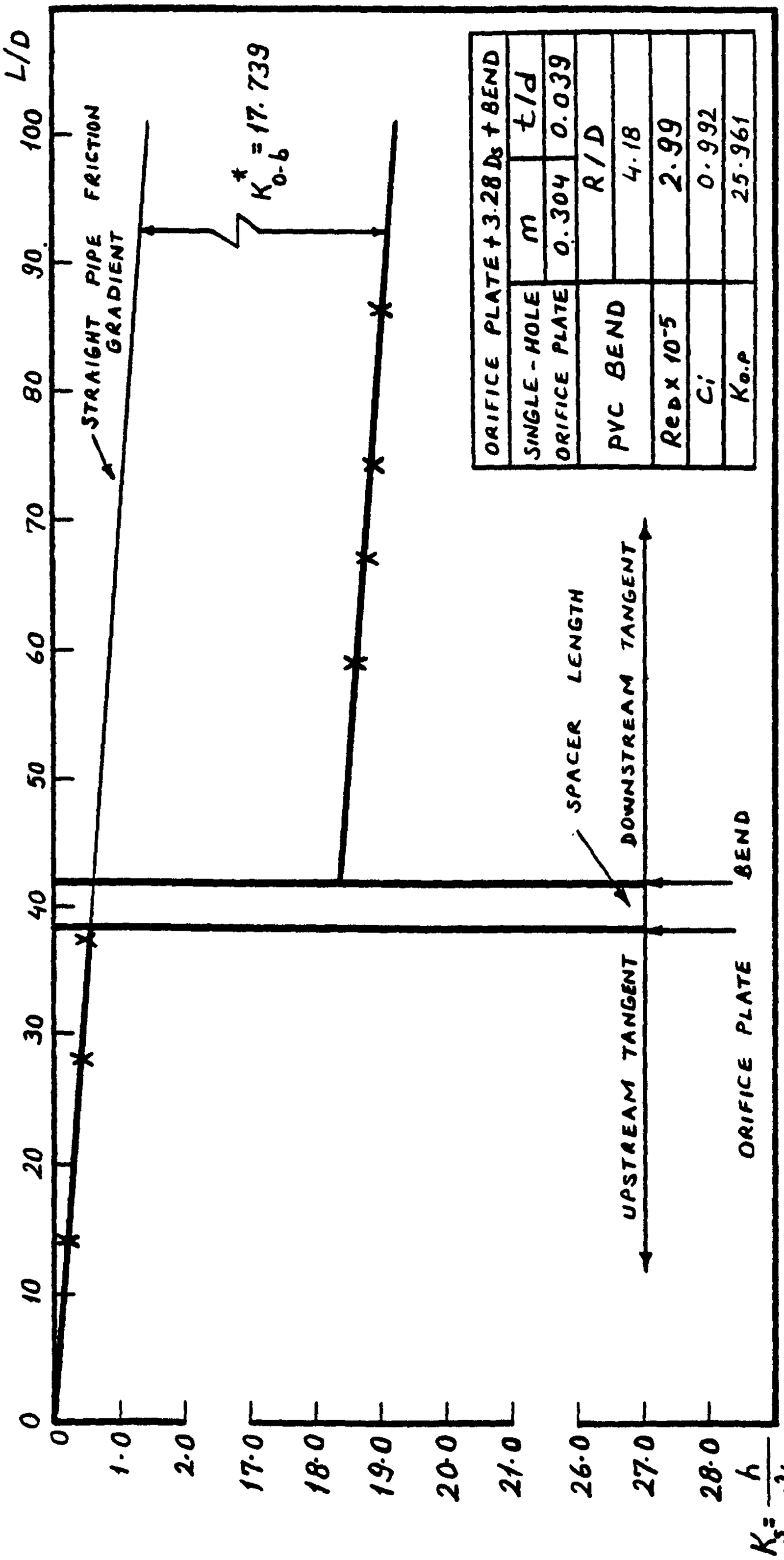

Fig. 238. Variation of system head loss coefficient with axial length

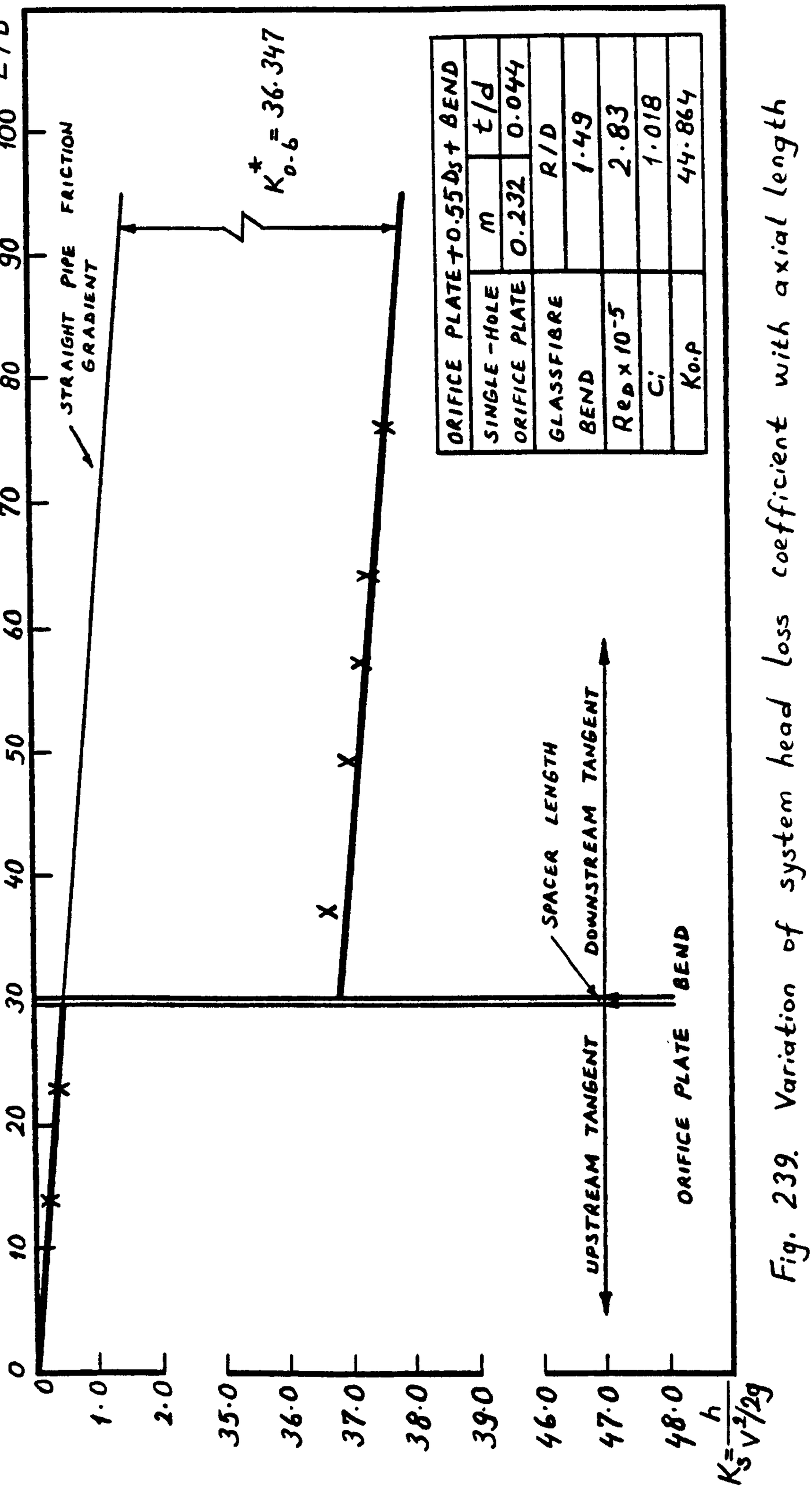

Fig. 239. Variation of system head loss coefficient with axial length

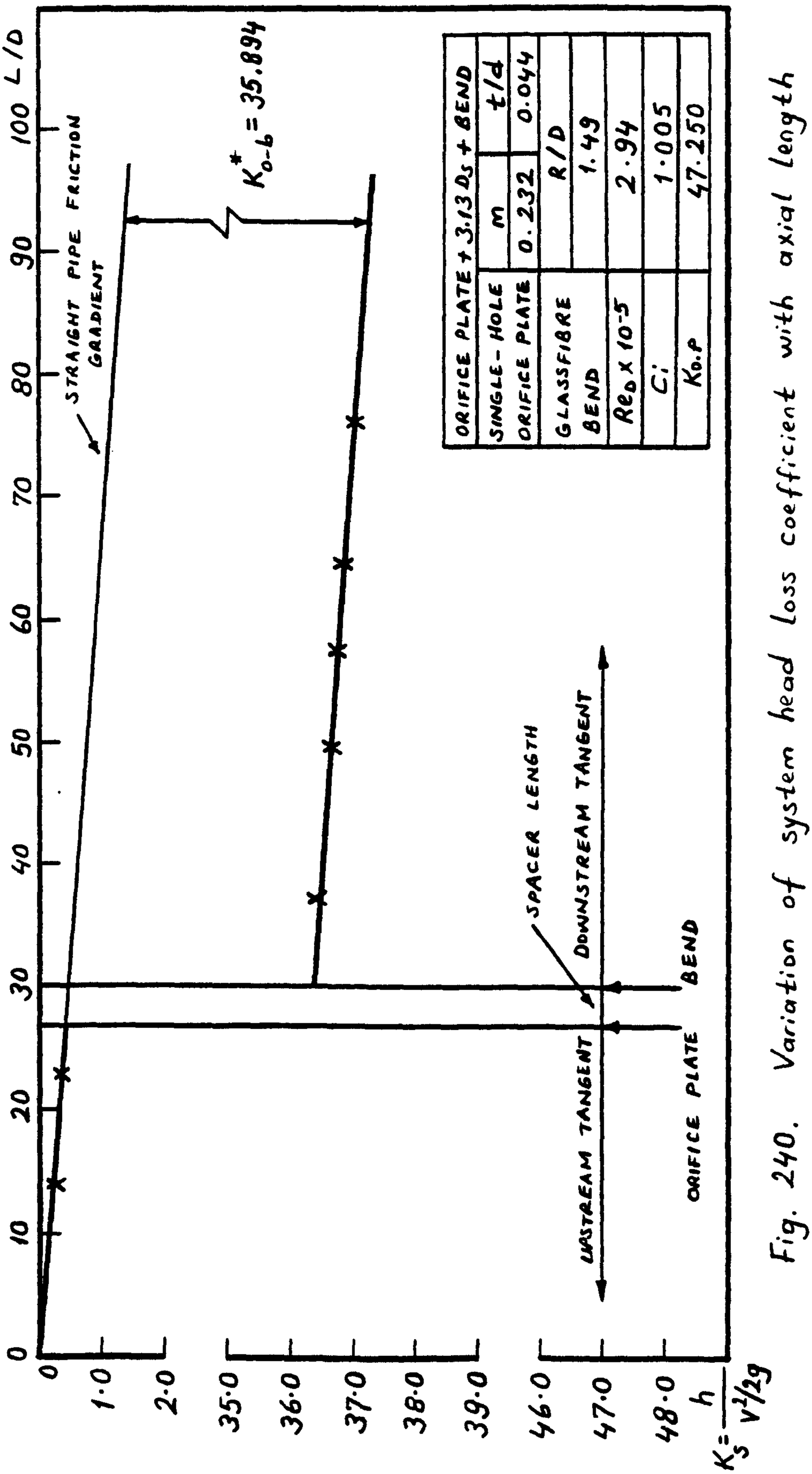
100 L/D
90
80
70
60
50
40
30
20
10
0
FRICTION
STRAIGHT PIPE FRICTION GRADIENT
$K^*_{0-6} = 35.894$
SPACER LENGTH
DOWNSTREAM TANGENT
BEND
ORIFICE PLATE
UPSTREAM TANGENT
0
1·0
2·0
35·0
36·0
37·0
38·0
39·0
46·0
47·0
48·0
$K_s = \frac{h}{V^2/2g}$
Length
Variation of system head loss coefficient with axial
ORIFICE PLATE + 3.13 D_s + BEND
SINGLE-HOLE ORIFICE PLATE
m
0.232
t/d
0.044
GLASSFIBRE BEND
R/D
1.49
2.94
1.005
47.250
$Re_D \times 10^{-5}$
Ci
$K_{0.P}$

Fig. 240.

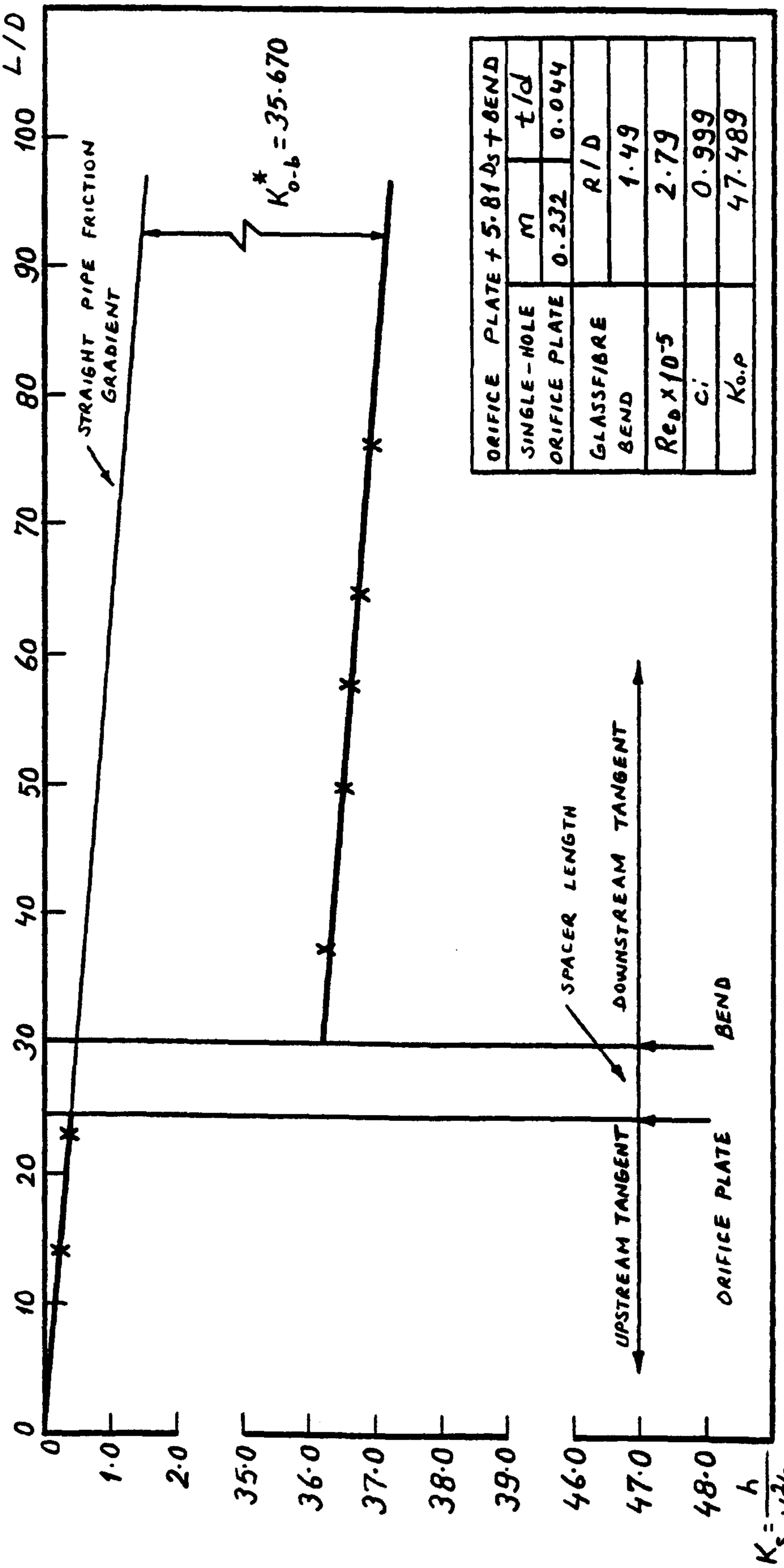

Fig. 241. Variation of system head loss coefficient with

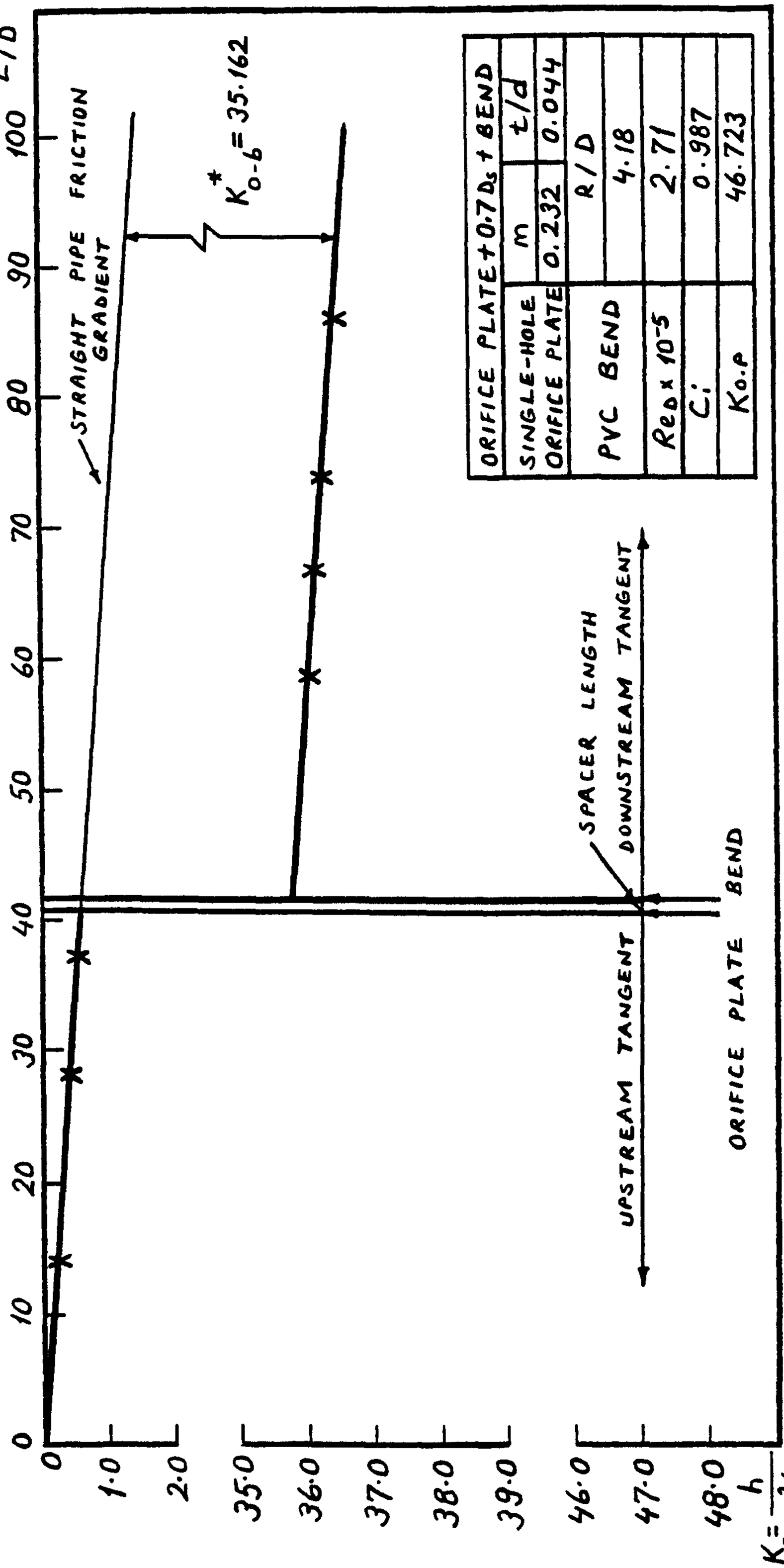

Fig. 242. Variation of system head loss coefficient with axial length

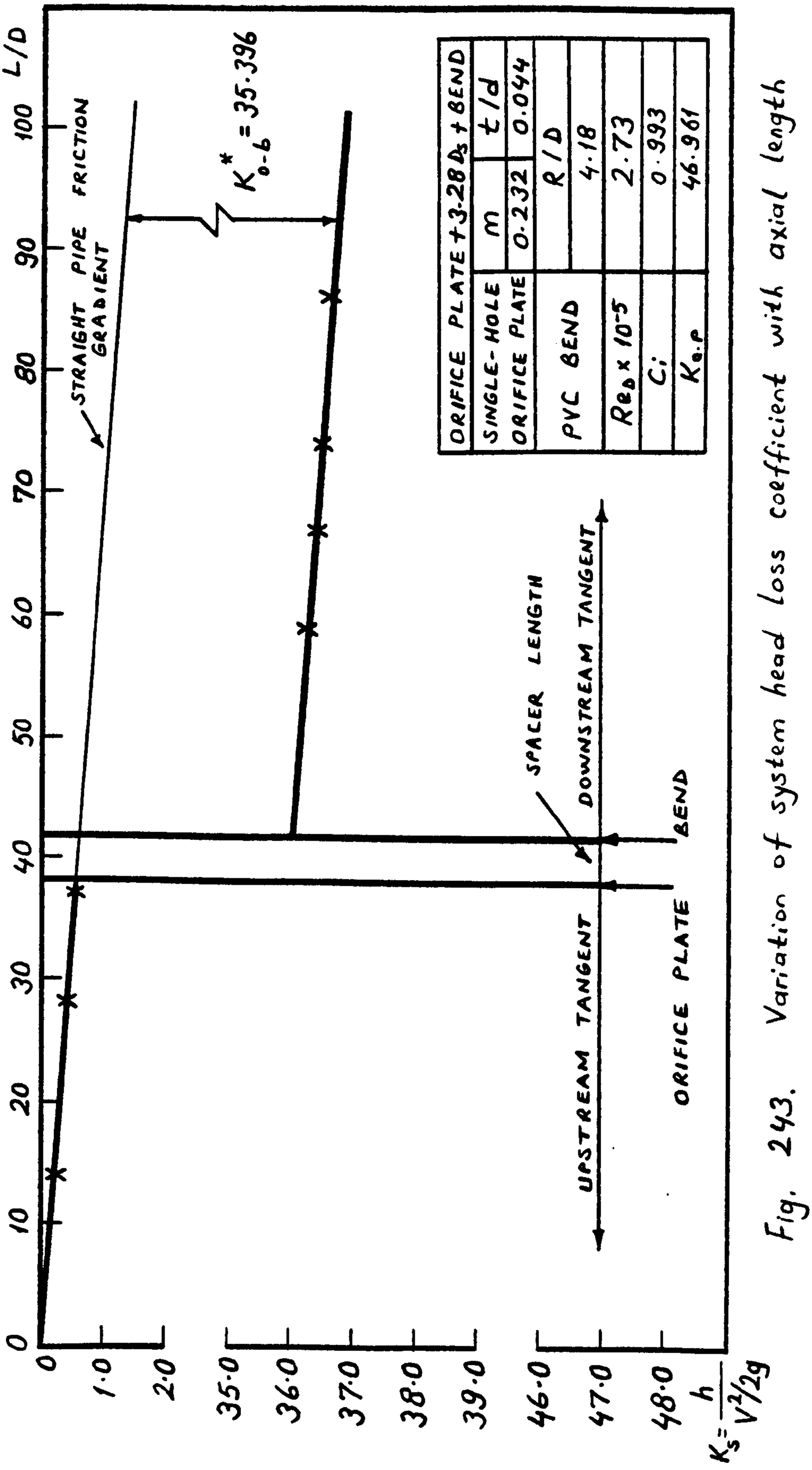

Fig. 243. Variation of system head loss coefficient with axial length

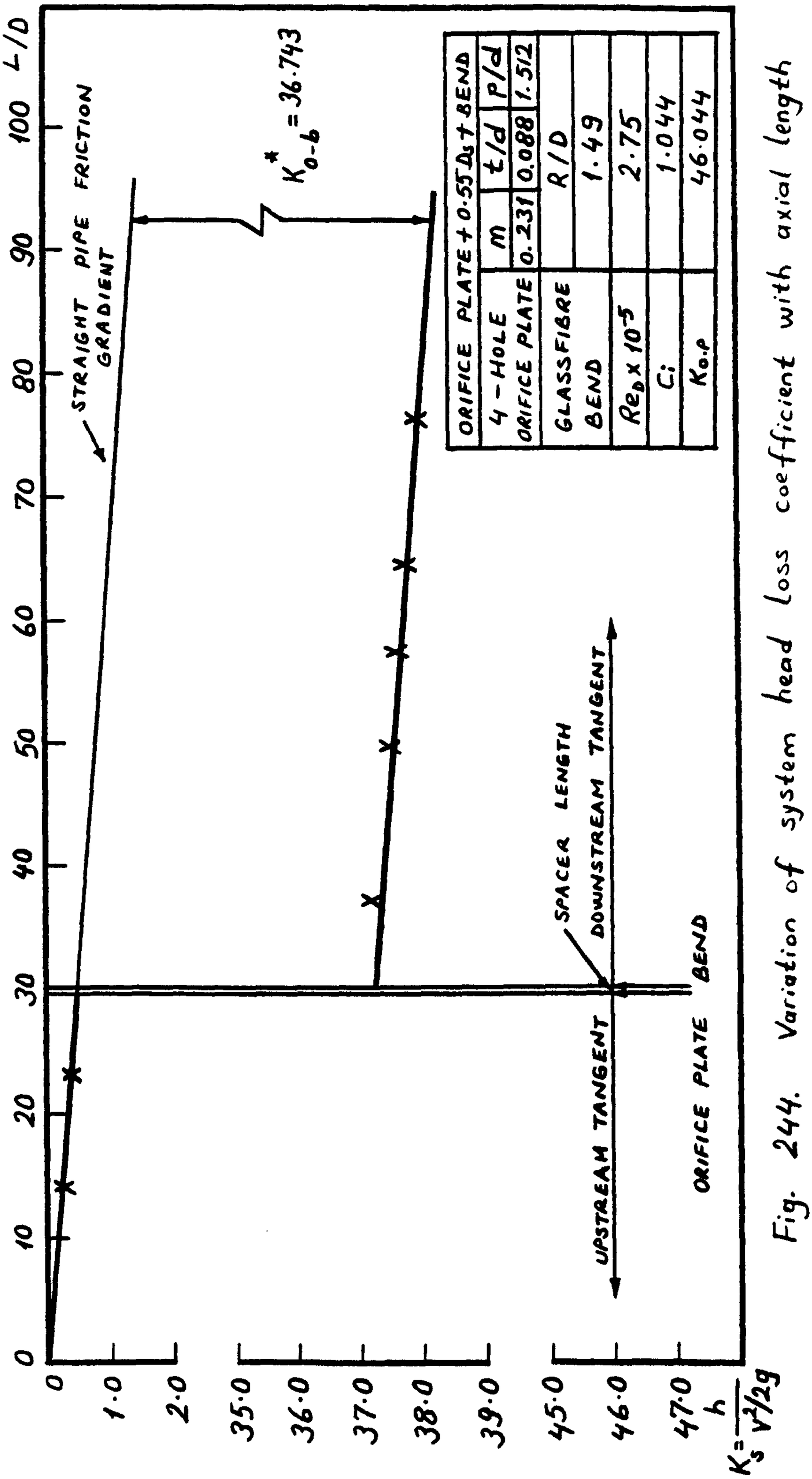

Fig. 244. Variation of system head loss coefficient with axial length

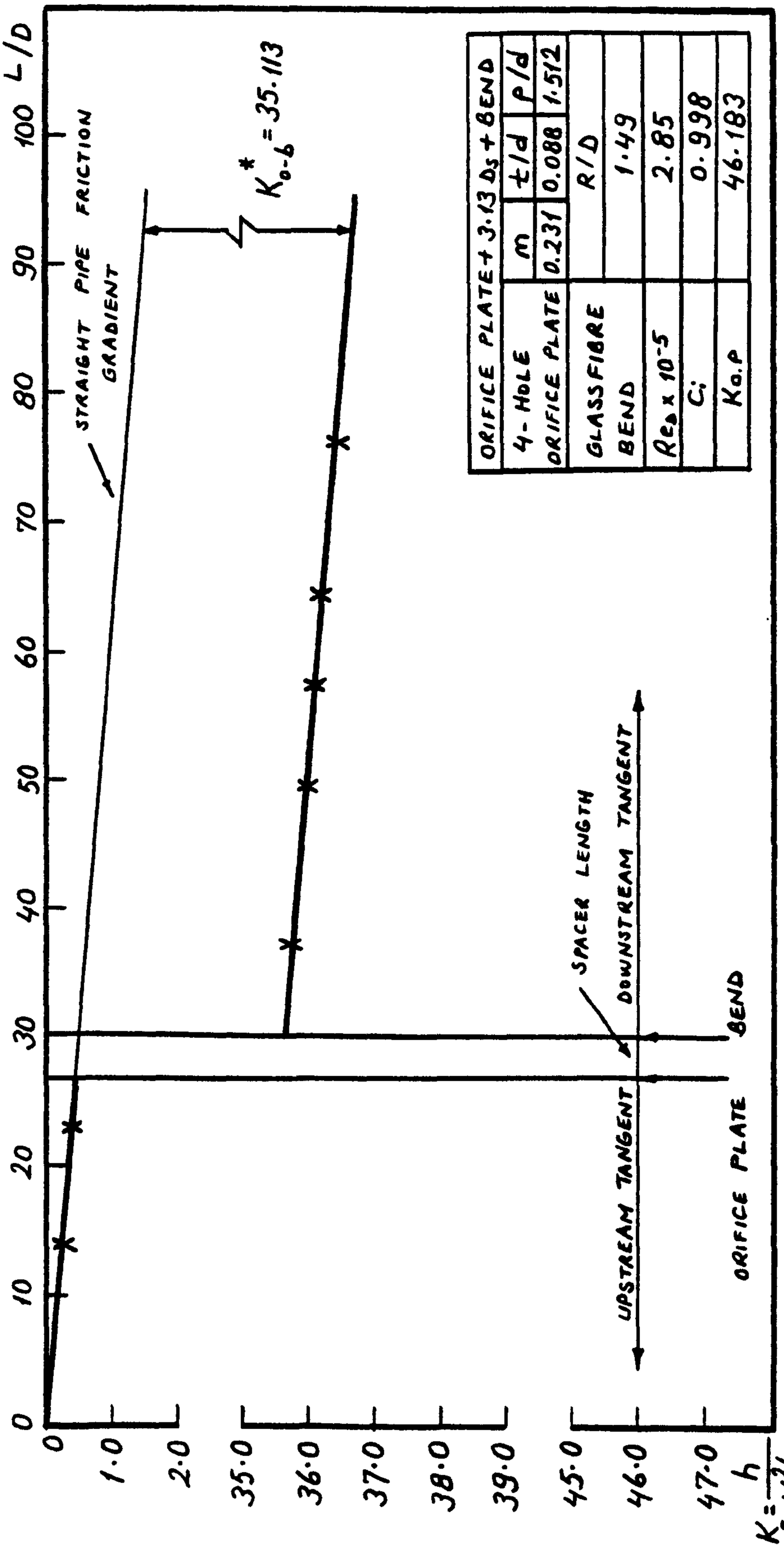

Fig. 245. Variation of system head loss coefficient with

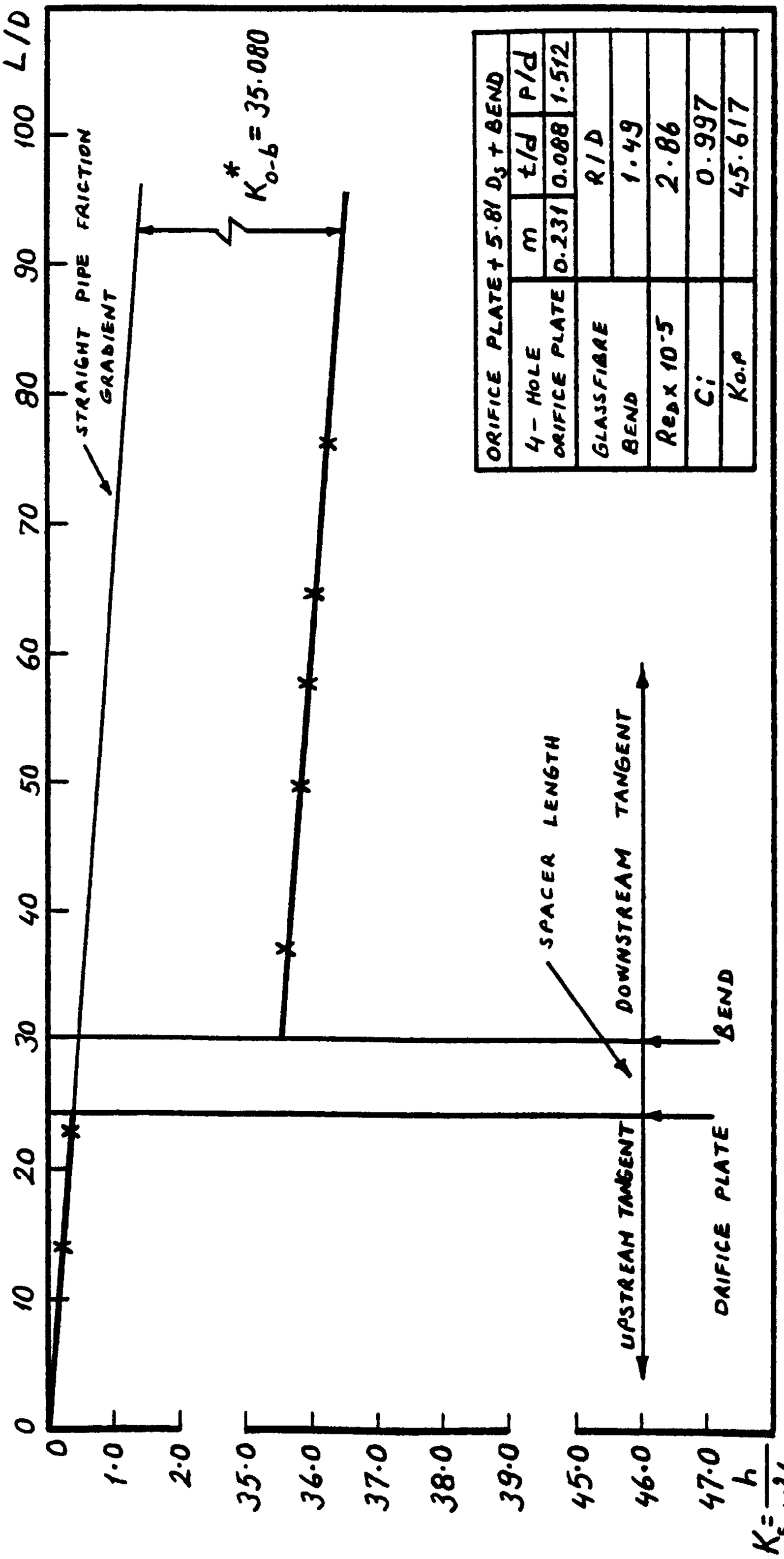

Fig. 246. Variation of system head loss coefficient with axial length

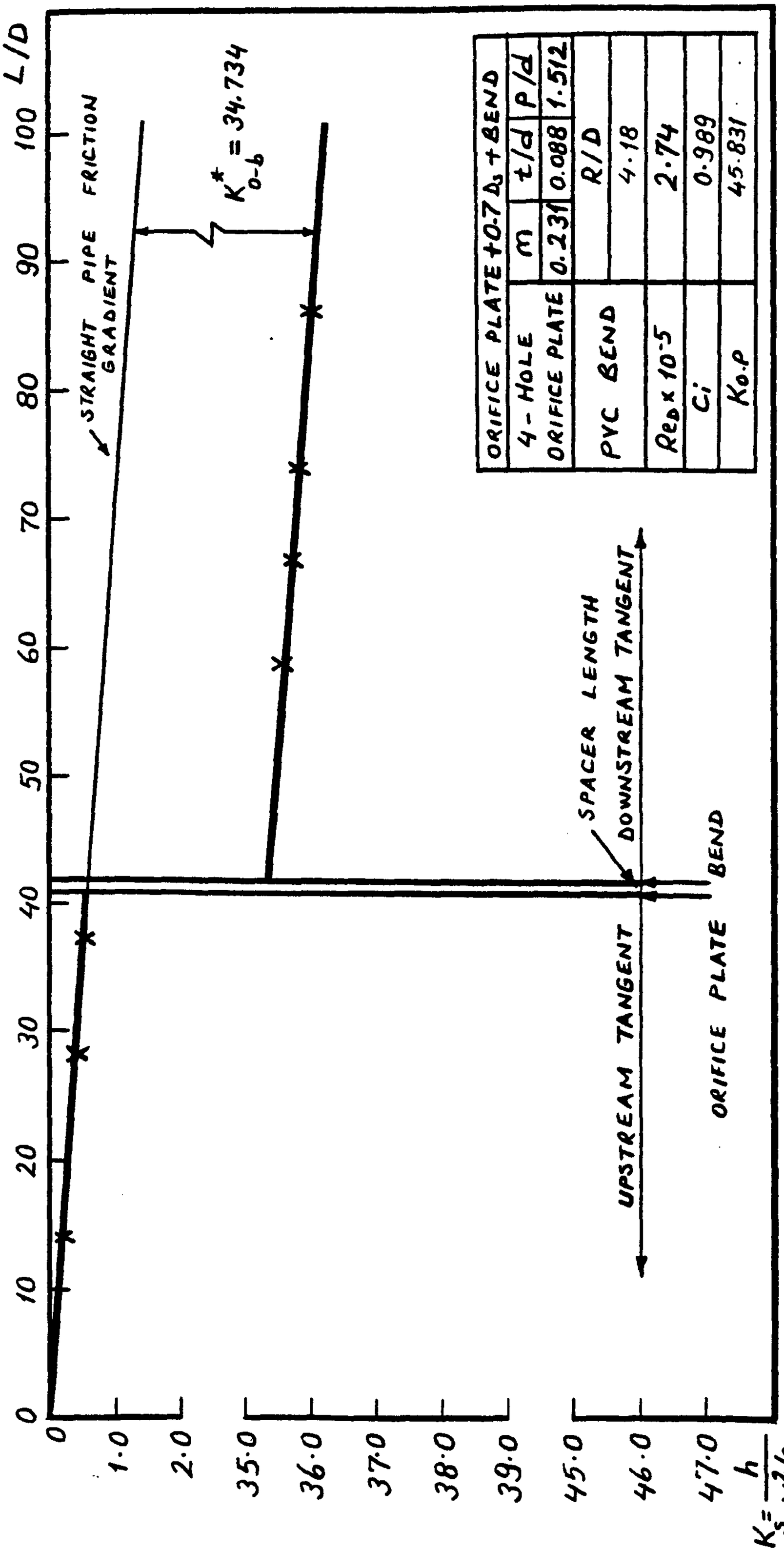

Fig. 247. Variation of system head loss coefficient with axial length

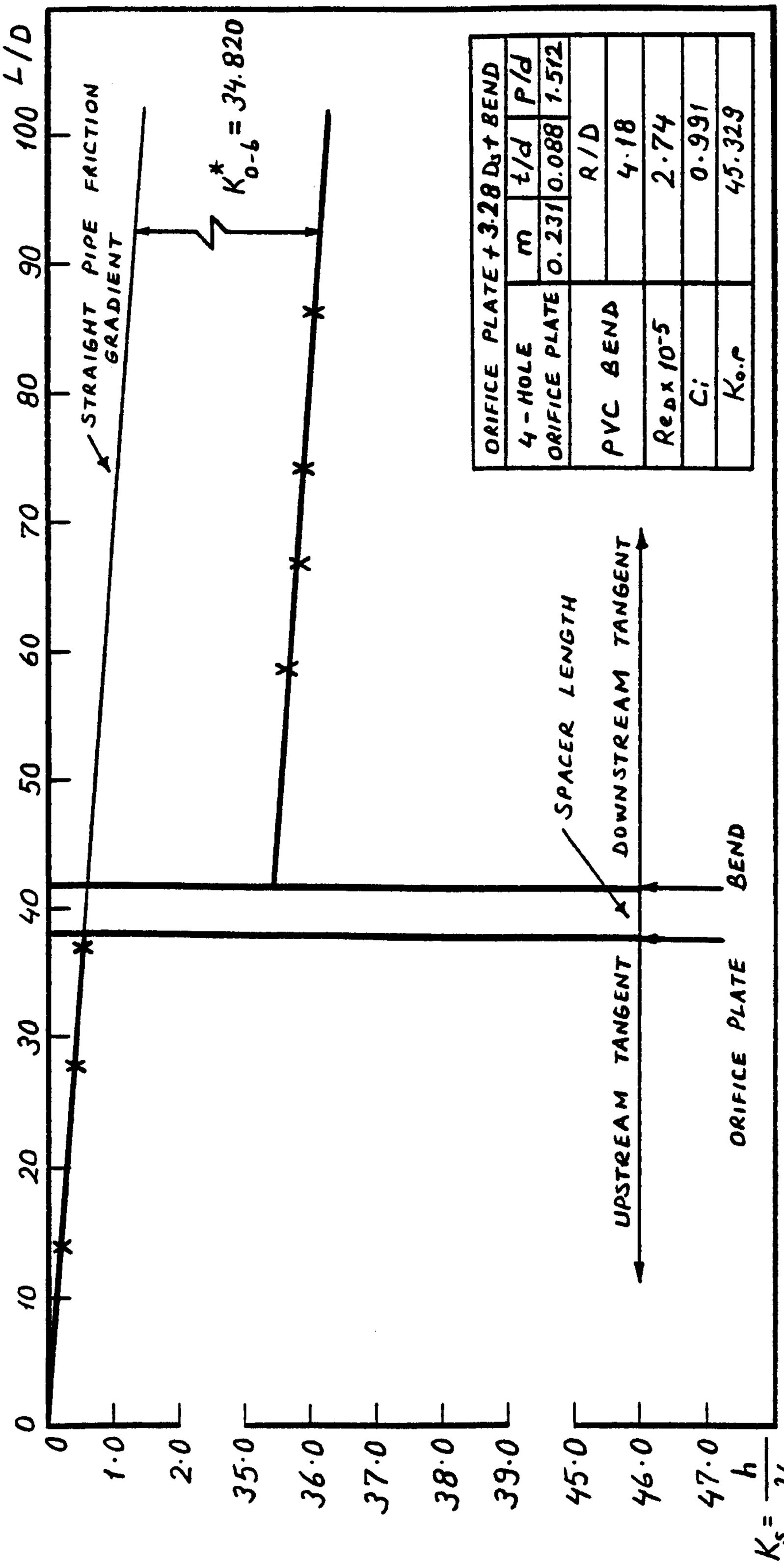

Fig. 248. Variation of system head loss coefficient with axial length

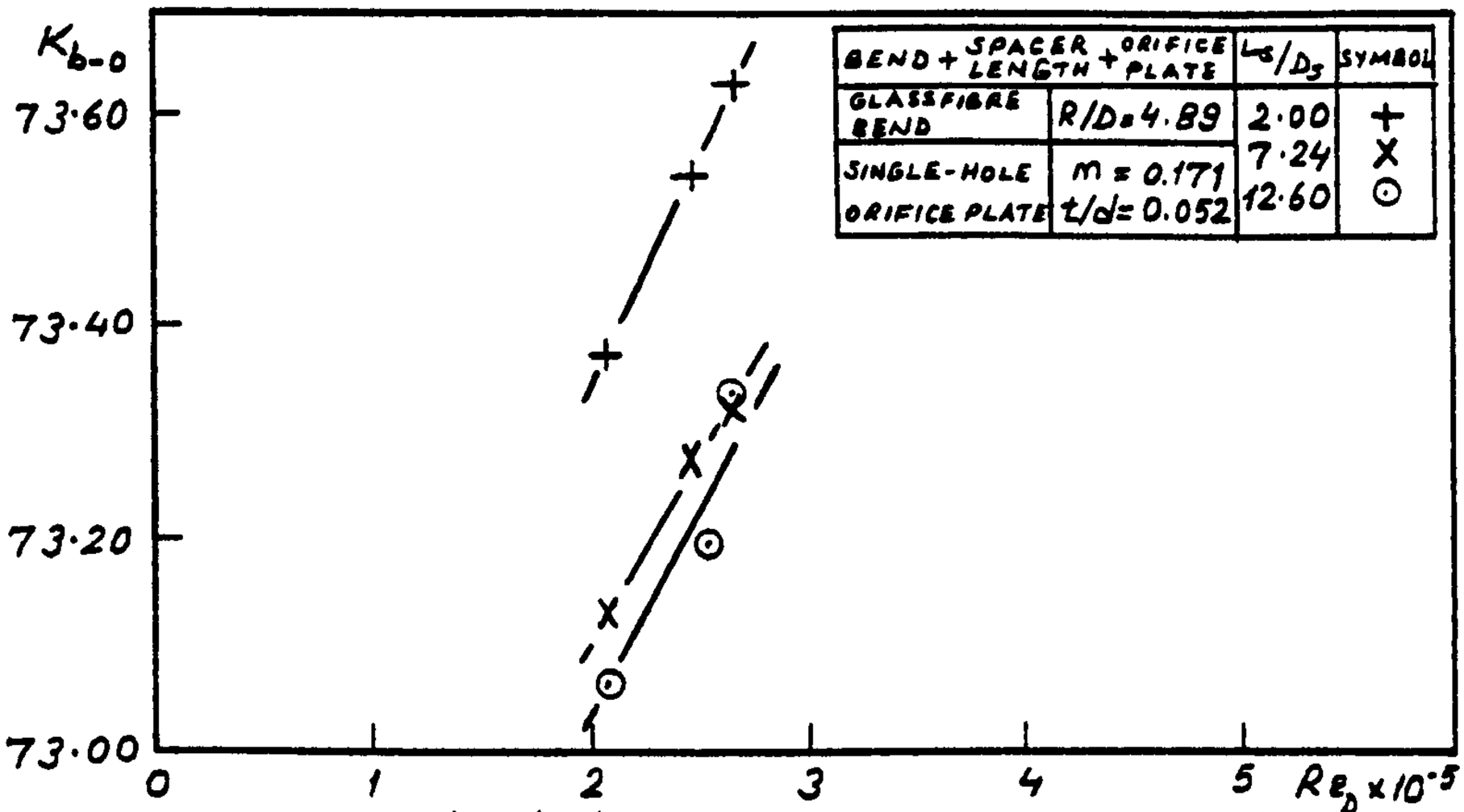

Fig. 249. Head loss coefficients for bend-orifice plate combinations

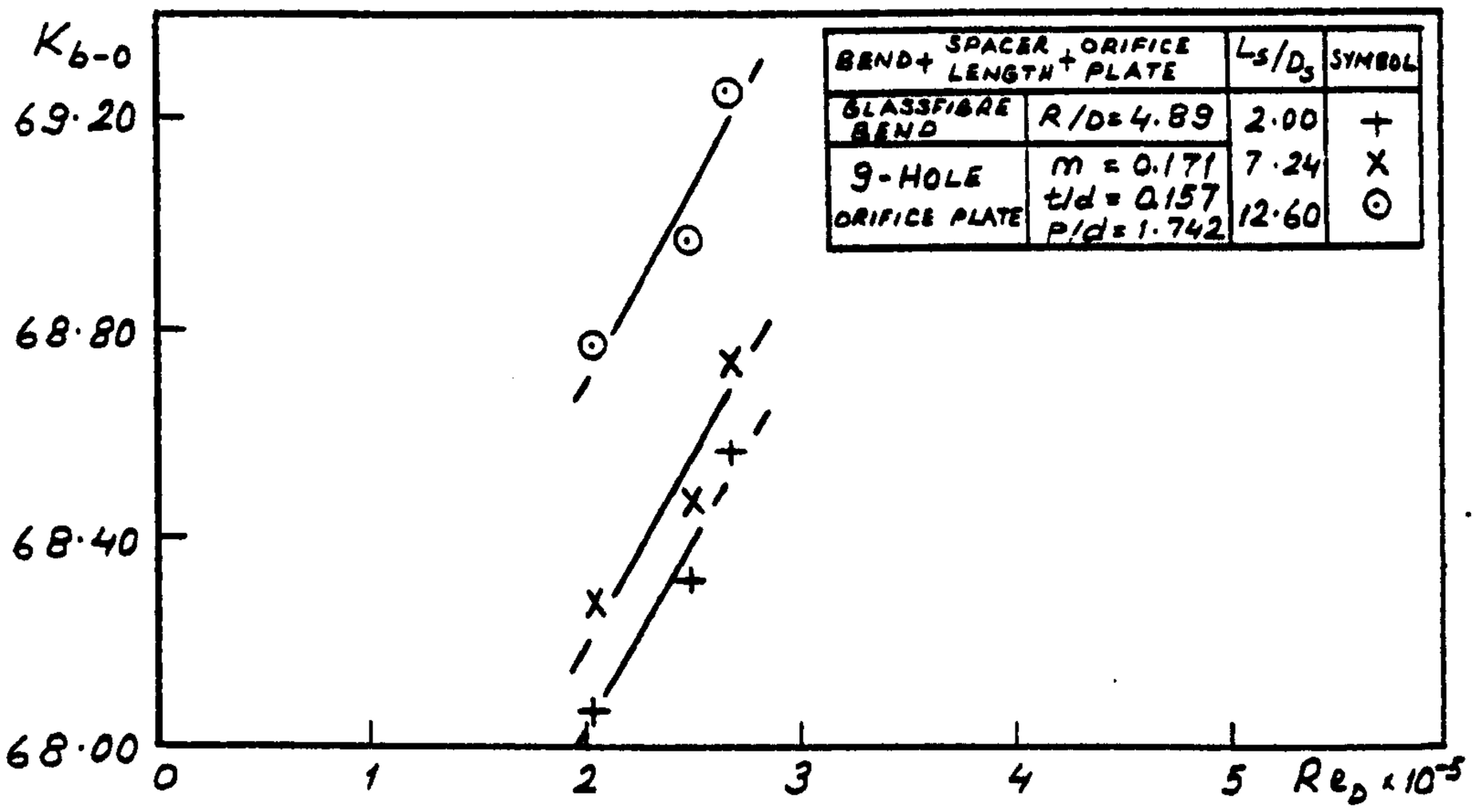

Fig. 250. Head loss coefficients for bend-orifice plate combinations

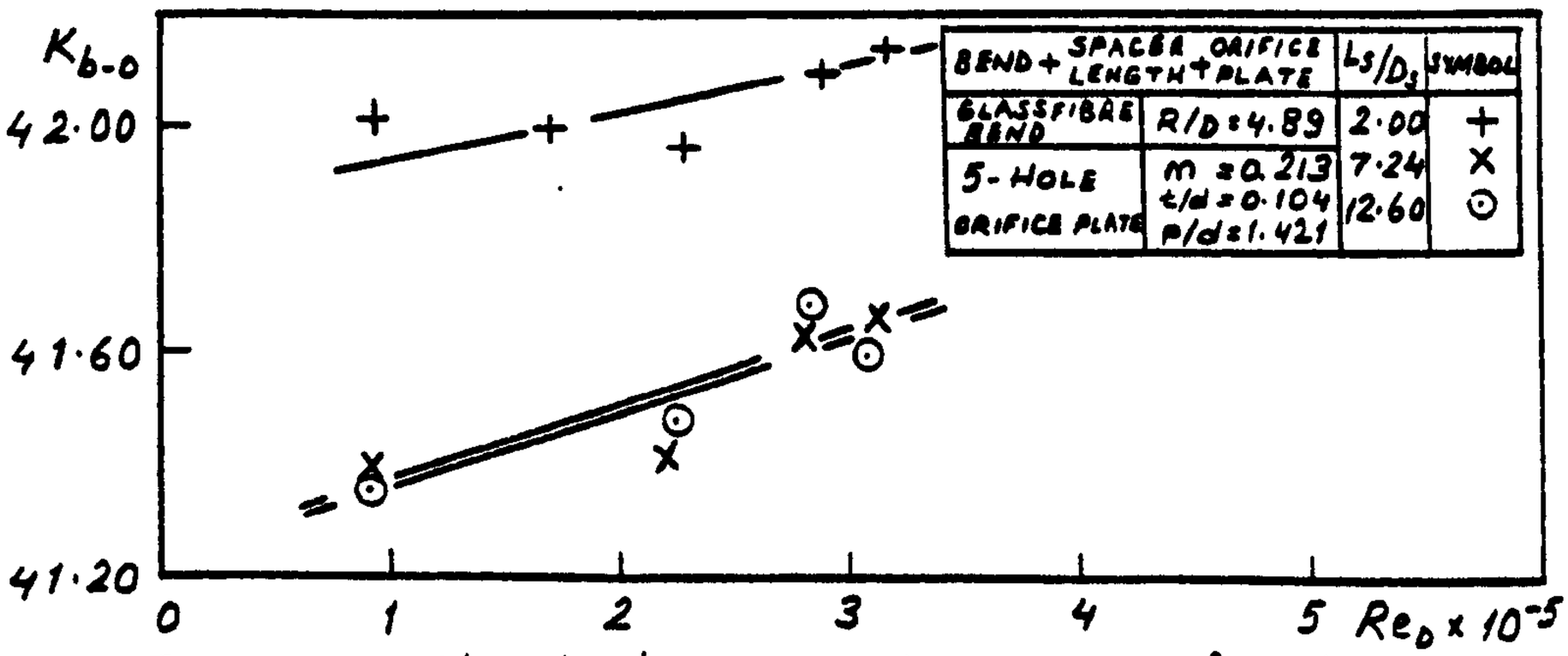

Fig. 251. Head loss coefficients for bend-orifice plate combinations

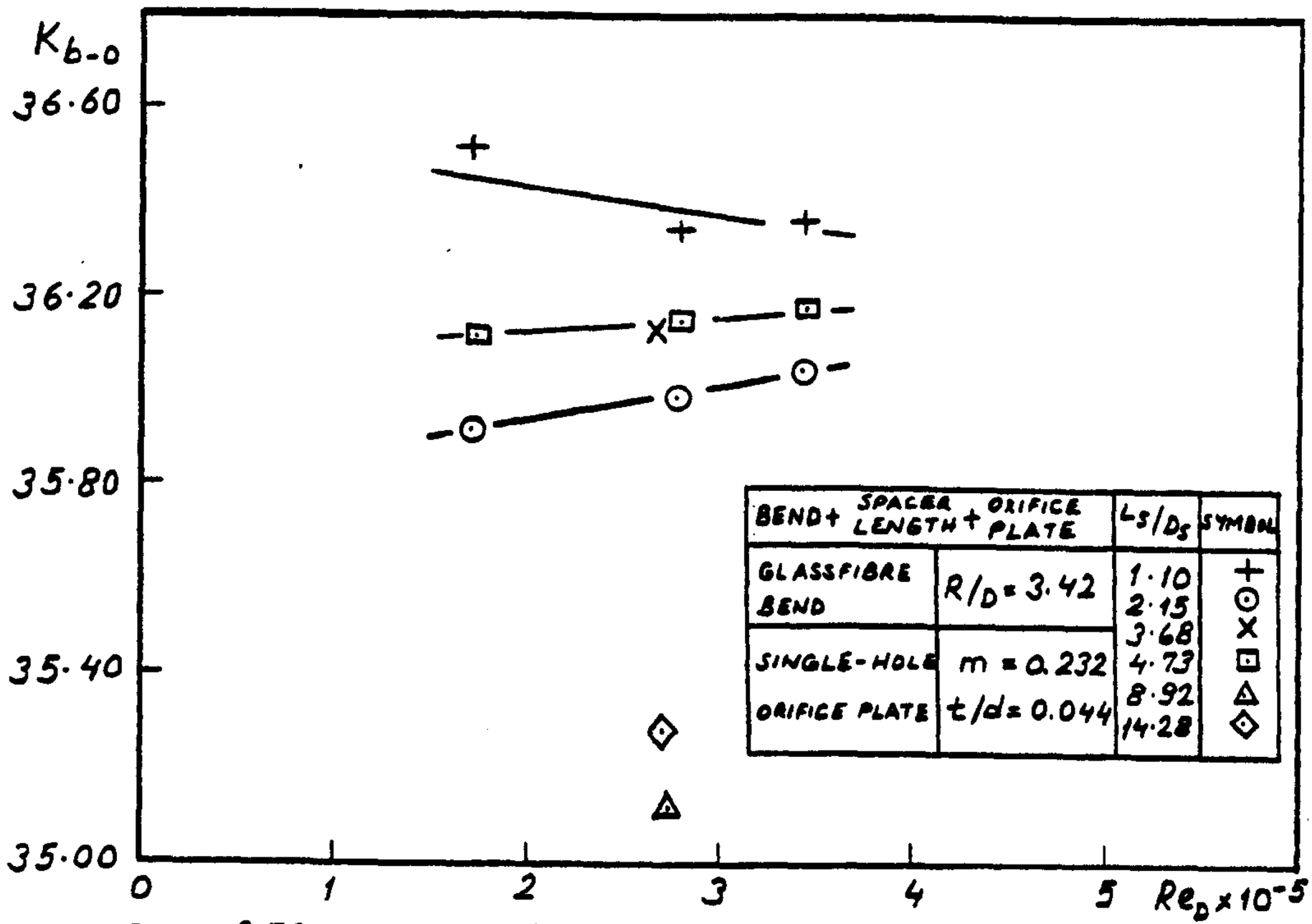

Fig. 252. Head loss coefficients for bend-orifice plate combinations

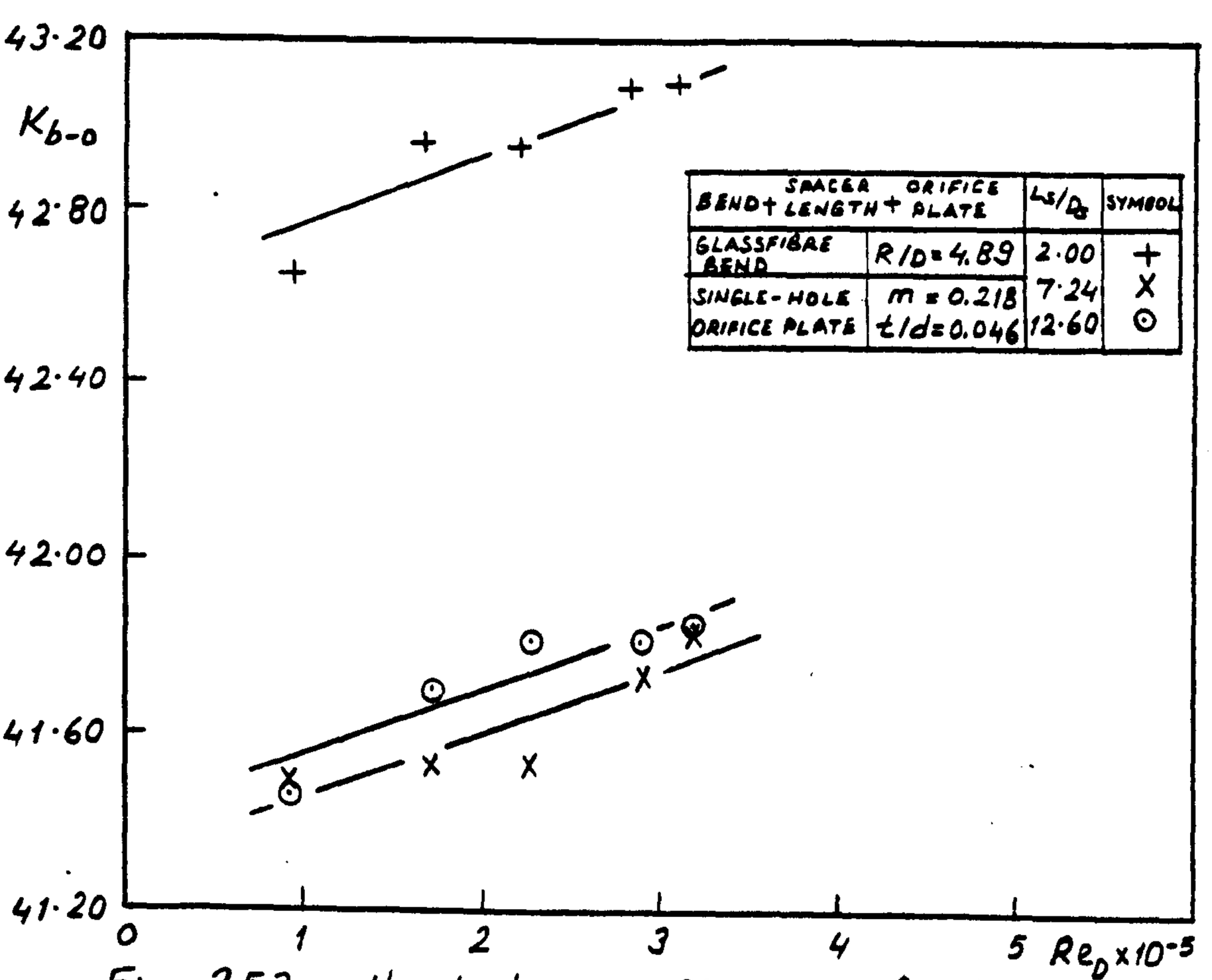

Fig. 253. Head loss coefficients for bend-orifice plate combinations

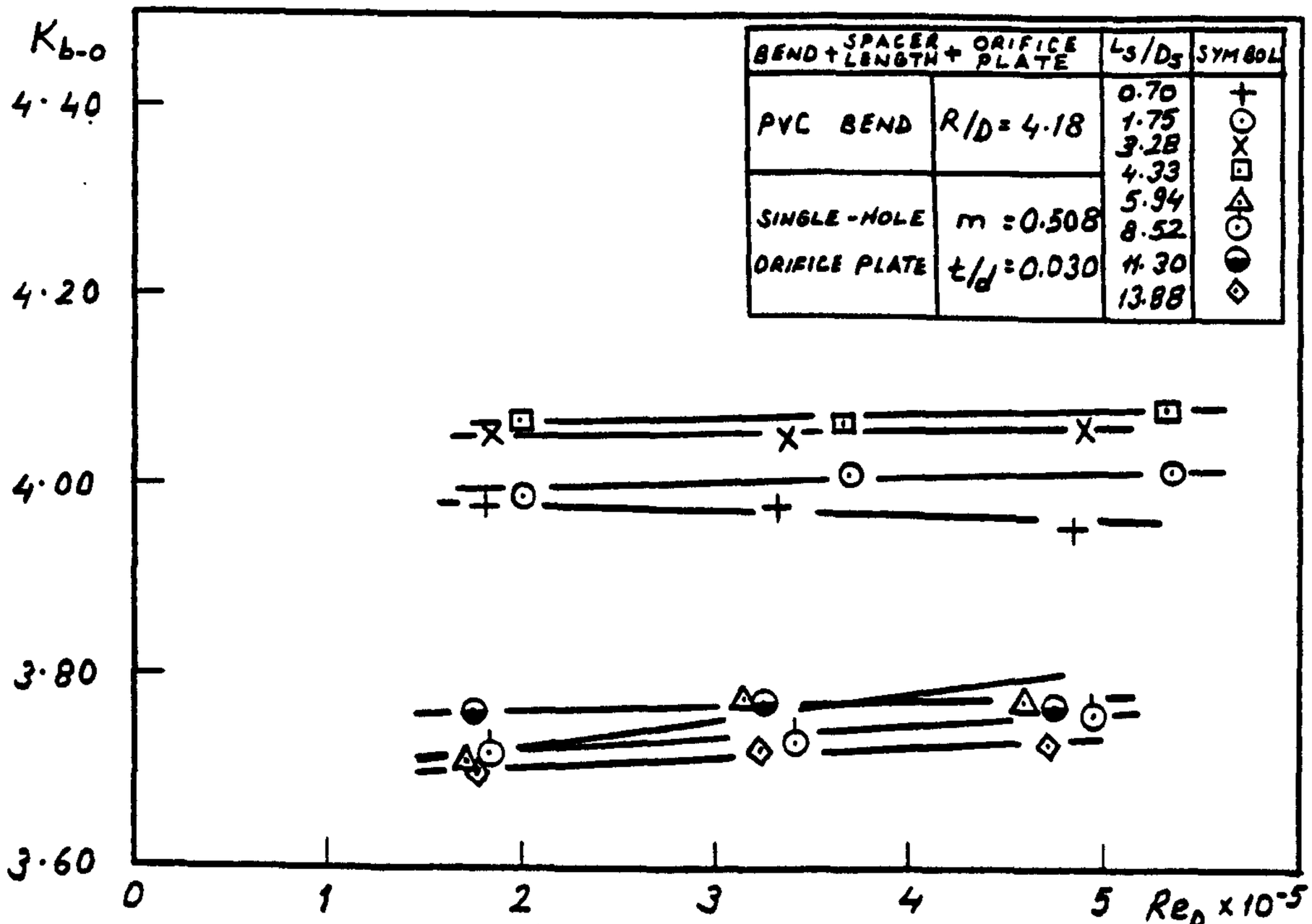

Fig. 254. Head loss coefficients for bend-orifice plate combinations

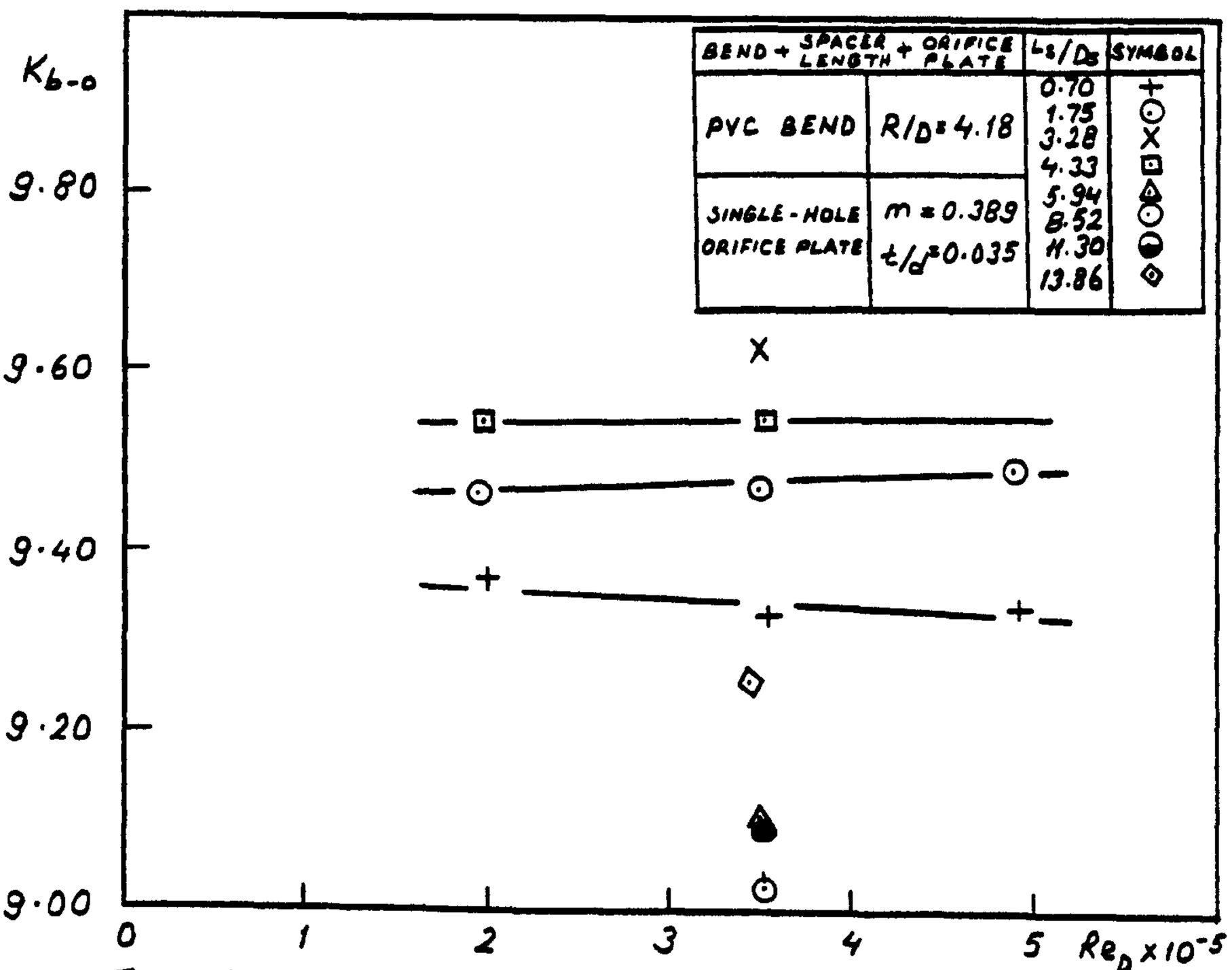

Fig. 255. Head loss coefficients for bend-orifice plate combinations

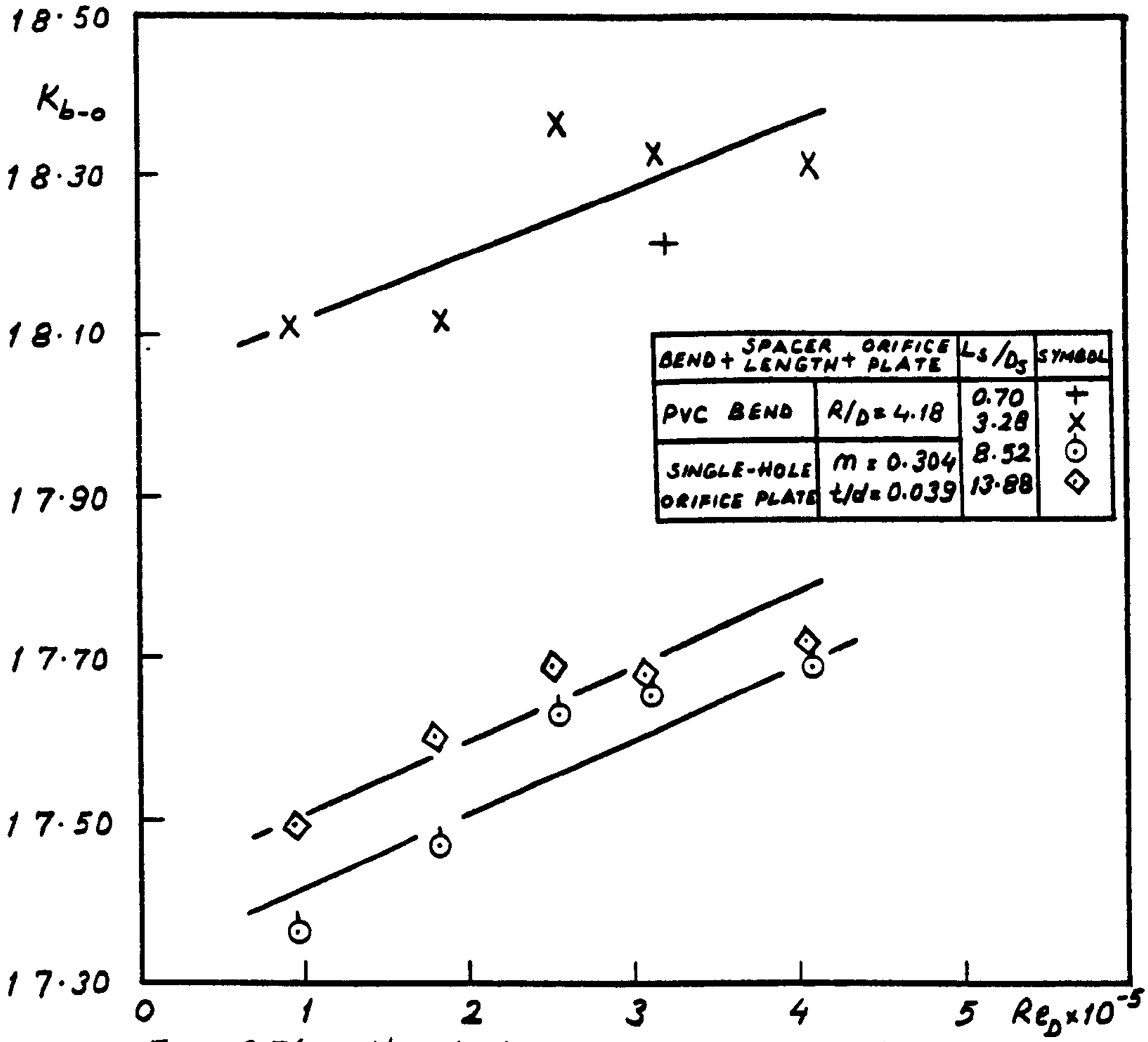

Fig. 256. Head loss coefficients for bend-orifice plate combinations

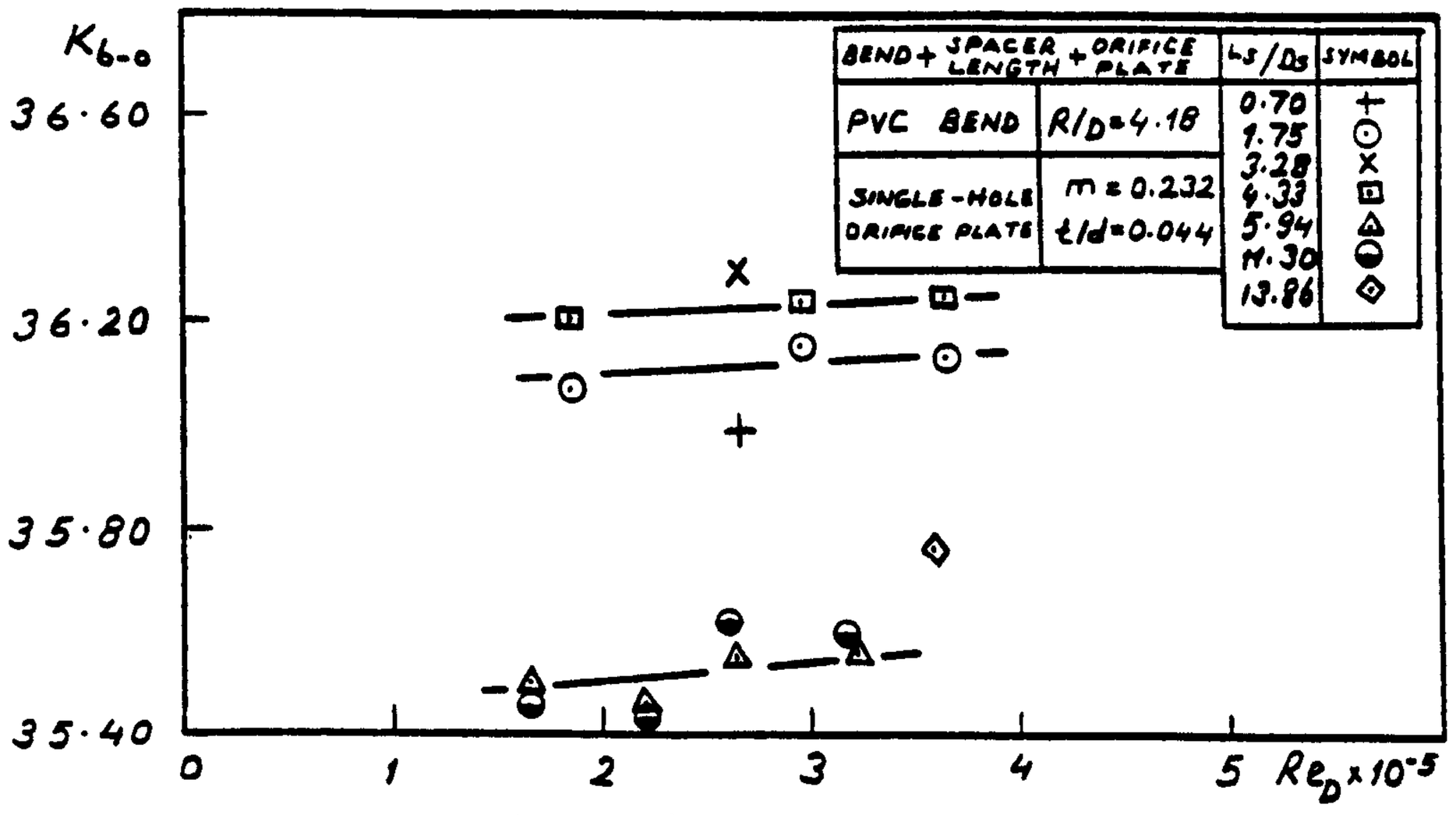

Fig. 257. Head loss coefficients for bend-orifice plate combinations

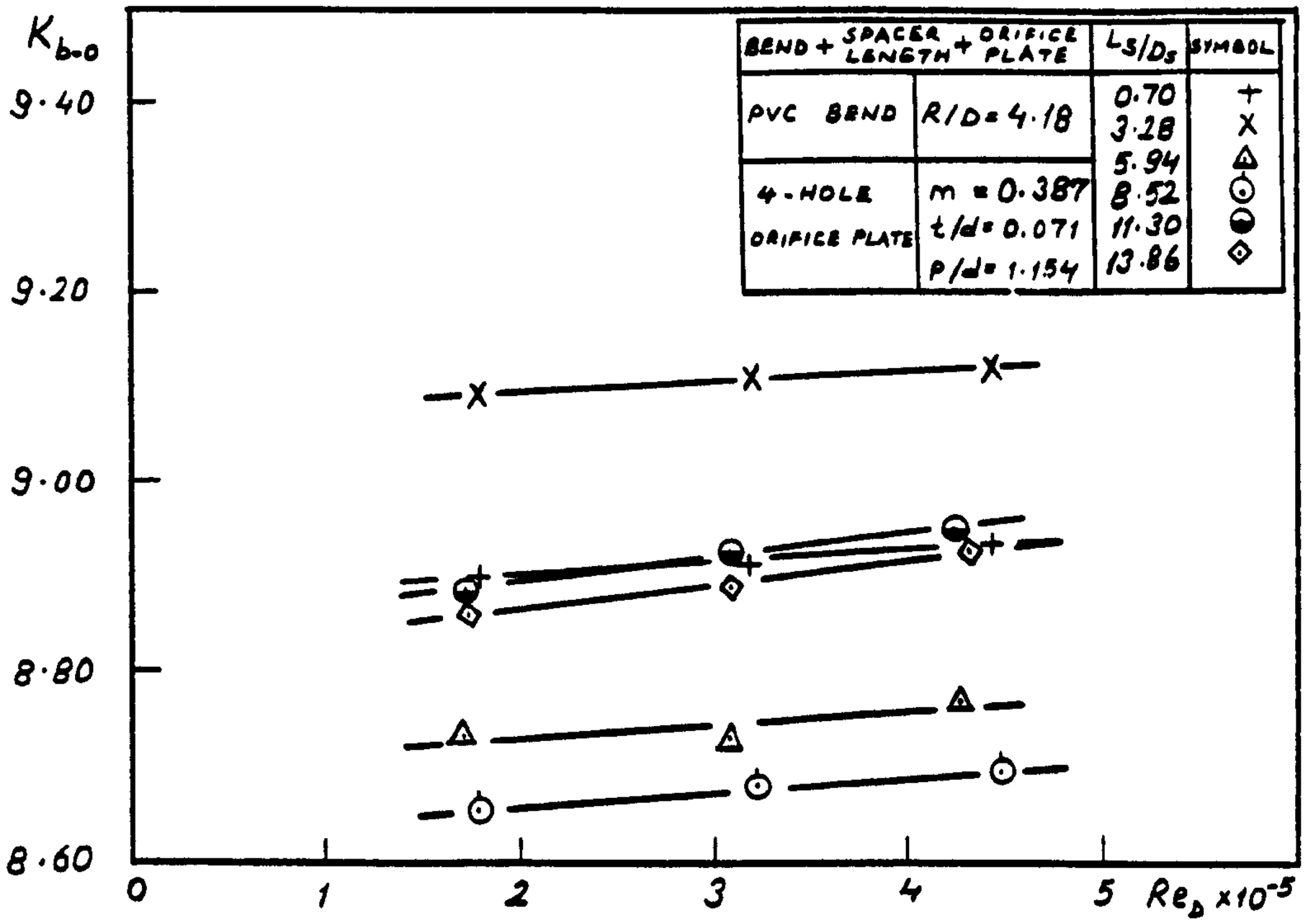

Fig. 258. Head loss coefficients for bend-orifice plate combinations

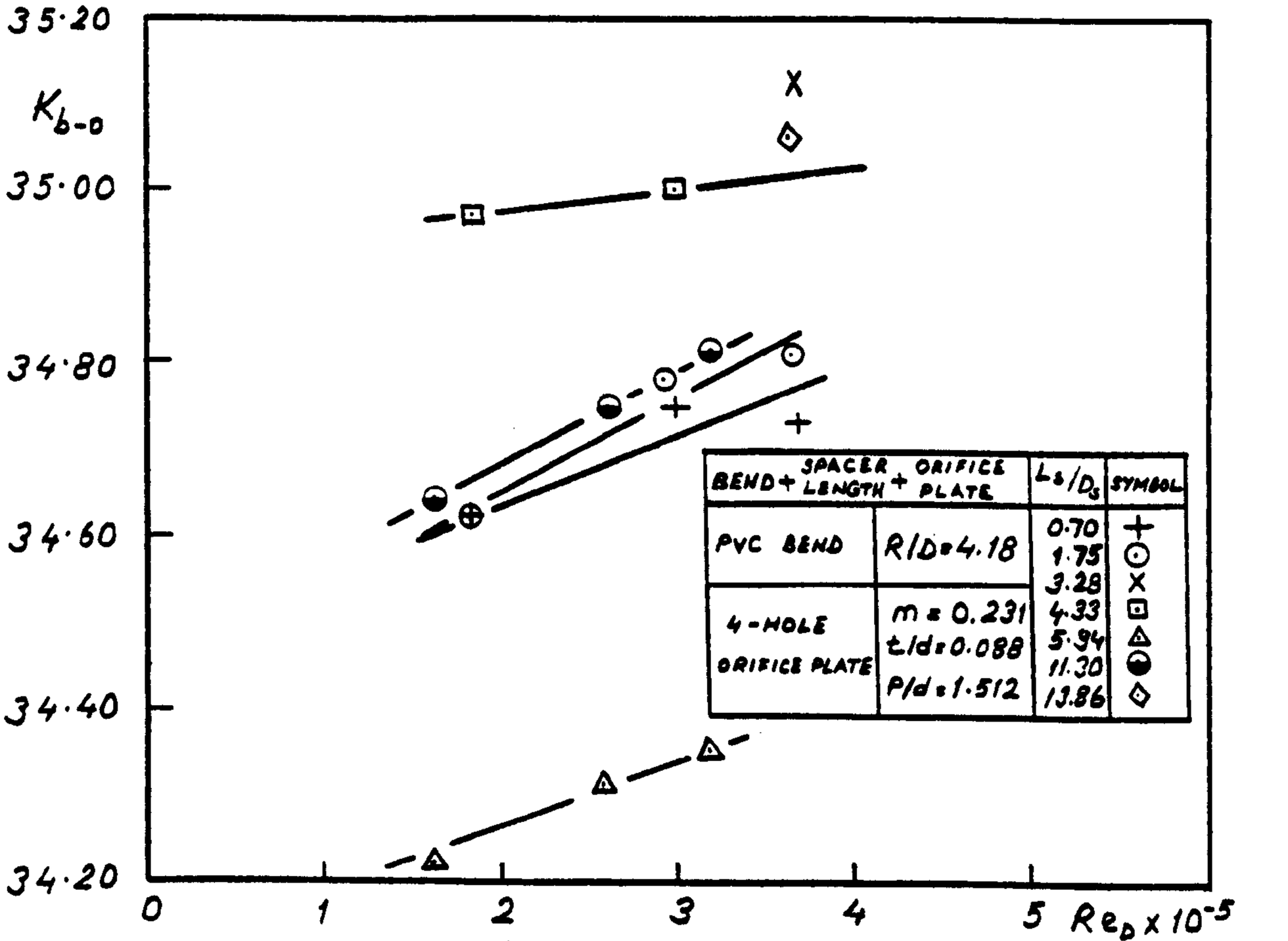

Fig. 259. Head loss coefficients for bend-orifice plate combinations

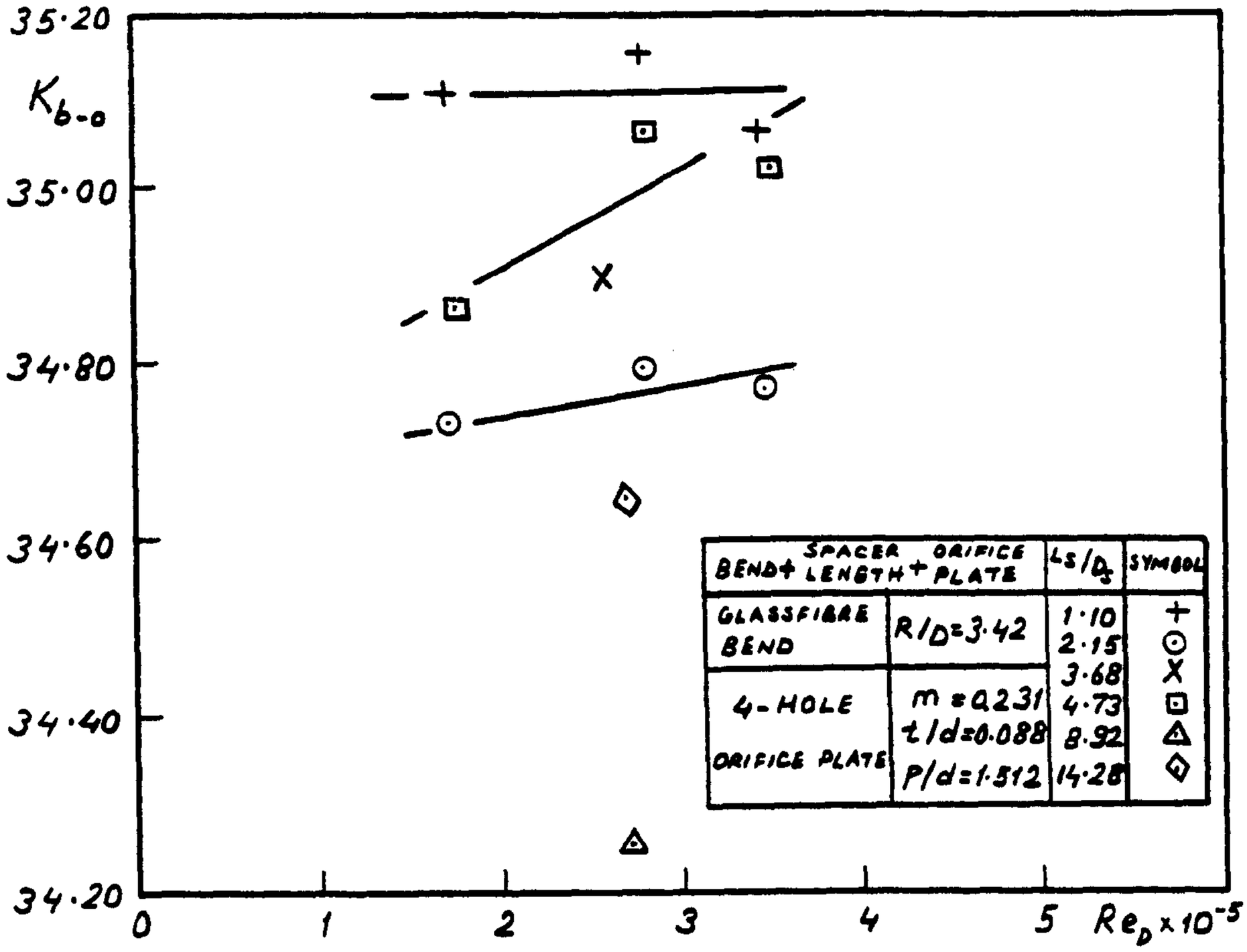

Fig. 260. Head loss coefficients for bend-orifice plate combinations

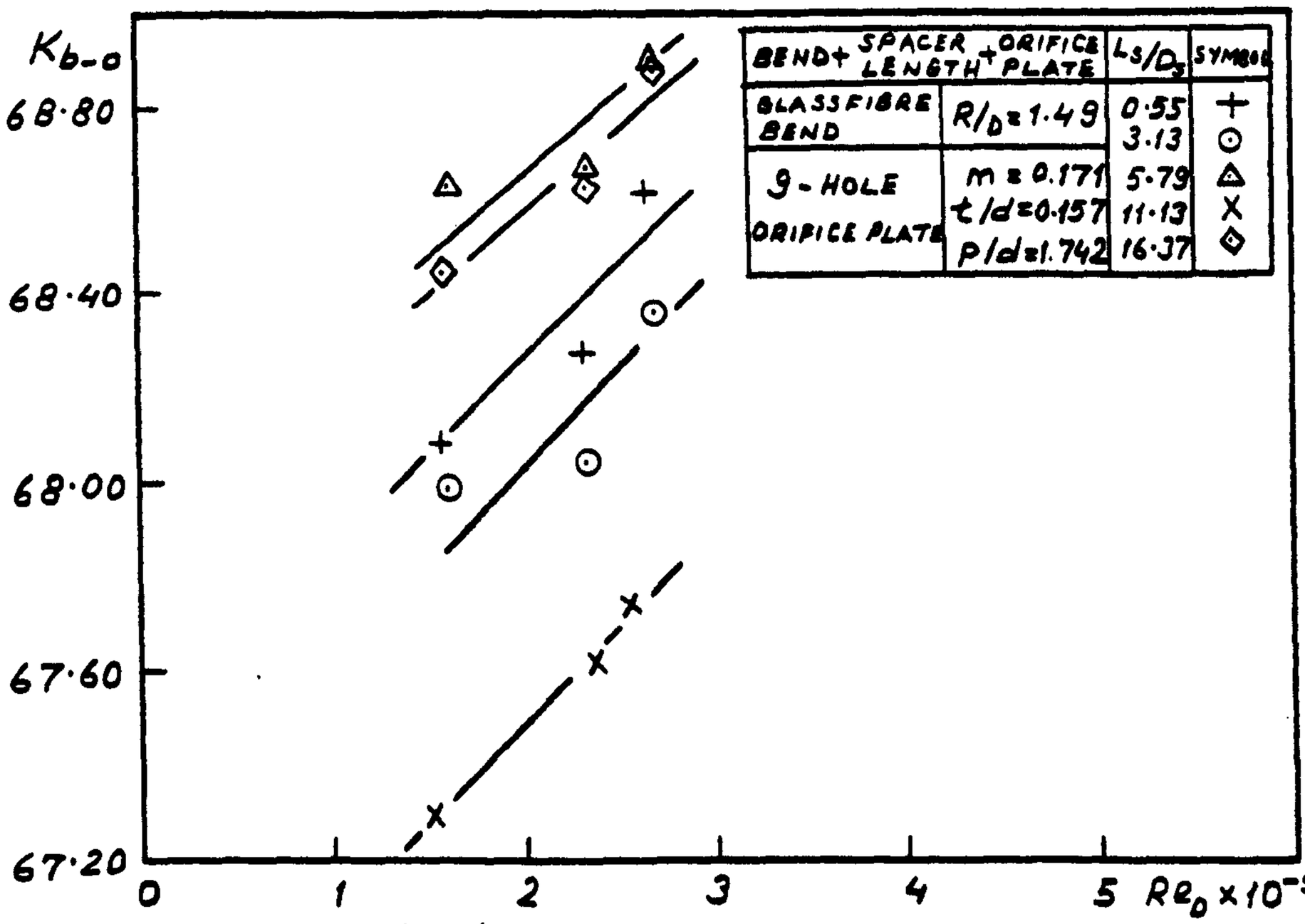

Fig. 261. Head loss coefficients for bend-orifice plate combinations

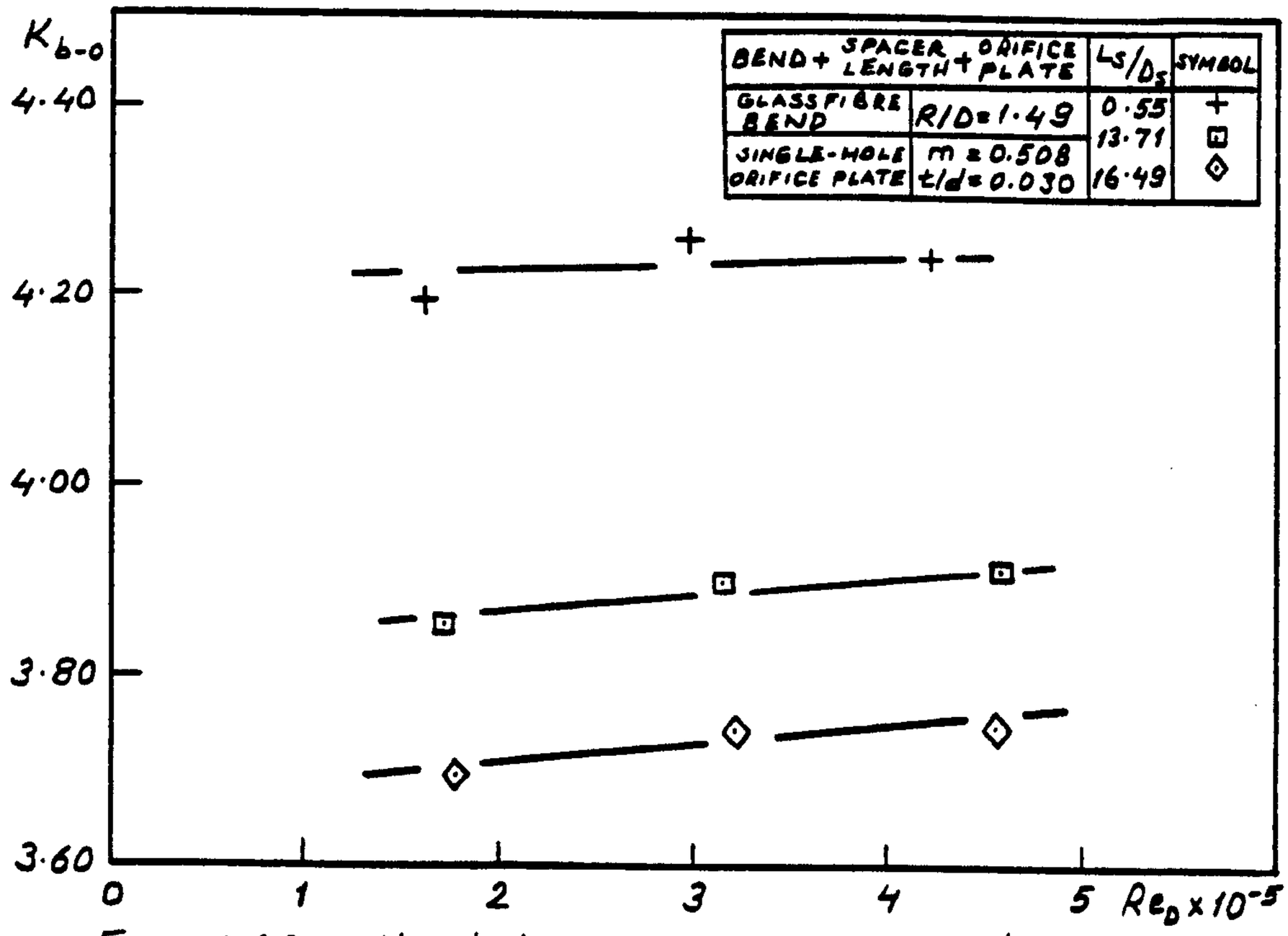

Fig. 262. Head loss coefficients for bend-orifice plate combinations

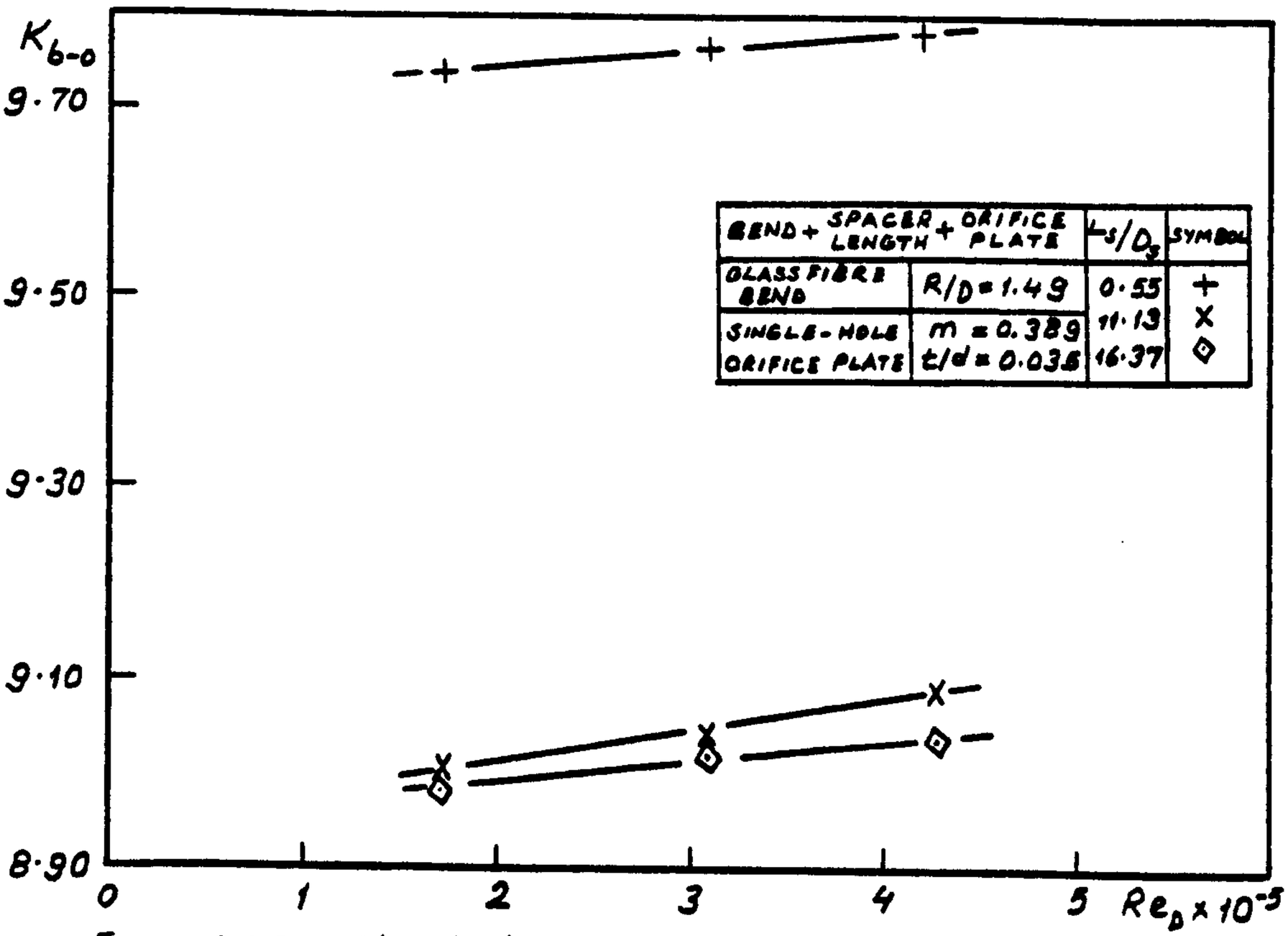

Fig. 263. Head loss coefficients for bend-orifice plate combinations

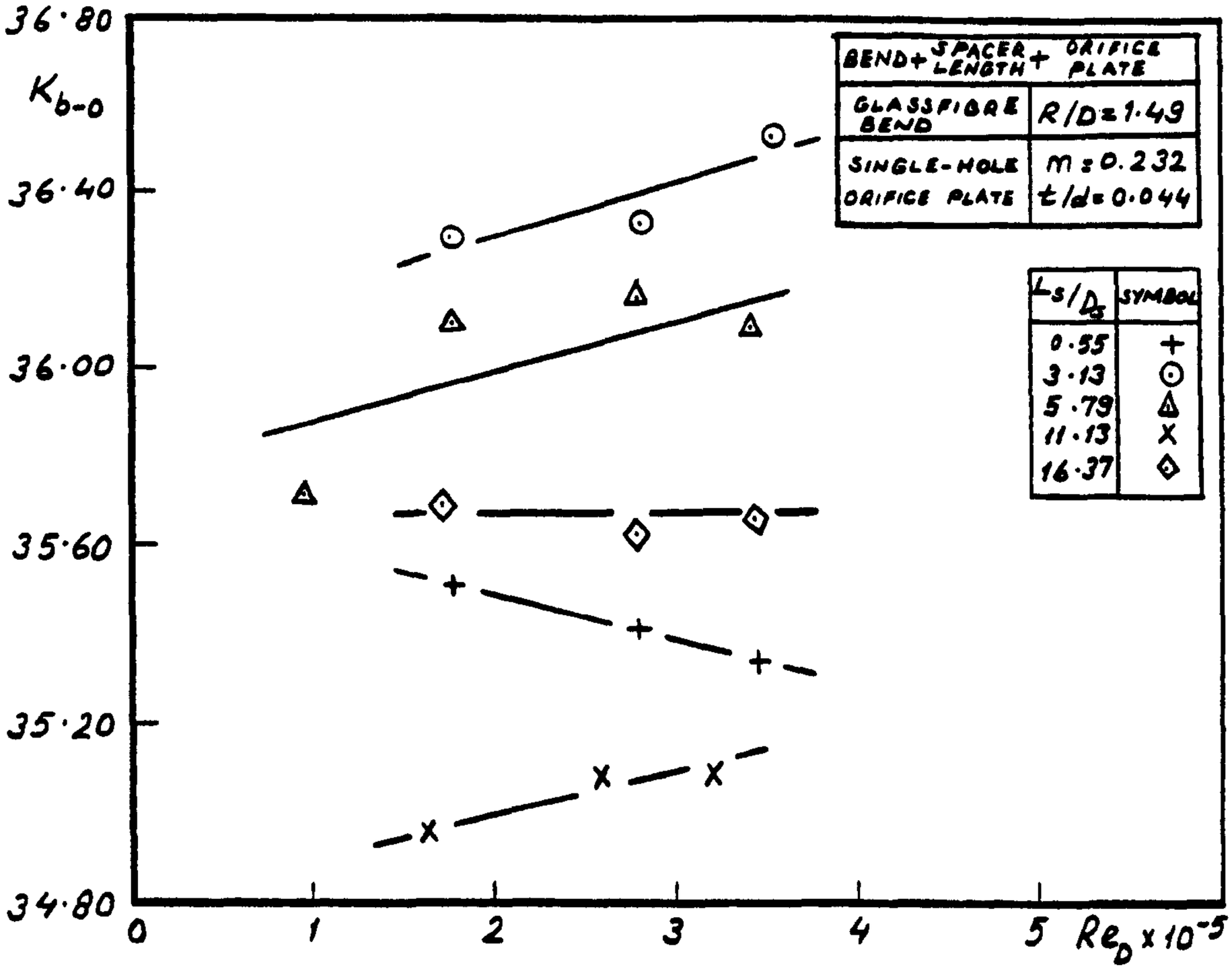

Fig. 264. Head loss coefficients for bend-orifice plate combinations

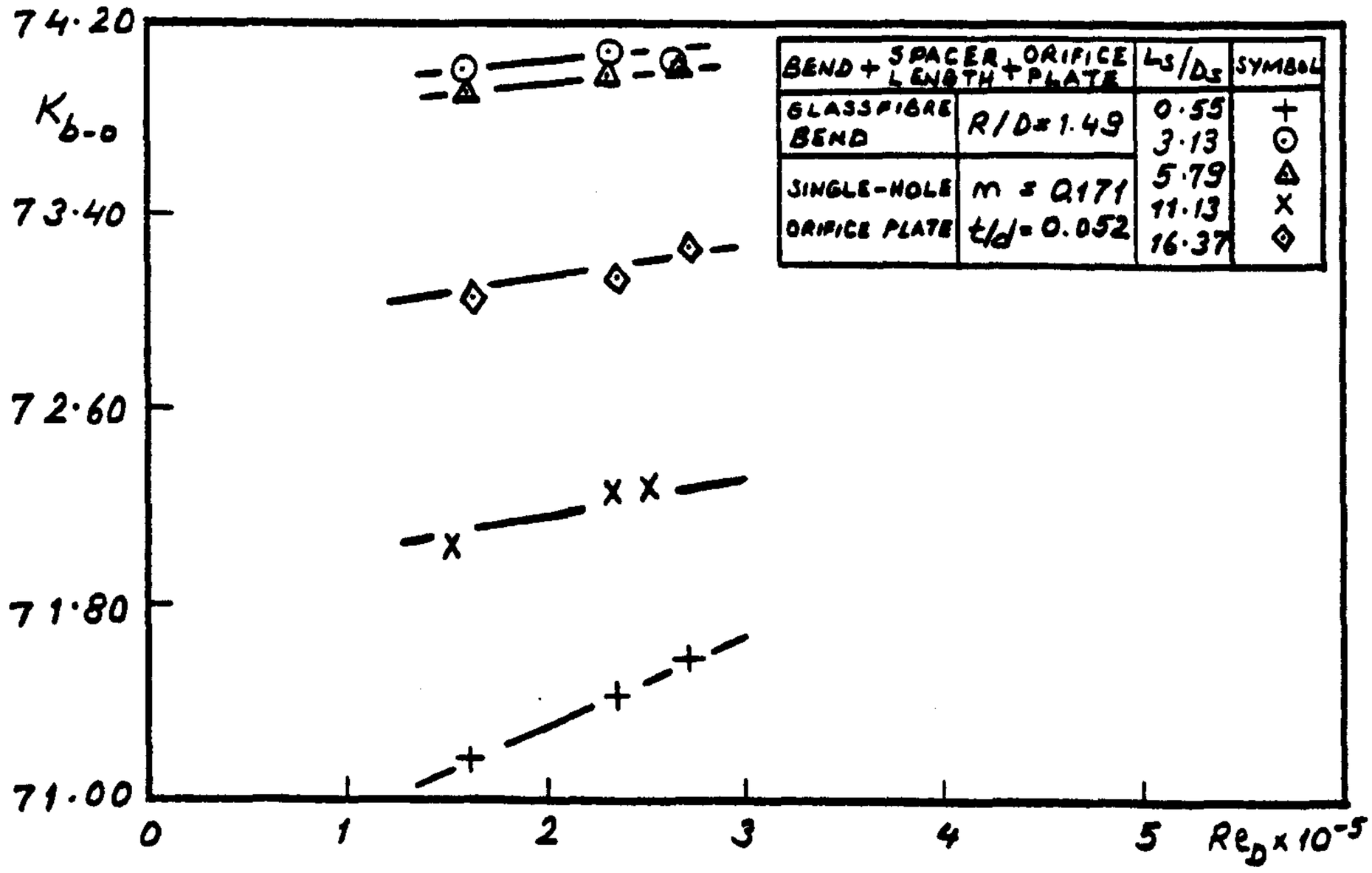

Fig. 265. Head loss coefficients for bend-orifice plate combinations

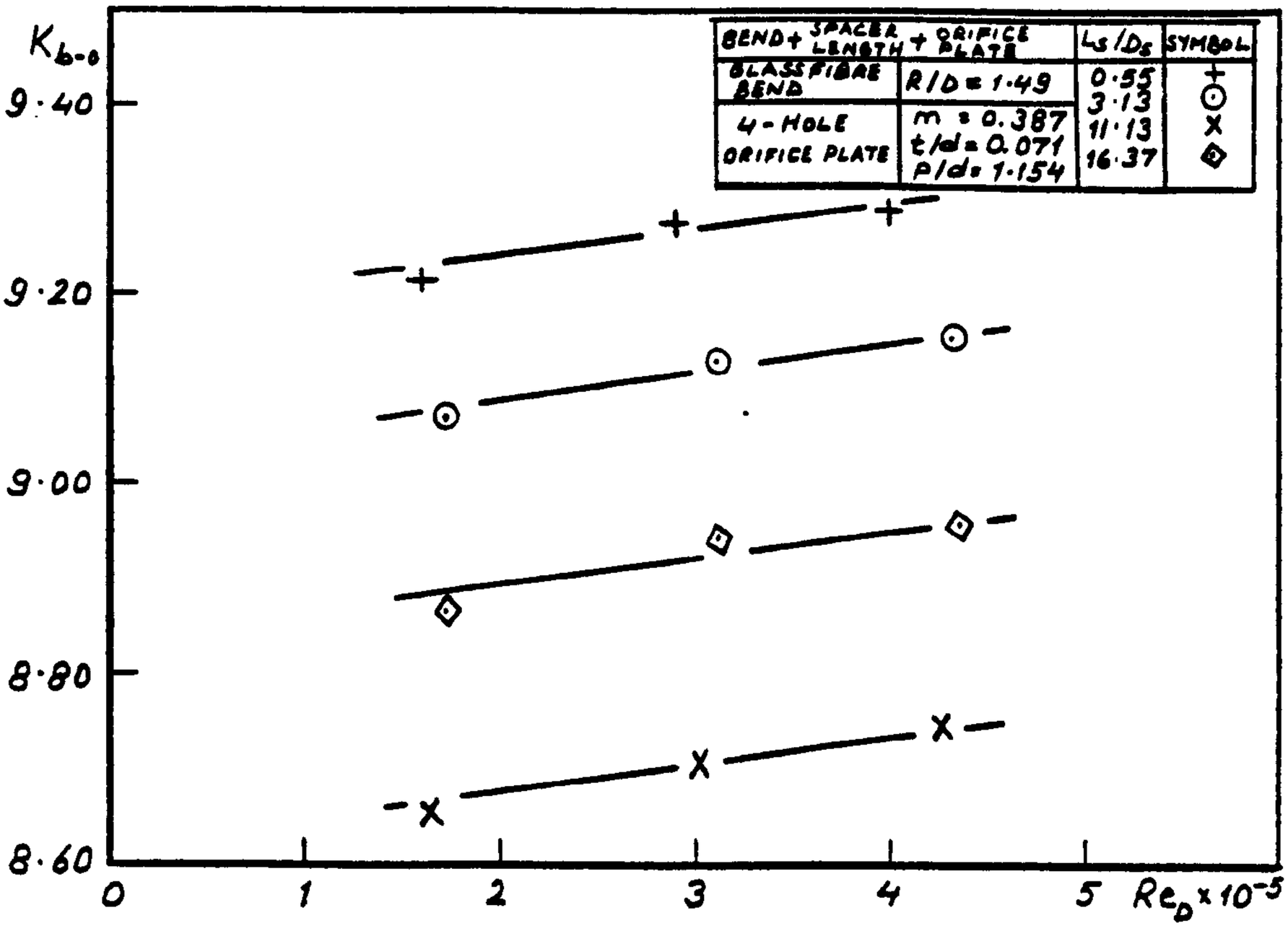

Fig. 266. Head loss coefficients for bend-orifice plate combinations

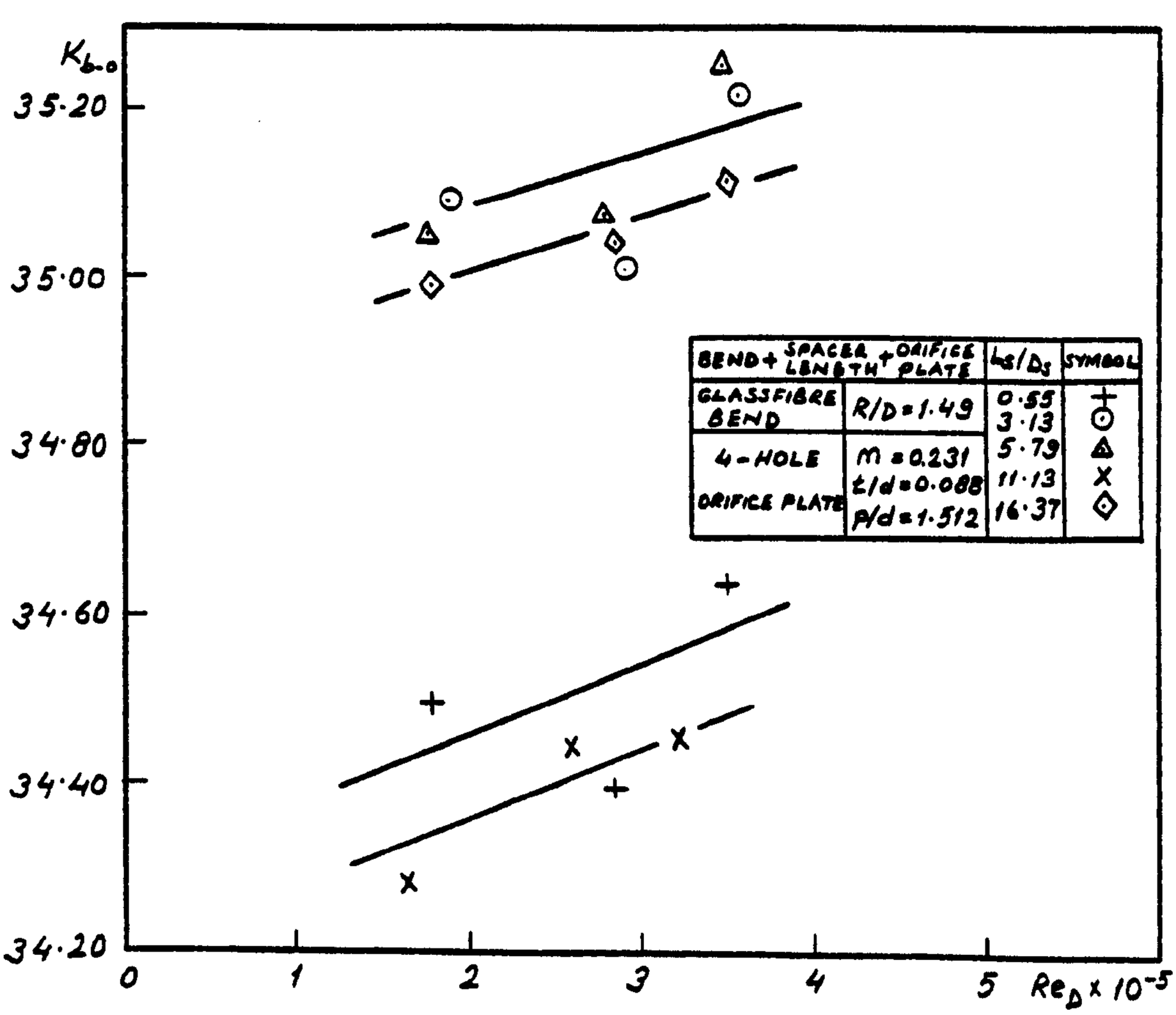

Fig. 267. Head loss coefficients for bend-orifice plate combinations

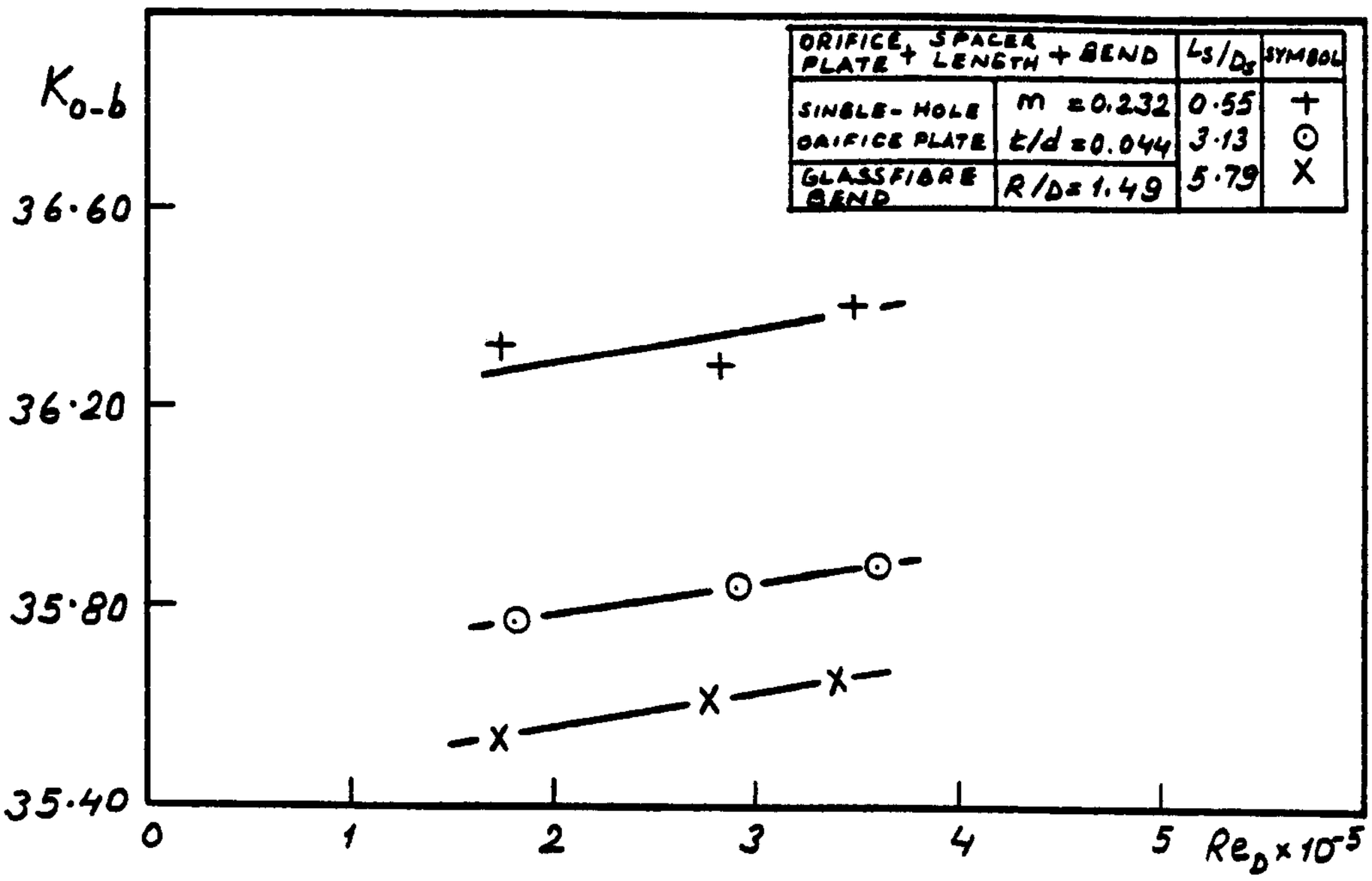

Fig. 268. Head loss coefficients for orifice plate - bend combinations

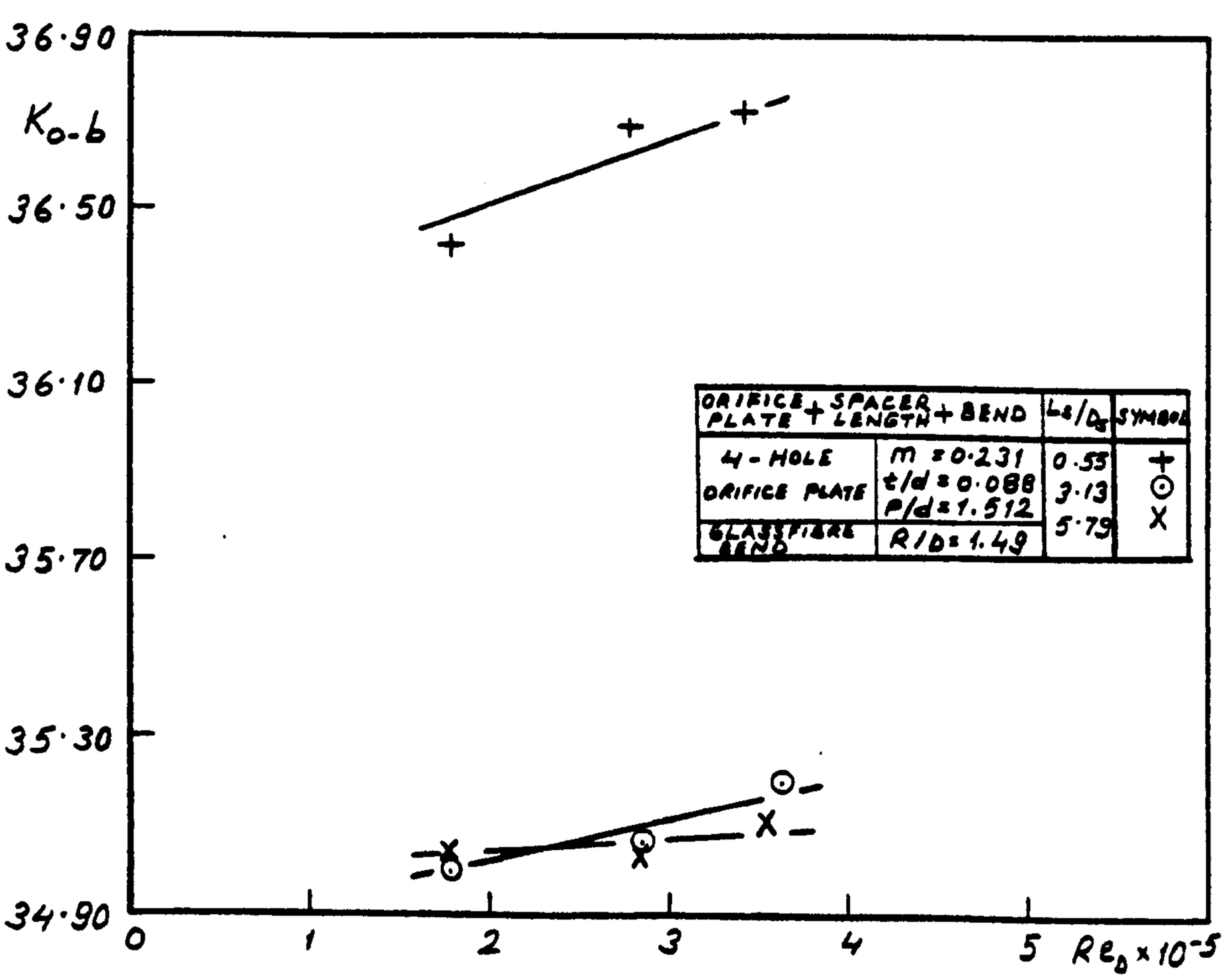

Fig. 269. Head loss coefficients for orifice plate - bend combinations

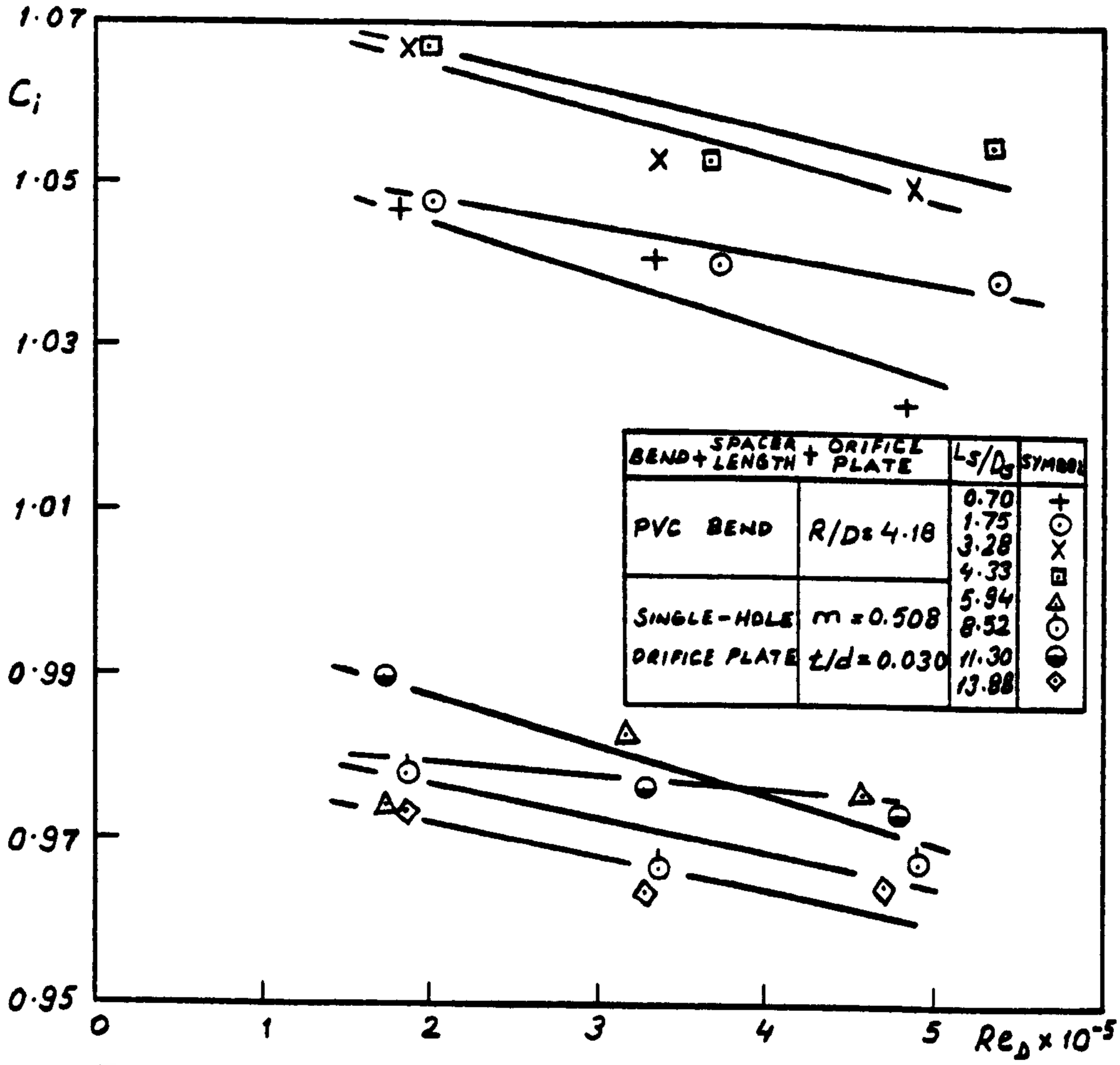

Fig. 270. Interaction coefficients for bend-orifice plate combinations

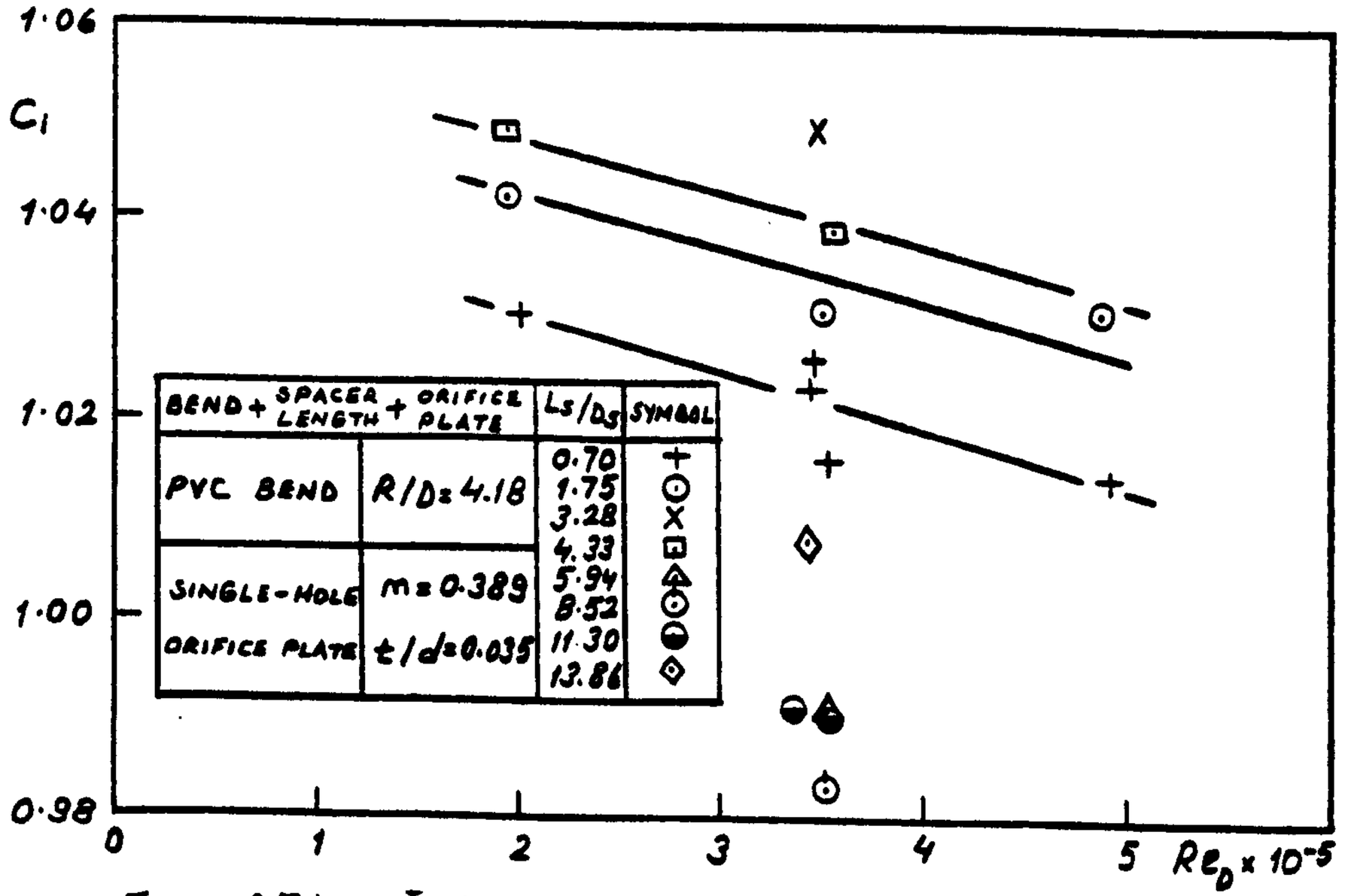

Fig. 271. Interaction coefficients for bend-orifice plate combinations

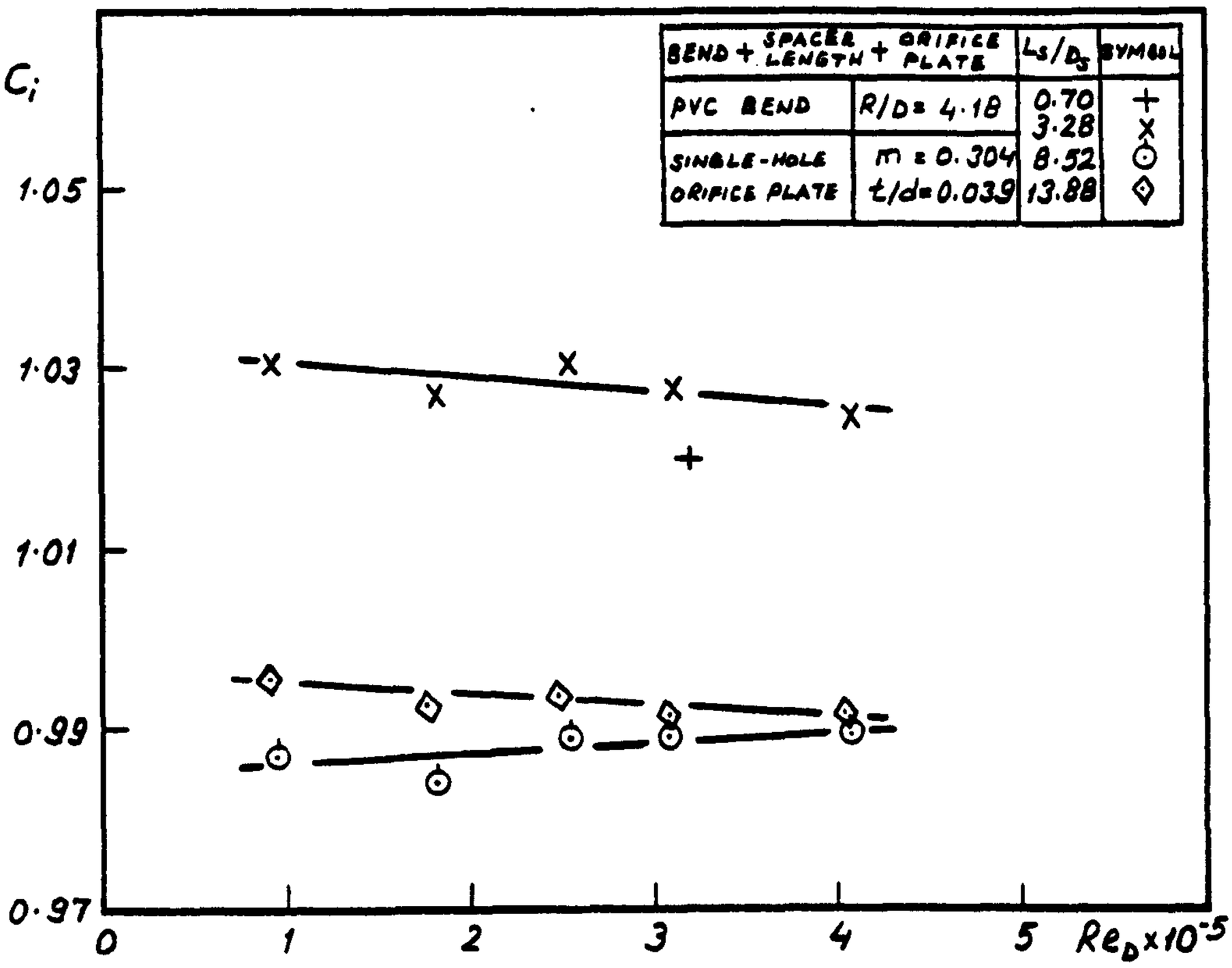

Fig. 272. Interaction coefficients for bend-orifice plate combinations

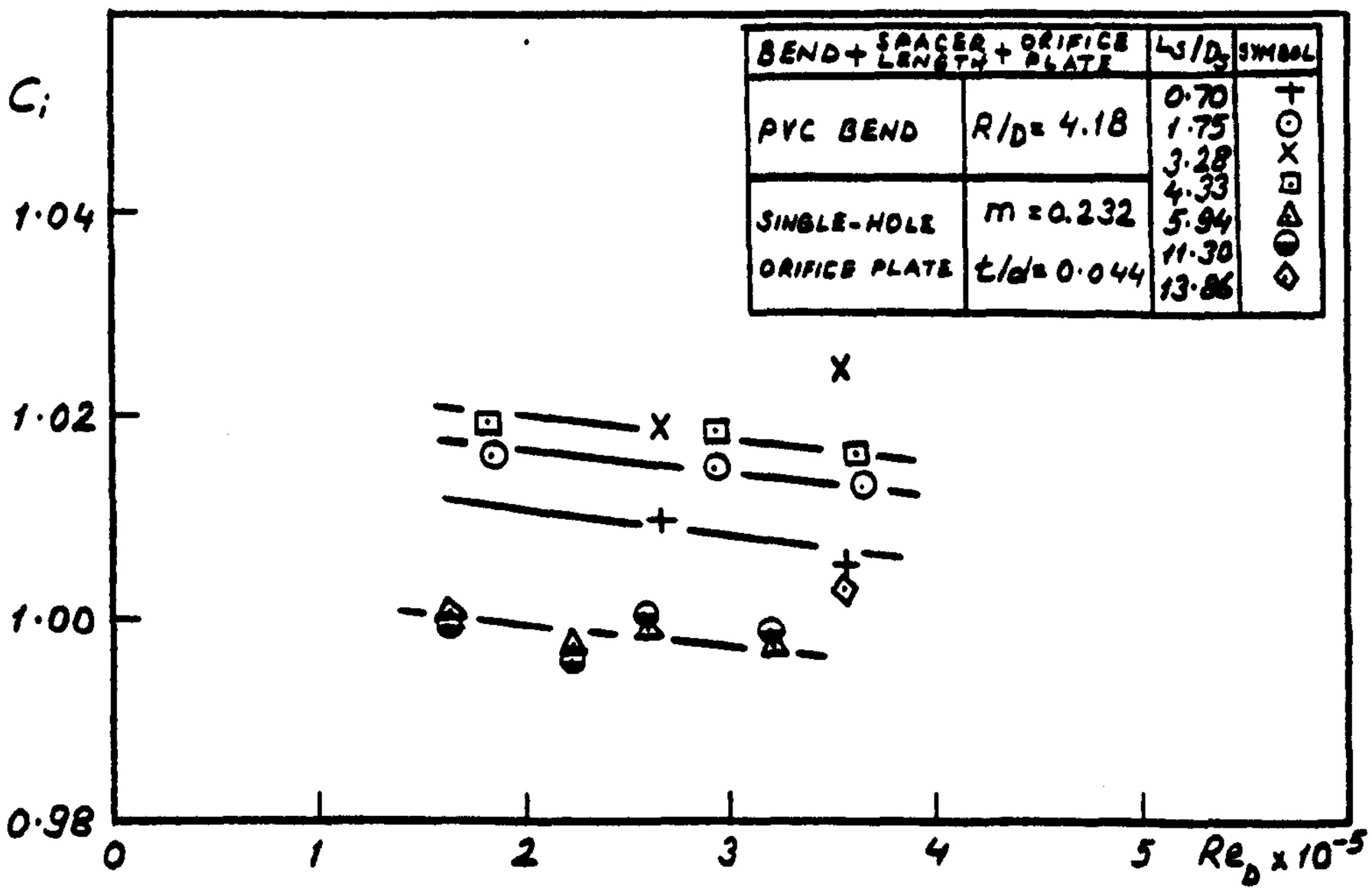

Fig. 273. Interaction coefficients for bend-orifice plate combinations

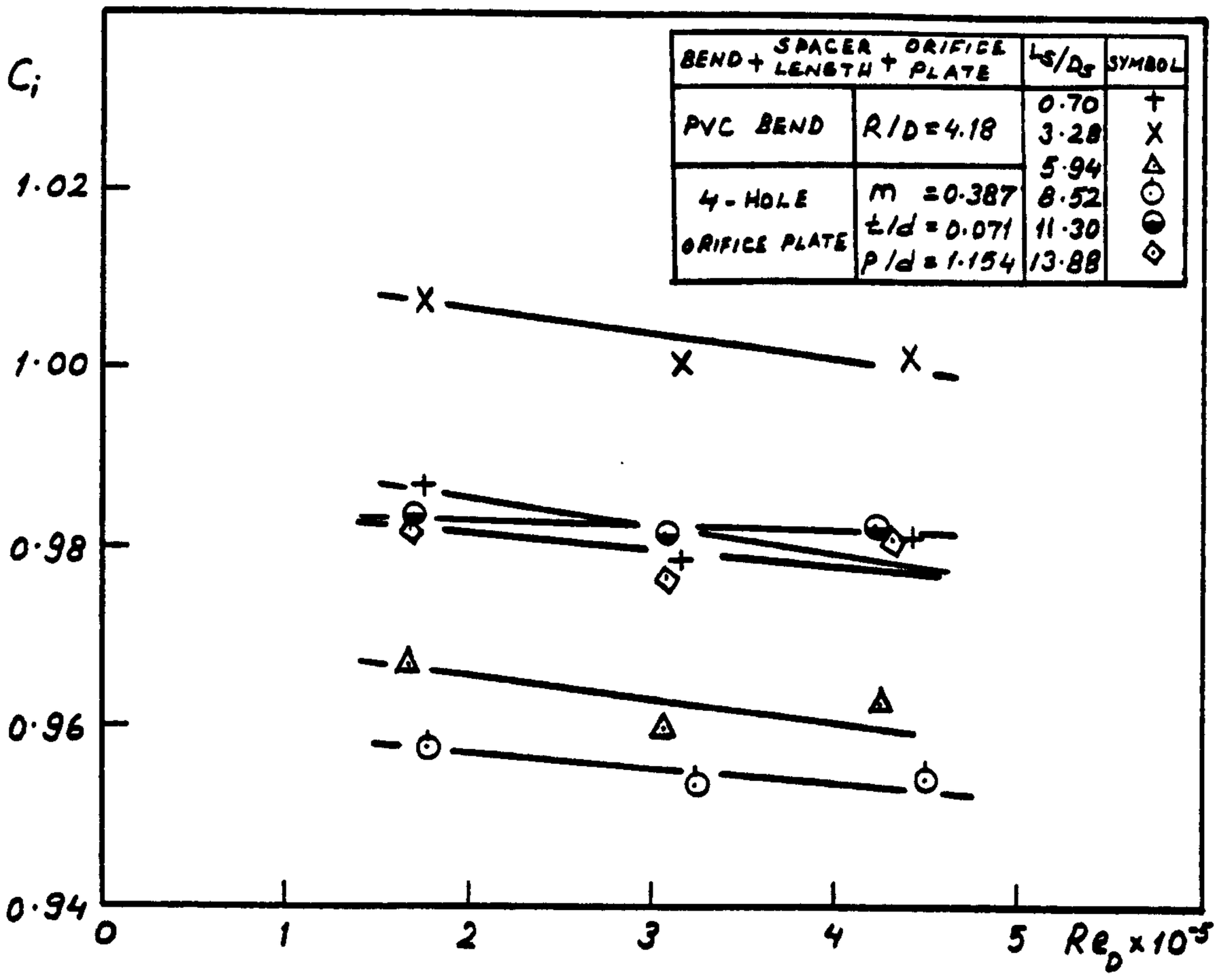

Fig. 274. Interaction coefficients for bend-orifice plate combinations

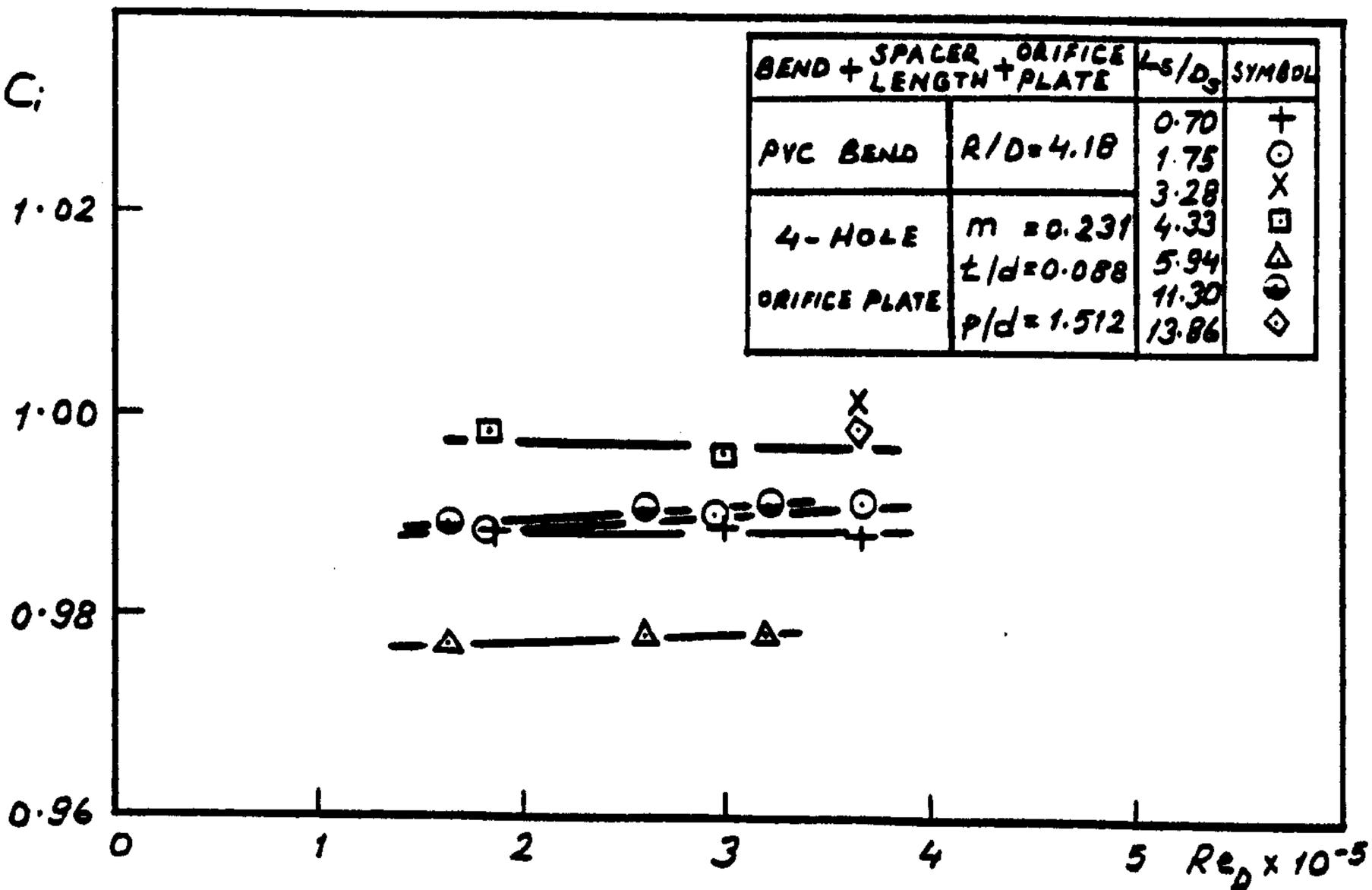

Fig. 275. Interaction coefficients for bend-orifice plate combinations

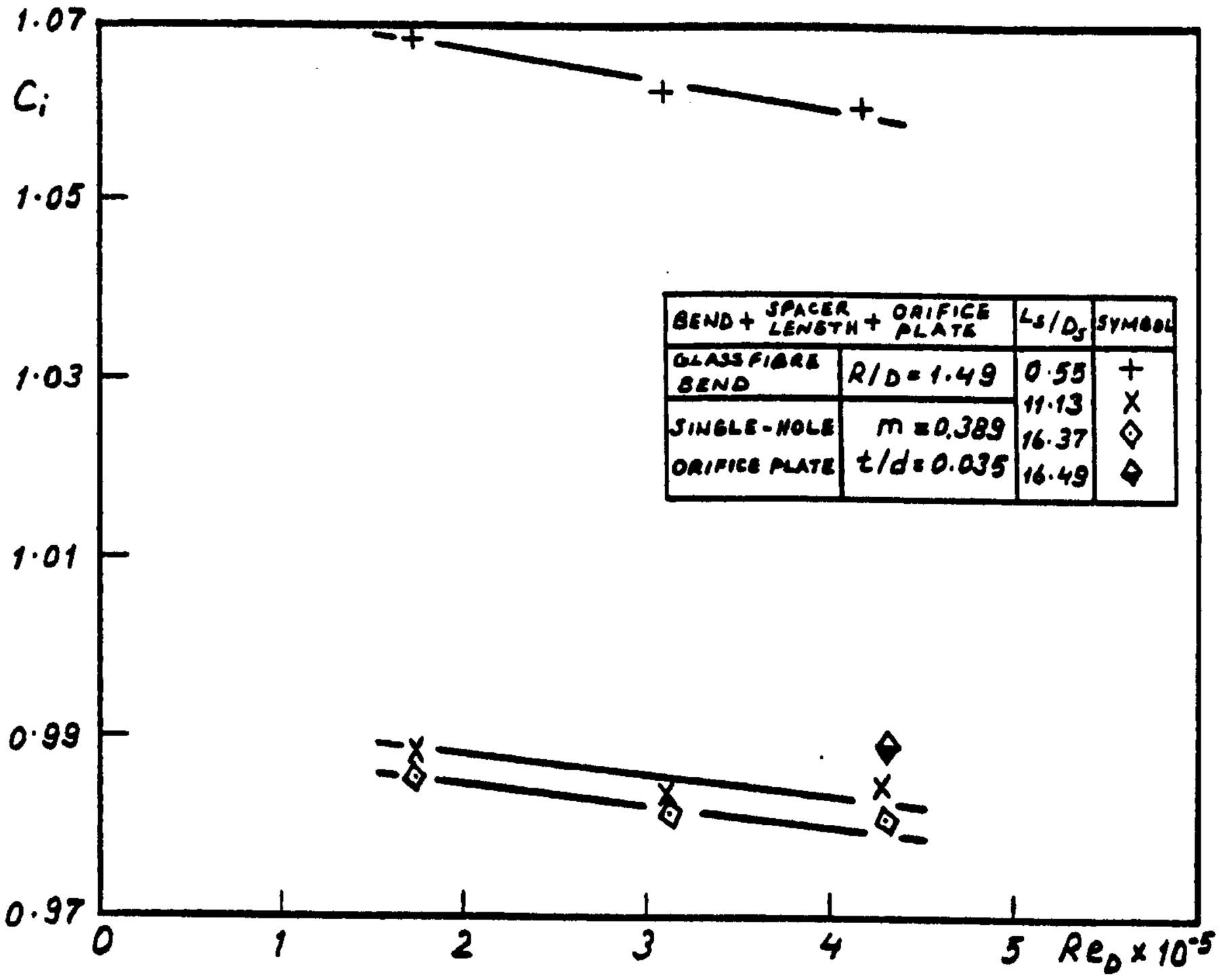

Fig. 276. Interaction coefficients for bend-orifice plate combinations

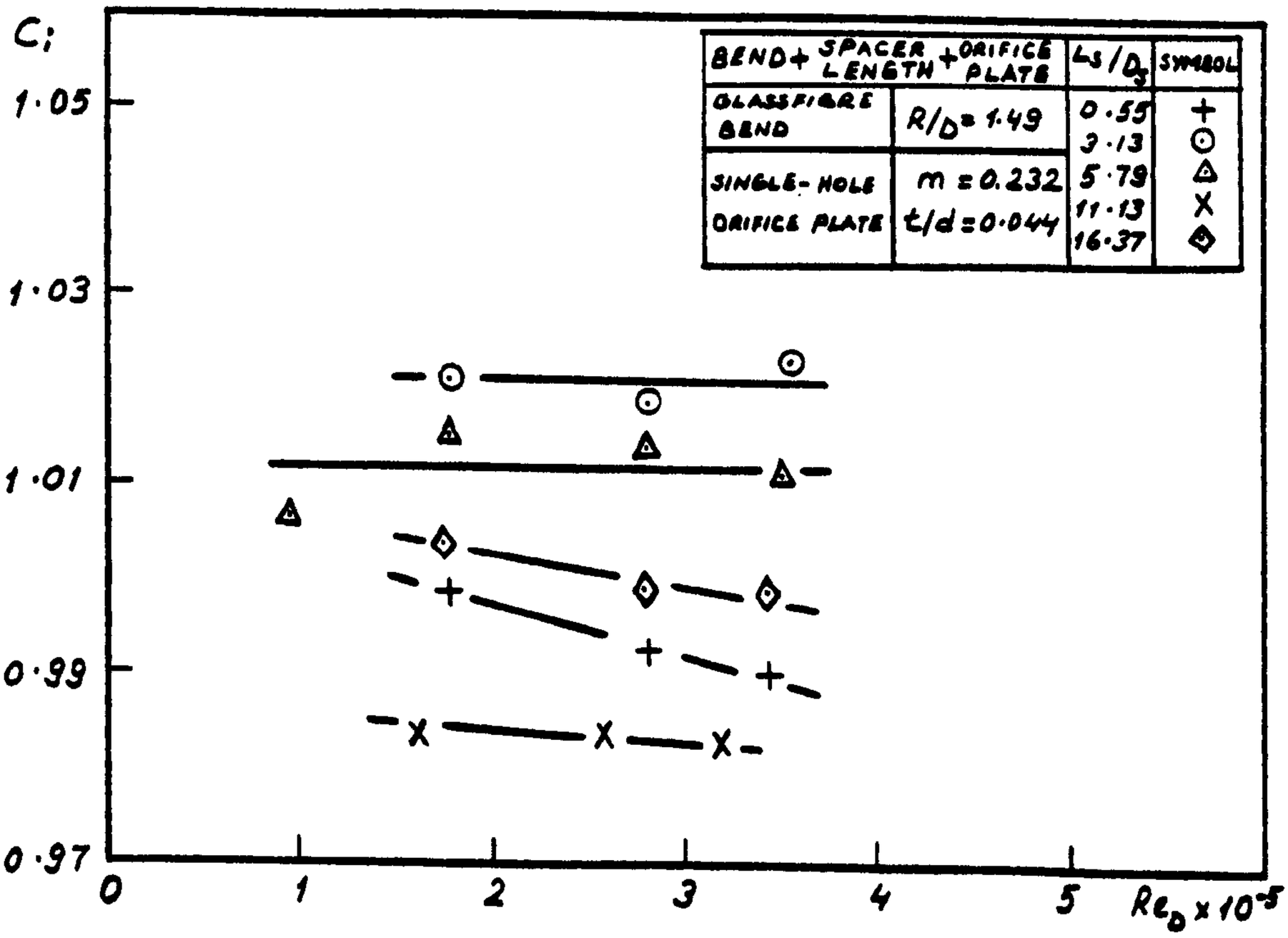

Fig. 277. Interaction coefficients for bend-orifice plate combinations

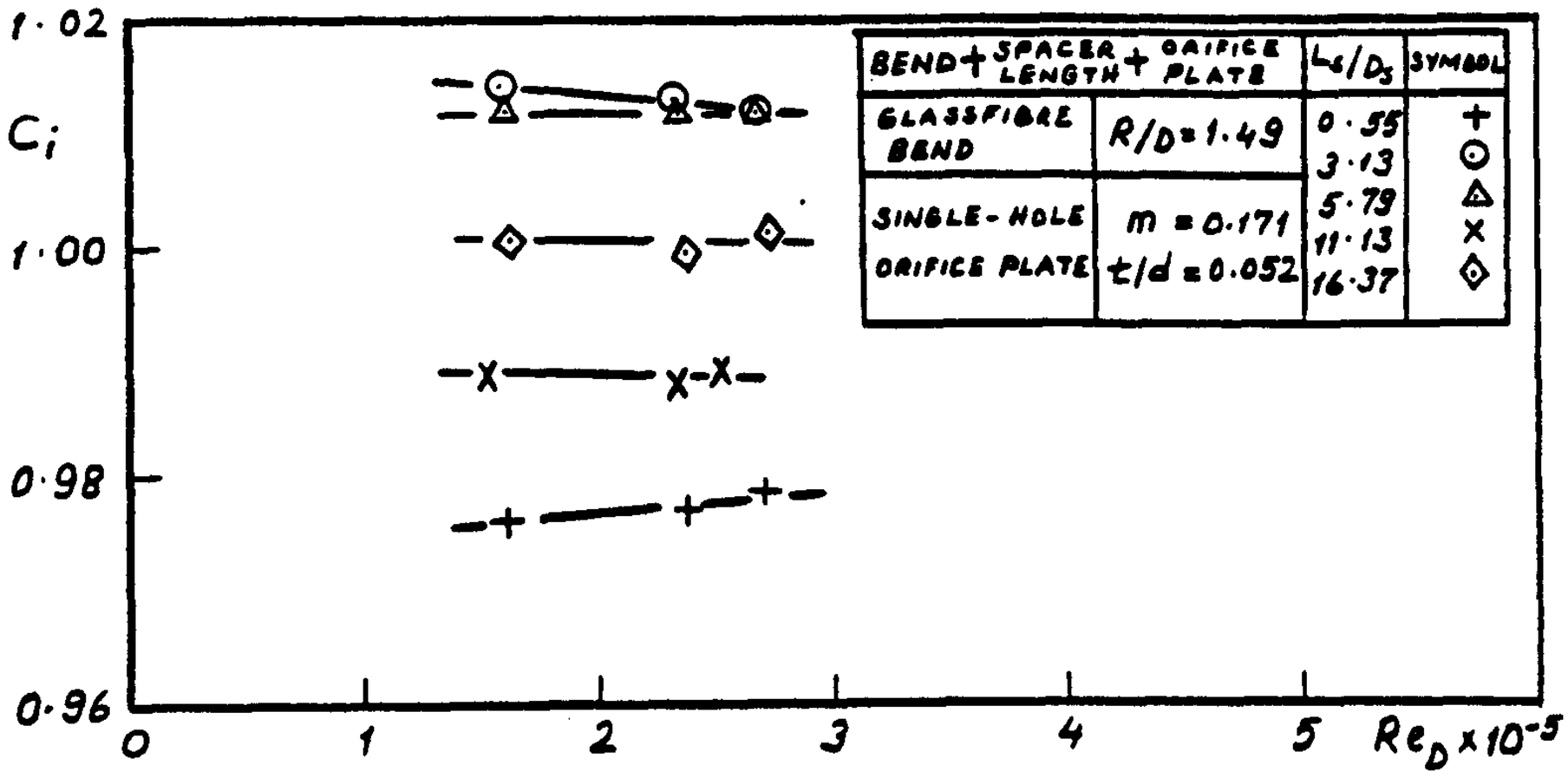

Fig. 278. Interaction coefficients for bend-orifice plate combinations

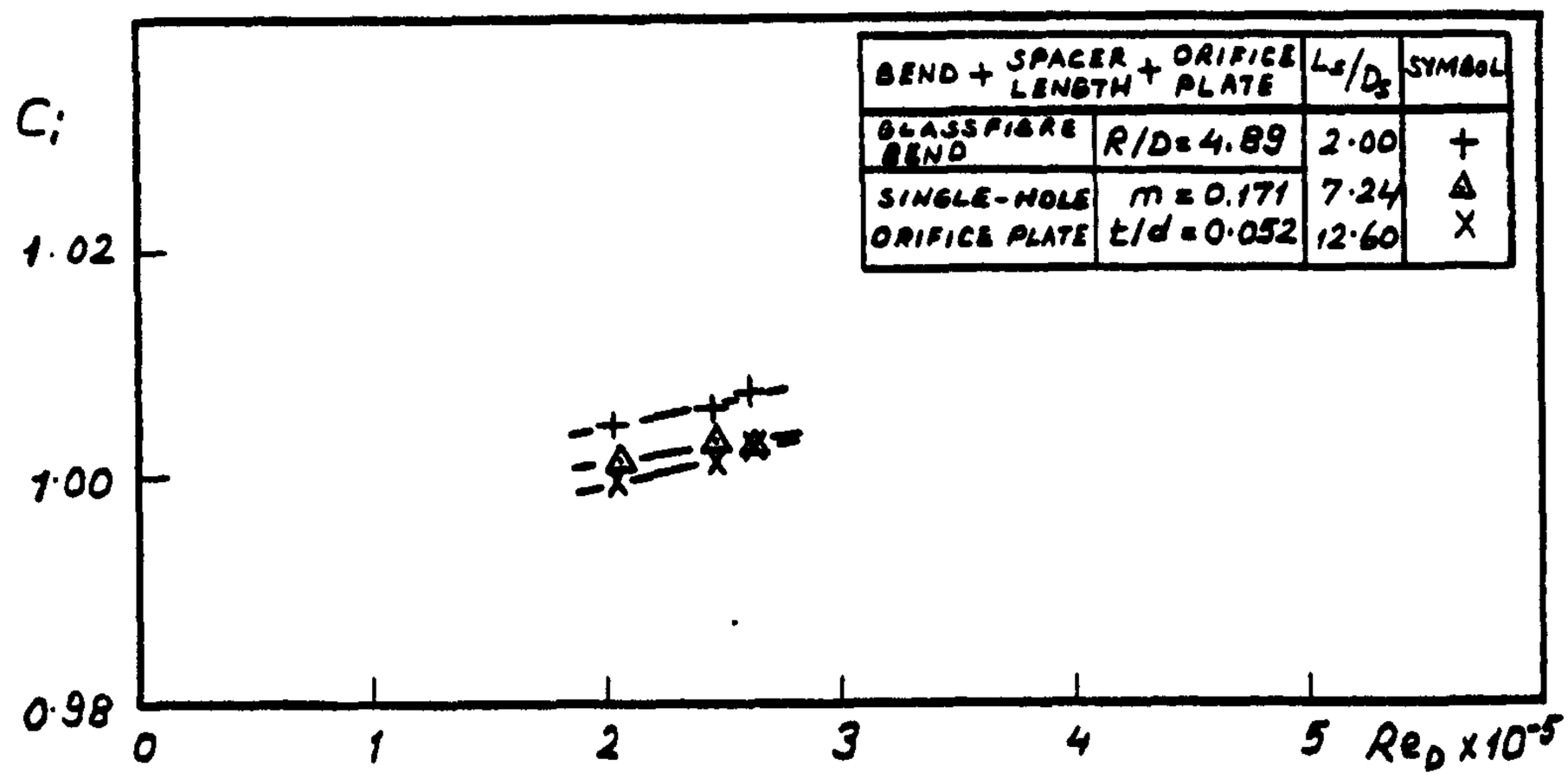

Fig. 279. Interaction coefficients for bend-orifice plate combinations

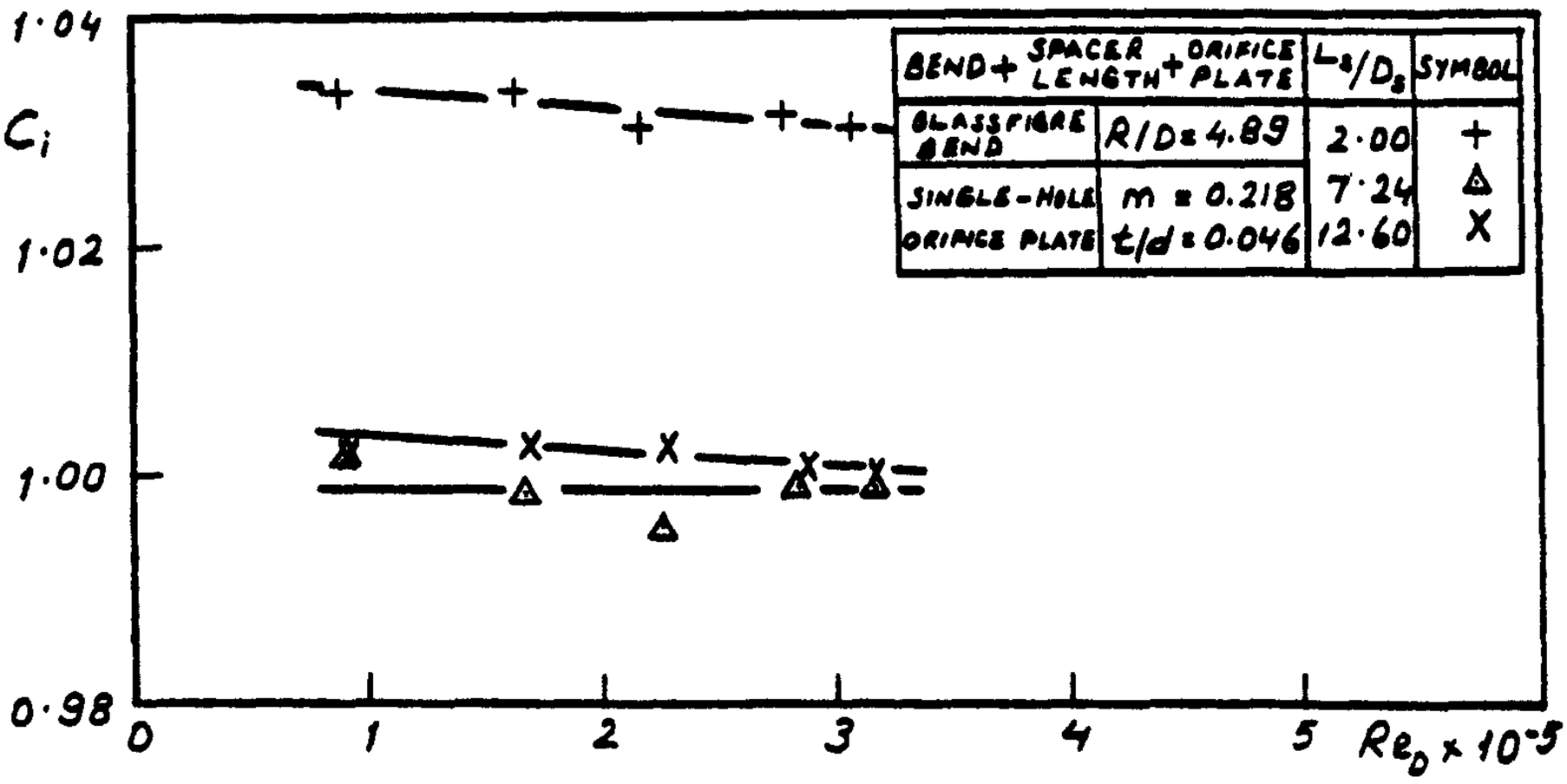

Fig. 280. Interaction coefficients for bend-orifice plate combinations

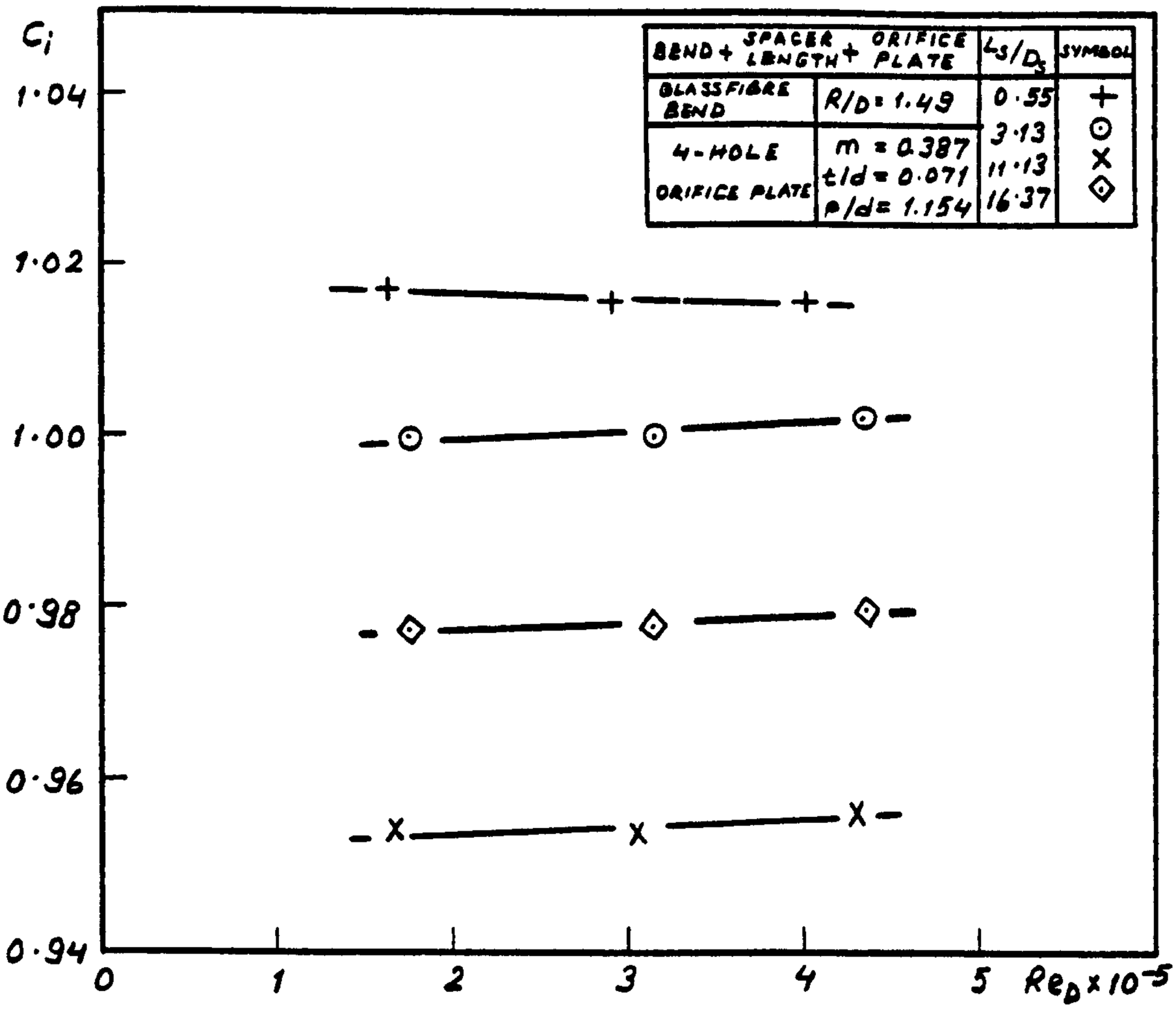

Fig. 281. Interaction coefficients for bend-orifice plate combinations

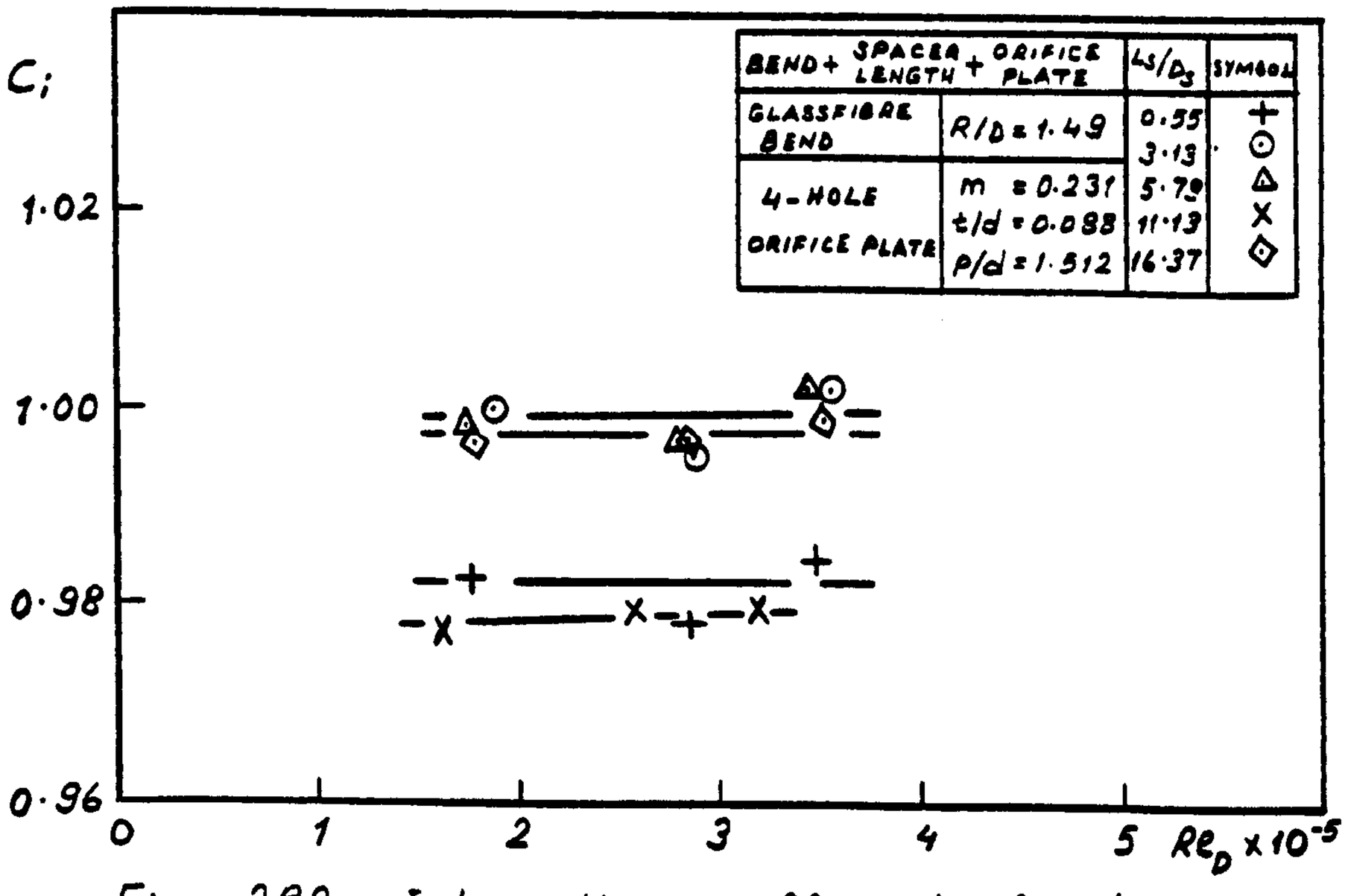

Fig. 282. Interaction coefficients for bend-orifice plate combinations

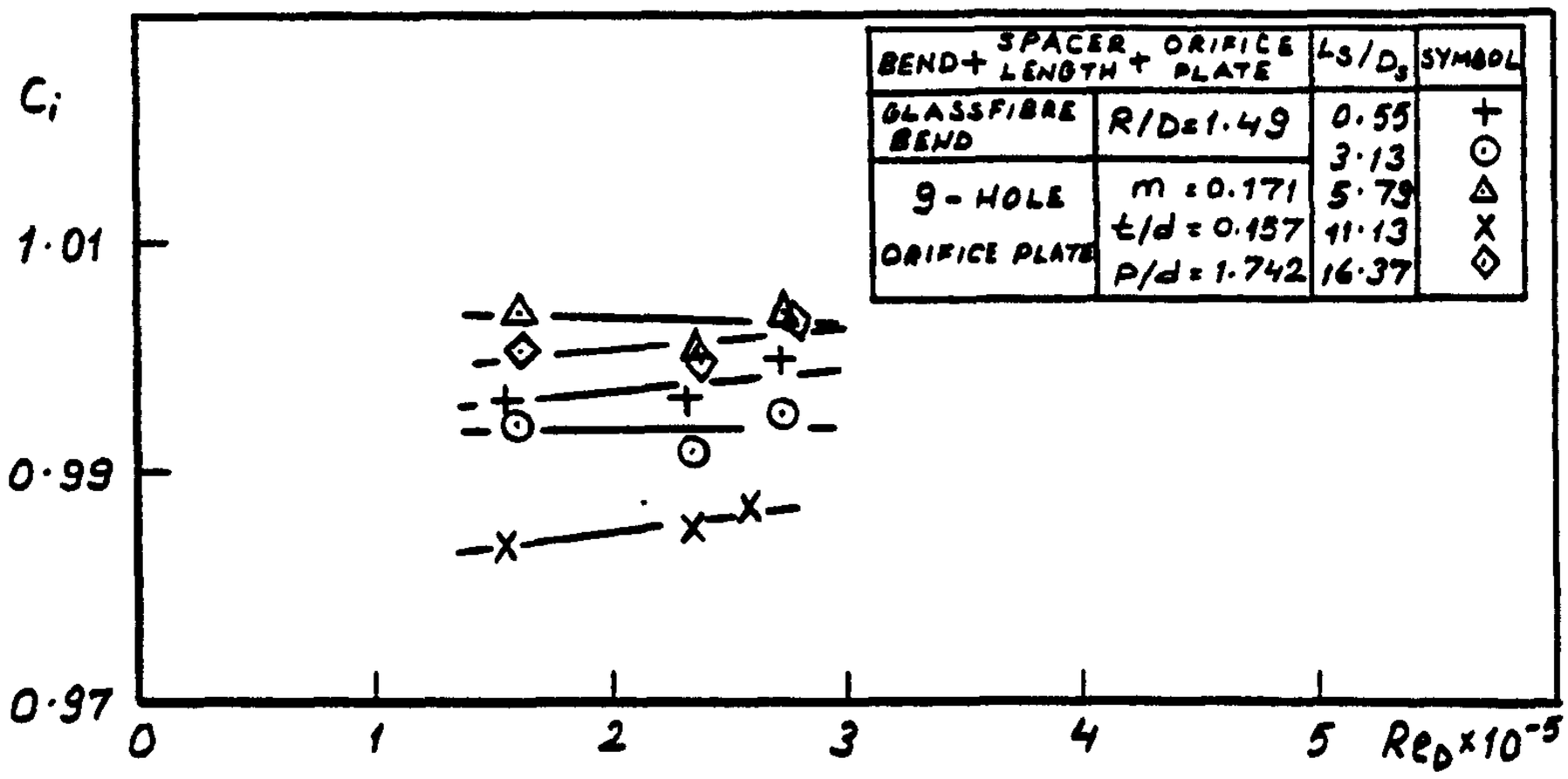

Fig. 283. Interaction coefficients for bend-orifice plate combinations

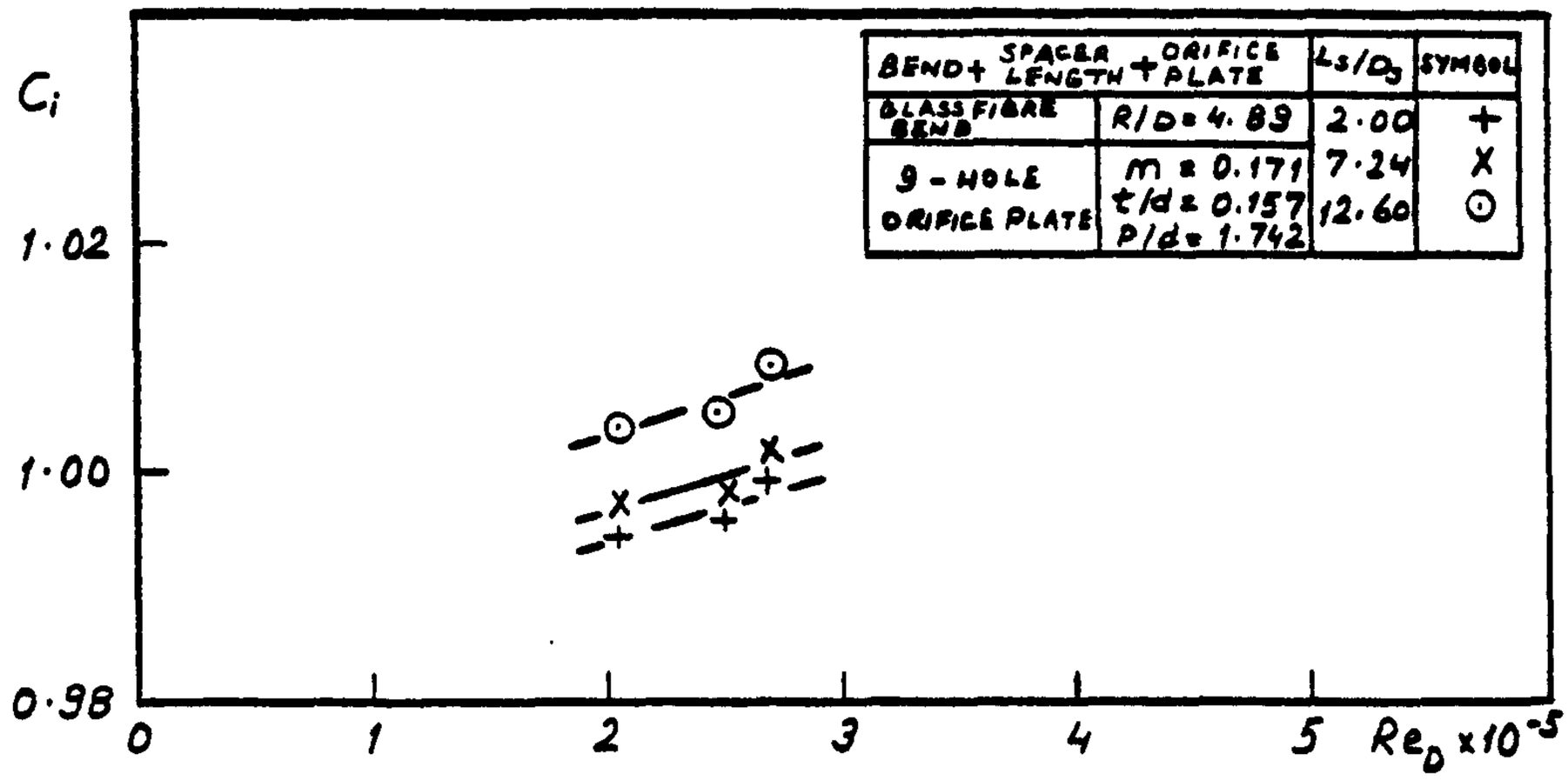

Fig. 284. Interaction coefficients for bend-orifice plate combinations

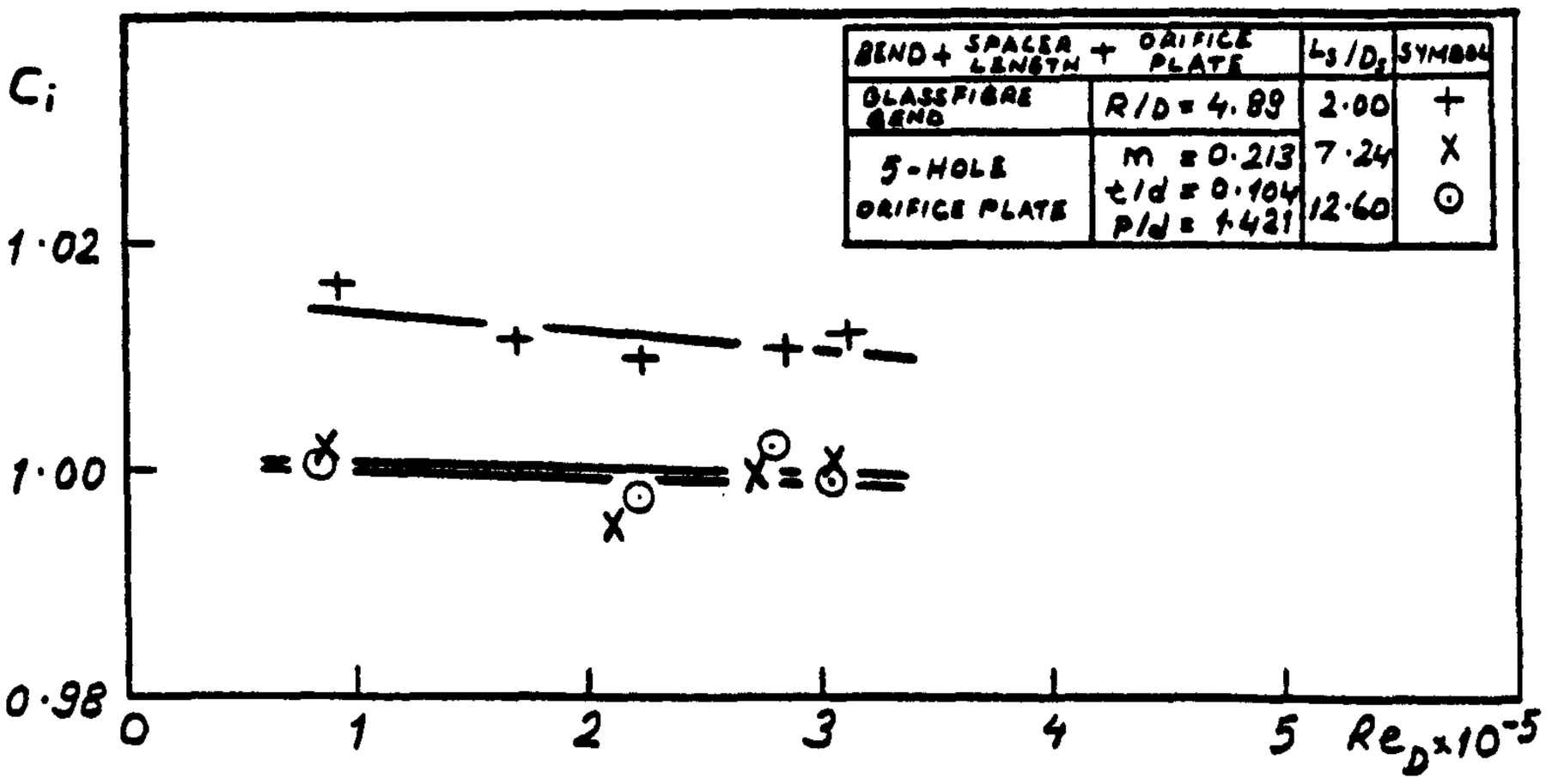

Fig. 285. Interaction coefficients for bend-orifice plate combinations

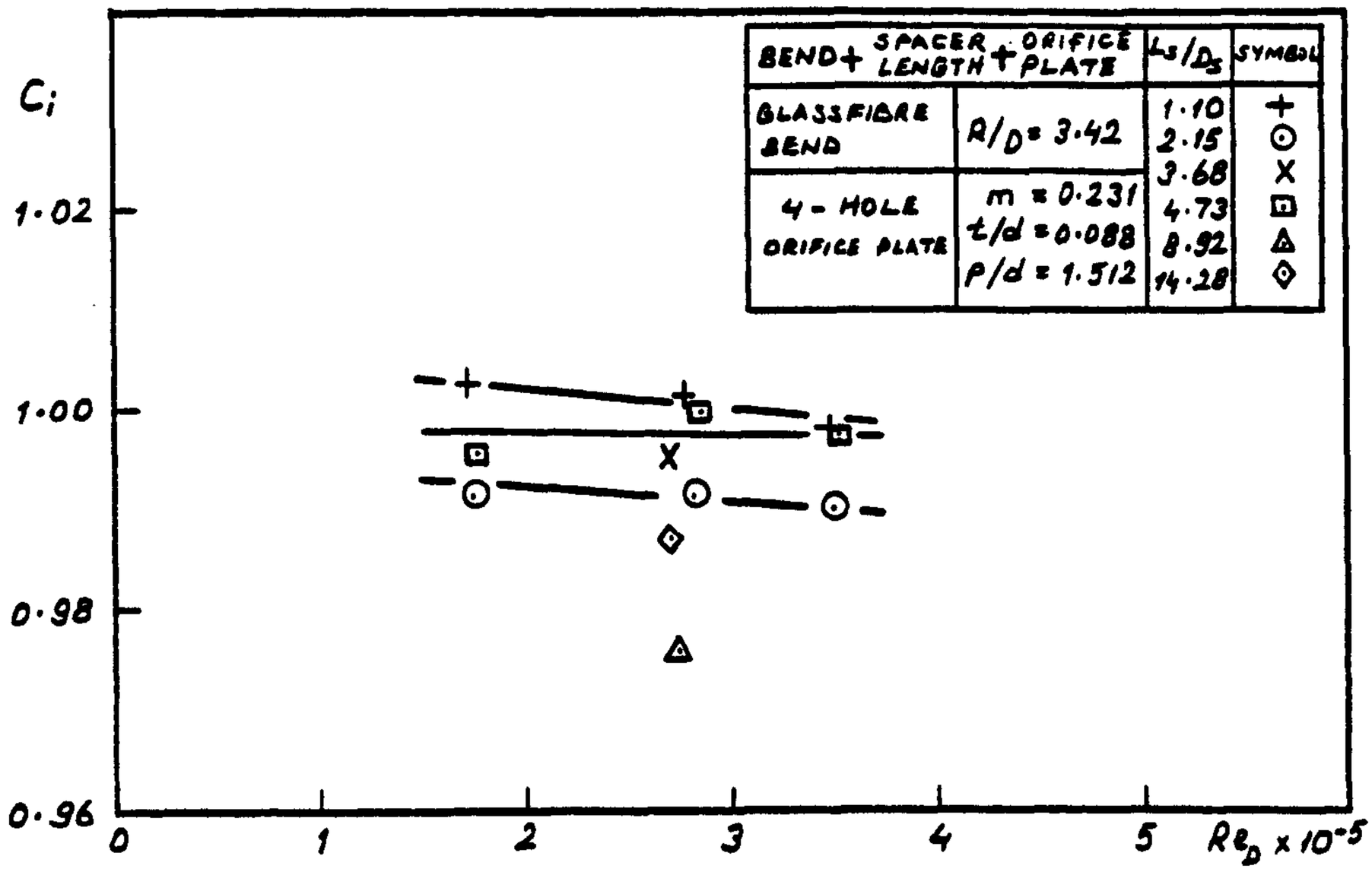

Fig. 286. Interaction coefficients for bend-orifice plate combinations

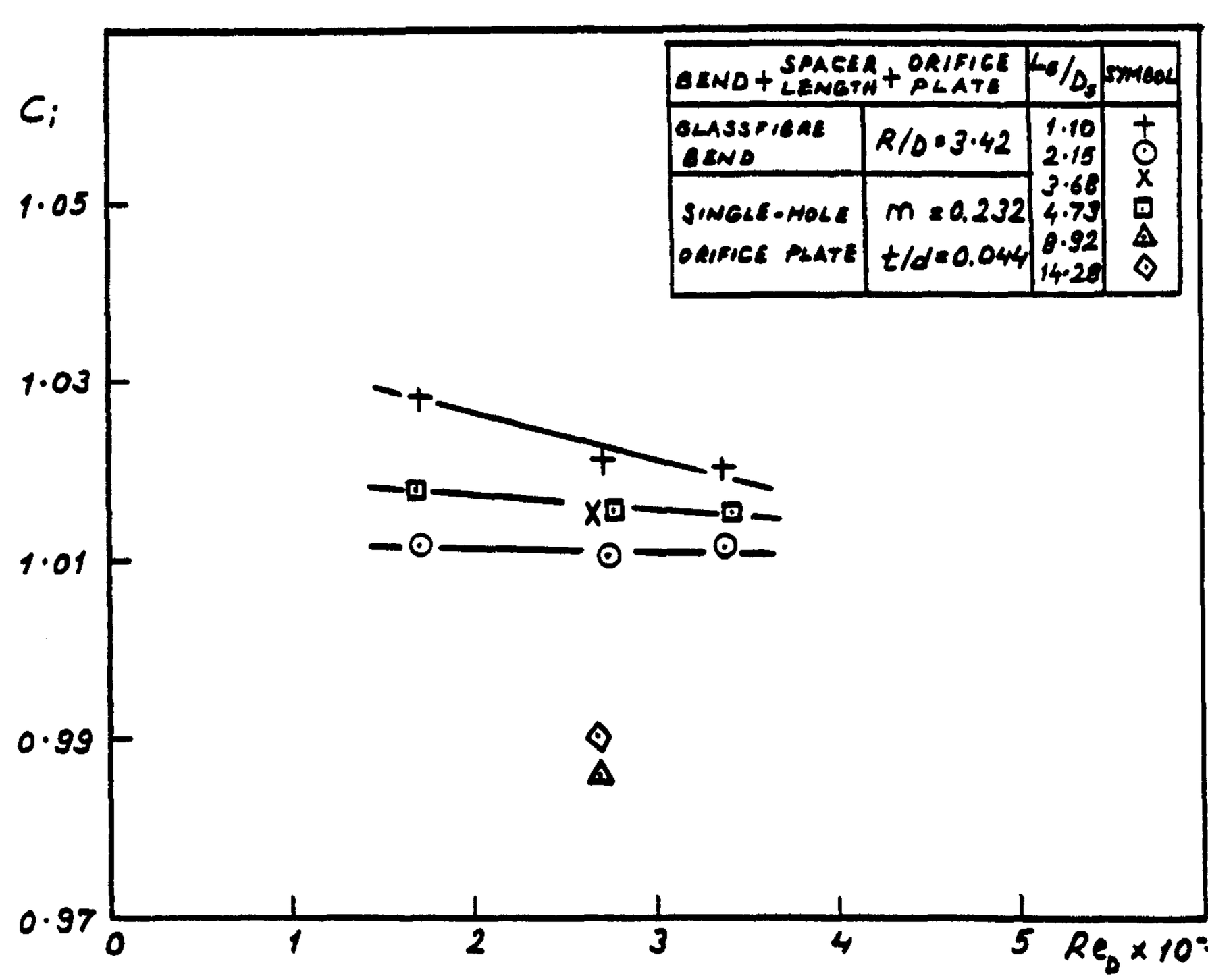

Fig. 287. Interaction coefficients for bend-orifice plate combinations

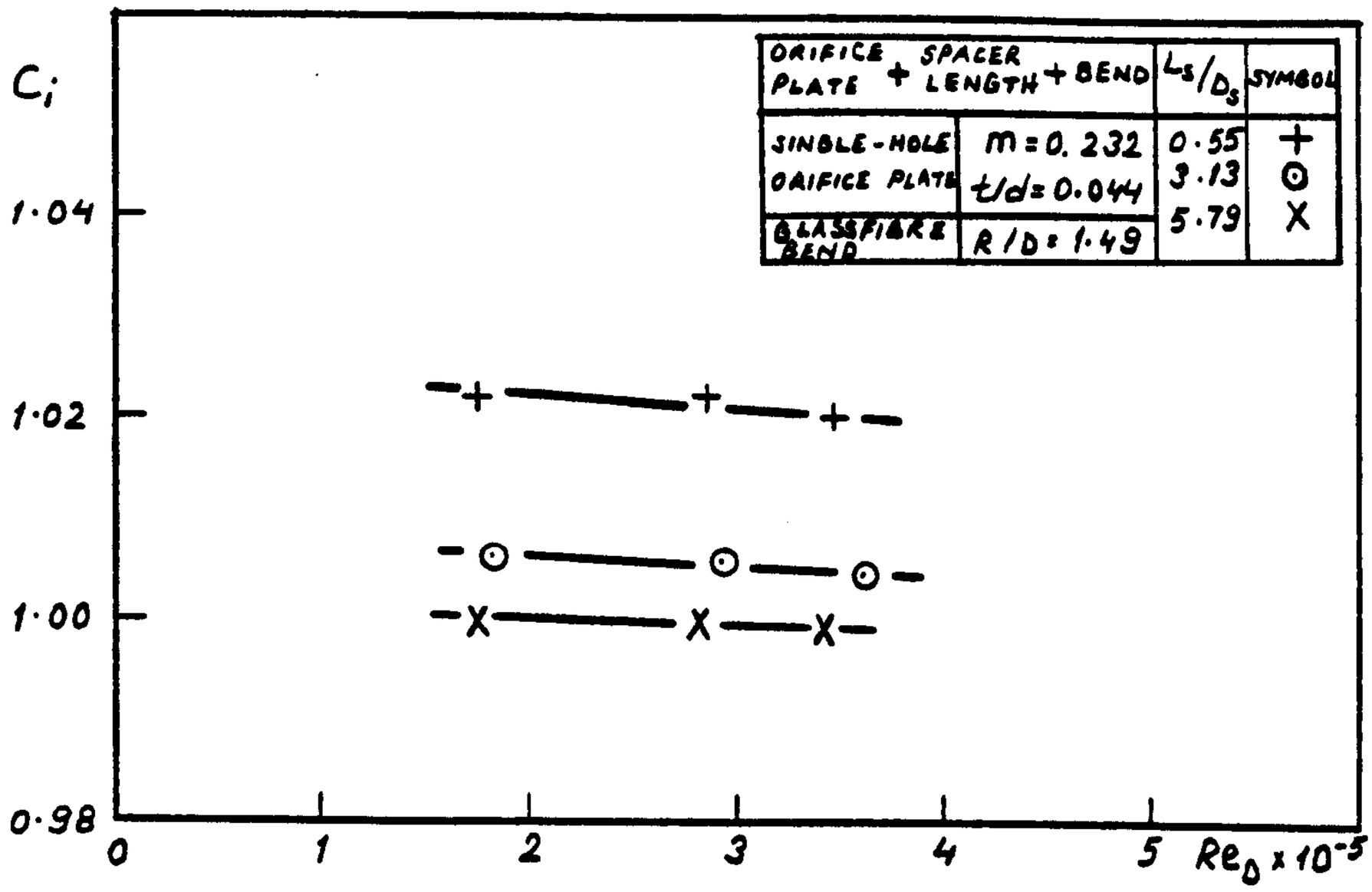

Fig. 288. Interaction coefficients for orifice plate – bend combinations

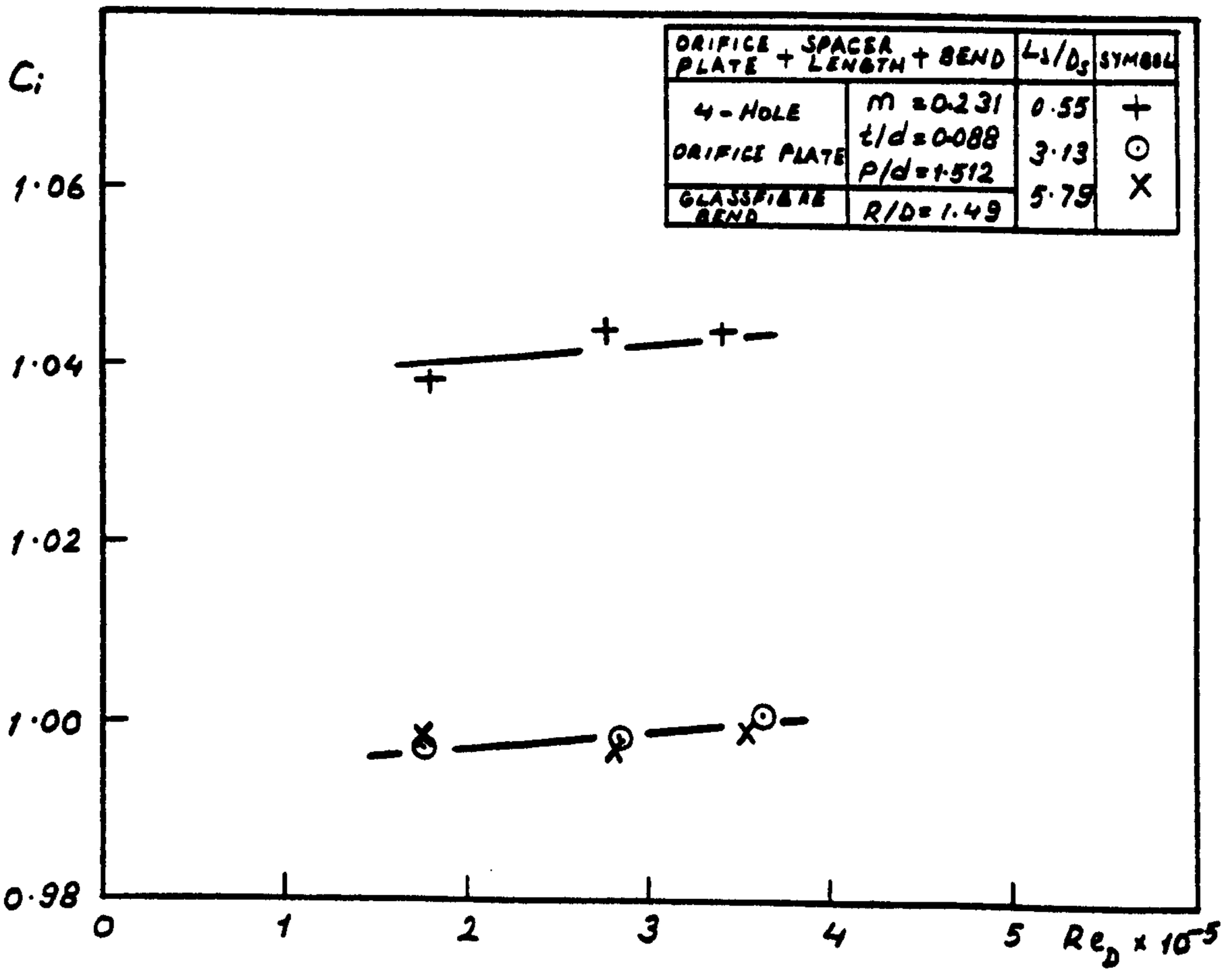

Fig. 289. Interaction coefficients for orifice plate - bend combinations

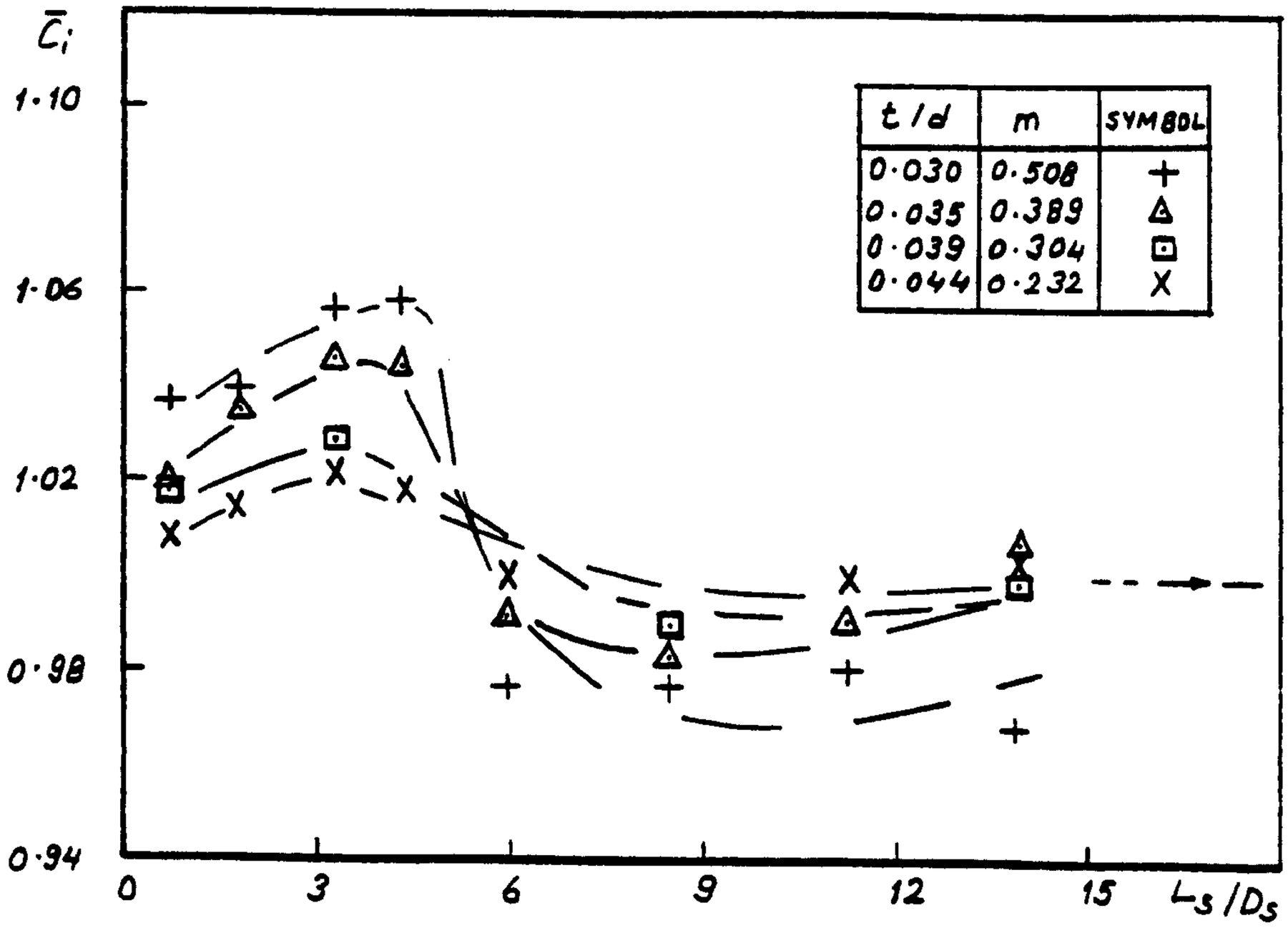

Fig. 290. Effect of spacer length on interaction coefficient (PVC bend of R/D = 4.18 upstream of various single-hole orifice plates)

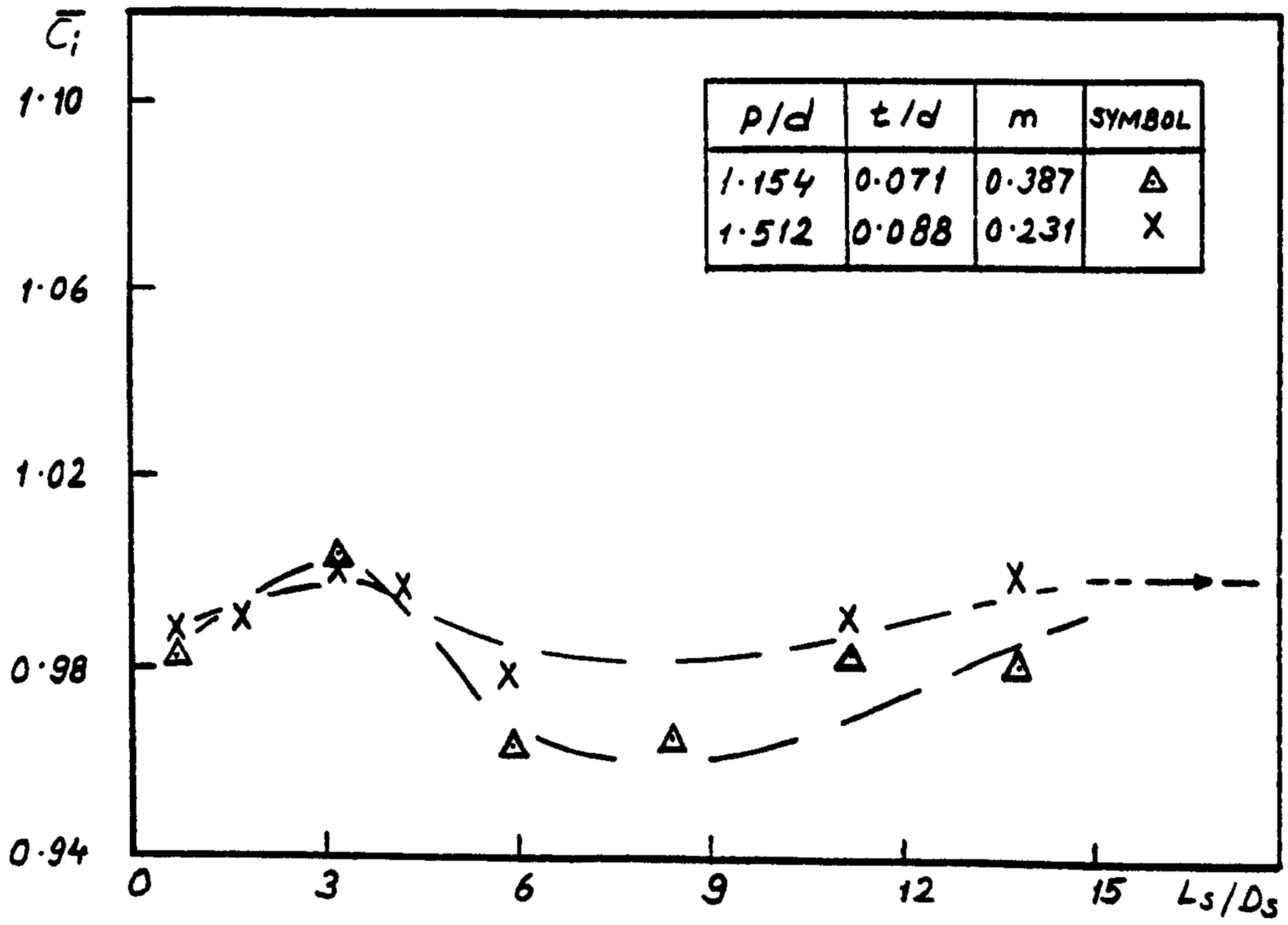

Fig. 291. Effect of spacer length on interaction coefficient (PVC bend of R/D = 4.18 upstream of various multi-hole orifice plates)

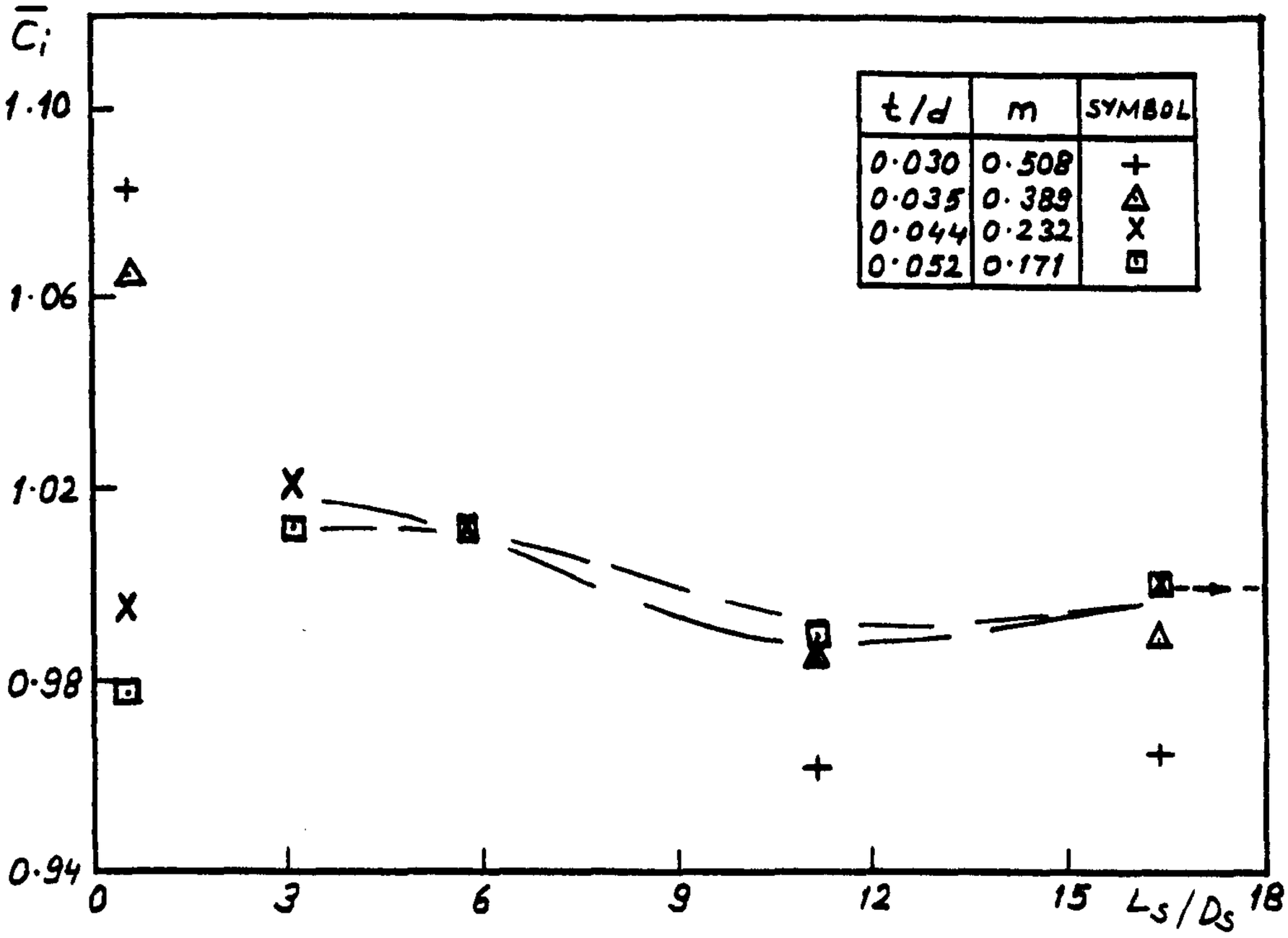

Fig. 292. Effect of spacer length on interaction coefficient (glassfibre bend of $R/D = 1.49$ upstream of various single-hole orifice plates)

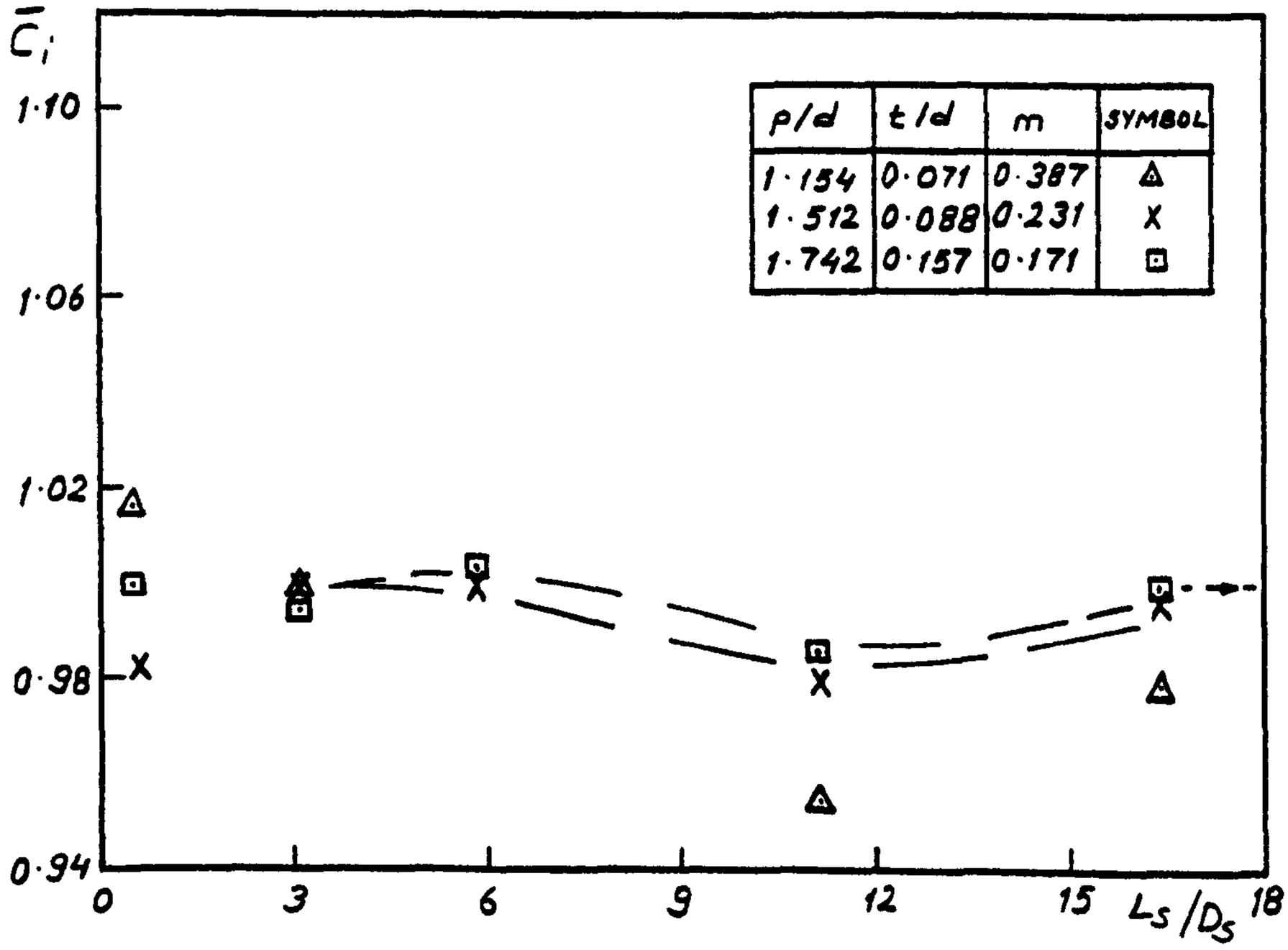

Fig. 293. Effect of spacer length on interaction coefficient (glassfibre bend of $R/D = 1.49$ upstream of various multi-hole orifice plates)

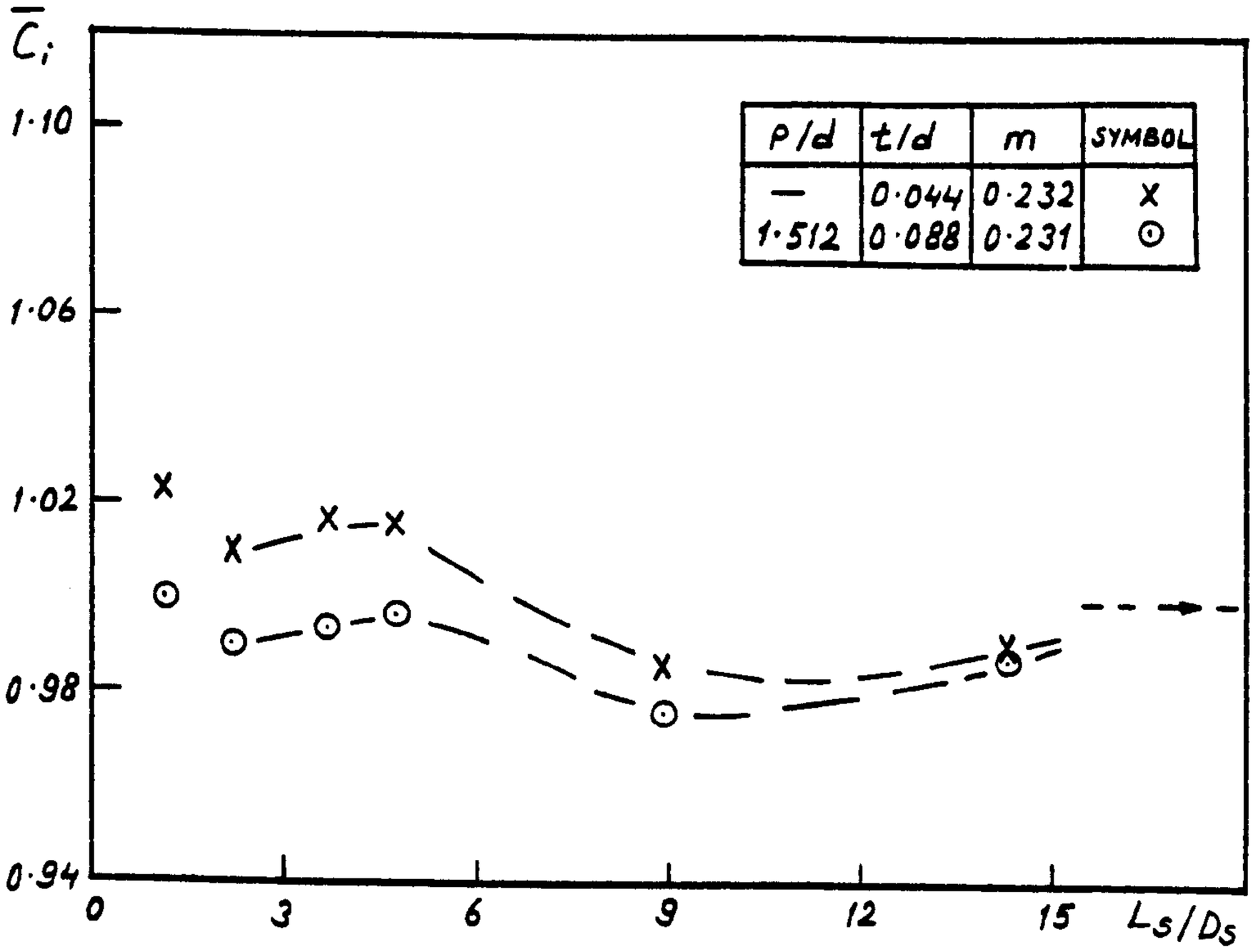

Fig. 294. Effect of spacer length on interaction coefficient (glassfibre bend of R/D=3.42 upstream of various orifice plates)

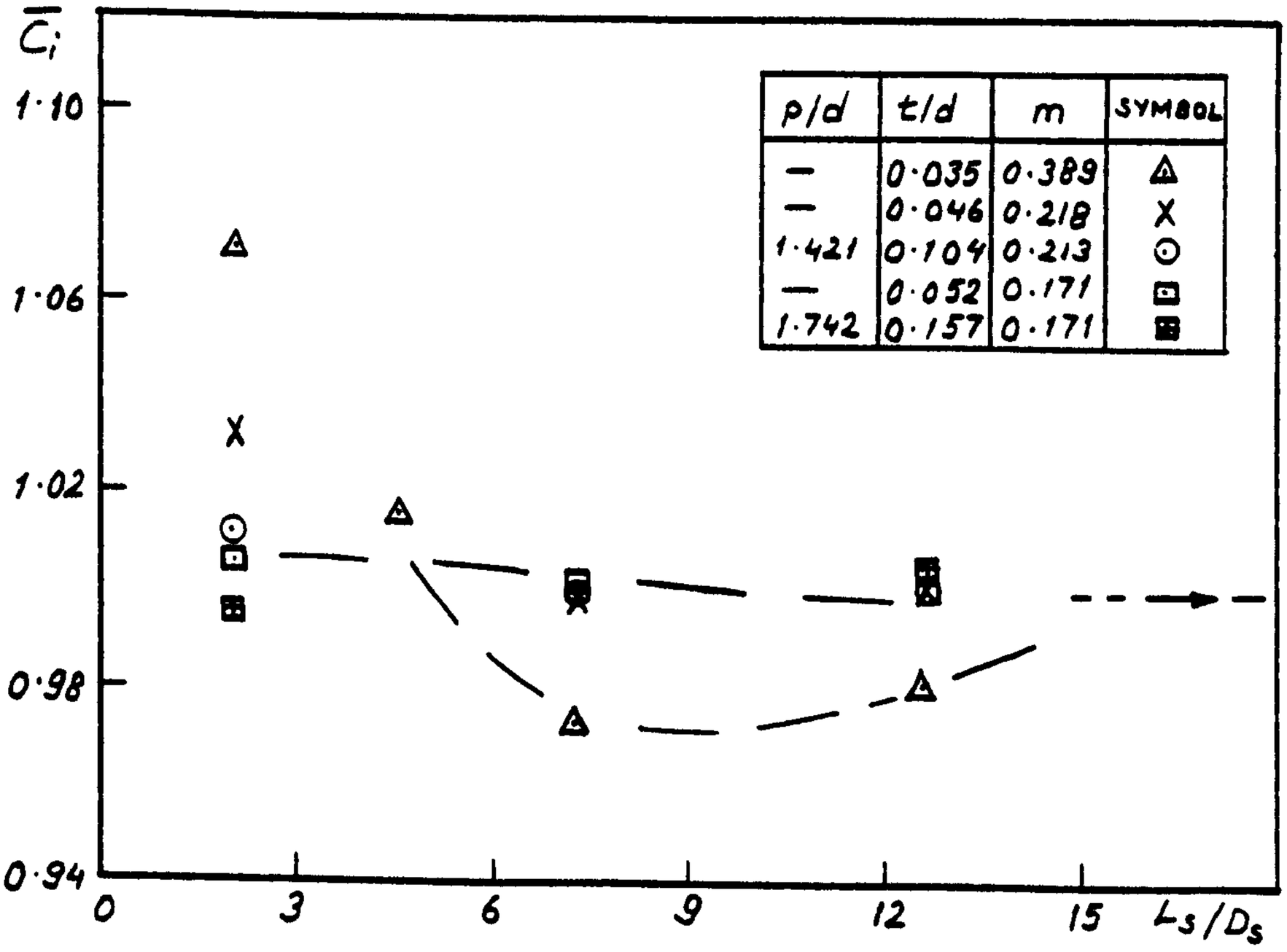

Fig. 295. Effect of spacer length on interaction coefficient (glassfibre bend of R/D=4.89 upstream of various orifice plates)

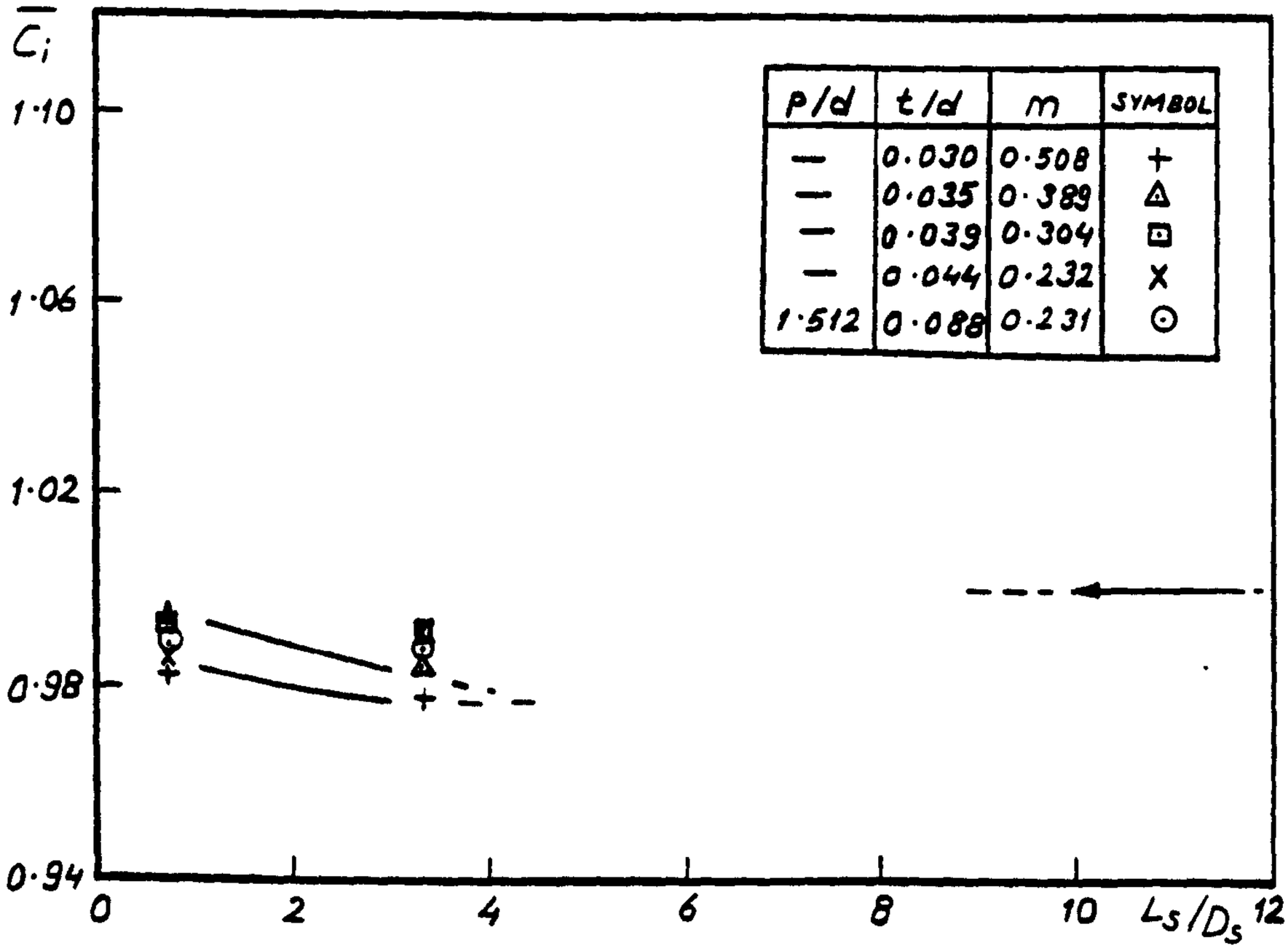

Fig. 296. Effect of spacer length on interaction coefficient (PVC bend of R/D=4.18 downstream of various orifice plates)

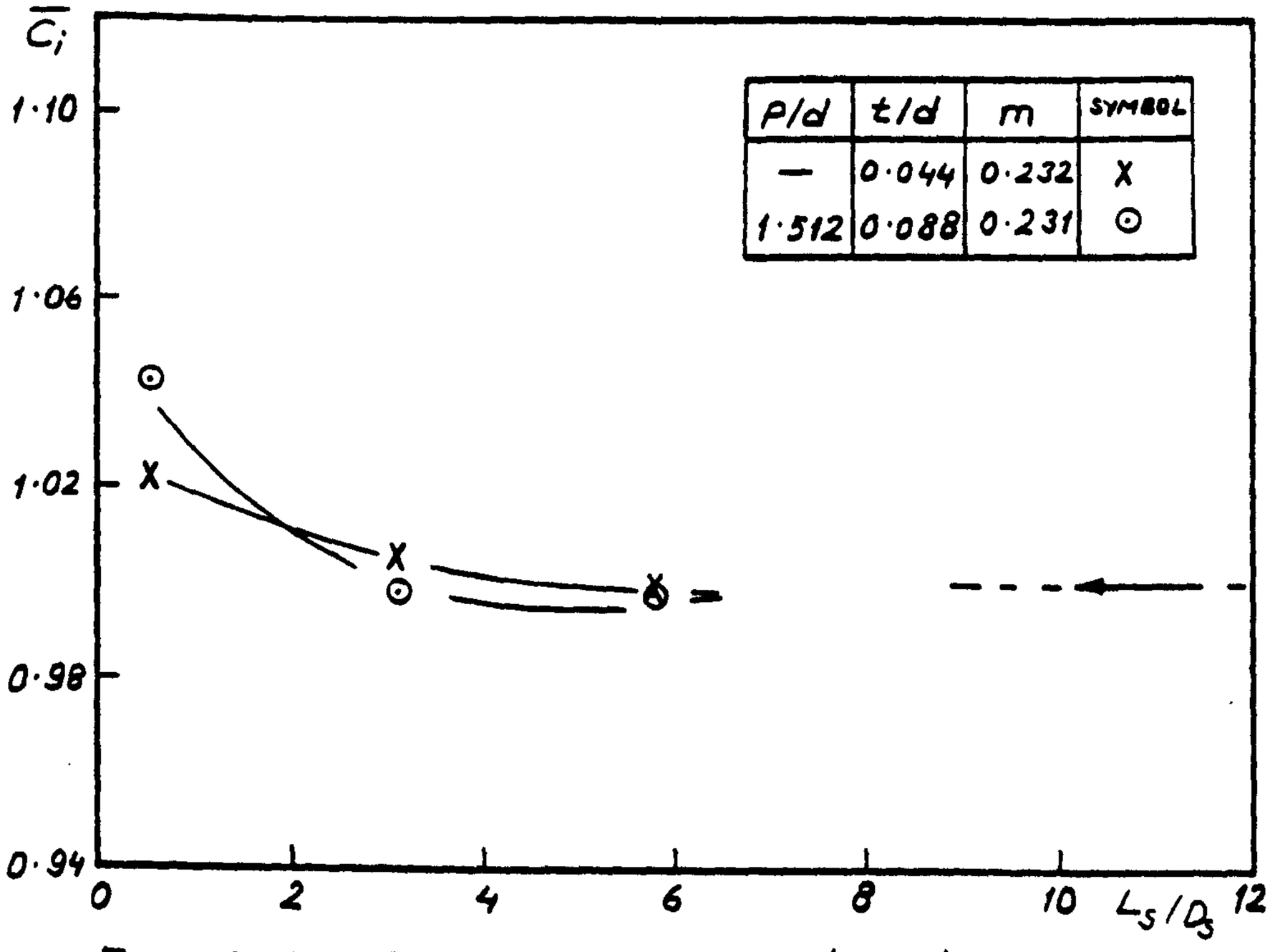

Fig. 297. Effect of spacer length on interaction coefficient (glassfibre bend of R/D=1.49 downstream of various orifice plates)

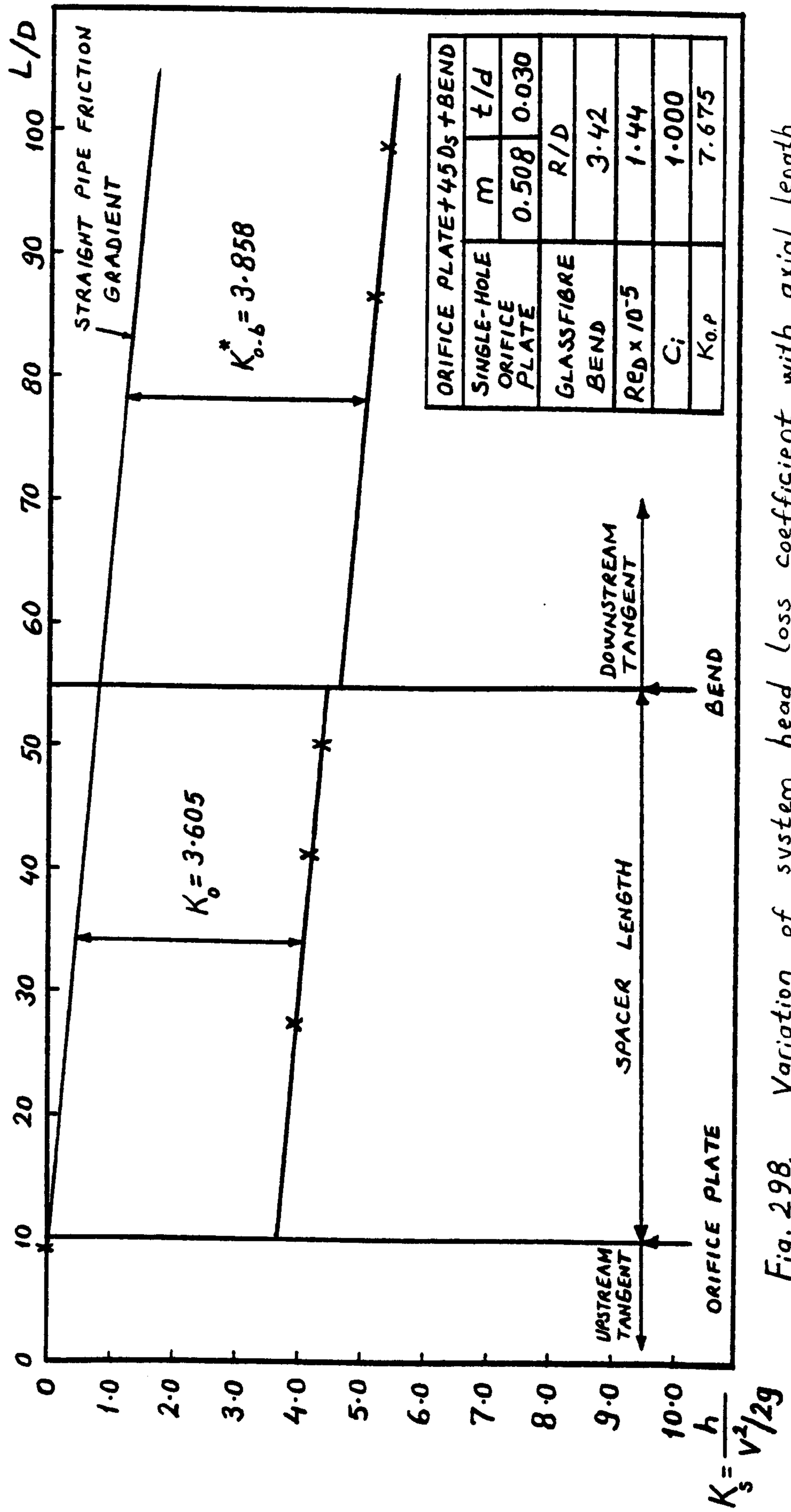

Fig. 298. Variation of system head loss coefficient with axial l

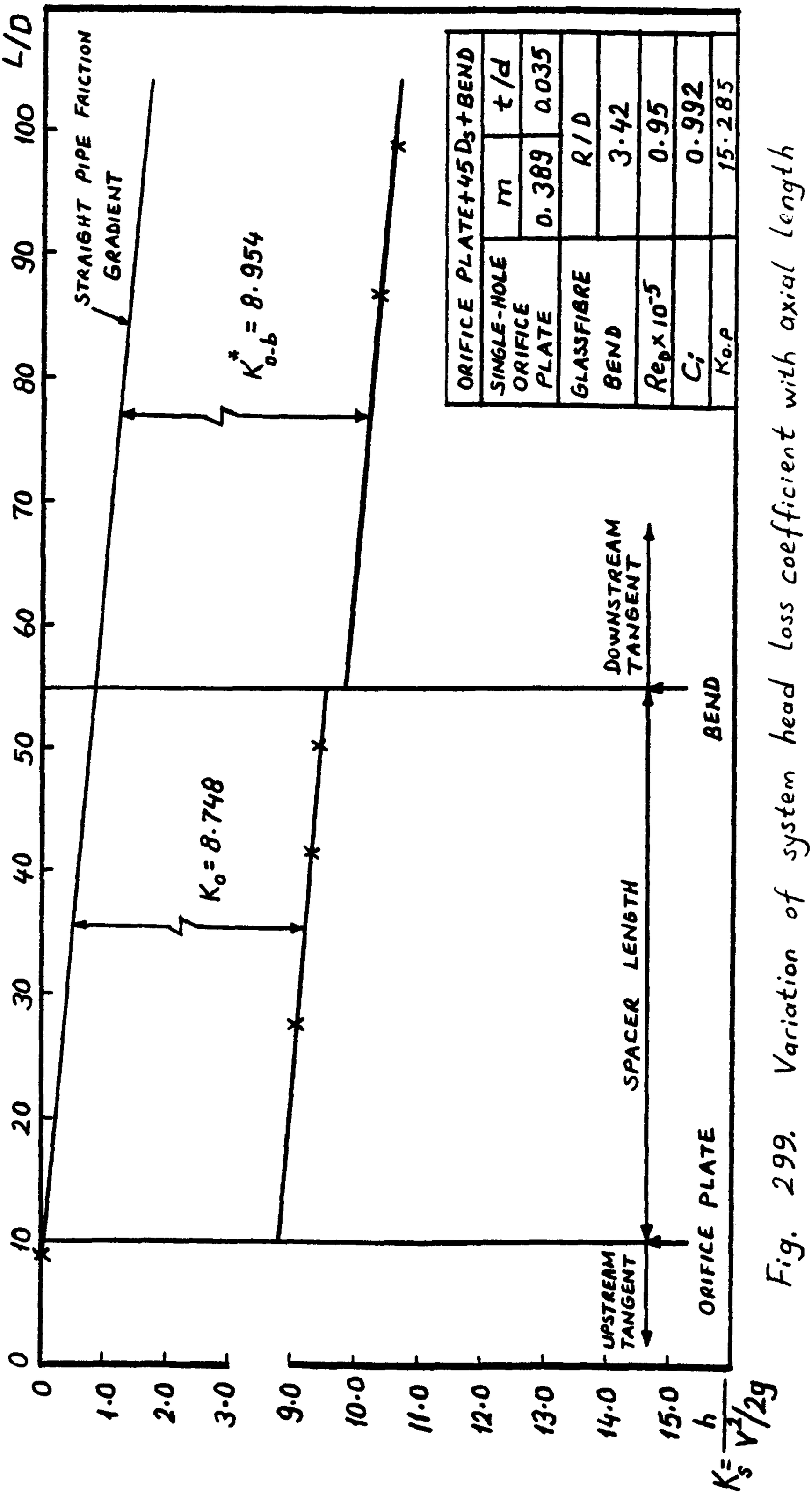

Fig. 299. Variation of system head loss coefficient with axial length

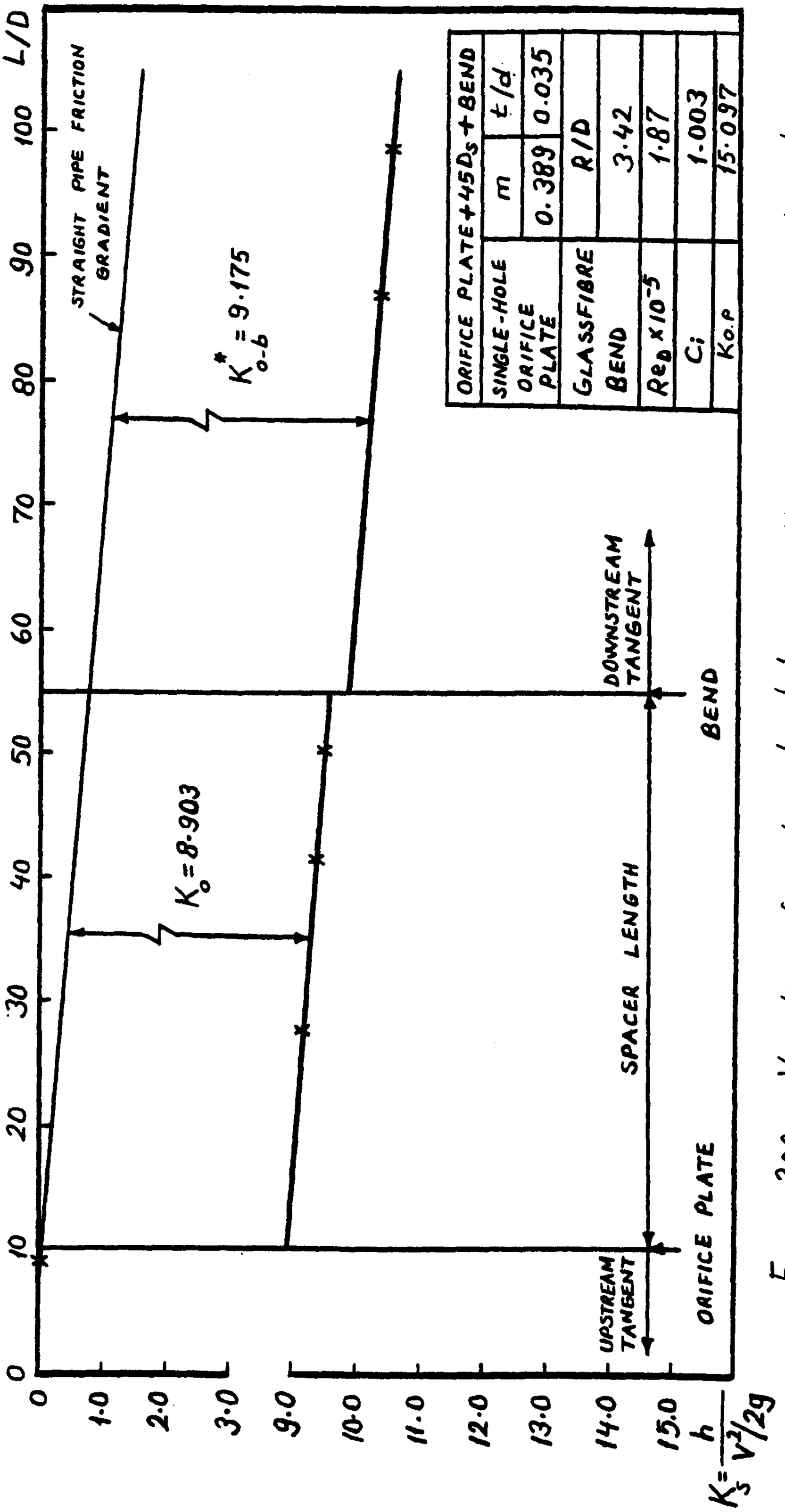

Fig. 300. Variation of system head Loss coefficient with axial length

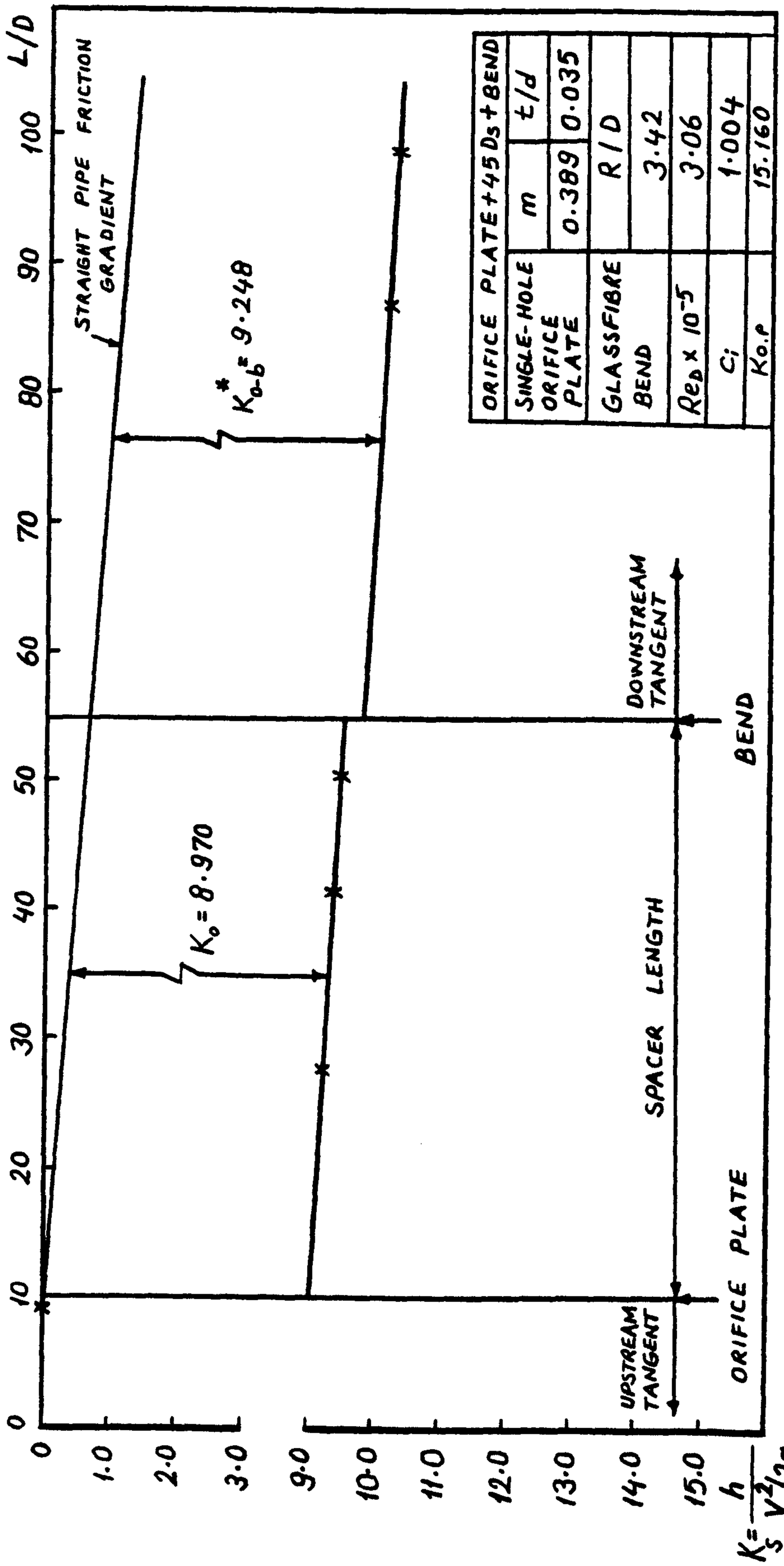

Fig. 301. Variation of system head loss coefficient with axial length

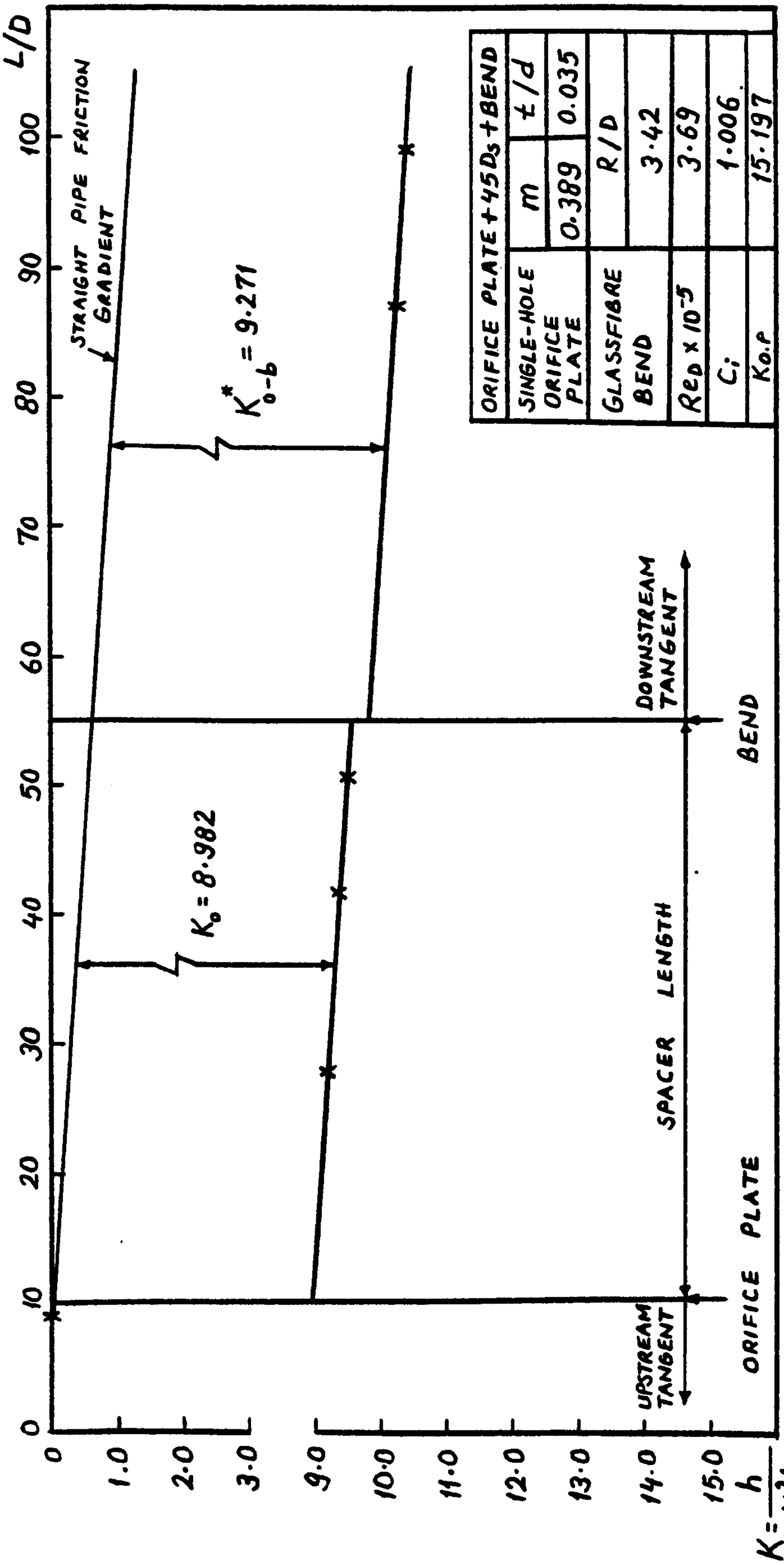

Fig. 302. Variation of system head loss coefficient with axial length

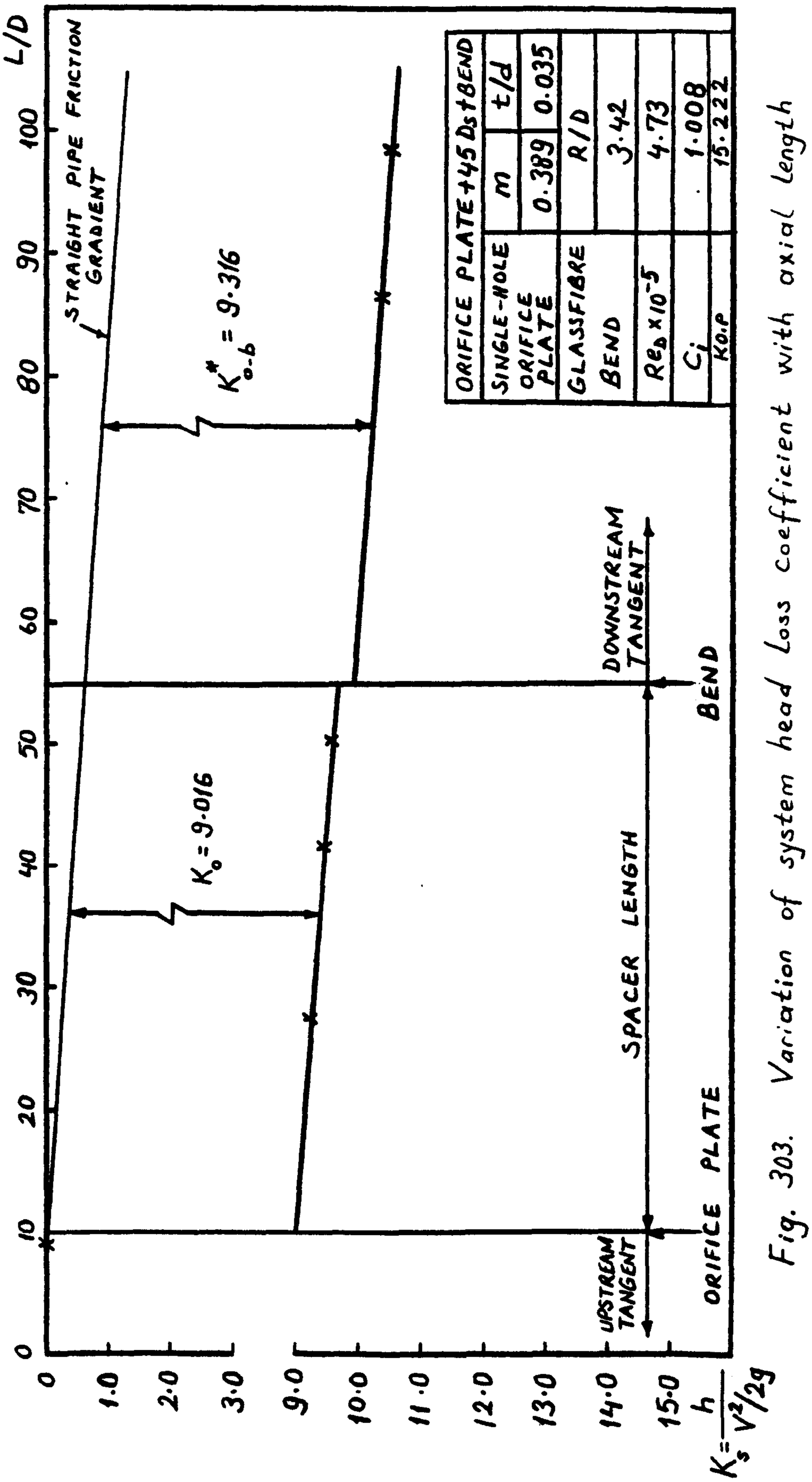

Fig. 303. Variation of system head Loss coefficient with axial length

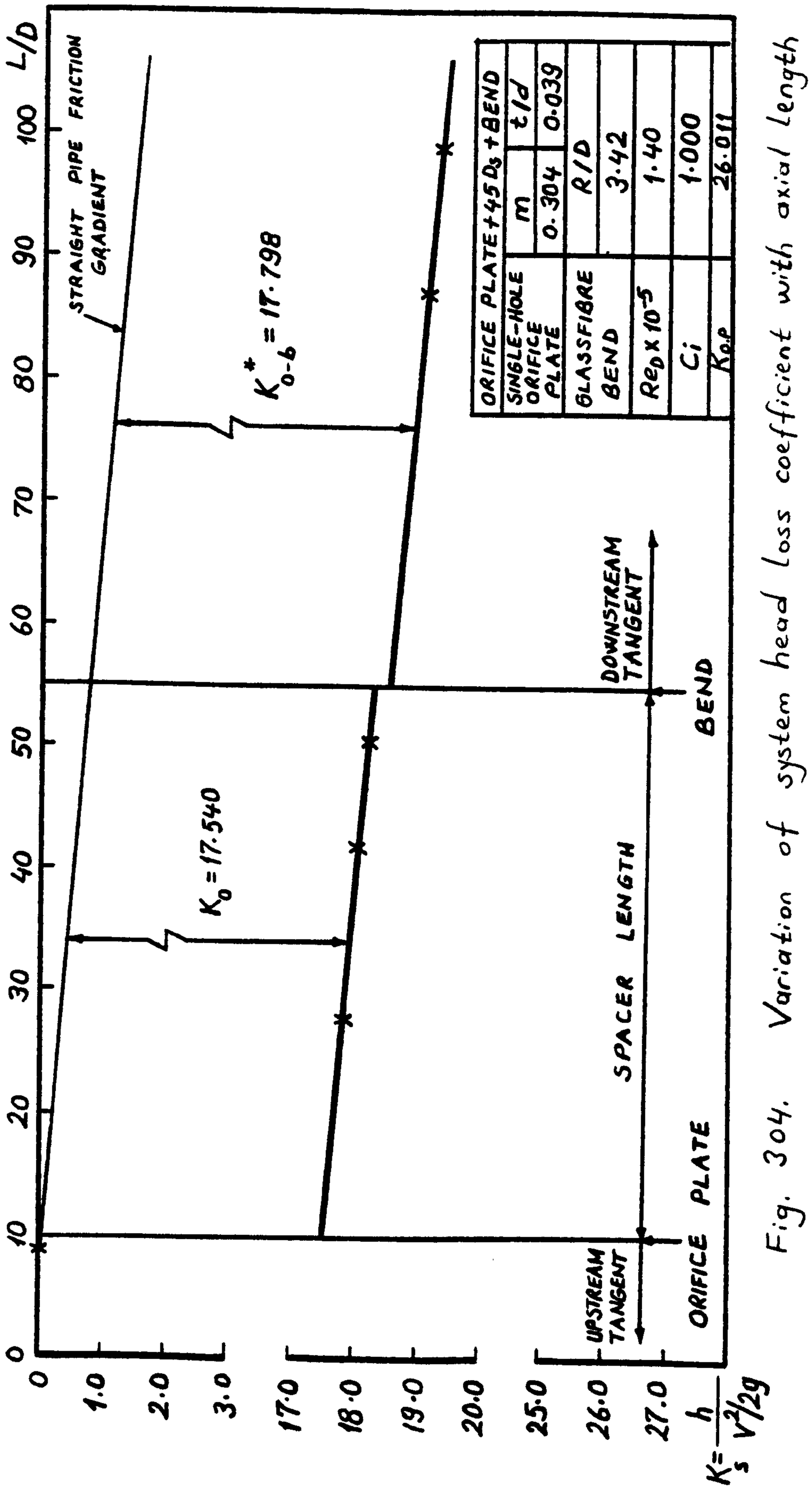

Fig. 304. Variation of system head loss coefficient with axial length

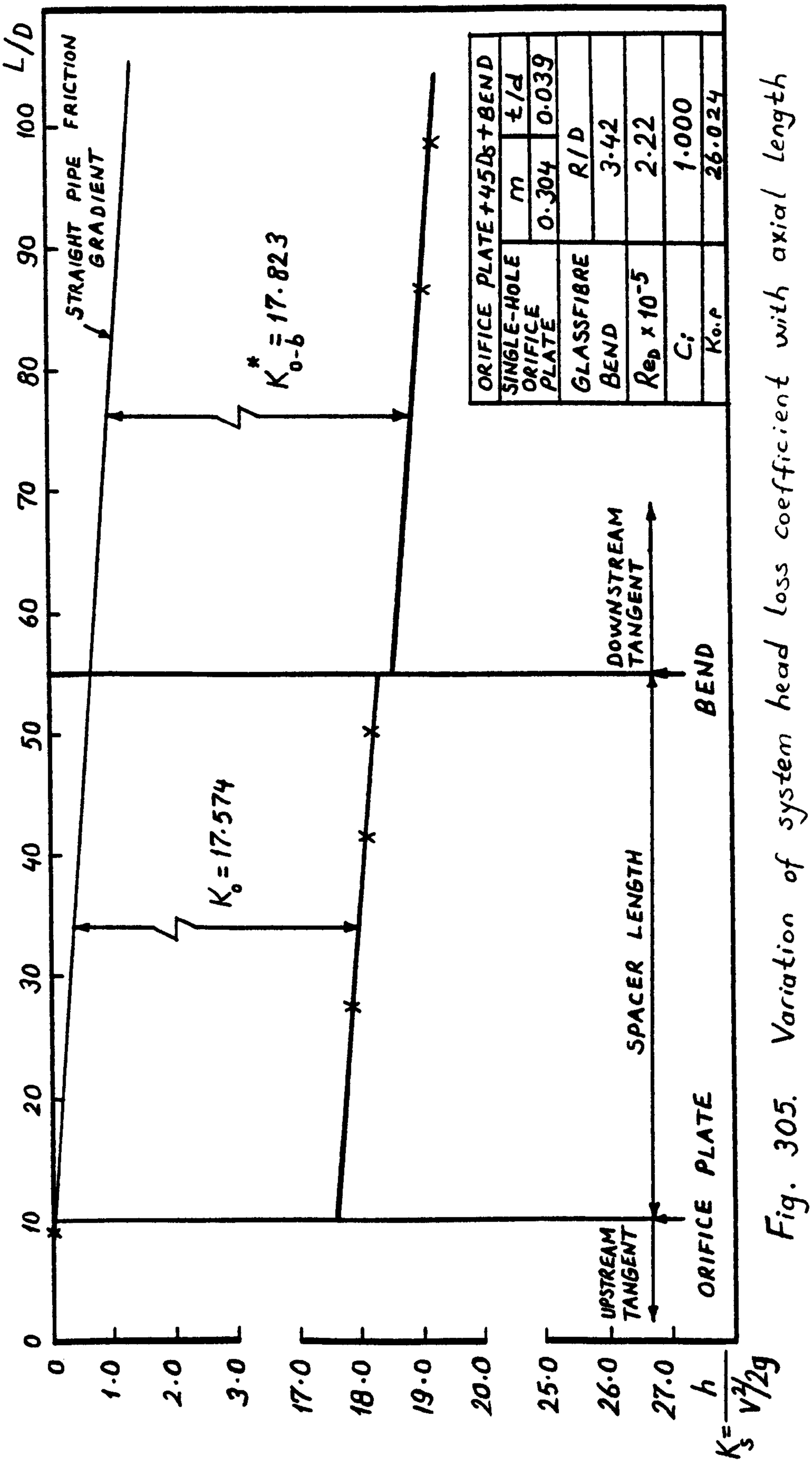

Fig. 305. Variation of system head loss coefficient with axial length

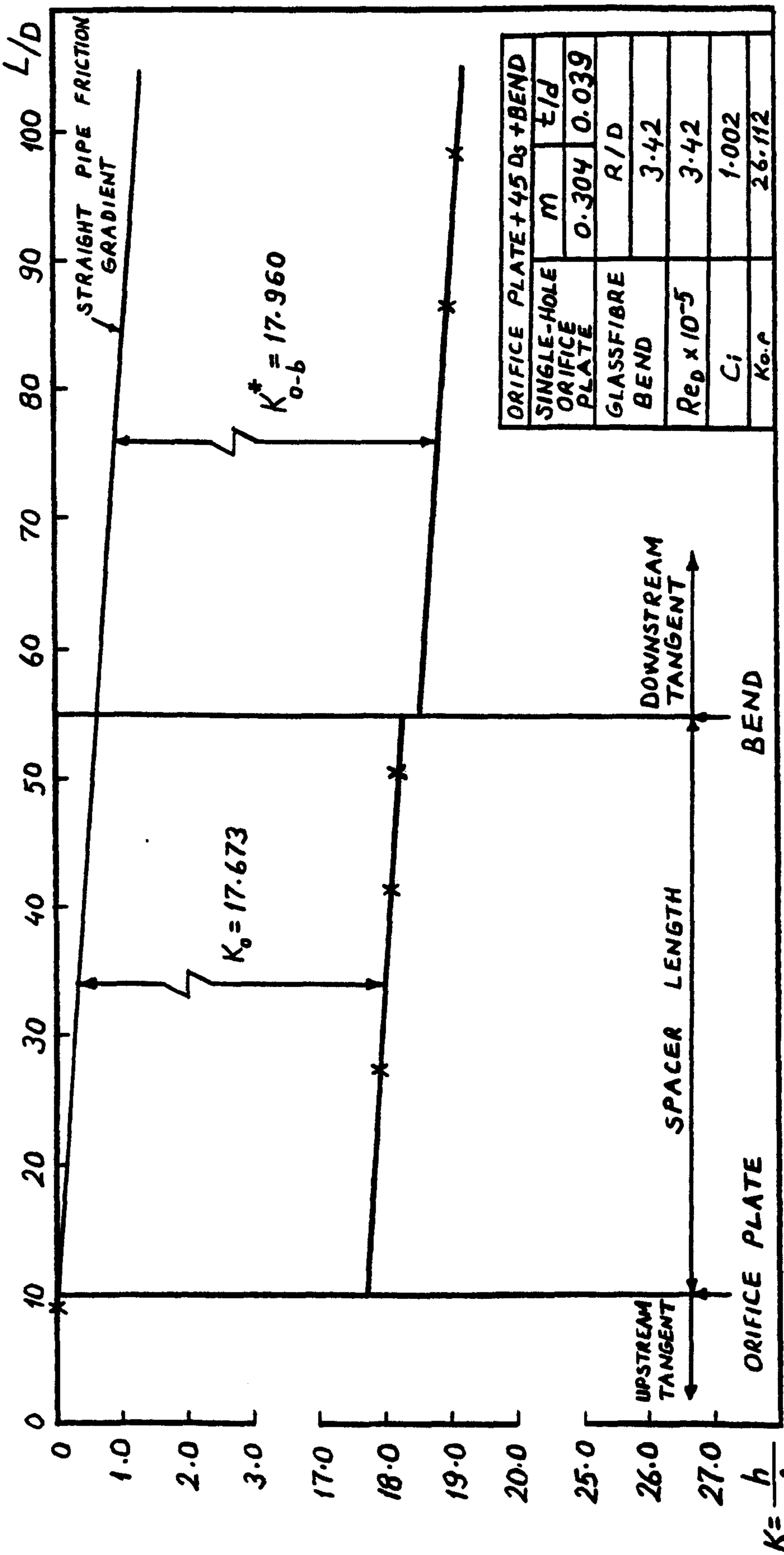

Fig. 306. Variation of system head loss coefficient with axial length

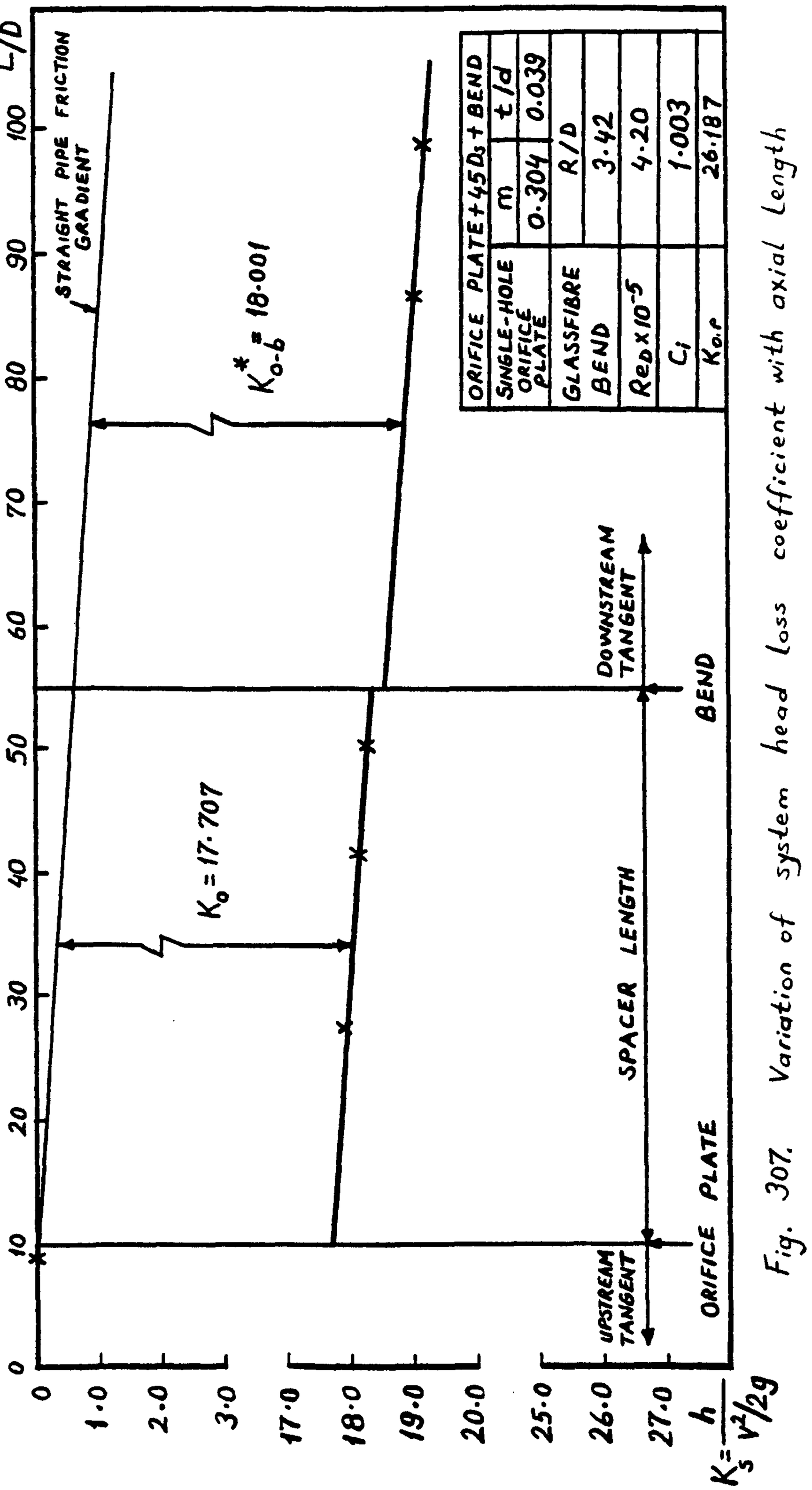

Fig. 307. Variation of system head loss coefficient with axial length

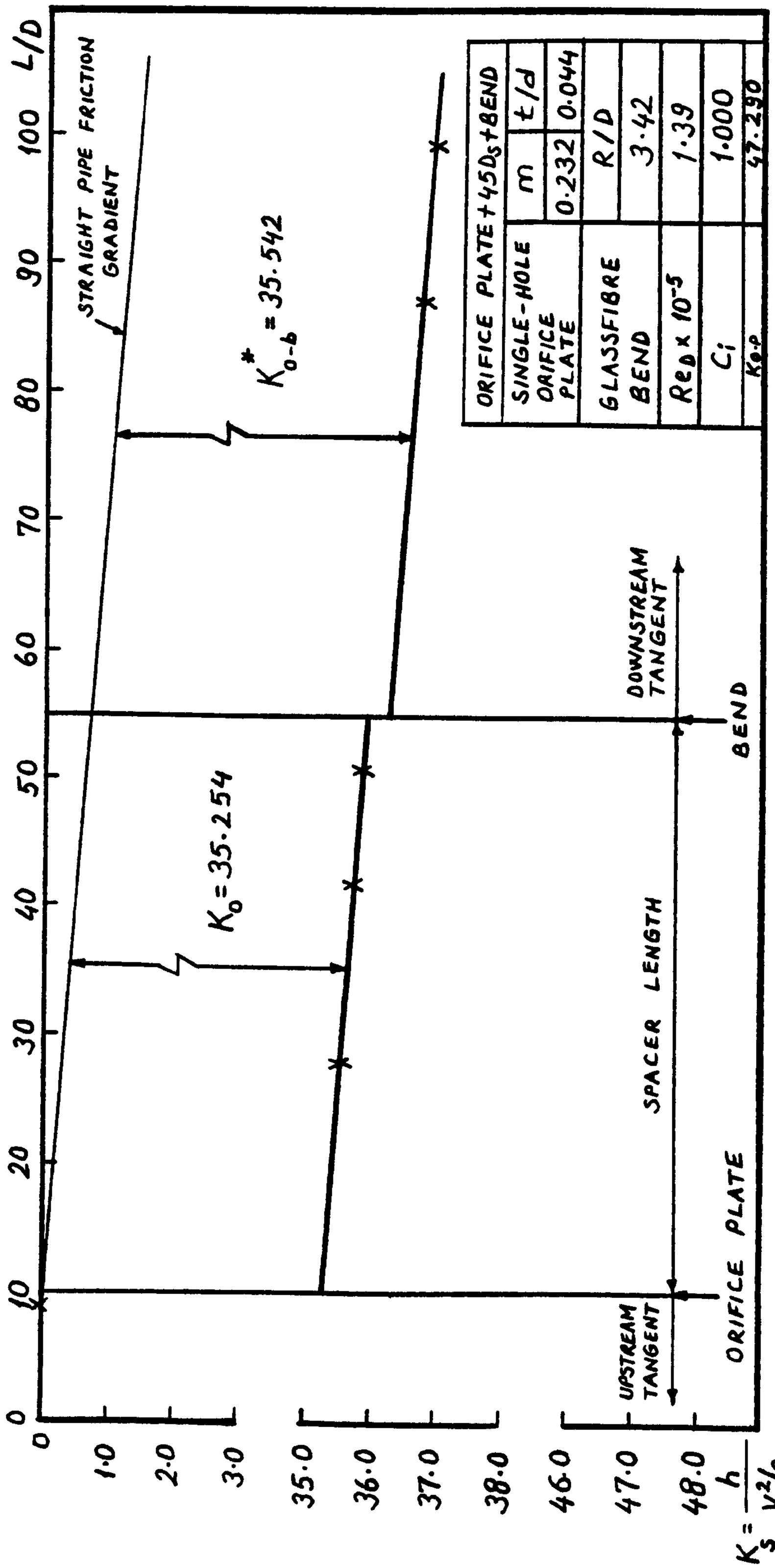

Fig. 308. Variation of system head loss coefficient with axial Length

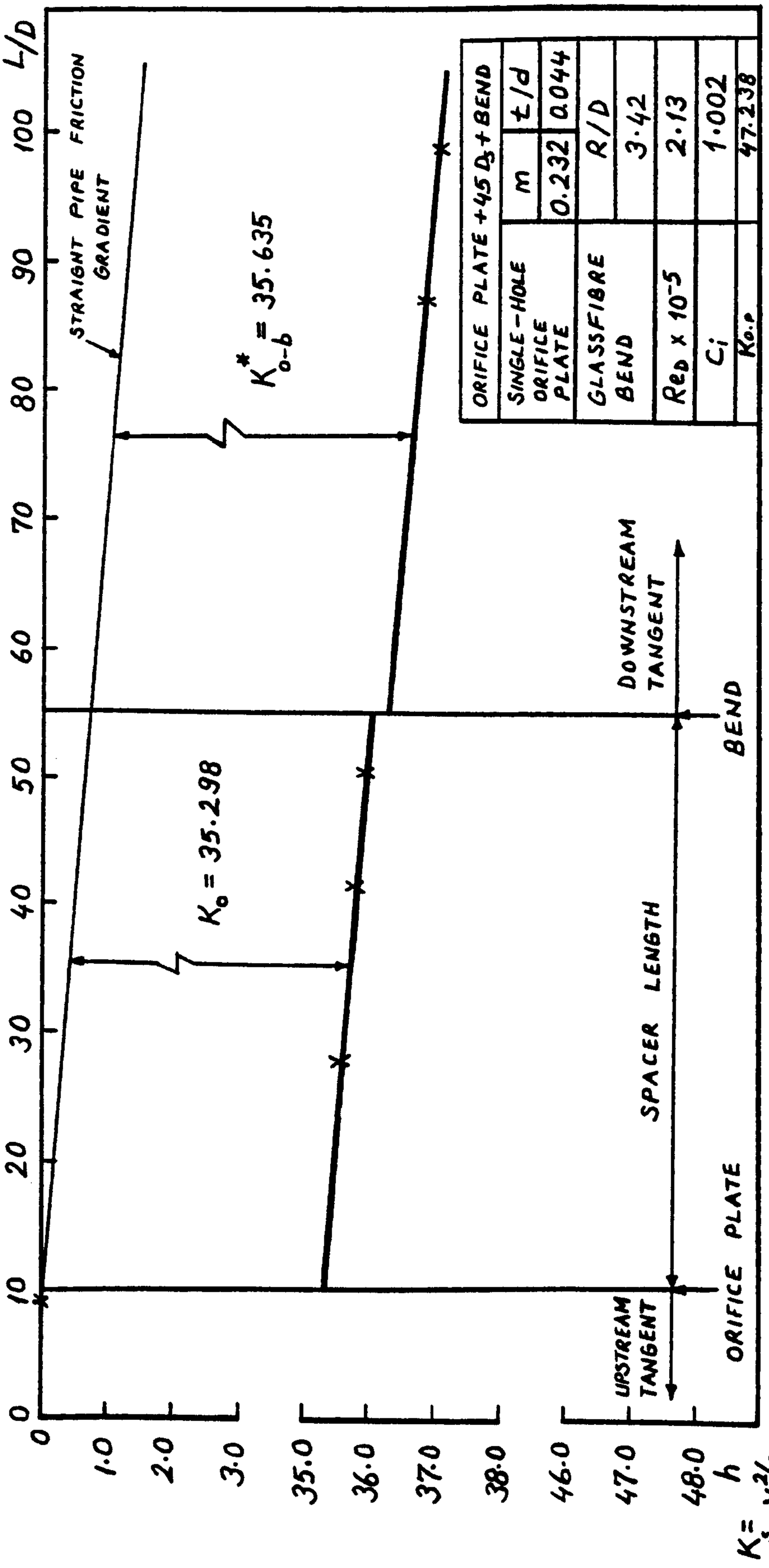

Fig. 309. Variation of system head loss coefficient with axial length

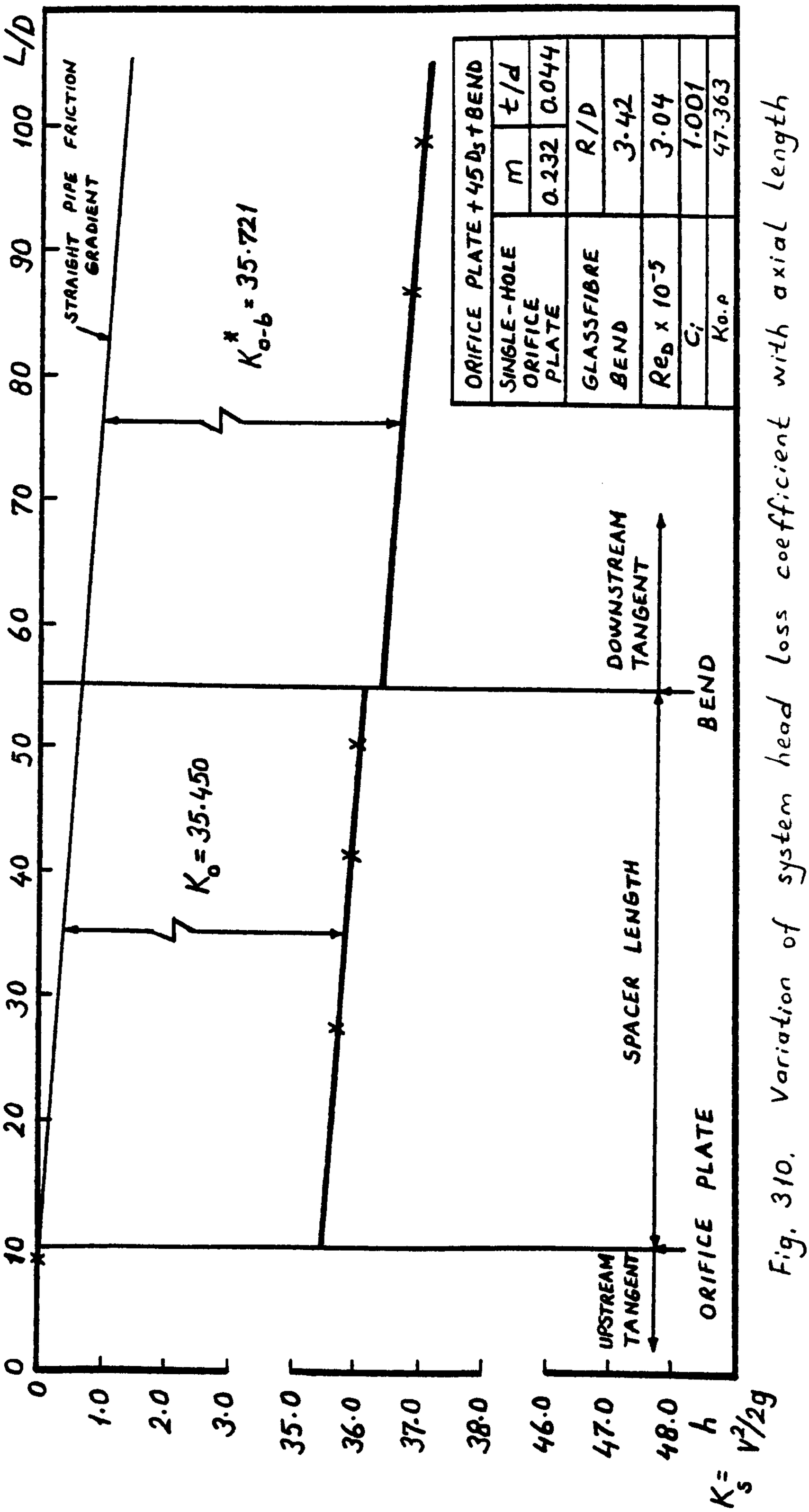

Fig. 310. Variation of system head loss coefficient with axial length

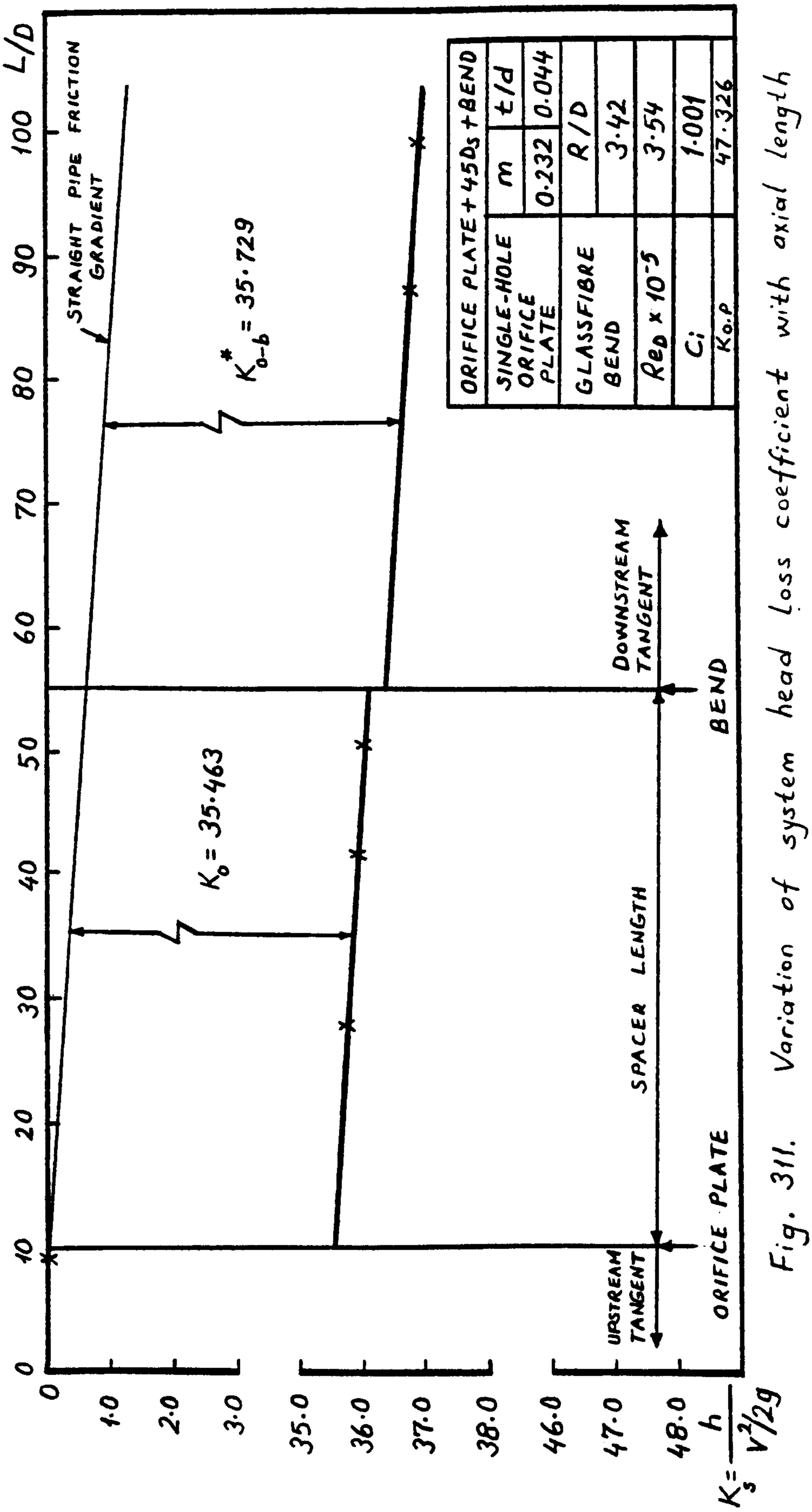

Fig. 311. Variation of system

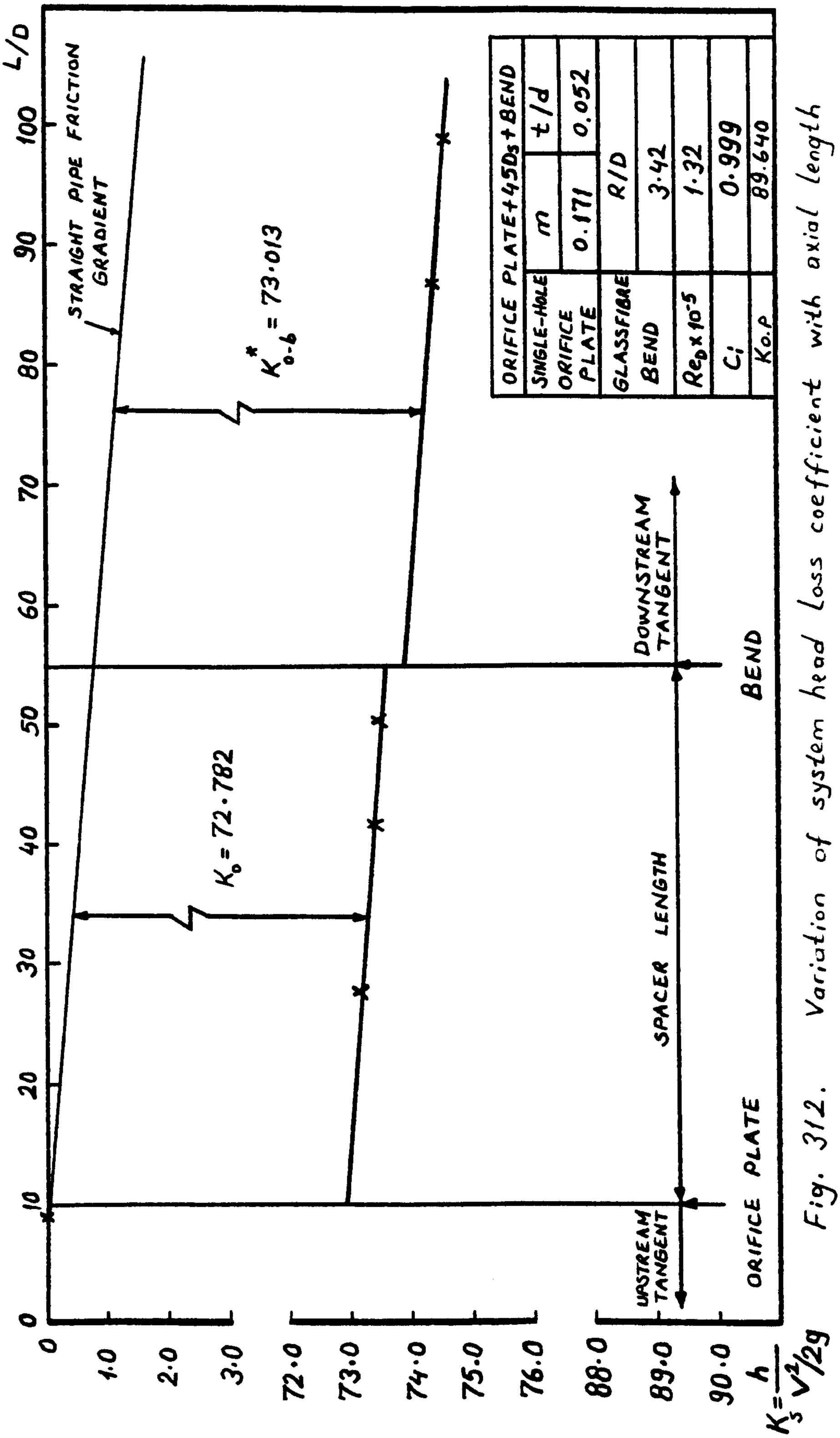

Fig. 312. Variation of system head loss coefficient with axial length

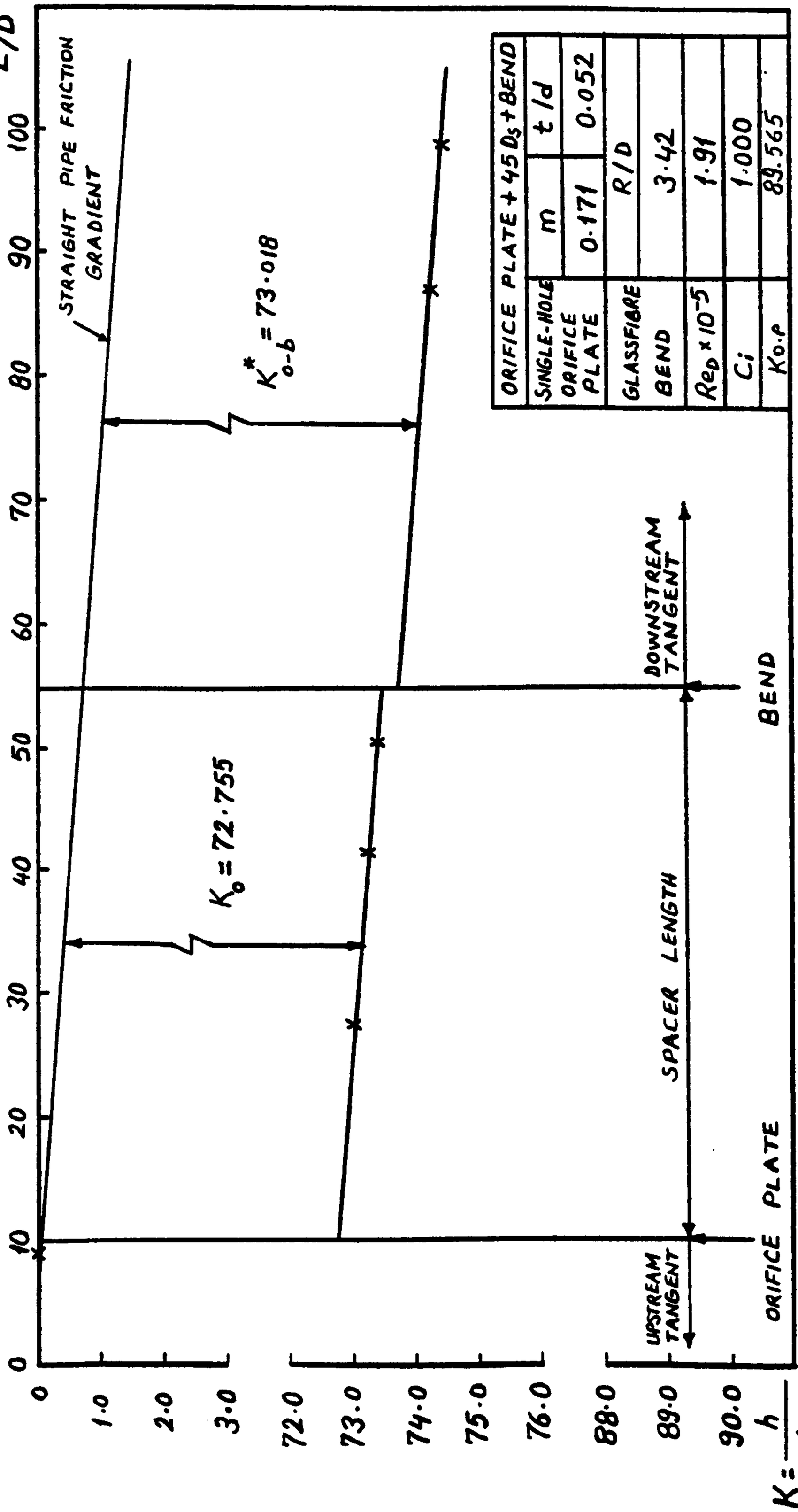

Fig. 313. Variation of system head loss coefficient with axial

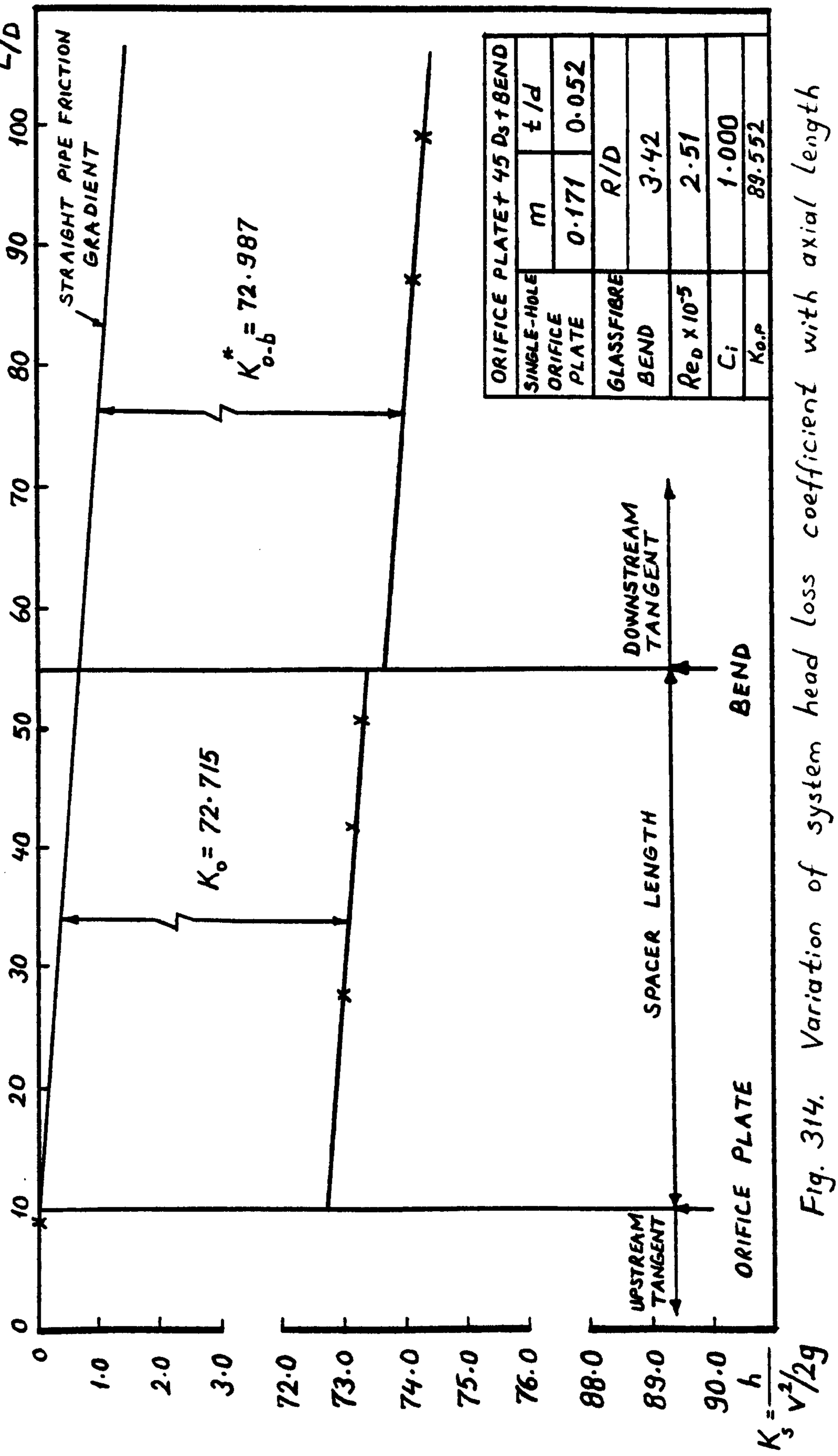

Fig. 314. Variation of system head loss coefficient with axial length

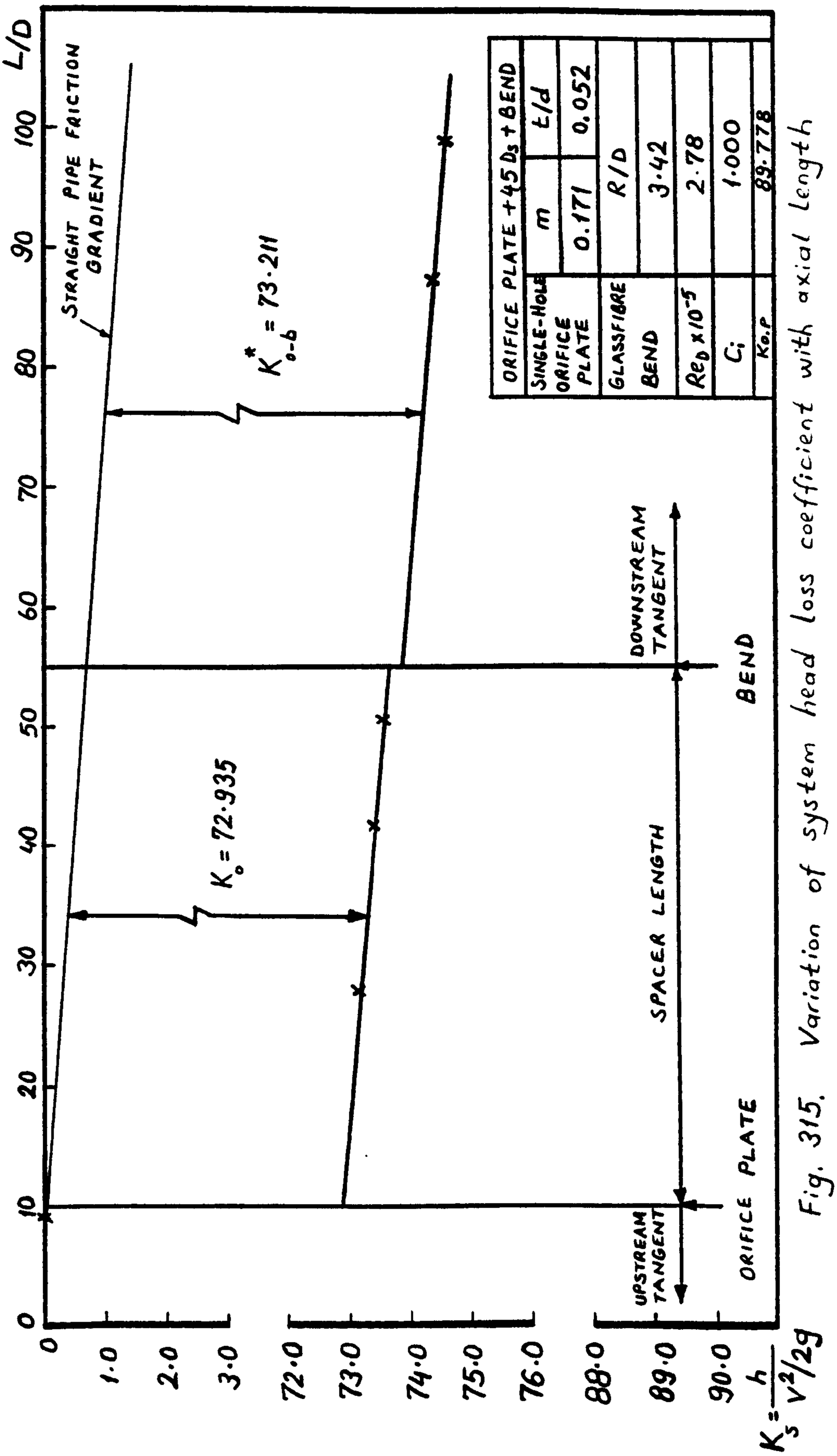

Fig. 315. Variation of system head loss coefficient with axial l

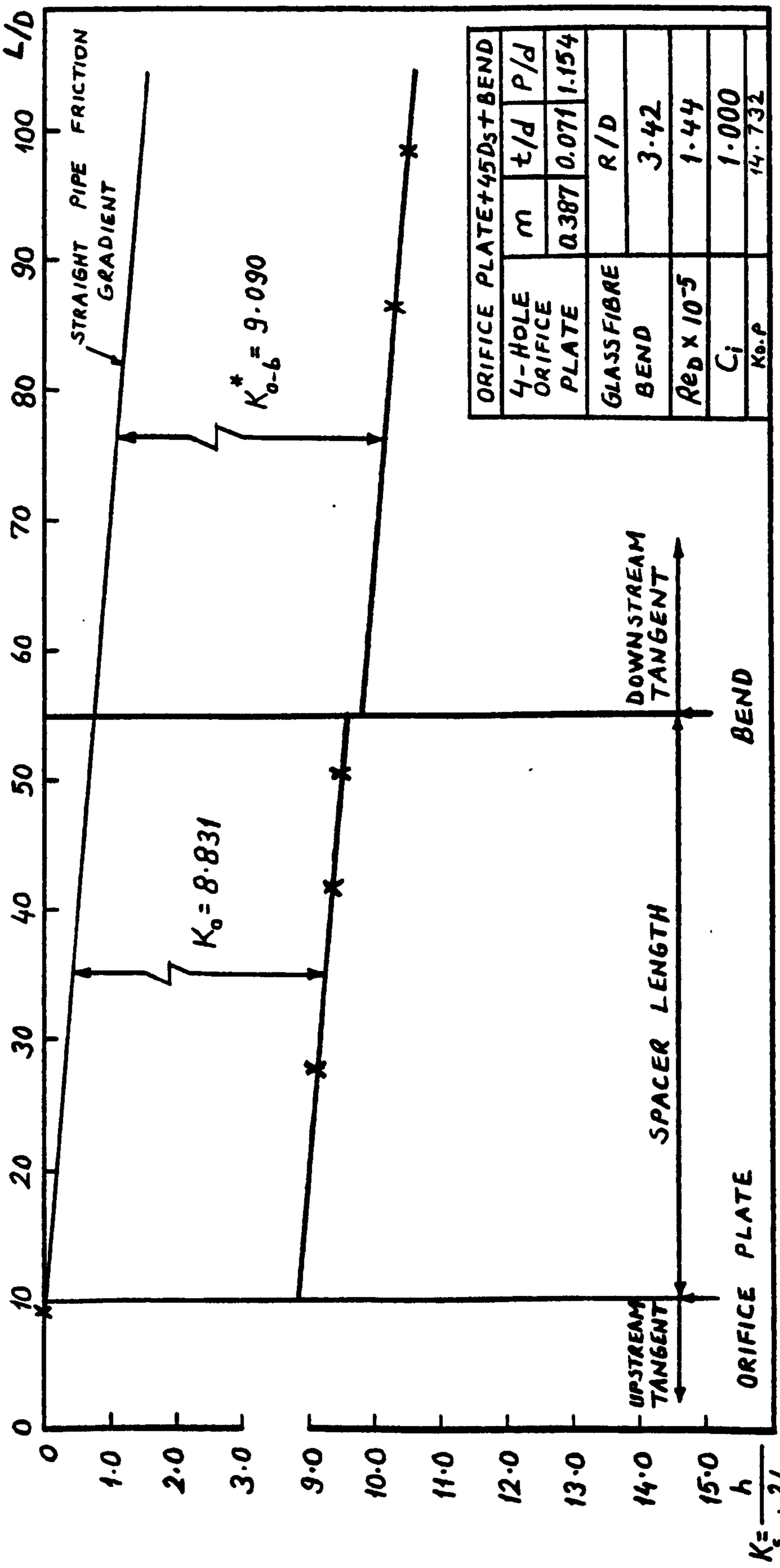

Fig. 3/6. Variation of system head loss coefficient with axial L

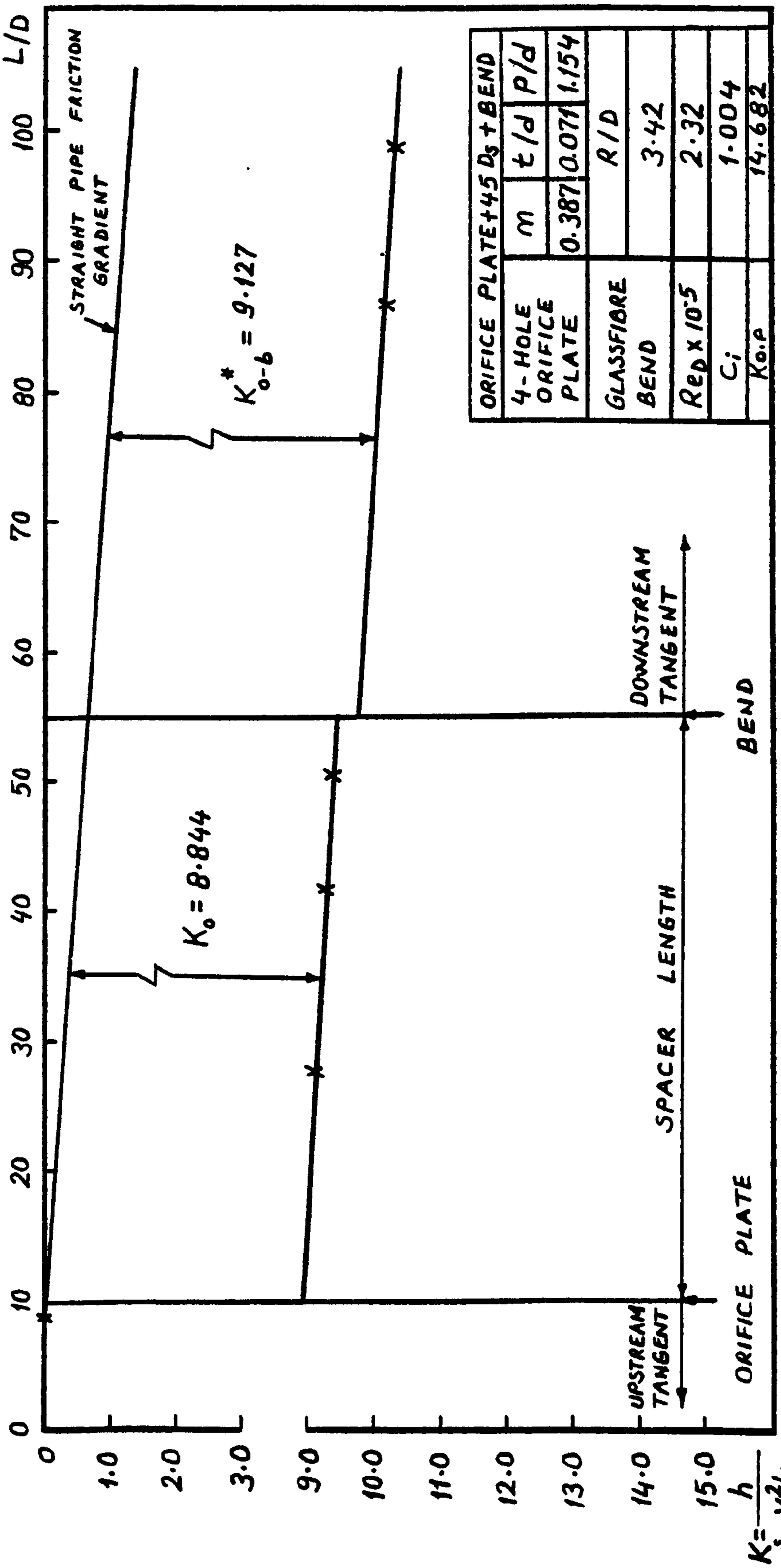

Fig. 317. Variation of system head loss coefficient with axial length

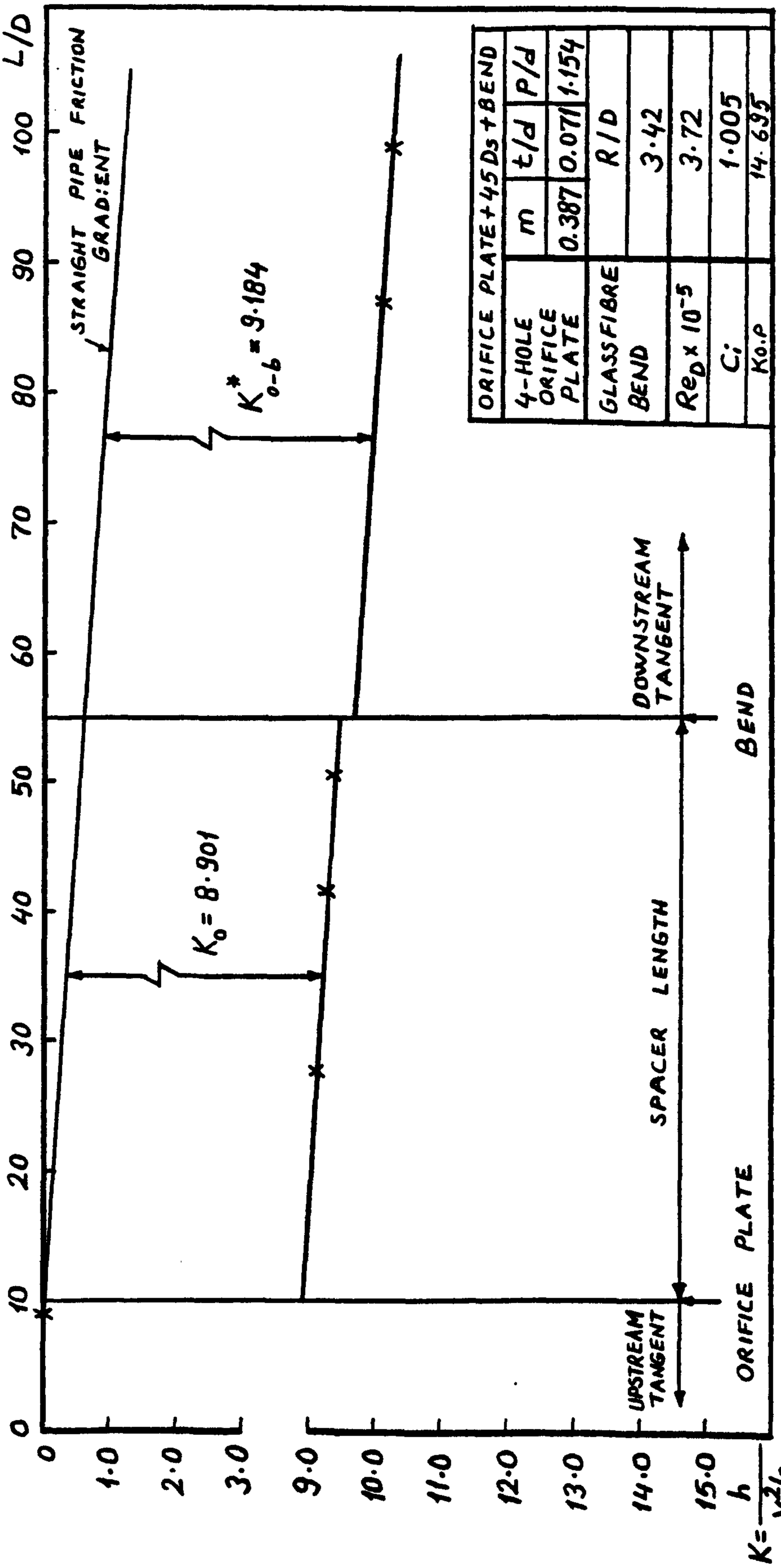

Fig. 318. Variation of system head loss coefficient with axial length

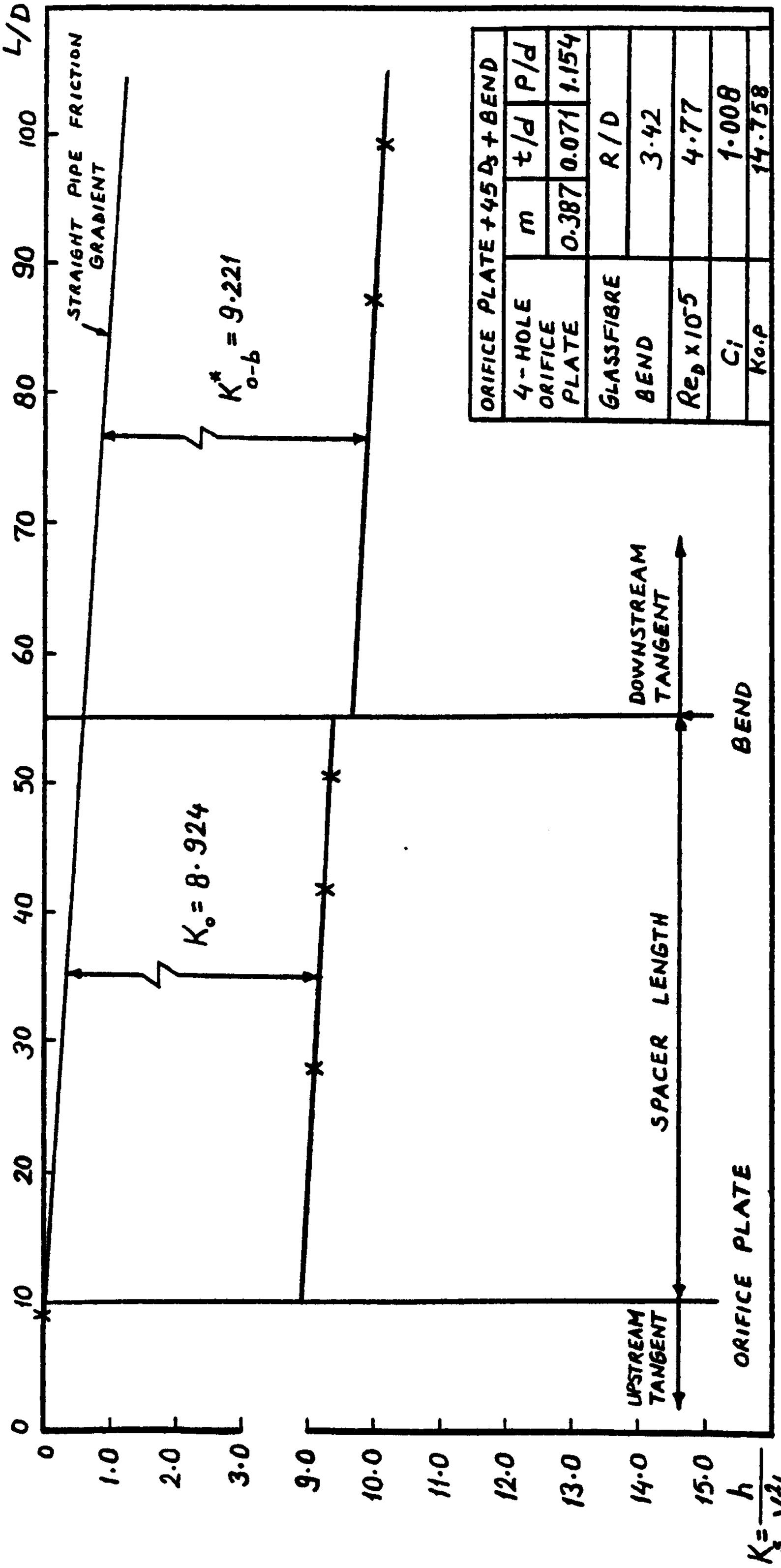

Fig. 319. Variation of system head Loss coefficient with axial Length

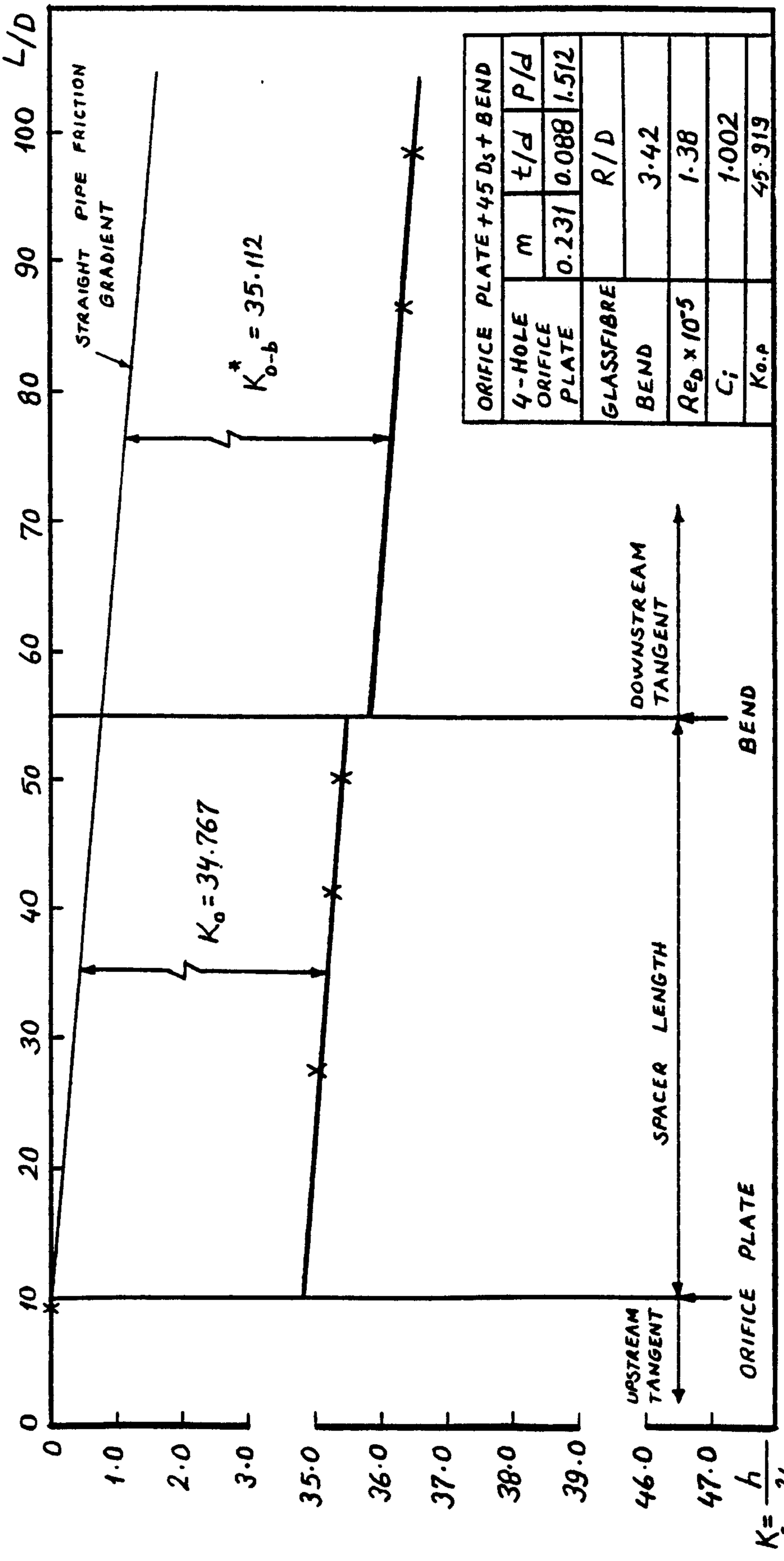

Fig. 320. Variation of system

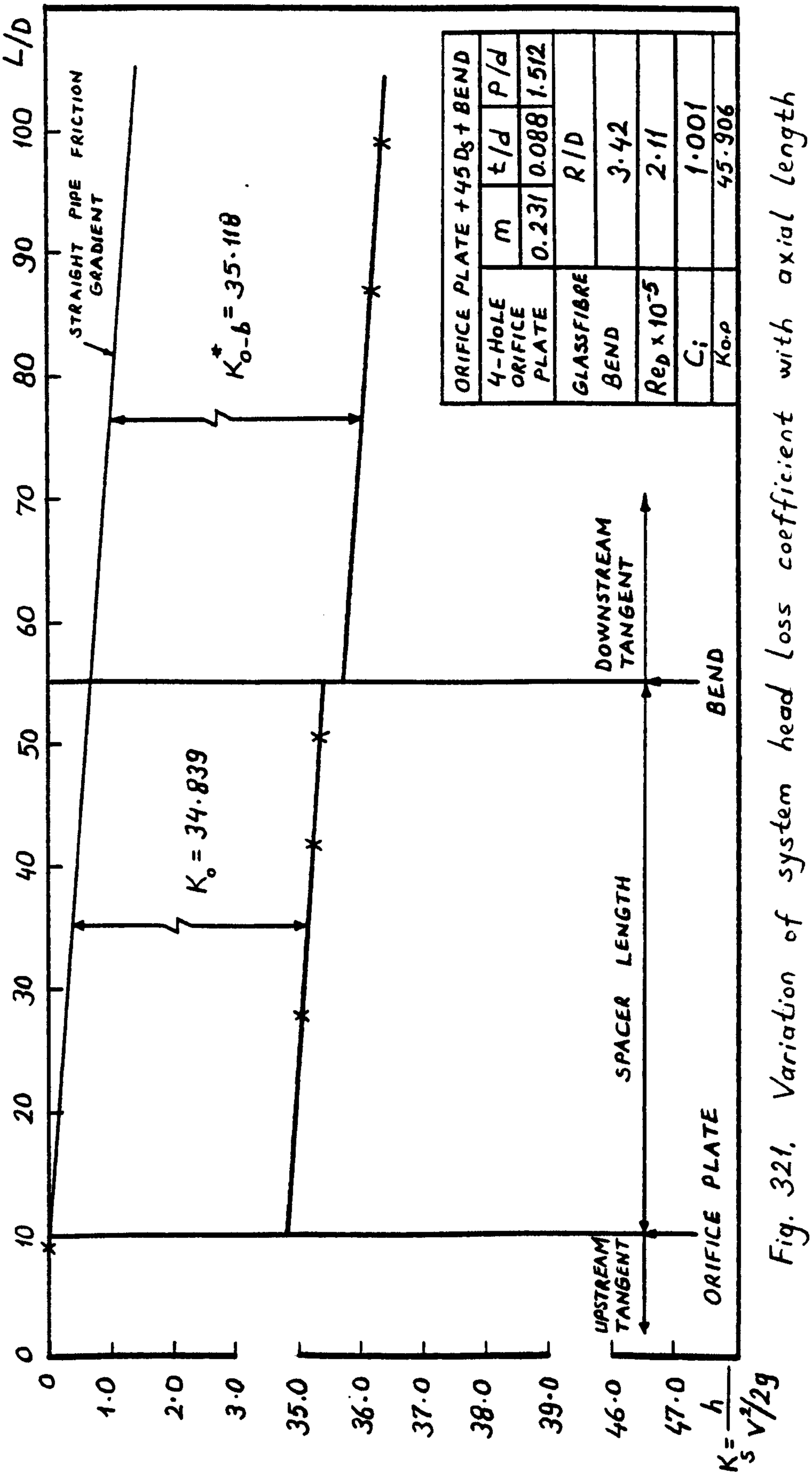

Fig. 321. Variation of system head loss coefficient with

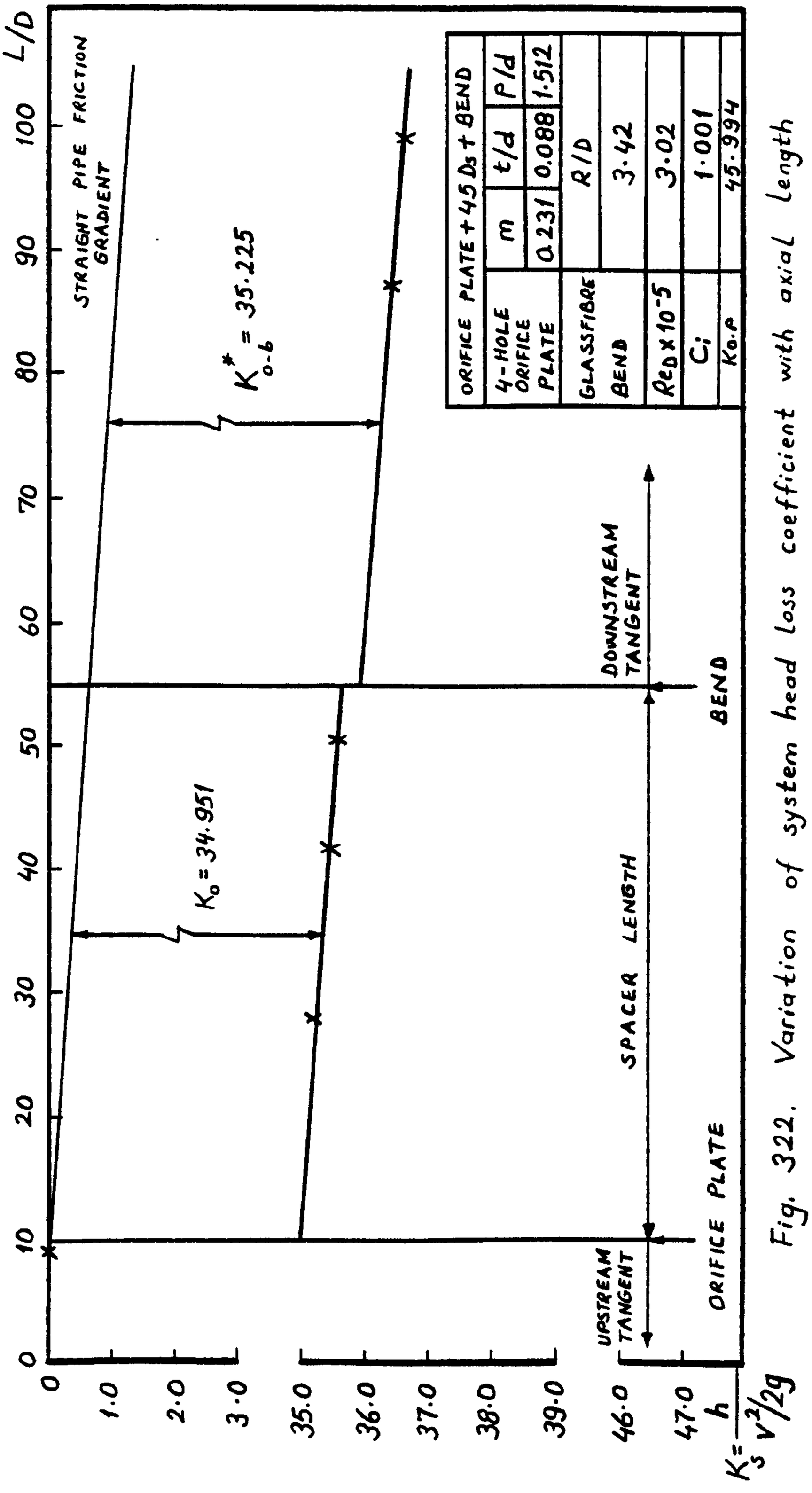

Fig. 322. Variation of system head loss coefficient with axial

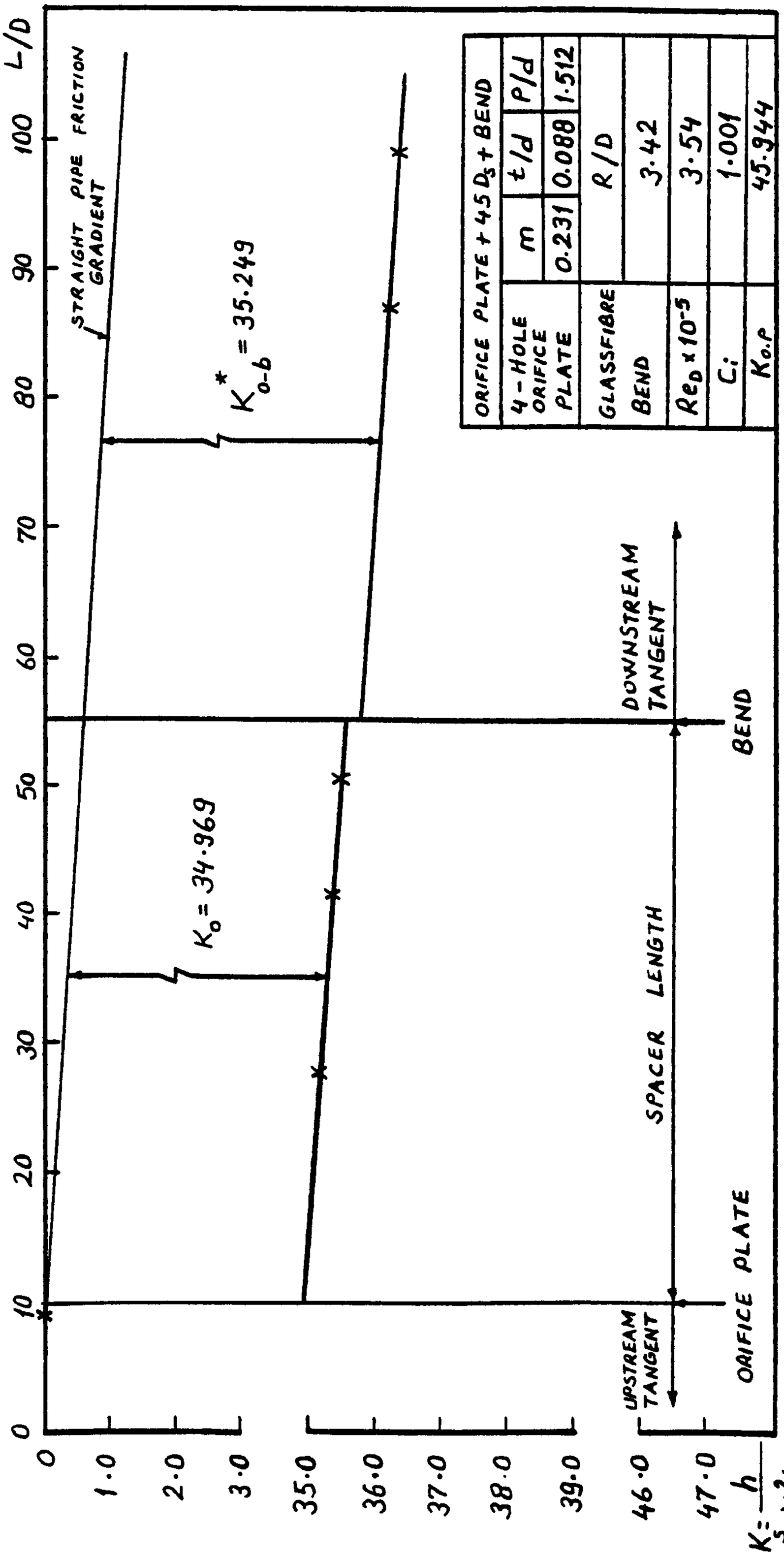

Fig. 323. Variation of system head loss coefficient with a

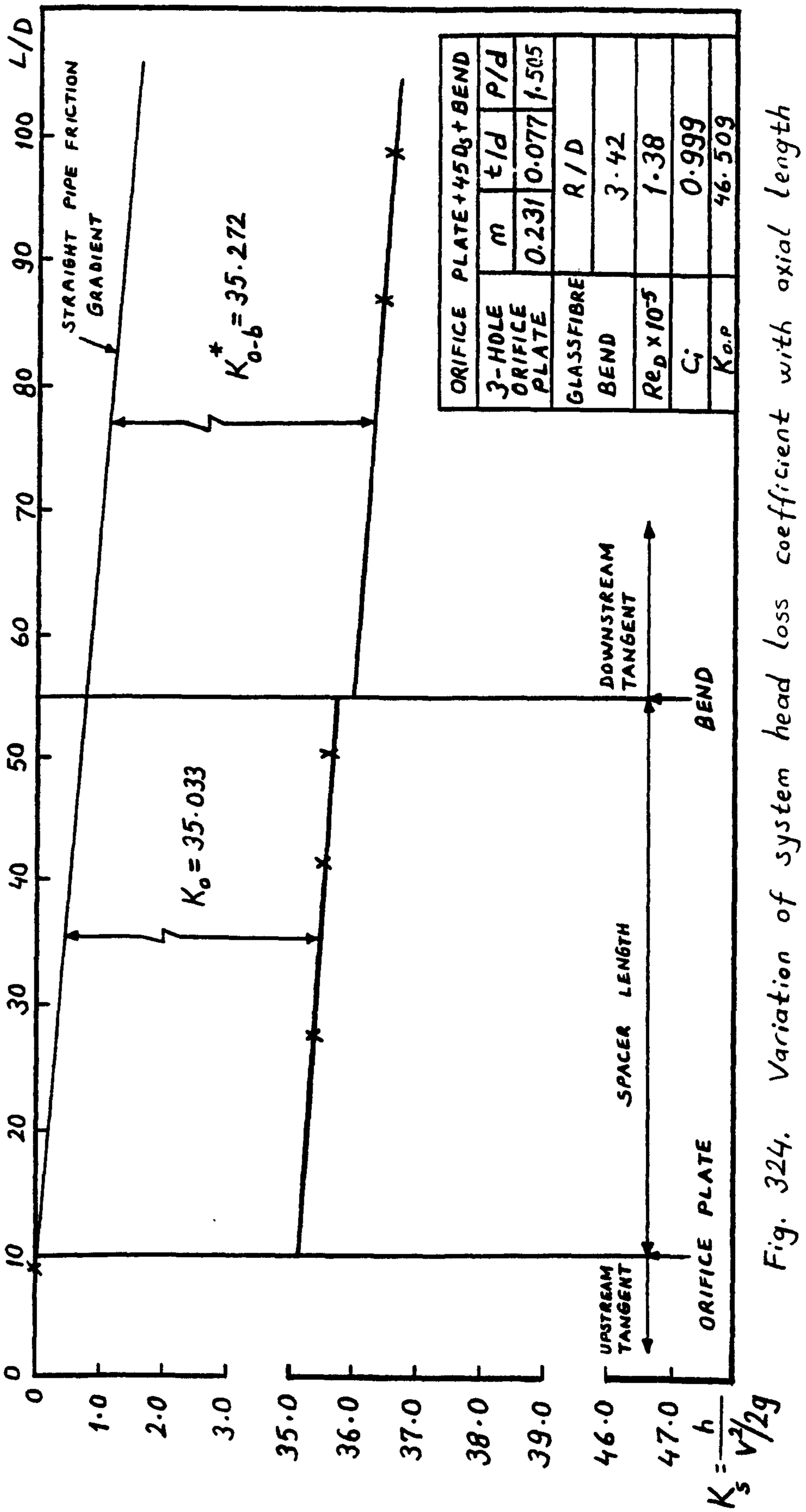

Fig. 324. Variation of system head loss coefficient with axial length

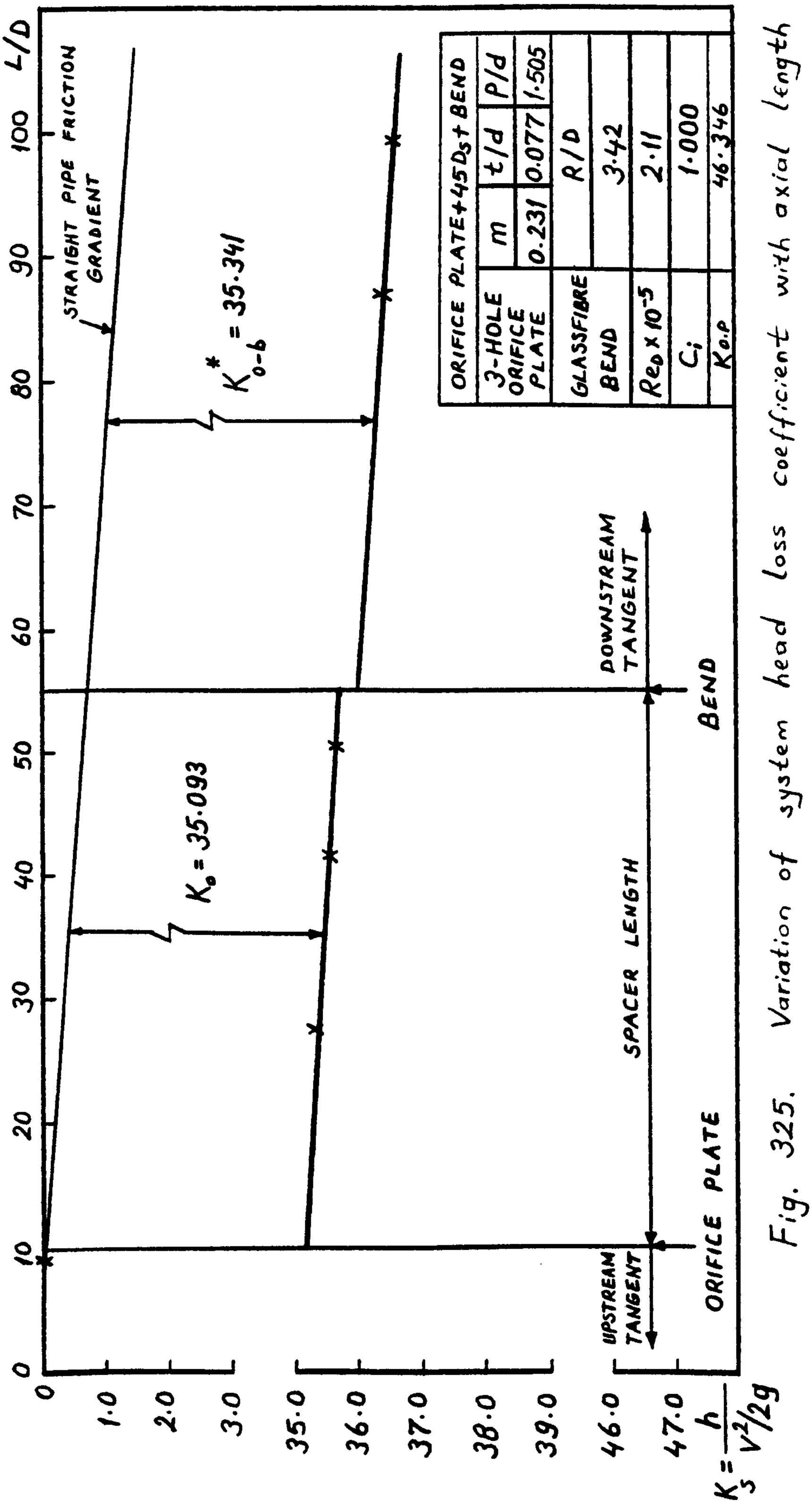

Fig. 325. Variation of system head loss coefficient with a

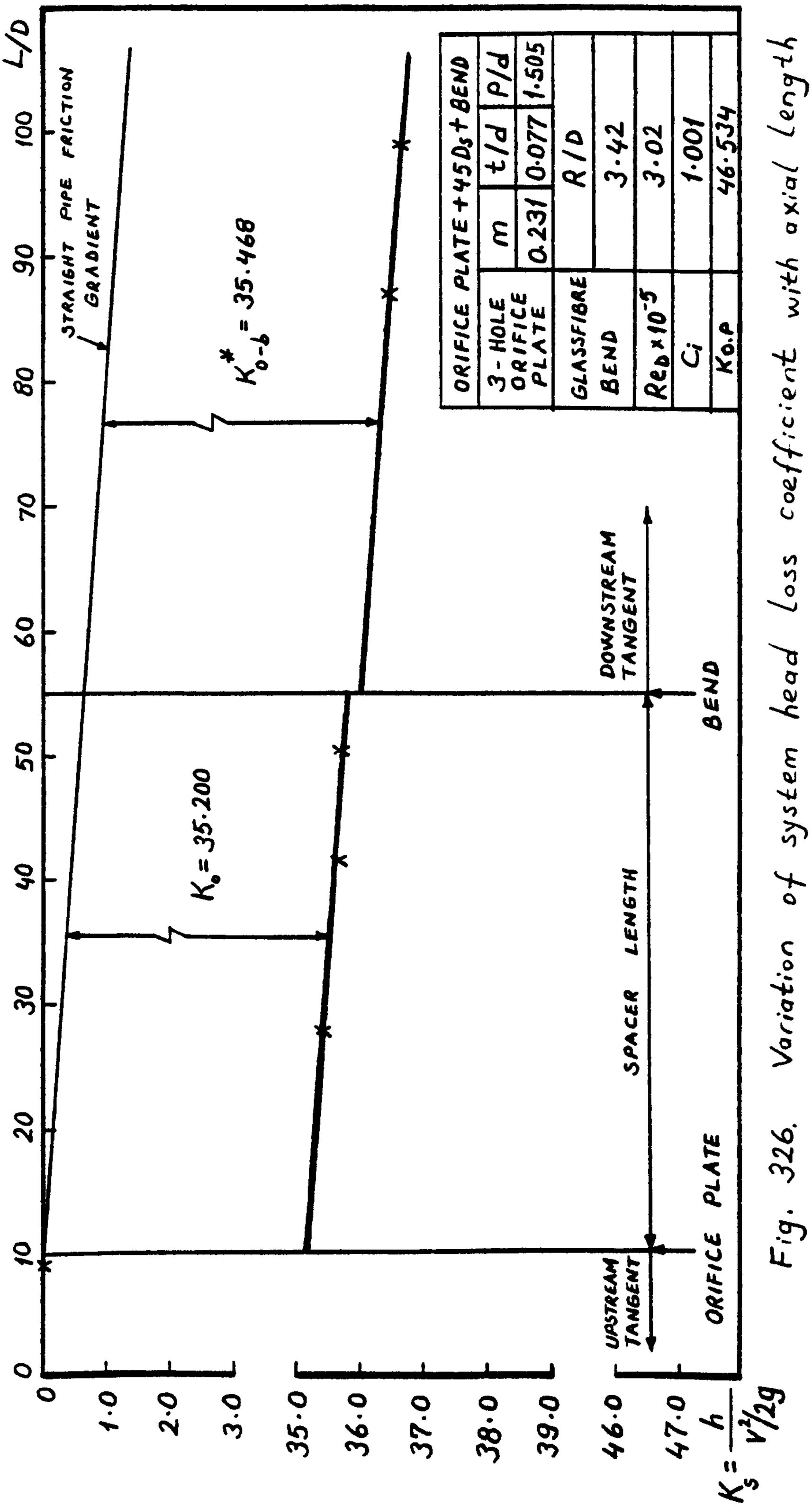

Fig. 326. Variation of system head loss coefficient with axial length

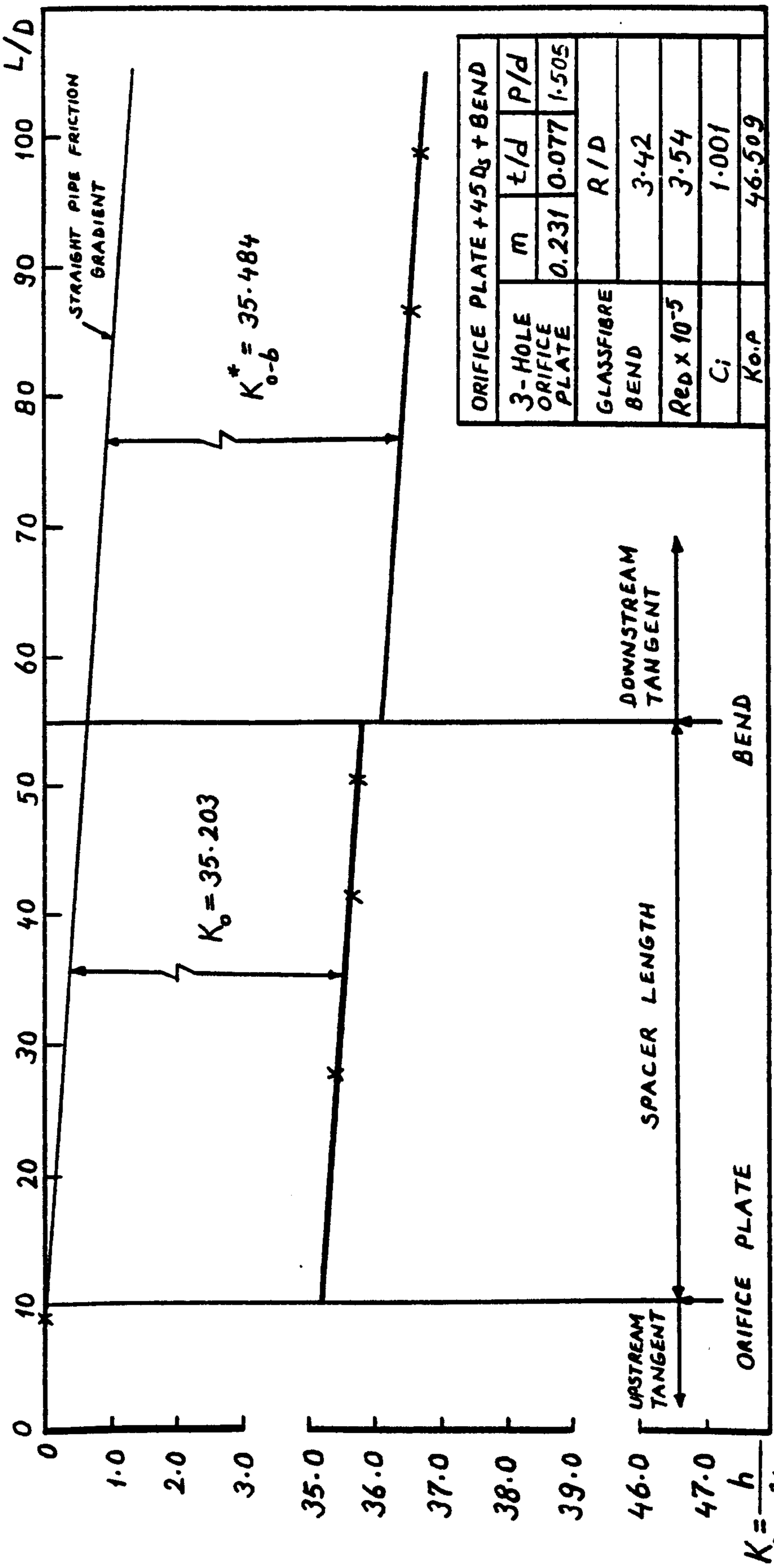

Fig. 327. Variation of system head loss coefficient with

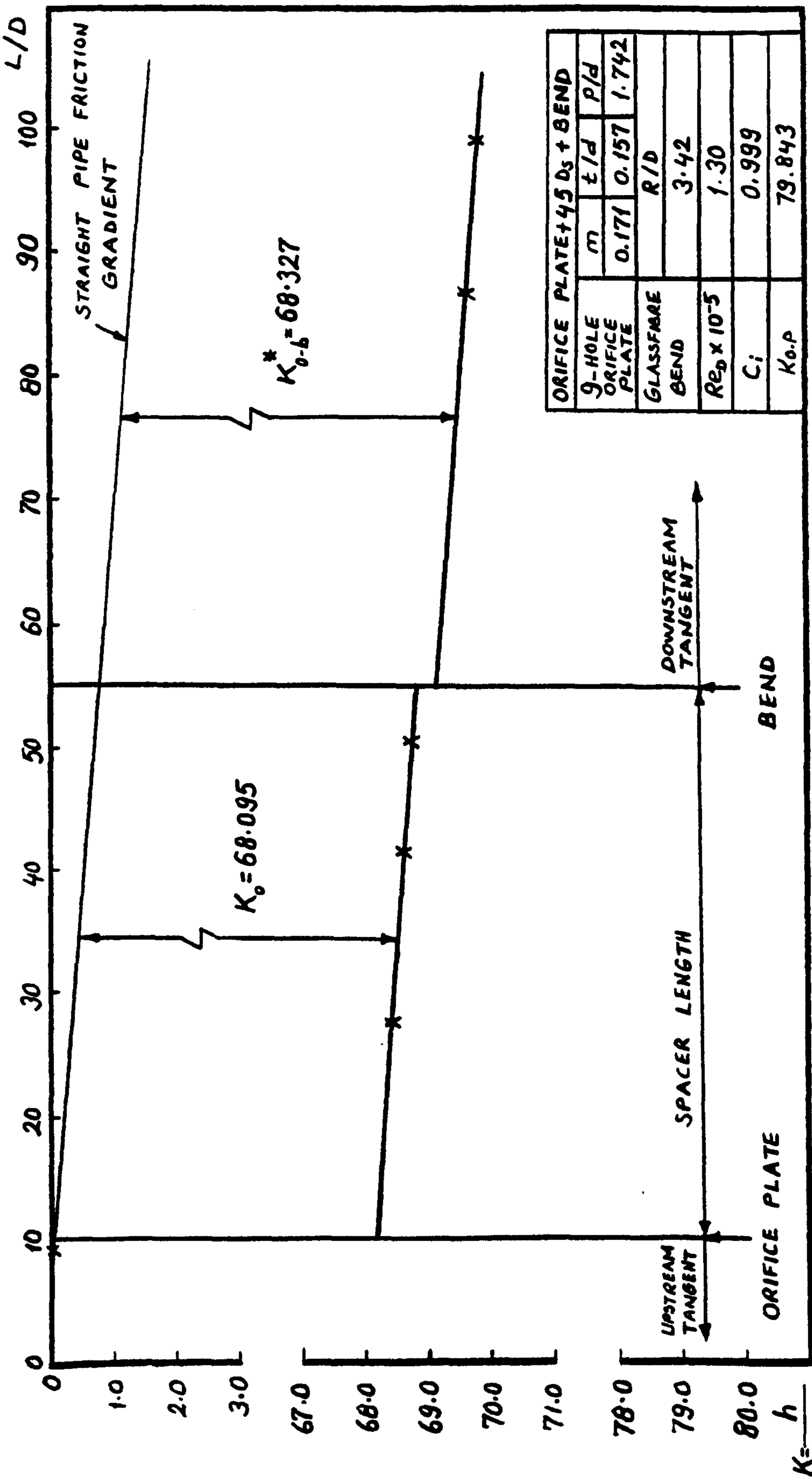

328. Variation of system head loss coefficient with

Fig.

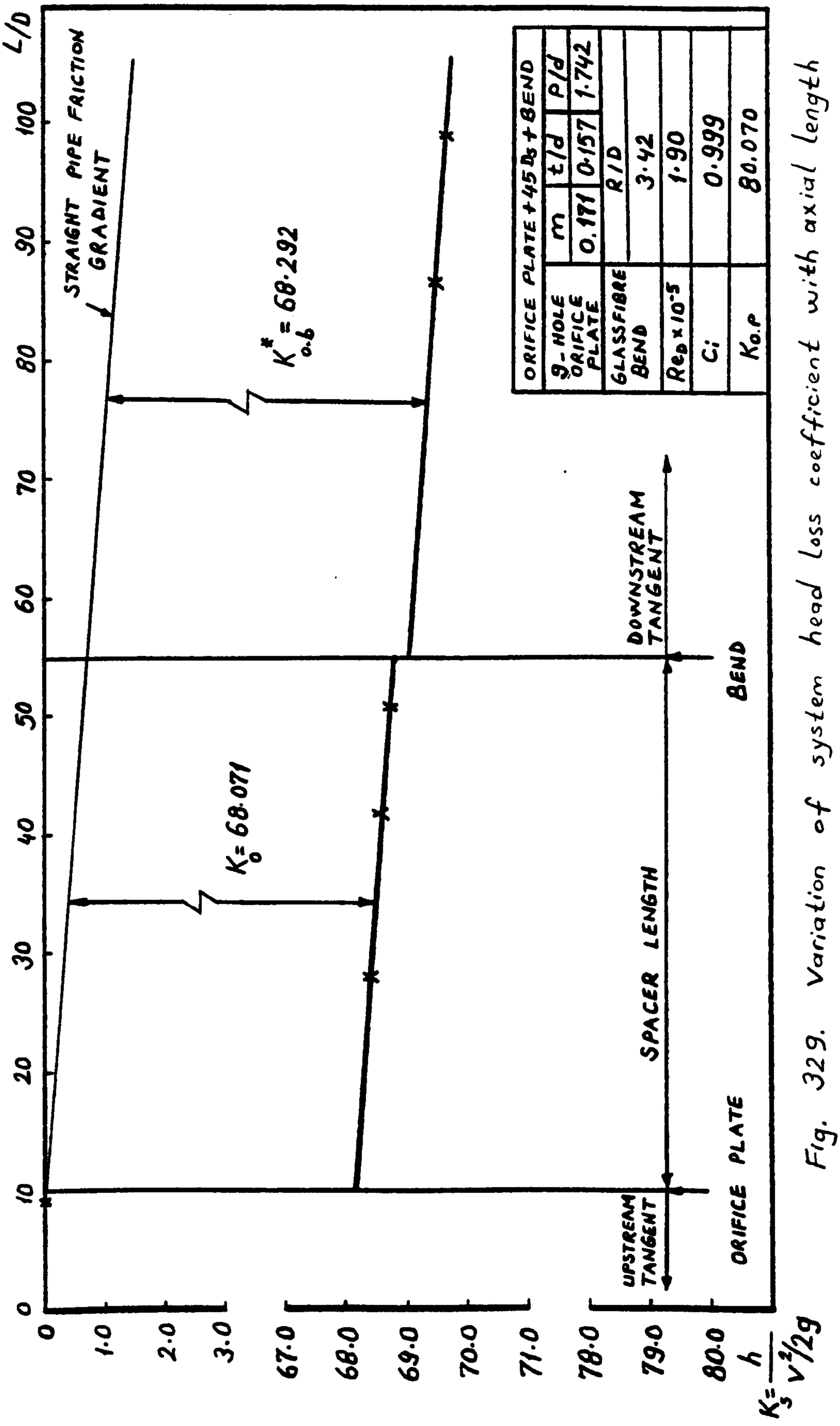

Fig. 329. Variation of system head loss coefficient with axial length

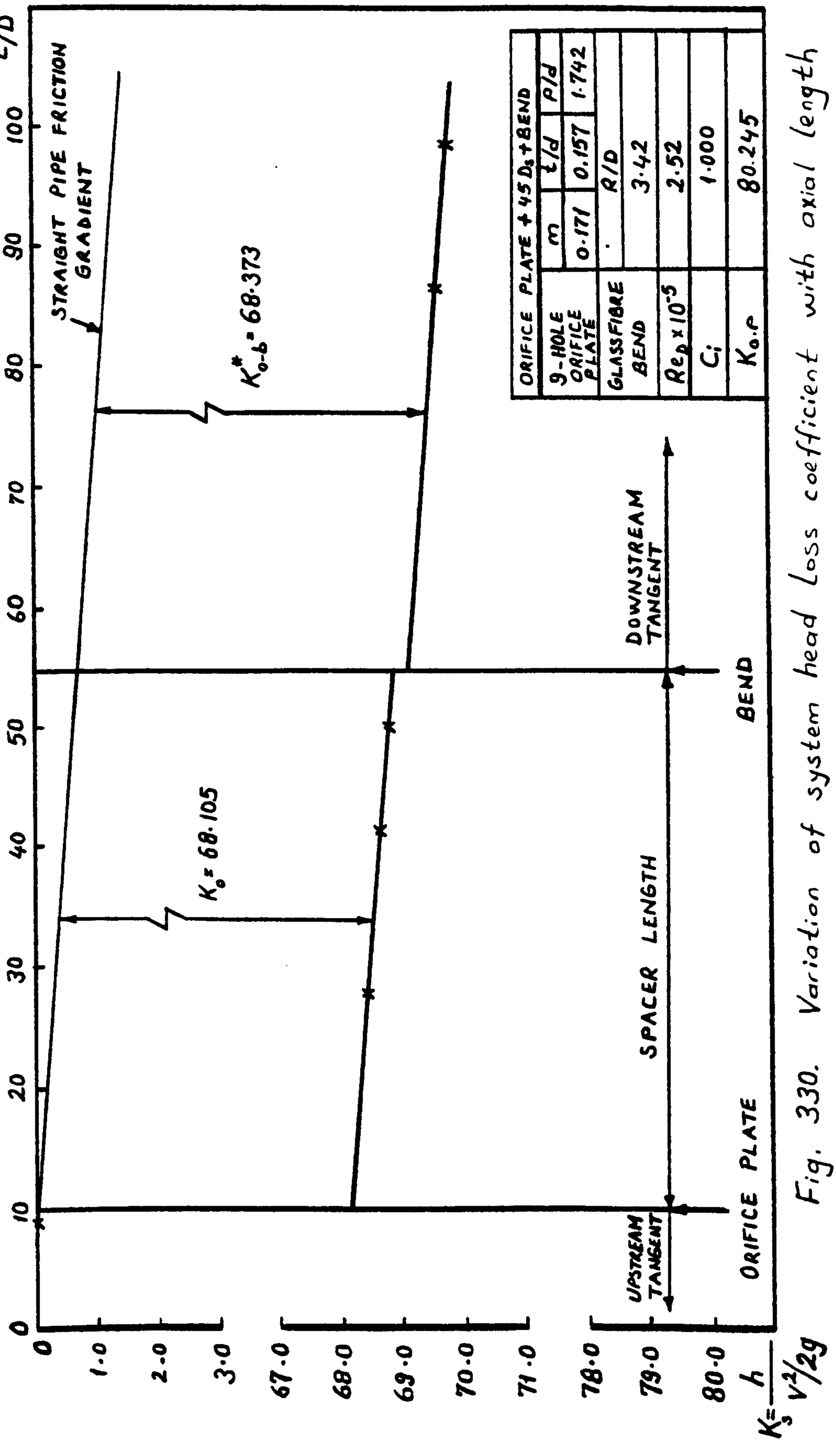

Fig. 330. Variation of system head loss coefficient with axial length

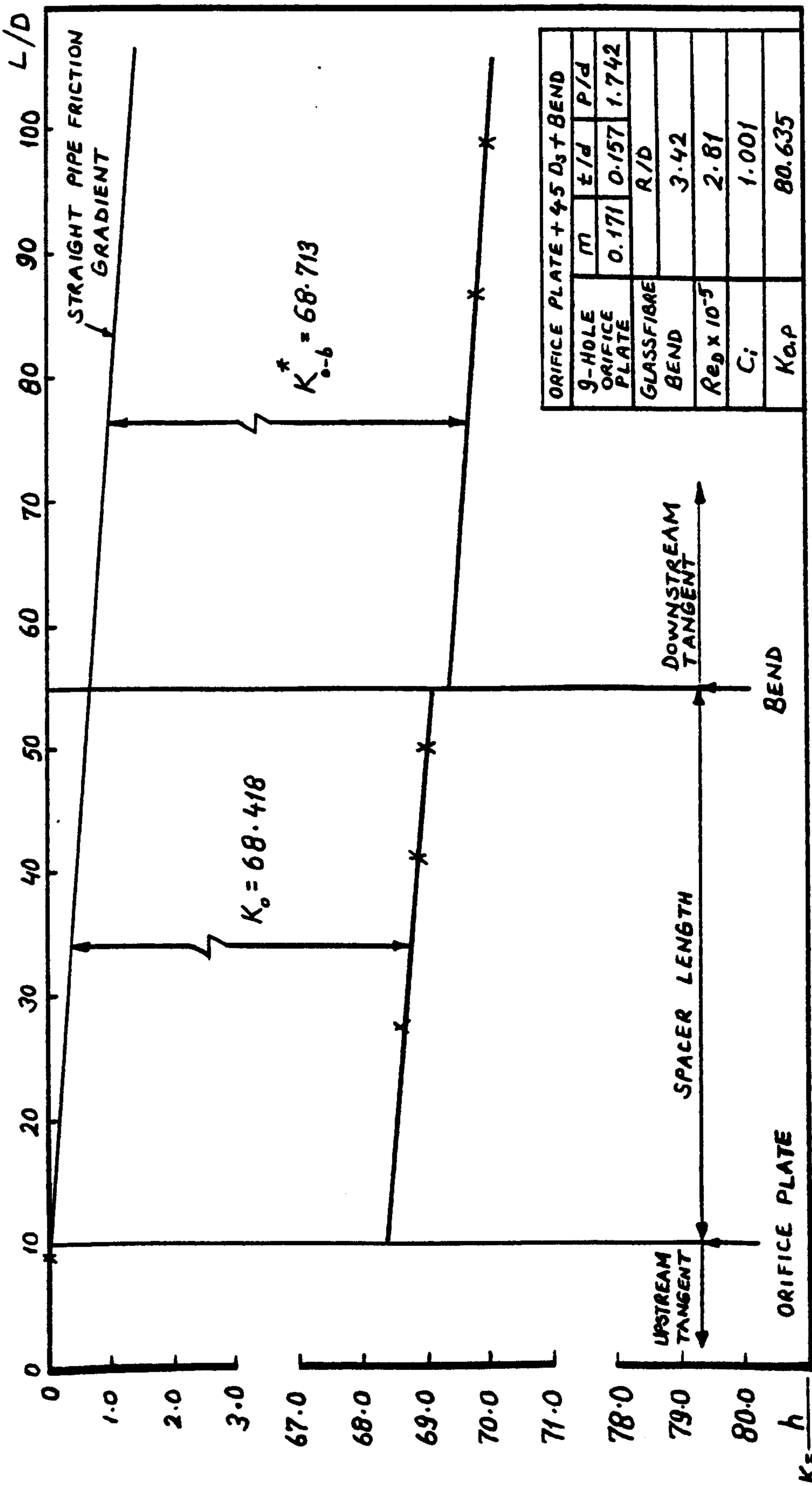

Fig. 331. Variation of system head loss coefficient with axial length

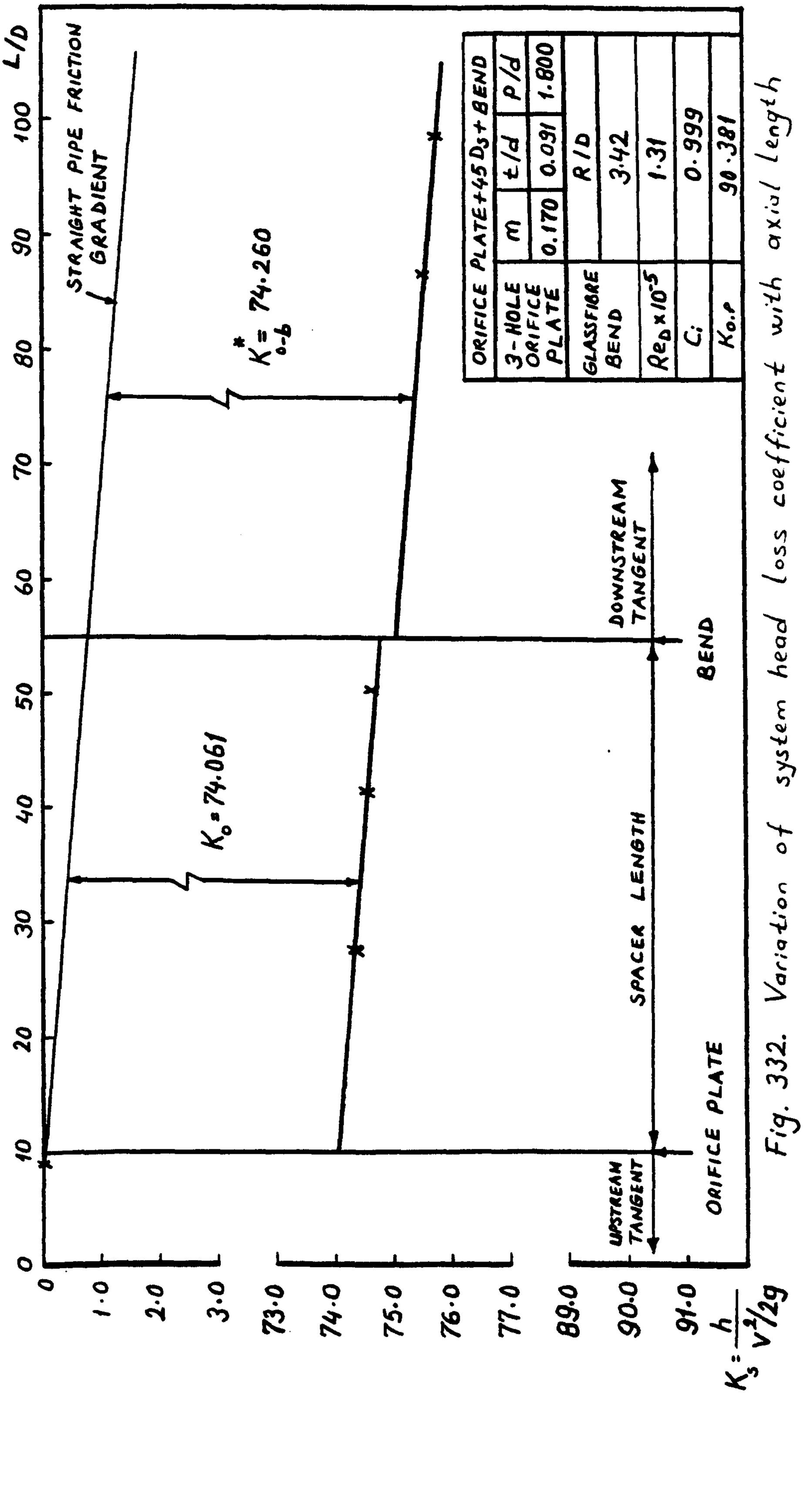
L/D
100
90
80
70
60
50
40
30
20
10
0
STRAIGHT PIPE FRICTION GRADIENT
K^*_{o-b} = 74.260
K_o = 74.061
ORIFICE PLATE+45 D_3+ BEND
m
0.170
t/d
0.091
P/d
1.800
ORIFICE PLATE
3-HOLE ORIFICE PLATE
GLASSFIBRE BEND
R/D
3.42
1.31
0.999
90.381
$Re_D \times 10^{-5}$
C_i
$K_{o.p}$
DOWNSTREAM TANGENT
BEND
SPACER LENGTH
UPSTREAM TANGENT
ORIFICE PLATE
0
1.0
2.0
3.0
73.0
74.0
75.0
76.0
77.0
89.0
90.0
91.0
$K_3 = \frac{h}{v^2/2g}$
Fig. 332. Variation of system head loss coefficient with axial length

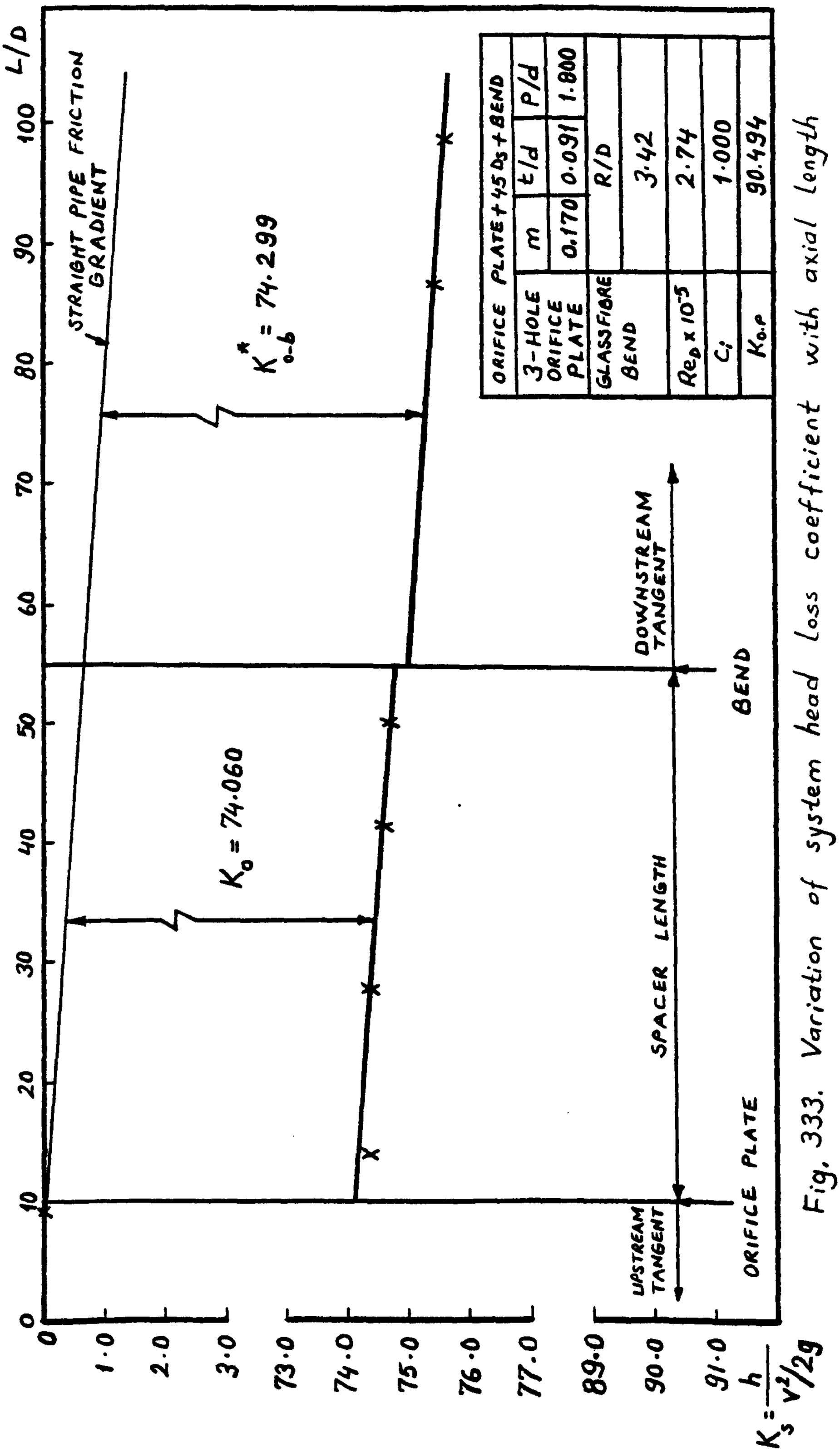

Fig. 333. Variation of system head loss coefficient with axial length

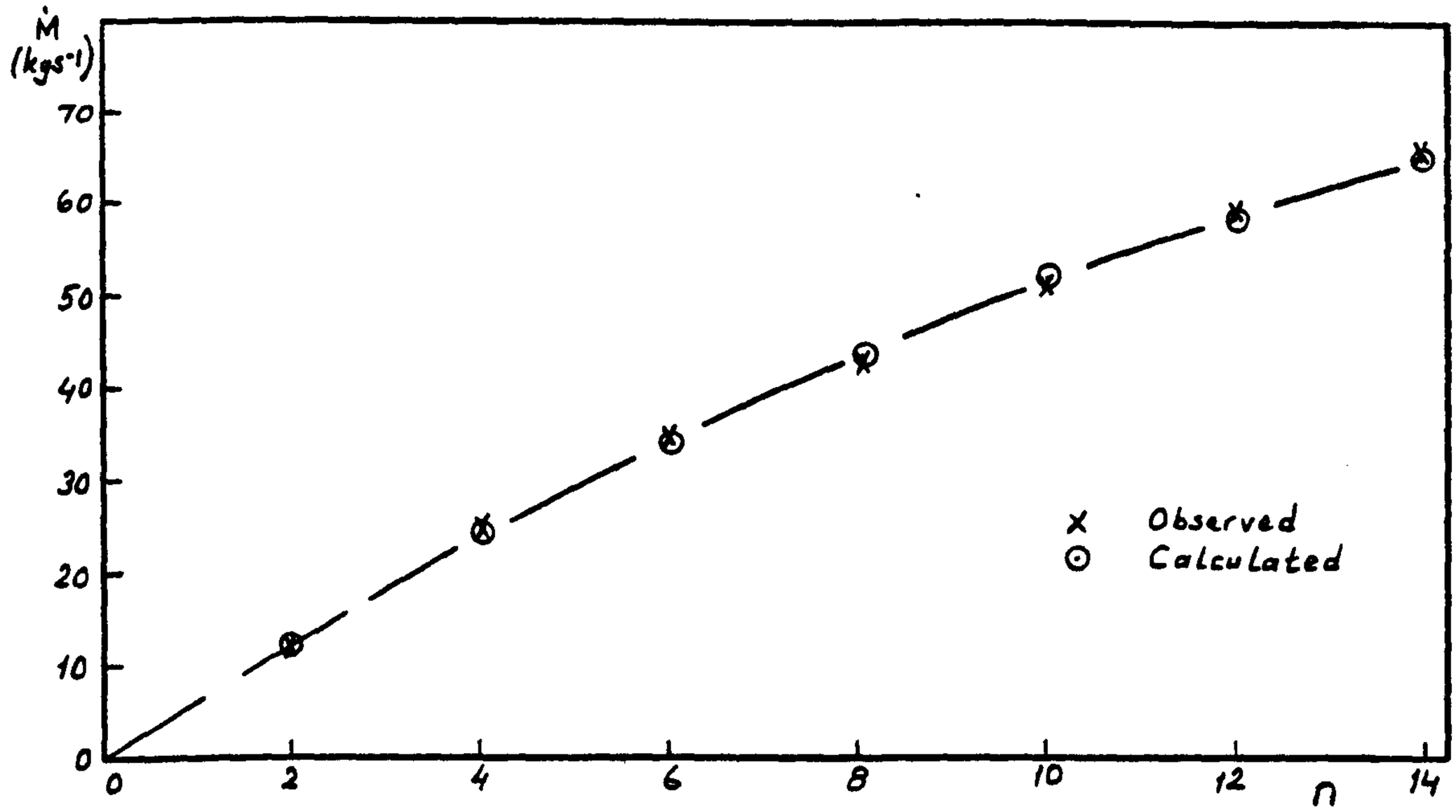

Fig. 334. Mass flow rate versus the number of valves open

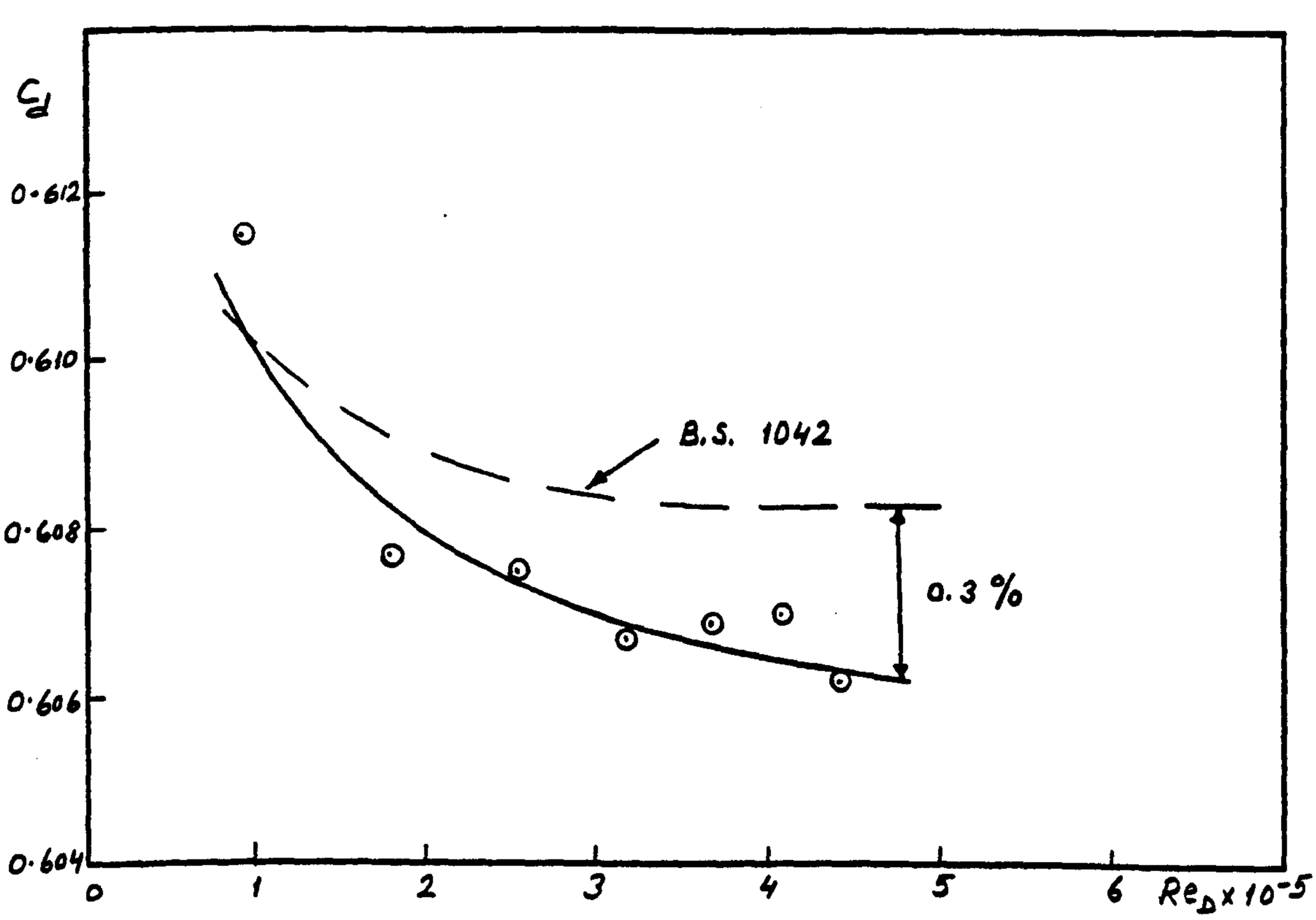

Fig. 335. Comparison of discharge coefficient for single-hole orifice plate of m = 0·386

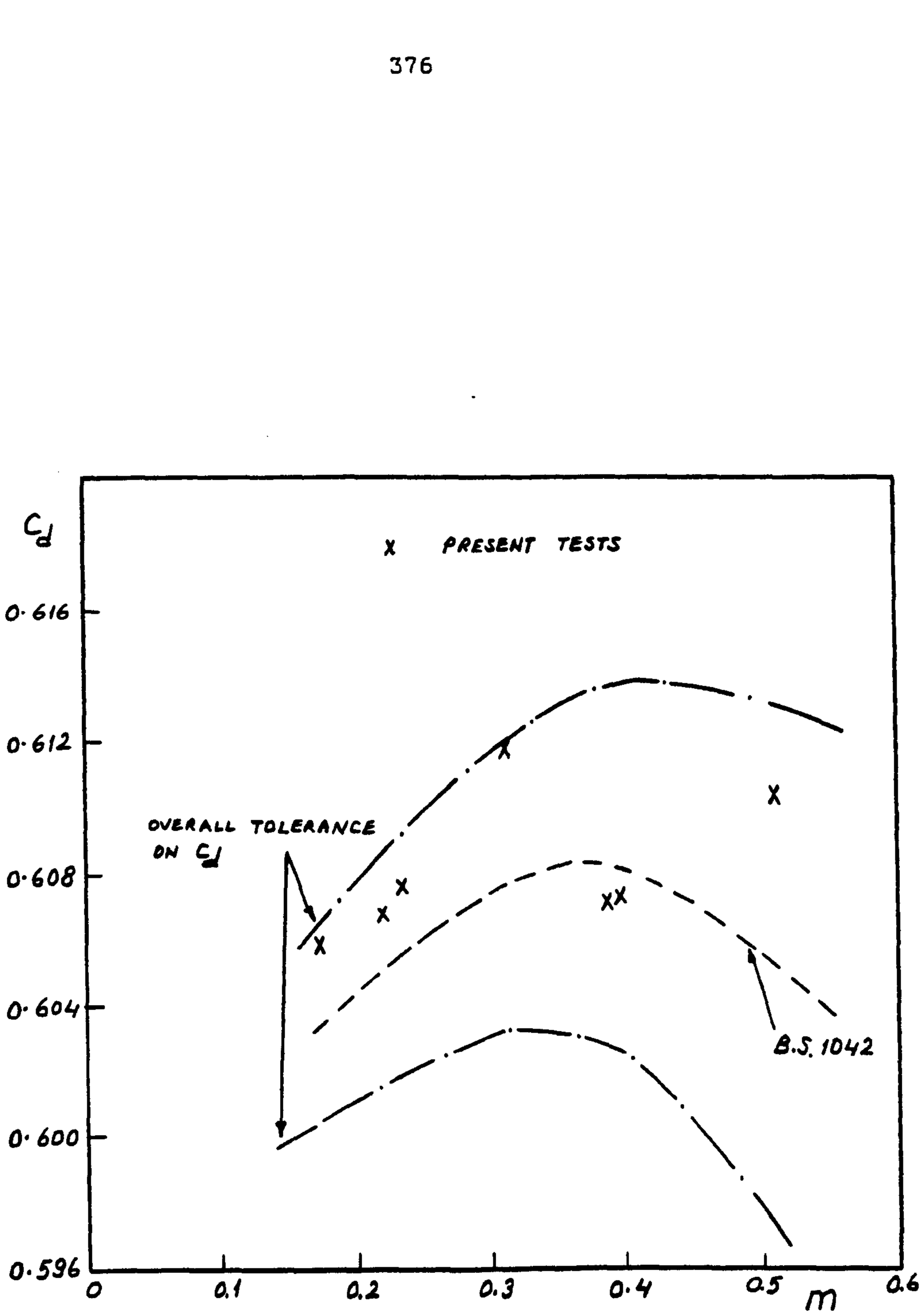

Fig. 336. Comparison of discharge coefficients for various single-hole orifice plates ($Re_d = 5 \times 10^5$)

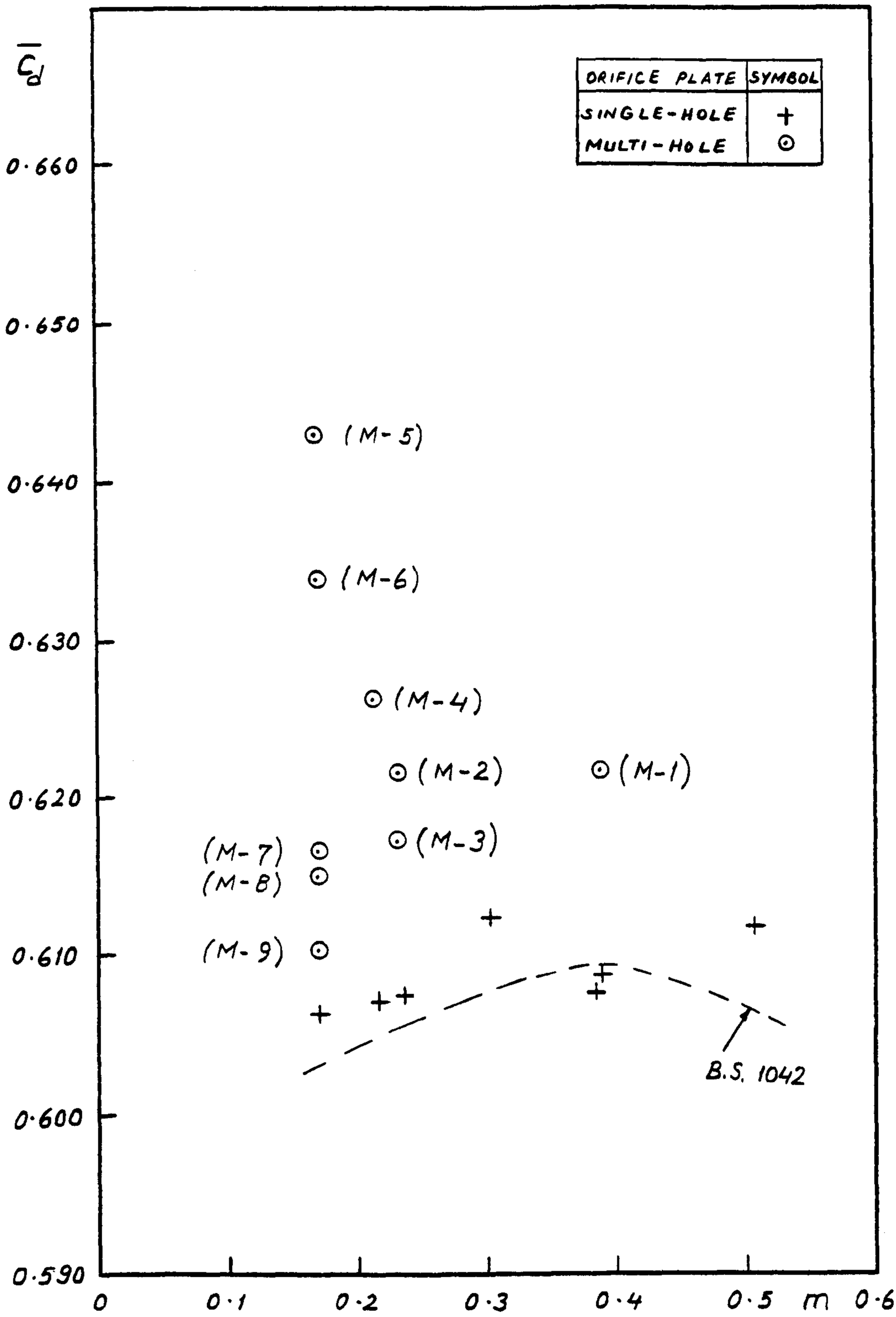

Fig. 337. Comparison of discharge coefficients for orifice plates tested (M- = name of multi-hole orifice plate, see Table 1)

SYMBOL	m	P/d	t/d	No. OF HOLES
□	0.171	1.742	0.157	9
◇	0.170	1.503	0.130	6
⊙	0.170	1.753	0.105	4
+	0.170	1.496	0.104	4
△	0.170	1.800	0.091	3

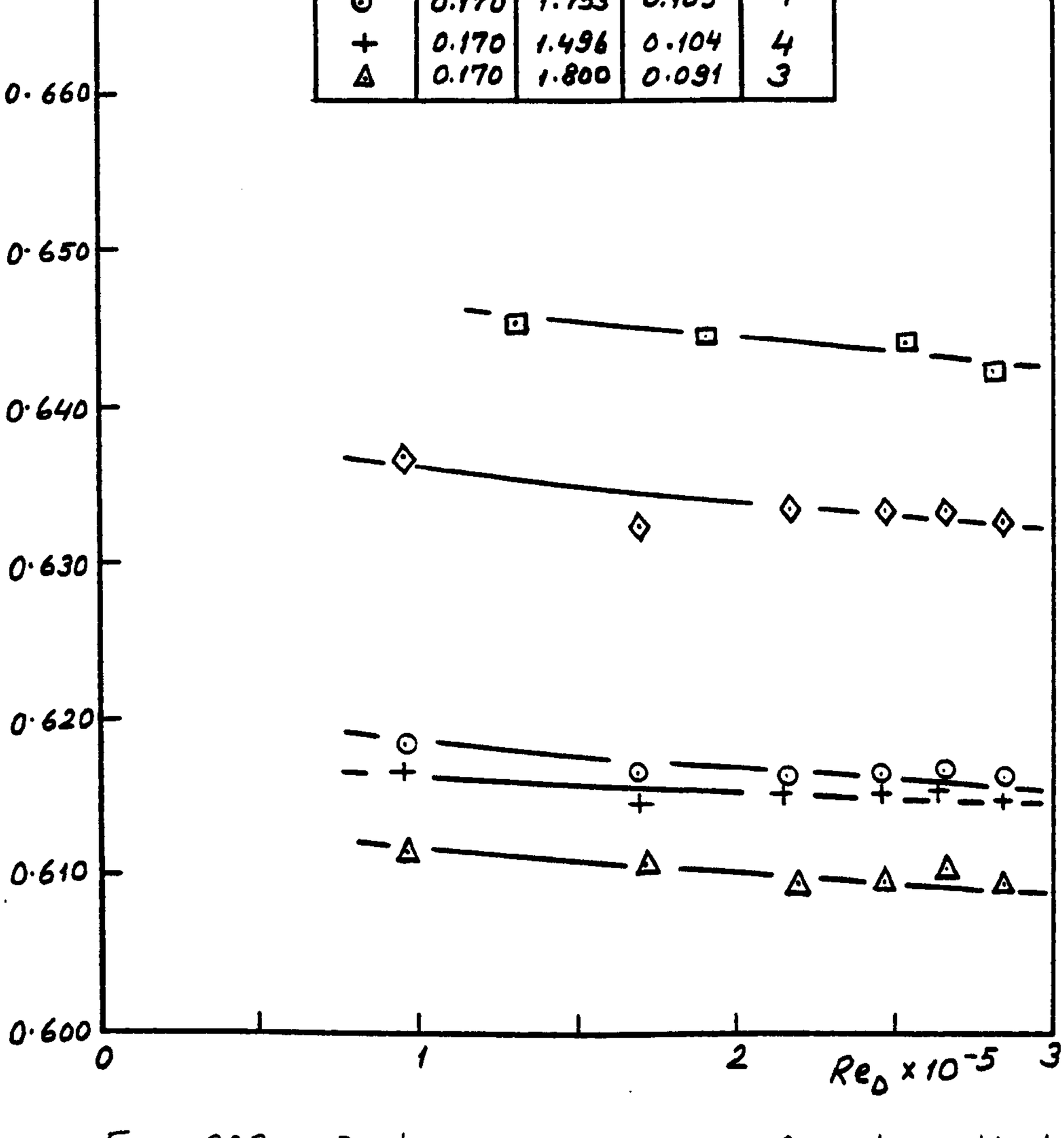

Fig. 338. Discharge coefficients for the multi-hole orifice plates of the same area ratio

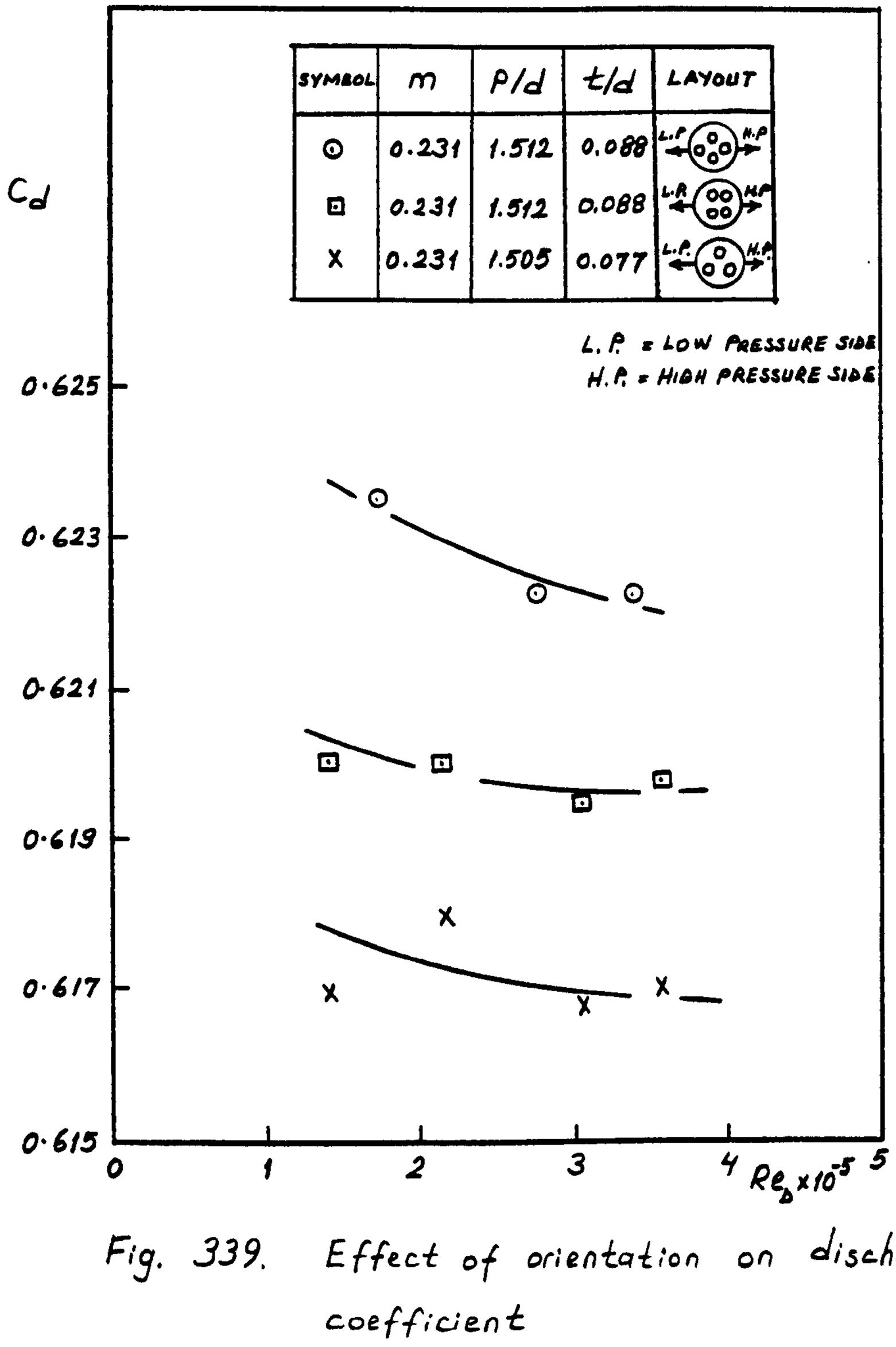

Fig. 339. Effect of orientation on discharge coefficient

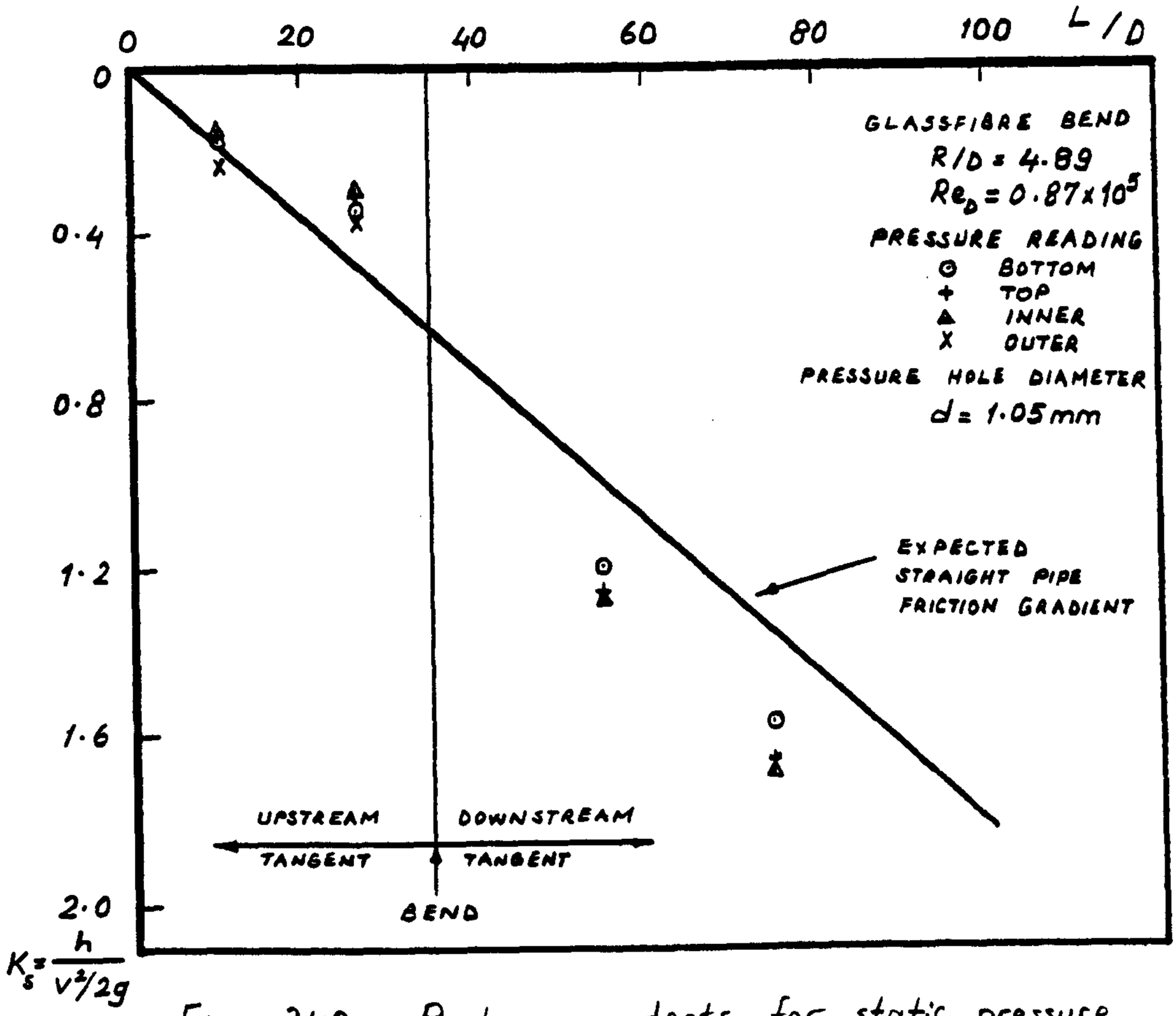

Fig. 340. Preliminary tests for static pressure tappings

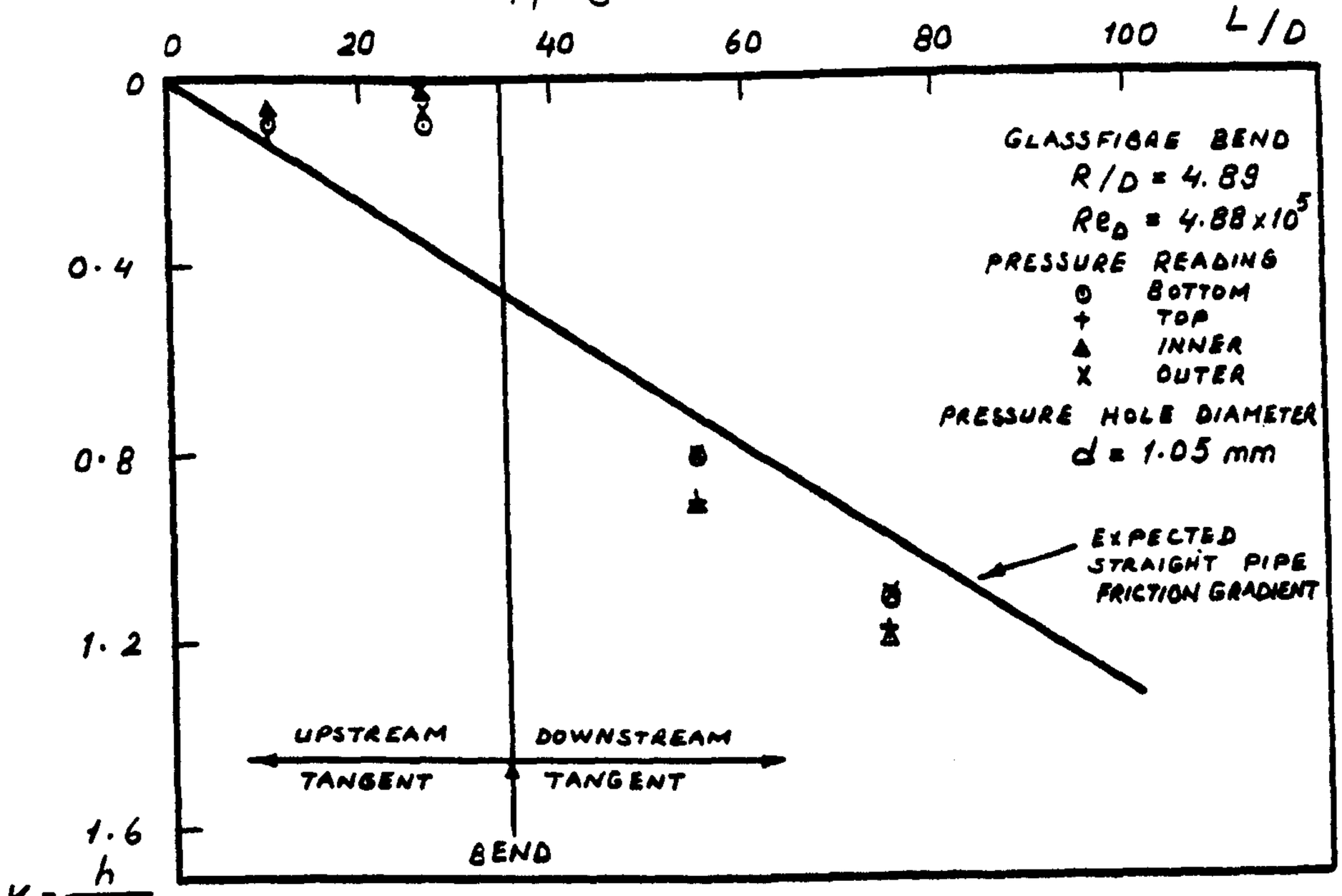

Fig. 341. Preliminary tests for static pressure tappings

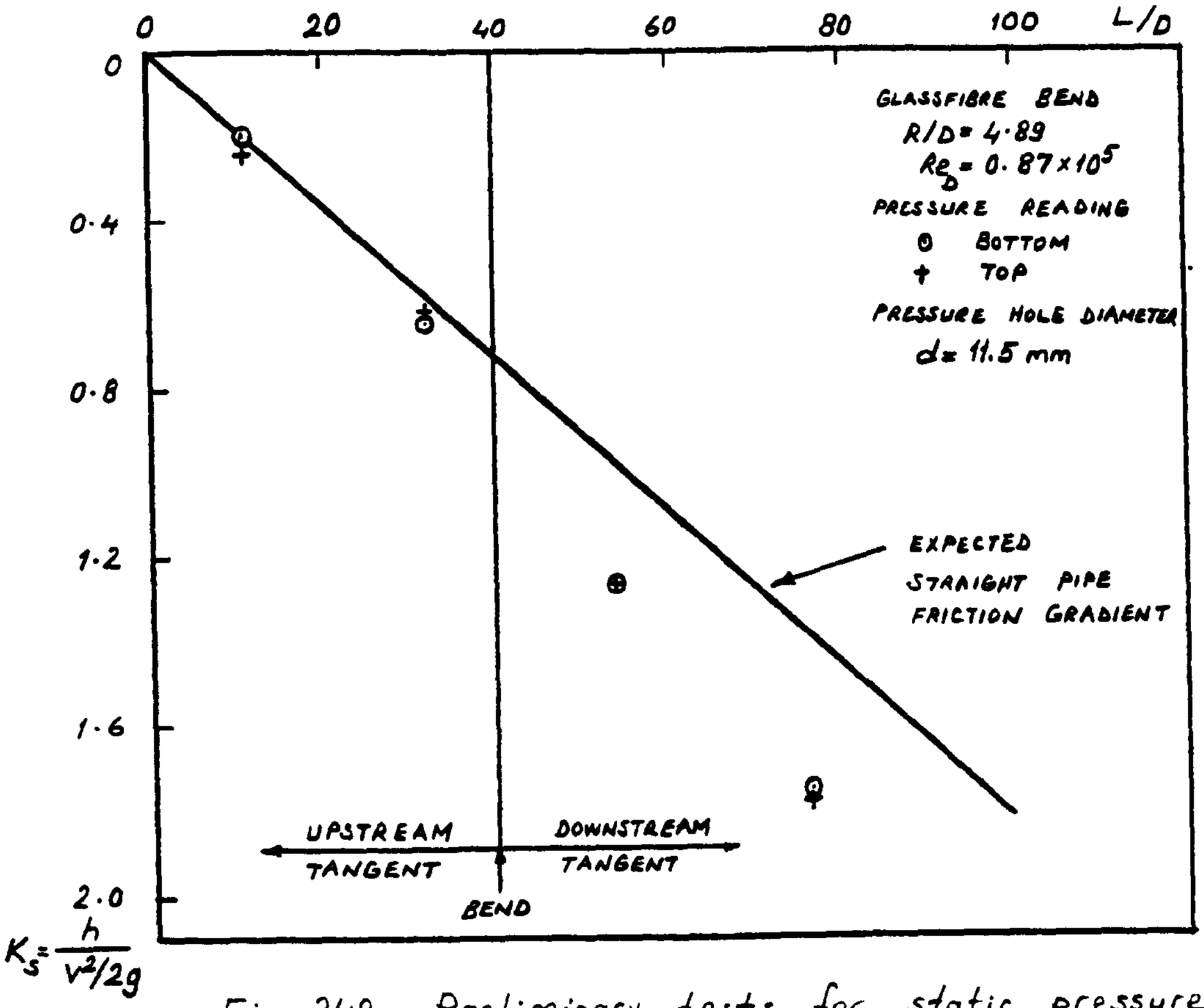

Fig. 342. Preliminary tests for static pressure tappings

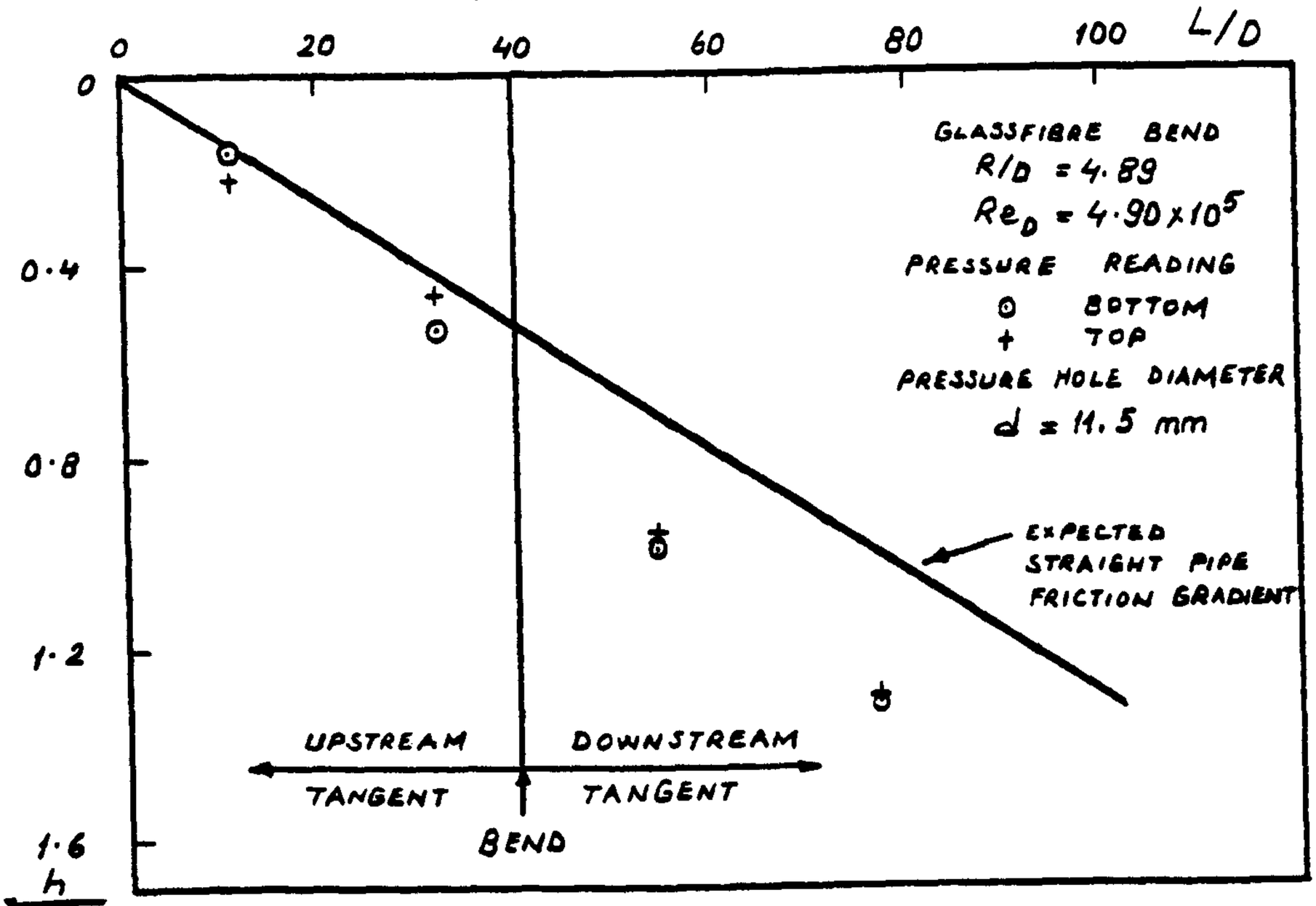

Fig. 343. Preliminary tests for static pressure tappings

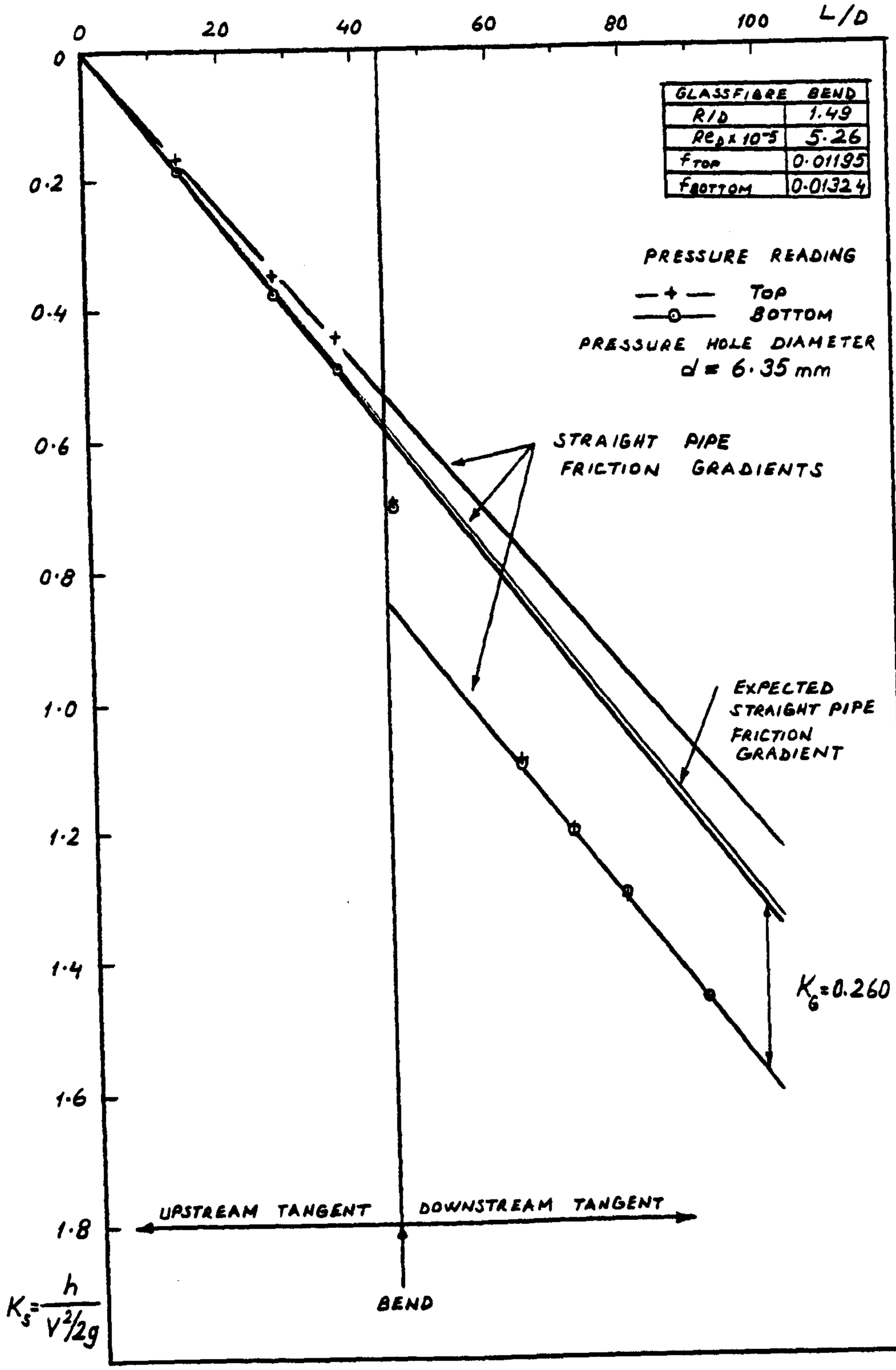

Fig. 344. Preliminary tests for static pressure tappings

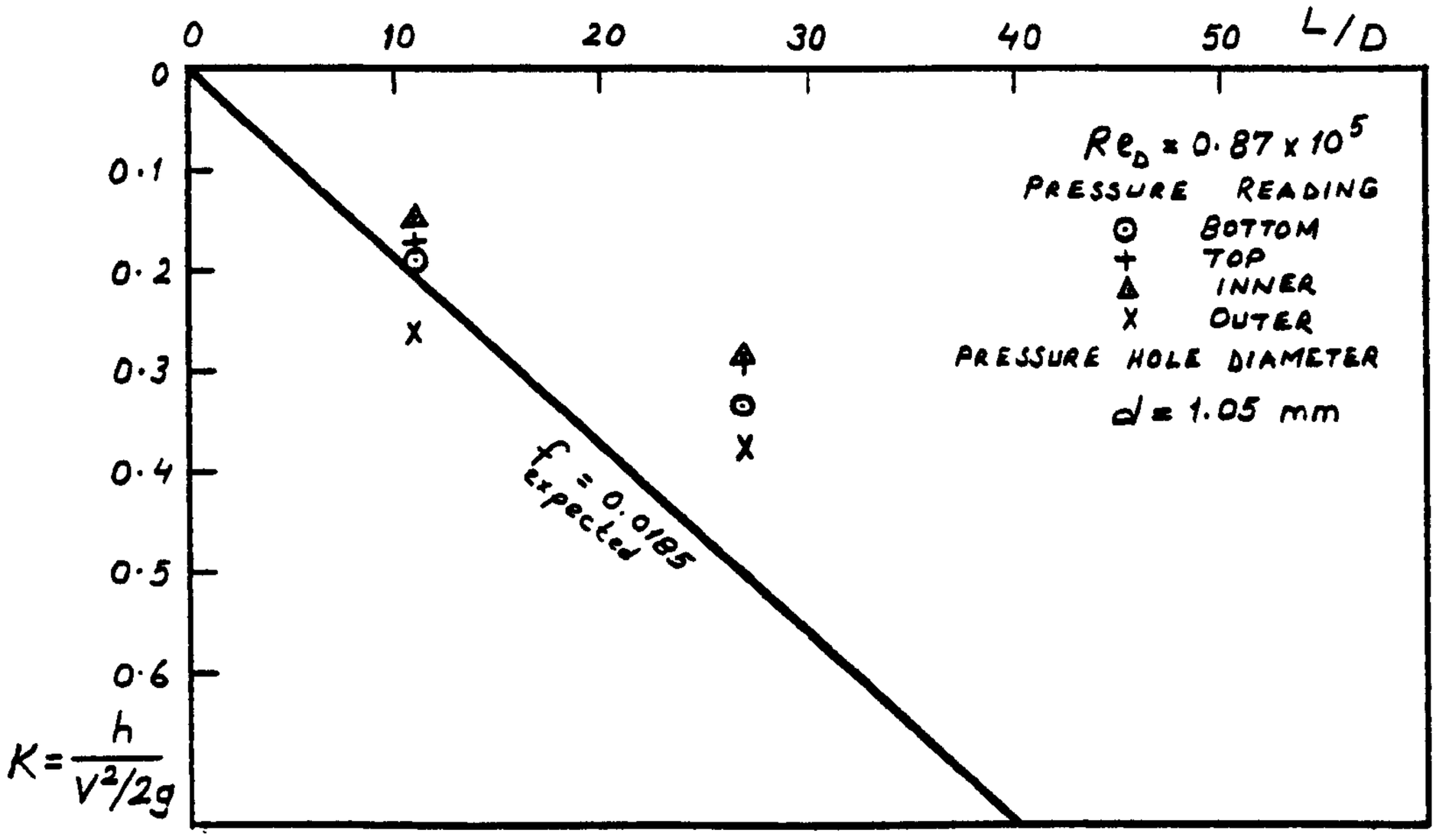

Fig. 345. Friction loss coefficient versus axial length for preliminary tests

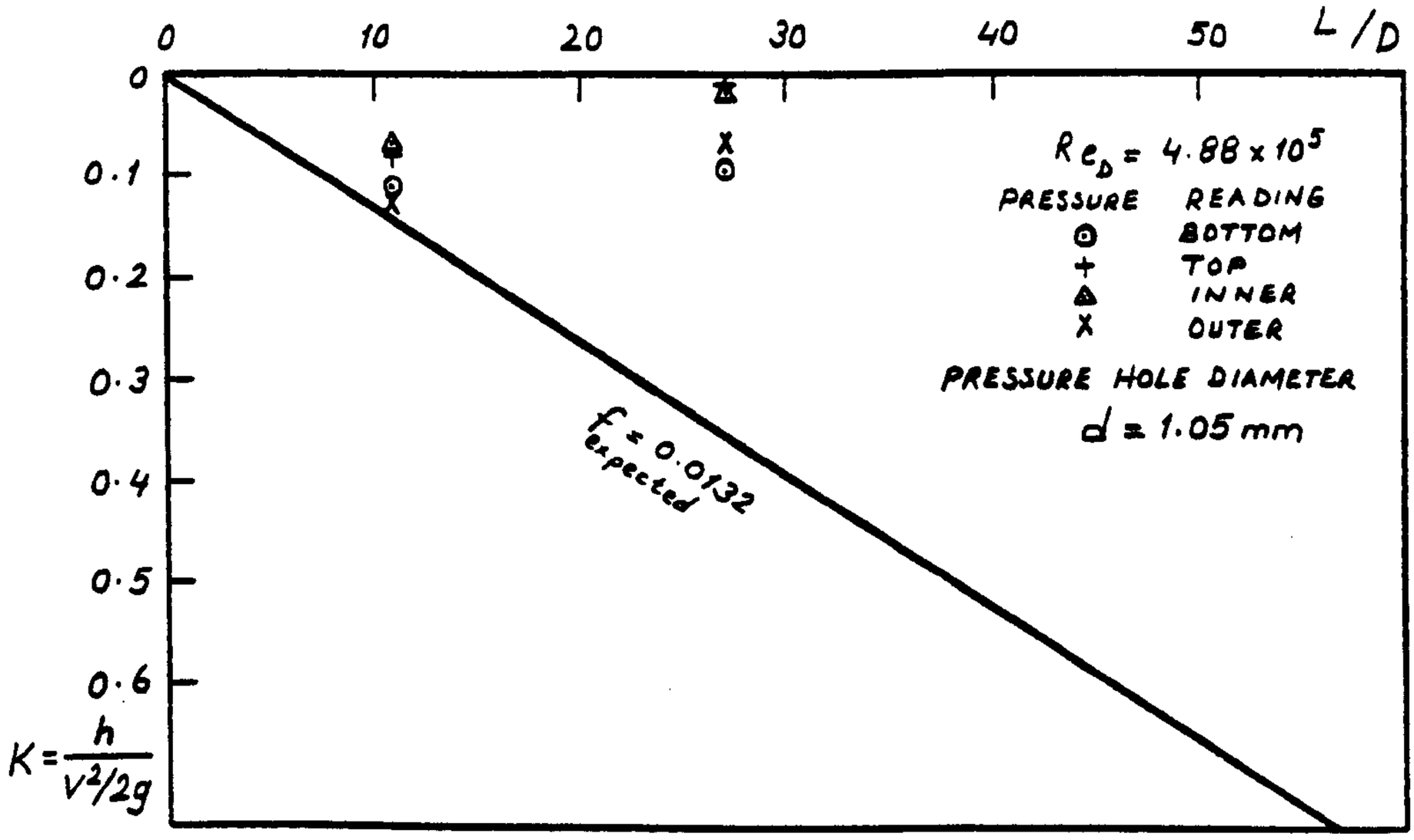

Fig. 346. Friction loss coefficient versus axial length for preliminary tests

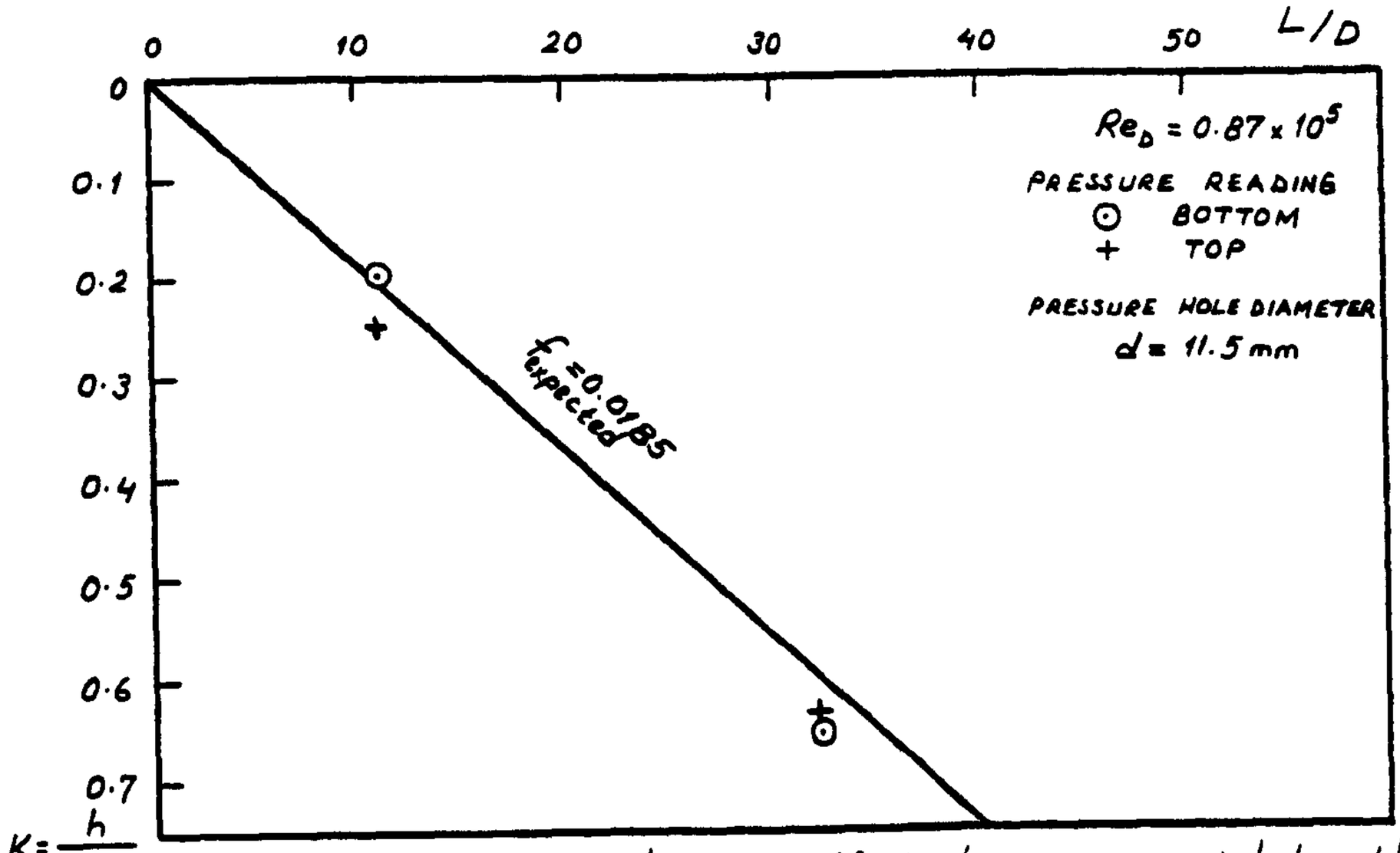

Fig. 347. Friction loss coefficient versus axial length for preliminary tests

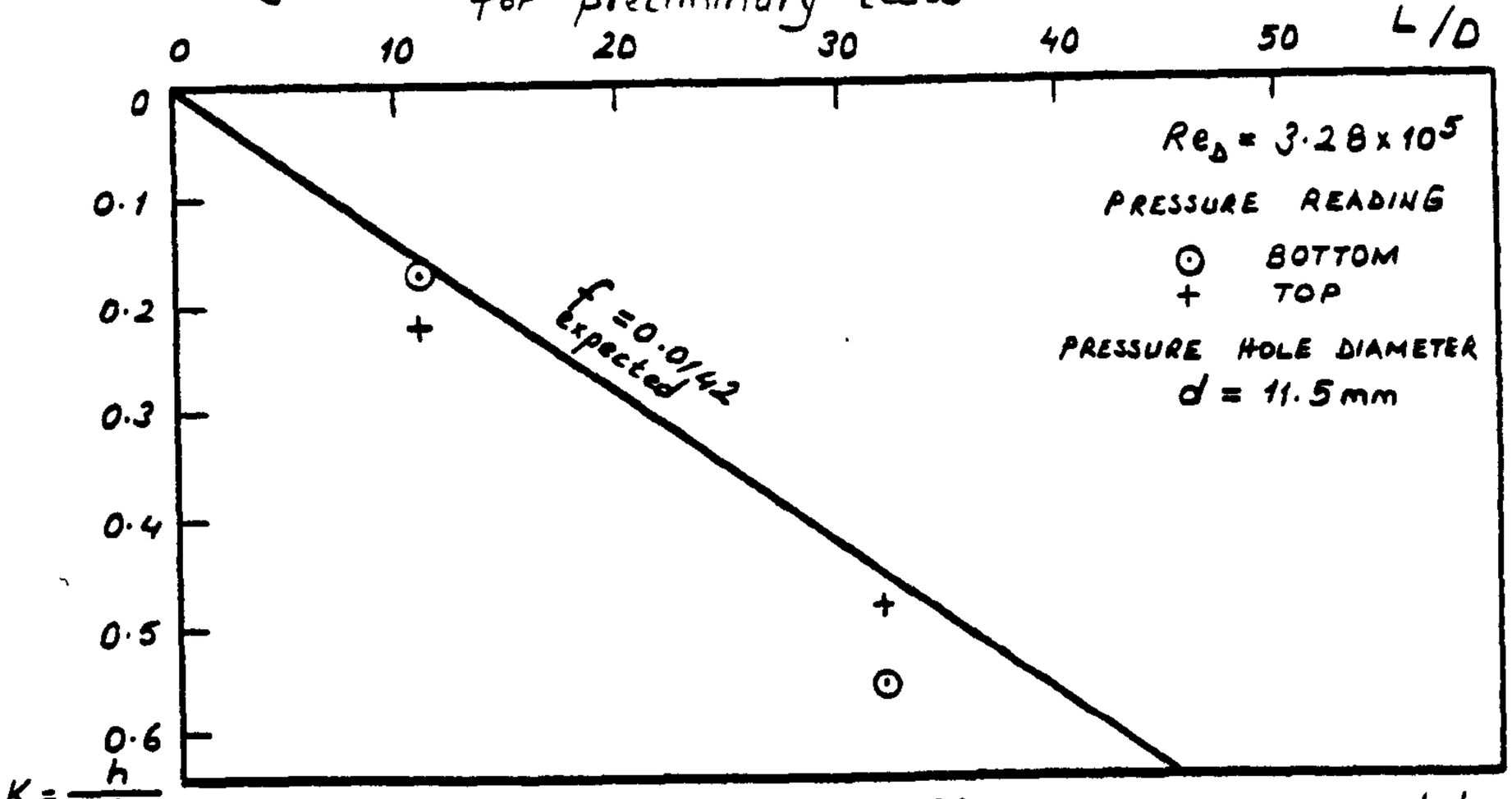

Fig. 348. Friction loss coefficient versus axial length for preliminary tests

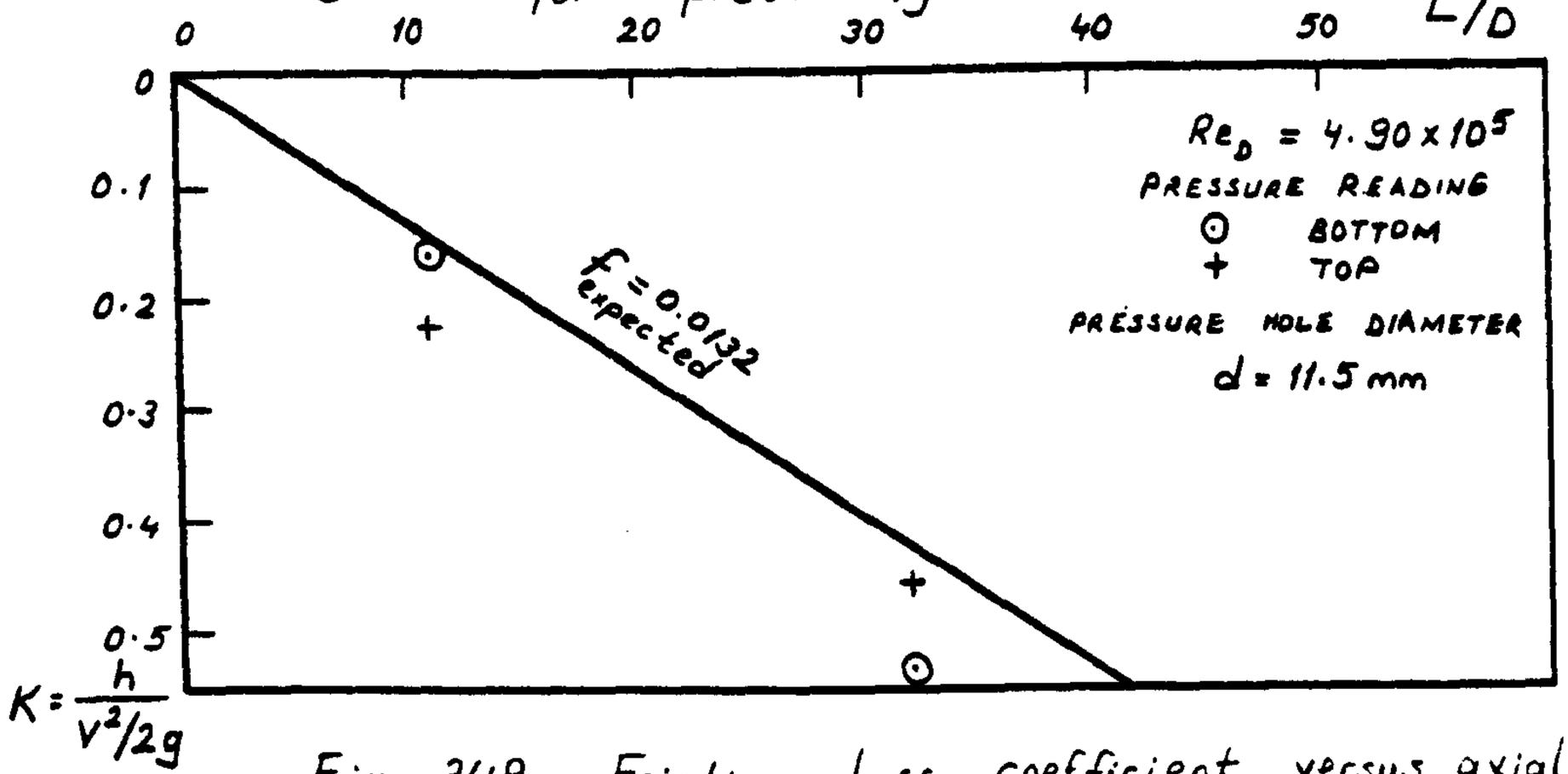

Fig. 349. Friction loss coefficient versus axial length for preliminary tests

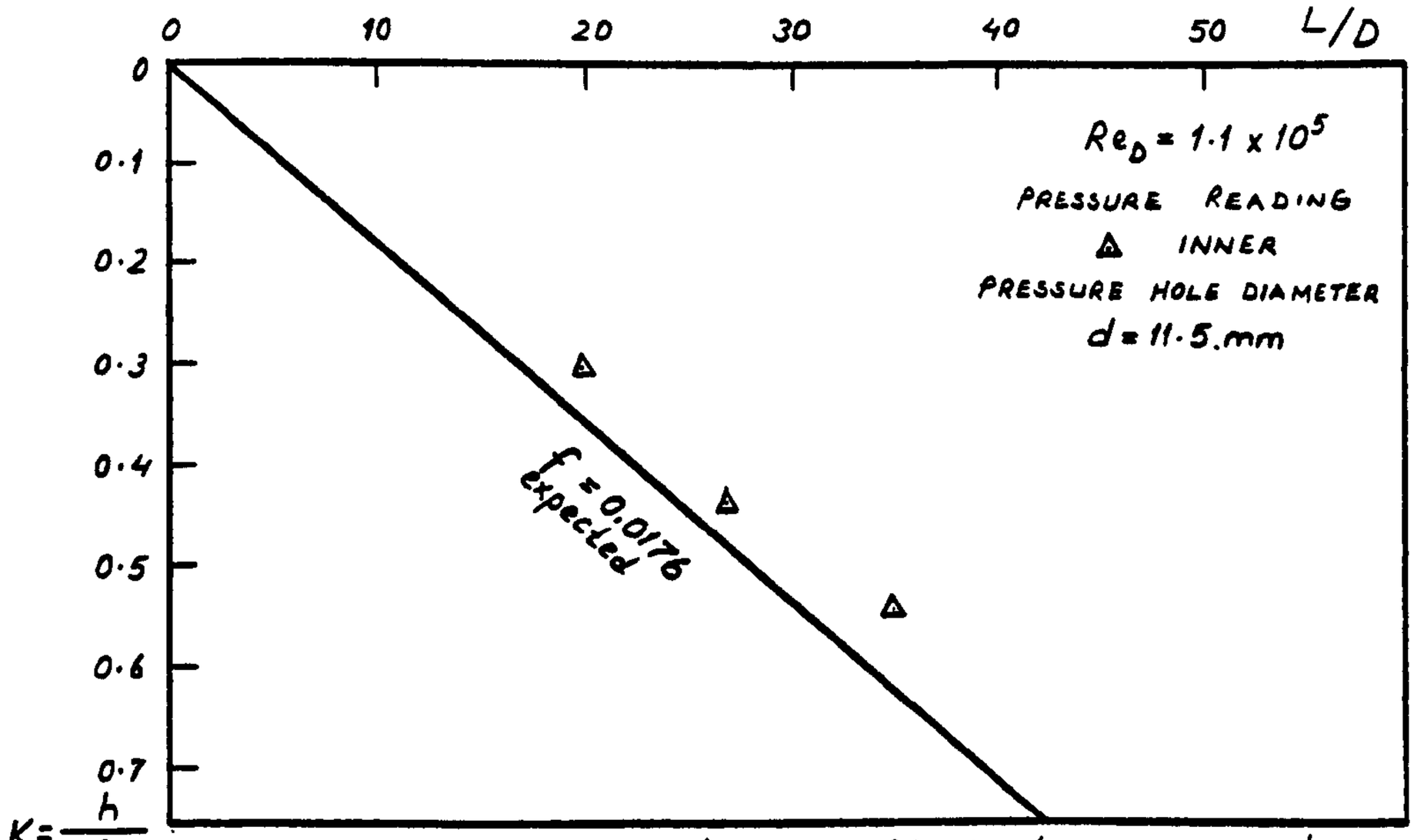

Fig. 350. Friction loss coefficient versus axial length for preliminary tests

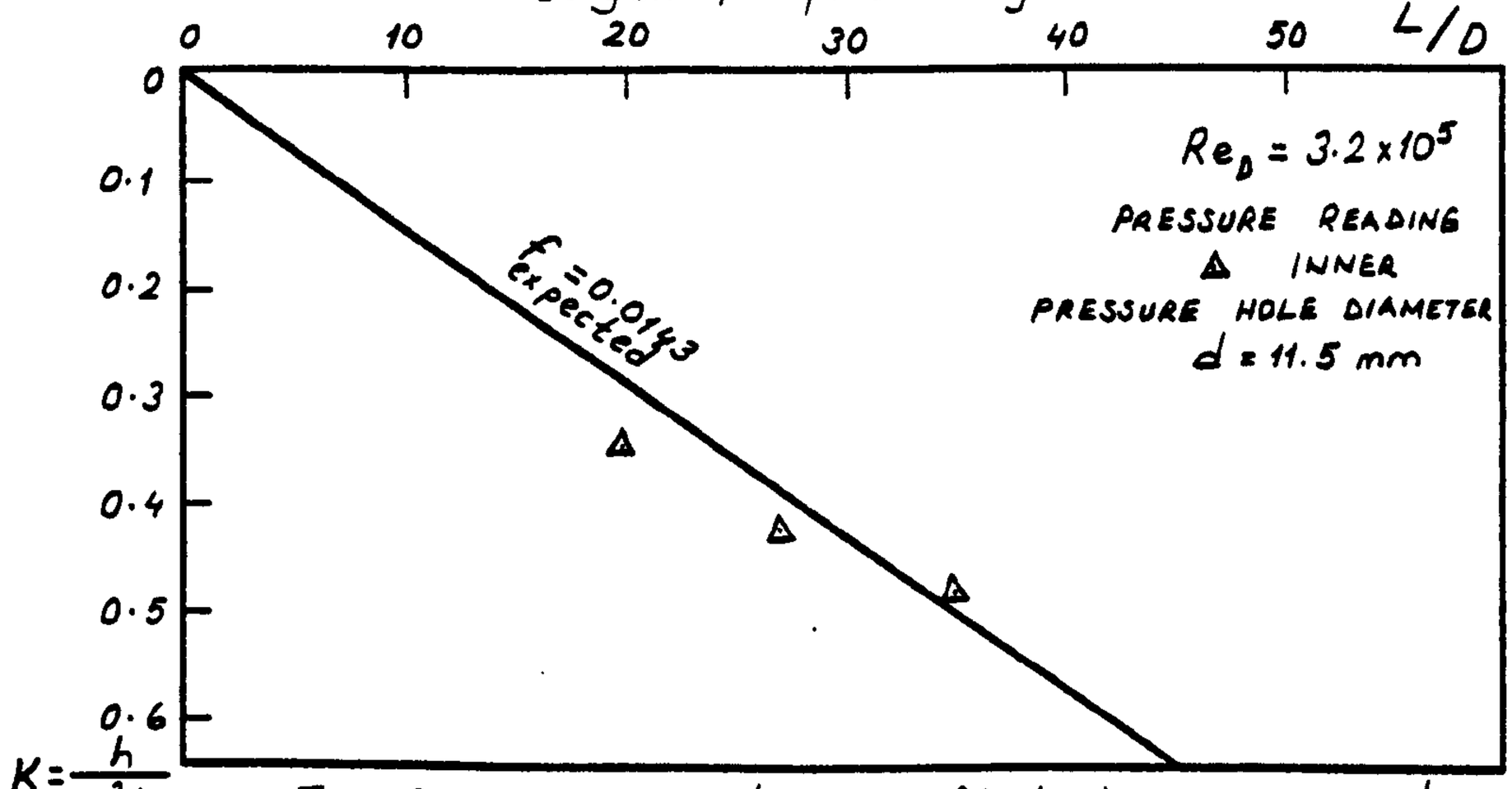

Fig. 351. Friction loss coefficient versus axial length for preliminary tests

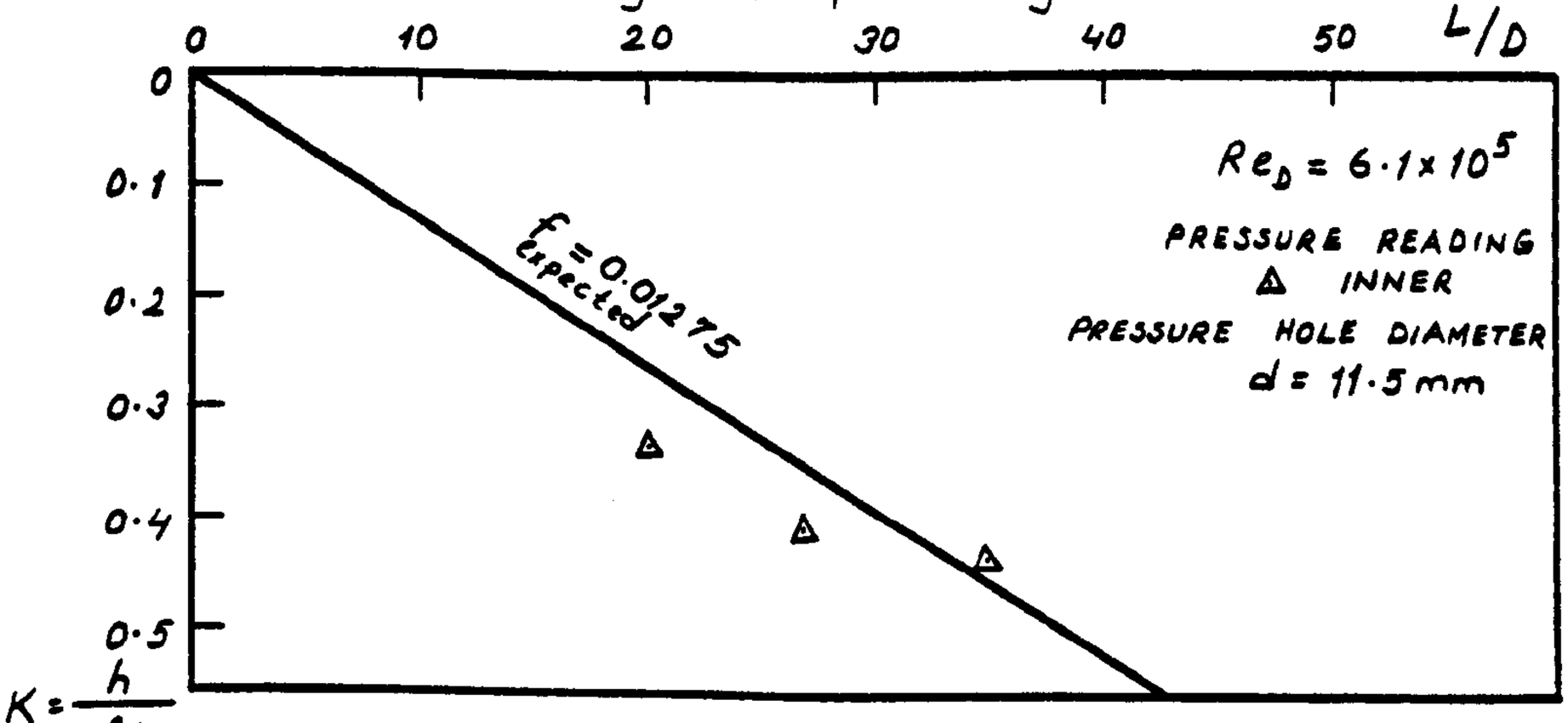

Fig. 352. Friction loss coefficient versus axial length for preliminary tests

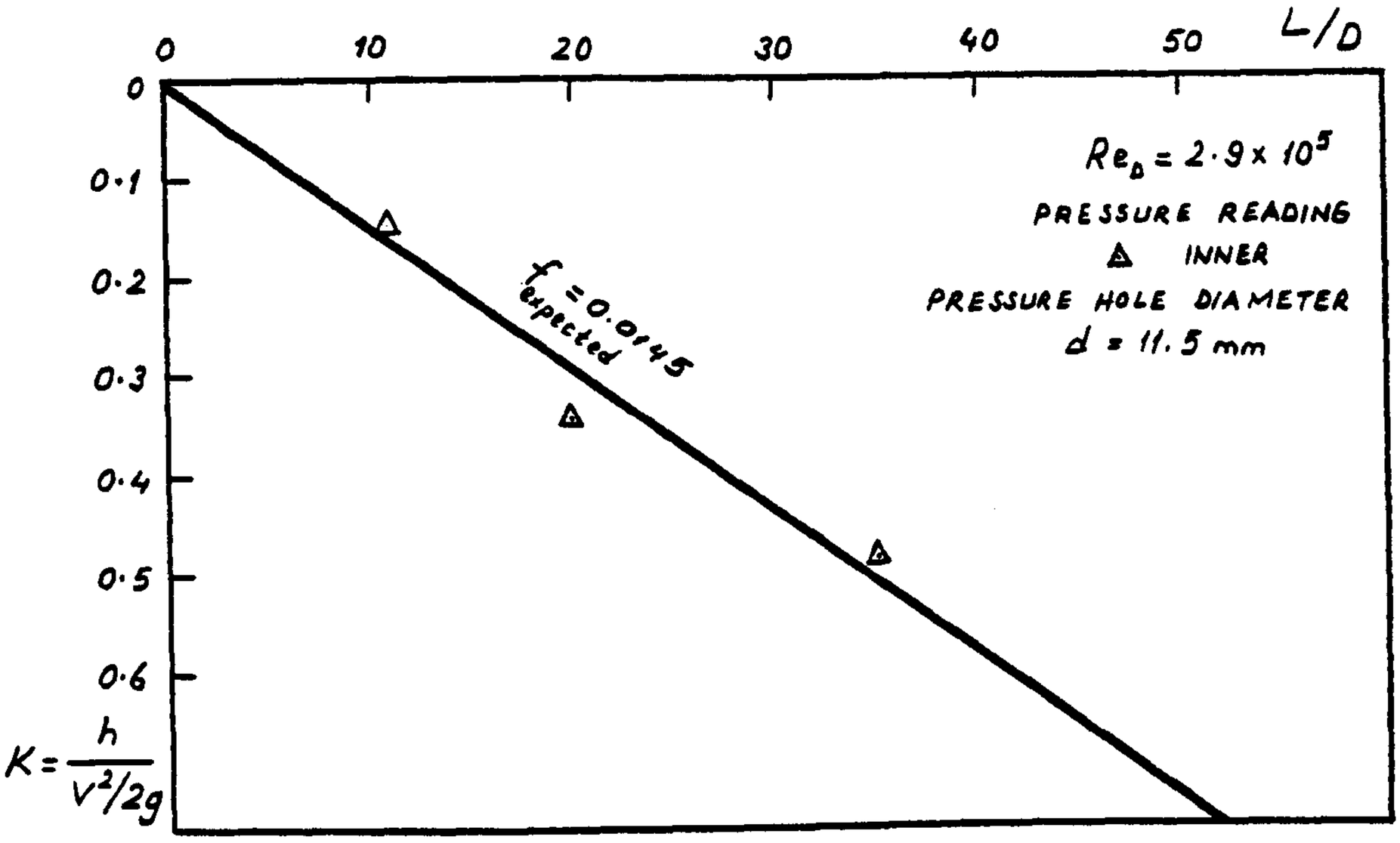

Fig. 353. Friction loss coefficient versus axial length for preliminary tests

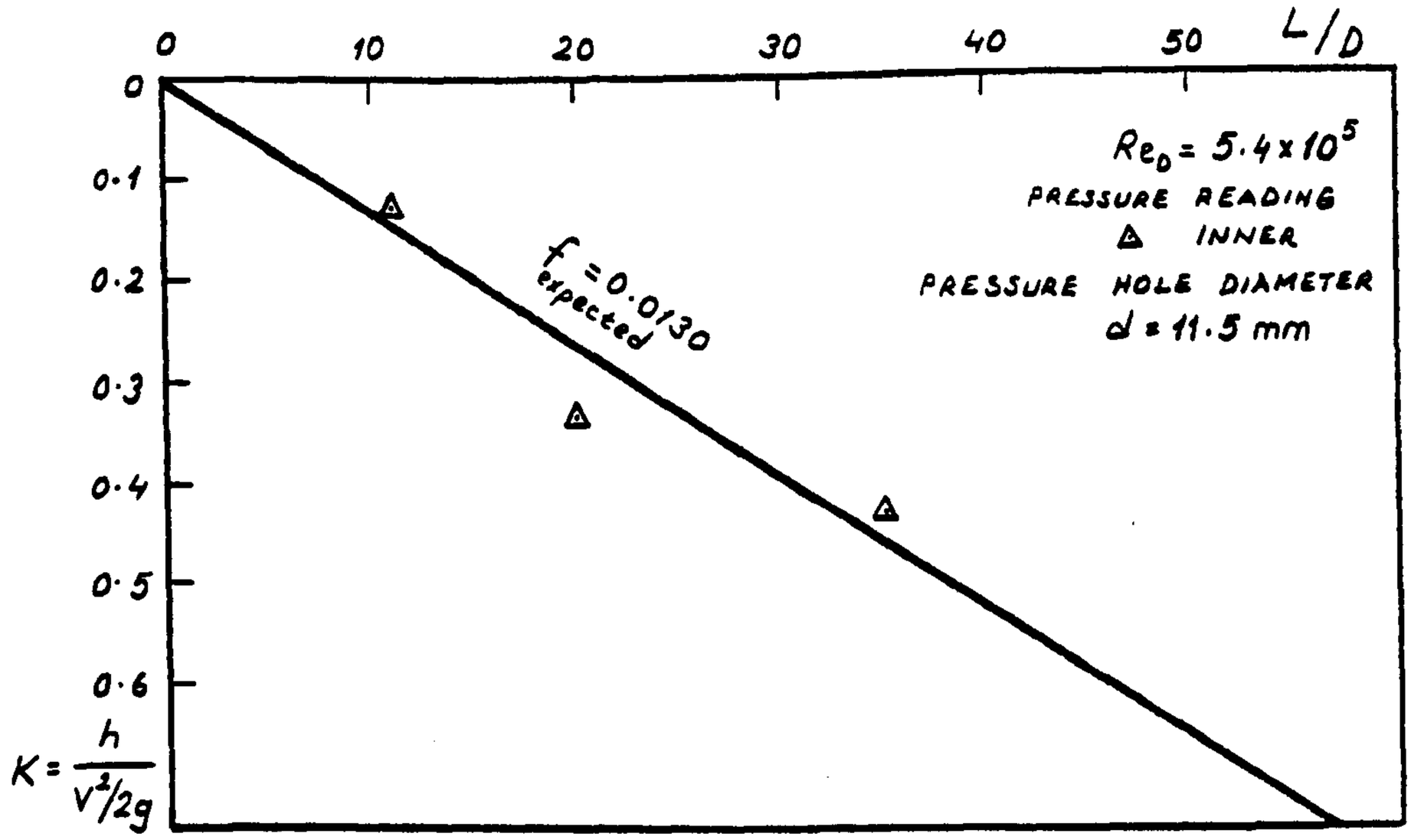

Fig. 354. Friction loss coefficient versus axial length for preliminary tests

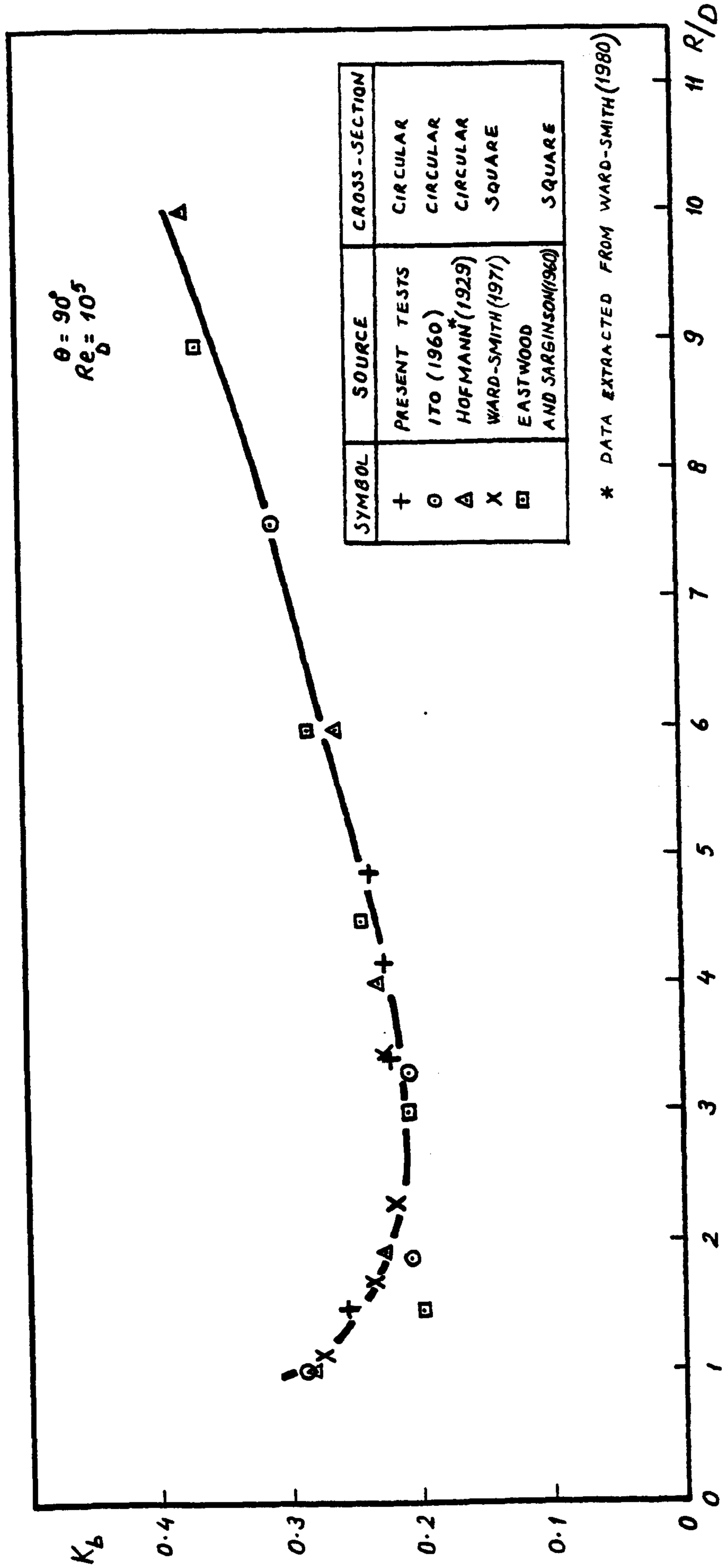

Fig. 355. Comparison of bend head loss coefficients ($\theta = 90^\circ$, $Re_D = 1 \times 10^5$)

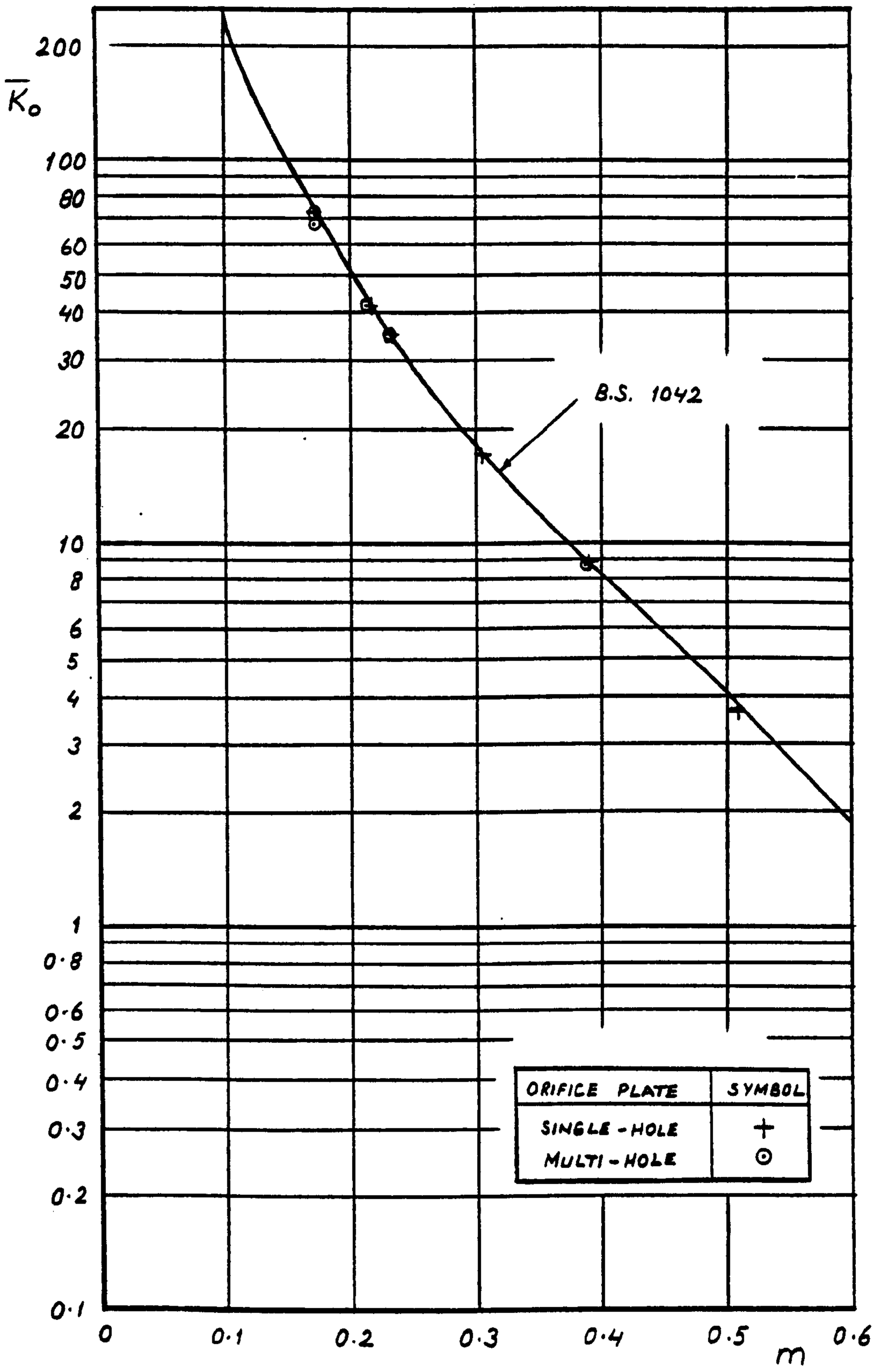

Fig. 356. Comparison of orifice plate head loss coefficients

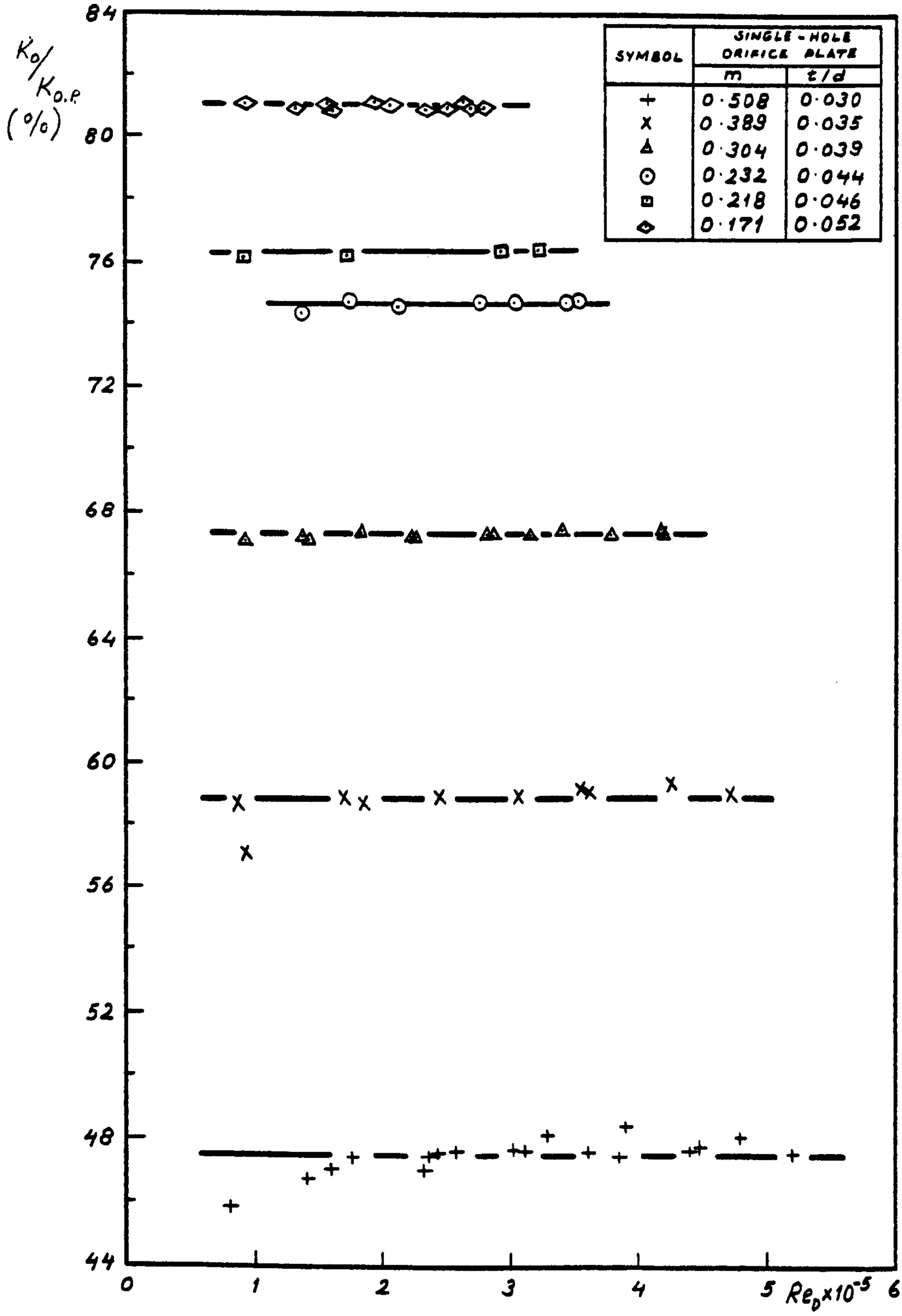

Fig. 357. Percentage net pressure loss versus Reynolds number for various single-hole orifice plates

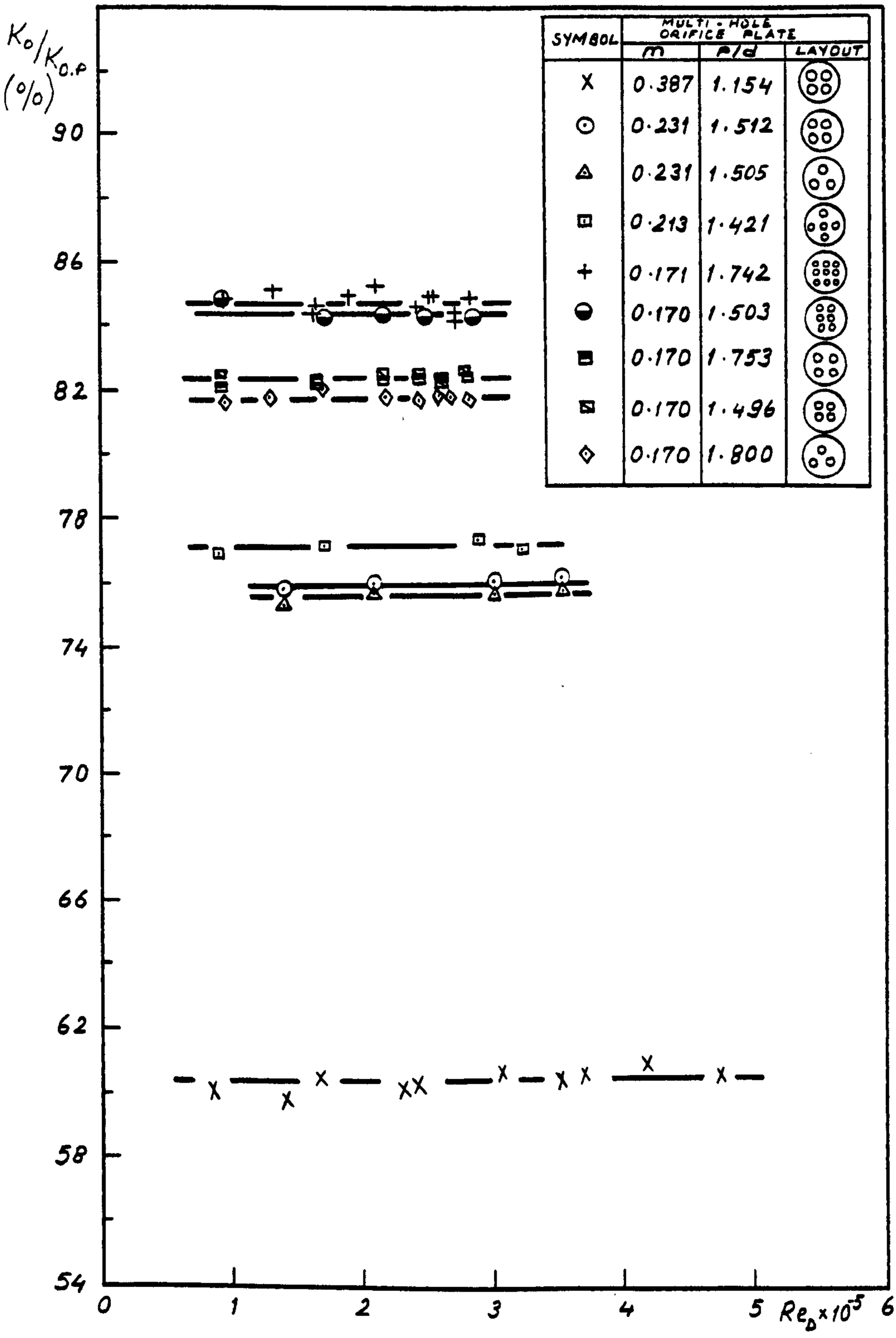

Fig. 358. Percentage net pressure loss versus Reynolds number for various multi-hole orifice plates

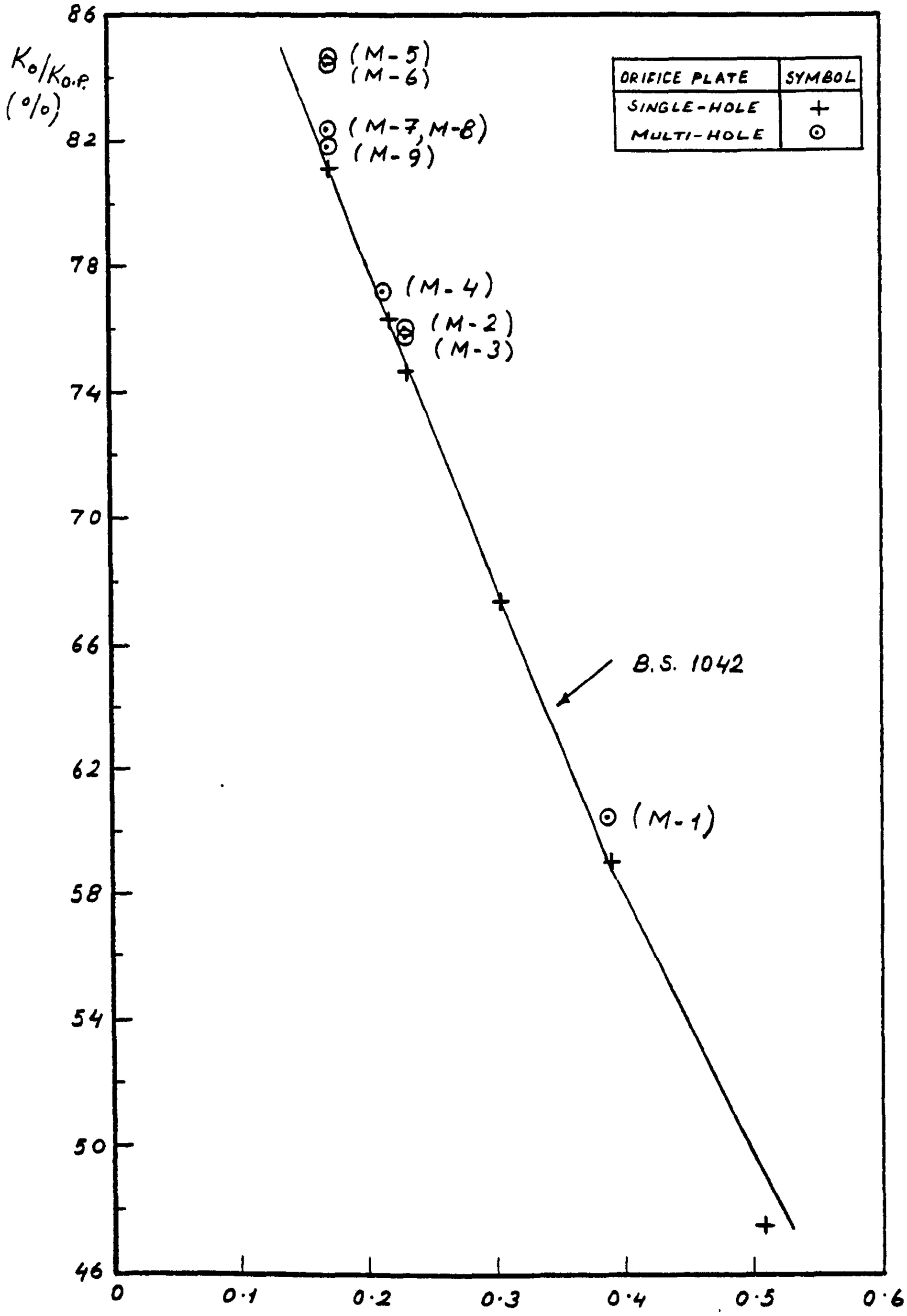

Fig. 359. Comparison of percentage net pressure loss for orifice plates (M- = name of multi-hole orifice plate, see Table 1)

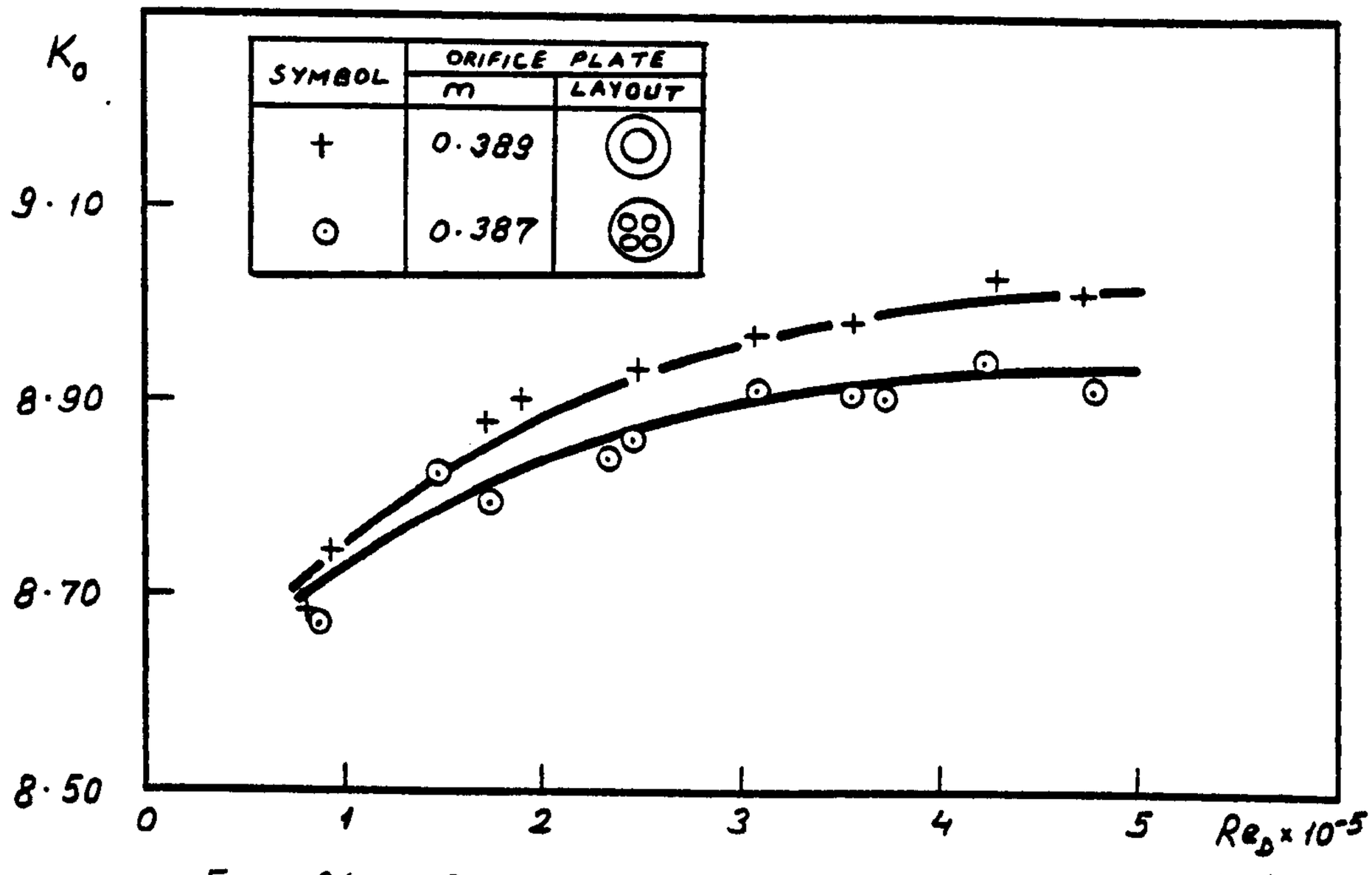

Fig. 360. Comparison of orifice plate head loss coefficients (Reynolds number based on duct diameter)

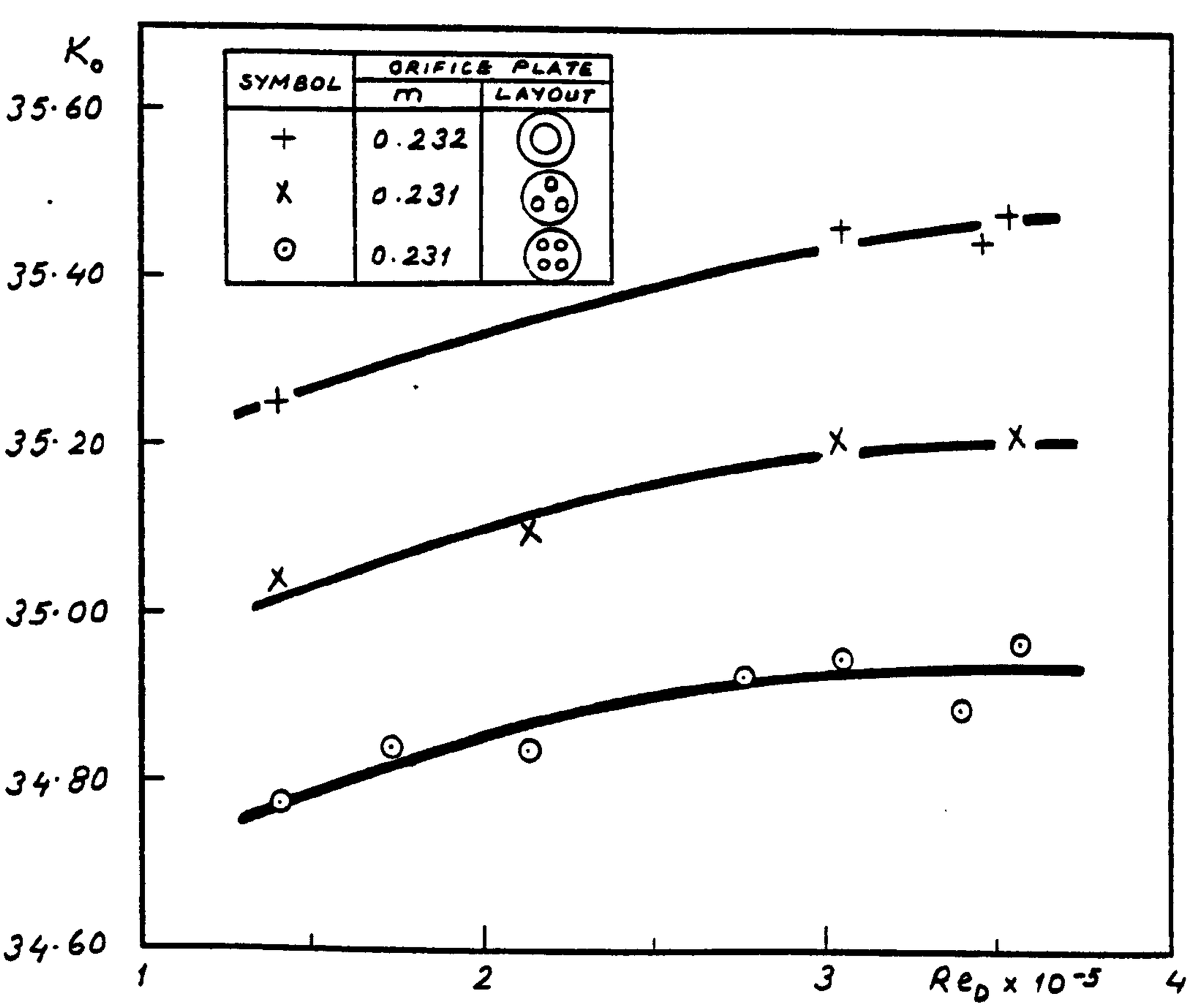

Fig. 361. Comparison of orifice plate head loss coefficients (Reynolds number based on duct diameter)

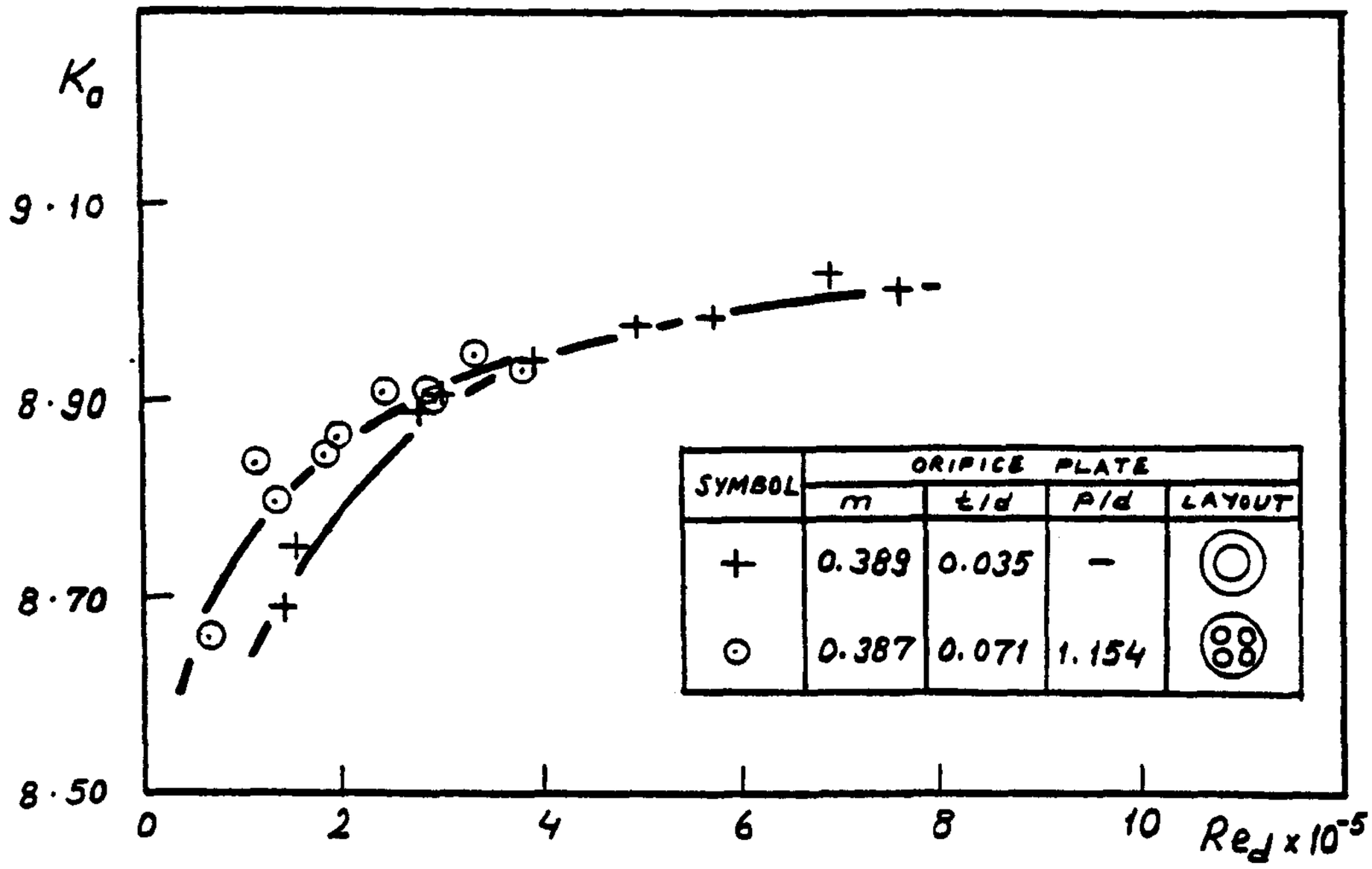

Fig. 362. Comparison of orifice plate head loss coefficients (Reynolds number based on hole diameter)

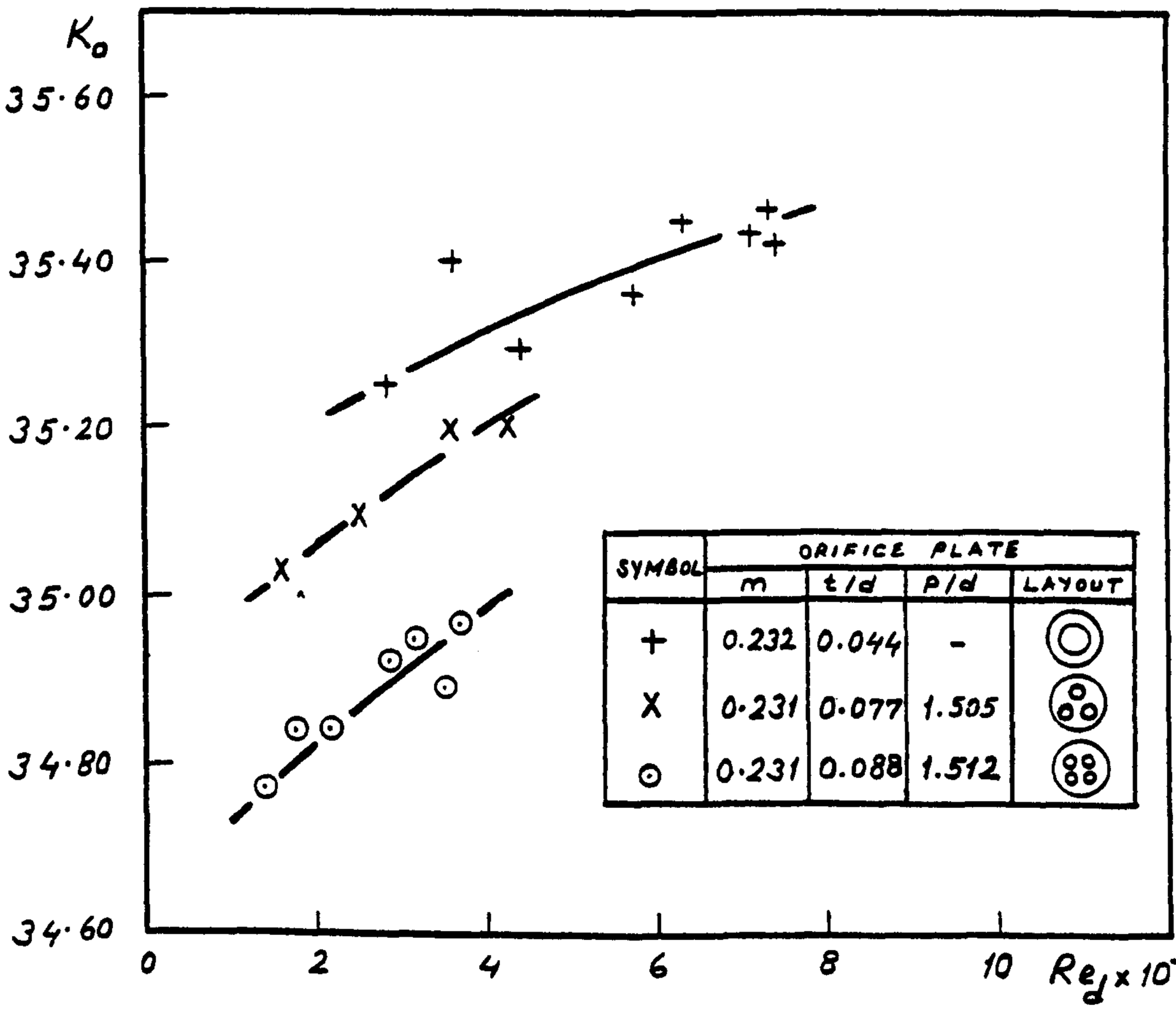

Fig. 363. Comparison of orifice plate head loss coefficients (Reynolds number based on hole diameter)

SYMBOL	ORIFICE PLATE			
	m	t/d	P/d	LAYOUT
△	0.170	0.091	1.800	
◇	0.170	0.104	1.496	
▭	0.170	0.105	1.753	
⊙	0.170	0.130	1.503	
X	0.171	0.157	1.742	

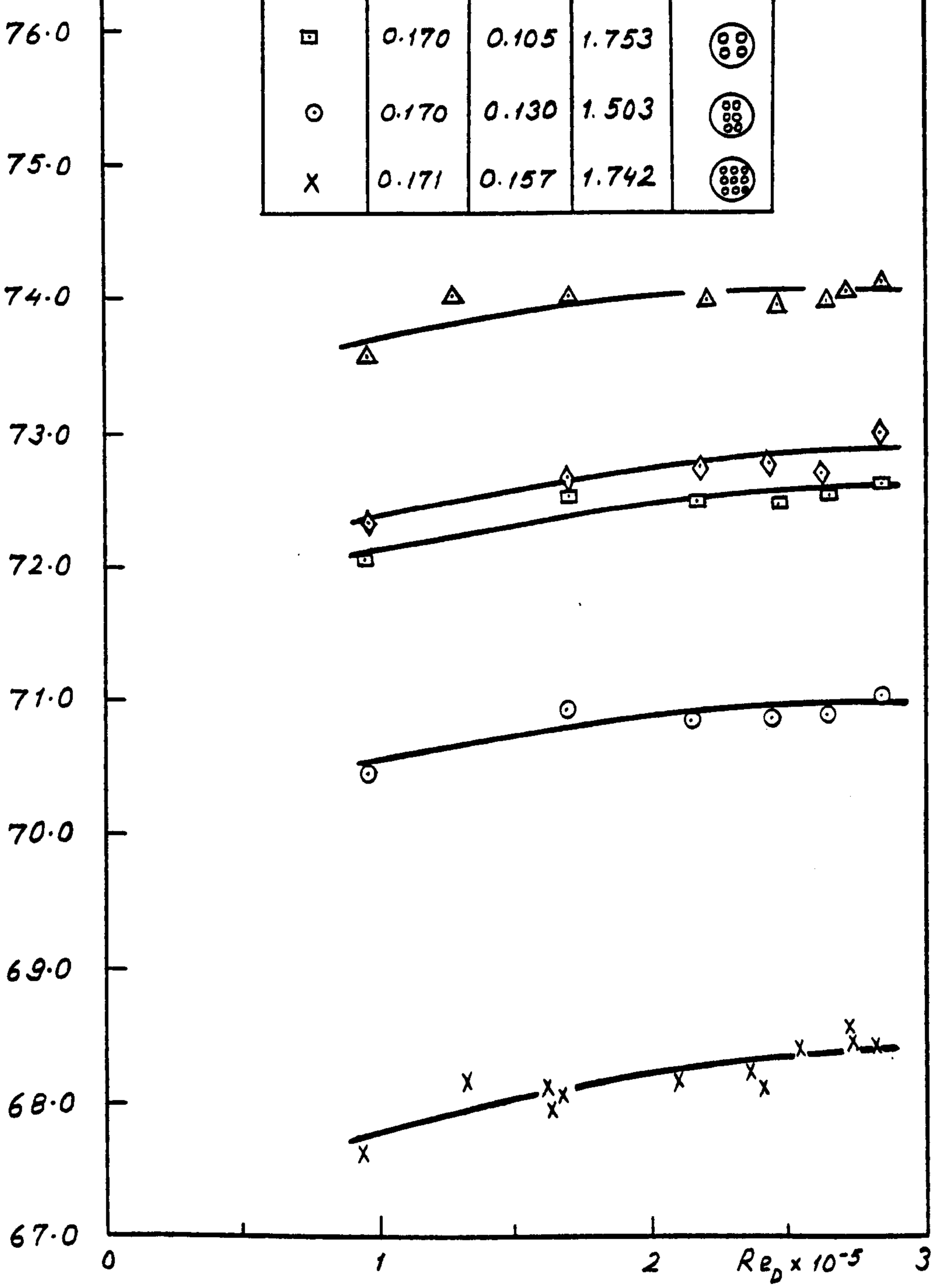

Fig. 364. Head loss coefficients for the multi-hole orifice plates of the same area ratio

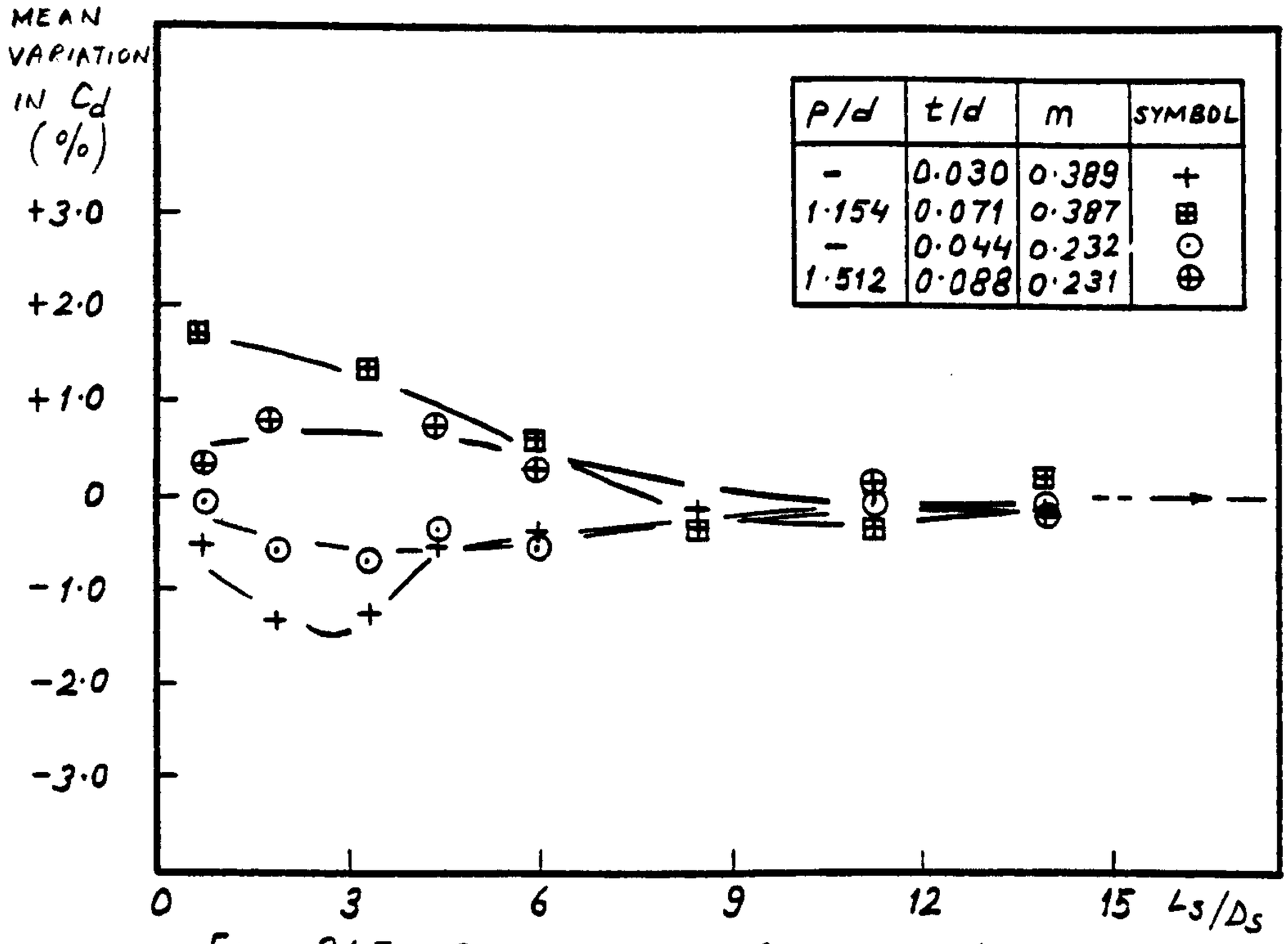

Fig. 365. Comparison of percentage variation in discharge coefficients for single- and multi-hole orifice plates of the same area ratios (PVC bend of R/D=4.18 upstream of orifice plates)

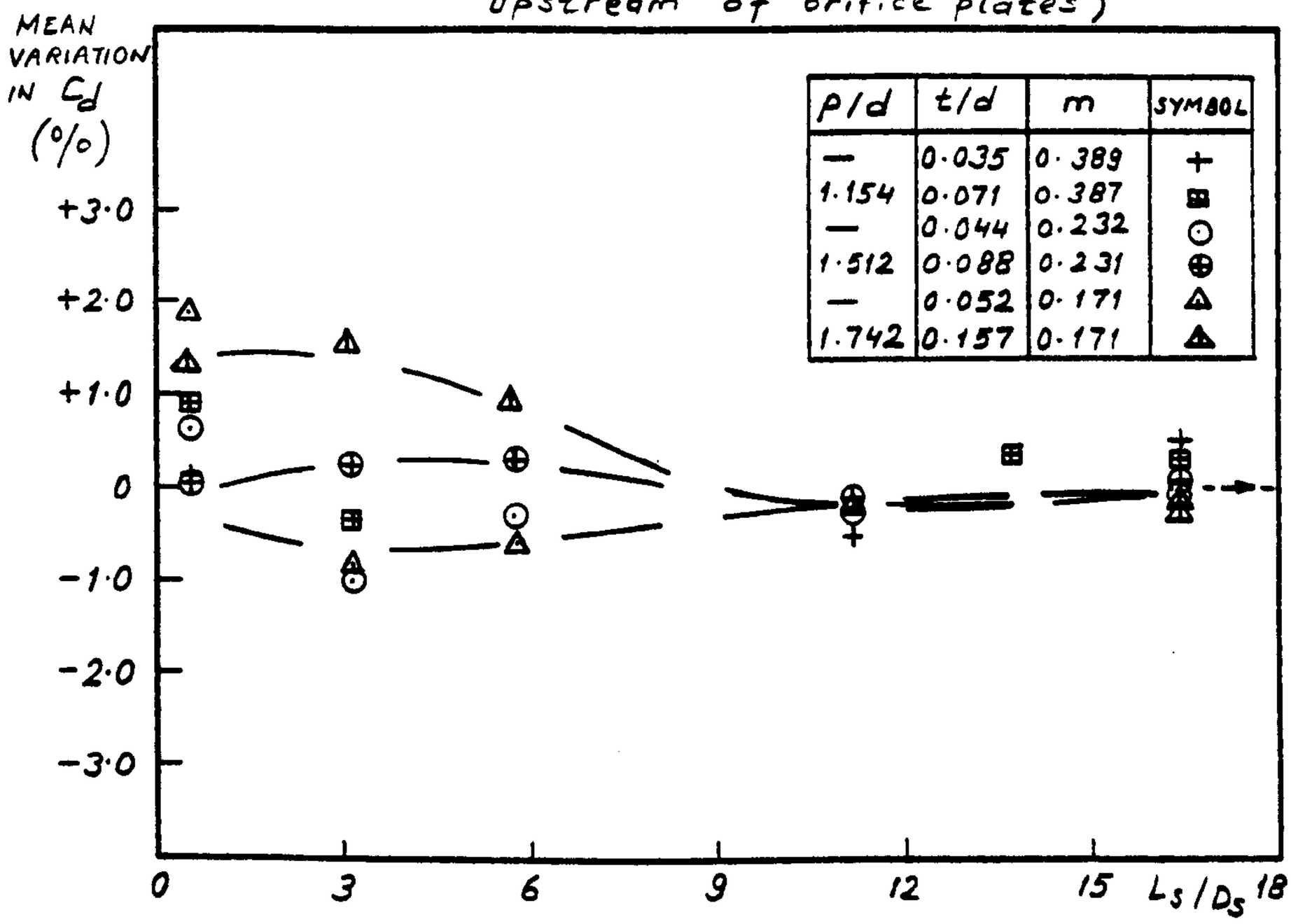

Fig. 366. Comparison of percentage variation in discharge coefficients for single- and multi-hole orifice plates of the same area ratios (glassfibre bend of R/D = 1.49 upstream of orifice plates)

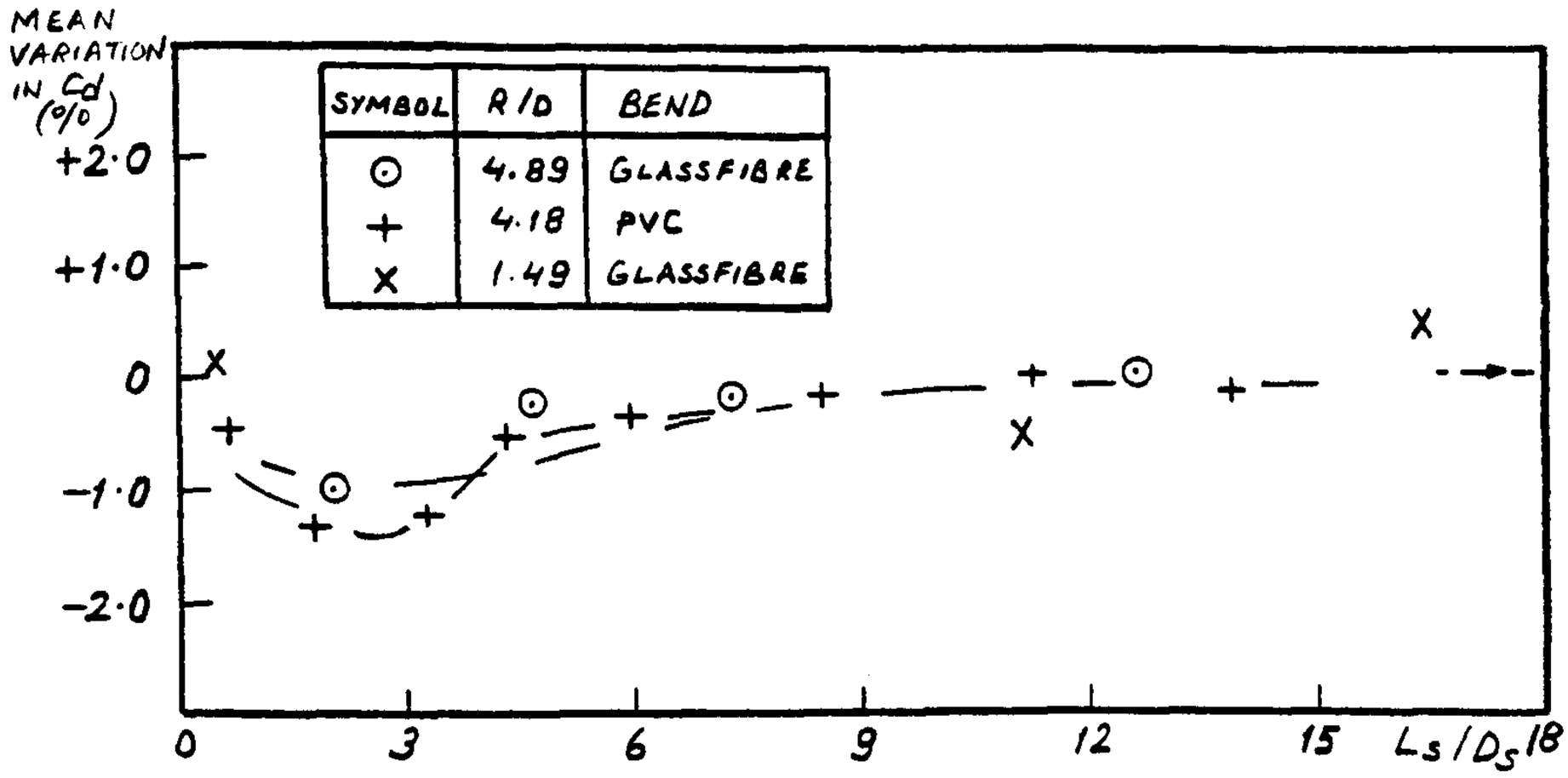

Fig. 367. Percentage variation in discharge coefficients (single-hole orifice plate of m = 0.389 downstream of various bends)

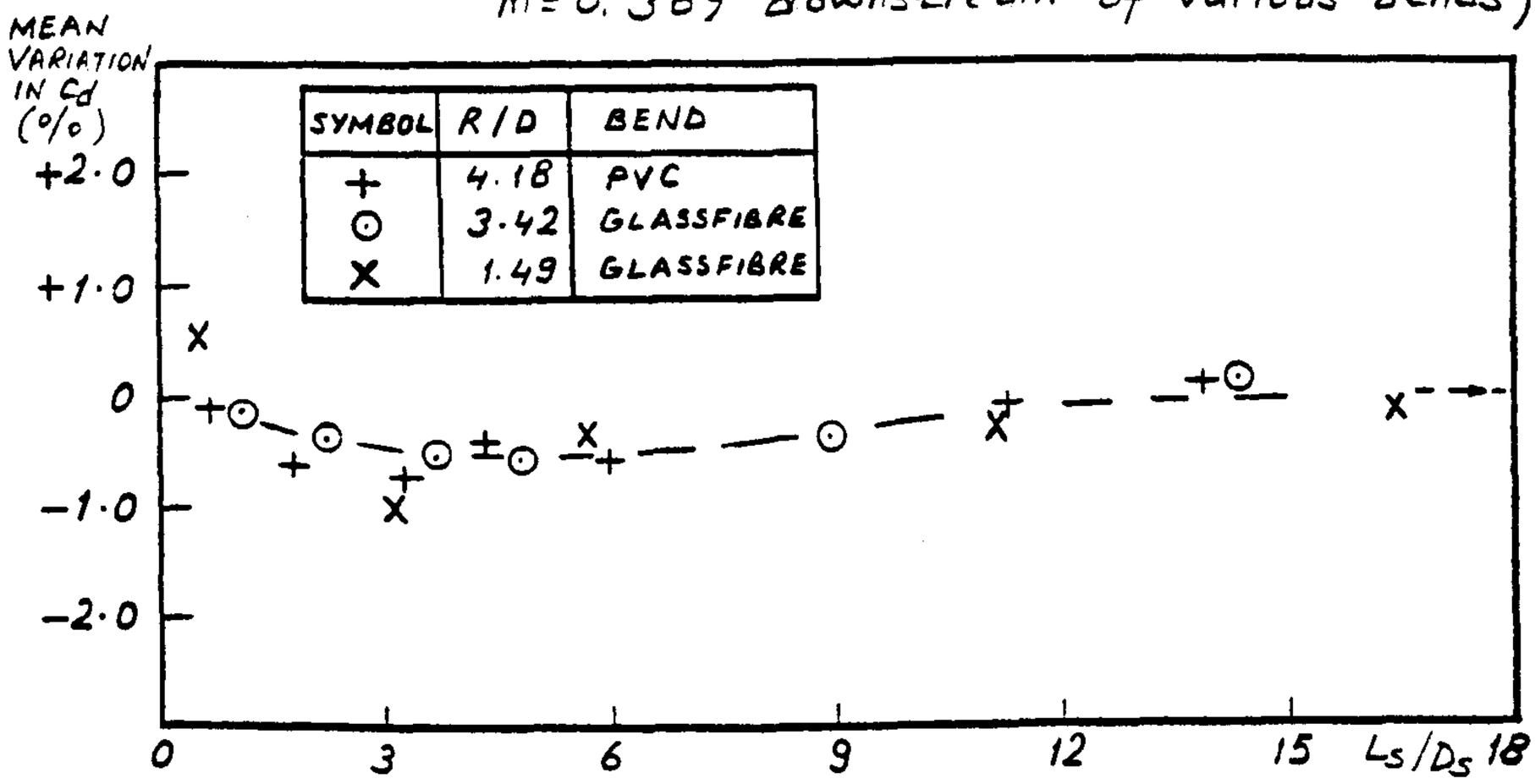

Fig. 368. Percentage variation in discharge coefficients (single-hole orifice plate of m = 0.232 downstream of various bends)

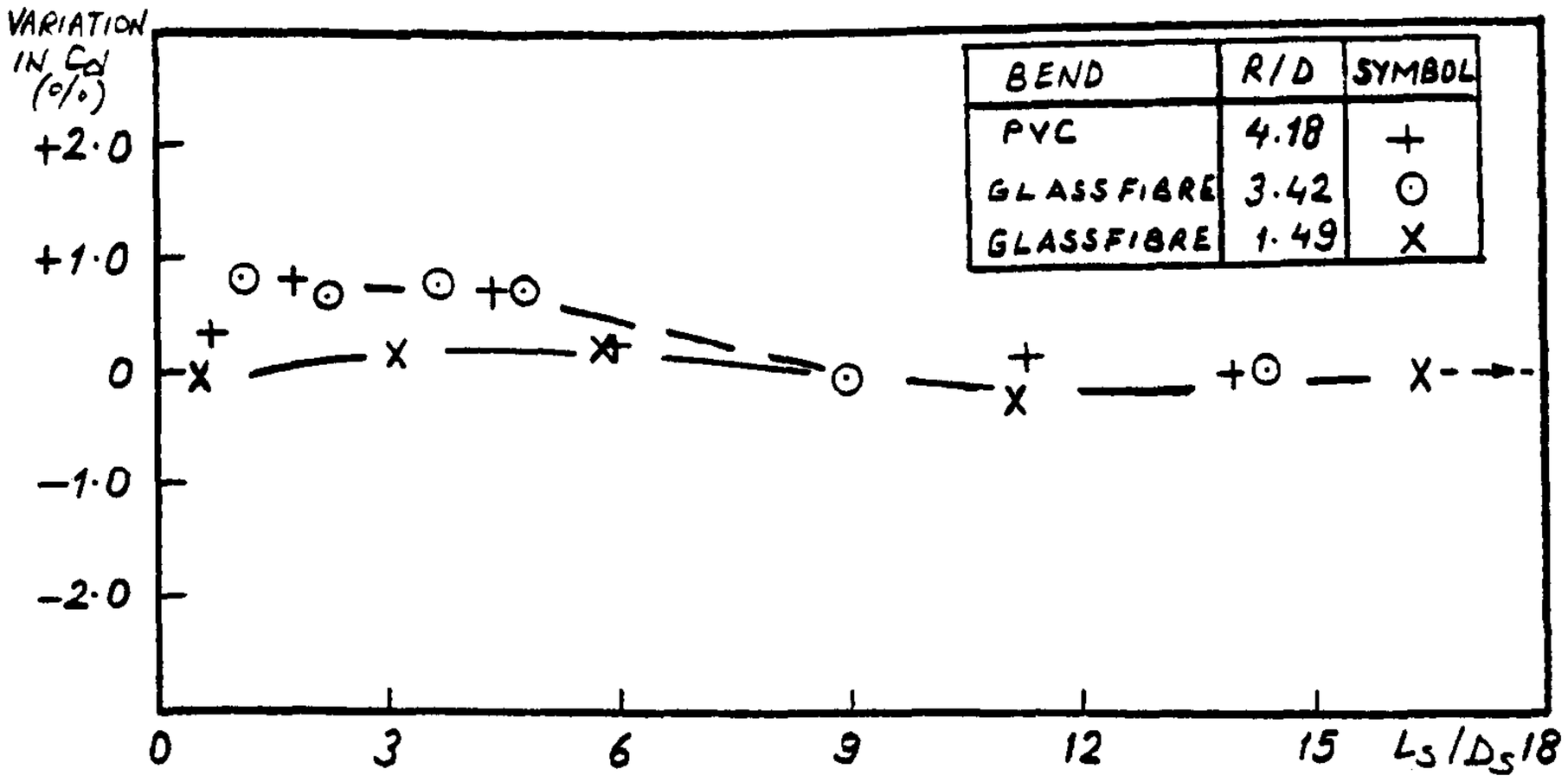

Fig. 369. Percentage variation in discharge coefficients (4-hole orifice plate of m = 0.231 downstream of various bends)

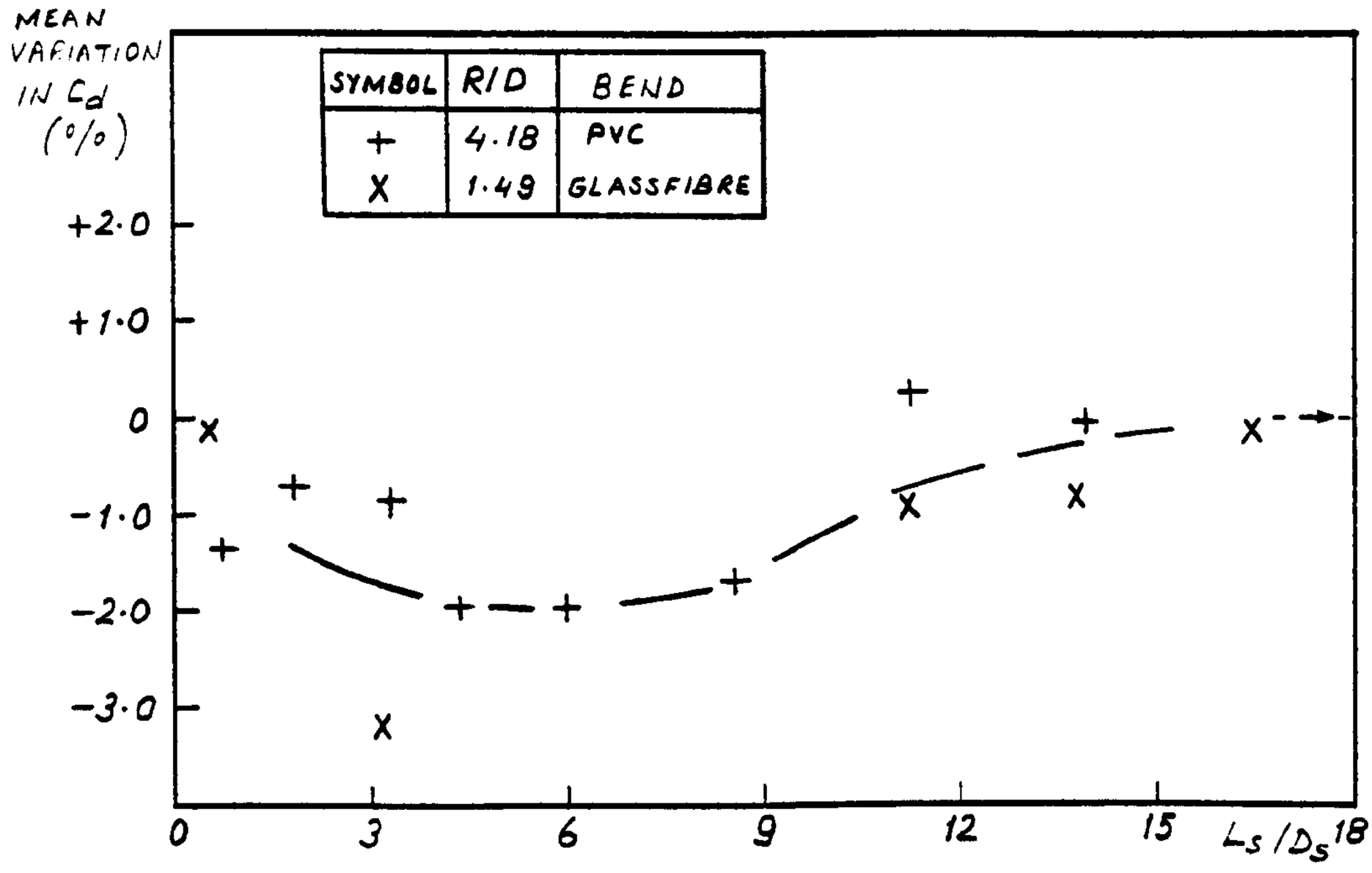

Fig. 370. Percentage variation in discharge coefficients (single-hole orifice plate of $m = 0.508$ downstream of various bends)

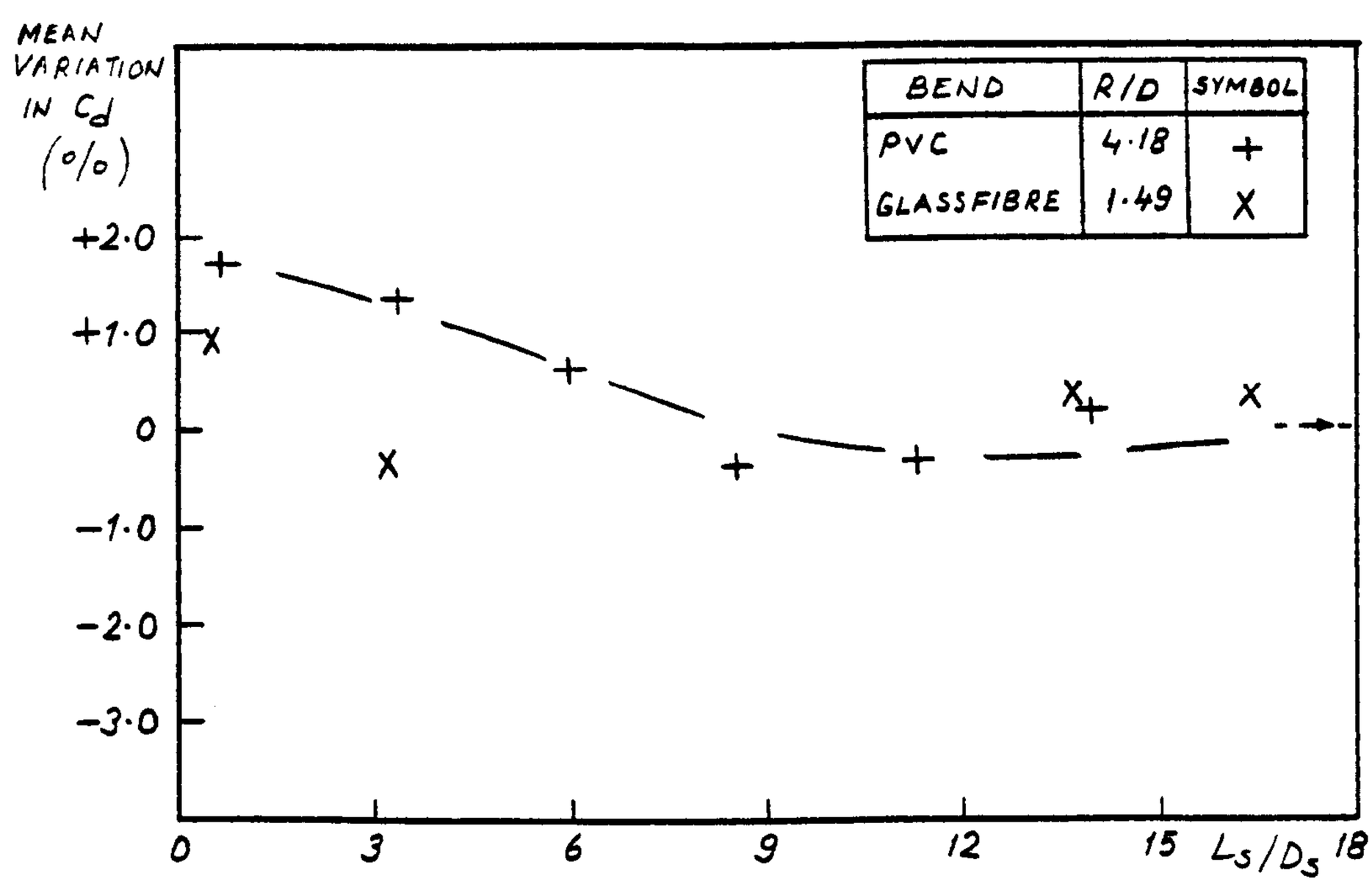

Fig. 371. Percentage variation in discharge coefficients (4-hole orifice plate of $m = 0.387$ downstream of various bends)

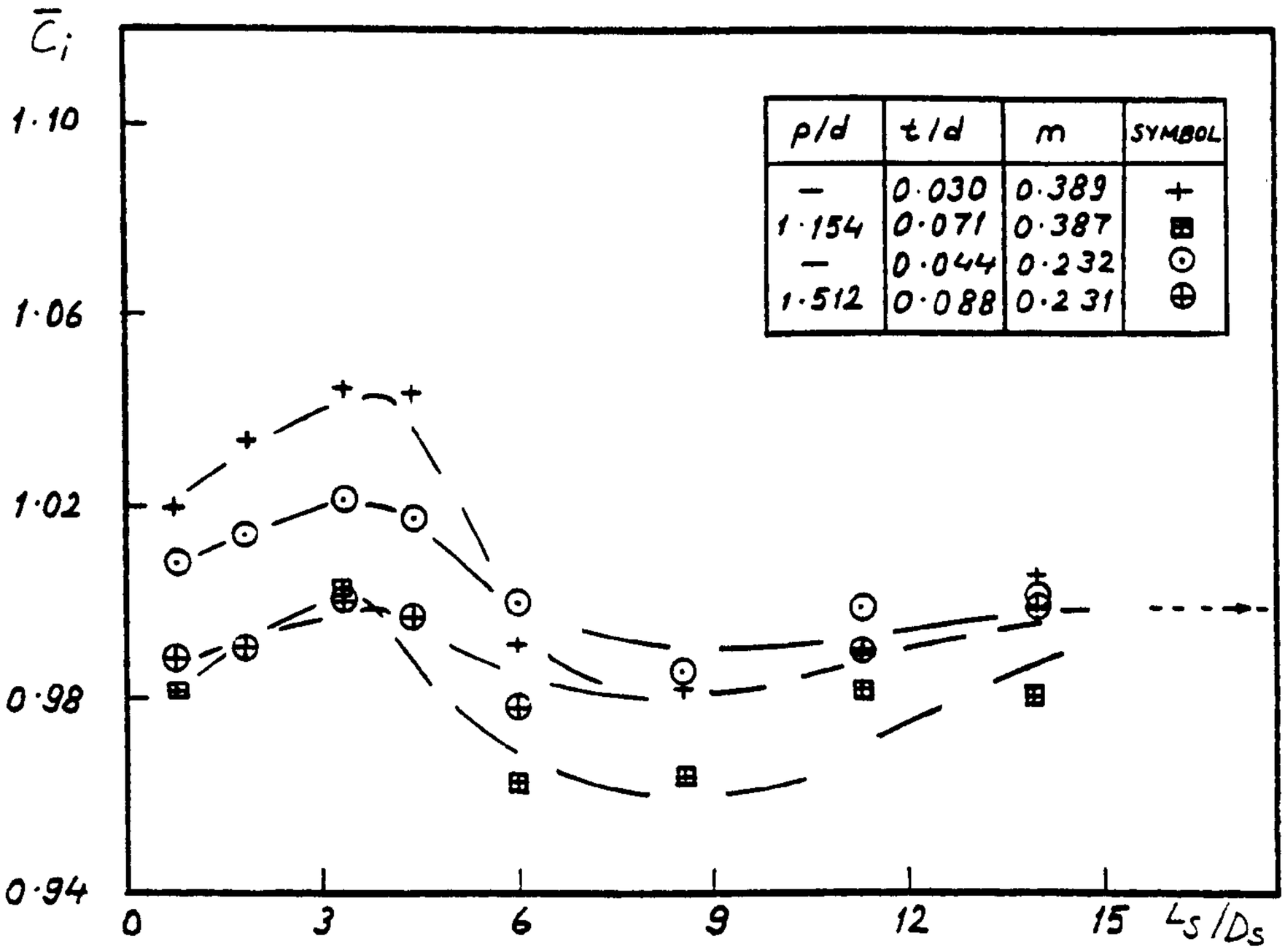

Fig. 372. Comparison of interaction coefficients for single- and multi-hole orifice plates of the same area ratios (PVC bend of R/D = 4.18 upstream of orifice plates)

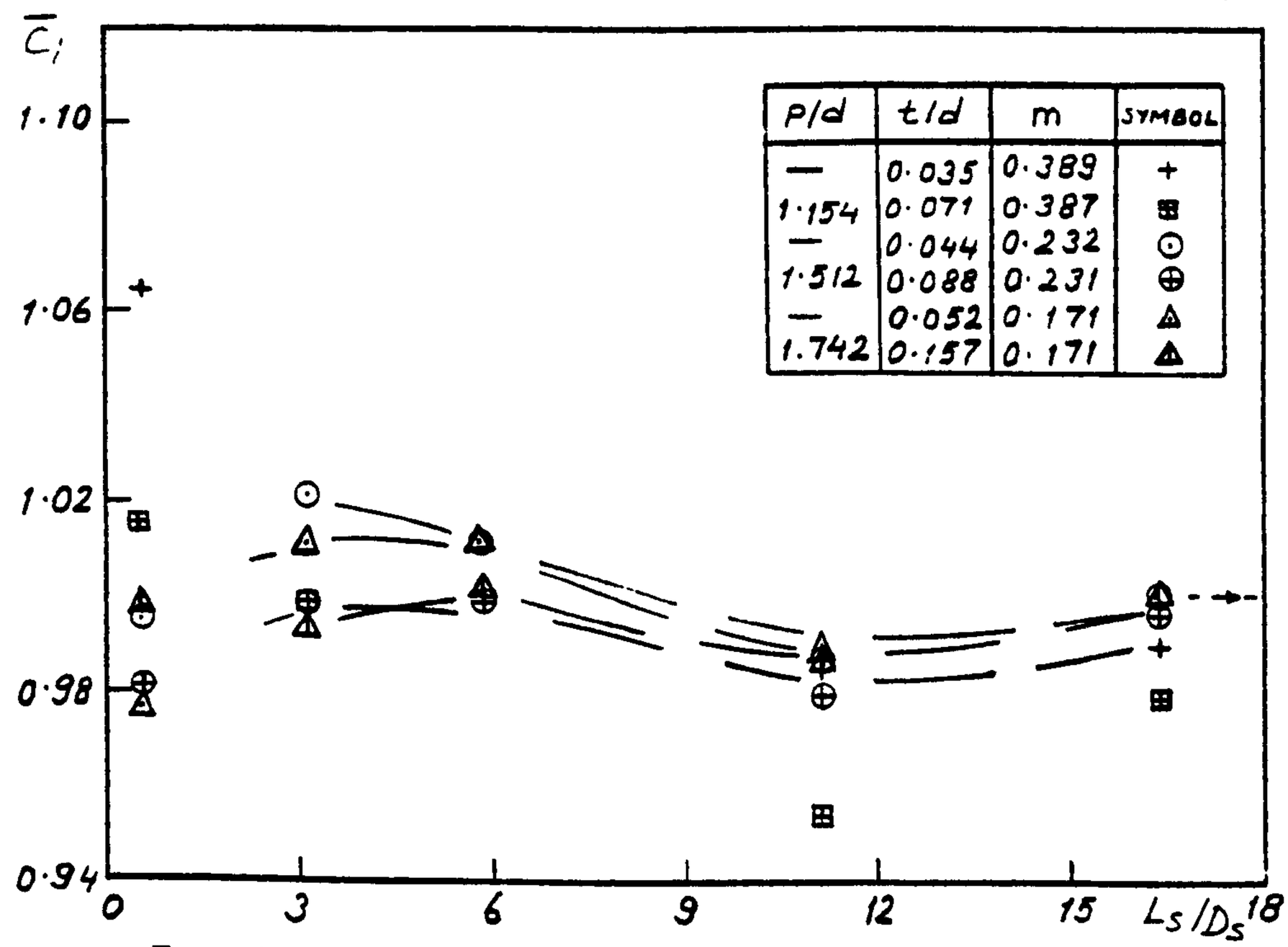

Fig. 373. Comparison of interaction coefficients for single- and multi-hole orifice plates of the same area ratios (glassfibre bend of R/D = 1.49 upstream of orifice plates)

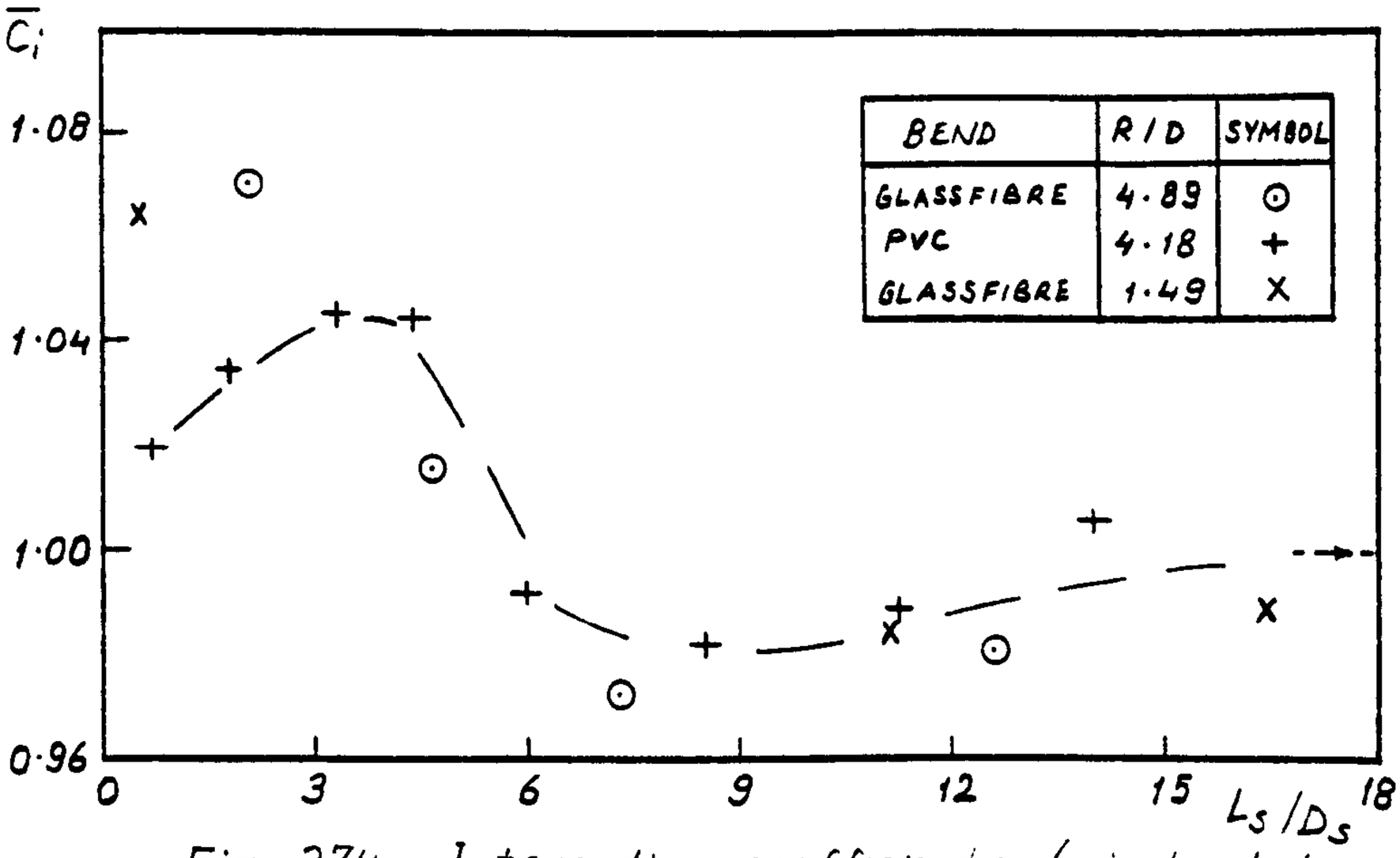

Fig. 374. Interaction coefficients (single-hole orifice plate of m=0.389 downstream of various bends)

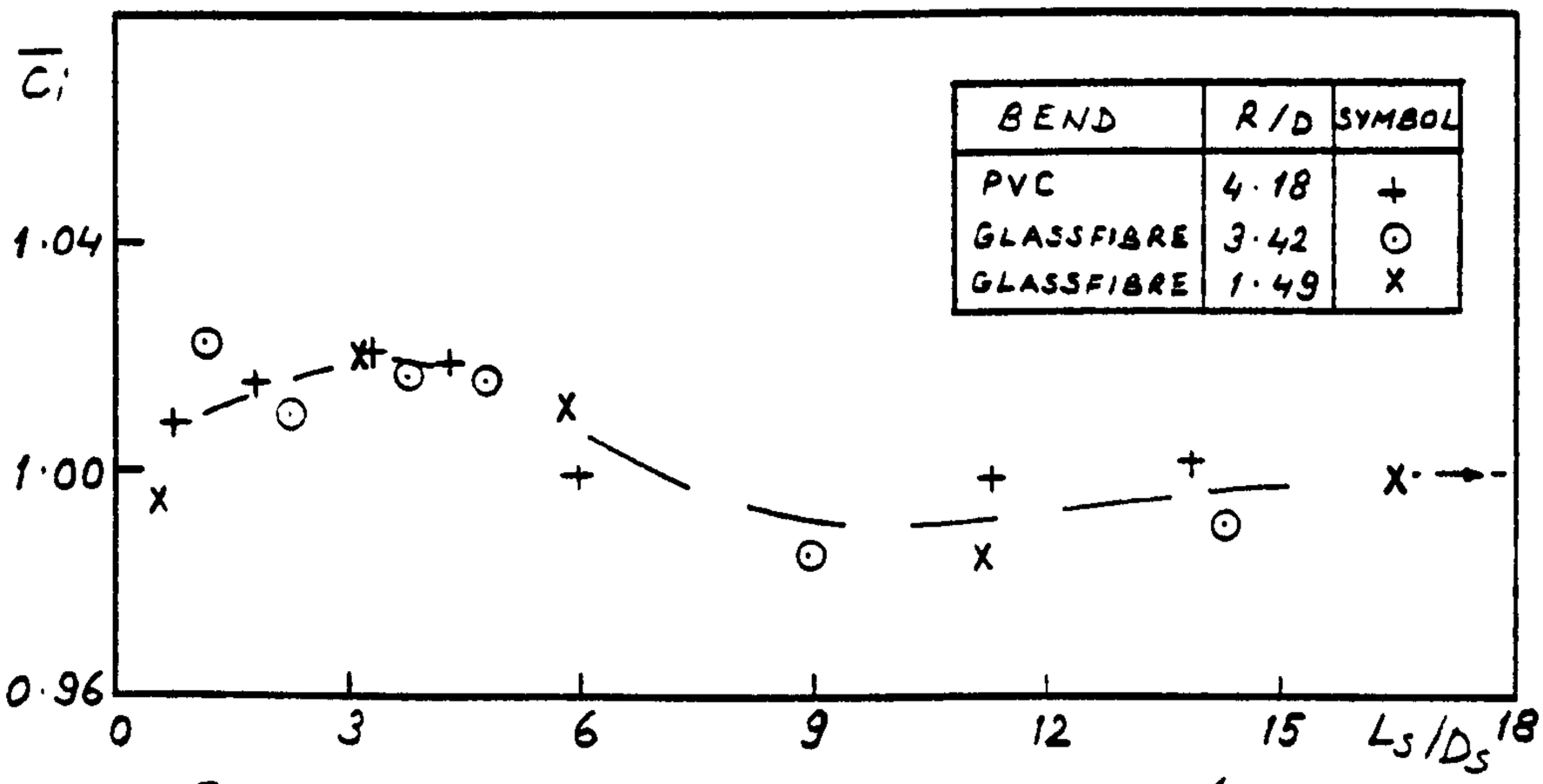

Fig. 375. Interaction coefficients (single-hole orifice plate of m=0.232 downstream of various bends)

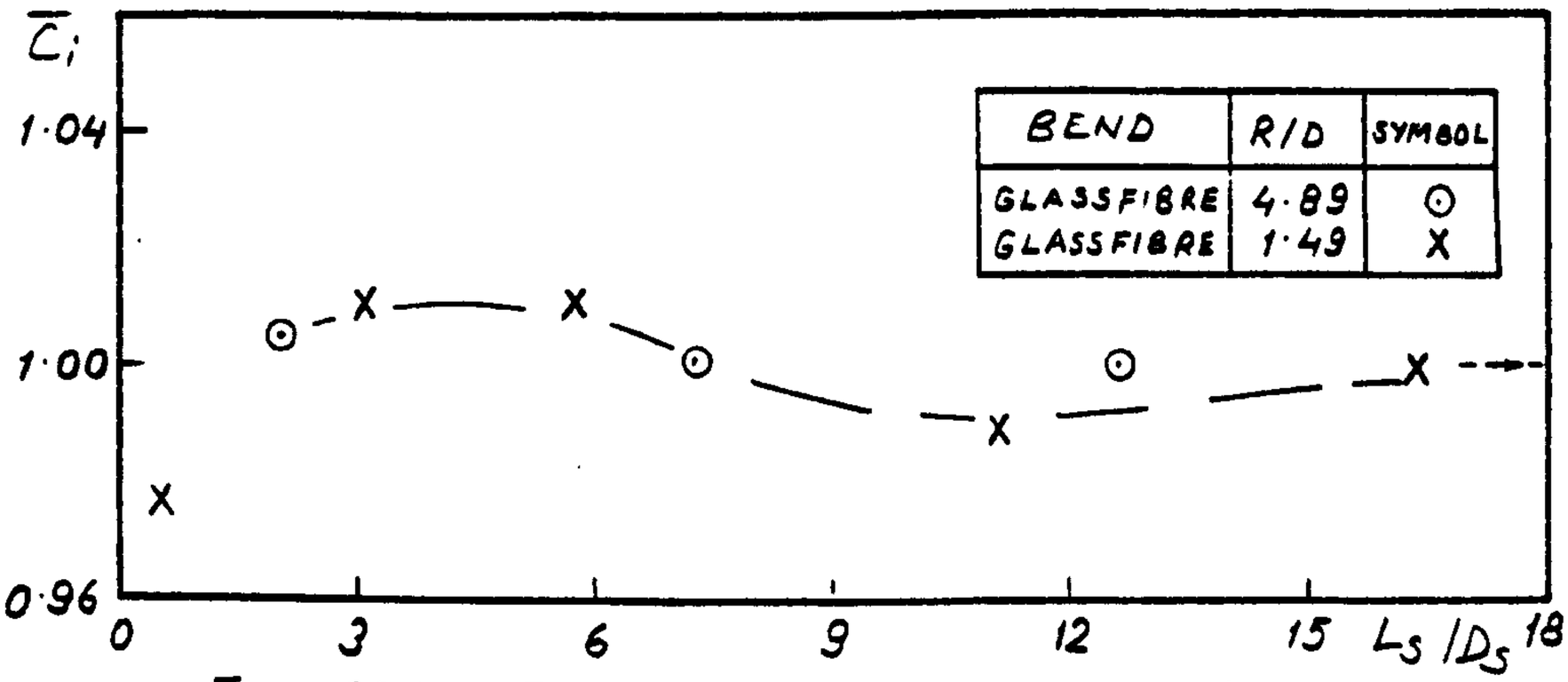

Fig. 376. Interaction coefficients (single-hole orifice plate of m=0.171 downstream of various bends)

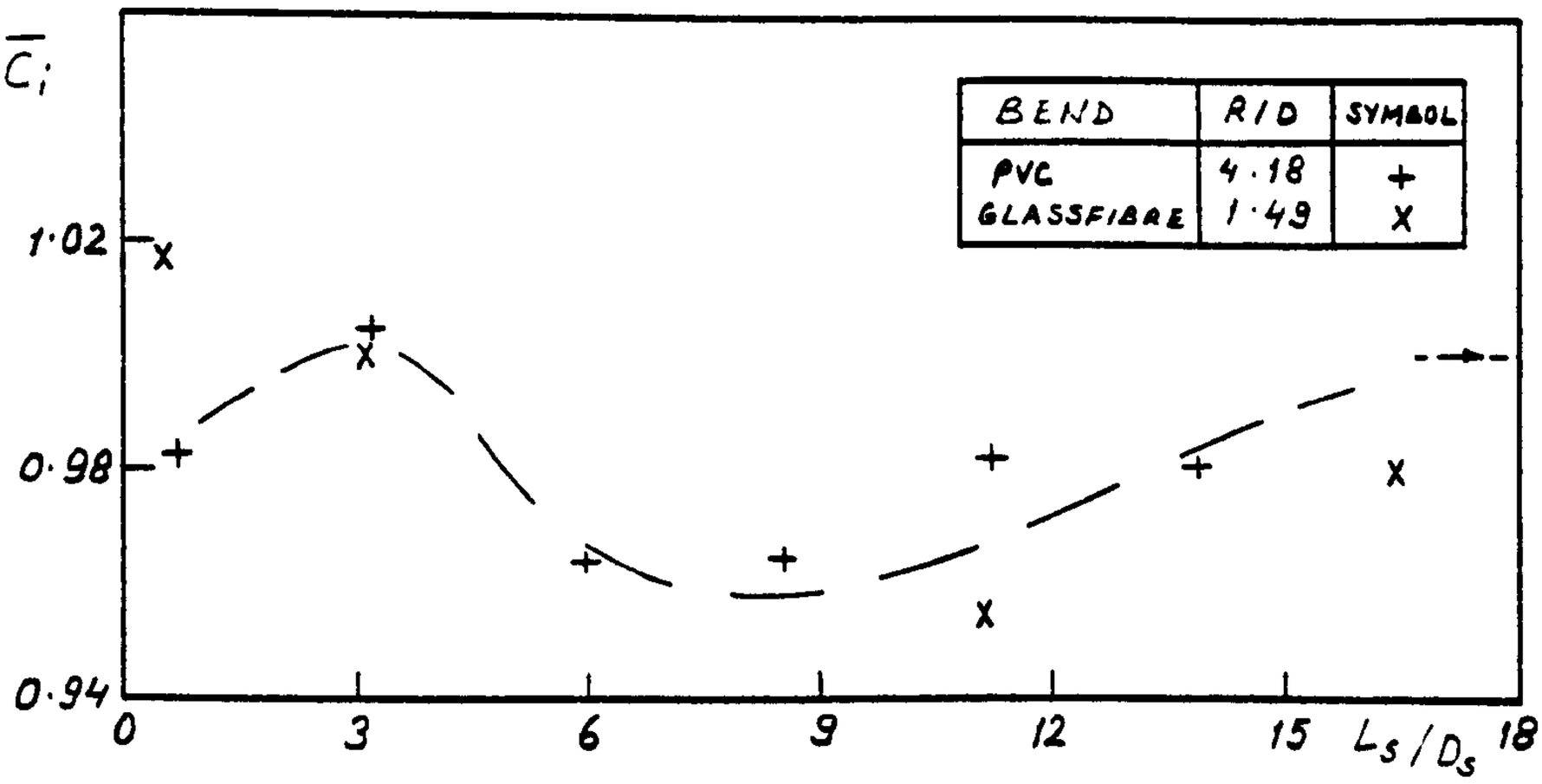

Fig. 377. Interaction coefficients (4-hole orifice plate of m = 0.387 downstream of various bends)

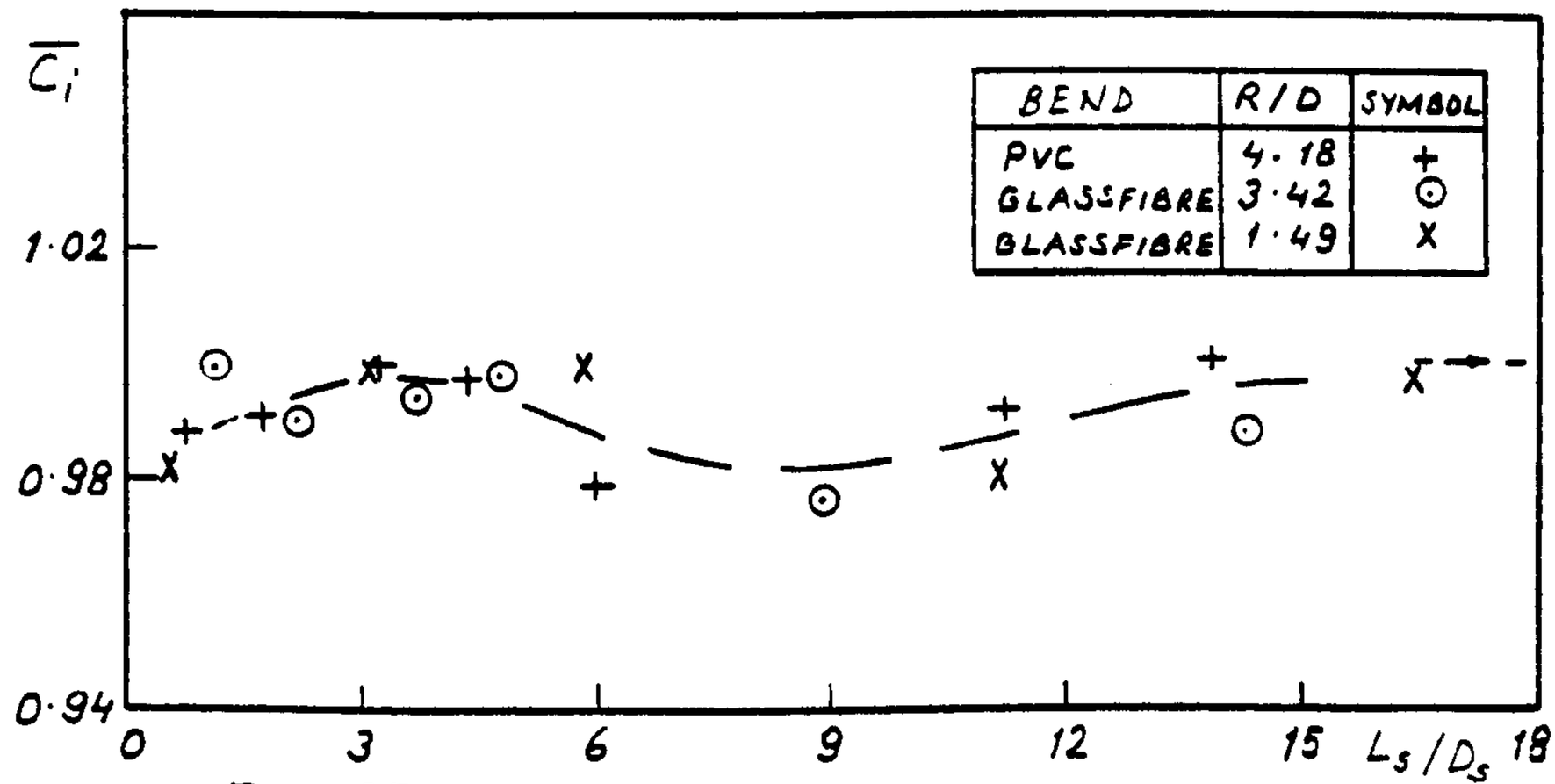

Fig. 378. Interaction coefficients (4-hole orifice plate of m = 0.231 downstream of various bends)

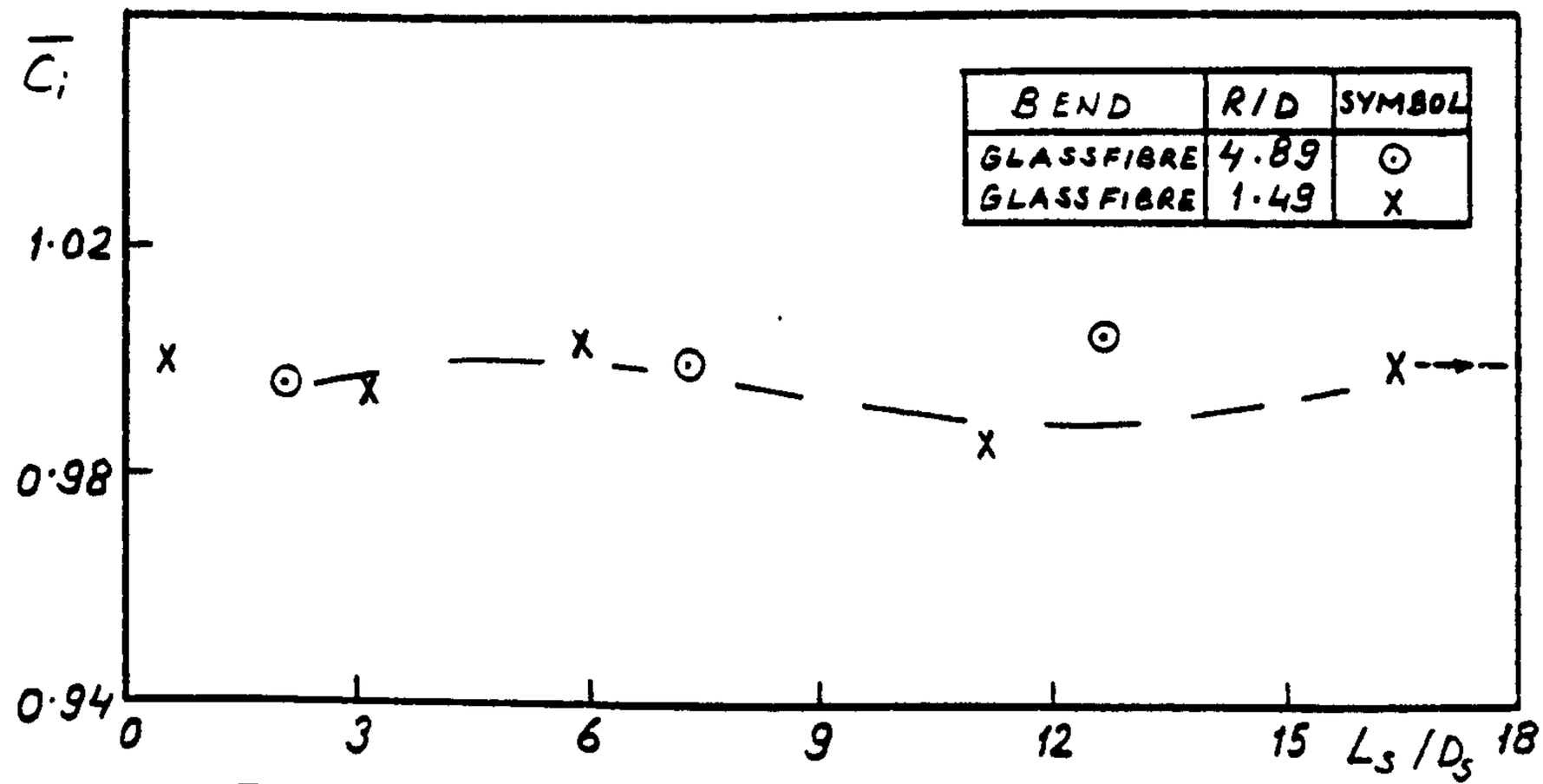

Fig. 379. Interaction coefficients (9-hole orifice plate of m = 0.171 downstream of various bends)

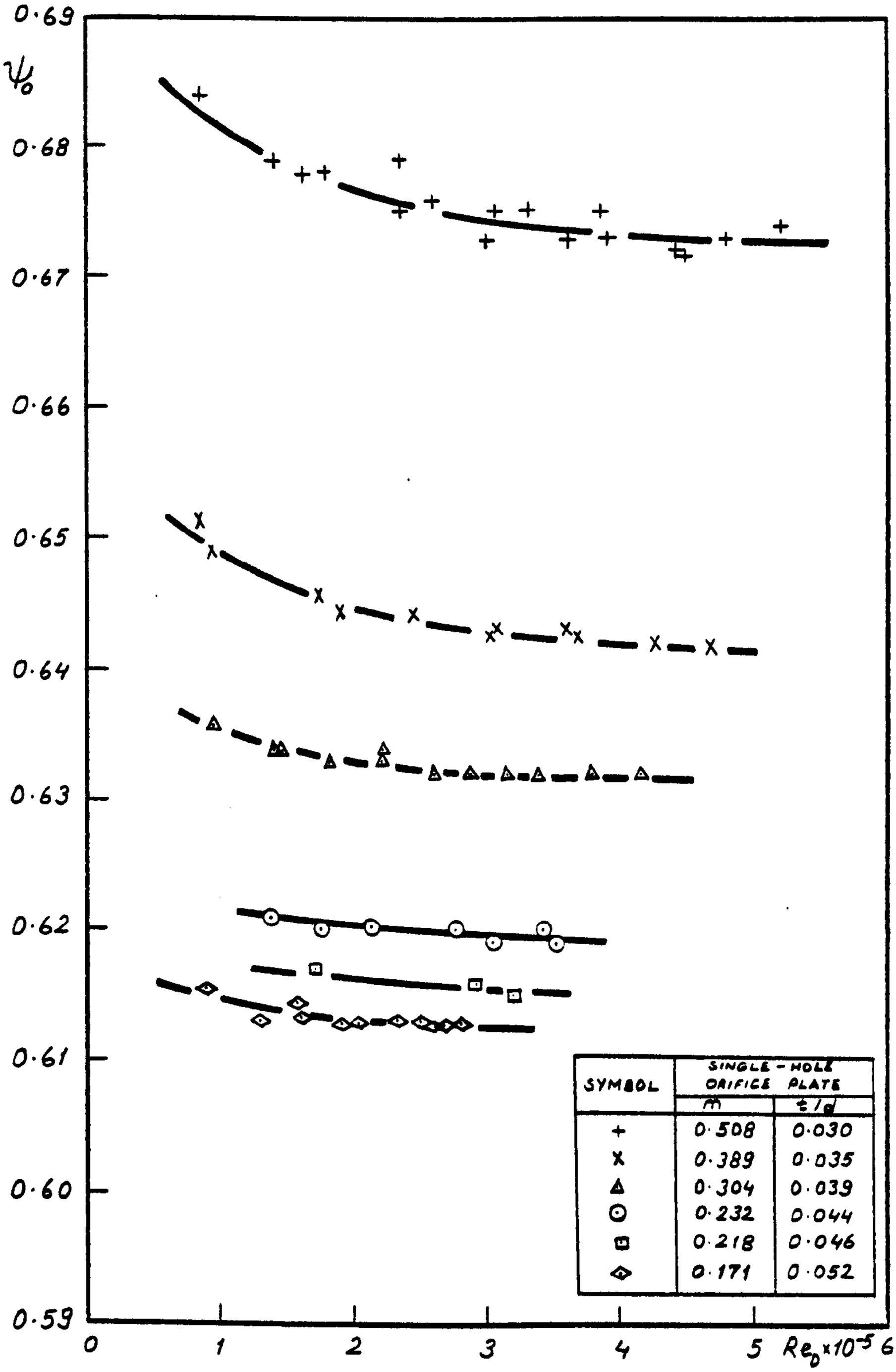

Fig. 380. Variation of pressure drop parameter with Reynolds number for single-hole orifice plates tested

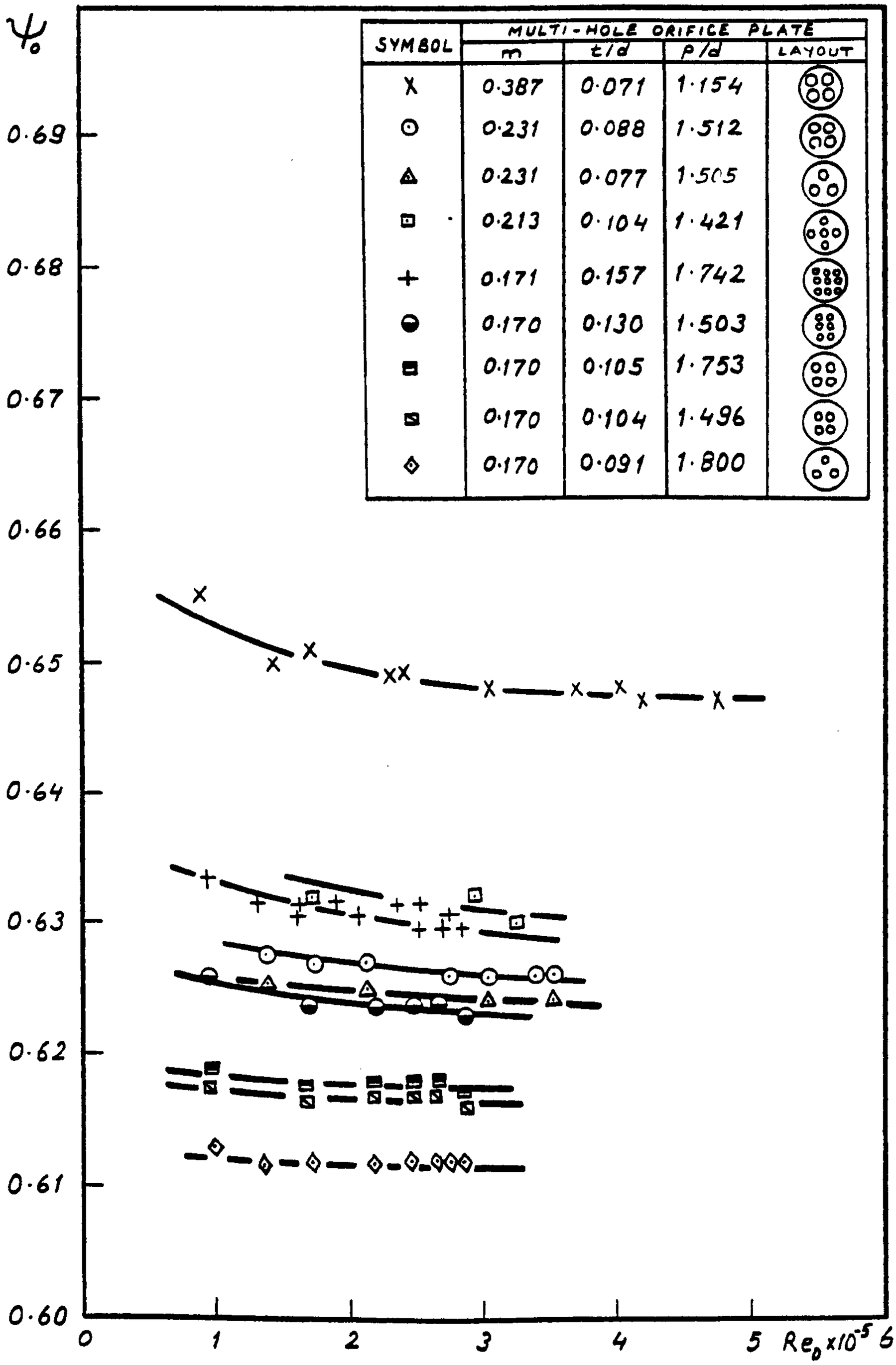

SYMBOL	MULTI-HOLE ORIFICE PLATE			
	m	t/d	p/d	LAYOUT
X	0·387	0·071	1·154	
⊙	0·231	0·088	1·512	
△	0·231	0·077	1·505	
⊡	0·213	0·104	1·421	
+	0·171	0·157	1·742	
◒	0·170	0·130	1·503	
▭	0·170	0·105	1·753	
▨	0·170	0·104	1·496	
◈	0·170	0·091	1·800	

Fig. 381. Variation of pressure drop parameter with Reynolds number for multi-hole orifice plates tested

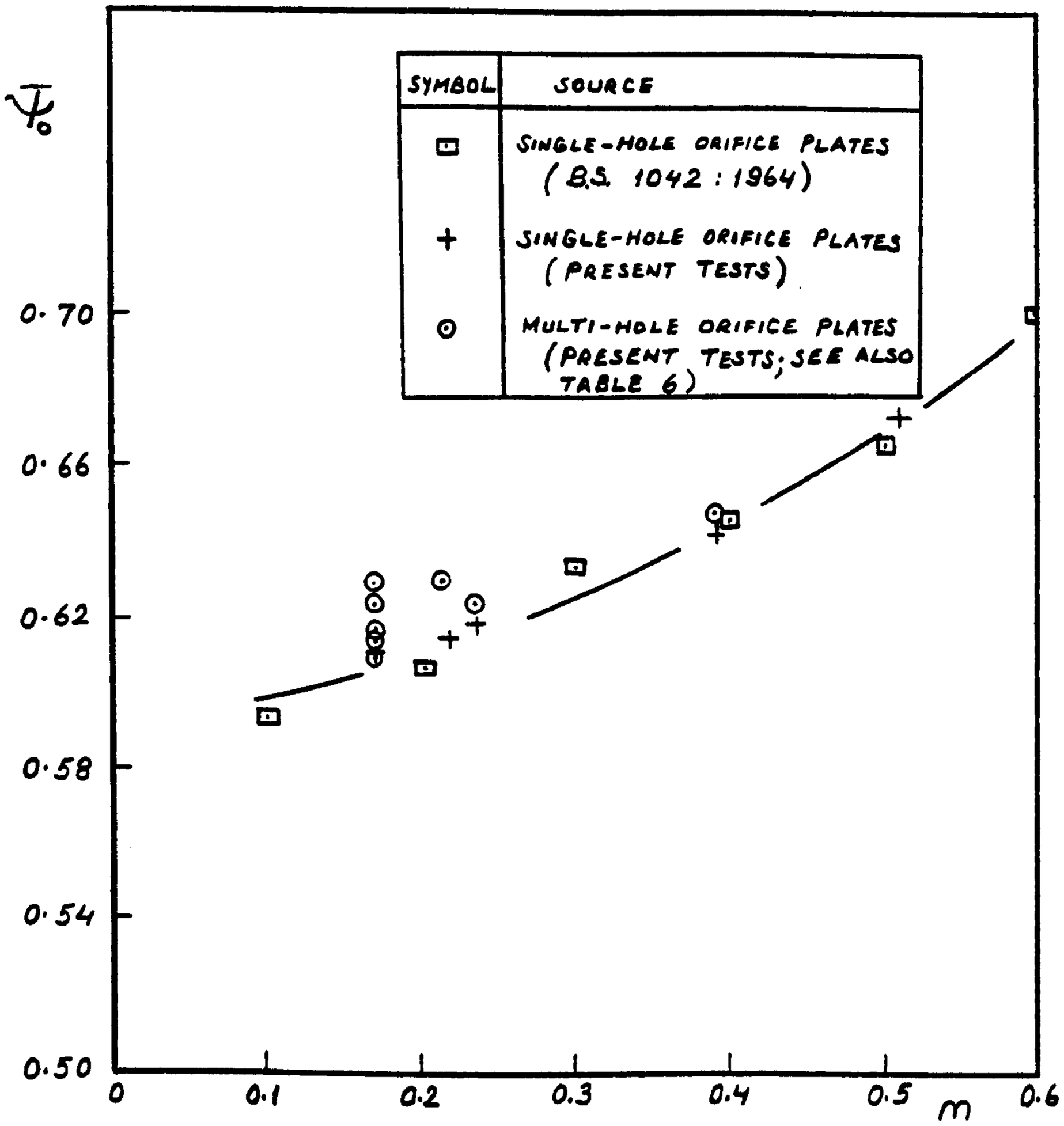

Fig. 382. Comparison of pressure drop parameters for both single- and multi-hole orifice plates

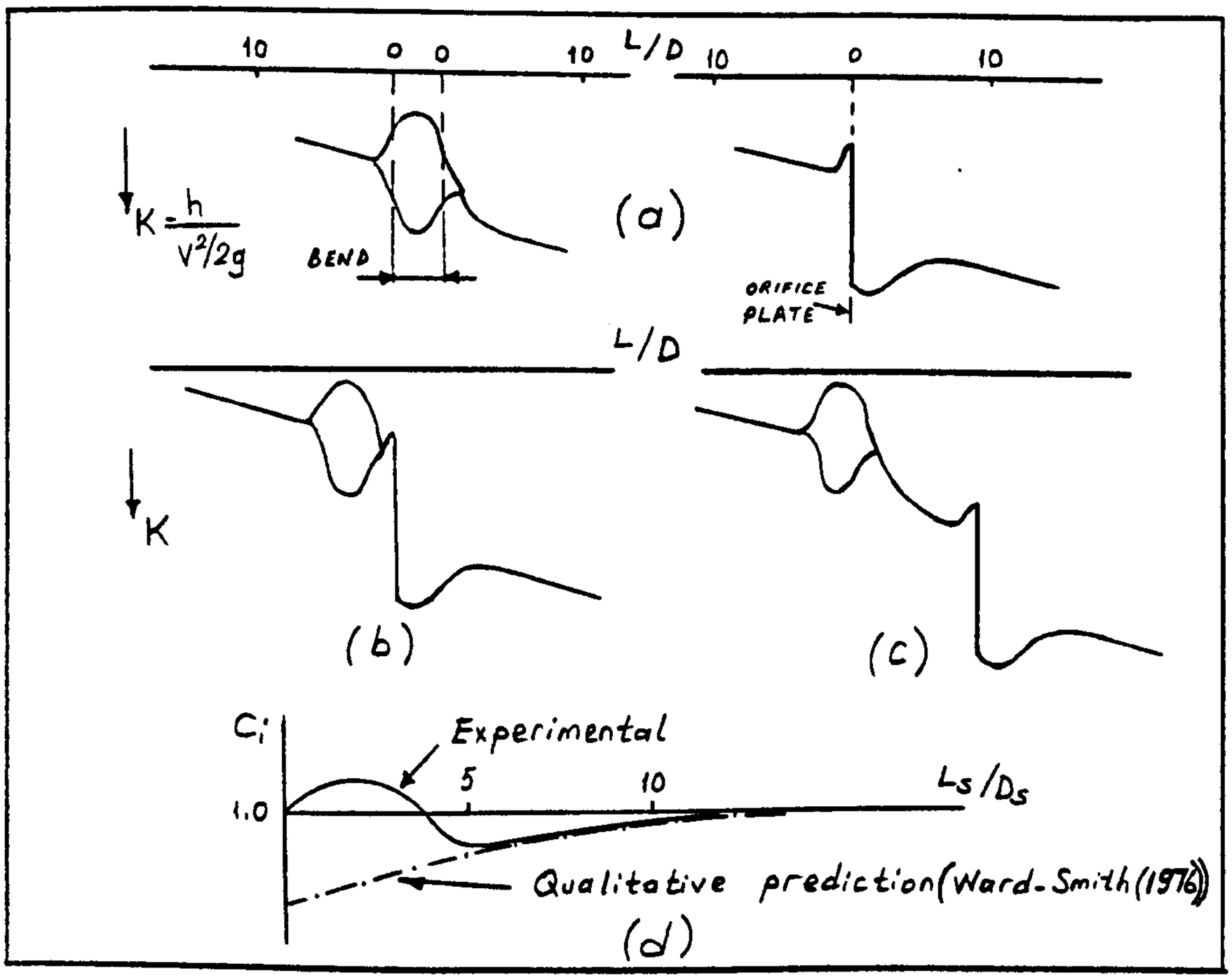

Fig. 383. Schematic representation of effects of spacer length and bend-orifice plate combination on the static pressure distribution

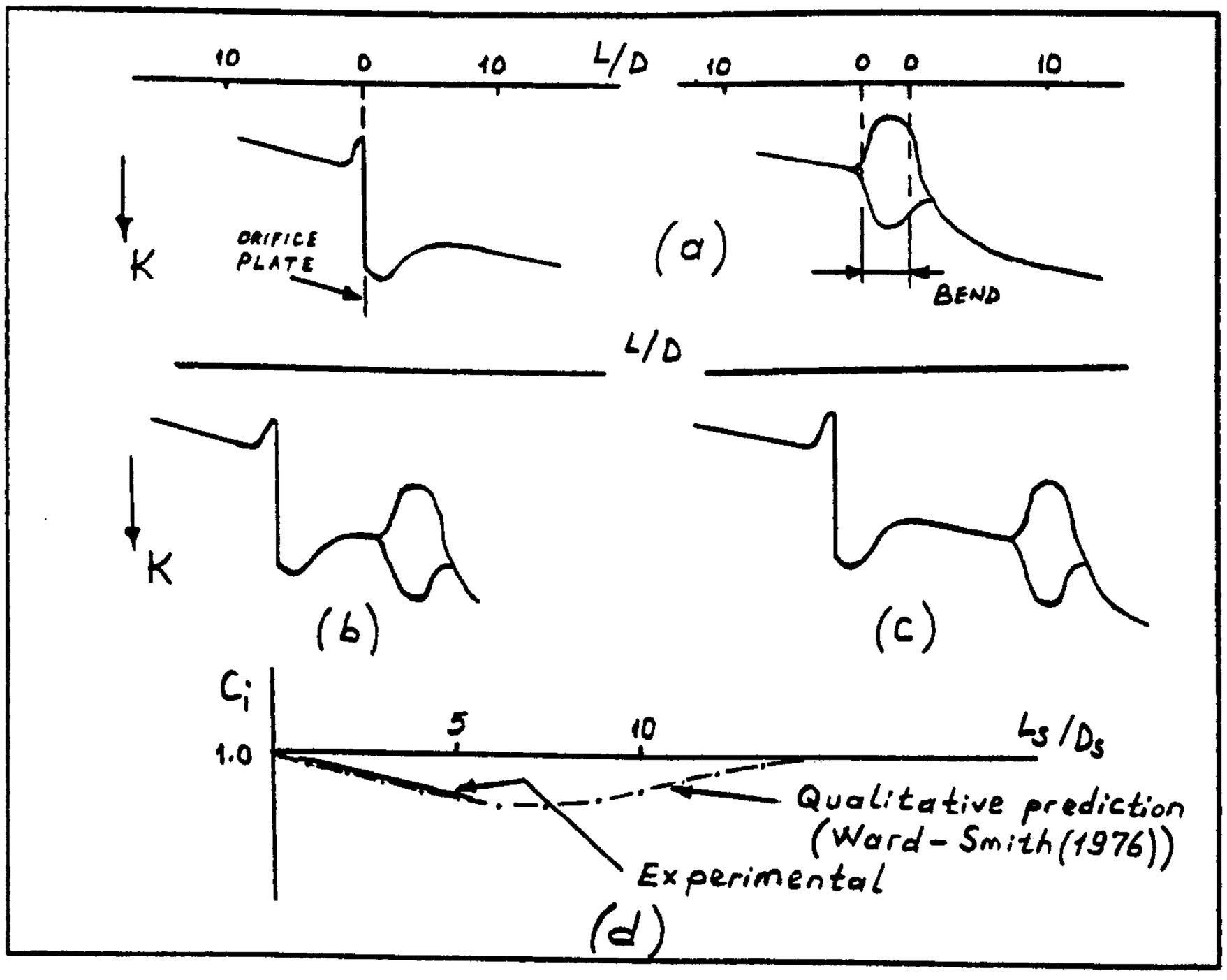

Fig. 384. Schematic representation of effects of spacer Length and orifice plate-bend combination on the static pressure distribution

Fig. 385. Test bends

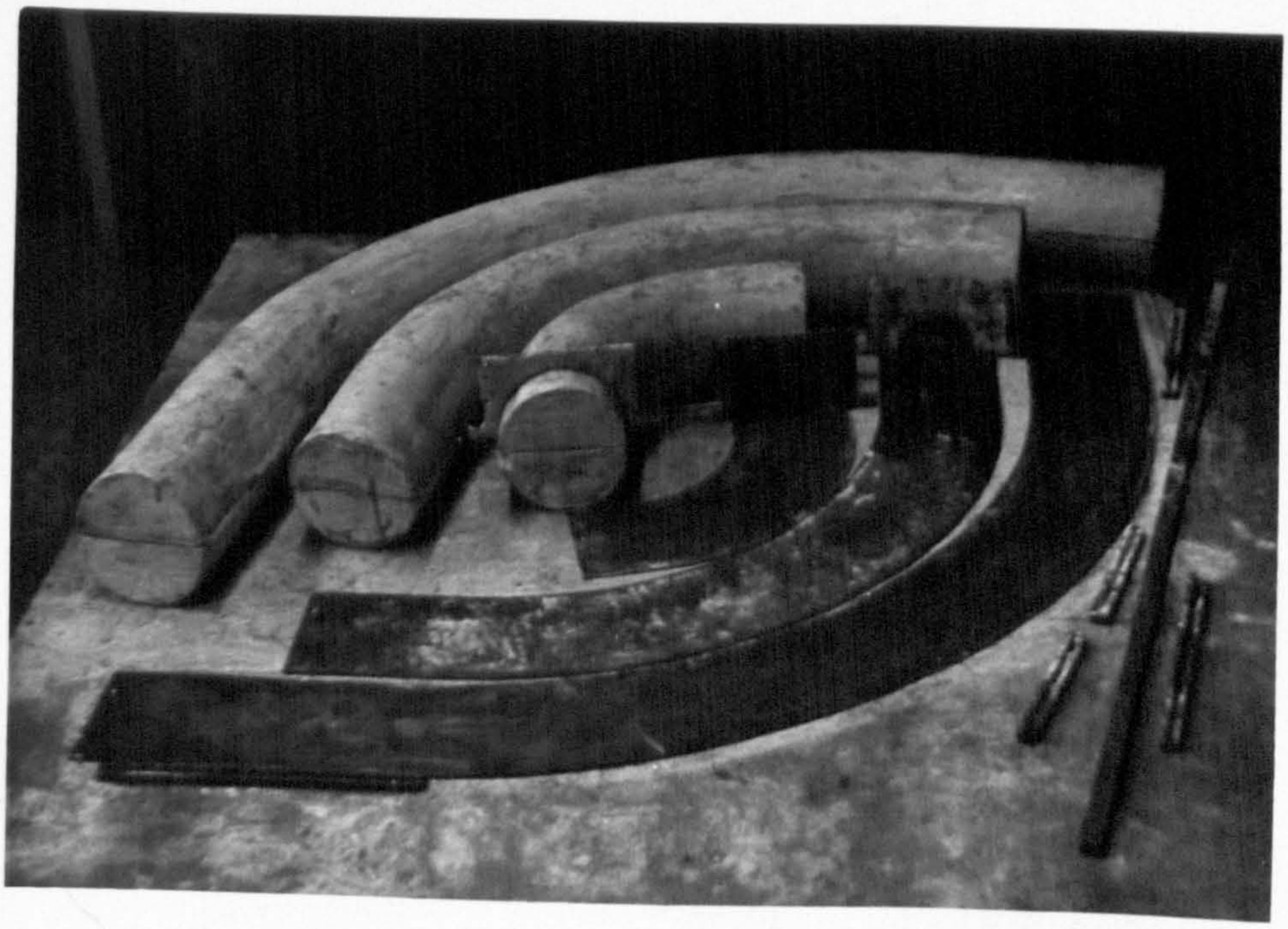

Fig. 386. Materials used for making glassfibre bends

APPENDIX A BENDS

All the bends required for the test work could not be obtained commercially and a number were made in glassfibre. The bends are circular bore, 90 degree, and have short integral tangents. Bends of R/D = 1.49, 3.42, and 4.89 were made in glassfibre, and one PVC bend of R/D = 4.18 was purchased. All bends tested are shown in Fig. 385.

The glassfibre bends were made up from two halves which were butted together and joined by wrapping with glassfibre tape and resin. The halves were made on plaster of Paris moulds which themselves were made on the base plate shown in Fig. 386. The base plate is arranged both with a pivot, and with slot plates for striking out the integral tangents. Technical details of the processes are recorded in Appendix B. Satisfactory bends were produced but difficulties were encountered in maintaining a circular bore, and smooth surfaces by way of the joints.

APPENDIX B PROCESSES FOR MAKING GLASSFIBRE BENDS

1. Making Moulds

Master moulds were made from the plaster of Paris. The instruction for the preparation of plaster is given as follows:

(i) Warm water and a thinner mix of plaster was used;

(ii) Solution of "Glue Size" was added to water before mix (Glue Size" is a retarding agent);

(iii) Plaster was added to water until powder remained all over the surface, was left to stand without mixing for approximately 10 minutes, was used portions with a platter knife without disturbing bulk - lasts approximately 30 minutes.

When the plaster was prepared some appropriate amount of plaster was put on to the template track and was swept by the smallest striker plate with radius of r = 50.8mm. Then, the half of the mould was completed by the striker plate with radius of r = 76.2mm. To make the integral tangents of the moulds at both ends the striker plate was moved in the appropriate slot plates. All the materials used are shown in Fig. 386 .

After the two halves of the moulds were set they were polished for a smooth surface by using a glass paper. Then the halves were ready to produce a bend.

2. Making Complete Glassfibre Bends

To have made the glassfibre bends the instructions were followed as advised by the manufacturer [see, for more information Strand Glassfibre Brochure (1976)]:

(i) The surface of the plaster mould was fully sealed by "Release Agent No. 1". Before applying "Release Agent No. 2", three to four coats of "Release Agent No. 3" were applied by a soft cloth, then one coat of "Release Agent No. 2" was sponged on and allowed to dry.

(ii) Gel Coat (Resin B) and hardener were brushed on to the dry release agent;

(iii) When the Gel Coat was set "Resin A" (the hardener was added into the resin in the proportion supplied by approximately 1 part to 150) was brushed thickly over the surface, and "Mat" was placed on top and pushed into the resin with a stippling action. More resin was put on top until the Mat was thoroughly wetted out and all air bubbles removed by a roller. The next layer was put straight on top, and the resin was again added, and then the same procedure was followed for the next 2 or 3 layers;

(iv) The first half of the bend was released from the mould when it was fully hardened and release agent was washed off with warm water;

(v) It was then polished by rubbing down with a 600 grade wet and dry paper used wet, and followed by polishing compound;

(vi) For a better inside surface, 1 to 2 layers of surfacing tissue were applied;

(vii) The laminate was cut with a jigsaw (or hacksaw).

(viii) When the two halves were ready they were jointed in the form of bend by using a glassfibre tape, and then applied to more 3 layers on.

Finally, each PVC flange was jointed on to both ends of each glassfibre bend by using "Microseal T17".